



HAL
open science

Quantitative imaging methods to investigate photosynthetic cells

Clarisse Uwizeye

► **To cite this version:**

Clarisse Uwizeye. Quantitative imaging methods to investigate photosynthetic cells. *Vegetal Biology*. Université Grenoble Alpes [2020-..], 2020. English. NNT : 2020GRALV043 . tel-03199259

HAL Id: tel-03199259

<https://theses.hal.science/tel-03199259>

Submitted on 15 Apr 2021

HAL is a multi-disciplinary open access archive for the deposit and dissemination of scientific research documents, whether they are published or not. The documents may come from teaching and research institutions in France or abroad, or from public or private research centers.

L'archive ouverte pluridisciplinaire **HAL**, est destinée au dépôt et à la diffusion de documents scientifiques de niveau recherche, publiés ou non, émanant des établissements d'enseignement et de recherche français ou étrangers, des laboratoires publics ou privés.

THÈSE

Pour obtenir le grade de

DOCTEUR DE L'UNIVERSITE GRENOBLE ALPES

Spécialité: Biologie Végétale

Arrêté ministériel: 25 mai 2016

Présentée par

CLARISSE UWIZEYE

Thèse dirigée par **Denis FALCONET**, CNRS
codirigée par **Giovanni FINAZZI**, CNRS
encadrée par **Pierre-Henri JOUNEAU**, CEA
et **Johan DECELLE**, UGA

préparée au sein du **Laboratoire de Physiologie Cellulaire et Végétale**
dans l'**École Doctorale Chimie et Sciences du Vivant**

Approches quantitatives d'imagerie pour explorer les cellules photosynthétiques

Quantitative imaging methods to investigate photosynthetic cells

Thèse soutenue publiquement le **16 décembre 2020**,
devant le jury composé de:

Monsieur Denis FALCONET
CHARGE DE RECHERCHE, CNRS,
Directeur de thèse

Monsieur Giovanni FINAZZI
DIRECTEUR DE RECHERCHE, CNRS,
Co-directeur de thèse

Madame Christelle BRETON
PROFESSEUR DES UNIVERSITES, UNIVERSITÉ DE GRENOBLE ALPES,
Président

Monsieur Samuel ZEEMAN
PROFESSEUR, UNIVERSITÄTSTRASSE ZURICH,
Examineur

Madame Cécile RAYNAUD
DIRECTEUR DE RECHERCHE, CNRS,
Rapporteuse

Monsieur Benjamin ENGEL
DOCTEUR EN SCIENCES, MAX PLANCK INSTITUTE OF BIOCHEMISTRY,
Rapporteur



UNIVERSITÉ DE GRENOBLE ALPES

EDCSV

École doctorale Chimie Sciences du Vivant

THÈSE

pour obtenir le titre de

docteur en sciences

de l'Université Grenoble Alpes

Spécialité : BIOLOGIE VÉGÉTALE

Présentée et soutenue par

Clarisse UWIZEYE

**Approches quantitatives d'imagerie pour explorer les cellules
photosynthétiques**

Thèse dirigée Denis FALCONET, CNRS

codirigée par Giovanni FINAZZI, CNRS

encadrée par Pierre-Henri JOUNEAU, CEA et Johan DECELLE, UGA

préparée au sein du Laboratoire de Physiologie Cellulaire et Végétale

soutenue le 16 décembre 2020

Composition du Jury :

<i>Président :</i>	Madame Christelle BRETON	- CERMAV, Université Grenoble Alpes
<i>Rapporteurs :</i>	Madame Cécile RAYNAUD	- CNRS
	Monsieur Benjamin ENGEL	- Max Planck Institute of Biochemistry
<i>Examineurs :</i>	Monsieur Samuel ZEEMAN	- Universitätstrasse, Zurich
<i>Directeurs :</i>	Monsieur Denis FALCONET	- CNRS
	Monsieur Giovanni FINAZZI	- CNRS
<i>Invités :</i>	Monsieur Pierre-Henri JOUNEAU	- IRIG, CEA Grenoble
	Monsieur Johan DECELLE	- Université Grenoble Alpes

*This work is dedicated to my father, my mother and my brother,
we have lost. May God, the Highest grant you peace.*

Acknowledgments

First of all, I would like to thank my supervisors, Dr Denis Falconet and Dr Giovanni Finazzi, to help me carry out this thesis in collaboration with their respective teams at the Cell and Plant Physiology Lab. I am also grateful for their scientific qualities, patience and sincerity. I would also like to thank my co-director, Prof. Samuel Zeeman, for the numerous stays at ETH Zurich, his kindness, and all his great enthusiasm concerning my work. I would also like to thank my advisors, Dr Pierre-Henri Jouneau and Dr Johan Decelle, who may have been instrumental in completing this work. I thank Dr Johan Decelle for his availability, his good humour and all the support he gave me during these three long years of the thesis. I sincerely hope that, once he gets his licence to direct research, his work atmosphere could continue to the future generation of PhD students in his team.

I want to express my gratitude to my two thesis reporters, Dr Benjamin Engel and Dr Cécile Raynaud, for taking the time to revise this large document and for their very positive and relevant feedback. I would also like to thank all the other jury members: the president of the jury Prof. Christelle Breton and for accepting to go through this work and give their time despite the complicated situation of the pandemic Covid.

I owe my gratitude to Dr Leandro Estrozi for being part of the follow-up thesis committee and bringing a fresh look at this project during the two years. His criticism has helped me to communicate better the results of this project.

I don't forget all the laboratory staff for guiding me through this work without a problem. First of all, I would like to thank the IT staff, especially Vincent Dolffer, for the quick resolution of all these little everyday computer problems. I would also like to thank all the secretariat staff: Tiffany, Sophie, and Alexandre, to keep our day-to-day life simple.

I also want to thank the people who gravitated around this thesis project: Benoît Gallet, Serena Flori, Jean-Baptiste Keck, Davide dal Bo, Christine Moriscot, Claire Seydoux, Fabien Chevalier, Nicole L. Schieber, Rachel Templin, Guillaume Allorent, Florence Courtois, Gilles Curien, Yannick Schwab, Guy Schoehn, for the growing of algae, sample preparation, image acquisition and these numerous exchanges which significantly contributed to the completion of the work. Special mention to Benoît for his unfailing support in sample preparation; to Jean-Baptiste Keck for his feedback on writing the python code used in this project. I owe my gratitude to Nicole L. Schieber Yannick Schwab for working tirelessly to provide the images that contributed to the completion of chapter 4 of this thesis.

I want to express my gratitude to the lipid team for their enthusiasm and high spirits. It helped me quickly feel at home in the lab. I loved the time I spent with you. Juliette, Eric, thanks, you are great people. I am also grateful to the other members of the photosynthesis team. In particular, Marie, Chloé and Erika, for their sense of humour and friendly atmosphere. Guillaume and Cécile, who, no matter what, the jokes still offer some sweets to accompany the coffee and the pizza party; Gilles for always sharing science.

Approches quantitatives d'imagerie pour étudier la physiologie des cellules photosynthétiques

Résumé — Le phytoplancton est composé de micro-organismes photosynthétiques (microalgues et cyanobactéries) vivant en suspension dans les eaux marines et douces. Grâce à la photosynthèse, le phytoplancton produit de grandes quantités d'oxygène indispensable à la vie marine et terrestre, et fixe le CO₂ de l'atmosphère. Les microalgues marines sont également des organismes prometteurs pour les applications biotechnologiques (alimentation humaine et animale, biocarburants). En raison de leur importance écologique et économique, l'étude des réponses du phytoplancton aux défis environnementaux (y compris ceux induits par l'activité humaine et le réchauffement climatique) est un domaine de recherche en plein développement. L'activité du phytoplancton est influencée par les changements dans la stratification verticale de la colonne d'eau qui module, en fonction de la température, la disponibilité de l'énergie lumineuse ainsi que l'apport de nutriments aux cellules du phytoplancton. En raison de la disponibilité de la lumière et des nutriments, les cellules du phytoplancton ont évolué vers différents modes de vie : phototrophie (activité photosynthétique), mixotrophie (utilisation simultanée de la photosynthèse et de la respiration de sources de carbone organique extérieures pour la croissance) et photosymbiose (interactions symbiotiques à l'intérieur de cellules animales). Dans cette thèse, j'ai étudié les réponses physiologiques des cellules du phytoplancton aux changements environnementaux en regardant aux niveaux cellulaires et subcellulaires. Pour atteindre cet objectif, j'ai mis au point un processus d'imagerie complet permettant d'effectuer des analyses morphométriques quantitatives de cellules entières d'algues représentatives à la fois d'espèces à succès écologique et de modèles de laboratoire. Le protocole commence avec l'acquisition de séries d'images hautes résolutions soit par FIB-SEM (Focused Ion Beam - Scanning Electron Microscopy) ou SBF-SEM (Serial Block Face - Scanning Electron Microscopy). Le protocole d'analyse d'images 3D développé dans ce travail permet d'obtenir des modèles tridimensionnels à haute résolution de cellules entières permettant la réalisation d'analyses quantitatives. Grâce à ces outils, j'ai pu imager des cellules du phytoplancton dans diverses conditions environnementales révélant ainsi : 1) le changement de taille et de morphologie des plastes et des mitochondries lors de l'acclimatation à la lumière dans les diatomées, 2) le changement dans l'interaction des organites chez *Nannochloropsis* lors de l'acclimatation aux nutriments, 3) les changements morphologiques qui surviennent lors de la photosymbiose dans l'algue *Phaeocystis*. Ces travaux révèlent plusieurs scénarios d'acclimatation du phytoplancton au niveau cellulaire et subcellulaire. J'ai également pu valider l'utilisation de ce protocole chez les plantes pour répondre à deux questions biologiques principales : la transition étioplaste - chloroplaste dans les cellules du cotylédon et le processus de formation des granules d'amidon dans les feuilles matures d'*Arabidopsis*.

Mots clés : Imagerie 3D, Analyse morphométriques, Phytoplancton, Photosymbiose, Organites, Plantes.

Plant & Cell Physiology lab (LPCV) - UMR 5168 - IRIG
17 rue des Martyrs
38054 Grenoble cedex 9
France

Quantitative imaging methods to investigate the physiology of photosynthetic cells

Abstract — Phytoplankton is composed of photosynthetic microorganisms (microalgae and cyanobacteria) living in suspension in marine and fresh waters. Through photosynthesis, phytoplankton produce large amounts of the oxygen essential for marine and terrestrial life, and captures CO₂ from the atmosphere. Marine microalgae are also promising organisms for biotechnological applications (human and animal food, biofuels). Because of their ecological and economic importance, the study of the phytoplankton responses to environmental challenges (including the ones induced by human activity and global warming) is a developing field of research. Phytoplankton activity is influenced by changes in the vertical stratification of the water column, which modulate light energy availability as well as nutrient supply to phytoplankton cells in a temperature-dependent manner. Based on light and nutrient availability, phytoplankton cells have evolved different lifestyles: autotrophy (photosynthetic activity), mixotrophy (simultaneous use of photosynthesis and respiration of exogenous organic carbon sources for growth) and photosymbiosis (endosymbiotic interactions within animal cells). In this thesis, I have studied phytoplankton cells and their responses to environmental changes at the cellular and subcellular levels. To achieve this goal, I have developed a complete imaging workflow to perform quantitative morphometric analyses of entire algal cells, representatives of ecologically-successful and laboratory-model microalgal species. This protocol starts with FIB-SEM (Focused Ion Beam-Scanning Electron Microscopy) or SBF-SEM (Serial Block Face-Scanning Electron Microscopy), to acquire high-resolution images. By implementing the 3D image analysis protocol, it is possible to obtain high-resolution whole cells models in three dimensions, suitable to perform quantitative analyses. Thanks to these tools, I have been able to image phytoplankton cells in various environmental conditions: (i) changes in the size and morphology of plastids and mitochondria during light acclimation in diatoms, (ii) Changes in organelles interaction during nutrient acclimation in *Nannochloropsis*, (iii) morphological changes occurring during photosymbiosis in *Phaeocystis*. Overall, this work reveals several scenarios of phytoplankton acclimation at both the cellular and subcellular levels. I have also validated the use of this protocol in plants to answer two main biological questions: the etioplast - chloroplast transition in cotyledon cells and the process of starch granule formation in mature leaves of *Arabidopsis*.

Keywords: 3D imaging, Morphometric analyses, Phytoplankton, Photosymbiosis, Organelles, Plants.

Plant & Cell Physiology lab (LPCV) - UMR 5168 - IRIG
17 rue des Martyrs
38054 Grenoble cedex 9
France

Contents

1	Introduction	1
1.1	Origin of photosynthesis	2
1.2	General history of microscopy	5
1.2.1	From photons to electrons	6
1.2.2	Volume imaging in biology	8
1.3	Objective of the Thesis project	13
2	Materials and methods	15
2.1	Introduction	16
2.2	Algal growth	16
2.3	Sample preparation methods	17
2.3.1	Chemical Fixation	17
2.3.2	Cryo-substitution	17
2.4	FIB-SEM acquisition	18
2.5	Equipment and software tools	18
2.6	Image processing and 3D reconstruction	19
2.6.1	Image pre-processing methods	19
2.6.2	Segmentation and 3D reconstruction	33
2.6.3	3D visualization and model editor	42
2.7	Geometry Processing	45
2.7.1	Surface and volume metrics	45
2.7.2	Proximity distance between two meshes	49
2.7.3	Splitting method	52
2.8	Image processing methods with sample preparations	55

3	Assessing subcellular features and their dynamics in microalgae	57
3.1	Introduction	60
3.2	Results and Discussion	62
3.2.1	Cellular architectures of phytoplankton	62
3.2.2	Subcellular features of energy managing organelles	67
3.2.3	Remodelling of the subcellular architecture of microalgae	69
3.3	Conclusion and perspectives	78
3.4	Supplementary Materials	80
4	Photosymbiosis	95
4.1	Introduction	96
4.2	Results and Discussion	99
4.2.1	Integration of the microalgae into the host cell	99
4.2.2	The architecture of <i>Phaeocystis</i> cell in free-living phase	100
4.2.3	Morphological change of <i>Phaeocystis</i> cells in symbiotic phase	102
4.3	Conclusion and perspective	112
5	3D imaging to investigate chloroplast biogenesis	113
5.1	Introduction	114
5.2	Preparation of plant material for SBF-SEM imaging	114
5.3	Background model	115
5.4	Segmentation and 3D analysis of SBF-SEM image datasets	116
5.5	Results and Discussion	117
5.5.1	Plastid development in germinating seedlings	117
5.5.2	Control of starch granule numbers in <i>Arabidopsis</i> chloroplasts	121
5.6	Conclusion and perspective	122
	Conclusion and perspectives	125

A Appendices	131
A.1 Algal Remodeling in a Ubiquitous Planktonic Photosymbiosis	131
A.2 Cytoklepty in the plankton	148
A.3 A multifaceted analysis reveals two distinct phases of chloroplast biogenesis. .	186
 Bibliography	 236

List of Figures

1.1	Schematic representation of the endosymbiosis event.	3
1.2	Nimrud lens British Museum Geni - Photo by user: geni.	5
1.3	Evolution of optic microscope to the compound light microscope.	6
1.4	Image formation in electron microscopy.	7
1.5	Summary of the different scales of observation.	7
1.6	EM volume imaging techniques as described by (Briggman et al. 2012). . . .	10
1.7	FIB-SEM imaging of <i>Phaeodactylum tricornutum</i> cells.	12
1.8	Tree of eukaryotes with phytoplankton lineages.	14
2.1	Open image sequences in Fiji.	20
2.2	Add voxel size information in Fiji.	21
2.3	Grey-shading toners from black to white just as the bits channel.	22
2.4	Grey image and the graphic representation of values distribution.	22
2.5	Adjust image contrast in Fiji.	23
2.6	z -stack preview in Fiji using the orthogonal view module.	24
2.7	Alignment with template matching.	25
2.8	Alignment with SIFT.	26
2.9	Alignment with MultiStackReg.	27
2.10	2D FIB-SEM images were binned using different regrouping factor methods.	29
2.11	Comparison of the image filtering methods.	30
2.12	Image convolution using a specific kernel in Fiji.	32
2.13	Grey images and histograms highlighting the distribution of grey values in AOI.	34
2.14	Representation of 3D Slicer interface.	36
2.15	The volume module includes many possibilities to adjust image settings.	37

2.16	3D Slicer Editor modules.	38
2.17	Painting with a circle brush	39
2.18	Painting with a sphere brush	39
2.19	Adaptive thresholding segmentation.	40
2.20	Smooth 3D reconstructed model.	40
2.21	Volume computation in 3D Slicer.	41
2.22	MeshLab interface and post-opening of a 3D model.	42
2.23	Cleaning and editing 3D model in MeshLab.	43
2.24	Quantification and computation of mesh metrics in MeshLab.	44
2.25	Mesh simplification, refinement or decimation in MeshLab.	45
2.26	Voxelized model with voxel unity.	46
2.27	3D reconstructed model represented by polygons.	47
2.28	Minimum distance between two meshes.	49
2.29	Proximity distance estimation.	50
2.30	Contact area computation.	51
2.31	<i>3D Object Counter plugin</i> form Fiji	53
2.32	Mesh splitting using Trimesh python package.	54
2.33	Chemically fixed image of <i>Phaeodactylum tricornerutum</i>	55
2.34	3D architecture organization of <i>Emiliania huxleyi</i>	56
3.1	Cellular volume and external features of selected phytoplankton cells.	62
3.2	Internal cell architecture of phytoplankton cells.	64
3.3	Morphometric analysis of phytoplankton members.	65
3.4	Contact surface areas between plastids and mitochondria in phytoplankton.	67
3.5	Organization/architecture of the mitochondria and plastids of phytoplankton.	68
3.6	Light acclimation in <i>Phaeodactylum tricornerutum</i>	70
3.7	Plastid mitochondria interactions are modified by trophic regimes.	71

3.8	Flowchart of image processing from data acquisition to morphometric analysis.	80
3.9	The different morphologies of mitochondria in three <i>Emiliania</i> cells.	81
3.10	Volumes and surfaces relationship in different subcellular compartments.	82
3.11	Subcellular features of different phytoplankton taxa.	82
3.12	Nucleus features.	83
3.13	Dinoflagellate cellular system.	84
3.14	Nucleus architecture in <i>Symbiodinium pilosum</i> cell.	85
3.15	Thylakoid membranes are modified under different light regimes.	86
4.1	The integration of the alga <i>Phaeocystis</i> in the host.	99
4.2	Cell ultrastructure of <i>Phaeocystis</i> in the free-living phase.	101
4.3	The correlation between the cell volume and organelles.	101
4.4	Cellular architectures of <i>Phaeocystis</i>	102
4.5	3D reconstructed model of <i>Phaeocystis</i> organelles	103
4.6	Morphological transformation of the microalga in symbiosis.	104
4.7	The plastids division in symbiotic <i>Phaeocystis</i>	105
4.8	Plastid architecture in <i>Phaeocystis</i> cell in free-living vs symbiotic phase.	106
4.9	The plastid-mitochondria interaction.	108
4.10	Mitochondria features in both phases.	109
4.11	Nucleus features in both phases.	110
4.12	Plastid-nucleus interactions.	111
5.1	3D reconstruction of thylakoid membranes of an etioplast from 3 day-old.	116
5.2	SBF-SEM images processing and 3D reconstruction.	117
5.3	3D reconstructions of plastid and thylakoid membrane during de-etiolation.	118
5.4	Quantitative analysis of plastid and thylakoid membrane during de-etiolation.	119
5.5	3D reconstruction of a 3–days old cotyledon cell revealed by SBF-SEM imaging.	120

- 5.6 Starch granules initiation in developing leaf cells of *Arabidopsis* WT vs. *ss4*. . 122

List of Tables

1.1	Comparison of different volume imaging methods.	9
2.1	The transformation methods provided in registration plugins of Fiji.	24
2.2	The transformation methods provided in registration plugins of Fiji.	32
2.3	Saving module of 3D Slicer.	41
2.4	Exported different file formats, size, volume information of the 3D model. . .	44
2.5	Comparison of metrics obtained from 3Dslicer, MeshLab and Python script. .	49
3.1	Taxonomy, cell size and FIB-SEM resolution of the phytoplankton cells. . . .	87
3.2	Volumetric data of micro-algae Cells.	88
3.3	Surface metrics information of the organelles.	89
3.4	Surface metrics information of the organelles.	90
3.5	Sub-organelle in plastid volume.	91
3.6	Sub-organelle compartment ratio in mitochondria volume.	92
3.7	Quantitative analysis of <i>Phaeodactylum</i> cells growing under high light regime.	93
3.8	Quantitative analysis of <i>Nannochloropsis</i> cells growing in two trophic regime.	94

Acronyms and abbreviations

2D	Two-dimensional
3D	Three-dimensional
EM	Electron Microscopy
TEM	Transmission Electron Microscopy
SEM	Scanning Electron Microscopy
FIB-SEM	Focused Ion Beam-Scanning Electron Microscopy
SBF-SEM	Serial Block Face-Scanning Electron Microscopy

Introduction

Contents

1.1	Origin of photosynthesis	2
1.2	General history of microscopy	5
1.2.1	From photons to electrons	6
1.2.2	Volume imaging in biology	8
1.3	Objective of the Thesis project	13

My Thesis project was financed in the frame of a call from the IDEX University Grenoble Alpes International Strategic Partnerships. My project is part of the SCruTINy project, and aims at unveiling Single-Cell phytoplankton eco-physiological responses with high-resolution chemical and structural imaging. The international partner of the project is the Plant Biochemistry Laboratory at the Swiss Federal Institute of Technology of Zurich (ETHZ). Both laboratories, The LPCV in Grenoble and the PBL at ETH of Zurich are developing research with photosynthetic eukaryotes to understand how phytoplankton (LPCV) and higher plants (PBL) respond to changes in their environment for different physiological pathways such as photosynthesis and carbohydrates storage and degradation.

The objective of the project is to develop subcellular imagery approaches to better understand responses of phytoplankton facing abiotic and biotic (symbiosis) constraints. During my PhD, I focused on the 3D reconstruction pipeline. First, I developed a full workflow to analyse single phytoplankton cells and then I transposed this pipeline to microalgal and higher plant cells.

My introduction chapter is therefore divided into two parts. In the first part, I present the biological material and its evolutionary origin since it is important to know these organisms if we want to understand their subcellular organization and physiological responses. In the second part, I present the history and development of the imaging techniques (acquisition and image processing) used in this project.

1.1 Origin of photosynthesis

Eukaryotic cells are complex organisms containing organelles and multiple cellular compartments, which are the result of more than two billion years of evolution. Nuclei, mitochondria (present in all eukaryotic cells) and plastids (present only in photosynthetic cells: plants and algae) are major organelles known as the ‘control room’, the ‘power house’ and the ‘energy captor/transformer’, respectively of the cell (Archibald 2015; Dyaal et al. 2004). Mitochondria and plastids are issued from distinct endosymbioses. Mitochondria originate from the engulfment of an α -proteobacterium-like organism in a Archea-type host cell about 2.2 billion years ago, giving rise to all modern eukaryotes (Degli Esposti 2014; Falconet 2012).

Plastids probably originated from the symbiotic association between a cyanobacterium (a photosynthetic bacteria) and a mitochondriate eukaryote having occurred between 1.6 and 0.6 billion years ago (Gray et al. 1999; Poole et al. 2007; Archibald 2015; Keeling 2013), reviewed in (Falconet 2012). This event leads to the development of plants, green and red algae, and glaucophytes, which contain the so-called primary plastids.

Multiple endosymbiotic events occurred between red and green algae as endosymbionts engulfed by non-photosynthetic eukaryotes leading to the so-called secondary plastids (Keeling 2010; De Clerck et al. 2012; Falconet 2012) (see Figure 1.1). The consequence of successive endosymbiosis is reflected by the number of membranes, which are limiting the primary and secondary plastids. While primary plastids are limited by two membranes, secondary plastids are generally surrounded by four membranes (Petroutsos et al. 2014; Flori et al. 2016).

Tertiary endosymbiosis introduces additional layers of associations after secondary endosymbiosis. These phenomena are common in dinoflagellates, which once had a red secondary plastid. However, some lines have apparently lost or reduced this plastid and have either taken another secondary alga to form a tertiary plastid or taken another primary alga to form a series of secondary plastids (Keeling 2013).

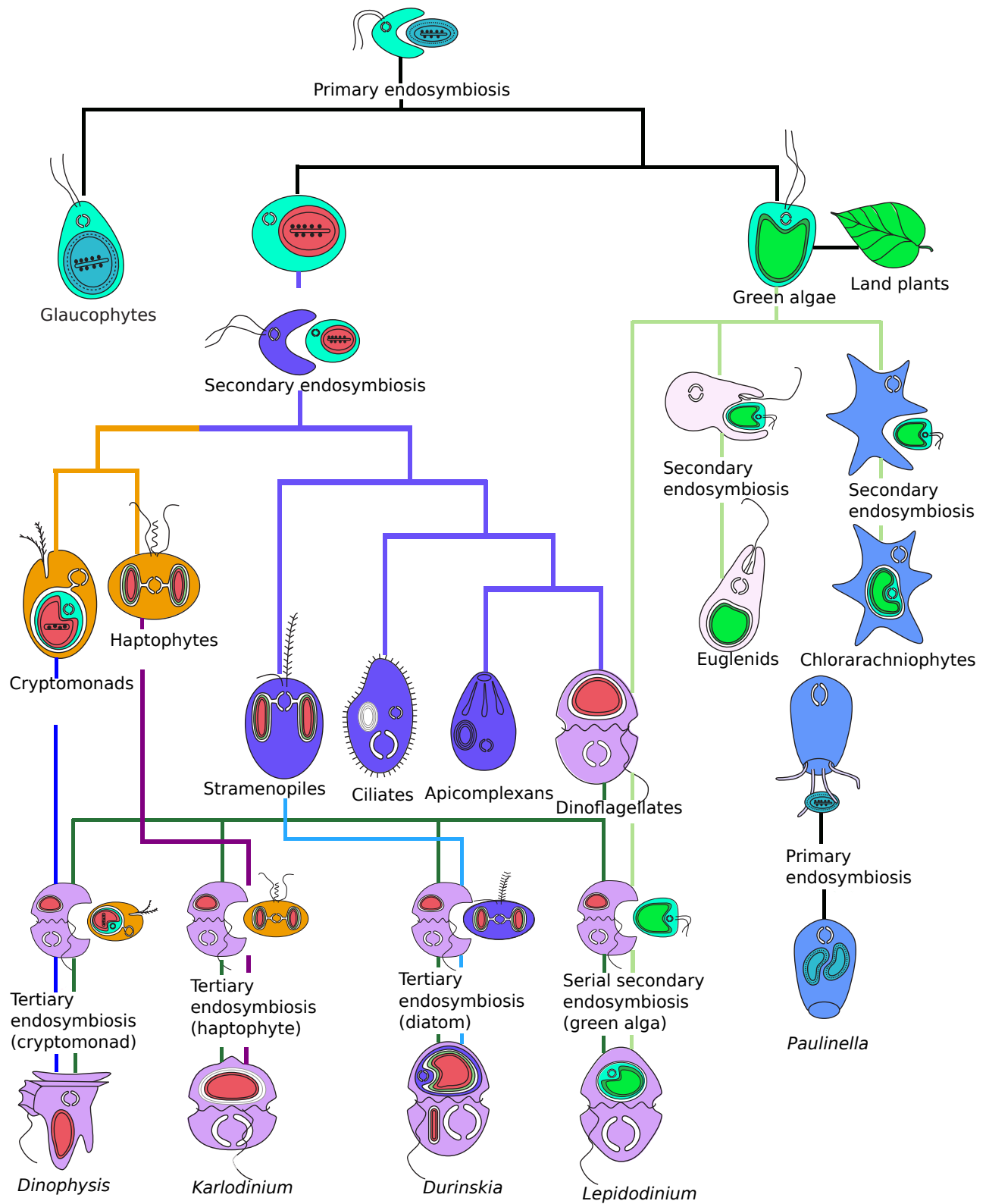


Figure 1.1 – Schematic representation of the endosymbiosis event. Representation of the primary endosymbiosis event, secondary and tertiary endosymbiosis event and their consequences in the photosynthetic organism’s apparition on Earth. Adapted from (Keeling 2013).

The different evolutionary origin translates into different plastid structures, functions and interactions with other cellular organelles, which in some cases (Bailleul et al. 2015), deeply affect the photosynthetic activity.

All unicellular photosynthetic organisms, which are highly diverse and present both on terrestrial and in aquatic environments, play a critical role as primary producers. These organisms, collectively named ‘phytoplankton’, are producing the oxygen of the atmosphere and are key players for the organic matter flux on Earth (Knoll et al. 2007; Falkowski et al. 2004).

Phytoplankton cells exhibit different lifestyles: autotrophy (photosynthetic activity), mixotrophy (simultaneous use of photosynthesis and respiration of exogenous carbon sources for growth) and photosymbiosis (symbiotic interactions with animal cells) (Dionísio 2017). Because of their ecological and economic importance, the question of photosynthetic responses to changing environments is becoming more and more relevant. Owing to climate changes, increasing temperatures at the surface of the Earth (both in the ocean and on land) could be detrimental for the growth rate and biomass production (Falkowski 2002; Field et al. 1998). These changes could impact the entire food web and the efficiency of the biologically driven sequestration of carbon from the atmosphere to the deep sea (Basu et al. 2018).

Therefore, it is very important to fully understand the physiological responses of the photosynthetic organisms exposed to different environmental challenges from the cellular to the subcellular level. Transcriptome and genome analyses have provided valuable information about the potential consequences of climate change on phytoplankton communities (Maor-Landaw et al. 2017; Stillman et al. 2015), but much less is known about responses at the single-cell level. In addition, bulk analyses (e.g. transcriptomics, metabolomics) can only reflect an average among cell populations and organelles, and cell heterogeneity cannot be distinguished. By contrast, subcellular imaging carries spatial information at the subcellular level about an ultrastructural component that provides invaluable information to highlight and decipher physiological mechanisms in an individual cell. Without this level of understanding, it is not possible to fully interpret the significance of “omics” analyses, and to understand the phytoplankton responses in general.

1.2 General history of microscopy

Although the inventor of the single-lens is unknown, it made it possible to see objects that are too small to be observed by the naked eyes. The oldest optical instrument known could be the 3000 years old Nimrud lens found in Mesopotamia by Austen Henry Layard and exposed at the British museum in London (Figure 1.2). However, it is only more recently, in the mid-17th century, that Robert Hooke and then Antoni van Leeuwenhoek investigate the world of the small living cells using artisanal magnifying microscopes (Figure 1.2).

Antoni van Leeuwenhoek showed the link between the focal length of the microscope and the lens diameter. Since then, efforts have been made to build a powerful microscope based on this theory. The use of curved lens instead of flat lens allowed a magnification of x270 instead of x50 with a flat lens. It was then possible to reduce the focal length while keeping the lens diameter building microscopes with many lenses. The new devices allow higher magnifications. Thanks to these new microscopes, biologists were able to observe single-cell organisms (bacteria) or cells of mammalian brain (Van Leeuwenhoek 1800; Dall'Oglio et al. 2010; O'Mara 1979; Gest 2004).

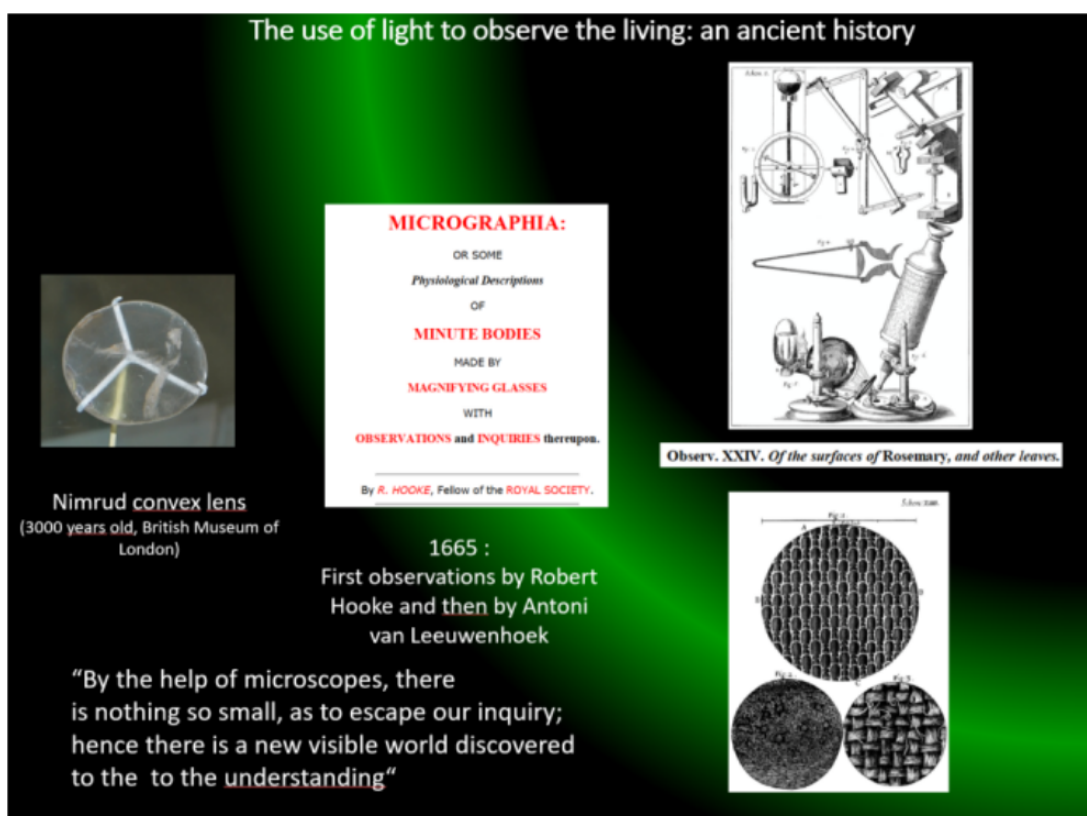


Figure 1.2 – Nimrud lens British Museum Geni - Photo by user: geni. Licensed under GFDL via Wikimedia Commons. R. Hooke, *Micrographia: or, some physiological descriptions of minute bodies made by magnifying glasses*. London: J. Martyn and J. Allestry, first edition (1665).

It was only at the end of the 19th century that Ernst Abbe formulated the theory of the image formation in the microscope. Abbe's theory considers the phenomena of light diffraction and interference in microscopy imaging. It states that to achieve a spatial resolution of $187\text{--}200\text{nm}$ in the microscope, it is necessary to use lenses of high-quality with thin specimens (Abbe 1873; Fornasiero et al. 2015; Kremer et al. 2015). Years later, a new microscope will be created allowing to see colours and to control light for the first time. Nowadays, modern light microscopes can magnify up to 1000x with a spatial resolution of 200 nm (see (Figure 1.3) for the different scales of observation). However, to address some biological problems, it is essential to have a higher spatial resolution.

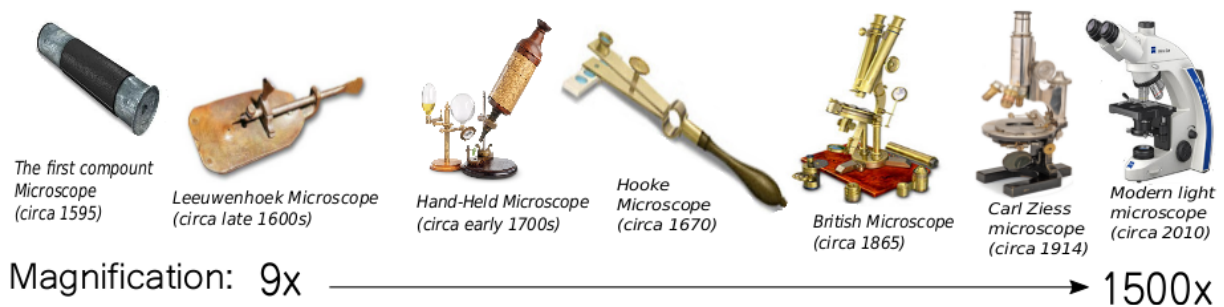


Figure 1.3 – Evolution of optic microscope to the compound light microscope. The modern devices magnify the image up to x1500 from its original size.

1.2.1 From photons to electrons

At the beginning of the 20th century, the wave-particle theory developed by De Broglie (De Broglie 1924) attracted Ernst Ruska's attention. Under the supervision of Dr. Max Knoll, Ruska performed experiments on the wave-like physical effect of particles, concluding that optical microscopes do depend on the wavelength of the light beams used to view the sample. He was able to show that since electrons have much shorter wavelengths than light, they could provide better resolutions. Ruska and Knoll built the first electron lens, which use the magnetic field to focus the electron beam as if it were light. Trying several lenses, they could greatly increase magnification (Knoll et al. 1932). Two-years later, their work led to the building of the first Transmission Electron Microscope (TEM) (for a review see (Kremer et al. 2015)). In TEM, electrons pass through a plastic-embedded specimen and are directed to the sample to create an image with a spatial resolution that extends to 0.1nm (Flegler et al. 1997; Reimer 2013).

A few years later, Max Knoll worked on the theory of backscattering electrons and found that electron beams can scan the surface of sample and resolve its structure in the nm range (Stadtländer 2007; Bogner et al. 2007). This work led to the making of a Scanning Electron Microscope (SEM) prototype, with a 250 000x magnification and a spatial resolution of 20 nm. At the same time, TEM was improved, becoming able to magnify an object up to 500 000x its original size with a spatial resolution of 0.1 nm (Stadtländer 2007; Erdman et al. 2019). SEM generates an image that gives the impression to see the surface of the sample in three-dimensions, while in TEM, electrons are transmitted through a thin section producing a magnified two-dimensional image (Smith 2010; Bogner et al. 2007)(Figure 1.4).

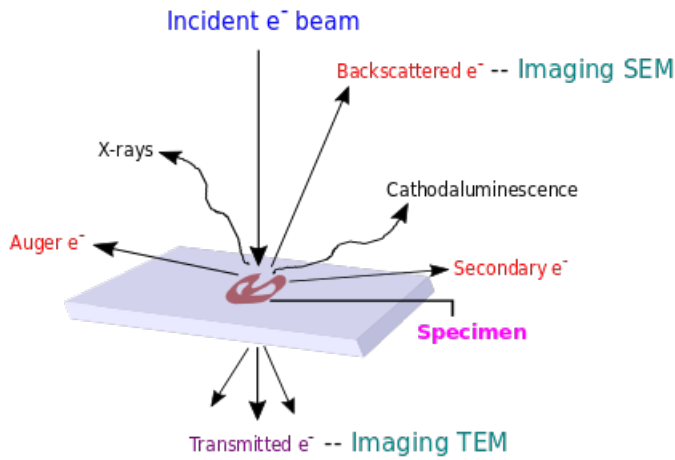


Figure 1.4 – Image formation in electron microscopy. When an electron beam interacts with the sample surface, they generate different types of signals from the interaction of particles with specimens. The produced secondary atoms (backscattered electron, transmitted electron, auger electrons, and X-ray radiations) contain the information of sample topography. The information is then analyzed via a numerical processing device and provides a 2D image (Murata et al. 1987).

Different scales of observation can be generated depending on the instrument used to perform the observations, as summarized in (Figure 1.5).

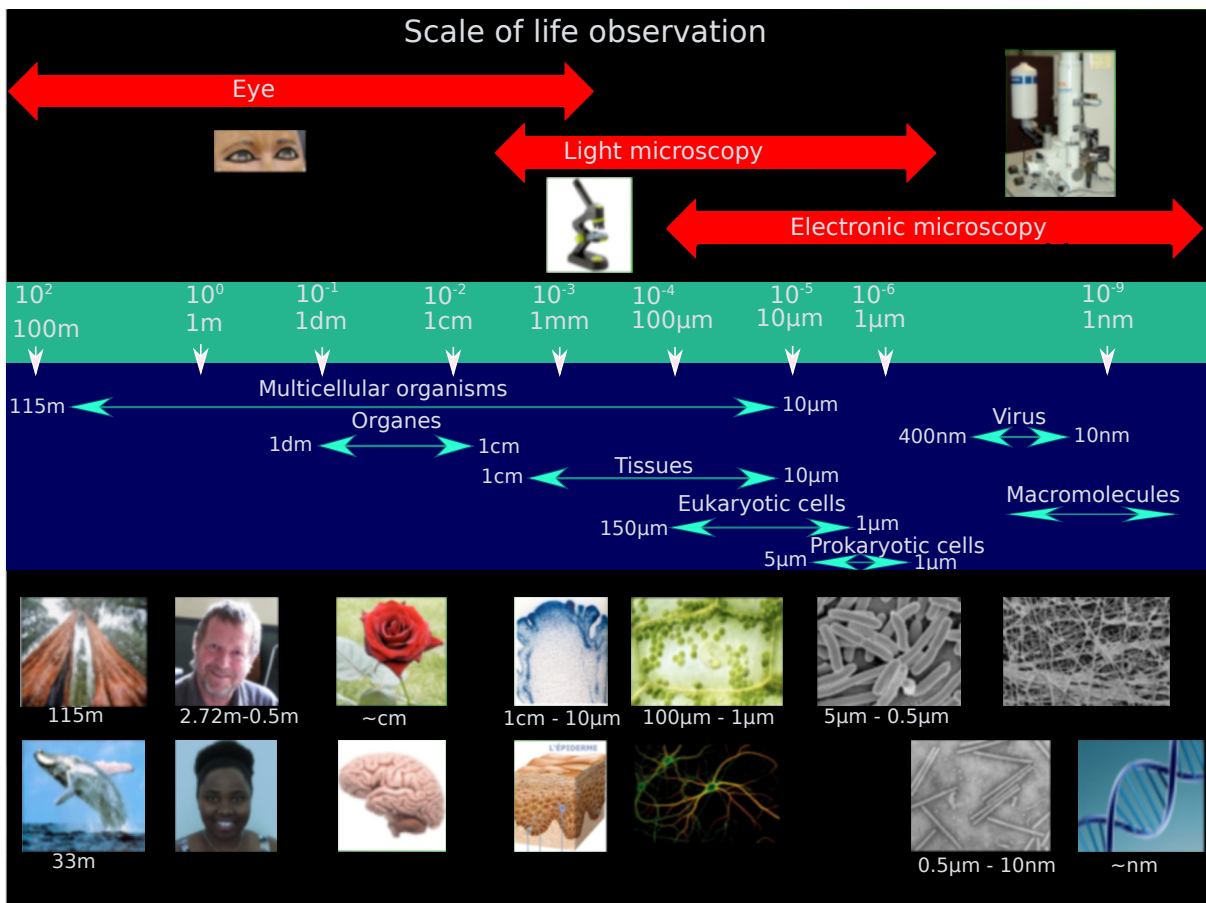


Figure 1.5 – Summary of the different scales of observation.

1.2.2 Volume imaging in biology

The above-mentioned development in light and electronic microscopy allows a two-dimensional (2D) observation of the objects. In biology, however, the function of a cell is often associated with its structure. To decipher the function of cells or organs, it is essential to obtain precise information about their three-dimensional (3D) structures. In light microscopy, the development of confocal laser scanning microscopes (CSLM) has made it possible to reconstruct 3D organization at the cellular and, to some extent, subcellular level. The use of immune-histochemical techniques has allowed to localize labelled proteins of interest them within anatomic structures (Sands et al. 2005). More recently, super-resolution microscopy (SRM) encompassing a variety of methods such as stochastic optical reconstruction microscopy (STORM), structured illumination microscopy (SIM) and stimulated emission depletion (STED) has been developed, generating images with higher (a few nanometers) resolution. Nonetheless, SRM methods have some limitations and EM is still a method of choice to address the structure of biological objects at the nm scale, offering a resolution not provided by SRM (Knott et al. 2013; Nellist et al. 2004).

Volume imaging by EM

Observation of objects with EM is limited by the fact that the maximum thickness that can be explored is $\sim 0.5\mu m$. When samples are thicker, electrons diffuse inelastically, thus reducing the information provided by the image. It is therefore important to find a specific imaging technique to image larger samples with variable thickness ($nm \rightarrow \mu m$).

This difficulty can be circumvented by a slicing approach, which divides the sample in manageable sections (Helmchen et al. 2005; Kanaya et al. 1972) for EM analysis. The first volume imaging was developed in the 1950's and known as serial section TEM (ssTEM) (Figure 1.6). This approach uses a manual sectioning of $\simeq 100nm$ layers of the resin-embedded sample, followed by an individual imaging section in TEM. Acquired images are manually aligned to obtain a 3D representation of the tissue volume with high-resolution in x- and y-planes and limited z-resolution because of the slice thickness (Harris et al. 2006; Frank 2013). Later advances have led to electron tomography, making it possible to acquire high-resolution 3D images with a thickness up to $1\mu m$. The technique uses a high-voltage TEM in which the object on the grids is tilted along one or two axes and a series of images is acquired at various tilt angles. Image analysis allows reconstructing the volume of the section (Hoppe 1974; McEwen et al. 2001).

The two above methods are complementary, since while electron tomography provides higher resolution in the z-axis, the ssTEM gives a continuous view in larger depth volume (Bock et al. 2011). Both methods are very labor intensive and use expensive equipment (Bock et al. 2011; Takemura et al. 2013). In addition, long exposure with a high-energy electron beam (100-200 kV) as typically used with a TEM can cause cell distortion and damage (Briggman et al. 2006). Imaging biological samples with thicknesses in the order of several μm was a challenge, which led to other more or less semi-automatic strategies based on the use of a Scanning Electron Microscope (SEM).

The SEM-based methods

In the Automated Tape-collecting Ultra Microtome SEM (ATUM-SEM) technique, sections are automatically collected and mounted in the right order on silicon wafers and then scanned in an SEM (Figure 1.6) (Hayworth et al. 2006). SEM provides surface information since the electron beam (with low energy, $\sim 1 - 3kV$) is scanned across the surface of the sample and the backscattered electrons are detected with a detector placed above the sample. This technique reduces the 3D EM acquisition time considerably compared to the previous approach and enabled biologists to explore in 3D the cell architecture with high structural and molecular details.

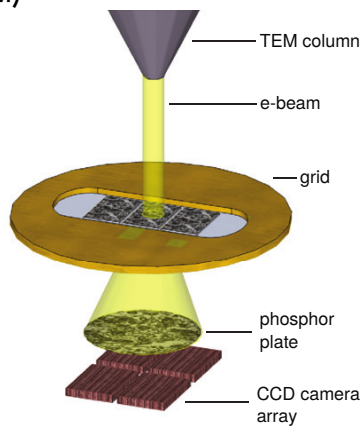
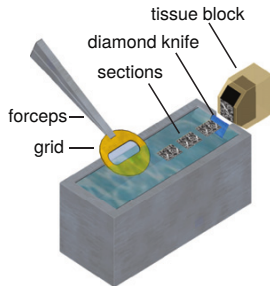
Over the last two decades, the development of two other automated EM volume imaging have emerged and led to a tremendous increase in 3D EM studies. The automated EM volume imaging is the technique which allows the acquisition of serially sectioned, imaged and digitally aligned ultrastructural data (Cocks et al. 2018; Deerinck et al. 2010; Tapia et al. 2012). The technique includes two similar and complementary approaches called Serial Block Face-Scanning Electron Microscopy (SBF-SEM) and Focused Ion Beam-Scanning Electron Microscopy (FIB-SEM) (Denk et al. 2004; Leighton 1981). In the SBF-SEM method, the automated sectioning with a diamond knife and imaging of the sample are performed within the vacuum chamber of the SEM. In the FIB method the sections are removed by a Gallium (Ga^+) beam. These two methods repeatedly remove and discard sections of the sample surface. Both techniques are destructive. FIB-SEM can provide a 3D reconstructed model with an excellent resolution in-depth compared to what a diamond knife in SBF-SEM can do. The choice of the thickness and number of serial sections depend on the method and the size of the sample (Young et al. 1993; Bushby et al. 2011).

FIB-SEM offers a higher voxel resolution of automated serial imaging compared to SBF-SEM (Peddie et al. 2014; Titze et al. 2016). Its higher resolution makes FIB-SEM the reference volume EM technique for imaging microscopic structures and specific areas of tissue. Its z-resolution could achieve $< 4nm$ while SBF-SEM sections thickness is $20nm$. A summary of the different methods is presented in (Table 1.1).

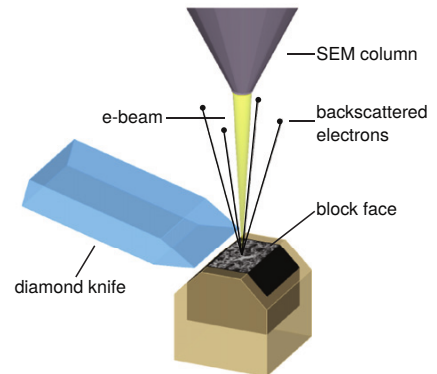
	Serial-section electron microscopy		Serial block-face electron microscopy		Super-resolution light microscopy	
	Section collection on TEM grids, TEM imaging	Section collection on solid support, SEM imaging	Diamond-knife cutting, SEM imaging	Focused ion beam ablation, SEM imaging	Stimulated-emission depletion nanoscopy and variants	Photo-activation localization microscopy (also known as STORM)
Depth (z) resolution	40nm section thickness, improved by tilts	<30nm section thickness	23 nm section thickness	5 nm ablation thickness	~30 nm (strongly dependent on fluorophore properties)	15 nm (strongly dependent on single-fluorophore brightness)
Lateral (xy) resolution	2 nm	< 4 nm	< 10 nm	< 10 nm	~30 nm	~20 nm
Advantages	Staining of sections possible after cutting, sections available for re-imaging, parallelized imaging possible		Negligible distortion, no loss of sections, fully automated cutting and acquisition		Multiple colours, optical sectioning possible	
	Highest lateral resolution, fastest imaging rate (TEMCA)	automatic section collection, large section areas, lower likelihood of section loss	Large areas possible	Highest isotropic resolution	Live cell imaging	Cheap
Drawbacks	Section distortion, folding and loss		En-block staining necessary, sections destroyed during cutting		Limited sample thickness, high fluorophore density needed	
	Section loss and distortion more severe	Tilt series more difficult than in TEM	Cutting de-bris on block face	Limited field of view	Limited speed (point scanning)	Many images of the same field needed
<small>SEM: scanning electron microscope; STORM: stochastic optical reconstruction microscopy; TEM: transmission electron microscope; TEMCA: transmission electron microscope fitted with a fast camera array. J. Lichtman, personal communication, H. Hess, personal communication.</small>						

Table 1.1 – Comparison of different volume imaging methods. Volume electron microscopy methods and two super resolution light-microscopy methods (Denk et al. 2012).

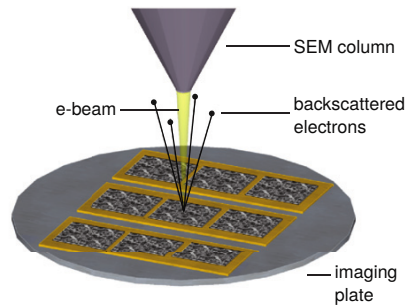
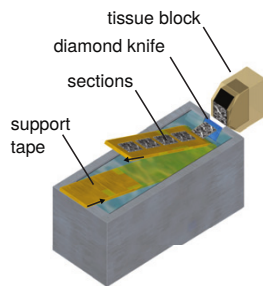
Serial section transmission electron microscopy (ssTEM)



Serial block-face scanning electron microscopy (SBEM)



Automated tape-collecting ultramicrotome scanning electron microscopy (ATUM-SEM)



Focused ion beam milling scanning electron microscopy (FIB-SEM)

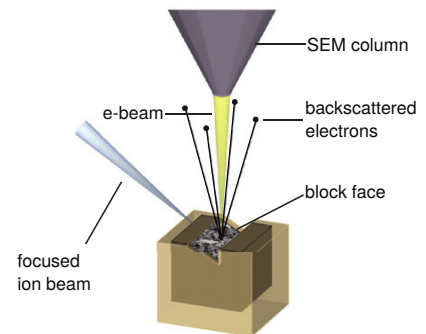


Figure 1.6 – EM volume imaging techniques as described by (Briggman et al. 2012).

Achievements of 3D EM imaging in cell biology

Electron Microscopy Tomography (EMT) has been principally used to investigate macromolecules, viral particles and the molecular organization of the cytoplasm (Baumeister 2002; Phan et al. 2016). A few 3D reconstruction of plant (Liang et al. 2018) with emphasis on thylakoids organization (Austin et al. 2011; Daum et al. 2010; Kowalewska et al. 2016; Shimoni et al. 2005) and algae cells (Moisan et al. 2006; Moisan et al. 1999; Ota et al. 2016a; Ota et al. 2016b) have been obtained and specific protocols described (Toyooka et al. 2014).

Early studies using manual serial sectioning and EM observations revealed the organization of the brain and its connectivity, first at the level of few synapses in the mouse cortex (White et al. 1981) and then the connectome of *Caenorhabditis elegans* formed by hundreds of neurons (White et al. 1986). At that time, sections were photographed and reconstructions were done by hand from prints. To perform such a reconstruction, 8000 prints were used; thus requiring a huge effort to achieve the 3D reconstruction. Manual sections have also been used to reconstruct algal cells (Ota et al. 2016a; Ota et al. 2016b; Wayama et al. 2013).

To study larger volumes of the brain, the ATUM device (see above) was used (Kasthuri et al. 2015) in association with a computer-assisted manual space-filling segmentation and annotation program (<https://neurodata.io/data/kasthuri15/>). Such an approach was at the same time simplified by the use of an ultramicrotome localized inside the microscope chamber (SBF, see above) allowing to address functional connectomics (Briggman et al. 2011).

The technology has been adopted by plant biologists with new preparation procedures suitable for plant tissue (Kittelmann et al. 2016) and was recently used to study chloroplast anatomical features in (Harwood et al. 2020) and in this thesis report, to study the chloroplast biogenesis during de-etiolation in *Arabidopsis thaliana* (see Chapter 5 and (Pipitone et al. 2020)).

The FIB-SEM technique was initially developed for materials science (Lopez-Haro et al. 2013) and later found promising applications in biology. One initial application of the ion-beam milling was to prepare thin lamella for imaging by cryo-EM (Rigort et al. 2012) revealing the native architecture of the *Chlamydomonas* chloroplast (Engel et al. 2015; Schaffer et al. 2015). Recently an improvement of this approach was proposed with an automated cryo-lamella preparation for high-throughput in-situ structural biology (Buckley et al. 2020).

Another important application was the possibility (with SBF) to scan the surface of the block after removing as little as 2nm , capturing images at isotropic resolution. This approach has been applied to different types of cells such as mammalian cells (Heymann et al. 2009), Human hepatoma cells (Vihinen et al. 2013), Mouse retina (Briggman et al. 2011), *Plasmodium chabaudi* infected erythrocytes (Medeiros et al. 2012), 3T3 fibroblast cells (Wierzbicki et al. 2013), yeast cells (Wei et al. 2012), for exhaustive reviews see (Hughes et al. 2014; Kizilyaprak et al. 2014; Narayan et al. 2015).

Recently FIB-SEM has been used to reveal the 3D structure of photosynthetic cells either with chemically fixed samples as in rice (Oi et al. 2017; Yamane et al. 2018), the green alga *Chlamydomonas* (García-Cerdán et al. 2020; Xu et al. 2017), the diatom *Phaeodactylum tricornutum* (Flori et al. 2017; Flori et al. 2016) (Figure 1.7, or cryo-fixed and freeze substituted *Phaeocystis* cells (Decelle et al. 2019) and Chapter 3 and Chapter 4 of this thesis. Cryo-FIB-SEM of high-pressure frozen marine algae such as coccolithophores (Sviben et al. 2016) and dinoflagellates (Jantschke et al. 2019; Jantschke et al. 2020) have also been used to study biomineralization pathways.

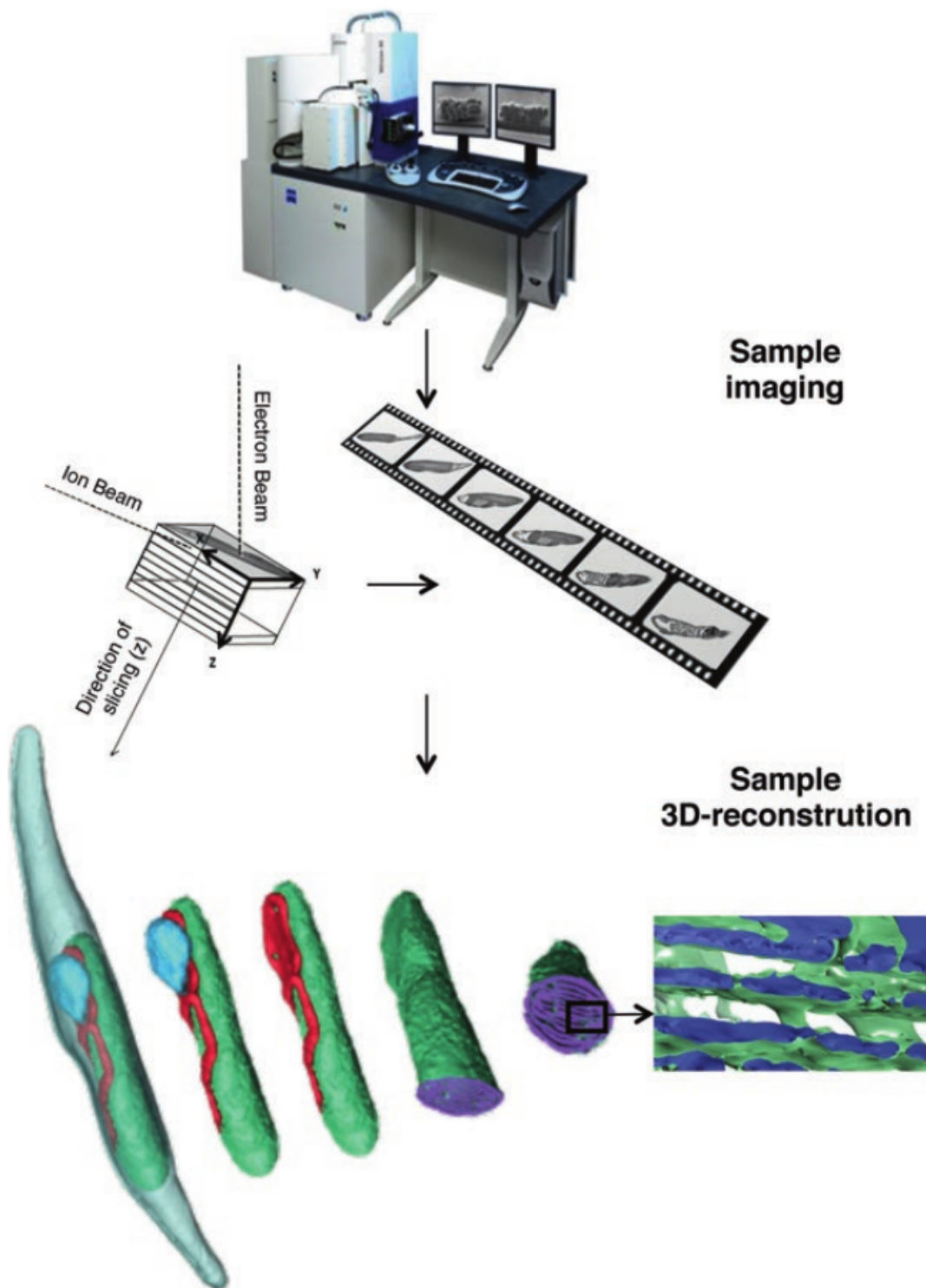


Figure 1.7 – FIB-SEM imaging of *Phaeodactylum tricornutum* cells. The representation shows the three-dimensional organization of the cell and reveals the contacts between the chloroplast (green), mitochondrion (red), and nucleus (blue), together with internal chloroplast structures (violet: semi-transparent plane, green: thylakoid volume) (Figure adapted from (Flori et al. 2018)).

Image analyses and 3D reconstruction

Volume imaging produced large datasets, which require very long machine times for analysis. Therefore advances in 3D EM imaging have generated new technological challenges related to “what to do with all the data” (Cocks et al. 2018). The complexity of the task can be explained by the following reasons:

- *Image analysis tools.* Over the past two decades, a significant number of automatic segmentation approaches have arisen. However the tools used are poorly described in the literature and inaccessible to the community of microscopists. The methodology proposed is often designed to analyse a specific dataset and not necessary suitable for studying other living systems. Actually, there is no suitable dataset that reflects the realities of all features observed in plant or animal cell structures. Although we need an impartial criterion to evaluate the automated segmentation algorithms performance, we still validate the automatic segmentation process by comparing it with manual procedures.
- *Segmentation.* The segmentation process allows separating a digital image into sets of pixels, i.e. to change the image representation into something more meaningful and easier to analyse. Upon segmentation, sets of pixels within an image will be assigned a label, in such a way that pixels with the same label share specific characteristics. Starting from a labelled area, it is possible to reconstruct the object volume, as required to represent biological objects in three-dimension and help biologists to explore structural features, state hypotheses and plan targeted experiments to relate cellular structures and functions. It is, therefore, crucial to increase data reproducibility by quantifying a large number of samples. The approach should avoid bias from the user/experimenter. Thus, the segmentation process should be automatic to get unbiased information fast. However, the reality is that capture of good quality images from a biological sample not only depends on image analysis, but also on the physiological state of the sample itself, the reagents used during fixation and the parameters of image acquisition.
- *Image quality.* Image acquisition provides complex grayscale images in which it is often possible to find two different Regions of Interests (ROIs) with the same pixel intensity or small areas with a significant variation in grey intensities. Therefore, often automated image segmentation does not lead to the desired results, and it is preferable and more straightforward to do manual segmentation to obtain 3D structure estimation close to reality.

1.3 Objective of the Thesis project

The main objective of my project was to implement the 3D image-processing pipeline for images datasets obtained by FIB-SEM or SBF-SEM using only free-access softwares. The images datasets were obtained through international collaborations involving different samples (microalgae and plants), and different samples preparation and different image acquisition protocols. The developed pipeline include sample preparation and image processing (see

material and methods, Chapter 2 of this thesis). It allowed us to get cell representation in three dimensions and obtain quantitative (volume, surface, contact) information.

These datasets allowed to investigate different photosynthetic organisms (see eukaryotic tree (Figure 1.8)), revealing: i) - the structural and metabolic responses of phytoplankton to abiotic stresses (Results, Chapter 3), ii) - the morphological changes occurring during photosymbiosis in *Phaeocystis* in its acantharians host (Results, Chapter 4) and iii) - plastid biogenesis during de-etiolation and transitory starch granule formation in *Arabidopsis thaliana* (Results, Chapter 5).

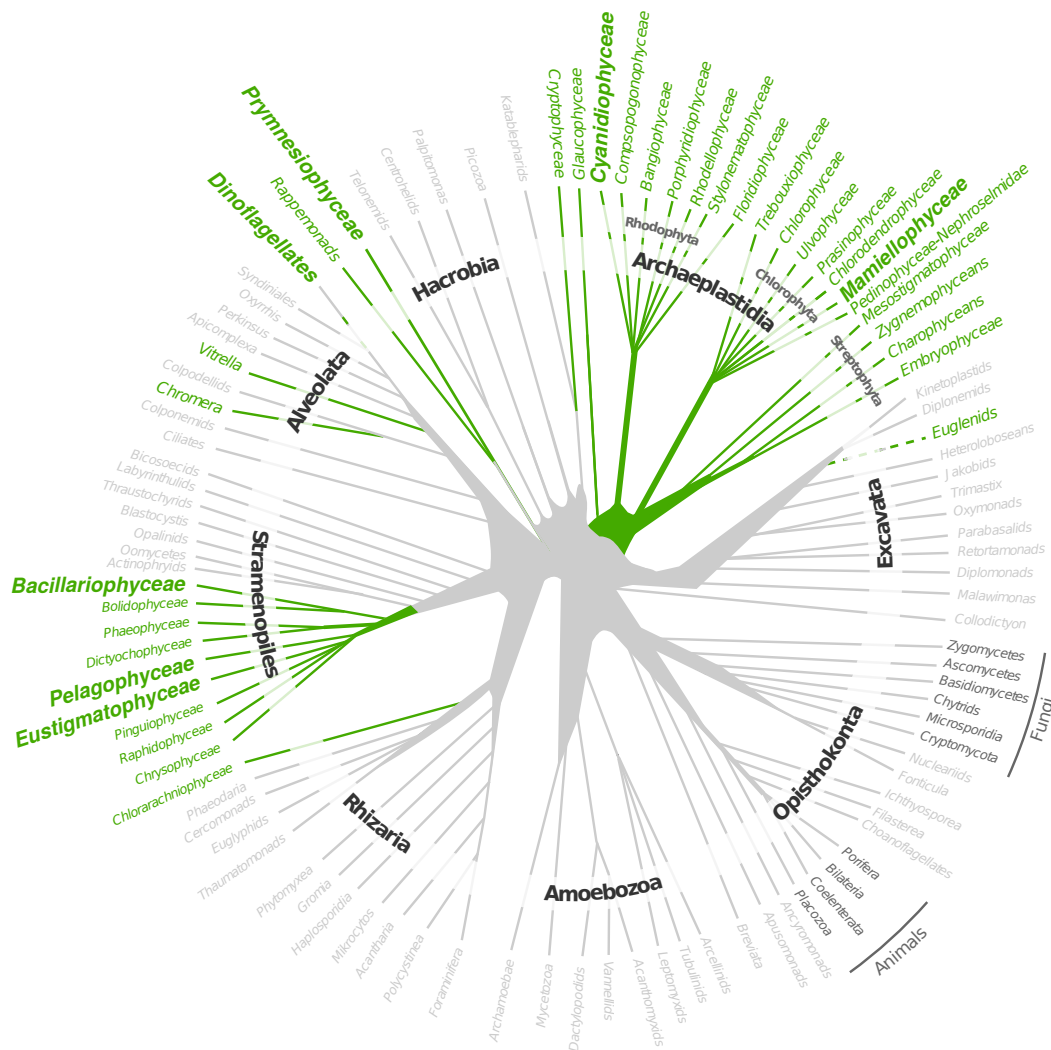


Figure 1.8 – Tree of eukaryotes with phytoplankton lineages. Tree of eukaryotes with phytoplankton lineages in green (adapted form (Decelle et al. 2015b)).

Materials and methods

Contents

2.1	Introduction	16
2.2	Algal growth	16
2.3	Sample preparation methods	17
2.3.1	Chemical Fixation	17
2.3.2	Cryo-substitution	17
2.4	FIB-SEM acquisition	18
2.5	Equipment and software tools	18
2.6	Image processing and 3D reconstruction	19
2.6.1	Image pre-processing methods	19
2.6.2	Segmentation and 3D reconstruction	33
2.6.3	3D visualization and model editor	42
2.7	Geometry Processing	45
2.7.1	Surface and volume metrics	45
2.7.2	Proximity distance between two meshes	49
2.7.3	Splitting method	52
2.8	Image processing methods with sample preparations	55

Summary

In the previous chapter, I have presented the state of the art on volume imaging. In this chapter, I describe the materials, procedures, methods and tools I have implemented to extract three-dimensional information from high-resolution 3D EM datasets. First, I briefly describe the protocol for cell culturing. Then I continue with the procedures for 3D reconstruction and quantitative analysis. The crucial steps to consider in quantitative imaging methods are (i) image pre-processing, (ii) image segmentation, and (iii) geometry processing. The principal goal of the segmentation is to extract relevant features based on pixel intensities distribution and reconstruct the 3D model corresponding to the features extraction. The proposed 3D imaging protocol can be applied to samples from any environment and can be used for quantitative comparative analysis of different species, which represent a link between cell structures and physiological/metabolic responses.

Keywords: [sample preparation], [FIB-SEM], [Segmentation], [Geometry processing]

2.1 Introduction

In this chapter, I present the materials, procedures, methods and tools needed to get three-dimensional information from high-resolution EM data. It starts with details on cell culturing. I discuss how image preprocessing steps may be different depending on the sample preparation methods. The chapter ends with examples of the various sample preparation methods used for this thesis and the corresponding image processing methods. Footnotes acknowledge the help of people involved in the different steps of the workflow as well as the laboratory where experiments have been performed.

2.2 Algal growth¹

Phaeodactylum tricornerutum Pt1 strain (CCAP 1055/3) was obtained from the Culture Collection of Algae and Protozoa, Scottish Marine Institute, UK. Cells were grown in 50 mL flasks in a growth cabinet (Certomat BS-1, Sartorius Stedim, Germany), at 19°C, a light intensity of 20 μmol photon m⁻²s⁻¹, a 12 – h light /12 – h dark photoperiod and shaking at 100 rpm, using the ESAW (Enriched Seawater Artificial Water) medium (Berges et al. 2001).

Galdieria sulphuraria SAG21.92 was obtained from the University of Dusseldorf (Germany) and was grown in a sterile 2XGS modified Allen medium, pH 2.0 (Allen 1959) at 42°C. Cells were grown in 250 mL flasks (50 mL culture volume).

Nannochloropsis gaditana CCMP526 was cultivated in artificial seawater (ESAW) using ten times enriched nitrogen and phosphate sources (5.49 × 10⁻³ M NaNO₃ and 2.24 × 10⁻⁴ NaH₃PO₄; called “10X ESAW” (Dolch et al. 2017). Cells were shifted from photoautotrophic to mixotrophic conditions by adding 5% of Lysogeny Broth (LB) to the growth medium.

Micromonas commoda RCC 827, *Pelagomonas calceolata* RCC 100, *Emiliania huxleyi* RCC 909 were grown in the K medium. *Symbiodinium pilosum* RCC 4014 cells were grown in the F/2 medium. Cells were grown at 20°C without agitation. All lines were obtained from the Roscoff Culture Collection (Vaulot et al. 2004).

Symbiotic acantharians harboring intracellular microalgal cells (*Phaeocystis*) were collected from surface seawaters (Mediterranean Sea, Villefranche-sur-Mer, France) as described in (Decelle et al. 2019). After collection, individual cells were isolated under a microscope with a micropipette, rapidly transferred into natural seawater, and maintained in the same controlled conditions (light intensity: 100 μmol photon m⁻²s⁻¹, temperature: 20°C) as the free-living stage. In parallel, cultures of the haptophyte *Phaeocystis cordata* RCC 1383 (the symbiont of Acantharia in the Mediterranean Sea) were maintained at 20°C in K/5 culture medium at 100 μmol photon m⁻²s⁻¹ without shaking.

¹**Cell culture and growth:** Gilles Curien, Johan Decelle, Claire Seydoux, Davide Dal Bo - Plant & Cell Physiology lab - IRIG /CEA Grenoble / France

2.3 Sample preparation methods

2.3.1 Chemical Fixation²

Phaeodactylum tricornutum and *Nannochloropsis gaditana* cells were fixed in 0.1 M Phosphate Buffer (PB) containing 2.5% glutaraldehyde, for at least 1h at room temperature and then prepared according to the modified protocol from T. J. Deerinck (<https://ncmir.ucsd.edu/sbem-protocol>) (see (Flori et al. 2018)).

2.3.2 Cryo-substitution³

1. Microalga cells were cryofixed using high-pressure freezing (HPM100, Leica).
2. Cells were subjected to high-pressure freezing, i.e. exposed to a pressure of 210MPa at -196°C , followed by freeze-substitution (EM ASF2, Leica).
3. Prior to cryo-fixation, microalgal cultures were concentrated by gentle centrifugation (800 rcf) for 10 *min*
4. For the freeze substitution, we used a mixture of 2% osmium tetroxide and 0.5% uranyl acetate in dried acetone. The freeze-substitution machine was programmed as follows: 60 – 80 *h* at -90°C , heating rate of 2°C h^{-1} to -60°C (15 h), 10 – 12 *h* at -60°C , heating rate of 2°C h^{-1} to -30°C (15 h), and 10 – 12 *h* at -30°C , quickly heated to 0°C for 1 h, to enhance the staining efficiency of osmium tetroxide and uranyl acetate and then back at -30°C .
5. Cells were washed four times for 15 *min* in anhydrous acetone at -30°C and gradually embedded in anhydrous araldite resin.
6. A graded resin/acetone (v/v) series was used (30, 50 and 70% resin) with each step lasting 2 h at increased temperature: 30% resin/acetone bath from -30°C to -10°C , 50% resin/acetone bath from -10°C to 10°C , 70% resin/acetone bath from 10°C to 20°C .
7. Samples were finally placed in 100% resin for 8 – 10 *h* and in 100% resin with the accelerator BDMA for 8 *h* at room temperature. The resin polymerization occurred at 65°C for 48 *h*.

Note: *The sample preparation protocol was adapted from (Decelle et al. 2019) to optimize the contrast for 3D electron microscopy imaging and therefore facilitate image segmentation.*

Note: *For TEM observations, ultrathin sections (50 – 70 nm) were prepared with an ultra-diamond knife, collected with an appropriate loop, and prepared following the protocol of (Flori et al. 2018).*

²**Chemical fixation:** Denis Falconet PCV - Plant & Cell Physiology laboratory - IRIG /CEA Grenoble

³**Cryo-substitution:** Johan Decelle (PCV), Benoit Gallet , Christine Moriscot, Guy Schoehn - Structural Biology platforms @ IBS - IRIG Grenoble

2.4 FIB-SEM acquisition⁴

FIB tomography was performed with either a Zeiss NVision 40 or a Zeiss CrossBeam 550 microscope, both equipped with the Fibics Atlas 3D software for tomography. The resin block containing cells was fixed on a stub with carbon paste, and surface-abraded with a diamond knife in a microtome to obtain a perfectly flat and clean surface. The entire sample was metalized with 4 nm of platinum to avoid charging during the observations. Inside the FIB, a second platinum layer (1 to 2 μm) was deposited locally on the analysed area. The sample was abraded slice by slice with the Ga^+ ion beam (generally with a current of 700 nA at 30 kV). Every freshly exposed surface was imaged with a SEM at 1.5 kV and with current of ~ 1 nA using the in-lens EsB backscatter detector. For algae, we generally used the simultaneous milling and imaging mode for better stability, with an hourly automatic correction of focus and astigmatism. For every slice, a thickness of a few nm was removed, and the SEM images were recorded with an adequate pixel size to obtain an isotropic voxel size.

2.5 Equipment and software tools

The reagents and equipment needed to prepare cell cultures for EM are described at <https://ncmir.ucsd.edu/sbem-protocol> for chemical fixation and in (Nicolas et al. 2018) for cryo-preparation.

Computers

Linux platform	Windows platform
CPU: 2x Intel Xeon E5-2695 v4 (36 cores total)	CPU: Intel 3.7 GHz (8 cores)
GPU: NVIDIA GeForce 980Ti 6GB	GPU: NVIDIA Quadro P4000 8GB
RAM: 128 GB	RAM: 256 GB
Storage: 4TB HDD	Storage: 2TB PCIe SSD

Software

1. The Fiji program for images pre-processing (cropping in 3D images, image alignment and filtering) can be downloaded [here](#)
2. Fiji(ImageJ v1.53c) additional plugins:
 - a. MultiStackReg for 3D data registration (available [here](#)) MultiStackReg uses TurboStackReg Plugin. You can download the [TurboStackReg](#) plugin and drop it directly in the plugin folder.
 - b. Template Matching and Slice Alignment for 3D data registration (available [here](#)).
 - c. 3D Object counters for multiple objects counting (download [here](#)).
3. [3 DSlicer 4.10.0](#) software for segmentation.

⁴**FIB-SEM acquisition:** Pierre-Henri Jouneau - The Nanocharacterization platform - IRIG Grenoble - Rachel Templin, Nicole Schieber, Yannick Schwab - Electron Microscopy Core Facility- EMBL-Heidelberg

4. [MeshLab v1.3.2 – 64bit](#) for 3D model editing/cleaning/re-meshing.
5. [Paraview 5.7.0](#) to capture a 2D representation of 3D dimension of cell ultrastructure.
6. [Blender 2.82](#) for animation using its [BlendLuxCore 2.3](#) module.
7. [Python 2.7.12](#).
8. Python modules:
 - **Matplotlib**: for data plotting and visualization (<https://matplotlib.org/>).
 - **NumPy**: N-dimensional linear algebra library (www.numpy.org/).
 - **STL**: access to geometry data of the STL format (<https://pypi.org/project/numpy-stl/>).
 - **Trimesh**: load and handle triangular meshes with an emphasis on watertight surfaces (<https://trimsh.org/install.html>).
 - **SciPy**: for image processing and interpolation (<https://www.scipy.org/>).

2.6 Image processing and 3D reconstruction

To get high quality 3D tomograms, it is crucial to have high quality samples for EM acquisition but also to correctly perform the image acquisition process. A poor sample preparation or a poor image acquisition leads to a poor representation of the sample, ultimately biasing any attempt to perform quantitative analysis.

FIB-SEM acquisition produces large datasets, which need to be simplified to get rid of useless information for image analysis. The acquisition methods automatically generate 3D images with good z -axis resolution with an isotropic voxel size. Most of the time, data need minimal image registration and a few steps to extract information from the 3D data.

Conversely, SBF-SEM images produce 3D data having big slice depth with a small $x - y$ pixel size. These features generate an anisotropic voxel (Gu erin et al. 2019). Therefore, yielding data needs additional image registration to realign the slices in data volume.

Both techniques produce huge datasets (between 50 to 100 GB), while existing softwares for 3D reconstruction can only efficiently handle datasets around 1 GB. Therefore, as a first step of data analysis, we need to find a way to extract smaller data volumes, while preserving the image details. This requires investigating the images content before starting the segmentation process. The pipeline I designed for this purpose includes noise reduction, feature extraction, 3D reconstruction and quantitative analysis.

2.6.1 Image pre-processing methods

The image pre-processing step has the role of ‘improving’ images by enhancing contrast or by highlighting important features. This step also includes stack registration and noise reduction with the overall purpose of facilitating the user in the process of identifying and

characterizing Regions Of Interest (ROIs). Using some plugins of Fiji, we can display images features, adapt settings to improve image resolution and perform stack registration.

Adjust image parameter settings.

1. Upload images sequences in Fiji by selecting “*File* → *import* → *Image sequences*”. In the sequence window check “*virtual stack*” mode → *press ok* (see Figure 2.1).

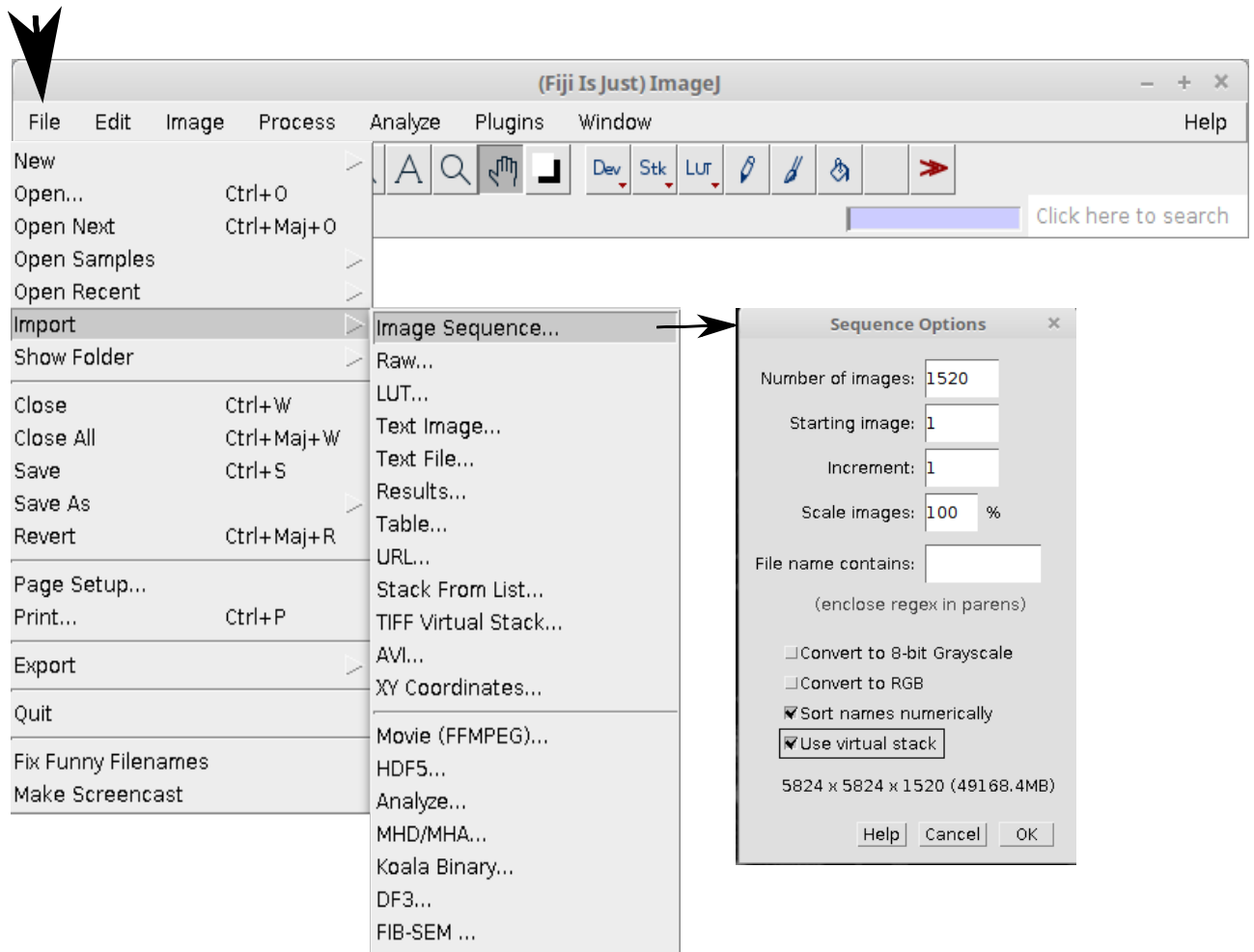


Figure 2.1 – Open image sequences in Fiji.

2. The volume of interest is isolated by specifying a landmark in an area of the current displayed image and right clicking on the mouse to select “*crop* → *check duplicate the stack*”. This technique helps creating a sub-stack without losing the displayed raw data in the virtual stack mode.
3. Set the voxel size information in “*Image* → *Properties*” (see Figure 2.2).

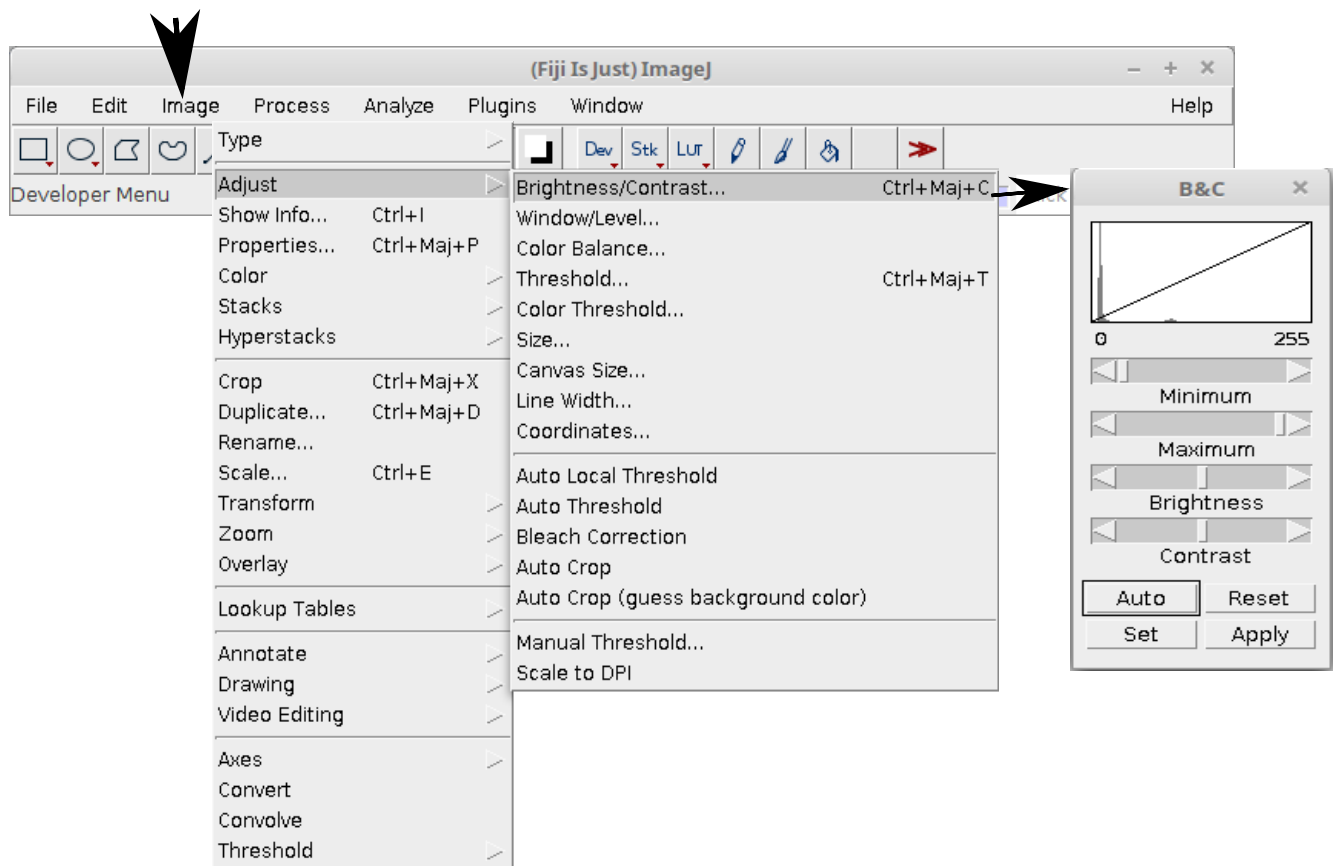


Figure 2.2 – Add voxel size information in Fiji.

Image features enhancement, observation and compression.

4. An image is an array of multi-dimensional points and every dimension represents a spatial dimension (the height, the width and the thickness) and resolution. For an image of two dimensions, the points are “pixels” while in three-dimensional, the points are “voxels”. The image resolution is the number of pixels per length normally represented as *dpi* (*dots per inch*). When the *dpi* is high, the image content and feature are important. To adjust “*dpi*” go to “*Image* → *Adjust* → *scale to dpi*”.
5. FIB-SEM/SBF-SEM acquires 16-bit colour images. This means that in 16-bit images, there are $2^{16} = 65536$ possible grey values per pixel. Working with 16-bit images requires managing large file size. 16-bit images can be reduced to 8-bit images in Fiji by choosing “*Image* → *Type* → 8-bit”. 8-bit images are “cheaper” in memory and represent images with only $2^8 = 256$ grey values for every pixel, effectively dividing required memory by two (see Figure 2.3).

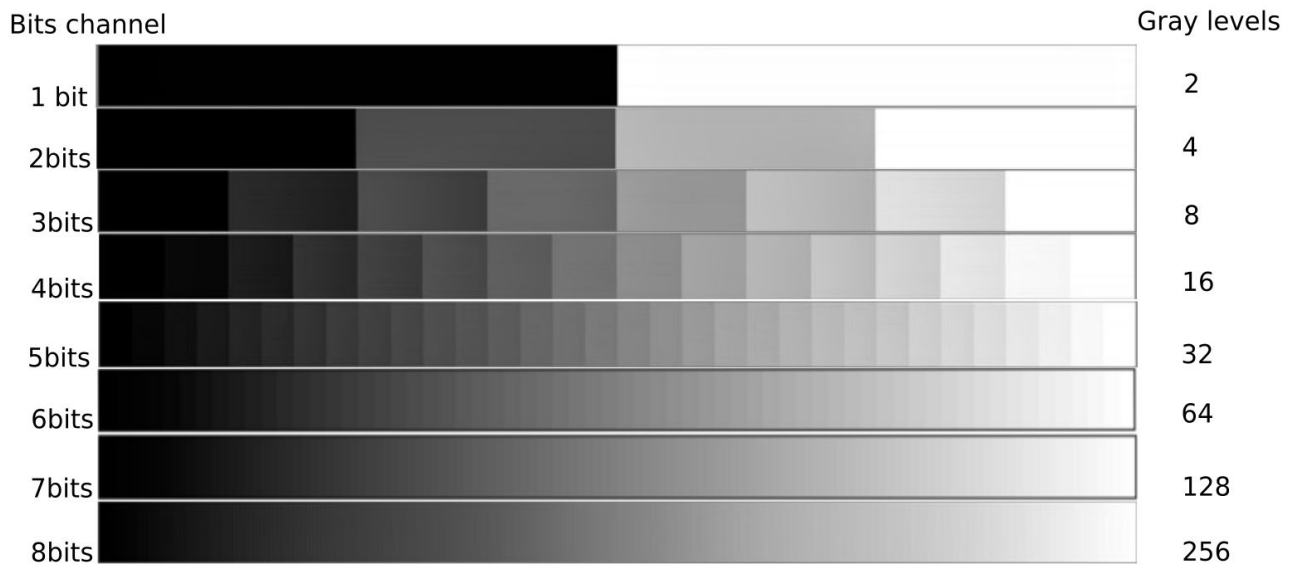


Figure 2.3 – Grey-shading toners from black to white just as the bits channel.

- EM images vary significantly in terms of pixel intensities from one area to another. For example, in one image we distinguish groups of global properties, which are easy to distinguish based on image histogram analysis, and local properties, which are undistinguishable (“*Analyze* → *Histogram*”, see Figure 2.4). Image histogram allows visualizing the distribution of the number of pixels in terms of their grey values and histogram thresholding is important in the segmentation process. However, the image histogram provides only quantitative information.

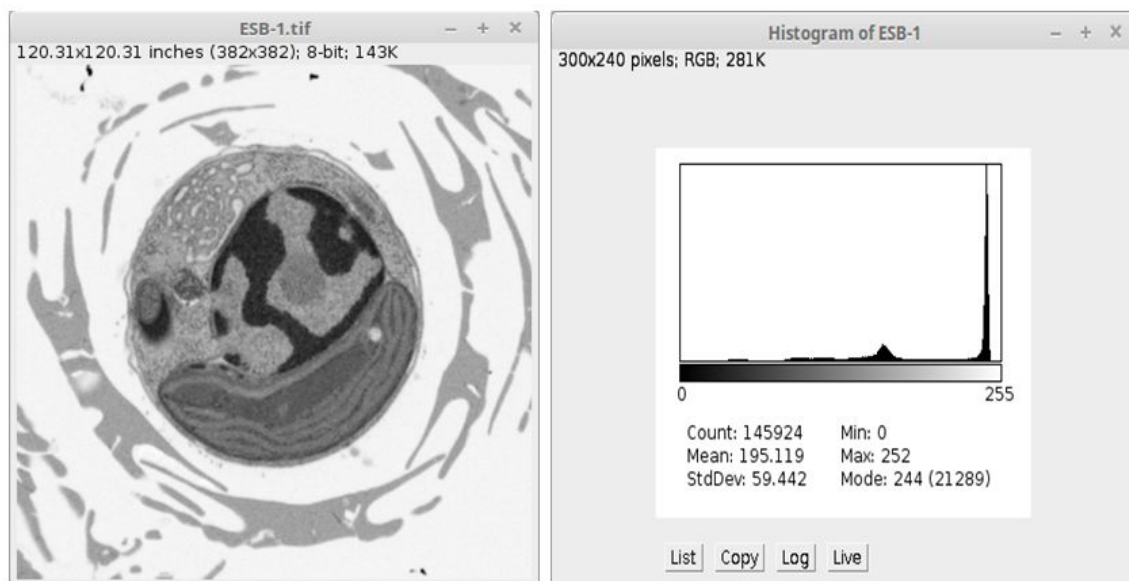


Figure 2.4 – Grey image and the graphic representation of values distribution.

- Image contrast is increased by the “*Image → Adjust → Brightness/contrast*” module to visualize and distinguish black and white by remapping the pixels values of the image to the (minimum, maximum, brightness or contrast) range of the data type (see Figure 2.5).

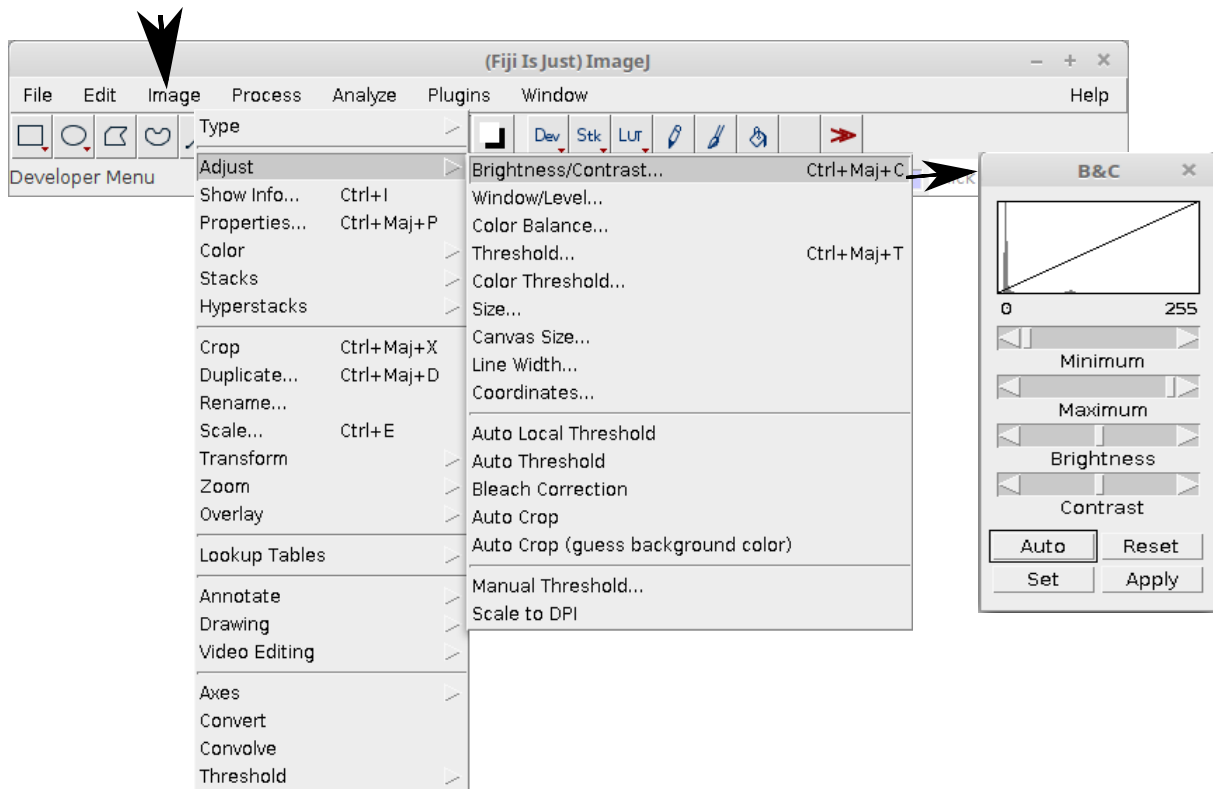


Figure 2.5 – Adjust image contrast in Fiji. Brightness-contrast window and contrast adjustment in the range of the data type.

- Depending on the image, we may want to give more weight to features strongly represented, with the “*Process / Enhance Contrast*” module and perform “*histogram equalization*”. This function increases the image contrast by equalizing histogram. It is also possible to set the “%” number of pixel saturation in the “*Saturated Pixels boxfg*”. When the “normalize” and “*equalize Histogram*” options are not checked, the pixel intensity is not changed.
- EM images must have a scale bar to give a clear visual indication of the size of the content. A scale bar is added to the image, by drawing a line on a specific location and choosing the “*Analyze → Tools Scale Bar*” module. The opened window will ask to add the scale bar and to adjust the settings at will.

Registration

- Preview the z-stack alignment in Fiji by opening “*Image → Stacks → orthogonal views*”(see Figure 2.6).

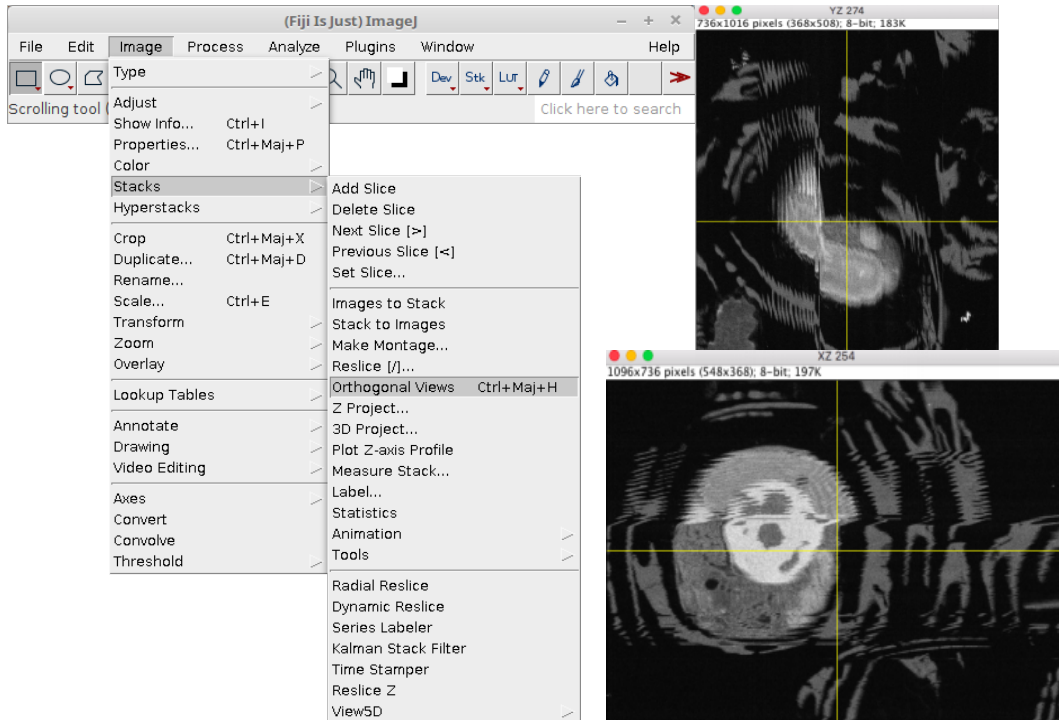


Figure 2.6 – z-stack preview in Fiji using the orthogonal view module.

2. If the z-stack is misaligned, find the proposed registration methods in Fiji choosing “*Plugins* → *Registration* → define the alignment methods”. Stack registration methods proposed in Fiji use different image transformation as shown below (Table 2.1).

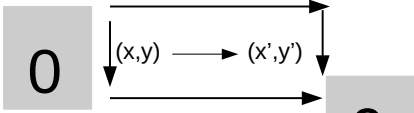
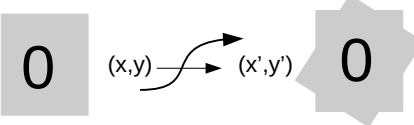
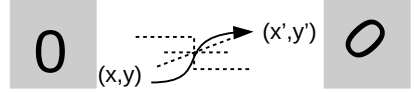
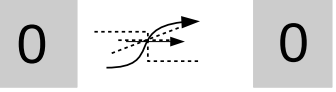
Translation	Rigid body
 <p>Image located at (x,y) in the original coordinate is shifted to a new position (x',y')</p>	 <p>Image which located at (x,y) in the original coordinate is rotated with an angle θ and shifted to the new position (x',y') while keeping the arrangements unchanged</p>
Affine	Similarity
 <p>Image which located at (x,y) in the original coordinate is projected to the new position (x',y'), by combining shift, turn with an angle θ, scale and shear operators.</p>	 <p>Image which located at (x,y) in the original coordinate is projected to the new position (x',y') by either rotation, translation, scaling, or reflection, without modifying the shape. It means that what is straight remain straight, and parallel lines remain parallel.</p>

Table 2.1 – The transformation methods provided in registration plugins of Fiji.

Example of the stack registration methods:

3. **Template matching plugin for Fiji.** The method works on a given landmark on the displayed image, which is taken as a reference slice. Use “*plugins* → *Template matching* → *run Align slices*” and matches with normalized correlation coefficient. Try subpixel displacements with bilinear interpolation to obtain best possible registration (Figure 2.7). Verify *z*-stack registration. If the stack is still incorrectly aligned, keep launching template matching mode until *z*-stack is correctly aligned.

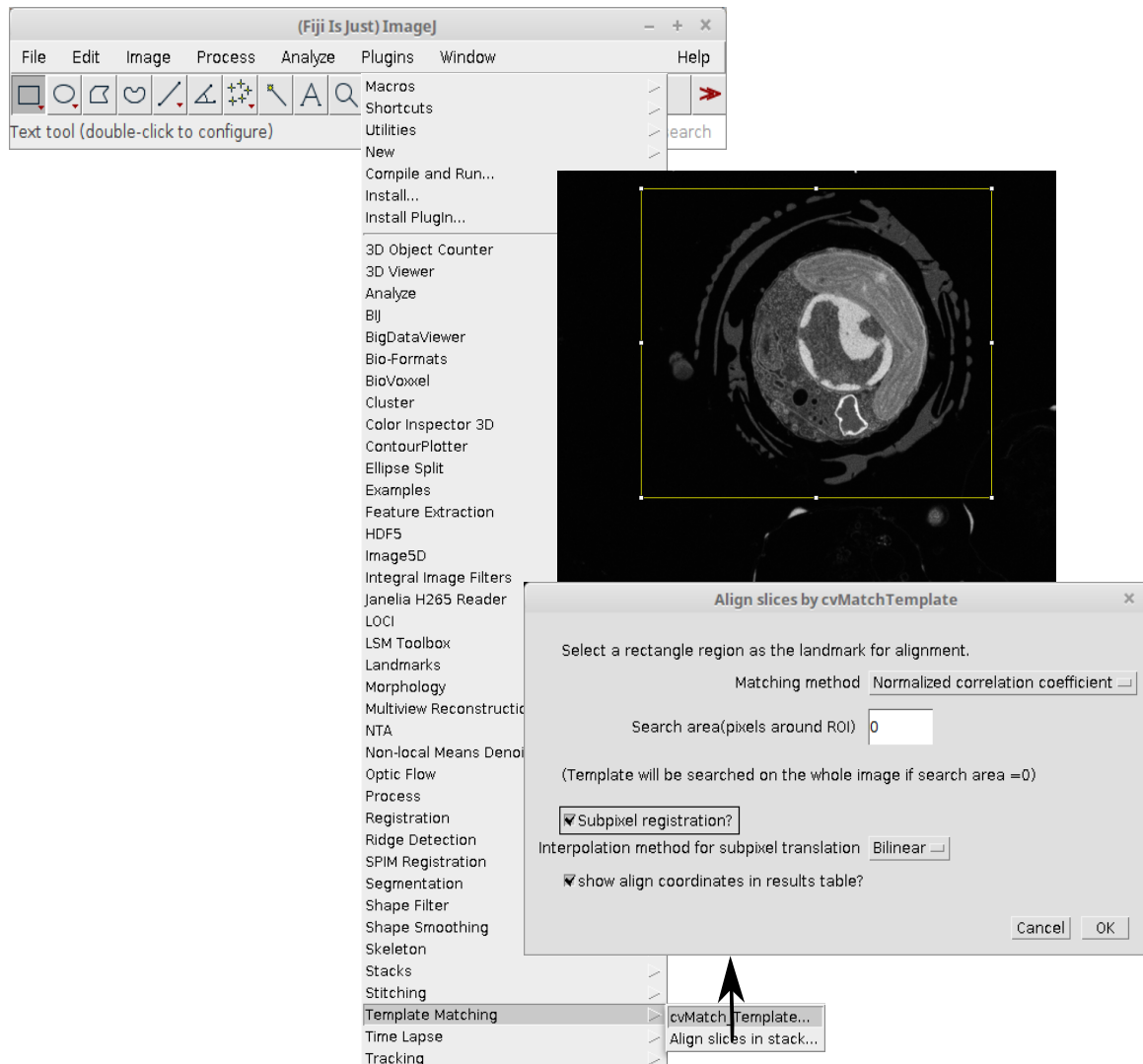


Figure 2.7 – Alignment with template matching. Stack registration using the template matching additional plugin from Fiji.

4. **Linear stack Alignment with SIFT from Fiji.** This method works by: (i) Selecting “*Plugin* → *Registration* → *Linear stack Alignment with SIFT*” (ii) Choosing appropriate image transformation methods (Table 2.1) and (iii) Defining the parameters (Figure

2.8). For more information on how to adjust the parameters and their meaning read details “[here](#)”. After each alignment round, verify the z-stack.

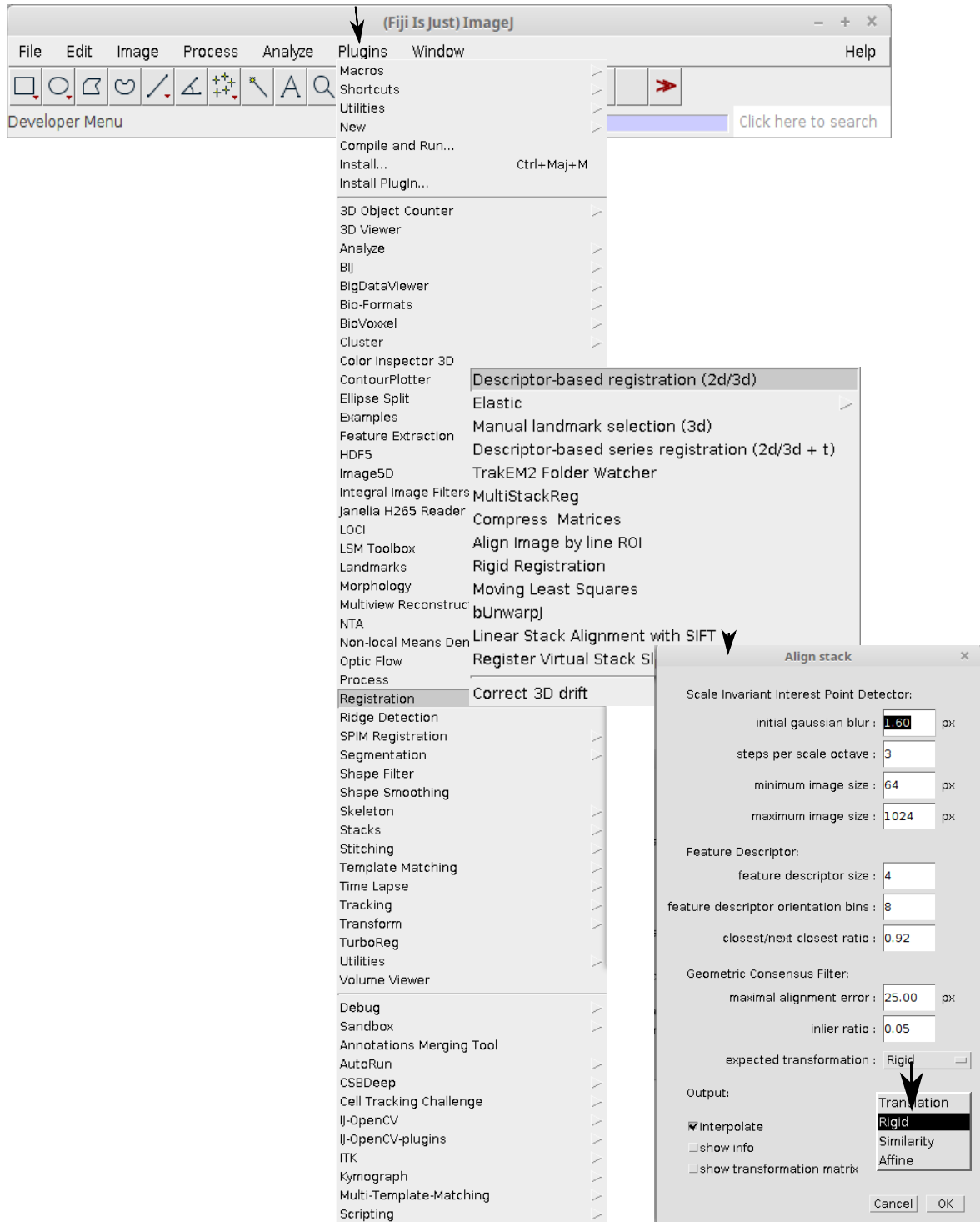


Figure 2.8 – Alignment with SIFT. Stack registration using Linear Stack Alignment with SIFT from Fiji.

5. **MultiStackReg plugin for Fiji.** The module works by selecting “*Plugin* → *Registration* → *MultiStackReg*” and choosing image transformation methods (see Figure 2.9 and Table 2.1).

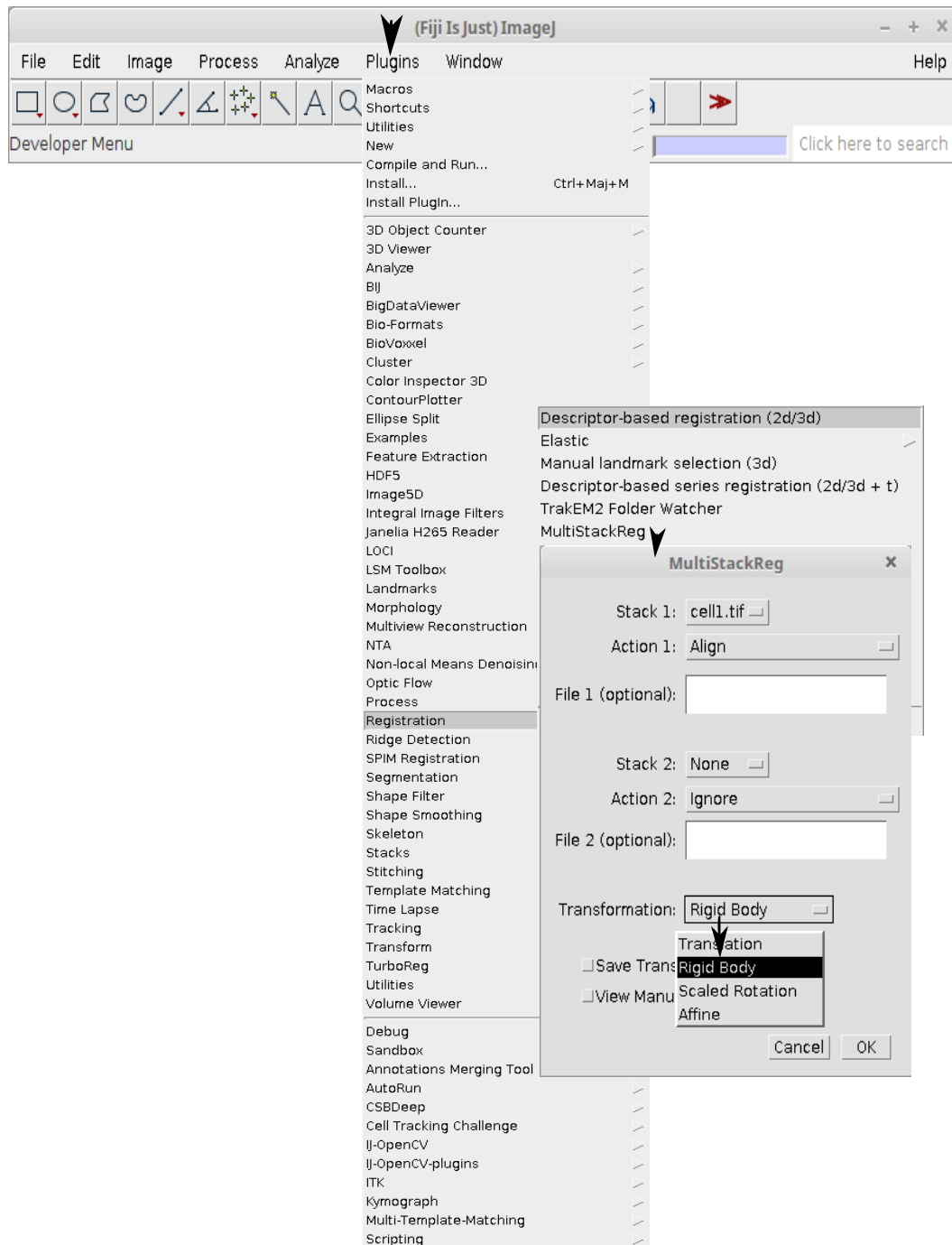


Figure 2.9 – Alignment with MultiStackReg. Stack registration using MultiStackReg additional plugin from Fiji.

Image filtering

1. *Binning transformation* is the process that works by regrouping adjacent pixels either by average, sum, or median methods, depending on the binning factor. In Fiji, a binning transformation for a big stack file is done using: “*Image* → *Transformation* → *Bin.*” and applying an average method. Binning by $2 \times 2 \times 2$ will reduce the stack by a factor of 2^3 and binning by $3 \times 3 \times 3$ reduces the stack by a factor of 3^3 . Binning method helps attenuating random image noise as well. Depending on the image content, the binning transformation provides a stack that can be further processed without applying any additional filter.

Several filtering methods exist for EM images, e.g. the work of Sim and collaborators on noise types in EM images (Sim et al. 2004a), and noise variation estimation (Sim et al. 2004b). Noise can be reduced using either a linear or a nonlinear filter. In most cases, the decision on ‘good’ or ‘bad quality’ images depends on human eyes. Despite this, “*the intensity profile*” module of Fiji can help evaluating the extent of ‘damage’ done on a given image every time its content is modified.

2. *The intensity profile of an image* is obtained using the profile plots function of Fiji. After drawing a line in a specific area, go to “*Analyze* → *plot profile*”. A plot describing the variation of the grey values at that location will appear. If the grey values of a ROI show sharp changes near the edges, that edge is identifiable using the first order derivative methods (see Figure 2.10).
3. Fiji proposes linear and nonlinear filters accessible in the “*Process* → *Filters* → *select filters*” module. Every selected filter will ask to define the window size. Different filters have advantages and drawbacks.

For example, (see Figure 2.11), when the window size becomes too large for the Gaussian filter, additional blurs appear in the image and edges are less visible. The median filter completely removes ‘shot noises’ without attenuating significantly the edges. When the histogram equalization is applied to both Gaussian and median filters, a small change in image observability is found. This change reflects the reorganisation of the density distribution of the grey value of the image. Therefore, it can be difficult to detect and localize the contour of the objects. In this case, image derivative methods can help to detect object contours in the image.

Note: *in some cases, binning should be avoided because the high-resolution information is modified or lost.*

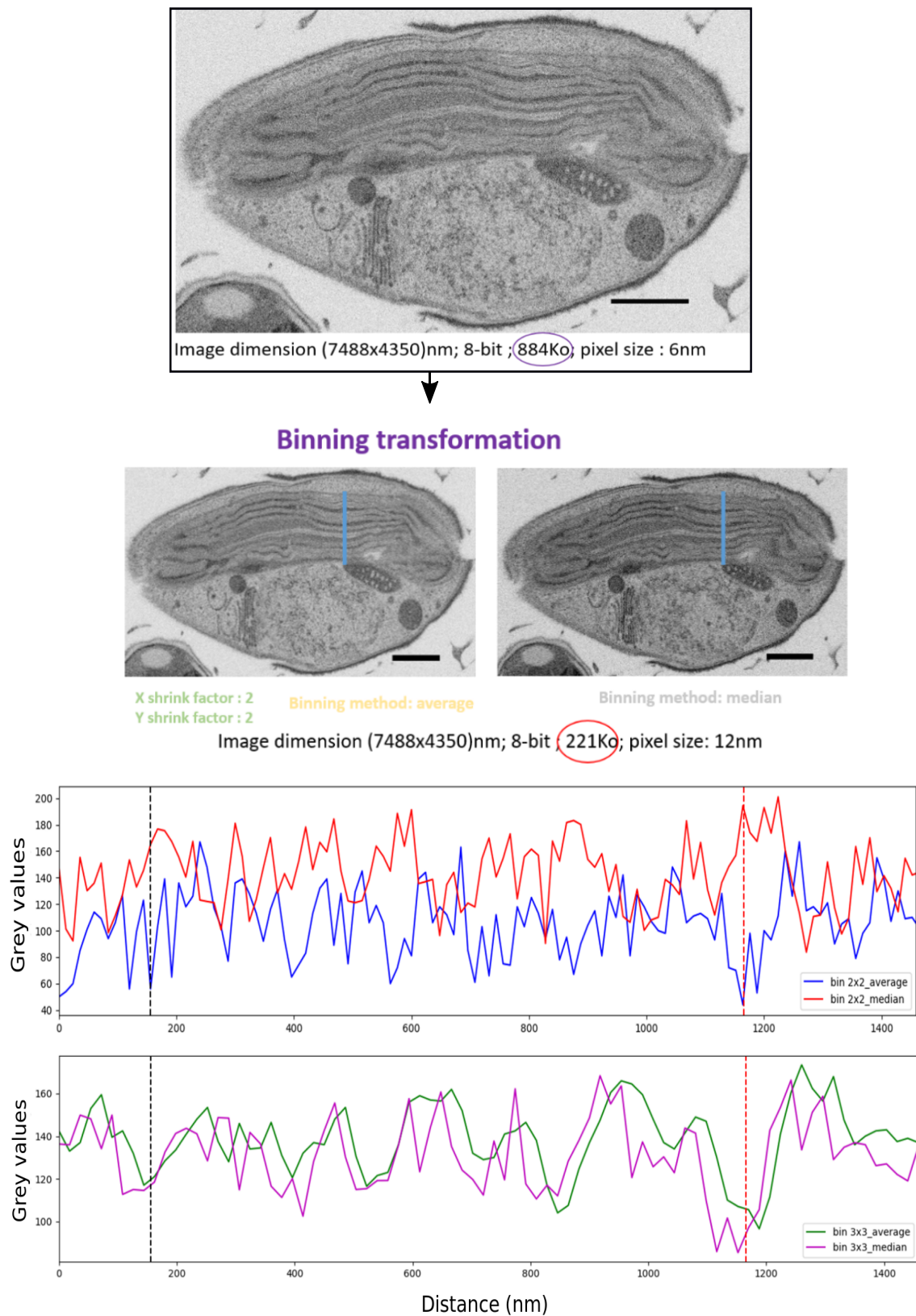


Figure 2.10 – 2D FIB-SEM images were binned using different regrouping factor methods. A line (in blue) of 1458 nm scans through the 2D slices in an area. The profile analysis represents the variation of grey values and local binning-impact.

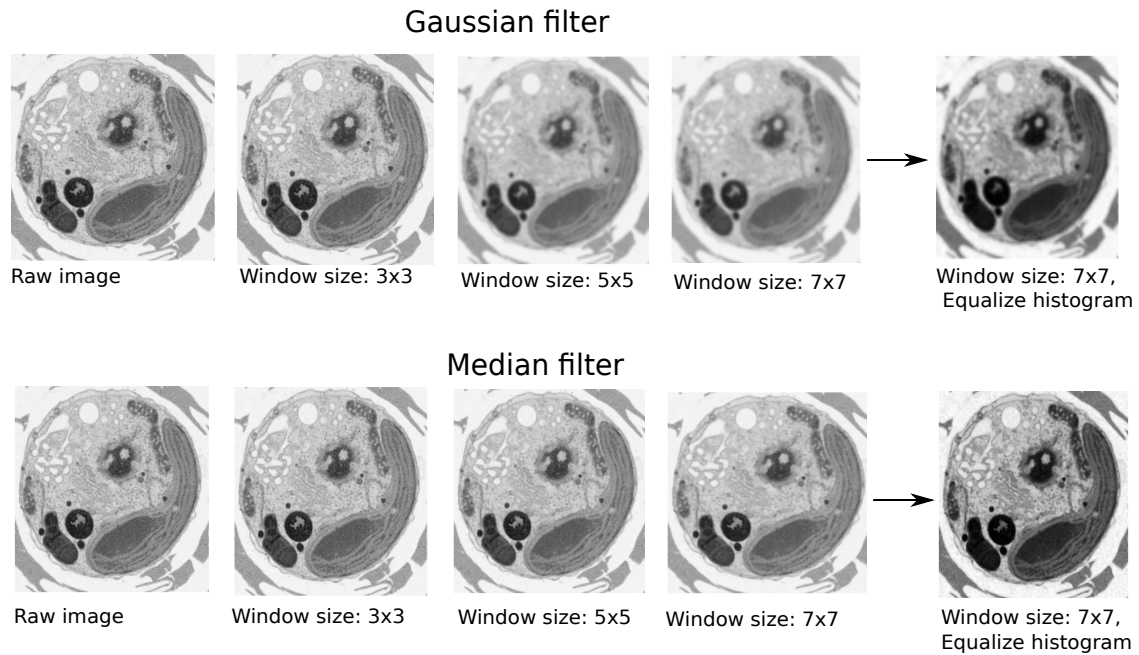


Figure 2.11 – Comparison of the image filtering methods. Gaussian and Median filters with a different window size.

4. *Image derivative for edge detection.* The edge based technique consists in identifying high variation intensities (edges or contours) through the so-called “first-order derivative” of the image function. We compute, image derivative by convolving the original image with a specific kernel.

2D Convolution

$$\begin{array}{c}
 \begin{bmatrix} 1 & 4 & 3 & 2 & 1 \\ 0 & 5 & 1 & 1 & 0 \\ 1 & 2 & 2 & 2 & 1 \\ 7 & 5 & 6 & 1 & 2 \\ 1 & 1 & 2 & 2 & 2 \end{bmatrix} \\
 \text{Original image}
 \end{array}
 *
 \begin{array}{c}
 \begin{bmatrix} -1 & -1 & -1 \\ -1 & 15 & -1 \\ -1 & -1 & -1 \end{bmatrix} \\
 \text{Kernel: Edge enhancement}
 \end{array}
 =
 \begin{array}{c}
 \begin{bmatrix} 6 & 50 & 32 & 24 & 12 \\ -10 & 61 & -6 & 3 & -7 \\ -4 & 3 & 7 & 16 & 9 \\ 95 & 53 & 73 & -4 & 22 \\ 2 & -6 & 15 & 17 & 25 \end{bmatrix} \\
 \text{Output image}
 \end{array}
 \quad (2.1)$$

How to calculate a 2D convolution manually?

We add outside pixels (0–padding), then we overlap the kernel over the image, advancing pixel-by- pixel.

$$\begin{bmatrix} 0 & 0 & 0 & 0 & 0 & 0 & 0 \\ 0 & 1 & 4 & 3 & 2 & 1 & 0 \\ 0 & 0 & 5 & 1 & 1 & 0 & 0 \\ 0 & 1 & 2 & 2 & 2 & 1 & 0 \\ 0 & 7 & 5 & 6 & 1 & 2 & 0 \\ 0 & 1 & 1 & 2 & 2 & 2 & 0 \\ 0 & 0 & 0 & 0 & 0 & 0 & 0 \end{bmatrix} \quad \begin{matrix} \text{Image}_{1,1} \\ \begin{bmatrix} 0 & 0 & 0 \\ 0 & 1 & 4 \\ 0 & 0 & 5 \end{bmatrix} \end{matrix} * \begin{matrix} \text{Kernel} \\ \begin{bmatrix} -1 & -1 & -1 \\ -1 & 15 & -1 \\ -1 & -1 & -1 \end{bmatrix} \end{matrix}$$

$$\begin{aligned} \text{Im}_{1,1} &= 0 * (-1) + 0 * (-1) + 0 * (-1) + 0 * (-1) + 1 * 15 + \\ &= (-1) * 4 + 0 * (-1) + 0 * (-1) + 5 * (-1) \\ &= 6 \end{aligned}$$

$$\begin{aligned} \text{Im}_{1,2} &= 0 * (-1) + 0 * (-1) + 0 * (-1) + 1 * (-1) + 4 * 15 + \\ &= 3 * (-1) + 0 * (-1) + 5 * (-1) + 1 * (-1) \\ &= 50 \end{aligned}$$

$$\begin{aligned} \text{Im}_{1,3} &= 0 * (-1) + 0 * (-1) + 0 * (-1) + 4 * (-1) + 3 * 15 + \\ &= 2 * (-1) + 5 * (-1) + 1 * (-1) + 1 * (-1) \\ &= 32 \end{aligned}$$

⋮

$$\begin{aligned} \text{Im}_{5,5} &= 1 * (-1) + 2 * (-1) + 0 * (-1) + 2 * (-1) + 2 * 15 + \\ &= 0 * (-1) + 0 * (-1) + 0 * (-1) + 0 * (-1) \\ &= 25 \end{aligned}$$

$$\begin{bmatrix} \text{Im}_{1,1} & \text{Im}_{1,2} & \text{Im}_{1,3} & \text{Im}_{1,4} & \text{Im}_{1,5} \\ \text{Im}_{2,1} & \text{Im}_{2,2} & \text{Im}_{2,3} & \text{Im}_{2,4} & \text{Im}_{2,5} \\ \text{Im}_{3,1} & \text{Im}_{3,2} & \text{Im}_{3,3} & \text{Im}_{3,4} & \text{Im}_{3,5} \\ \text{Im}_{4,1} & \text{Im}_{4,2} & \text{Im}_{4,3} & \text{Im}_{4,4} & \text{Im}_{4,5} \\ \text{Im}_{5,1} & \text{Im}_{5,2} & \text{Im}_{5,3} & \text{Im}_{5,4} & \text{Im}_{5,5} \end{bmatrix} = \begin{bmatrix} 6 & 50 & 32 & 24 & 12 \\ -10 & 61 & -6 & 3 & -7 \\ -4 & 3 & 7 & 16 & 9 \\ 95 & 53 & 73 & -4 & 22 \\ 2 & -6 & 15 & 17 & 25 \end{bmatrix}$$

The results will depend on the choice of the kernel. The common edge operators used in image processing are “Roberts, Prewitt and Sobel (see below) and Robinson (not shown)” (Gonzalez et al. 2002; Haralick et al. 1985; Rogowska 2000).

$$\begin{matrix} \text{Roberts} & & \text{Prewitt} & & \text{Sobel} \\ \begin{bmatrix} 0 & -1 \\ 1 & 0 \end{bmatrix} \begin{bmatrix} 1 & 0 \\ 0 & -1 \end{bmatrix} & & \begin{bmatrix} -1 & 0 & 1 \\ -1 & 0 & 1 \\ -1 & 0 & 1 \end{bmatrix} \begin{bmatrix} -1 & -1 & -1 \\ 0 & 0 & 0 \\ 1 & 1 & 1 \end{bmatrix} & & \begin{bmatrix} -1 & 0 & 1 \\ -2 & 0 & 2 \\ -1 & 0 & 1 \end{bmatrix} \begin{bmatrix} -1 & -2 & -1 \\ 0 & 0 & 0 \\ 1 & 2 & 1 \end{bmatrix} \end{matrix} \quad (2.2)$$

G_y G_x G_y G_x G_y G_x

The edge strength is given by the gradient magnitude $|G| = \sqrt{(G_x^2 + G_y^2)}$ to give the approximations of the first derivative (Malathi et al. 2011). Therefore, when it is difficult to define an image contour, the object contours can be sharpened either by combining edge-enhanced images with the original image (Table 2.2) or by convoluting the original image with the sharpen kernel to help the user eyes to identify the object boundaries.

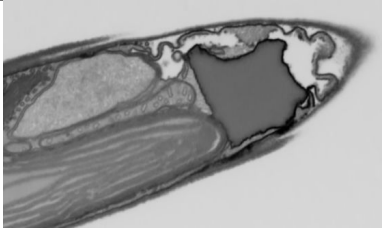
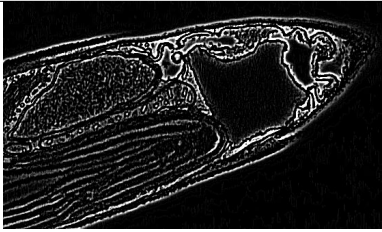
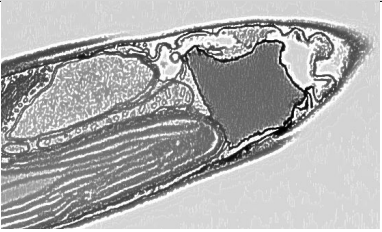
Original image	Edge enhancement kernel
	$\begin{pmatrix} -1 & -1 & -1 & -1 & -1 \\ -1 & -1 & -1 & -1 & -1 \\ -1 & -1 & 24 & -1 & -1 \\ -1 & -1 & -1 & -1 & -1 \\ -1 & -1 & -1 & -1 & -1 \end{pmatrix}$
Im = Original * Kernel	(Original + Im)
	

Table 2.2 – The transformation methods provided in registration plugins of Fiji.

In Fiji, image convolution is computed with “*Process* → *Filters* → *Convolve*” (Figure 2.12).

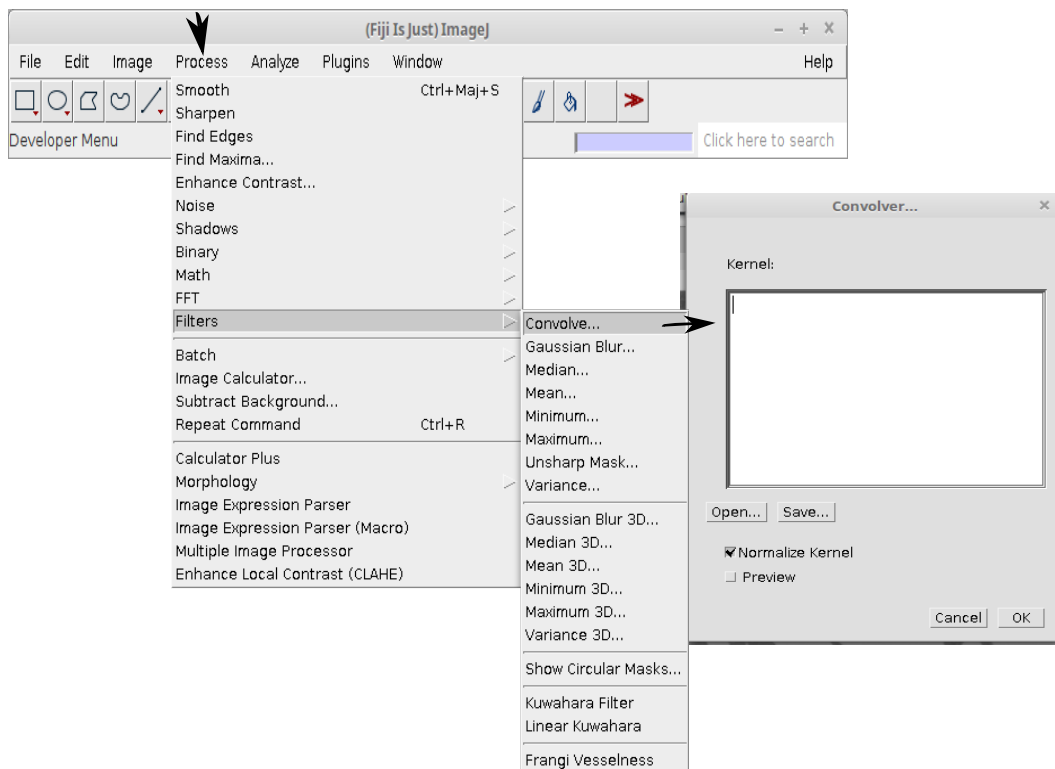


Figure 2.12 – Image convolution using a specific kernel in Fiji.

2.6.2 Segmentation and 3D reconstruction

Segmentation techniques are defined depending on object characteristic and classification design. We distinguish: manual, semi-automatic, and automatic techniques (Suetens et al. 1993), which use pixel-based or region-based selection methods (for a review see (Awcock et al. 1995; Rajapakse et al. 1997)). The thresholding technique classifies global methods based on grey-level histograms and global methods are based on local properties (Pal et al. 1993).

Objects classification

To process EM images, we need an adaptive segmentation method to process all datasets in the same way, to ensure data reproducibility and allow data comparison between species or within cells. The datasets analysed in this PhD project contain different cell types with different features. The goal is therefore to isolate Volumes Of Interest (VOI), annotate Areas Of Interest (AOI) and, finally, to link these regions to specific cellular and subcellular features in order to reconstruct a corresponding three-dimensional representation of the cell.

Manual segmentation

A manual pixel classification using the segmentation plugin “TrakEM2” of Fiji was tested. This technique was useful to process small stacks of few images (Cardona et al. 2012). The method consists in using the brush tool to draw an outline around the selected object in the image and then, fill the object area by using the keyboard and the mouse. The process is iteratively repeated on the next slices (for more details see (Cocks et al. 2018)). This method is labour-intensive to build a 3D model from 2000 images. It was therefore replaced by an automatic segmentation of the AOI.

Automatic segmentation

I tested an automatic segmentation process using the “*autocontext*” module of Ilastik to speed up the segmentation (Kreshuk et al. 2011; Tu et al. 2009). This module allows annotating the AOI in two steps. The first step is to separate the AOI from other structures using a pixel classification module (the extracted region does not have to be perfect and can be used as a training dataset). The second step uses the training dataset to select the region vs. the background. This technique was used to segment synaptic contacts and the quantitative validation of the automatic detection of synapse (Kreshuk et al. 2011). I noticed that this process is particularly greedy in RAM and pretty slow for both steps. Indeed, it was difficult to individualize cell features within an image stack containing mixtures of cells from different species. Moreover, some features (i.e., membranes and intracellular structures of small cells) were difficult to extract. Hence, the semi-automatic segmentation turned out to be the best choice to annotate the AOIs independently and perform quantitative analysis.

Semi-automatic segmentation

To avoid problems of low contrast and a large variation in pixel intensities of AOI, image pre-processing was performed to improve image visibility. Based on the notion that all pixels in a given AOI share a common property, thresholding methods were used to extract objects with respect to the pixel intensities range of grey values.

Global thresholding

Let $I(x, y)$ be the image with global properties represented in the histogram (Figure 2.13 A-C), the easiest way to extract the AOI from the background is to set the pixel intensity at a thresholding range “ T ” which separates the two regions (Figure 2.13). Therefore, the segmentation of the AOI will be defined as:

$$M_{ij} = \begin{cases} 1 & \text{if } I_{ij} \in [v_{\min}, v_{\max}] \\ 0 & \text{Otherwise} \end{cases} \quad (2.3)$$

The result is a binary image M (image mask) where the pixels with “1” value correspond to the AOI while those with “0” reflect the background. When an image contains more than two types of AOI with almost the same intensity, the histogram modes fail to separate regions, and the threshold selection becomes difficult. However, it is still possible to split the image into patches and set sub-thresholding range (see Figure 2.13).

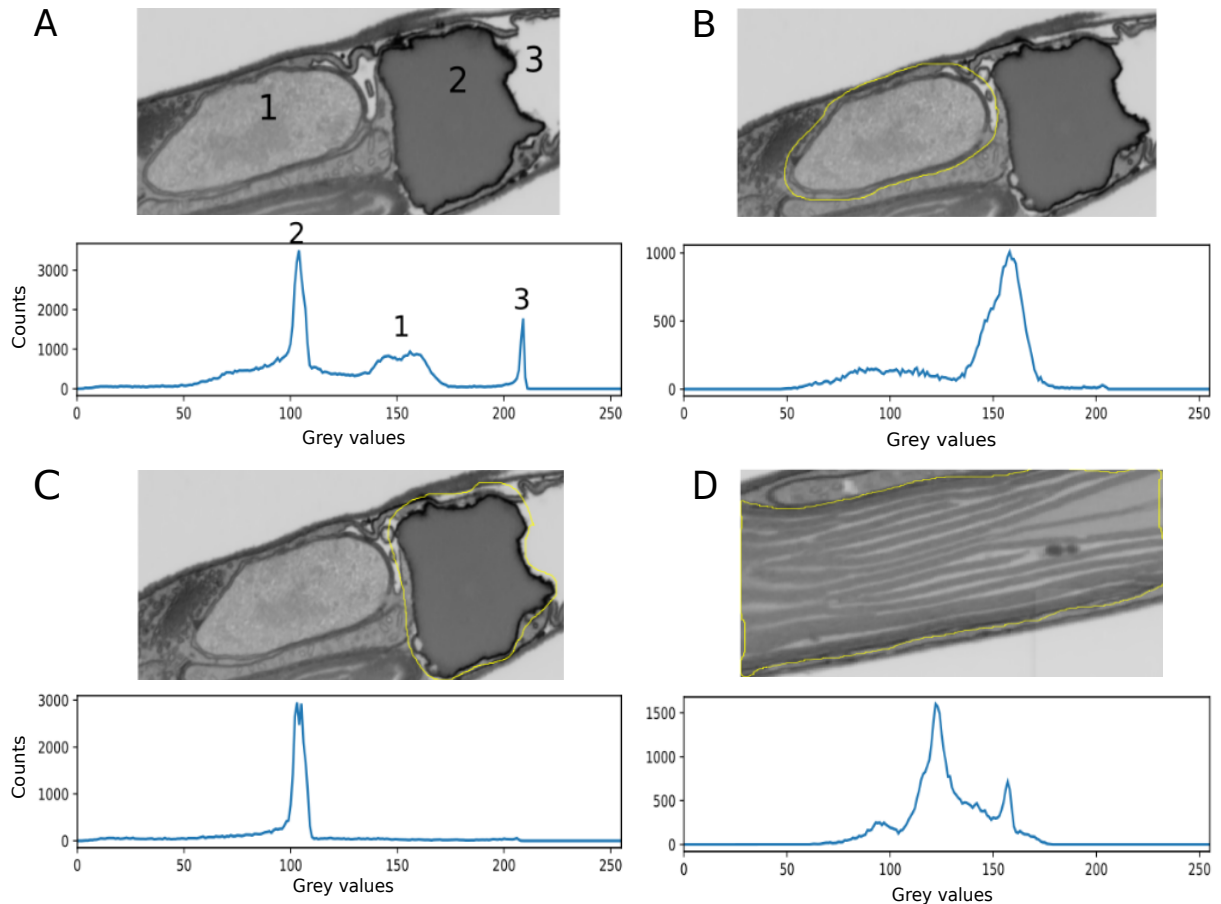


Figure 2.13 – Grey images and histograms highlighting the distribution of grey values in AOI. (A-D) illustrate the different image contents and AOIs characteristics.

Note: *If the background pixel intensities vary significantly across the image (see Figure 2.13 D) or if AOIs have low contrast the thresholding method fails. Therefore, a manual segmentation is advisable. In this situation it may also be worth trying adaptive thresholding.*

Adaptive thresholding

When image characteristics contain a heterogeneous grey value distribution in the background and structures that vary across the image (see Figure 2.13 D), the thresholding method well in one part of the image, will provide unsatisfactory results for other areas. In this case, it is important to get insight on the grey values distribution to correctly set the thresholding range or add missing pixels manually. To do that, it is crucial to use a segmentation software that offers possibilities to remove easily or add misclassified pixels and avoid the under/overestimation of AOI.

To perform supervised semi-automatic segmentation we use the 3Dslicer software (Fedorov et al. 2012). Among the different modules contained in the 3DSlicer software platform (see Figure 2.14), we have chosen to present only those that will help to speed up the segmentation process.

Note: *for other usages, please refer to [the tutorial training](#).*

Segmentation using the Editor module of 3D Slicer

The Editor module of 3D Slicer was used to segment a complete tomogram of 3D EM data. To segment correctly the AOI, we have developed a technique based on image characteristics to optimize the thresholding ranges selection.

1. Using 3D Slicer, import data volume (.tiff format) “→ *Load data module* → *choose the file to add*”. The module displays in the three windows the image volume in axial (XY), sagittal (YZ) and coronal (XZ) views. Adjust the image contrast for better visibility by ticking in any window and scroll the mouse from the top to bottom.
2. Set voxel size information using “*welcome to slice module* → *volume* → *add voxel size information*” in the image spacing window and press “*center volume*” to set data volume to the origin coordinate (Figure 2.14).

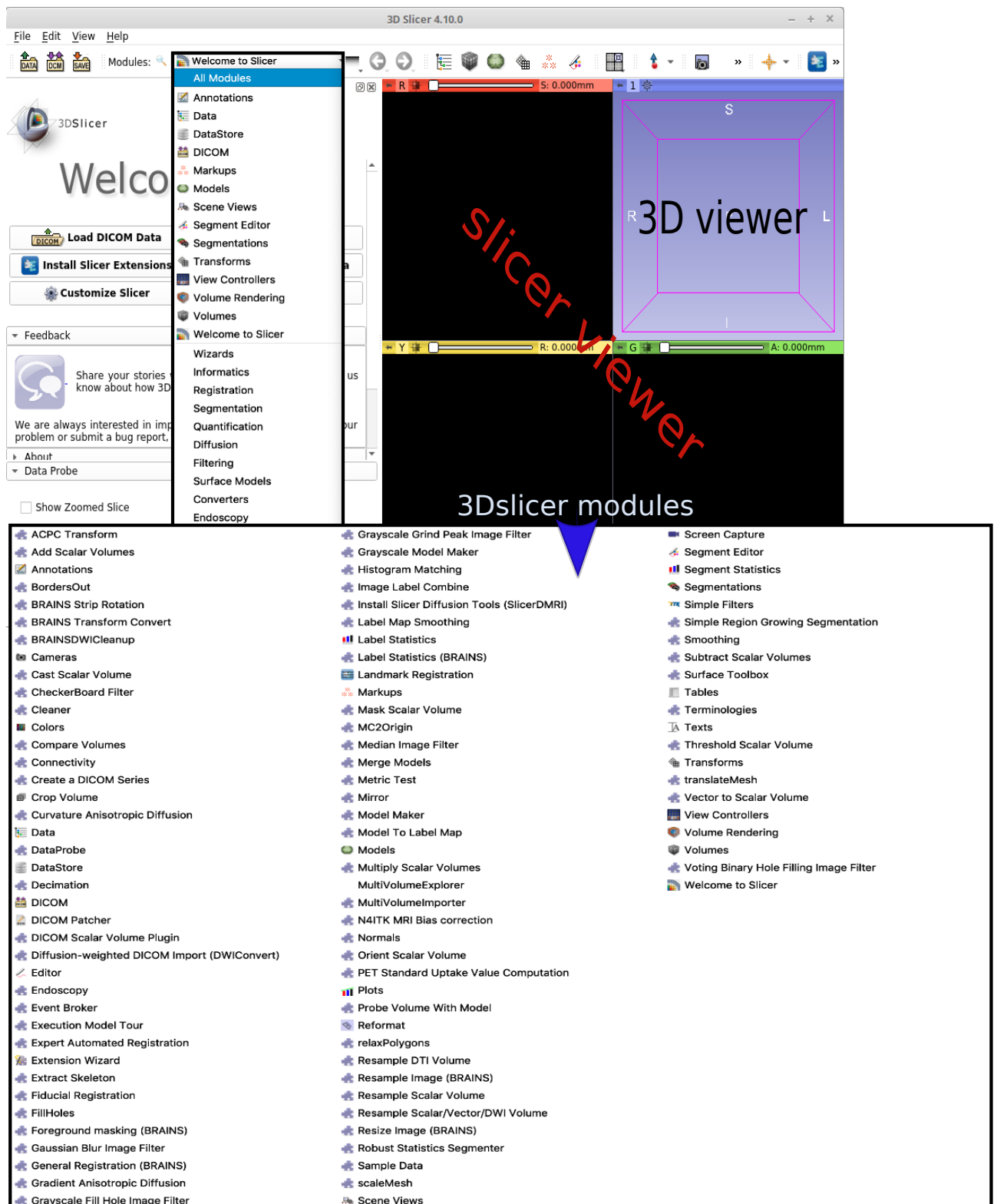


Figure 2.14 – Representation of 3D Slicer interface. The interface represents different view modes: the axial ($z - y$ plane) in red, the sagittal ($y - z$ plane) in yellow and the coronal ($x - z$ plane) in green (view together with all welcome modules).

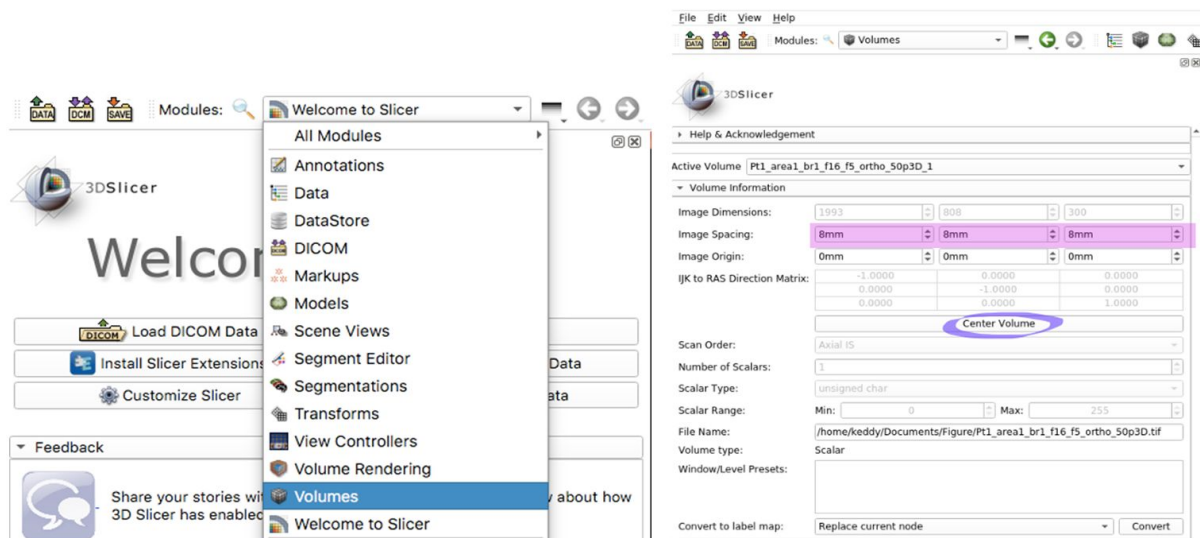


Figure 2.15 – The volume module includes many possibilities to adjust image settings.

Note: When one changes the properties of the unity in 3D Slicer, the software changes only the displayed values. So, it is simple if the pixel unity of the image equal to the default unity “mm” (i.e. $8 \text{ nm} = 8 \text{ mm}$ or $5 \text{ }\mu\text{m} = 5 \text{ mm}$).

3. Run the editor module selecting “welcome to slice module → Editor”. A label map of an AOI is generated in the “per – structure” editor module. A new structure is added with a new labelling colour. The process generates automatically a file with the same name. The segmented AOI corresponds to the binary images. Switch the view mode if necessary, to improve the view (Figure 2.16).
4. In the painting tools, select the brush to manually colour the AOI. In the active tools select the “paint effect” and in additional settings box check “paint over” to draw on the image. Choose “threshold paint” and a range of grey values in 0...256 will appear. Adapt the thresholding range to select ranges, which correspond to grey values of the AOI. Draw a line on the AOI to test if your thresholding range is well adjusted (Figure 2.16).
5. In the “paint effect” additional settings, check “sphere”. Adapt the painting brush setting to be able to work with more than one image at a time. (See the comparison in Figure 2.17 and Figure 2.18).

3D reconstruction

- i. If necessary, adapt and modify the thresholding range to fit with all grey values of the AOI, and perform segmentation using a sphere painting brush (Figure 2.19).
- ii. Build the 3D model using active tools and select “Make model effect”. If you want to generate a smoothed 3D model, use “Model maker” default parameters and check

“smooth model → apply”. Otherwise go to “Model maker” adjust settings and choose filter type (*Sinc* or *Laplacian filter*) and check smoothing % then “apply” in the “model maker” panel (Figure 2.20).

The volume computation

- To automatically clean and remove the isolated misclassified pixels, use the active tools and select the “*dentify Islands effect*”. In the displayed setting check “*Fully connected*” mode and “*apply*”. The function will assign a new colour to all detected disconnected components (see Figure 2.21).
- Compute the volume of the reconstructed 3D model, by selecting “*Welcome to slice modules* → *Label statistic* → select the label name of the AOI → *apply*”.

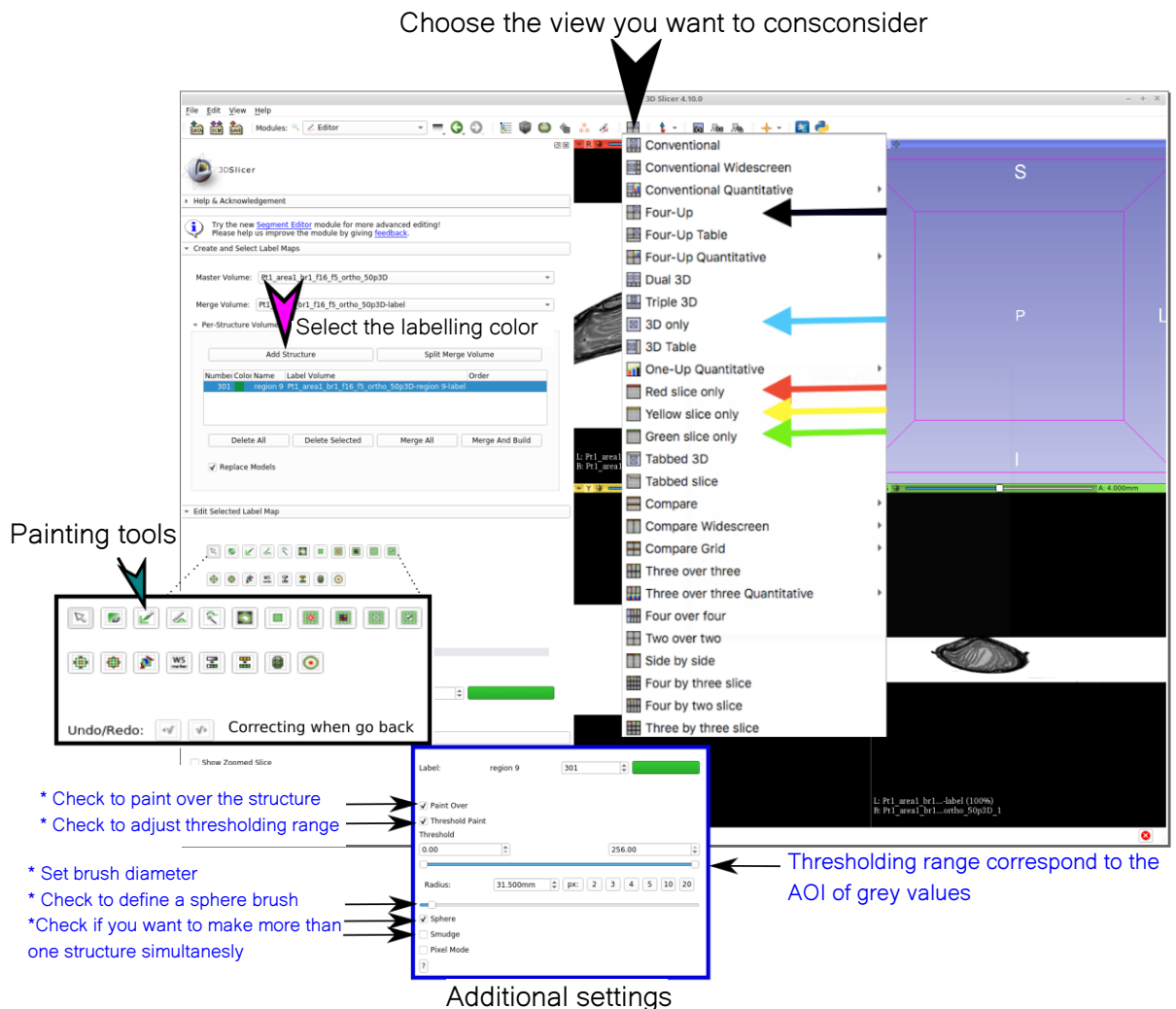


Figure 2.16 – 3D Slicer Editor modules. Additional settings in (pink arrow) are used to paint the AOI. Painting tools (green arrow) help controlling the brush. The icon shown by the black arrow opens a window with tools to enable switching the view modes.

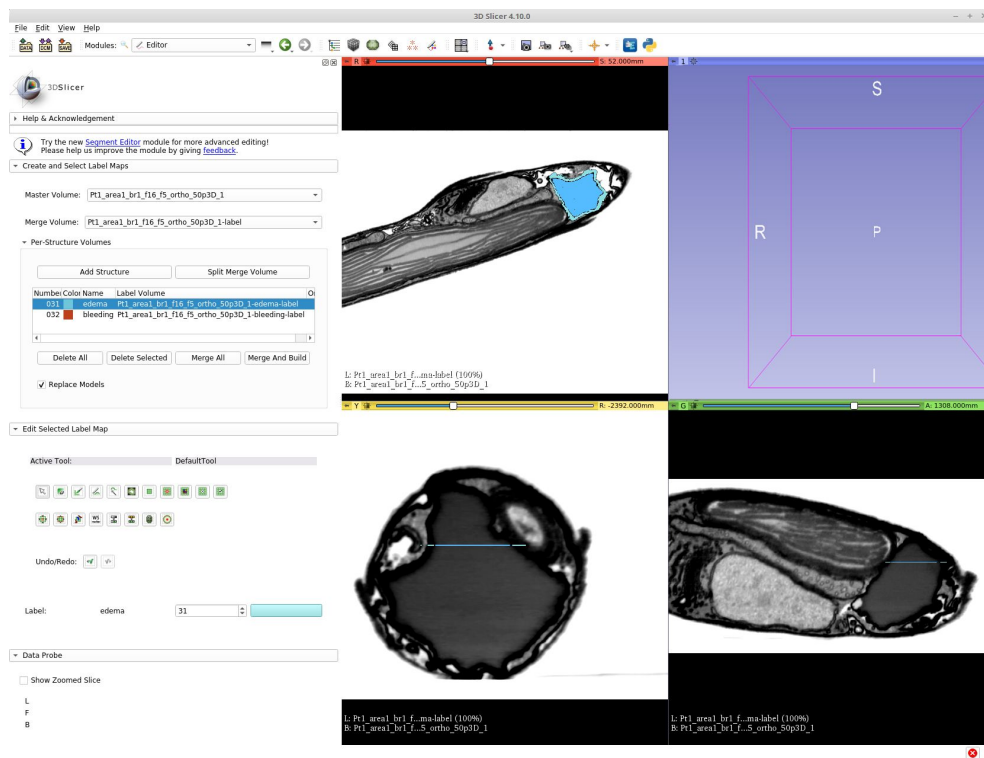


Figure 2.17 – Painting with a circle brush of diameter 87 nm on a stack with the voxel size: $8 \times 8 \times 8 \text{ nm}^3$. It takes 1 image at a time for 1 move.

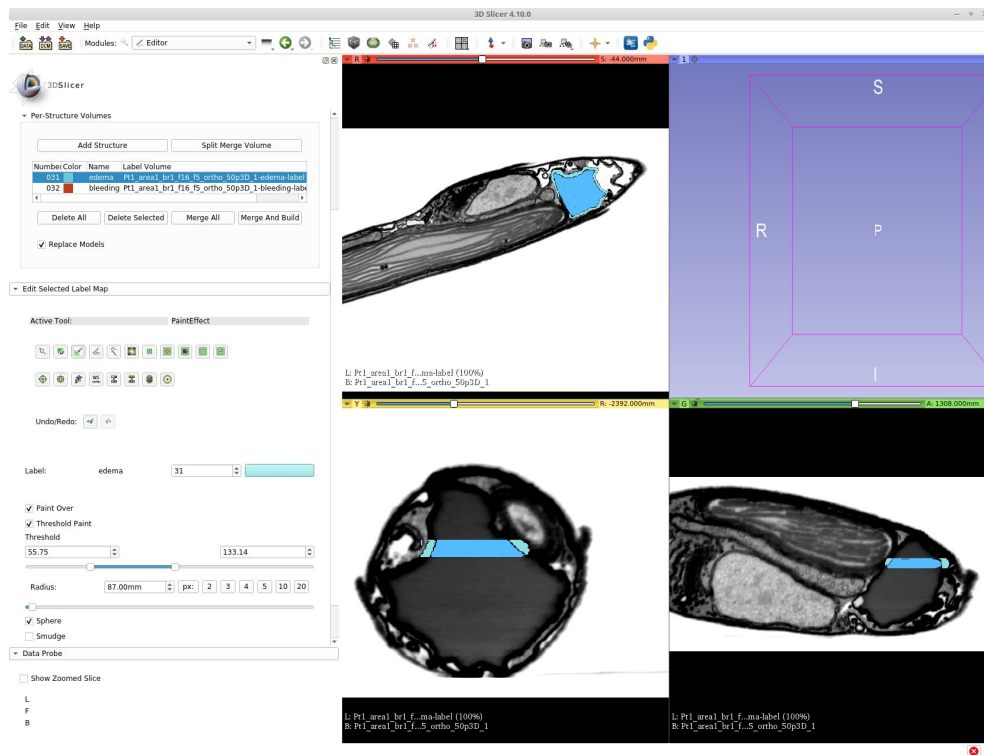


Figure 2.18 – Painting with a sphere brush of diameter 87 nm on a stack with the voxel size: $8 \times 8 \times 8 \text{ nm}^3$. It takes 10 image at a time for 1 move.

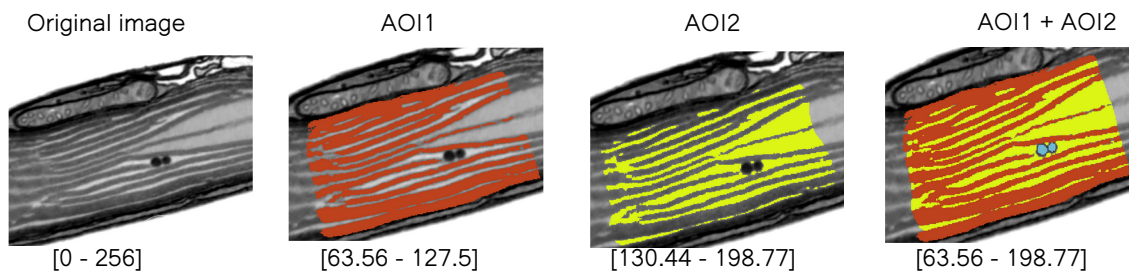


Figure 2.19 – Adaptive thresholding segmentation. The pixel intensities distribution was separated into sub-thresholding ranges to classify different objects in the AOI.

Save file in 3D Slicer

CTRL+S then choose the directory for selected “*files* → *save*”. 3D Slicer generates different type of file formats:

- The *.mrm1 format contains all the information of the 3D reconstruction and segmentation (label map + 3D models). If you want to rework on previously unfinished segmentations, upload only .mrm1 file in 3D Slicer interface and all files will be included.
- The *.nrrd format contains binary images generated during the segmentation of the AOI. They are named automatically every time a label volume for a structure to edit is selected.
- Generated 3D models can be saved as poly data in (.vtk) format, which is a default format. The 3D model can be saved as either as XML poly data (.vtp), STL (.stl), PLY (.ply) or wavefront OBJ (.obj) as well. These file formats are read with other image analysis software (see Table 2.3).

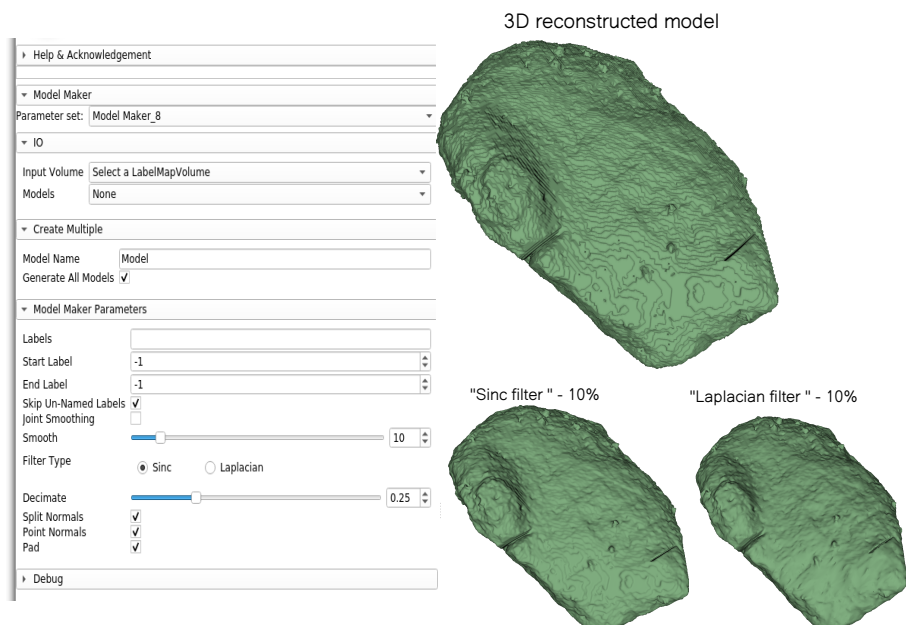
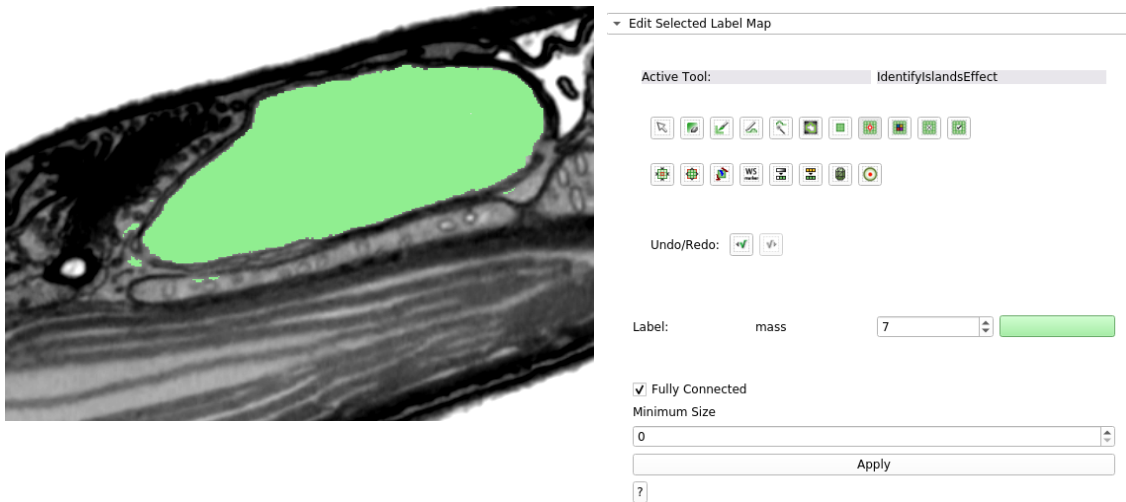


Figure 2.20 – Smooth 3D reconstructed model. Welcome modules provide tools to smooth generated models.



(a) Here classified pixels are mixed with wrong pixels in the AOI.



(b) Fully connected classified pixels in a group of clusters.

Figure 2.21 – Volume computation in 3D Slicer. The output table contains the number of voxels, the volume of the model and all the information related to the AOI annotation and pixel intensities distribution properties.

	Fiji/TrakEM2	Ilastik	3D Slicer
Datasets format	130 file formats	.tif, HDF	.tif, .nrrd, DICOM
Segmentation tools	Manual	Automatic	Manual, semi-automatic, automatic
Export 3D file format	.obj	.tif, .obj, .h5	.obj, .stl, .vtk, .vtp, .ply, .tif, .nrrd
Tested compatible software	ParaView, 3D Slicer, MeshLab, Blender	ParaView, 3D Slicer, MeshLab, Blender	Paraview, Ilastik, MeshLab, Blender, Amira, Fiji

Table 2.3 – Saving module of 3D Slicer. The different image formats and segmentation techniques offered by 3D image analysis open-source softwares tested in this project.

2.6.3 3D visualization and model editor

Segmentation and 3D reconstruction generate model files, which reach up to 2 GB ca and therefore cannot fit easily into memories of the 3D visualization and animation software. We need to reduce them to an ‘easy to manage’ size. The memory size may vary considerably from file to file depending on the features used in a model (see Table ??). Moreover, to clean the model in 3DSlicer, it is necessary to rerun the “*model make*” module to reconstruct a cleaned 3D structure. We therefore propose an additional technique in this pipeline, which involves editing and cleaning the 3D model in the MeshLab software.

Editing 3D model in MeshLab

- i. In MeshLab software go to “*File* → *Import mesh file format (*.stl, *.obj, *.ply)*” or drag and drop the 3D model into the window and in the “post-open processing” window, check “*unify duplicate vertices*” (Figure 2.22). A project will be created and the mesh will appear in the MeshLab interface. The interface displays the model’s name, number of vertices and faces.

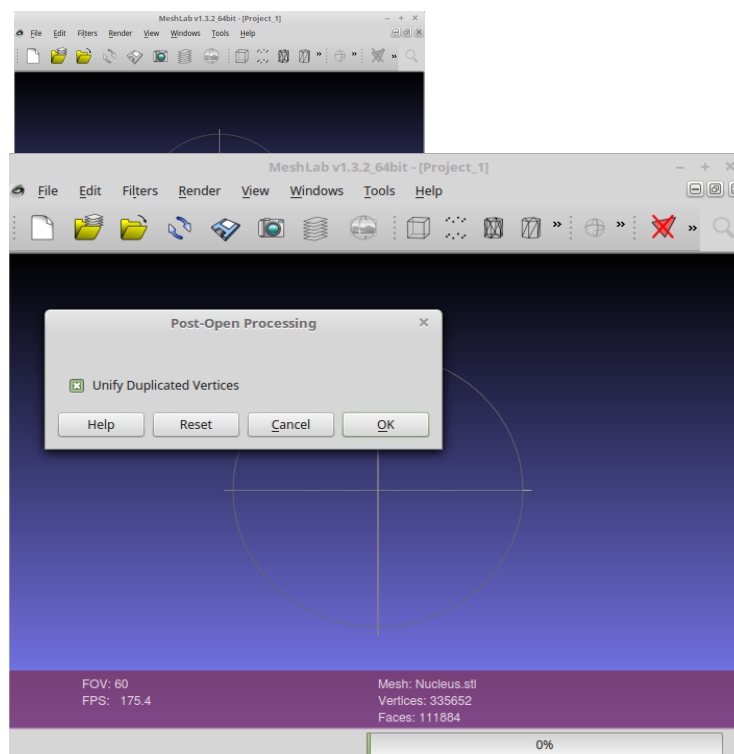
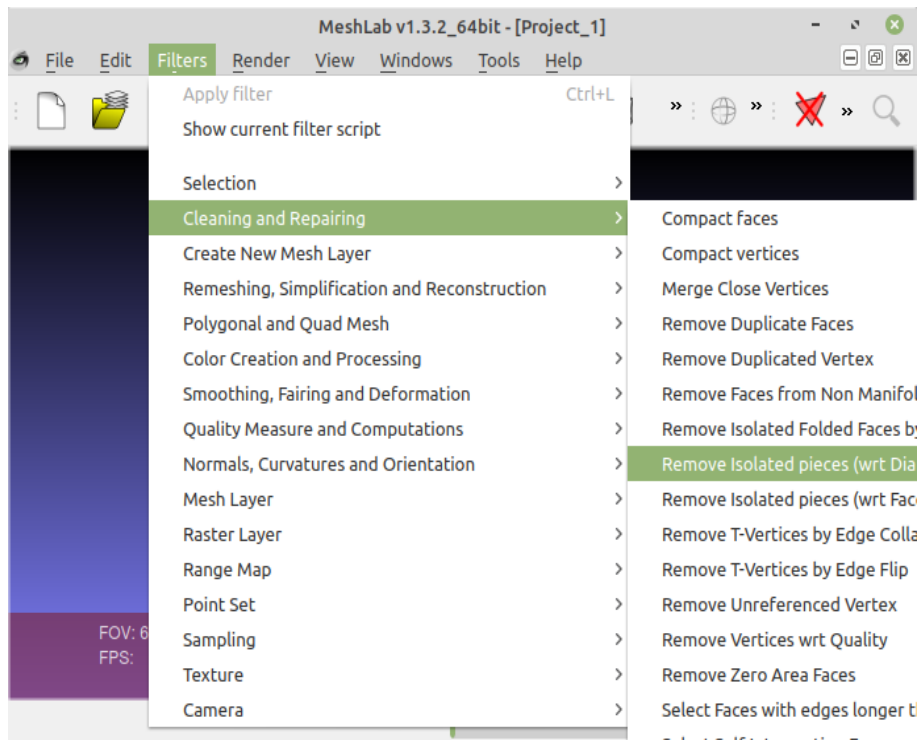
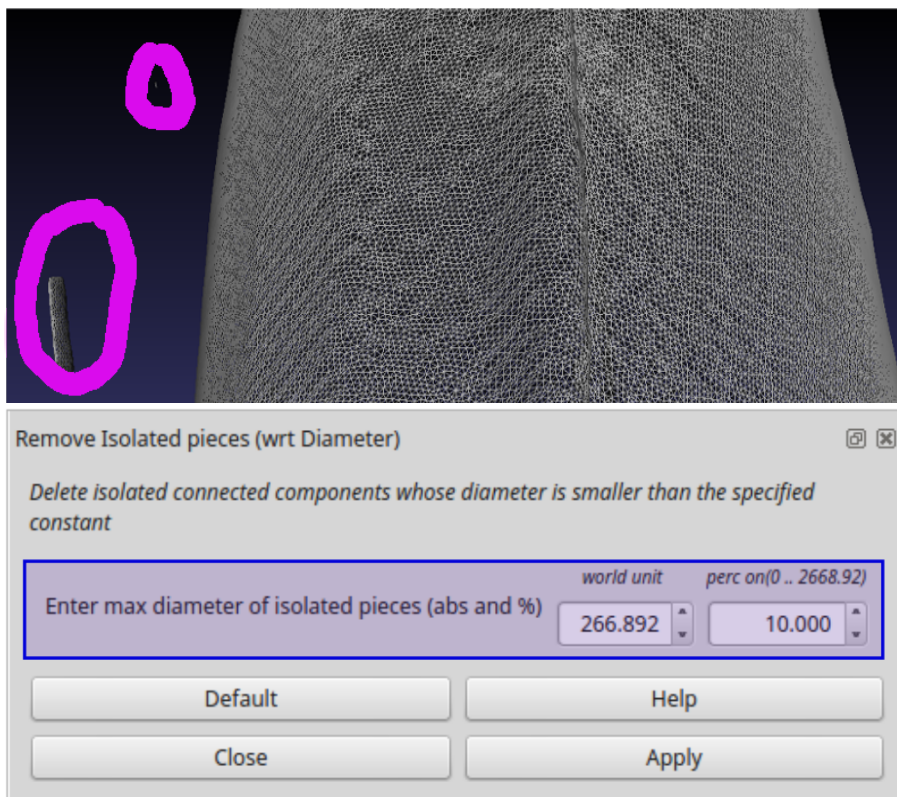


Figure 2.22 – MeshLab interface and post-opening of a 3D model.

- ii. Clean and edit the mesh by selecting the “*Filters*” module → choose “*cleaning and repairing*” function. This module removes unreferenced and unclean components with respect to the diameter of isolated pieces (Figure 2.23). Add the maximum diameter “**d**” of isolated pieces. The program will delete the isolated component having a diameter smaller than or equal to the specified distance “**d**”.



(a) The clean and edit module removes isolated pieces



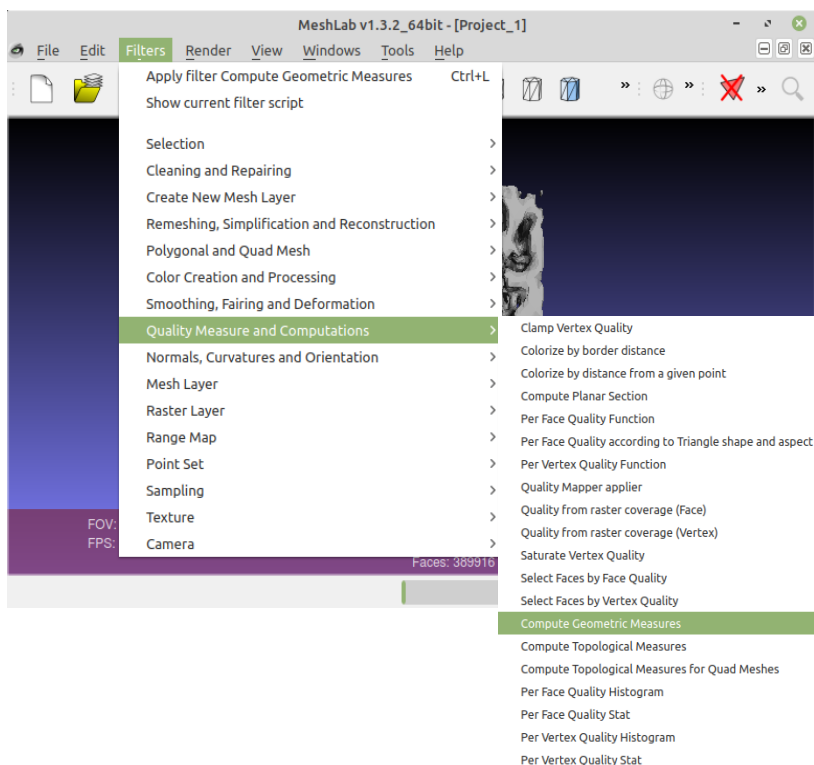
(b) Removing unstructured triangle meshes in MeshLab

Figure 2.23 – Cleaning and editing 3D model in MeshLab.

- iii. Once the model is clean, select the “*quality measure and computations*” module → then the “*compute geometric measures*” function. On the top of the menu click on the “*show layer dialog*” icon and the information of the model will appear on the right side of the interface (Figure 2.24).
- iv. To reduce the size of the mesh, go to the “*Remeshing, Simplification and Reconstruction*” module and select the “*Quality Edge Collapse Decimation*” function to open the corresponding window. Set the minimum faces you want to consider in “*the target number of faces*” box → “*apply*” (see example in Figure 2.25 and Table 2.4).

	STL format	PLY format	OBJ format
3D model size	22.1 Mo 204617 meshes	8.78 Mo 204087 meshes	35.2 Mo 204087 meshes
Volume information	$1.22669 \times 10^9 \text{ nm}^3$	Mesh is not 'watertight'	Mesh is not 'watertight'
Model decimation information	7.15 Mo 150000 meshes	2.71 Mo 150000 meshes	10.8 Mo 150000 meshes

Table 2.4 – Exported different file formats, size, volume information of the 3D model.



The screenshot shows the MeshLab v1.3.2_64bit interface. The 'Filters' menu is open, and 'Quality Measure and Computations' is selected. The 'Compute Geometric Measures' option is highlighted. The 'Show layer dialog' window is open on the right, displaying the following information:

```

-510.014587 1.469603
Center of Mass is 21.768322
-512.367981 0.429020
Inertia Tensor is :
| 2328952320.000000 -36555916.000000
-6336933.500000 |
| -36555916.000000 2080780160.000000
24839976.000000 |
| -6336933.500000 24839976.000000
1678304128.000000 |
Principal axes are :
| 0.989449 0.144745 0.006290 |
| -0.144102 0.987693 -0.060797 |
| -0.015013 0.059249 0.998130 |
axis momenta are :
| 2334372352.000000
2076913024.000000 1676751232.000000

```

Figure 2.24 – Quantification and computation of mesh metrics in MeshLab.

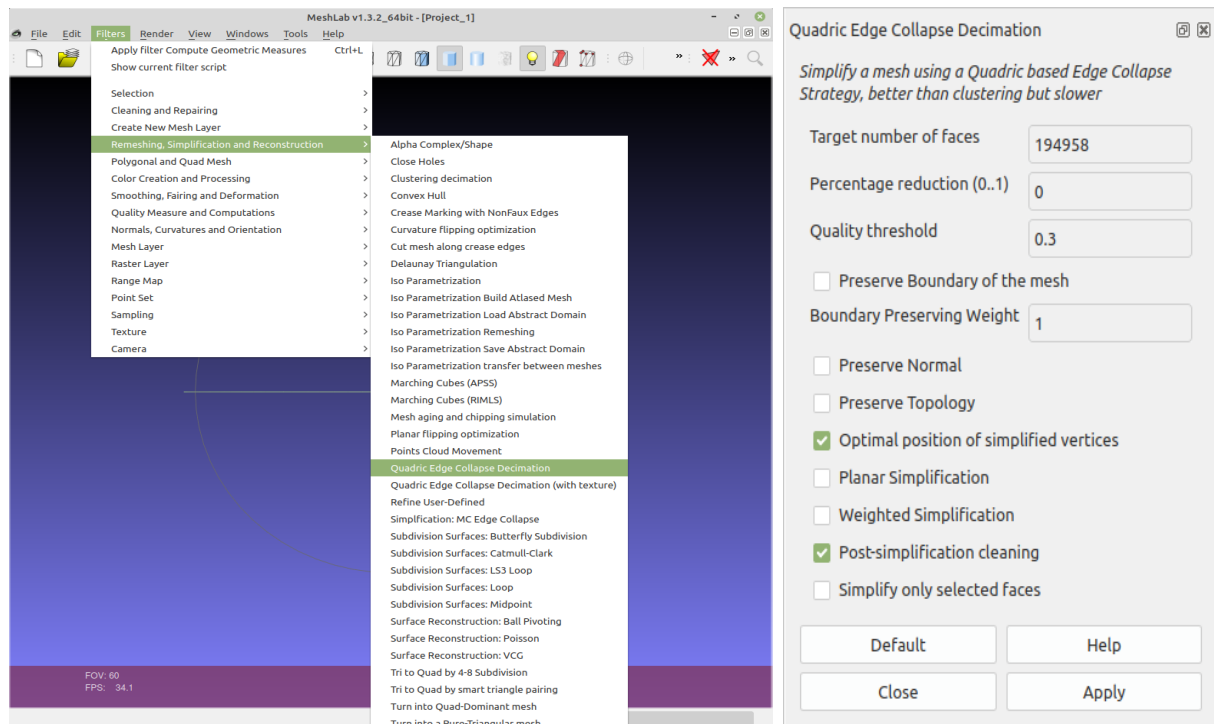


Figure 2.25 – Mesh simplification, refinement or decimation in MeshLab. Set the target number of faces in the “*Quality Edges Collapse Decimation*” window.

Animation

After editing the 3D model in MeshLab, the model file is imported into the ParaView software to capture a 2D representation of a three-dimensional description. For animation, we used Blender and its “*LuxCoreRender*” module for realistic rendering.

2.7 Geometry Processing

In this protocol, 3DSlicer and MeshLab softwares compute model geometry using two different methods. The 3DSlicer method is based on the voxel size information while the MeshLab method uses the information of triangle points of a tetrahedron. To understand and evaluate the “pro” and “cons” of the two methods, I implement a third method, which uses python packages to get quantitative data after image segmentation and volume reconstruction.

2.7.1 Surface and volume metrics

Fist method

3DSlicer uses label map and counts all voxels as if the model is voxelized (see Figure 2.26).

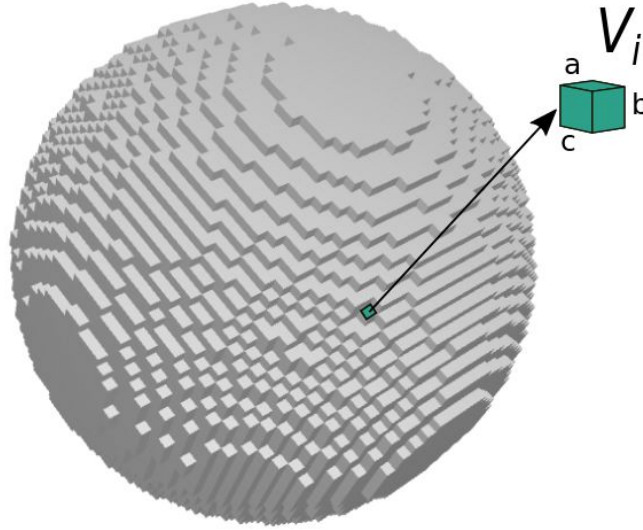


Figure 2.26 – Voxelized model with voxel unity.

The volume

Given d_x , d_y , d_z the width, length and height, the voxel size volume V_i is computed as:

$$V_i = d_x \times d_y \times d_z (\text{unity}^3) \quad (2.4)$$

Therefore, the total volume V_I of the model in (Figure 2.26) will be:

$$V_I = (\text{nbre of voxels in the object I}) \times (\text{the voxel size } V_i) \quad (2.5)$$

The surface area

Taking a voxelized object I , the area measurement is computed as follow:

- first, draw the boundary of the AOI on the surface.
- second, identify the region that is surrounded by the border.
- third, calculate the area of the region

These steps take into account the topological properties of a discrete surface by:

- counting all the voxels which are covered.
- ensuring that no path of the adjacent voxels are connected.
- taking into account hidden faces.

These tasks are not trivial but for additional information read (Prepelitã et al. 2016; Schwarz et al. 2010).

Second method

MeshLab reads a 3D model as a collection of vertices, edges and faces, which represent a polyhedral structure (Figure 2.27).

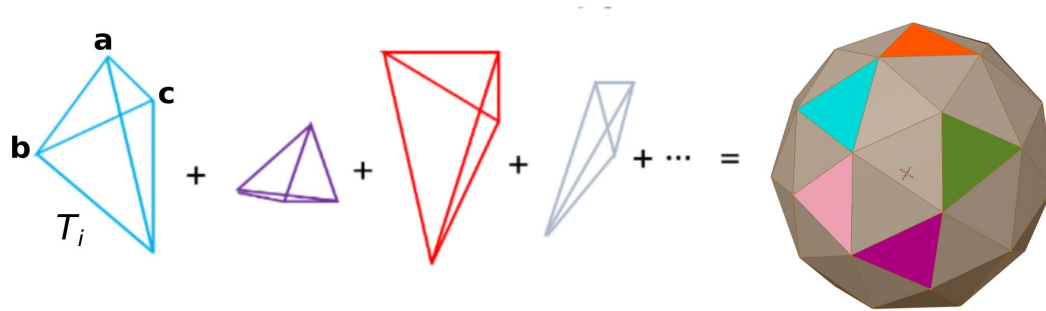


Figure 2.27 – 3D reconstructed model represented by polygons.

The volume

Let a, b, c be the triangle vertices of the tetrahedrons of object J . The volume of T_i :

$$T_i = \frac{1}{6}(\vec{a} \times \vec{b}) \cdot \vec{c} \Rightarrow V_J = \sum_{i=1}^N T_i \quad (2.6)$$

The process involves summing N polygons faces. Those pointing in will be added on V_I and those pointing out will be subtracted. Thus, V_I is the volume inside.

The surface area

The surface area S_I of the object in (Figure 2.27) is the number of faces unity defining the polygon. The area surface of one face A_i is computed as:

$$S_J = \sum_{i=1}^{\text{all faces}} A_t, \text{ where } A_t = \frac{1}{2}|\vec{AB} \times \vec{AC}| \quad (2.7)$$

Third method

Surface and volume metrics computation using STL python module.

Requirements:

1. Download the source code on GitLab: https://gitlab.com/clariaddy/stl_statistics


```

import numpy as np
from stl import mesh

mesh_file = 'a.stl' # add here the location path of your STL file.
mesh = mesh.Mesh.from_file(mesh_file)
def compute_surface(mesh):
    surface = 0.0
    for triangle in mesh.vectors:
        X0,X1,X2 = triangle
        u, v = X1-X0, X2-X0
        w = np.cross(u, v)
        surface += np.sqrt(np.dot(w, w)) / 2.0
    return surface
def compute_volume(mesh):
    volume = 0.0
    for triangle in mesh.vectors:
        X0,X1,X2 = triangle
        volume += np.dot(X0, np.cross(X1, X2)) / 6.0
    return volume
def compute_surface_fast(mesh):
    Vt = mesh.vectors
    U = Vt[:,1]-Vt[:,0]
    V = Vt[:,2]-Vt[:,0]
    W = np.cross(U,V)
    S = np.sum(np.sqrt(np.sum(W*W, axis=1))) / 2.0
    return S
def compute_volume_fast(mesh):
    Vt = mesh.vectors
    V = np.sum(Vt[:,0]*np.cross(Vt[:,1], Vt[:,2])) / 6.0
    return V

shape = mesh.vectors.shape
pts = mesh.vectors.reshape(shape[0]*shape[1], shape[2])
pmin = np.min(pts, axis=0)
pmax = np.max(pts, axis=0)
L = pmax - pmin

S = compute_surface_fast(mesh)
V = compute_volume_fast(mesh)
print '''
Mesh '{}' statistics:
pmin: {}
pmax: {}
L:      {}
S:      {}
V:      {}
S/V:    {}
'''.format(mesh_file, pmin, pmax, L, S, V, S/V)

```

2. Make sure you have Python on your computer
3. Install numpy-stl by just `pip3 install numpy-stl`
4. Install sublime Text

5. Open Sublime Text
6. Copy and paste the code in the sublime text interface and add the path of your STL file and save (CTRL + S) the work in a specific directory
7. Run the code with (CTRL + B)

When we compared the volume computed using the voxel (3DSlicer) and mesh (MeshLab and Python script) based methods, results are comparable (see Table 2.5)

	3DSlicer (Label statistics)	MeshLab geometric measures module	Python script
Model test volume	$1.20689 \times 10^9 nm^3$	$1.22669 \times 10^9 nm^3$	$1.21272 \times 10^9 nm^3$

Table 2.5 – Comparison of metrics obtained from 3Dslicer, MeshLab and Python script.

2.7.2 Proximity distance between two meshes

After building the 3D model of the cellular system, we wished to evaluate distances between two organelles in the cells to hypothesize a possible functional relationship. In the following pipeline, I describe how to integrate the proximity distance computation between two meshes and implement the surface contact surface below the thresholding.

Given two meshes A and B , we computed the pointwise distance from mesh A to mesh B . For each vertex in the mesh A , we computed the minimal distance to the mesh B using the Trimesh python module. Using this method, every vertex of mesh A is compared to all vertices contained in mesh B to calculate the intermesh distance (Figure 2.28).

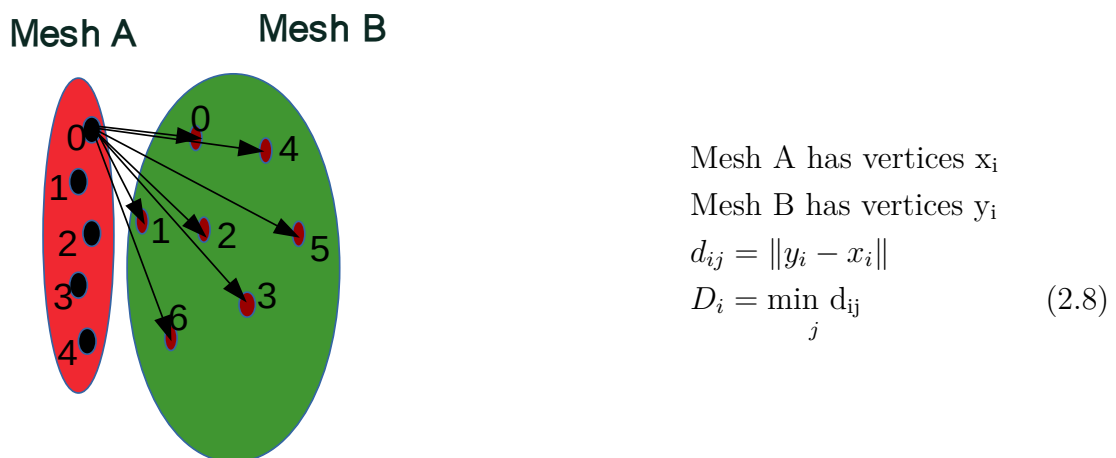


Figure 2.28 – Minimum distance between two meshes.

After having set a biological meaningful threshold distance (here $\leq 90 \text{ nm}$), we generate subsets of $A - B$ points that meet this criterion:

$$x_i \text{ close to } B \Leftrightarrow D_i \leq D_{\text{threshold}} \quad (2.9)$$

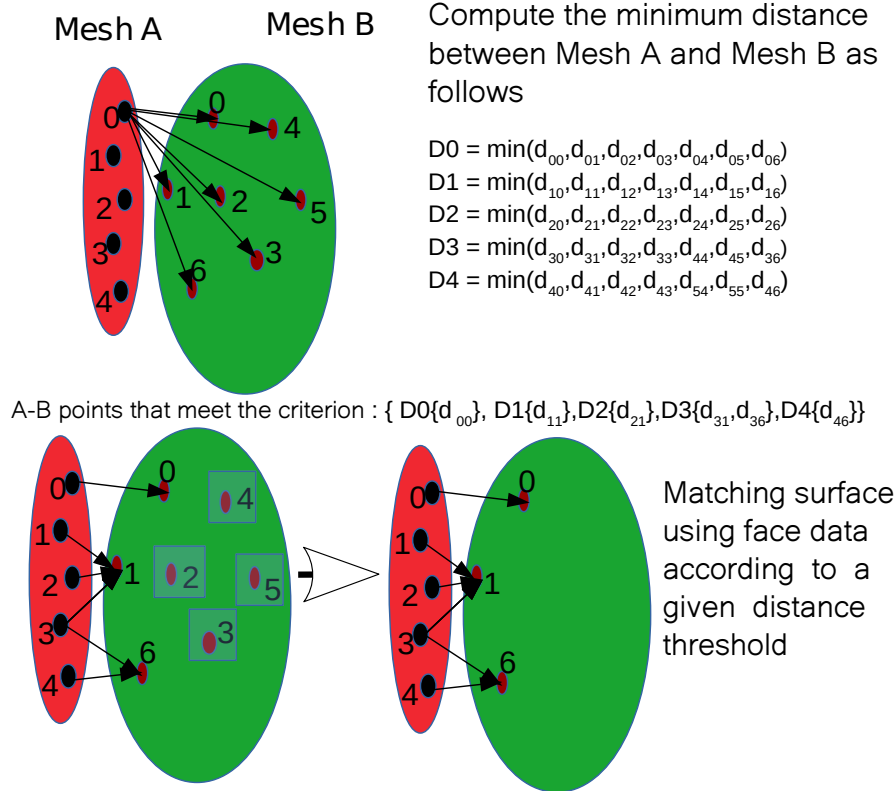


Figure 2.29 – Proximity distance estimation. Computation of the minimum distance between two meshes using pointwise distance from mesh A to mesh B .

Using the python code provided at: <https://gitlab.com/clariaddy/mindist>, we reconstruct the matching surface using face data (see Figure 2.29) also the example in Figure 2.30).

The code scripts and implementation

The algorithms implement the minimum distance between two meshes either by providing the minimum distance between mesh A and mesh B or implementing the area corresponding to the proximity distance between them. What you need to implement the code:

1. Download the python code on GitLab: <https://gitlab.com/clariaddy/mindist>
 - `mindist`: allows to compute the distance between two meshes.

- minsurf: allows to extract a surface below a threshold distance.
2. Install all packages in the text file “deps.txt”:
 - sudo apt-get install libspatialindex-dev
 - sudo pip3 install rtree
 - sudo pip3 install svg.path
 - sudo pip3 install bashplotlib
 3. Make the python code executable by opening the terminal CTRL + ALT+ T and add location path of the code + run:
 - chmod +x mindist
 - chmod +x minsurf
 4. The main parameter, we need to run the code:
 - mindist [-h] [-n NPTS] [-u UNIT] [-prec PREC] [-plt] [-nv] mesh0 mesh1
 - minsurf [-h] [-d MAX_DISTANCE] [-af] [-cd] [-n NPTS] [-ss SPACE_SCALING] [-ps PLOT_SCALING] [-prec PREC] [-nv] [-plt] [-bc BASE_COLOR] [-ba BASE_ALPHA] [-s SUBDIVISIONS] [-cc CUSTOM_COLORS] [-vc] [-dm DISPLAY_MODE] mesh0 mesh
 5. Run the command below:


```
./minsurf Mitochondria.stl Chloroplast.stl -ss 1
-d 50 -plt -dm all -cc black,green -bc red -ba 0.2
```



Figure 2.30 – Contact area computation. Dark spots show the contact points between mitochondria and plastid.

2.7.3 Splitting method

During the segmentation process, we noticed that an AOI may contain several structures that can be individualized only upon several rounds of segmentation. Individualizing ~ 100 structures, one by one, even using the semi-automatic segmentation to speed up the process is a tedious task. Therefore, the protocol to implement quantitative analysis, as detailed below:

Region splitting in 3DSlicer use “*3DSlicer/Editor module*”

1. Add a label map for a structure to edit in a *per-structure* module panel.
2. While keeping the same label map, annotate different structures from the AOI using different labelling colours (see Figure 2.17 and 2.18)
3. Select “*Welcome to Slicer modules → label statistic*” and indicate in “*the Grayscale volume*” the name of your stack and in the “*Label Map*” the name of the label map, which corresponds to the segmented clusters of the AOI and → apply.
4. A table appears displaying volume information of the topology of individualized structures and the corresponding pixel intensities distribution. The module displays information with respect to the segmentation order.

Region splitting in Fiji use “*Fiji/3D objects counter plugin*”

During the segmentation of multiple clusters in the AOI, we may choose to annotate all clusters with one colour to avoid repetitive segmentation. External softwares may be required to get quantitative information of individual structure. The simplest way is to use the “*3D object counter*” plugin from Fiji.

Note:After segmentation save the `.nrrd` file which contains binary images of the AOI.

Count object number structures using “*3D objects counter*” plugin:

1. Download the 3D object counter plugin [here](#). Drag and drop the `3d-oc.jar` in the plugins folder of Fiji. Go to Plugins → install → `3d-oc.jar` and restart Fiji.
2. Import the `.nrrd` file in Fiji; go to *Image → Properties to set voxel size information*. Select “*Plugins → 3D Object Counter → Set Measurements*” and add statistical parameters then select “*3D Object Counter*” function.

- Adapt the thresholding value, which corresponds to your data and scroll the slice panel to see if the threshold value covers all objects individually (Figure 2.31) then press *ok*. A table, containing all the statistical measurements of the detected objects, will appear. Note that the object realignment is random, i.e. we cannot have the structures ordered exactly as they were originally modelled in 3DSlicer.



Figure 2.31 – *3D Object Counter* plugin from Fiji provides all geometric topology information of detected objects in the cluster.

Mesh splitting

After evaluating how much time it takes to get quantitative data in the cluster, we tried splitting a mesh model using Trimesh. The technique based on 3D model gives

good results in term of quantitative analysis and reduces the working time (see how the algorithm works and the example in Figure 2.32):

1. Load the mesh file in `.stl` format and cleans it if required.
2. Check if the loaded object is watertight, (i.e, it has true volume, count connected groups of vertices and compute the surface/volume).
3. Split mesh objects using connected faces (faces sharing an edge).
4. Sets up a minimum number of triangles considered as a sub-mesh. If it is not specified, the algorithm considers that a sub-mesh contains at least three triangles or 1% of base mesh triangles.
5. Iterate on face subgroups and build the sub-mesh. Clean the sub-mesh and save it.
6. Print the computed statistical measurements of individual generated sub-meshes.
7. The parameters, we need to run the code:

```
split_mesh [-h] -i INPUT_FILE [-o OUTPUT_BASENAME] [-c] [-nv]
[-mo MAX_OBJECTS] [-mt MIN_TRIANGLES] [-mtp MIN_TRIANGLES_PERCENTAGE]
```



3D models of plastids
in *Phaeocystis* cells



```

kedy@zephyr ~/Images/Documents/mesh_splitting-master
kedy@zephyr ~/Images/Documents/mesh_splitting-master $ ./split_mesh -i Group.stl
-o test -mo 10 -mt 100 -mtp 0.001
Loading mesh 'Group.stl'.
Input mesh contains 241238 triangles forming 12 connected components.

Detailed statistics
+-----+-----+-----+-----+-----+-----+
| Name | Volume | Surface | Surface/Vo | Triangles | Watertight |
|-----+-----+-----+-----+-----+-----+
| Group.stl | 8.163e+08 | 9945315.033 | 0.012 | 241238 | True/True |
+-----+-----+-----+-----+-----+-----+
| test_0.stl | 3.905e+08 | 3580808.784 | 0.009 | 79854 | True/True |
+-----+-----+-----+-----+-----+-----+
| test_1.stl | 1.043e+08 | 1420821.487 | 0.014 | 38168 | True/True |
+-----+-----+-----+-----+-----+-----+
| test_2.stl | 87679842.616 | 1267224.560 | 0.014 | 31740 | True/True |
+-----+-----+-----+-----+-----+-----+
| test_3.stl | 75936807.302 | 1115388.915 | 0.015 | 29662 | True/True |
+-----+-----+-----+-----+-----+-----+
| test_4.stl | 81548590.531 | 1119527.630 | 0.014 | 27900 | True/True |
+-----+-----+-----+-----+-----+-----+
| test_5.stl | 48529741.502 | 805684.704 | 0.017 | 18304 | True/True |
+-----+-----+-----+-----+-----+-----+
| test_6.stl | 16691987.783 | 360252.606 | 0.022 | 8834 | True/True |
+-----+-----+-----+-----+-----+-----+
| test_7.stl | 11113155.448 | 264131.568 | 0.024 | 6402 | True/True |
+-----+-----+-----+-----+-----+-----+

```

Figure 2.32 – Mesh splitting using Trimesh python package.

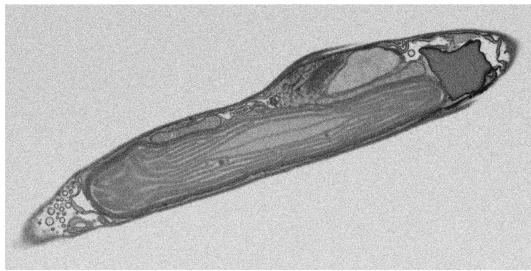
2.8 Image processing methods with sample preparations

The image processing has been applied to different sample preparations: either chemically fixed or frozen at high pressure and cryo-substituted cells.

Chemically fixed samples

When samples are chemically fixed, membranes are heavily stained and organelles envelopes are visible. However, the segmentation process may take a lot of time because the AOI is delimited by membrane structure. This information tends to add many details on the AOI and the human eye will use edges to delimit structures.

Therefore, image pre-processing needs to include filtering and edge detection methods to help the user extracting the AOI from other structures. Overall, a full segmentation of a cell can take a week (see example in Figure 2.33).



(Flori et al. 2017)

Image processing:

1. Image pre-processing steps:
 - Binning transformation
 - Gaussian filter
 - Edge enhancement
2. Image segmentation (3DSlicer) and reconstruct 3D model.
3. 3D representation (ParaView)

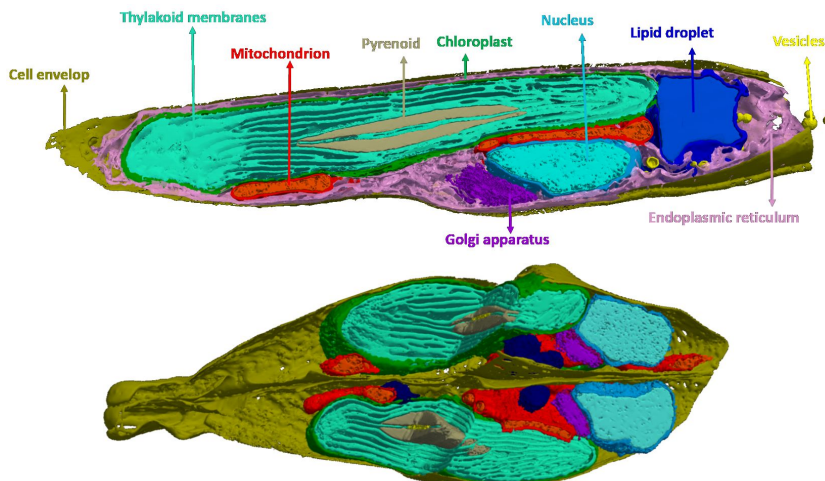
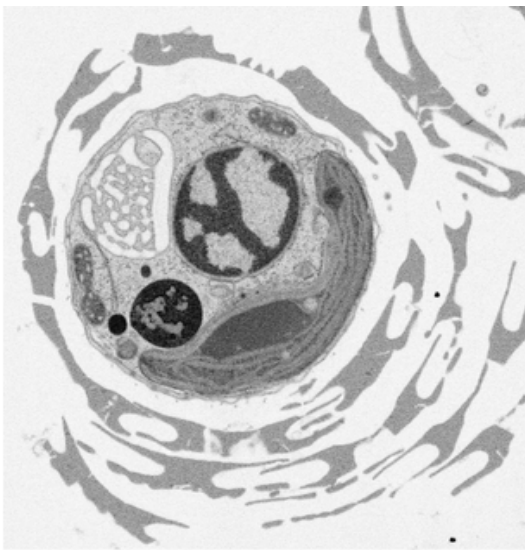


Figure 2.33 – Chemically fixed image of *Phaeodactylum tricornutum*. 3D cell architecture organization (bottom panel), together with indication on the image processing steps (top panel).

Cryo-substituted sample

If the sample preparation is improved to preserve cell structure (see above, sample preparation description), the image resolution is higher and the subcellular structures are well preserved.

Thus, the image pre-processing steps include fewer steps and the time required to segment a full tomogram of the cell is largely reduced (three days for an experienced user, Figure 2.34).



(Uwizeye et al. 2020)

Image processing:

1. Image pre-processing steps:
 - Crop 3D volume data.
 - Binning transformation could be enough to reduce noise.
2. Image segmentation (3DSlicer) and reconstruct 3D model.
3. 3D representation (Blender, LuxCoreRender)

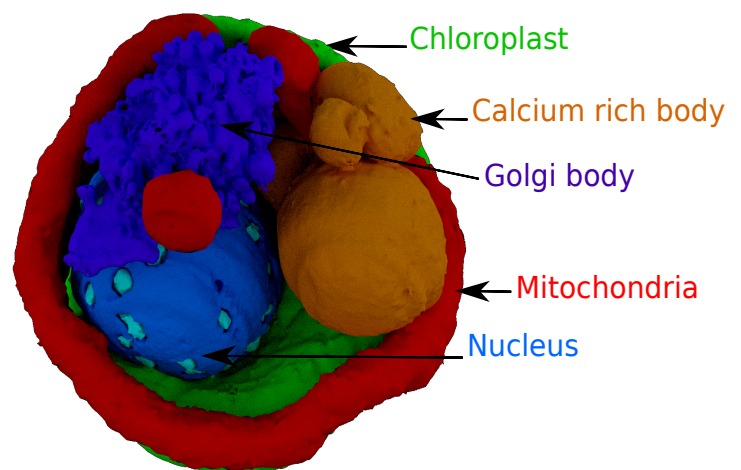
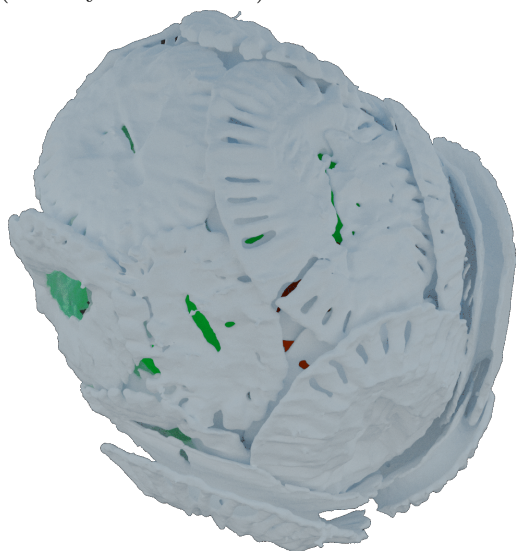


Figure 2.34 – 3D architecture organization of *Emiliana huxleyi*. The cells were frozen at high pressure and cryo-substituted.

Assessing subcellular features and their dynamics in planktonic microalgae using a FIB-SEM imaging approach

Contents

3.1	Introduction	60
3.2	Results and Discussion	62
3.2.1	Cellular architectures of phytoplankton	62
3.2.2	Subcellular features of energy managing organelles	67
3.2.3	Remodelling of the subcellular architecture of microalgae	69
3.3	Conclusion and perspectives	78
3.4	Supplementary Materials	80

Summary

Phytoplankton comprise microorganisms belonging to prokaryotes and to eukaryotes. Phytoplankton play an essential role on Earth through the process of photosynthesis, and support aquatic trophic networks. Despite a better understanding of their biodiversity, evolution and ecology, we still lack information about their response at the subcellular level. Nanoscale information can help understanding the internal cell organisation and its possible link to physiological responses. In this chapter, I employed the imaging workflow described in Chapter 2 to perform quantitative analyses of entire algal cells from different phytoplankton taxa. I focused on the relationships between the energy production compartments (plastids, mitochondria) and energy storage compartments. I found that they occupy constant volume fractions in the different lineages. I also identified interactions between plastids and mitochondria in all species, which change according to the cell energy demand. These findings revealed the role of plastid-mitochondria interactions and morphology adjustment as the critical parameters to understand how phytoplankton adapt to their environment. Moreover, this type of investigation opens new perspectives in the study of phytoplankton cellular structure and acclimation at the cellular and subcellular scale.

Keywords: [phytoplankton], [microalgae], [3D structure], [biometrics], [organelles]

Introduction

Phytoplankton are essential for life on Earth. By turning CO₂, sunlight and other nutrients into useful biomass and O₂, they are almost equivalent to forests and other land plants (Falkowski 2002; Field et al. 1998). These single-celled photosynthetic organisms are ubiquitous in the oceans, in aquatic and terrestrial ecosystems and they significantly contribute to food chains, and to the CO₂ feedstock pump. Phytoplankton include prokaryotes and eukaryotes. Eukaryotic phytoplankton group a wider variety of lineages (diatoms, dinoflagellates, haptophytes, rhodophytes, etc.) with different forms and sizes (Yoon et al. 2017). Under optimum conditions, phytoplankton growth is exponential (Mellard et al. 2012). However, it is affected by abiotic challenges, including global warming (Pörtner et al. 2014; Lewandowska et al. 2014; Cross et al. 2015), which affect nutrient availability by modulating the vertical stratification of the water column and ocean temperature (Pandey et al. 2017).

Phytoplankton growth is also regulated by biotic stresses, including e.g. the presence of biotoxins produced by other organisms, which are harmful to marine life (Hallegraeff 2010; Davidson et al. 2012). While our knowledge of population responses to abiotic and biotic is increasing, thanks e.g. to omics approaches, the cellular reactions behind these responses are less known. For these reasons, a major challenge of my PhD has been to develop a pipeline to access to the cellular and subcellular features of phytoplankton at the nanometric scale, based on FIB-SEM technique approach as reported e.g. in (Narayan et al. 2015; Kizilyaprak et al. 2014).

FIB-SEM has already been successfully applied to provide 3D models of eukaryotic cells (Decelle et al. 2019; Flori et al. 2017; Gavelis et al. 2019). As explained in chapter 2, the protocol developed here is suitable to carry out comparative studies of subcellular features. We applied it to several cell types, mainly focusing on three observables: (i) cell volume fractions occupied by the different organelles, (ii) constant volumetric ratios between plastids and mitochondria and (iii) plastid-mitochondria interactions at specific locations, suggesting the presence of contact points between the energy-producing compartments. In the following, I will present data that have been included in a manuscript that is in preparation plus additional information concerning other species/observables.

Structural bases of phytoplankton energy management and physiological responses unveiled by 3D Quantitative imaging

Clarisse Uwizeye¹, Johan Decelle^{1*}, Pierre-Henri Jouneau², Serena Flori^{1,3}, Benoit Gallet⁴, Jean-Baptiste Keck⁵, Davide dal Bo¹, Christine Moriscot^{4,6}, Claire Seydoux¹, Fabien Chevalier¹, Nicole L. Schieber⁷, Rachel Templin⁷, Florence Courtois¹, Gilles Curien¹, Yannick Schwab^{7,8}, Guy Schoehn⁴, Samuel C. Zeeman⁹, Denis Falconet^{1*}, Giovanni Finazzi^{1*}.

¹Univ. Grenoble Alpes, CNRS, CEA, INRAe, IRIG-LPCV, 38000 Grenoble, FRANCE.

²Univ. Grenoble Alpes, CEA, CNRS, IRIG-MEM, 38000 Grenoble, FRANCE.

³The Marine Biological Association, The Laboratory, Citadel Hill Plymouth, Devon, PL1 2PB, UK

⁴Univ. Grenoble Alpes, CNRS, CEA, IRIG-IBS, 38000 Grenoble, FRANCE.

⁵Univ. Grenoble Alpes, Laboratoire Jean Kuntzmann, 38000 Grenoble, FRANCE.

⁶Univ. Grenoble Alpes, CNRS, CEA, EMBL, Integrated Structural Biology Grenoble (ISBG) 38000, Grenoble, FRANCE.

⁷Cell Biology and Biophysics Unit, European Molecular Biology Laboratory, 69117 Heidelberg, GERMANY.

⁸Electron Microscopy Core Facility, European Molecular Biology Laboratory, 69117 Heidelberg, GERMANY.

⁹Institute of Molecular Plant Biology, Department of Biology, ETH Zurich, 8092 Zurich, SWITZERLAND.

*Corresponding authors:

johan.decelle@univ-grenoble-alpes.fr; denis.falconet@cea.fr;
giovanni.finazzi@cea.fr

Abstract

Eukaryotic phytoplankton is a minor fraction of the global biomass playing a major role in primary production and climate. Despite improved understanding of its diversity, evolution and ecology, we still miss information on 3D architectures of phytoplankton cells and their possible plasticity during physiological responses. Here, we developed an imaging workflow to perform quantitative morphometric analysis of subcellular structures using 3D electron microscopy (FIB-SEM). Comparative analysis across distant phylogenetic taxa representing major oceanic phytoplankton lineages and model-laboratory microalgae reveal *i*) conserved cell-volume fractions (40 – 50%) occupied by the main organelles (nucleus, plastid, mitochondria); *ii*) constant volumetric ratios between plastids and mitochondria; and *iii*) plastid-mitochondria interactions at specific locations, suggesting the presence of contact points between the energy-producing compartments. Hence, we propose that phytoplankton cell volume occupancy and organelles topology is governed by energy management rules. In line with this hypothesis, we observed a link between changes in cell volume occupancy of plastids and mitochondria, their interactions, and phytoplankton environmental acclimation. The comparison between diatom *Phaeodactylum tricornutum* cells grows under low light and high light show the enhancement of photosynthesis and respiration in parallel with increased of plastid-mitochondria interactions and larger volume occupancy by the mitochondria and the plastid CO₂-fixing pyrenoid. Changes in organelle architectures and interactions also accompany acclimation of *Nannochloropsis* to different trophic lifestyle, along with commensurate modifications in respiration and photosynthesis. Overall, by revealing the evolutionary- conserved architectures of microalgal energy managing organelles and the role of their structural plasticity in phytoplankton fitness and physiology, this study opens new perspectives to study acclimation responses at the subcellular scale.

Keywords: [phytoplankton], [microalgae], [3D structure], [FIB-SEM], [biometrics]

3.1 Introduction

Phytoplankton plays a critical role in supporting life on Earth. By converting CO₂, sunlight and nutrients into biomass and oxygen, unicellular phototrophs are responsible for about 50% of primary productivity (Field et al. 1998). They also contribute to food webs and to the biological CO₂ pump in the oceans. Phytoplankton members are ubiquitous in marine and freshwater ecosystems and include prokaryotes and eukaryotes, the latter having acquired photosynthesis capacity up to 1.5 billion years ago through endosymbiotic events (Sibbald et al. 2020). Eukaryotic phytoplankton encompasses a great diversity of lineages (e.g. diatoms, dinoflagellates, haptophytes, chlorophytes, and rhodophytes) with different morphologies and sizes (from 0.8 to a few tens of microns) (Not et al. 2012). Although our knowledge on phytoplankton biodiversity and ecological relevance in aquatic ecosystems has greatly improved in the recent

years e.g. (De Vargas et al. 2015), the cellular bases of ecological responses of these unicellular organisms remain undetermined. Moreover, we do not know how flexible the phytoplankton cellular (subcellular) architectures are facing environmental changes.

So far, phytoplankton morphological features have been mainly visualized by light microscopy and 2D electron microscopy studies (Andersen et al. 2015; Embleton et al. 2003; Rodenacker et al. 2006; Schulze et al. 2013; Sosik et al. 2007), often associated with assessment of photosynthetic activity (Hense et al. 2008; Schulze et al. 2013). A high-throughput confocal fluorescence 3D imaging has been developed to scan, classify and quantify phytoplankton cells collected in different oceanic regions (Colin et al. 2017). However, optical microscopy studies have insufficient resolution to reveal microstructural features, and 2D electron microscopy by definition cannot provide a comprehensive volumetric description of phytoplankton cells and their organelles. This is a critical aspect, as recent works have proposed that some phytoplankton physiological responses rely on the presence of peculiar 3D subcellular architectures (Engel et al. 2015; Bailleul et al. 2015). Thanks to the recent development of 3D Electron Microscopy (EM) studies, it is now possible to visualize small sections of native frozen cells at nearly-atomic resolution using cryo-Electron Tomography (cryo-ET, (Engel et al. 2015; Wietrzynski et al. 2020; Asano et al. 2016) or to provide 3D structures of entire cells with enough resolution (4 – 10 nm) to investigate subcellular architectures, using focused Ion Beam Scanning Electron Microscopy (FIB-SEM) (Flori et al. 2017; Decelle et al. 2019).

In this work, we applied a FIB-SEM-based workflow to seven monoclonal cultures of different eukaryotic microalgae representing major oceanic phytoplankton lineages and/or model-laboratory microalgae. By optimising every step of the workflow (sample preparation including cryofixation, 3D imaging, filtering, segmentation, and 3D modelling), we generated accurate 3D reconstructions, suitable for quantitative morphometric analysis (surfaces and volumes) of organelles and subcellular structures. Comparative analysis of the different lineages revealed preserved structural characteristics between the different species: (*i*) conserved cell-volume fractions occupied by the different organelles; (*ii*) constant volumetric ratios in energy-producing organelles (plastids, mitochondria); (*iii*) consistent plastid-mitochondria interactions. These relationships between cellular sub-compartments related to energy management likely represent evolutionary conserved features responsible for specific phytoplankton physiological responses. Consistent with this idea, physiological responses of microalgae acclimated to either different light regimes or trophic lifestyles were accompanied by substantial modifications in the structural features of plastids and mitochondria, as well as in their interactions.

3.2 Results and Discussion

3.2.1 Cellular architectures of phytoplankton

We reconstructed the 3D cellular architecture of different eukaryotic lineages representatives of ubiquitous phytoplankton taxa and laboratory model organisms: Mamiellophyceae (*Micromonas* RCC 827), Prymnesiophyceae (*Emiliana* RCC 909), Pelagophyceae (*Pelagomonas* RCC 100), Dinophyceae (*Symbiodinium* RCC 4014 clade A), Cyanidiophyceae (*Galdieria* SAG 21.92) and Bacillariophyceae (*Phaeodactylum* Pt1 8.6), Eustigmatophyceae (*Nannochloropsis* CCMP 526) (see supplementary Table 3.1). Prior to FIB-SEM imaging, live cells were fixed with high-pressure freezing (to maximise preservation of native structures) followed by slow freeze-substitution and resin embedding. FIB-SEM datasets were processed to 3D models using open-access software (supplementary Figure 3.8 and section 2.6 for more details). This imaging approach allows quantifying cell volumes in a wide range, from $3 \mu\text{m}^3$ ca in the mamiellophyceae *Micromonas*, to more than $200 \mu\text{m}^3$ in the dinoflagellate *Symbiodinium*.

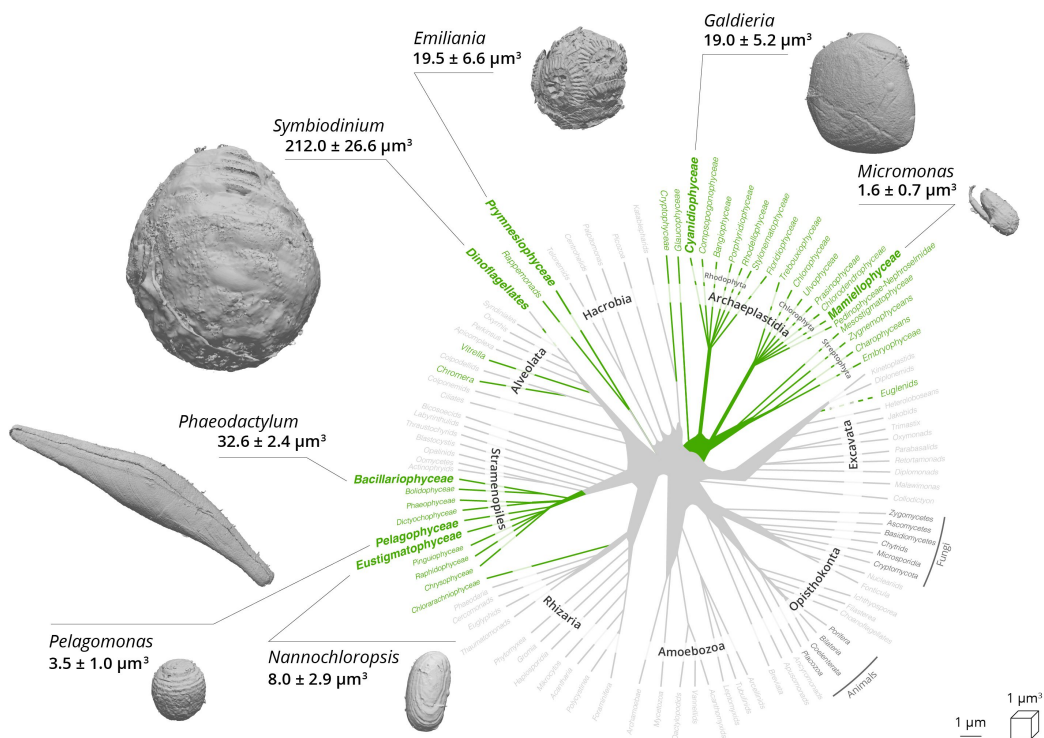


Figure 3.1 – Cellular volume and external features of selected phytoplankton cells. Green lineages of the phylogenetic tree of eukaryotes represent photosynthetic eukaryotes (adapted from (Decelle et al. 2015b)). A 3D scan view of cell morphology of selected phytoplankton members (Mamiellophyceae (*Micromonas* RCC 827), Prymnesiophyceae (*Emiliana* RCC 909), Bacillariophyceae (*Phaeodactylum* Pt1 8.6), Pelagophyceae (*Pelagomonas* RCC 100), Dinophyceae (*Symbiodinium* RCC 4014 clade A), Cyanidiophyceae (*Galdieria* SAG21.92) and Eustigmatophyceae (*Nannochloropsis* CCMP526)) is shown with a linear scale bar of $1 \mu\text{m}$ and a voxel scale of $1 \mu\text{m}^3$. Specific cellular features

We observed both external architectures of microalgae (e.g. coccoliths in *Emiliana*, the raphe in *Phaeodactylum*, the flagellum in *Micromonas*, Figure 3.1), and subcellular features, including the main organelles (Figure 3.3: nucleus -blue-, plastid-green- and mitochondria-red).

Other cellular features were observed (grey): storage bodies in *Emiliana* (Gal et al. 2018; Sviben et al. 2016), carbon-rich structures in *Pelagomonas* (Andersen et al. 1993), lipid droplets in *Phaeodactylum* (Lupette et al. 2019) and large oil bodies in *Nannochloropsis*, starch sheath surrounding the pyrenoid in *Micromonas* (Dos Santos et al. 2017) and *Symbiodinium* and vacuoles of different sizes in *Phaeodactylum*, *Galdieria* and *Micromonas* (the so-called impregnated bodies (Dos Santos et al. 2017)).

Different shapes were observed for the main organelles. Plastids were cup-shaped in *Galdieria*, *Pelagomonas*, *Emiliana*, lobed in *Symbiodinium* (Blank 1987); globular in *Micromonas* and *Nannochloropsis* and elongated in *Phaeodactylum* (Figure 3.2 B and Figure 3.2 A). When distinguishable, photosynthetic membranes (thylakoids) were organised in layers of a few stacks, without the clear subdivision into stacked and unstacked membrane domains observed in vascular plants (Mustárdy et al. 2003).

The nucleus had spherical/oval shape and was closely associated to the plastid via the fourth envelope membrane in secondary plastids (i.e. *Phaeodactylum* (Flori et al. 2016)). Mitochondria were characterized by more variable shapes not only between species but also within cells of the same species (e.g. Supplementary Figure 3.9 in the case of *Emiliana*). This likely reflects the dynamic nature of these organelles, which change their shape, undergo dislocations, and undergo fusion and fission within the cell (Bereiter-Hahn et al. 1994).

Concerning the main organelles, plastids always occupied the largest fraction (25 – 40%) of the cell (Figure 3.2 C and Supplementary Table 3.2), followed by the nucleus (5 – 15%) and the mitochondria (2.5 – 5%). Altogether, these three organelles (nuclei, plastids and mitochondria) filled a relatively constant fraction (40 – 55%) of the total cell volume, despite significant differences in the cell volumes of the different phytoplankton taxa (*Symbiodinium* e.g. is around 200 times bigger than *Micromonas*). Networks of internal vesicles, the Golgi apparatus, ER, vacuoles and storage compartments (e.g. lipid droplets, starch granules, nutrient storage, etc.) and the cytosol occupied the other half with a larger variability in terms of their relative volume occupancy. We interpret this conservation of the organelle volumes and the variability of the other compartments as the signature of evolutionary constraints that preserve essential cellular functions (gene expression, energy production, and anabolism/catabolism), while leaving metabolic flexibility to allow the storage of assimilated nutrients, particularly carbon and subcellular trafficking. The only exception was *Nannochloropsis*, where the large accumulation of oil bodies likely reduced the cell volume available to the main organelles (Figure 3.2, see below).

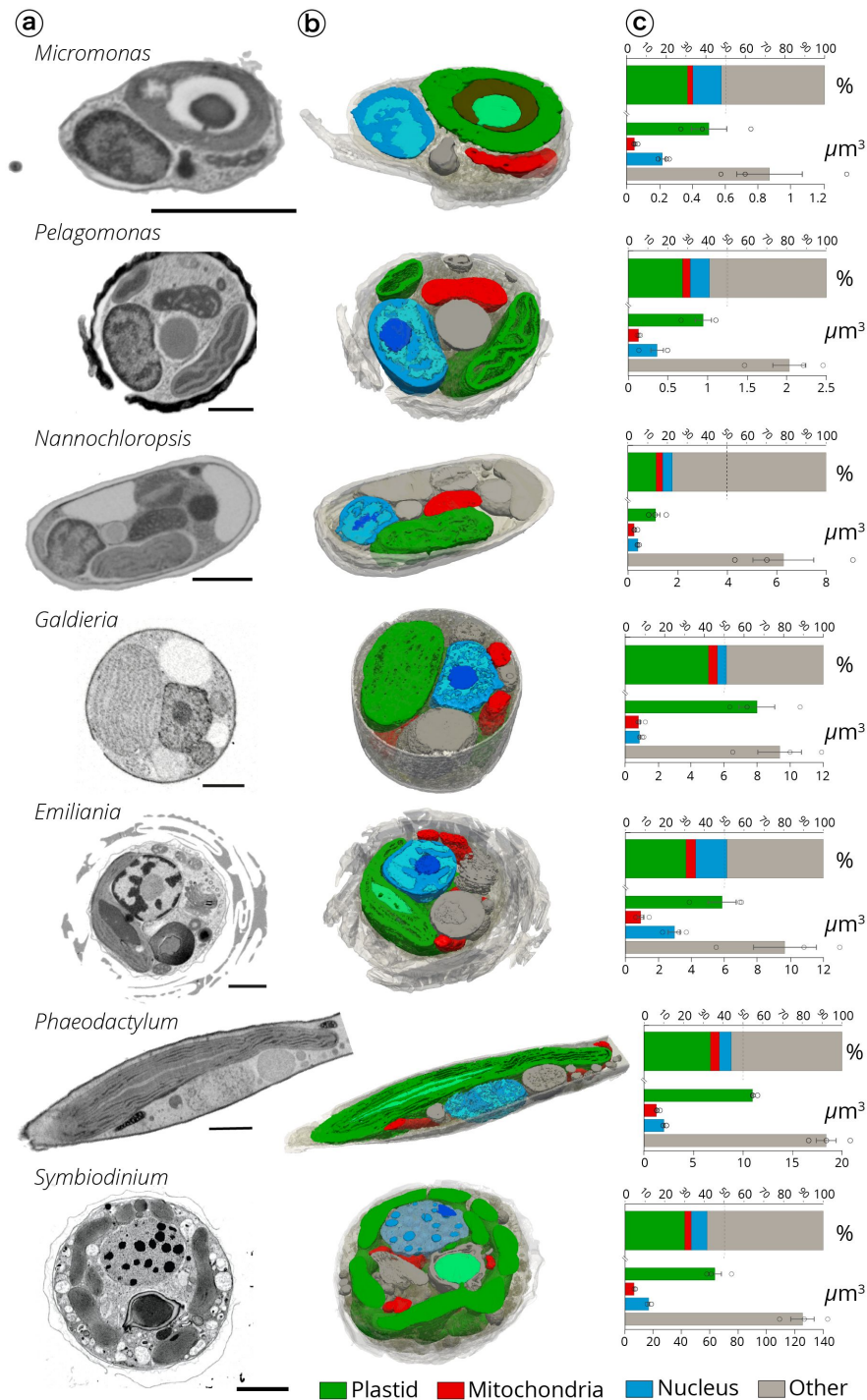


Figure 3.2 – Internal cell architecture of phytoplankton cells. (a) Sections through cellular 3D volumes, segmented from FIB-SEM images of whole cells of *Micromonas*, *Pelagomonas*, *Emiliana* (Supplementary Video 3), *Galdieria*, *Phaeodactylum*, *Symbiodinium*, and *Nannochloropsis* were imaged. (b) Segmentations highlight the main subcellular compartments: green: plastids (containing thylakoids and pyrenoids -light green- in some cell types); red: mitochondria; blue: nuclei (with different intensity of staining possibly corresponding to euchromatin -light blue- heterochromatin -blue- and the nucleolus -dark blue-); grey: other compartments. (c) Volume occupancy by the different subcellular compartments in different microalgal cells. Top plot: % of occupation; bottom plot: absolute volume sizes ($N = 3 \pm SD$).

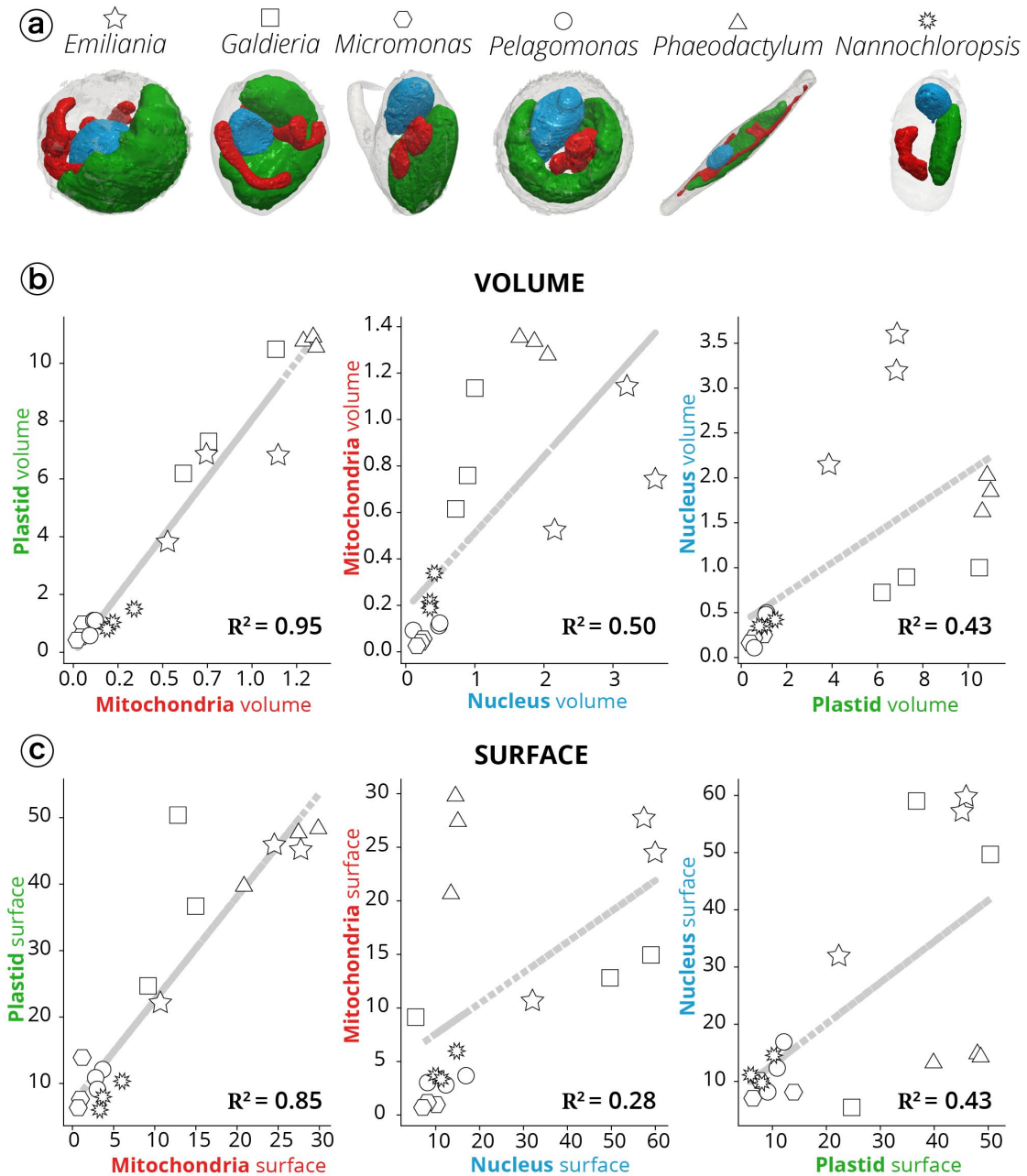


Figure 3.3 – Morphometric analysis of phytoplankton members. (a) 3D topology of the main organelles (green: plastids; red: mitochondria; blue: nuclei) in the different cell types. (b) Volume relationships in different subcellular compartments, as derived from quantitative analysis of microalgal 3D models. (c) Surface relationships in different subcellular compartments, as derived from quantitative analysis of microalgal 3D models. Three cells were considered for every taxum. Hexagons: *Micromonas*; circles: *Pelagomonas*; stars: *Emiliana*; squares: *Galdieria*; triangles: *Phaeodactylum*; suns: *Nannochloropsis*. *Symbiodinium* cells were not considered in this analysis, because their size, which largely exceeds the other (Supplementary Figure 3.10, prevents a meaningful analysis of the volume/surface relationships).

Thanks to the possibility offered by our approach to perform quantitative surface and volumetric estimates, we sought relationships between the three above mentioned organelles (Figure 3.2 A) in the different taxa, to identify possible evolutionary-preserved morphological characteristics. This analysis was initially biased by the presence of *Symbiodinium* (Supplementary Figure 3.10). These dinoflagellate cells, being much larger than the others, led to the clustering of data into two groups (*Symbiodinium* cells on one side, all the other ones on the other side), leading to the observation of apparent linear relationships between all the considered parameters.

Excluding *Symbiodinium* from the analysis removed this bias and unveiled the existence of a tight correlation between plastids and mitochondria in terms of volume (the coefficient of determination R^2 , being 0.95, Figure 3.3 B) and surface area ratios ($R^2 = 0.85$, Figure 3.3 C) (see also Supplementary Table 3.2 and 3.3). No significant correlation was found between the volume/surface ratio of the nucleus and the mitochondria or plastid ($R^2 \leq 0.5$).

Plastid-mitochondria relationships are of primary importance in diatoms (Bailleul et al. 2015; Kim et al. 2016), where interactions between the two organelles are relevant for carbon assimilation. Based on the findings above, we propose that this organelle-organelle relationship also exists in other microalgal species, possibly representing a conserved feature of phytoplankton bioenergetics. Plastid-mitochondria interactions may rely on physical contacts between the two organelles (Bailleul et al. 2015; Flori et al. 2017; Mueller-Schuessele et al. 2018).

We tested this possibility by a comparative analysis, where we quantified contacts between plastids and mitochondria in the different species analysed above (Figure 3.4 and see Supplementary 3.4 of this chapter). Distance criteria have been recently proposed to operationally track contact points between organelles (Scorrano et al. 2019).

The distance between two organelles that can reflect a contact site is in the 10 – 90 nm range, with distances of 30 nm can be found in most cases (Scorrano et al. 2019). Following this rule, we identified surface areas of contact between plastids and mitochondria. Areas of contact varied depending on the microalgal. At 30 nm, almost no contact points were detected in *Pelagomonas* and *Nannochloropsis* ($0.1 \pm 0.1\%$ and $0.16 \pm 0.3\%$ of the plastid surface being involved in contacts with mitochondria, respectively), while interactions were found in the other microalgae (up to $7.1 \pm 0.1\%$ in *Phaeodactylum*). At 90nm, plastid-mitochondria contacts became visible in all algae, reaching $15.7 \pm 1.4\%$ in the diatom. Despite changes in their size, contact points maintained the same localisation when calculated using the distance criteria. To us, this finding suggests that plastid-mitochondria interactions occur at specific locations, as already proposed in the case of other organelles-organelle interactions (Prinz 2014; Phillips et al. 2016; Rowland et al. 2012).

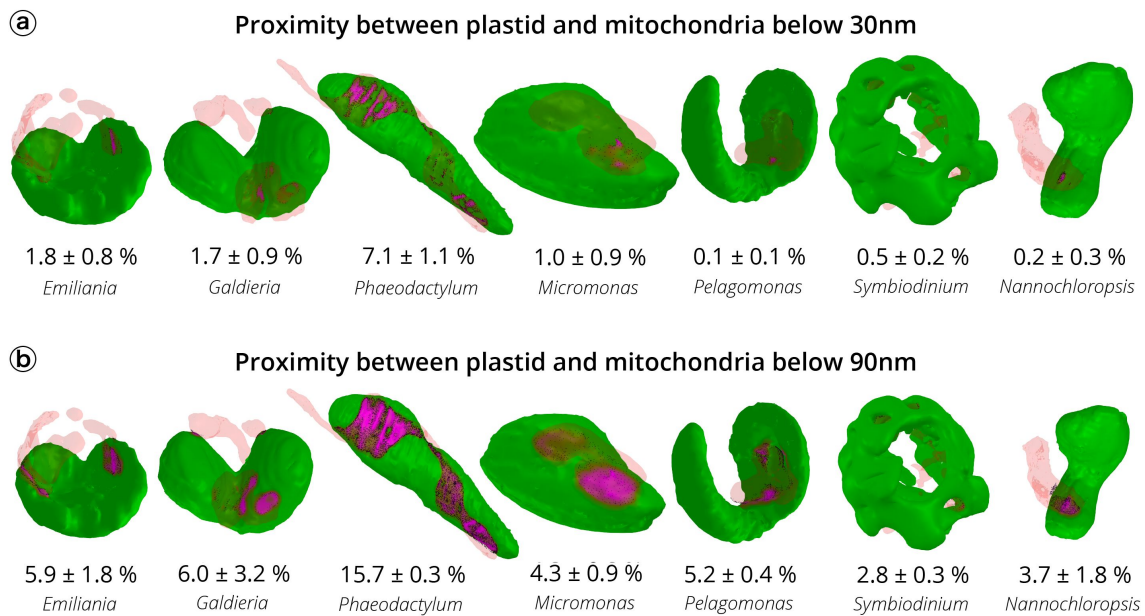


Figure 3.4 – Contact surface areas between plastids and mitochondria in phytoplankton. Green: plastid surface. Light red: mitochondria surface. Pink: contact points (i.e. points at a distance ≤ 30 nm, panel A or ≤ 90 nm) between mitochondria and plastids.

3.2.2 Subcellular features of energy managing organelles

Besides providing information on the topology of organelles, our 3D images had enough resolution to explore sub-organelle features. We exploit this possibility to investigate the possible conservation of structural architectures within plastids and mitochondria (Figure 3.5 and Supplementary Figure 3.11), seeking for signatures of structural constraints relayed to cellular energy management. Plastids were mostly occupied by thylakoid membranes and the stroma, and by the carbon-fixing pyrenoid (Figure 3.5 B), a Rubisco-rich matrix that was not observed in *Pelagomonas* (Andersen et al. 1993), *Galdieria* and *Nannochloropsis* (Merola et al. 1981; Mackinder et al. 2016).

In two taxa (*Phaeodactylum* and *Emiliana*), we observed thylakoids crossing the pyrenoid matrix (Figure 3.5 A). These pyrenoid membranes (also called pyrenoid tubules in *Chlamydomonas reinhardtii* (Engel et al. 2015)) display different topologies: we observed parallel stacks in the diatom and a more branched structure in *Emiliana*, reminiscent of that recently reported in *Chlamydomonas reinhardtii* (Engel et al. 2015; Meyer et al. 2016).

Micromonas and *Symbiodinium* contained thylakoid-free pyrenoids that were almost completely surrounded by starch sheaths (Figure 3.5 A). Few stalks ensure the connection between pyrenoid and the plastid, possibly to facilitate the diffusion of Rubisco substrates and products as previously proposed (Badger et al. 1994; Engel et al. 2015; Moroney et al. 1991), see also the review (Meyer et al. 2017). Unlike *Micromonas*, the pyrenoid of the dinoflagellate *Symbiodinium* was not centred in the plastid, but instead protruded towards the cytosol, being surrounded by a shell

of cytosolic rather than stromal starch (Dauvillée et al. 2009; Meyer et al. 2017; Van Thinh et al. 1986).

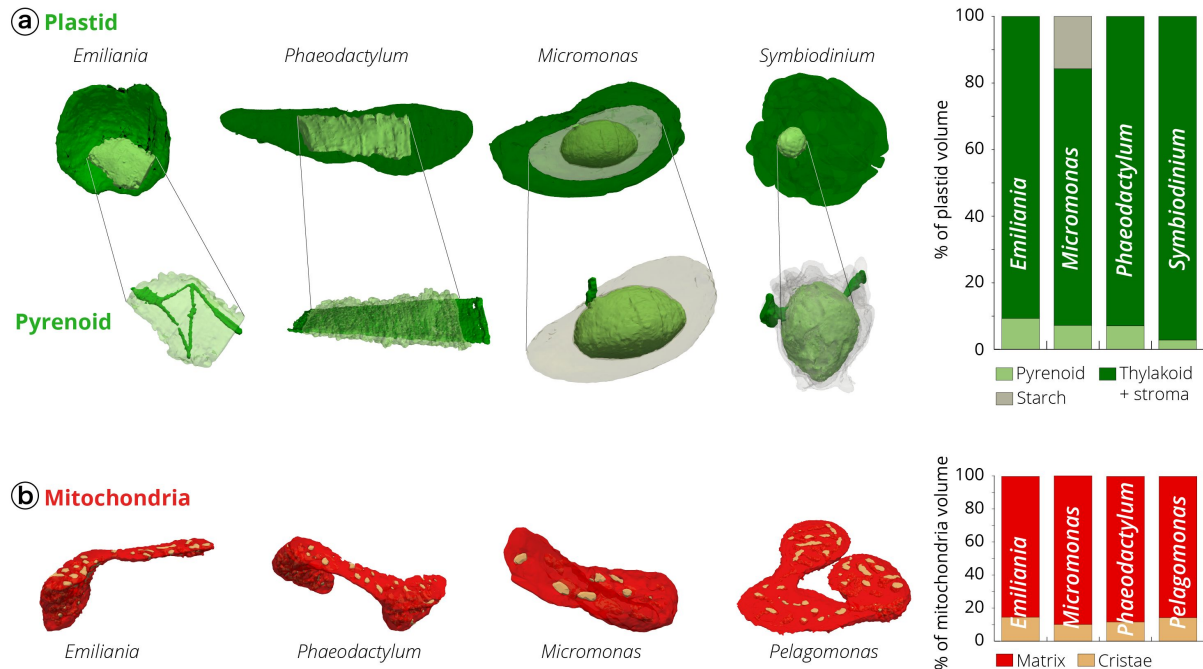


Figure 3.5 – Organization/architecture of the mitochondria and plastids of phytoplankton. (a) Topology of the plastid. Whole plastid images and focus on the CO₂-fixing compartment (pyrenoid) topology in *Phaeodactylum*, *Emiliana*, *Micromonas* and *Symbiodinium* cells. The 3D reconstruction displays the thylakoid network (dark green) crossing the pyrenoid matrix (light green). If present (*Micromonas* and *Symbiodinium*), a starch layer surrounding the pyrenoid is shown in grey. The histogram recapitulates volume occupancy by sub-plastidial structures (thylakoids, matrix, starch). Note that starch is cytosolic in *Symbiodinium*, and therefore its volume is not considered in the graph. (b) Mitochondrial features. Topology of mitochondrial compartments. Red: mitochondrial matrix; yellow: cristae. The histogram recapitulates volume occupancy by mitochondrial sub-compartments (in the matrix and within the cristae). Despite changes in the mitochondria morphology, likely reflecting the dynamic character of these organelles (Supplementary Figure 3.9), the ratio between the subcellular compartment volumes is relatively constant in the different cells.

Despite the differences in the pyrenoid topology, the ratio of pyrenoid/plastid volumes was preserved in three out of the four microalgae lineages where this compartment was present (7.1 ± 1.2 %, 9.3 ± 1.4 %, 7.2 ± 1.2 % for *Phaeodactylum*, *Emiliana*, *Micromonas*, respectively, Figure 3.5 A and Supplementary Table 3.5). This constant ratio highlights the importance of maintaining a proper balance between the sub-compartments performing light harvesting (the photosynthetic membranes) and CO₂ fixation (the pyrenoid). An exception to this observation is *Symbiodinium*, where the pyrenoid occupies a much lower fraction of the plastid volume (2.8 ± 0.2 %). Our

quantitative morphometric analysis provides a possible rationale for this exception. We found that the pyrenoid surface/volume ratio (an important parameter for gas exchange in this compartment, and therefore for CO₂ assimilation) is 20.6 ± 6 , 12.3 ± 2.6 and 15.1 ± 2.4 in *Phaeodactylum*, *Emiliana*, *Micromonas* but only around 4.7 ± 2.3 in the dinoflagellate.

This possibly explains why the large increase in the plastid volume of *Symbiodinium* ($63.5 \pm 9.5 \mu\text{m}^3$) when compared to *Phaeodactylum*, *Emiliana* and *Micromonas* ($11 \pm 0.3 \mu\text{m}^3$, $5.8 \pm 1.8 \mu\text{m}^3$, $0.5 \pm 0.2 \mu\text{m}^3$, respectively, Supplementary Table 3.5) is not followed by a commensurate expansion of the pyrenoid volume in the dinoflagellate ($2 \pm 0.2 \mu\text{m}^3$), when compared to the other algae ($0.8 \pm 0.1 \mu\text{m}^3$, $0.5 \pm 0.2 \mu\text{m}^3$ and $0.05 \pm 0.03 \mu\text{m}^3$ respectively). A much lower surface to volume ratio may represent a functional constraint for carbon assimilation.

Overall, our volumetric analysis of the pyrenoid suggests that both the surface to volume ratio and the volumetric ratio between the plastid and the pyrenoid are important parameters for the photosynthetic metabolism. This concept of constant volumetric ratios within energy producing organelles is corroborated by our analysis of mitochondria. In these organelles, we found that the ratio between the volume inside the cristae and the matrix (Figure 3.5 B and Supplementary Table 3.6) is relatively constant in all cells (11.6 ± 2.8 %, 14.2 ± 2.6 %, 14.5 ± 2.9 %, 10.1 ± 5.9 % in *Phaeodactylum*, *Pelagomonas*, *Emiliana* and *Micromonas*, respectively, Figure 3.5 B), despite differences in the shape (Figure 3.3 A) and overall volumes of their mitochondria (Figure 3.2 C and Supplementary Figure 3.9).

3.2.3 Remodelling of the subcellular architecture of microalgae following physiological responses

The finding that plastid-mitochondria interactions and sub-organelle volume partitioning are relatively well conserved features of phytoplankton suggest that these features could have been evolutionary-selected to ensure proper microalgal fitness. To test this hypothesis, we looked at possible modifications in the above mentioned parameters upon exposing microalgae of a given species to changing environmental conditions. For these experiments, we concentrated on laboratory model algae (*Phaeodactylum* and *Nannochloropsis*), which can easily be grown in different conditions.

We first focused on *Phaeodactylum* cells grown under different light intensities, i.e. a type of environmental modification that is often experienced by diatoms in their natural environment (Gallagher et al. 1984). Exposure to increasing light intensity enhanced both respiratory and photosynthetic performances (Figure 3.6), see Supplementary Table 3.7), in line with previous reports (Bailleul et al. 2015). Comparative analysis of 3D models of cells from low light ($40 \mu\text{mol photons m}^{-2}\text{s}^{-1}$) and high light ($350 \mu\text{mol photons m}^{-2}\text{s}^{-1}$) conditions revealed substantial changes in

the morphology of the two cell engines (Figure 3.6).

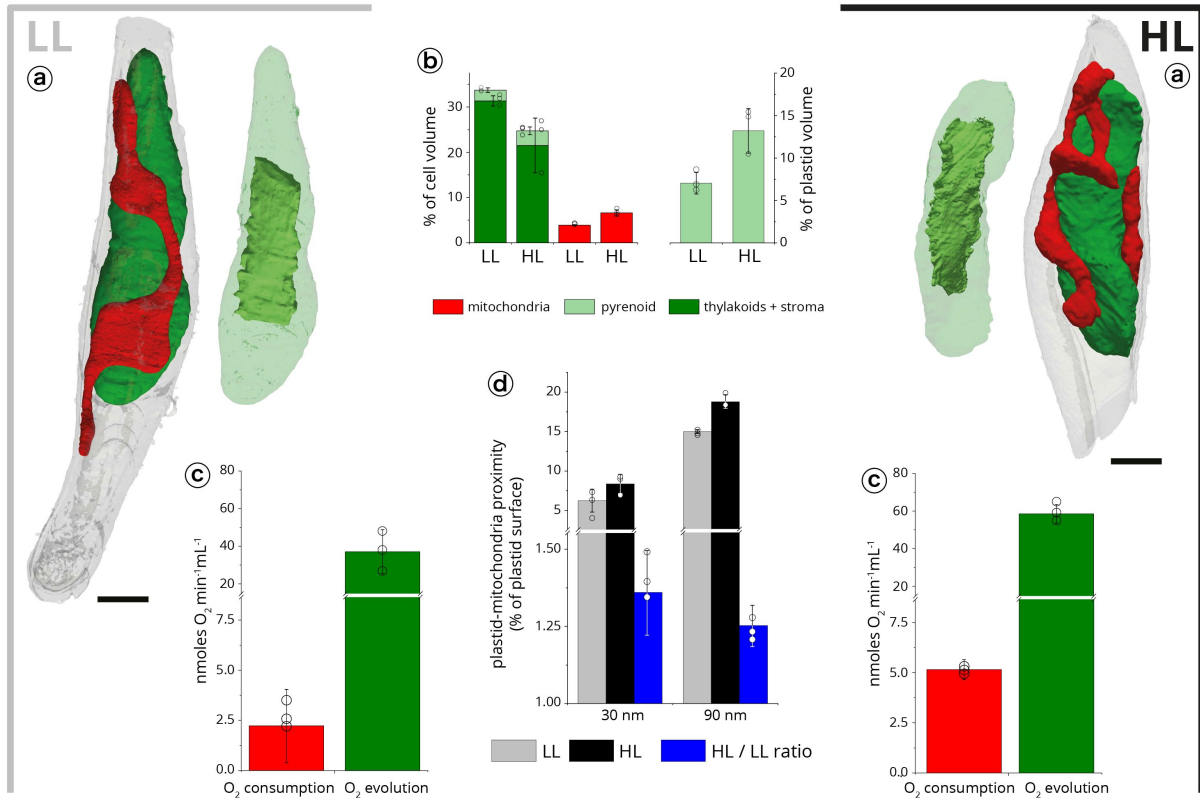


Figure 3.6 – Light acclimation in *Phaeodactylum tricornutum*. Cells were grown under two different regimes: LL ($40 \mu\text{mol photons m}^{-2}\text{s}^{-1}$, left) and HL ($350 \mu\text{mol photons m}^{-2}\text{s}^{-1}$, right). Photosynthetic capacities and respiratory activities are indicated in green and red, respectively. (a) Volume occupancy by the plastids (dark green), mitochondria (red) and pyrenoid (light green) in the two growth conditions. (b) plastid-mitochondria contact points in LL and HL cells, measured at 30 nm (grey) and 90 nm (black). At both distances, contact points are increased by around 25 % (blue) upon HL transition. $N = 3 \pm \text{s.d}$

The volume occupied by mitochondria showed an almost twofold increased (from 3.9 ± 0.2 to 6.6 ± 0.2 %), consistent with the enhanced respiratory activity. Conversely, the overall plastid volume slightly narrowed down from 31.3 ± 1.2 to 21.5 ± 5 %. This reduction already reported in the case of *Phaeocystis Antarctica* (Moisan et al. 2006) was not accompanied by changes in the pyrenoid volume occupancy (2.4 ± 0.6 vs 3.2 ± 1) leading to an almost twofold augmentation of the plastid volume occupied by the pyrenoid (from 7 ± 1.3 to 13.2 ± 2.5 %), at the expenses of the thylakoids + stroma. These increase likely accounts for the significant increase in photosynthetic activity (from $37 \pm 11 \mu\text{mol O}_2 \text{ mg Chl}^{-1}$ to $58 \pm 5 \mu\text{mol O}_2 \text{ mg Chl}^{-1}$) observed between low light and high light acclimated cells.

Indeed, photon capture by the thylakoids in high light no longer limits the photosynthetic flux, which is, instead, set by the turnover of the carbon assimilating enzymes. Enhanced photosynthetic performances are also expected based on the relative increase of plastid-mitochondrial contacts ($35 \pm 13\%$ at 30 nm and $25 \pm 6.7\%$) between HL and LL cells, in the frame of the hypothesis that organelle interactions improve photosynthesis by facilitating energetic interactions between the two cell engines (Bailleul et al. 2015).

Next, we compared the physiology and subcellular features of *Nannochloropsis* cells exposed to two trophic conditions. Previous studies have highlighted the ability of this alga to metabolize external carbon sources under photosynthetic conditions (mixotrophy) for a better growth (Sforza et al. 2012; Das et al. 2011; Fang et al. 2004).

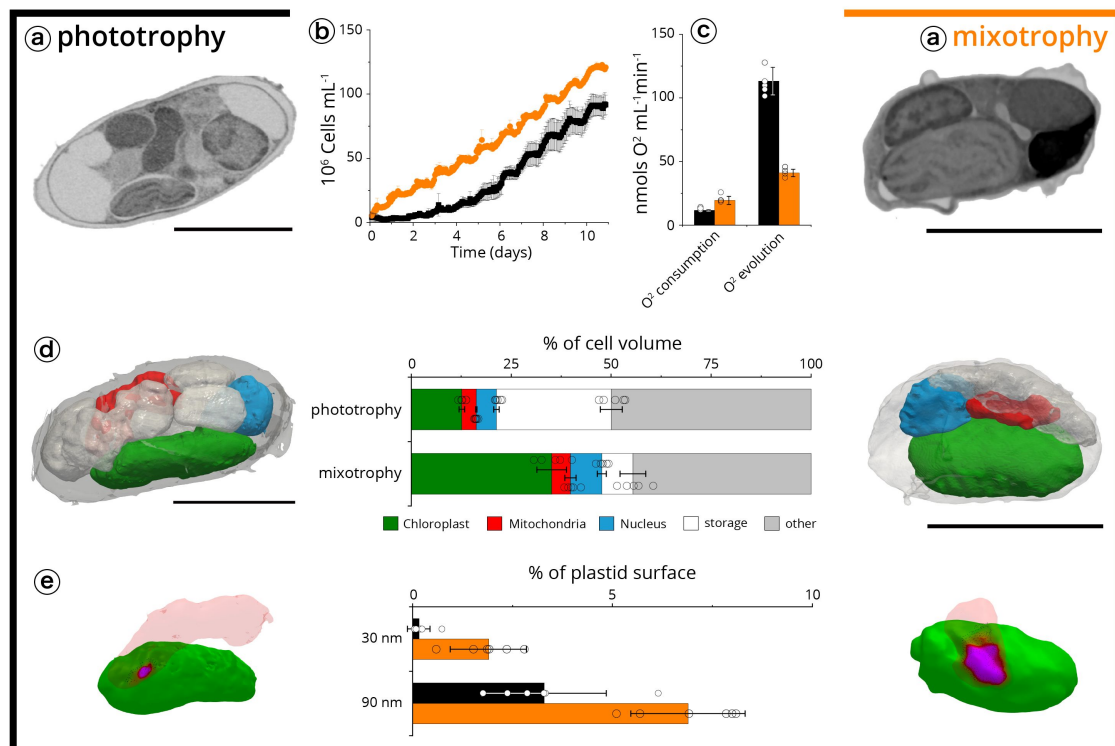


Figure 3.7 – Plastid mitochondria interactions are modified by trophic regimes. (a) 2D FIB-SEM section of *Nannochloropsis* cell. (b) Growth capacity. (c) Oxygen evolution and consumption in photoautotrophic conditions (black), and mixotrophic ones (orange). (d) Volume occupancy by the different subcellular compartments in different microalgal cell. Green: plastid; red: mitochondria; blue: nuclei; white storage vesicles; grey: other. (e) Analysis of plastid-mitochondria contact points in phototrophic (black) and mixotrophy (orange) conditions. $N = 5 \pm \text{s.d.}$

We reproduced the growth enhancement reported earlier when shifting cells from phototrophy (without organic carbon) and in a carbon rich medium (Marudhupandi et al. 2016) (Figure 3.7 and supplementary Table 3.8), and found that changes in the trophic lifestyle of this alga were also accompanied by substantial physiological and morphological changes. Shifting the algae to mixotrophy enhanced their respiratory capacity (from $11.5 \pm 0.5 \mu\text{mols O}_2 \text{ mg Chl}^{-1}$ to $18.5 \pm 2.5 \mu\text{mols O}_2 \text{ mg Chl}^{-1}$) while photosynthetic activity decreased (from $113.1 \pm 11.1 \mu\text{mols O}_2 \text{ mg Chl}^{-1}$ to $41 \pm 3.1 \mu\text{mols O}_2 \text{ mg Chl}^{-1}$).

In parallel, the volume occupied by organelles recovered a value (around 50%) similar to the one observed in the other algae (Figure 3.2), mainly due to a substantial decrease in the bulkiness of reserve vesicles. We interpreted this finding in terms of a higher consumption of lipid reserves in mixotrophy owing to the less favourable balance between photosynthesis and respiration. Moreover, we observed a substantial increase of plastid and mitochondria interaction upon acclimation to mixotrophy (Figure 3.7 C, Supplementary Table 3.8). The increase was huge when calculated for a distance of at 30 nm (from $0.16 \pm 0.3 \%$ to $1.776 \pm 0.9 \%$) and still two fold at 90 nm (from $3.3 \pm 1.7 \%$ to $6.9 \pm 1.4 \%$). We conclude that *Nannochloropsis* cells may increase organelles contacts under conditions where respiration is boosted to favour energy interactions between the two organelles and therefore improve cell energy usage for growth.

Conclusion and perspectives

Thanks to the optimisation of the different steps of the workflow (sample preparation, acquisition, segmentation and 3D reconstruction), the FIB-SEM tomograms reported here allows generating high-resolution whole cell 3D models of different phytoplankton species. These tomograms provide a unique resource to evaluate morphological differences and similarities between relatively distant phytoplankton organisms, and better assess their physiological responses in changing environment.

Besides structural differences, our analysis pinpoints conserved features: (i) conserved cell-volume fractions that are occupied by the main organelles (Figure 3.2); (ii) plastid-mitochondria contact points (Figure 3.3 - 3.4), (iii) constant surface/volumetric ratios inside the energy-producing organelles, as exemplified by the surface to volume ratio in mitochondria and in the pyrenoid (Figure 3.2). These characteristics suggest the existence of topological constraints on phytoplankton subcellular organisation, possibly reflecting functional constraints at the level of energy management for carbon assimilation. Consistent with this hypothesis, acclimation of *Phaeodactylum* cells to different light conditions and of *Nannochloropsis* to trophic lifestyles result in changes in their photosynthetic/respiratory activity, which we can explain based on topological changes in the two cell engines plastid and mitochondria. Overall these data clearly highlight the existing link between cell structures, cell energy balance and physiological responses.

The quantitative FIB-SEM tomography workflow developed here represents a unique approach to interpret physiological responses at the subcellular and even sub-organellar structures. Correlation of this approach with cryo-electron tomography, combination with chemical imaging (Decelle et al. 2020) and correlative microscopic studies on phytoplankton (Sartori et al. 2007; Stephens et al. 2003) may further improve the spectrum of applications of this technique, and enlarge its applications. We predict that it will be relevant to study climate change scenarios (Pachauri et al. 2014), where changes in temperature and nutrient availability may affect the subcellular features of phytoplankton, thereby disturbing their activity and acclimation capacity.

Material and methods

Species. The species used in this work (see Table 3.1) were chosen on the basis of their representativeness of phytoplankton taxa that are ecologically relevant or of their ability to successfully grow in variable laboratory conditions.

Algal cultivation. *Phaeodactylum* CCAP 1055/3 was obtained from the Culture Collection of Algae and Protozoa, Scottish Marine Institute, UK. Cells were grown in the ESAW (Enriched Seawater Artificial Water) medium (Berges et al. 2001) in 50 mL flasks in a growth cabinet (Minitron, Infors HT, Switzerland), at 19°C, a light intensity of 40 $\mu\text{mol photon m}^{-2}\text{s}^{-1}$, a 12-h light / 12-h dark photoperiod (unless otherwise specified) and shaking at 100 rpm. *Galdieria* SAG21.92 was obtained from the University of Dusseldorf (Germany) and was grown in sterile 2XGS modified Allen medium, pH 2.0 (Allen 1959) at 42°C under the same light conditions.

Cells were grown in 250 mL flasks (50 mL culture volume). *Nannochloropsis* CCMP526 was cultivated in artificial seawater ESAW using ten times enriched nitrogen and phosphate sources (5.49×10^{-3} M NaNO_3 and 2.24×10^{-4} M NaH_2PO_4); called “10X ESAW” (Dolch et al. 2017). Cells were shifted from photoautotrophic to mixotrophic conditions through the addition of 5% Lysogeny Broth (LB) to the growth medium. *Micromonas* 84 RCC 827, *Pelagomonas* RCC 100, *Emiliania* RCC 909 in K medium at 20°C, and *Symbiodinium* RCC 4014 in F/2 medium at 20°C were obtained from the Roscoff Culture Collection (Vaulot et al. 2004) and maintained in the same medium and temperature condition without agitation. Cells were kept at a light intensity of 60 – 80 $\mu\text{mol photon m}^{-2}\text{s}^{-1}$, a 12-h light / 12-h dark photoperiod, without shaking.

Nannochloropsis growth was measured following changes in the culture optical density at 650 nm. Changes were calibrated with cell numbers in both control and mixotrophic cultures. Oxygen exchanges were measured with a Clark-type electrode (Hansatech Instruments, UK) at 20°C. Respiration and gross photosynthesis were quantified by measuring the slope in the dark and upon light exposure (intensity 300 $\mu\text{mol photon m}^{-2}\text{s}^{-1}$).

Sample preparation for electron microscopy. Sample preparation protocols were adapted from (Decelle et al. 2019) to optimize the contrast for 3D electron microscopy imaging and therefore facilitate image segmentation through pixel classification. Live cells were cryofixed using high-pressure freezing (HPM100, Leica) in which cells were subjected to a pressure of 210 MPa at -196°C , followed by freeze-substitution (EM ASF2, Leica). Prior to cryo-fixation, the microalgal cultures were concentrated by gentle centrifugation for 10 min (800 ref). For the freeze substitution (FS), a mixture 2% osmium tetroxide and 0.5% uranyl acetate in dried acetone was used. The freeze-substitution machine was programmed as follows: 60 – 80 h at -90°C , heating rate of 2°C h^{-1} to -60°C (15 h), 10 – 12 h at -60°C , heating rate of 2°C h^{-1} to -30°C (15 h), and 10 – 12 h at -30°C , quickly heated to 0°C for 1 h to enhance the staining efficiency of osmium tetroxide and uranyl acetate and then back at -30°C . The cells were then washed four times in anhydrous acetone for 15 min each at -30°C and gradually embedded in anhydrous araldite resin. A graded resin/acetone (v/v) series was used (30, 50 and 70% resin) with each step lasting 2 h at increased temperature: 30% resin/acetone bath from -30°C to -10°C , 50% resin/acetone bath from -10°C to 10°C , 70% resin/acetone bath from 10°C to 20°C . Samples were then placed in 100%resin for 8 – 10 h and in 100% resin with the accelerator BDMA for 8 h at room temperature. Resin polymerization finally occurred at 65°C for 48 h.

FIB-SEM acquisition imaging. Focused ion beam (FIB) tomography was performed with either a Zeiss NVision 40 or a Zeiss CrossBeam 550 microscope, both equipped with Fibics Atlas 3D software for tomography. The resin block containing the cells was fixed on a stub with carbon paste, and surface-abraded with a diamond knife in a microtome to obtain a perfectly flat and clean surface. The entire sample was metallized with 4 nm of platinum to avoid charging during the observations. Inside the FIB, a second platinum layer (1 – 2 μm) was deposited locally on the area analysed. The sample is then abraded slice by slice with the Ga^{+} ion beam (generally with a current of 700 nA at 30 kV). Each freshly exposed surface is imaged by scanning electron microscopy (SEM) at 1.5 kV and with a current of ~ 1 nA using the in-lens EsB backscatter detector. For algae, we generally used the simultaneous milling and imaging mode for better stability, and with an hourly automatic correction of focus and astigmatism. For each slice, a thickness of 8 nm was removed, and the SEM images were recorded with a pixel size of 8 nm, providing an isotropic voxel size of $8 \times 8 \times 8 \text{ nm}^3$. Whole volumes were imaged with 800 to 1000 frames, depending on the species. Due to its reduced cell dimensions, the voxel size was reduced to $4 \times 4 \times 4 \text{ nm}^3$ in the case of *Micromonas*, resulting in higher resolution datasets with approximately 350 – 500 frames/cell.

Image processing. As a first step of image processing, ROIs containing cells were cropped from the full image stack. This was followed by image registration (stack alignment), noise reduction, semi-automatic segmentation of ROIs, 3D reconstruction of microalgae cells and morphometric analysis. Several problems may be

encountered during these steps. Raw stacks consist of big data (50 to 100 GB for the whole imaged volume, containing several cells) that do not necessarily fit into the computer main memory (RAM). Moreover, cryo-substituted cells generate less contrasted images than cells prepared with chemical fixation. Therefore, the first step in building a robust 3D model consists in ‘isolating’ a given ROI (e.g. an organelle) from other compartments, to obtain a smaller stack size that can be easily worked with (in practice, we worked with substacks that were around 10% of the original stack size).

Single cells were isolated by cropping in 3-dimensions using the open software **Fiji** (Supplementary Figure 3.8 A). Image misalignment was corrected using **template matching** (“align slices in stack”) option implemented in Fiji. This function tries to find the most similar image pattern in every slice and translates them to align the landmark pattern across the stack (Figure 2.7). Aligned image stacks were filtered to remove noise using Python (Oliphant 2007) and OpenCV (Minichino et al. 2015). Filtering techniques were chosen to highlight contours while removing noise in the images. Depending on the species, we found that the osmium staining was not homogeneously distributed. Therefore, it was not possible to filter raw datasets of every species with the same method. Based on the effectiveness in highlighting organelle boundaries, different filters were used for the different microalgae (Supplementary Figure 3.8 B). Application of a linear Gaussian filter followed by sharpening to remove noise and enhance contours, which is widely used and easy to implement (Russo 2002), was used to process raw datasets of *Emiliana*, *Micromonas*, *Nannochloropsis*, *Phaeodactylum* and *Pelagomonas*. However, this method was less effective when applied to raw datasets of *Galdieria* and *Symbiodinium*, where using the median filter turned out to be a better de-noising option. These choices reflect the different cellular features and biochemical composition of each taxon (e.g. the presence of a thick cell wall in *Galdieria*), which results in variable contrast.

Segmentation. Segmentation of organelles, vesicular networks, vacuoles and storage compartments was carried out with **3DSlicer** software (Kikinis et al. 2014) (Supplementary Figure 3.8 C), using a manually-curated, semi-automatic pixel clustering mode (3 to 10 slices are segmented simultaneously for a given Region Of Interest, (ROI)). We ‘coloured’ the ROIs using paint tools and adjusted the threshold range for image intensity values. The ROIs were annotated and the corresponding label map was run into the model maker module from 3D slicer (Supplementary Figure 3.8 C), to generate corresponding 3D models that were exported in different formats (.stl, .obj, .vtk, .ply, .mtl). For further analysis, we used the .stl mesh, which proved to be more suitable for 3D analysis in our workflow (Table 2.4).

3D reconstructed model. A 3D filtering process was needed to clean the model and reduce the size of the file (see Figure 2.1). In our case, 3D models generated by 3D Slicer were imported into the open source software MeshLab (Cignoni et al. 2008) to clean the model by automatically removing isolated islands and then edited

with the MeshLab software (Cignoni et al. 2008; Callieri et al. 2012) to eliminate “isolated islands”, which were erroneously annotated as ROIs. We also performed a remeshing process to facilitate 3D modelling, visualization and animation. Using MeshLab, we simplified meshes (‘mesh decimation’, Supplementary Figure 3.8 D) to reduce the model nodes and faces down to 25% of the original data without modifying morphometric values, such as surfaces and volumes (see Table 2.5). Every 3D model was imported into Paraview (Ahrens et al. 2005) (Supplementary Figure 3.8 D) to visualize 3D objects and understand their relationship. **Blender** was used for object animation.

Morphometric evaluations. Measurement of volumes, surface area, and the minimum distance between meshes were performed using **numpy-stl** and **Trimesh** packages of Python see the code script in the section 2.7.1. This Python package is faster than MeshLab, with obvious advantages in terms of analysis of large files (> 500 MB).

Surface and volume measurements. Surfaces and volumes were computed using the discrete mesh geometry, surface being computed directly from mesh triangles, and volume being obtained from the signed volume of individual tetrahedrons, assuming a closed surface (watertight mesh Supplementary Figure 3.8 E).

Briefly, to compute the surface, we iterated over all the triangles of the mesh. The computation of the cross product between two edges of a given triangle gives a vector whose magnitude is twice the area of said triangle. Then, the sum of all these areas provides the total surface area of the mesh. We then computed the signed volume of all tetrahedrons, which goes from the origin (0,0,0) to each triangle present in the mesh. Assuming a closed surface (watertight mesh), summing all those volumes give the volume of the mesh (Zhang et al. 2001). A simple implementation of those algorithms is provided by the authors [here](#).

Distance between organelles. Using the Trimesh Python module, the minimal distance between two meshes was calculated based on the closest points between two triangular meshes. Hence, the surface area contacts were quantified based on: *i*) calculating the minimal distance between each vertex of the plastid mesh to the mitochondria mesh (for 3 cells of every species), and then by *ii*) gathering mesh vertices according to a given distance threshold to generate contact surface. A distance threshold ≤ 90 nm was chosen as representative of an interaction between nearby organelles, on the basis of previously established morphometric analysis in animal and plant cells (Helle et al. 2013; Mueller-Schuessele et al. 2018; Scorrano et al. 2019). The corresponding surfaces were then compared to the total plastid surface. Mindist python code is provided [here](#).

Acknowledgements

The authors thank the Roscoff Culture Collection that provided phytoplankton strains and Noan Le Bescot (Ternog Design) for help in the conception and realisation of

the figures of this article. This project received funding from the European Research Council: ERC Chloro-mito (grant no. 833184) to G.F., D.F., G.C. Research was also supported by a Défi X-Life grant from CNRS to J.D., funds from the CEA DRF impulsion FIB-Bio program to J.D., P.-H.J., B.G., C.M., D.F., G.S.; the LabEx GRAL (ANR-10-LABX-49-01), financed within the University Grenoble Alpes graduate school (Ecoles Universitaires de Recherche) CBH-EUR-GS (ANR-17-EURE-0003) to C.W., J.D., P.-H.J., B.G., C.M., F.C., G.C., G.S., D.F., G.F. and the ANR ‘Momix’ (Projet-ANR-17-CE05-0029) to G.C., G.F. This project also received funds from the European Union’s Horizon 2020 research and innovation programme CORBEL under the grant agreement No 654248 to J.D. This work used the platforms of the Grenoble Instruct-ERIC centre (ISBG; UMS 3518 CNRS-CEA-UGA-EMBL) within the Grenoble Partnership for Structural Biology (PSB), supported by FRISBI (ANR-10-INBS-05-02) and GRAL to B.G., C.M., G.S. The electron microscope facility is supported by the Auvergne-Rhône-Alpes Region, the Fondation Recherche Medicale (FRM), the funds FEDER and the GIS-Infrastructures en Biologie Santé et Agronomie (IBISA) to B.G., C.M., G.S.; J.D. was supported by ATIP-Avenir program. C.U. is supported by a joint UGA-ETH Zurich PhD grant (to G.F. and S.C.Z.) in the framework of the “Investissements d’avenir” programme (ANR-15-IDEX-02).

Author contributions

C.U. designed the work, performed image treatment; made programming tasks and drafted the manuscript; J.D. designed the manuscript, prepared samples for FIB-SEM, interpreted data and drafted the manuscript; P.-H. J. conceived the work, performed FIB-SEM imaging and drafted the manuscript; S.F. characterised the physiological responses of LL and HL *Phaeodactylum* cells; B.G. performed cryo fixation; J.B.K. performed image treatment automation and programming tasks; D.dB. characterised the physiological responses of phototrophic and mixotrophic *Nannochloropsis* cells; C.M. performed cryo fixation. F.C. optimized samples growth; C.S. characterised the physiological responses of LL and HL *Phaeodactylum* cells; L.S. performed FIB-SEM imaging; R.T. performed FIB-SEM imaging; F.C. interpreted data; G.C. optimized samples growth and interpreted data; Y.S. performed FIB-SEM imaging and participated to manuscript drafting; G.S. designed the work and participated to manuscript drafting; S.C.Z. designed the work and participated to manuscript drafting; D.F. designed the work, prepared samples for FIB-SEM, interpreted data and drafted the manuscript; G.F. designed the work; interpreted data and drafted the manuscript. All authors revised and approved the text. The authors declare that all the data supporting the findings of this study are available within the paper and in its supplementary information files.

Competing financial interests

The authors declare no competing financial interests.

3.3 Conclusion and perspectives

Compared to other imaging approaches involving electron microscopy (ssTEM, cryo-TEM or SBF-SEM), the FIB-SEM technique presented here has the advantage of providing a 3D tomogram of full cells with high z -resolution in organisms of different sizes (in our case $< 2 \mu\text{m}$ to $15 \mu\text{m}$). Different cell types of closely related size can be mixed in the same block during the preparation of the sample, ensuring a fast and reliable comparison between species or conditions.

The pipeline described above is entirely based on open-source software and optimises the speed of image analysis and 3D reconstruction. This approach can be applied to samples from any environment and can be used for comparative quantitative analysis of different species, providing links between cell structures and physiological or metabolic responses. We observe for instance morphological rearrangements (concerning the volume, shape and size of the cell, mitochondria and plastid organization) during adaptation of cells to different light and trophic regime (*Phaeodactylum* and *Nannochloropsis*, respectively). In both cases, a significant increase in the contact surface between the plastid and mitochondria was observed, likely to enhance the traffic between these organelles. Exchanges between plastids and mitochondria have been proposed to optimize energy utilisation in diatoms for carbon assimilation (Bailleul et al. 2015). Based on our finding, it is tempting to propose that a similar phenomenon may also occur in other phytoplankton members. To better understand the significance of this plastid mitochondria interaction, we need to count the number of membranes which are limiting the primary and secondary plastids. While primary plastids are limited by two membranes, secondary plastids are in most of the cases surrounded by four membranes (McFadden 2001; Petroustos et al. 2014; Flori et al. 2016). However, in the contact points between the plastids and mitochondria observed in diatoms, we can only count less than six membranes (4 in the plastid +2 in the mitochondria). Unfortunately, all these membranes cannot be clearly distinguished by FIB-SEM tomography.

Despite its structural limits, FIB-SEM can provide information on suborganelle structures in some cases. This concept is clearly exemplified in cells grown under high light regime by the plastids harbouring thylakoid deformation, larger pyrenoid volume and increase in number and size of plastoglobules. These changes probably reflect an adaptation of the plastid to the light stress. The pyrenoid matrix is particularly interesting. We observe various features of the pyrenoid matrix and transpyrenoidal membranes (also called tubules (Meyer et al. 2017)). Based on the 3D reconstructed model, the different shape of the pyrenoid with transpyrenoidal membranes in *Phaeodactylum* and *Emiliana* and the presence of a starch sheath surrounding the pyrenoid in *Micromonas* and *Symbiodinium*, can be considered as defining characteristics of the pyrenoid and probably contribute to their ability to deliver high CO_2 concentrations to Rubisco (Meyer et al. 2017; Ramazanov et al. 1994).

As a final comment, I would like to point out that in this study, we focused on a limited set of cell types and a restricted set of growth conditions, because this approach is relatively time consuming. However, many conditions can potentially be compared to visualise the adaptation strategies of photosynthetic microorganisms eukaryotes (and prokaryotes) to their environment, to bridge the gap between physiology, cell biology, structure and function of the ecosystems (Mock et al. 2016; Hildrew et al. 2007). These findings may be relevant to predict the consequences of climate change on phytoplankton size and morphology by influencing temperature, acidity and nutrient supply (Rossoll et al. 2012) (Rossoll et al., 2012). An important challenge for the future will be to combine this approach with Cryo-EM tomography to improve the resolution of subcellular structures at molecular levels. Mixing it with chemical imaging (Decelle et al. 2019) and fluorescence measurements with fluorophores/antibodies (Zhang et al. 2017; Prieto et al. 2014) will allow correlative microscopy studies on phytoplankton (Robinson et al. 2009).

3.4 Supplementary Materials

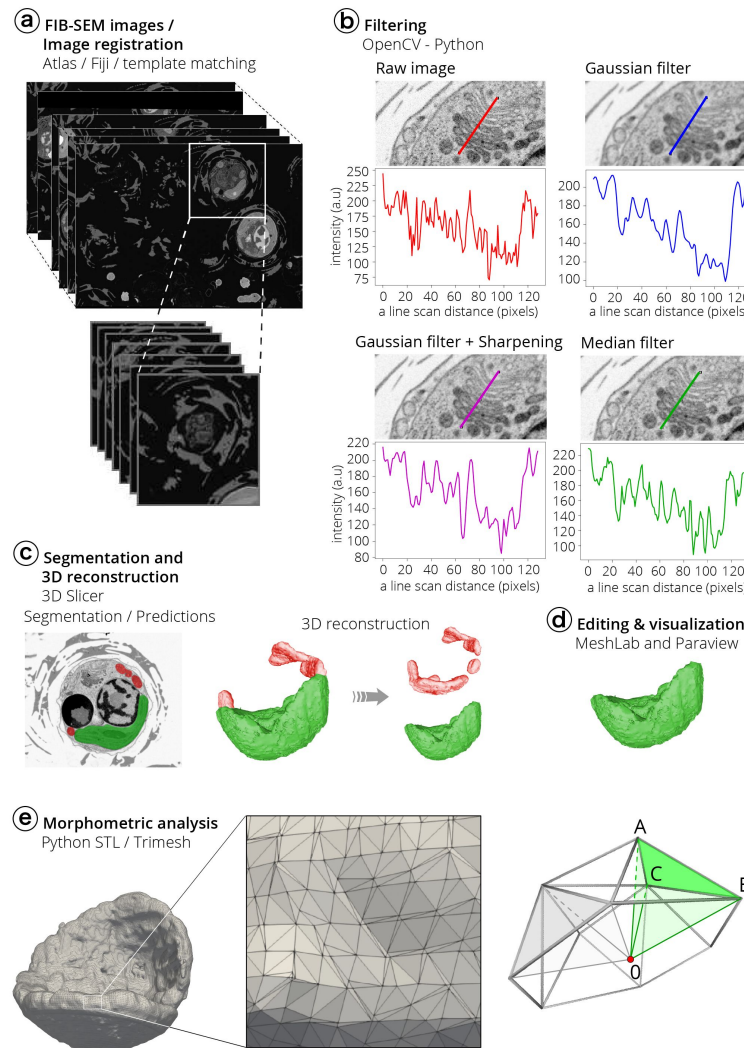


Figure 3.8 – Flowchart of image processing from data acquisition to morphometric analysis. (a) The pipeline includes data acquisition with FIB-SEM and registration with Fiji. (b) Single cells are selected from the whole FIB-SEM stack; images are registered before inverting their contrast. Stacks are filtered in Python using the PyOpenCV module. Linear (Gaussian) filter followed by edge enhancement (sharpening) or non-linear filters (median filter) are suitable in different species based on their cellular features (see text). A scan line of the Golgi apparatus drawn with Fiji in *Emiliania huxleyi* shows the impact of different filters on the profile plot of the flattened membrane-enclosed disks (the cisternae). Red: original image. Blue: A Gaussian filter smooths the edges and some membranes disappear. Purple: sharpening after application of the Gaussian filter allows recovery of some image details after smoothing edges. Green: The median filter is less sensitive to edges. (c) Image processing was done with 3D Slicer for segmentation and (d) MeshLab and ParaView, for editing and visualisation, respectively. (e) The STL and Trimesh python packages were used to quantify volumes, surfaces and distances. From a watertight mesh, surface is obtained by summing the surface of each individual triangle present in the mesh. Volume is computed with a volume integral formula discretized over tetrahedrons according to ref60. Distances between nearby point clouds of different objects within a cell were used to estimate organelle proximity. The whole process requires 10 to 15 days for a microalgal cell with a cell diameter comprised between $2 \mu\text{m}$ to $8 \mu\text{m}$.

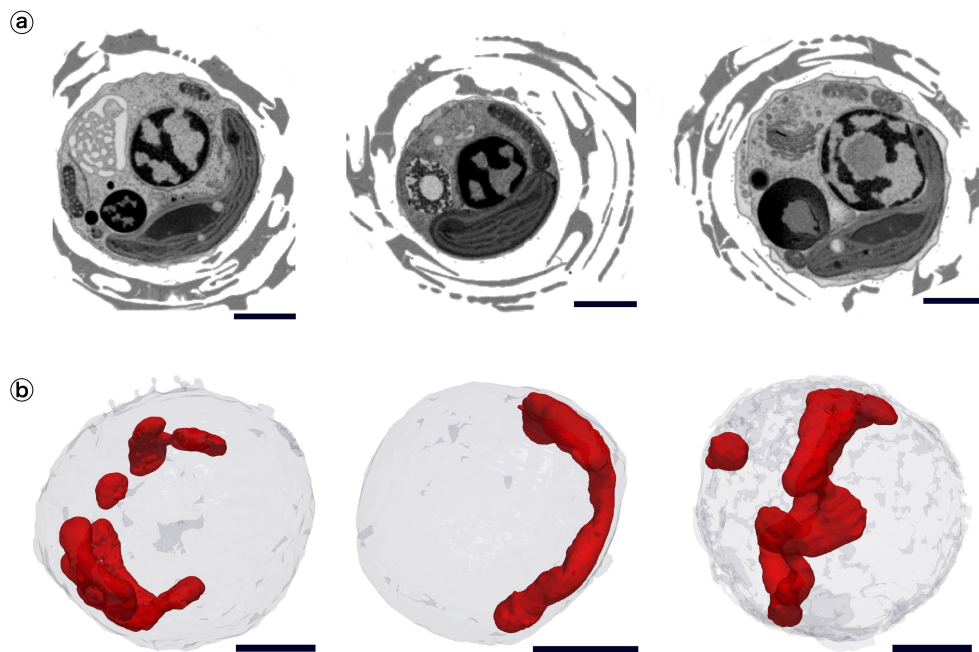


Figure 3.9 – The different morphologies of mitochondria in three *Emiliana* cells. (a) Sections through cellular 3D volumes. (b) Segmentations highlight the different 3D topology of the mitochondria (red) in the cell (light grey), consistent with the dynamic character of these organelles. Scale bar: 1 μm . Representatives micrographs and tomograms of an experiment repeated three times with similar results.

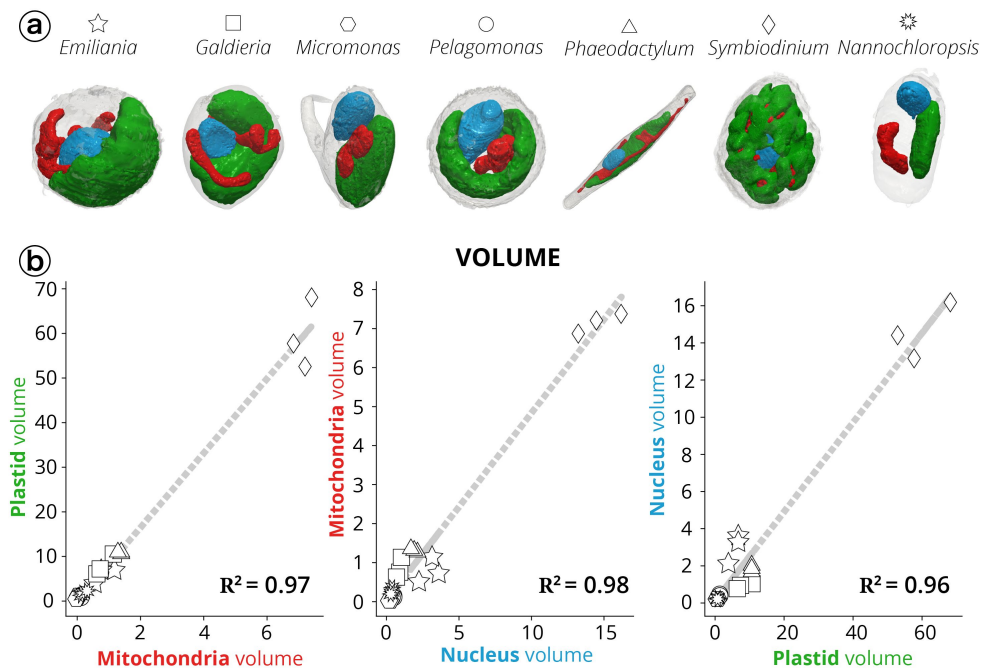


Figure 3.10 – Volumes and surfaces relationship in different subcellular compartments. Three cells are considered for every species. (a) stars: *Emiliana*; squares: *Galdieria*; hexagons: *Micromonas*; circles: *Pelagomonas*; triangles: *Phaeodactylum*; diamonds: *Symbiodinium*; suns: *Nannochloropsis*. (b) Because of the much larger size of *Symbiodinium* cells, all the other taxa are compacted in a bottom left cluster in the plot. The presence of these two clusters prevents the observation of correlation between the other cells (Figure 3.3).

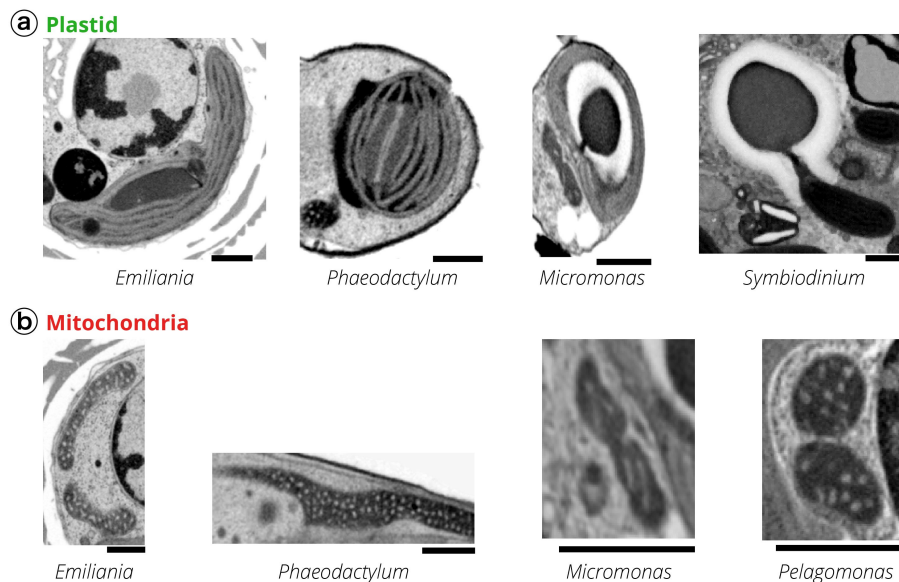


Figure 3.11 – Subcellular features of different phytoplankton taxa. 2D FIB-SEM frames of pyrenoids (a) and mitochondria (b). Scale bar: 500 nm.

Nucleus feature

In the nucleus, we observed regions with different affinity for heavy metal stain (Supplementary Figure 3.12), likely reflecting differences in DNA compactness (e.g. euchromatin vs heterochromatin). The compartments vary from the nucleus of *Phaeodactylum*, where low stained DNA was predominant (60 %) to the dinokaryon of dinoflagellates, which contained around hundreds of compact chromosomes of different sizes. The averaged surface to volume ratio was 30 ± 10 in *Symbiodinium* and 15 ± 3 in *Scrippsiella* (see Supplementary Figure 3.13 C).

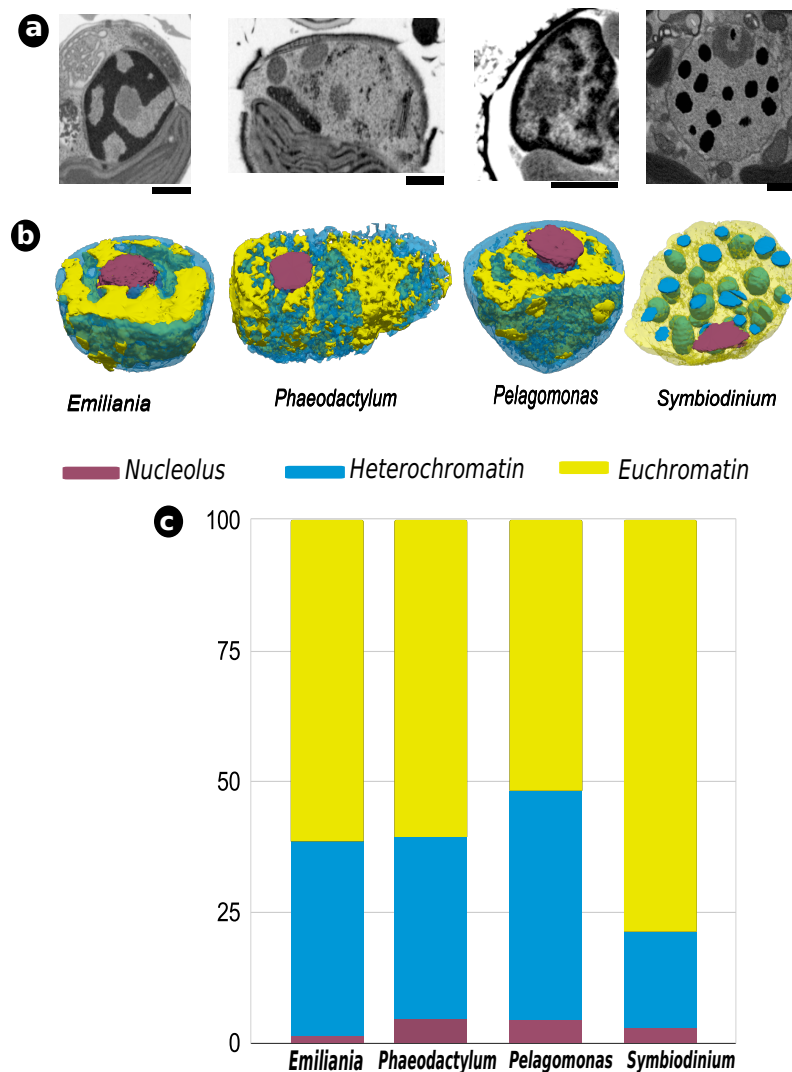


Figure 3.12 – Nucleus features. (a) 2D FIB-SEM frames of nucleus Nuclear features and the topology of the nucleus. (b) Yellow: euchromatin-low stained; blue: heterochromatin-heavy. Nucleoids-medium stained (magenta) are also visible. (c) Volume occupancy by the different types of chromatin. Different levels of DNA condensation are visible. DNA is present in the form of compact chromosomes in *Symbiodinium*, possibly leaving a fraction of the nucleoplasm without chromatin. Scale bar : 500 nm.

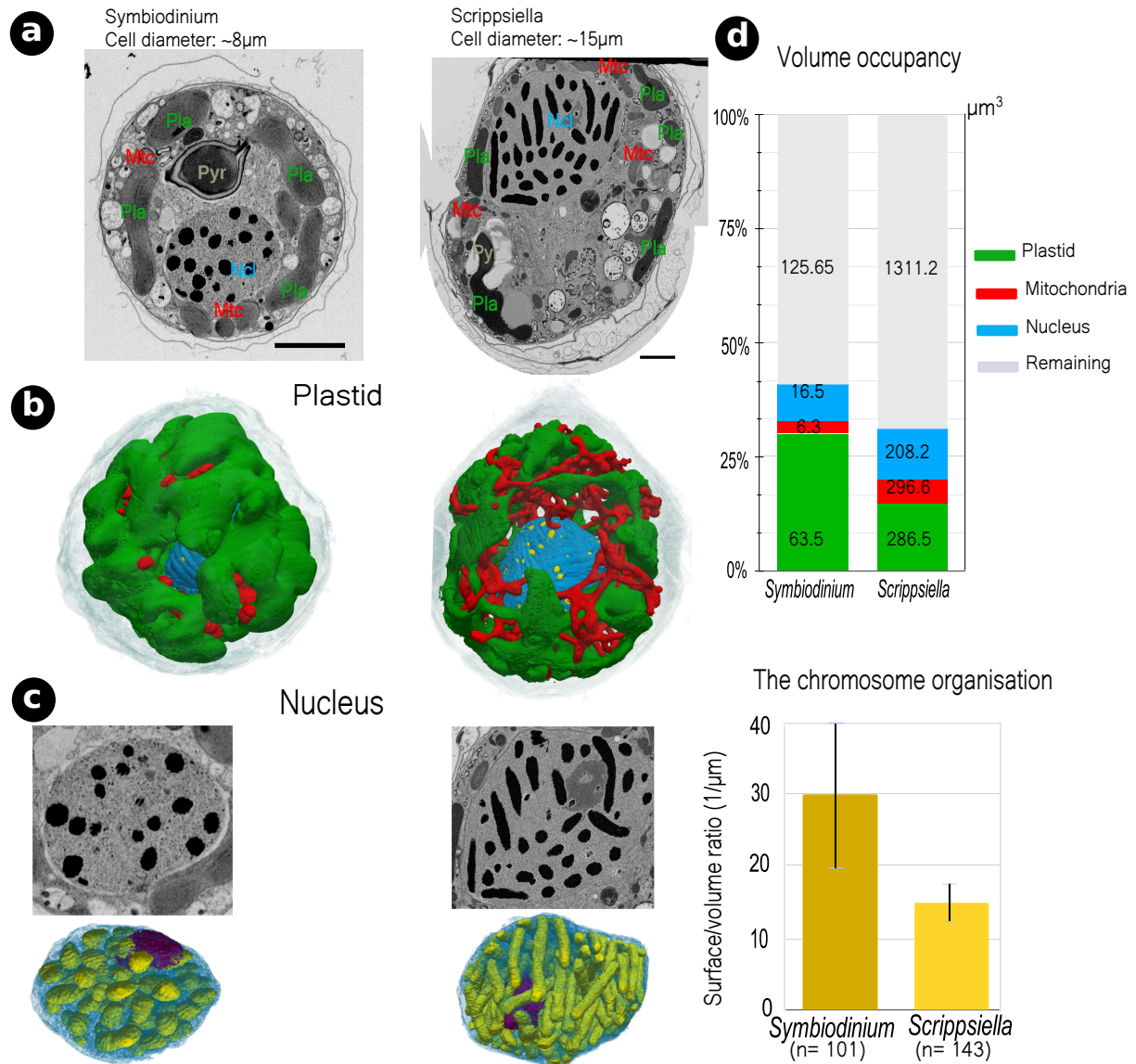


Figure 3.13 – Dinoflagellate cellular system. (a) 2D view of cell ultrastructure of *Symbiodinium*, and *Scrippsiella* cells. Abbreviation. Pla: plastid; Mtc: mitochondria; Ncl: nucleus and Pyr: pyrenoid. (b) The organelles of interest are labelled (plastid -green, mitochondria -red, nucleus -blue). 3D topologies represent the lobed plastids, mitochondria network and a dinokaryon nucleus in *Symbiodinium* and *Scrippsiella*. (c) Nuclear features. Yellow: euchromatin-low stained; blue: heterochromatin-heavy and Nucleoids-medium stained (magenta). Scale bar: $2\mu\text{m}$.

Inside the nucleus, chromosomes display a particular arrangement: most of them were in contact with the nuclear envelope, while only a few were ‘floating’ in the matrix (Supplementary Figure 3.14).

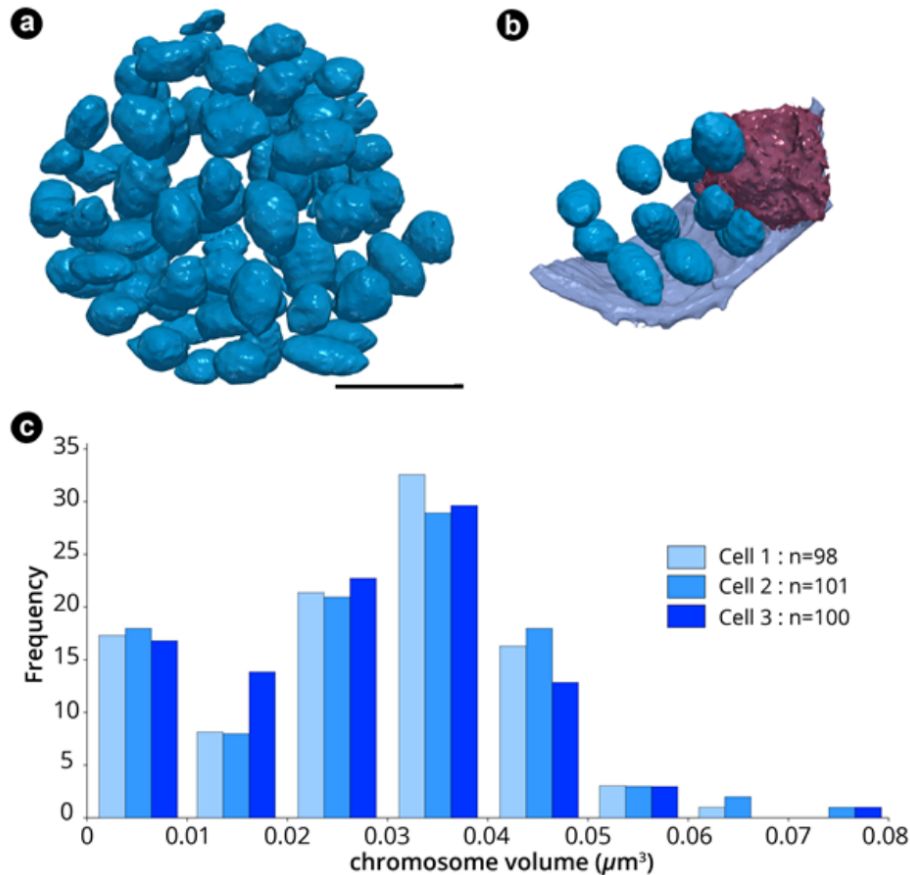


Figure 3.14 – Nucleus architecture in *Symbiodinium pilosum* cell. ((a) 3D arrangement of chromosomes (blue) inside the nucleus. ((b) Contact points with the nuclear envelope (purple) were detected for peripheral chromosomes 63 and for the nucleolus (wine) ((c) Chromosomes number and volume distribution in three cells. Scale bar: 1 μm .

Thylakoid structures in cells grown under low light and high light regimes

In chemical preparation at room temperature, osmium tends to be more effective to highlight organelles membrane envelopes compared to cryo-substitution at -30°C . We, therefore, used room temperature chemical fixation to compare the photosynthetic membranes of cells grown under low light (LL) and high light (HL) regimes (Supplementary Figure 3.15).

When *Phaeodactylum* cells are grown under a high light regime (Supplementary Figure 3.15), the global structure of the thylakoid membranes is rearranged and is somewhat more disorganised than that observed under a low light control (Supplementary Figure 3.15 A). These membranes being responsible for light absorption and utilisation, it is reasonable to think that the acclimation to high light leads to changes in the photosynthetic process associated with the structural thylakoids modification (Lodish et al. 2000). We also observe more plastoglobules, which appear larger in the

high light regime (Supplementary Figure 3.15 B). Increase in plastoglobule size and numbers reflects the reduced number of photosynthetic membranes per plastid in high light condition, and constitute probably a sign of stress as reported in the *Phaeocystis Antarctica* (Moisan et al. 2006).

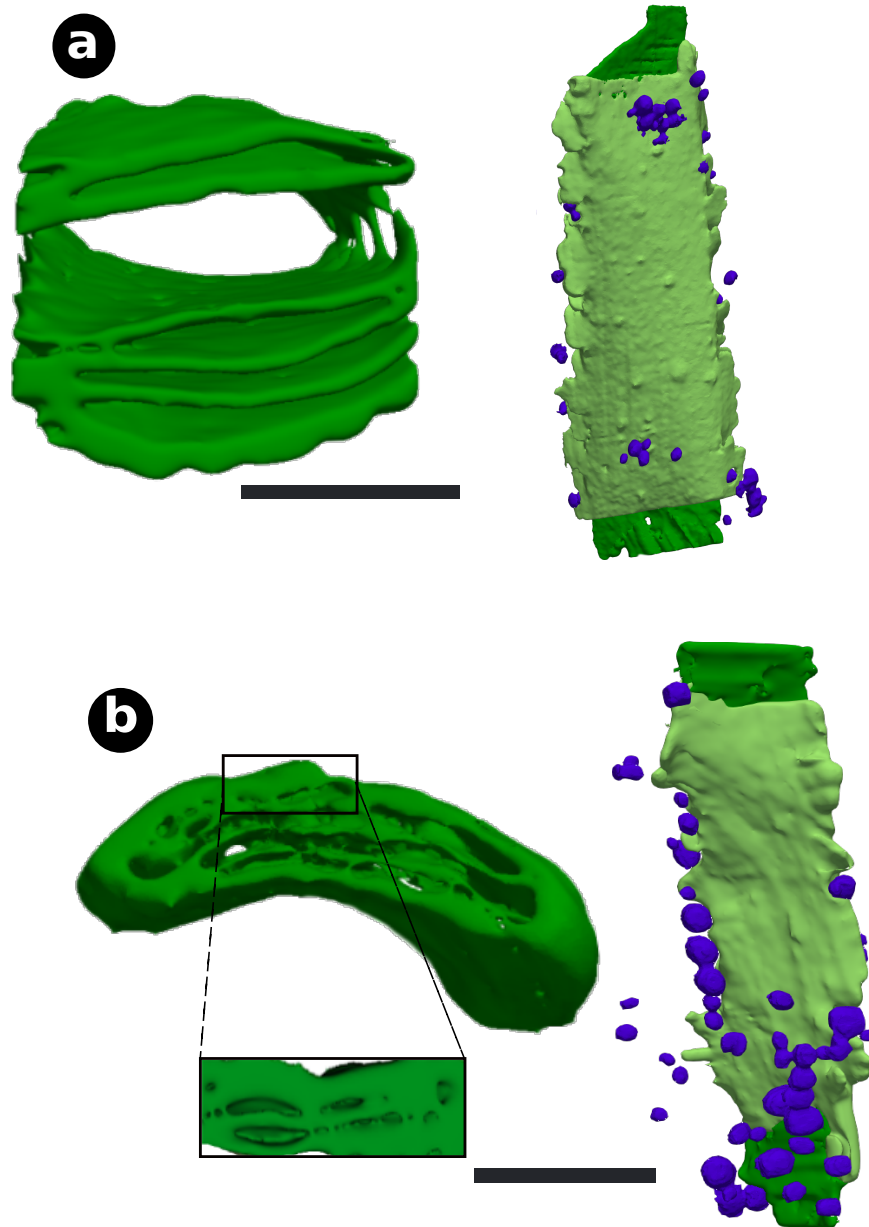


Figure 3.15 – Thylakoid membranes are modified under different light regimes. The internal plastid structures: the thylakoids (green), the pyrenoid (light green) and the plastoglobules (blue) are represented in (a) low light vs (b) high light conditions. Scale bar: 1 μm

Class	Species	Cell size	FIB-SEM z-resolution
Bacillariophyceae	<i>Phaeodactylum tricornutum</i> Pt1 8.6	13 – 15 μm of length	6nm
Pelagophyceae	<i>Pelagomonas</i> RCC 100	$\leq 3 \mu\text{m}$ in diameter	4nm
Dinoflagellates	<i>Symbiodinium</i> RCC 4014 clade A	7 – 8 μm in diameter	8nm
	<i>Scrippsiella</i>	11 – 15 μm in diameter	8nm
Prymnesiophyceae	<i>Emiliana huxleyi</i> RCC 909	3 – 8 μm in diameter	6nm
Mammiellophyceae	<i>Micromonas commoda</i> RCC 827	$\leq 2 \mu\text{m}$ in diameter	4nm
Cyanidiophyceae	<i>Galdieria</i> SAG21.92	3 – 9 μm in diameter	8nm
Eustigmatophyceae	<i>Nannochloropsis</i> CCMP526	2 – 4 μm in diameter	6nm

Table 3.1 – Taxonomy, cell size and FIB-SEM resolution of the phytoplankton cells.

<i>Micromonas</i>	Cell ₁ (μm^3)	Cell ₂ (μm^3)	Cell ₃ (μm^3)	Average(μm^3)	STD (μm^3)
Cell	2,38	1,09	1,43	1,63	0,67
Plastid	0,74	0,32	0,45	0,50	0,22
Mitochondria	0,06	0,03	0,04	0,04	0,02
Nucleus	0,25	0,18	0,23	0,22	0,04
Remaining	1,33	0,56	0,71	0,87	0,41
<i>Galdieria</i>	Cell ₁ (μm^3)	Cell ₂ (μm^3)	Cell ₃ (μm^3)	Average(μm^3)	STD (μm^3)
Cell	24,36	18,79	13,97	19,04	5,20
Plastid	10,48	7,272	6,20	7,980	2,23
Mitochondria	1,13	0,76	0,62	0,84	0,26
Nucleus	1,00	0,90	0,73	0,88	0,14
Remaining	11,75	9,86	6,42	9,34	2,70
<i>Pelagomonas</i>	Cell ₁ (μm^3)	Cell ₂ (μm^3)	Cell ₃ (μm^3)	Average(μm^3)	STD (μm^3)
Cell	4,16	3,91	2,34	3,47	0,81
Plastid	1,10	1,09	0,65	0,95	0,21
Mitochondria	0,13	0,14	0,11	0,13	0,01
Nucleus	0,49	0,48	0,12	0,36	0,17
Remaining	2,44	2,20	1,46	2,03	0,42
<i>Phaeodactyl.</i>	Cell ₁ (μm^3)	Cell ₂ (μm^3)	Cell ₃ (μm^3)	Average(μm^3)	STD (μm^3)
Cell	35,33	31,94	30,59	32,62	2,44
Plastid	11,28	10,80	10,84	10,97	0,27
Mitochondria	1,44	1,19	1,18	1,27	0,15
Nucleus	2,07	1,82	2,13	2,01	0,16
Remaining	20,54	18,13	16,44	18,37	2,06
<i>Emiliana</i>	Cell ₁ (μm^3)	Cell ₂ (μm^3)	Cell ₃ (μm^3)	Average(μm^3)	STD (μm^3)
Cell	22,12	24,35	11,98	19,48	6,597
Plastid	6,84	6,92	3,82	5,86	1,77
Mitochondria	0,94	1,34	0,58	0,95	0,38
Nucleus	3,63	3,20	2,15	2,99	0,76
Remaining	10,71	12,89	5,43	9,68	3,84
<i>Symbiodinium</i>	Cell ₁ (μm^3)	Cell ₂ (μm^3)	Cell ₃ (μm^3)	Average(μm^3)	STD (μm^3)
Cell	189,32	241,24	205,50	212,02	26,57
Plastid	56,56	74,45	59,59	63,53	9,57
Mitochondria	6,81	6,61	5,51	6,31	0,70
Nucleus	17,52	17,68	14,32	16,51	1,90
Remaining	108,43	142,50	126,08	125,67	17,04
<i>Nannochlorop.</i>	Cell ₁ (μm^3)	Cell ₂ (μm^3)	Cell ₃ (μm^3)	Average(μm^3)	STD (μm^3)
Cell	6,86	11,31	5,86	8,01	2,90
Plastid	0,79	1,51	1,04	1,11	0,37
Mitochondria	0,19	0,36	0,22	0,26	0,09
Nucleus	0,35	0,42	0,36	0,38	0,04
Remaining	5,53	9,02	4,24	6,26	2,47

Table 3.2 – Volumetric data of micro-algae Cells.

<i>Micromonas</i>	Cell ₁ (μm^3)	Cell ₂ (μm^3)	Cell ₃ (μm^3)
Cell	11,164	6,731	7,127
Plastid	13,92	6,36	7,65
Mitochondria	1,185	0,703	0,967
Nucleus	8,13	7,07	10,17
<i>Galdieria</i>	Cell ₁ (μm^3)	Cell ₂ (μm^3)	Cell ₃ (μm^3)
Cell	53,28	56,34	32,15
Plastid	36,69	50,39	24,76
Mitochondria	14,96	12,81	9,14
Nucleus	59	49,686	5,47
<i>Pelagomonas</i>	Cell ₁ (μm^3)	Cell ₂ (μm^3)	Cell ₃ (μm^3)
Cell	21,76	19,01	25,79
Plastid	12,11	10,876	9,136
Mitochondria	3,673	2,815	3,031
Nucleus	16,907	12,337	8,173
<i>Phaeodactylum</i>	Cell ₁ (μm^3)	Cell ₂ (μm^3)	Cell ₃ (μm^3)
Cell	132,07	97,89	97,74
Plastid	48,61	48,003	39,86
Mitochondria	29,88	27,47	20,85
Nucleus	14,52	15,07	13,48
<i>Emiliana</i>	Cell ₁ (μm^3)	Cell ₂ (μm^3)	Cell ₃ (μm^3)
Cell	53,947	60,5	34,421
Plastid	45,905	45,165	22,305
Mitochondria	24,532	27,741	10,677
Nucleus	59,963	57,388	32,033
<i>Symbiodinium</i>	Cell ₁ (μm^3)	Cell ₂ (μm^3)	Cell ₃ (μm^3)
Cell	185,477	236,402	183,631
Plastid	274,23	390,164	268,393
Mitochondria	69,41	55,085	88,466
Nucleus	41,56	32,51	38,56
<i>Nannochloropsis.</i>	Cell ₁ (μm^3)	Cell ₂ (μm^3)	Cell ₃ (μm^3)
Cell	20,8	30,2	27,2
Plastid	5,5	9,5	7,1
Mitochondria	2,7	5,2	3,3
Nucleus	4,3	6,0	4,5

Table 3.3 – Surface metrics information of the organelles.

<i>Micromonas</i>	Mitochondria (μm^2)	Plastid (μm^2)	Area % ($d \leq 30\text{nm}$)	Area % ($d \leq 90\text{nm}$)
Cell ₁	1,082	12,632	0,510	3,39
Cell ₂	0,658	6,000	0,390	4,62
Cell ₃	0,765	6,860	1,990	5,01
<i>Galdieria</i>	Mitochondria (μm^2)	Plastid (μm^2)	Area % ($d \leq 30\text{nm}$)	Area % ($d \leq 90\text{nm}$)
Cell ₁	12,12	31,05	0,79	3,47
Cell ₂	7,10	10,14	1,32	3,96
Cell ₃	8,27	22,38	2,83	10,50
<i>Phaeodactylum</i>	Mitochondria (μm^2)	Plastid (μm^2)	Area % ($d \leq 30\text{nm}$)	Area % ($d \leq 90\text{nm}$)
Cell ₁	21,482	41,009	5,660	15,350
Cell ₂	21,781	45,917	7,250	15,530
Cell ₃	18,887	38,773	8,410	16,090
<i>Emiliana</i>	Mitochondria (μm^2)	Plastid (μm^2)	Area % ($d \leq 30\text{nm}$)	Area % ($d \leq 90\text{nm}$)
Cell ₁	4,94	13,90	0,98	5,34
Cell ₂	6,63	14,27	2,78	8,24
Cell ₃	2,71	7,56	1,51	4,10
<i>Symbiodinium</i>	Mitochondria (μm^2)	Plastid (μm^2)	Area % ($d \leq 30\text{nm}$)	Area % ($d \leq 90\text{nm}$)
Cell ₁	65,86	255,29	0,36	2,50
Cell ₂	53,95	303,06	0,70	2,88
Cell ₃	55,01	261,05	0,32	3,13
<i>Pelagomonas</i>	Mitochondria (μm^2)	Plastid (μm^2)	Area % ($d \leq 30\text{nm}$)	Area % ($d \leq 90\text{nm}$)
Cell ₁	2,10	9,53	0,22	5,71
Cell ₂	1,89	8,64	0,00	4,87
Cell ₃	1,86	6,33	0,05	5,06
<i>Nannochloropsis</i>	Mitochondria (μm^2)	Plastid (μm^2)	Area % ($d \leq 30\text{nm}$)	Area % ($d \leq 90\text{nm}$)
Cell ₁	2,48	5,27	0,00	0,98
Cell ₂	4,41	9,00	0,00	1,21
Cell ₃	3,03	6,78	10,63	17,09

Table 3.4 – Surface metrics information of the organelles.

Plastid

<i>Phaeodactyl.</i>	Cell ₁ (μm^3)	Cell ₂ (μm^3)	Cell ₃ (μm^3)	Average(μm^3)	STD (μm^3)
Thylakoid + stroma	10,30	9,91	9,90	10,04	0,23
Pyrenoid	0,67	0,72	0,92	0,77	0,13
<i>Pyrenoid</i>	Volume (μm^3)		Surface (μm^2)		S/V ratio
Cell ₁	0,92		11,793		12,82
Cell ₂	0,67		18,327		27,35
<i>Emiliana</i>	Cell ₁ (μm^3)	Cell ₂ (μm^3)	Cell ₃ (μm^3)	Average(μm^3)	STD (μm^3)
Thylakoid + stroma	6,12	6,23	3,54	5,30	1,52
Pyrenoid	0,74	0,61	0,31	0,55	0,22
<i>Pyrenoid</i>	Volume (μm^3)		Surface (μm^2)		S/V ratio
Cell ₁	0,74		6,396		8,64
Cell ₂	0,61		8,748		14,34
<i>Micromonas</i>	Cell ₁ (μm^3)	Cell ₂ (μm^3)	Cell ₃ (μm^3)	Average(μm^3)	STD (μm^3)
Thylakoid + stroma	0,74	0,32	0,45	0,5	0,22
Pyrenoid	0,084	0,025	0,04	0,05	0,03
Starch	0,186	0,072	0,063	0,11	0,07
<i>Pyrenoid</i>	Volume (μm^3)		Surface (μm^2)		S/V ratio
Cell ₁	0,084		1,018		12,119
Cell ₂	0,025		0,448		17,92
<i>Symbiodinium</i>	Cell ₁ (μm^3)	Cell ₂ (μm^3)	Cell ₃ (μm^3)	Average(μm^3)	STD (μm^3)
Thylakoid + stroma	55,13	72,34	57,85	61,77	9,25
Pyrenoid	1,43	2,11	1,74	1,76	0,34
<i>Pyrenoid</i>	Volume (μm^3)		Surface (μm^2)		S/V ratio
Cell ₁	1,43		7,227		5,05
Cell ₂	2,11		9,537		4,52
Cell ₃	1,74		8,004		4,60

Table 3.5 – Sub-organelle in plastid volume.

Mitochondria

<i>Phaeodactyl.</i>	Cell ₁ (μm^3)	Cell ₂ (μm^3)	Cell ₃ (μm^3)	Average(μm^3)	STD (μm^3)
Cristae	14,6	11,1	9,2	11,6	2,8
Matrix	85,4	88,9	90,8	88,4	2,8
<i>Pelagomonas</i>	Cell ₁ (μm^3)	Cell ₂ (μm^3)	Cell ₃ (μm^3)	Average(μm^3)	STD (μm^3)
Cristae	11,8	13,7	17,0	14,2	2,6
Matrix	88,2	86,3	83,0	85,8	2,6
<i>Emiliana</i>	Cell ₁ (μm^3)	Cell ₂ (μm^3)	Cell ₃ (μm^3)	Average(μm^3)	STD (μm^3)
Cristae	16,0	16,4	11,2	14,5	2,9
Matrix	84,0	83,6	88,8	85,5	2,9
<i>Micromonas</i>	Cell ₁ (μm^3)	Cell ₂ (μm^3)	Cell ₃ (μm^3)	Average(μm^3)	STD (μm^3)
Cristae	16,7	10,0	4,9	10,1	5,9
Matrix	83,3	90,0	95,1	90,2	5,9

Table 3.6 – Sub-organelle compartment ratio in mitochondria volume.

Phaeodactylum cells growing under different regime

<i>Low light</i>	Cell ₁ (μm^3)	Cell ₂ (μm^3)	Cell ₃ (μm^3)	Average(μm^3)	STD (μm^3)
Cell	35,33	31,94	30,59	32,61	2,44
Plastid	11,28	10,8	10,84	10,97	0,27
Mitochondria	1,44	1,19	1,18	1,27	0,15
Nucleus	2,07	1,82	2,13	2,01	0,16
Pyrenoid	0,67	0,72	0,92	0,77	0,13
Thylakoid + stroma	10,61	10,08	9,92	10,20	0,36
<i>Proximity distance</i>	Mitochondria (μm^2)	Plastid (μm^2)	Area % (d \leq 30nm)	Area % (d \leq 60nm)	Area % (d \leq 90nm)
Cell ₁	17,023	39,387	4,61	11,01	14,73
Cell ₂	19,419	43,736	6,69	11,92	14,96
Cell ₃	17,242	38,036	7,5	11,91	15,33
<i>High light</i>	Cell ₁ (μm^3)	Cell ₂ (μm^3)	Cell ₃ (μm^3)	Average(μm^3)	STD (μm^3)
Cell	20,16	32,88	29,15	27,40	6,54
Plastid	3,43	9,32	8,41	7,05	3,17
Mitochondria	1,28	2,00	2,17	1,81	0,47
Nucleus	1,53	1,87	1,80	1,73	0,18
Pyrenoid	0,50	1,40	0,85	0,92	0,46
Thylakoid +stroma	2,93	7,92	7,56	6,14	2,78
<i>Proximity distance</i>	Mitochondria (μm^2)	Plastid (μm^2)	Area % (d \leq 30nm)	Area % (d \leq 60nm)	Area % (d \leq 90nm)
Cell ₁	12,562	16,467	6,96	14,27	18,29
Cell ₂	21,471	30,876	8,9	15,60	19,82
Cell ₃	19,26	34,271	9,29	14,53	18,25

Table 3.7 – Quantitative analysis of *Phaeodactylum* cells growing under high light regime.

Nannochloropsis cells grow in two trophic conditions

<i>Autotroph</i>	Cell ₁ (μm^3)	Cell ₂ (μm^3)	Cell ₃ (μm^3)	Cell ₄ (μm^3)	Cell ₅ (μm^3)	Average (μm^3)	STD (μm^3)
Cell	12,70	12,33	6,89	11,18	7,36	10,09	2,77
Plastid	1,71	1,43	0,86	1,50	0,91	1,28	0,38
Mitoch.	0,41	0,41	0,28	0,39	0,28	0,35	0,07
Nucleus	0,54	0,59	0,42	0,50	0,42	0,50	0,08
Remaining	10,04	9,90	5,33	8,79	5,76	7,96	2,27

<i>Proximity distance</i>	Mitochondria (μm^2)	Plastid (μm^2)	Area % (d \leq 30nm)	Area % (d \leq 60nm)	Area % (d \leq 90nm)
Cell ₁	4,93	11,49	0,15	0,94	2,83
Cell ₂	4,65	9,82	0,00	0,05	1,72
Cell ₃	2,91	5,61	0,66	1,74	3,29
Cell ₄	4,51	9,07	0,00	0,63	2,33
Cell ₅	3,56	6,48	0,01	2,56	6,09

<i>Mixotroph</i>	Cell ₁ (μm^3)	Cell ₂ (μm^3)	Cell ₃ (μm^3)	Cell ₄ (μm^3)	Cell ₅ (μm^3)	Average (μm^3)	STD (μm^3)
Cell	8,58	3,91	3,43	4,94	5,23	5,22	2,02
Plastid	3,07	1,27	1,04	1,83	2,10	1,86	0,80
Mitoch.	0,33	0,20	0,10	0,23	0,36	0,24	0,11
Nucleus	0,53	0,36	0,30	0,38	0,38	0,39	0,08
Remaining	4,65	2,08	1,99	2,50	2,39	2,72	1,10

<i>Proximity distance</i>	Mitochondria (μm^2)	Plastid (μm^2)	Area % (d \leq 30nm)	Area % (d \leq 60nm)	Area % (d \leq 90nm)
Cell ₁	4,03	12,94	0,50	2,73	5,65
Cell ₂	2,67	6,97	2,30	5,75	7,94
Cell ₃	1,23	5,51	1,46	3,10	5,03
Cell ₄	2,46	8,17	2,75	5,55	8,03
Cell ₅	3,47	9,45	1,87	5,54	7,81

Table 3.8 – Quantitative analysis of *Nannochloropsis* cells growing in two trophic regime.

Cellular architecture of a microalgal cell in planktonic photosymbiosis by FIB-SEM imaging

Contents

4.1	Introduction	96
4.2	Results and Discussion	99
4.2.1	Integration of the microalgae into the host cell	99
4.2.2	The architecture of <i>Phaeocystis</i> cell in free-living phase	100
4.2.3	Morphological change of <i>Phaeocystis</i> cells in symbiotic phase	102
4.3	Conclusion and perspective	112

Summary

*Endosymbiosis has been vital in the evolution of life on Earth and remains today a ubiquitous and ecologically significant process. Photosymbiosis is a relationship between hosts and endosymbiotic microalgae widespread in oceanic plankton, particularly in oligotrophic waters where nutrients are poorly available. However, the functioning of the host-symbiont interaction and the subcellular mechanisms by which the host harvests and benefits from its microalgae remains largely unknown. Using a quantitative subcellular imaging approach, we reconstructed the three-dimensional cell architecture of the Haptophyte *Phaeocystis* cell in free-living and symbiotic stages, and studied how microalgal cells are associated with hosts sampled in the sea. We have shown the invagination of the host-derived vacuole into the microalgal cell. This highlights cell-adaptation mechanisms in the host and provides strong evidence of host farming of algae. Inside the host, we observe algal cell volume by 80–times with a higher number of plastids (from 2 to 65 in symbiosis). Plastid multiplication lead to a 100–fold increase in the total volume of plastids in a cell. Cell division of the alga is blocked, suggesting that the cell cycle evolution and plastid division are uncoupled in symbiosis, possibly because of inhibition of communication between the plastid and the nucleus. The volume of the mitochondrial network increases up to 45 times in relation to the volume of the plastids. Altogether, these findings demonstrate a substantial morphological transformation of microalgae after their integration within a host that boost their bioenergetics, and suggest that this symbiosis could be a farming strategy in which the host exploits the microalgae for its own benefit.*

Keywords: [Photosymbiosis], [*Phaeocystis*], [Anchantarian], [3D structure], [FIB-SEM], [organelles]

4.1 Introduction

Symbiosis is living together with organisms of different species and represents one of the most intimate and sophisticated form of cellular interactions (Decelle et al. 2015a). Symbiosis was essential in the evolution of life (Margulis 1970; Decelle et al. 2015a), and it is common to almost all species and habitats. Photosymbiosis is a symbiotic interaction that arises when a photosynthetic organism is maintained within eukaryotic host cells. Through this process, many unicellular and multicellular heterotrophic species acquired a functioning mode by which they can assimilate organic carbon by phototrophy. Within plankton, mutualistic partnerships such as photosymbiosis are found everywhere in the ocean, provided that surface waters are deficient in nutrients (Taylor et al. 1982). The oligotrophy is likely to be a significant driving force in the development of these planktonic symbioses. Today, the interaction between host and microalgae is an ecologically important process in our ecosystem (Decelle et al. 2015a) because of their significant contribution to the biomass of plankton, carbon sequestration and exportation in the deep sea (Guidi et al. 2016; Lampitt et al. 2009).

Photosymbiosis is considered as a preliminary step leading to the acquisition of plastids and their propagation in photosynthetic lineages (Bhattacharya et al. 2007; Embley et al. 2006; Keeling 2004). The interplay between host and endosymbiont has eventually evolved into a parasitic relationship in which the host exploits a prokaryotic “primary endosymbiosis” or symbiont plastid “secondary or tertiary endosymbiosis”. Slowly, the symbiont cell size organelles and genomes are reduced until the host “steals” the symbiont plastid (Keeling 2013; Archibald 2015).

Among the plankton photosymbionths, Radiolaria, are commonly observed in the oligotrophic waters of the upper surface (Michaels et al. 1995; Decelle et al. 2015a). These hosts are reported to concentrate large numbers of actively photosynthesising microalgae (dinoflagellates or haptophytes) (Swanberg et al. 1991) and represent an important source of marine primary productivity. While the diversity of eukaryotic photosymbiosis is well known, the physiology and underlying cellular mechanisms, which enable a host cell to incubate and control algal cells, remain poorly understood. Here, the main objective of this chapter is to reveal the morphological changes of algal cells not in abiotic constraints as studied in the previous chapter but in biotic stress inside a host cell.

Algal remodelling in a ubiquitous planktonic photosymbiosis

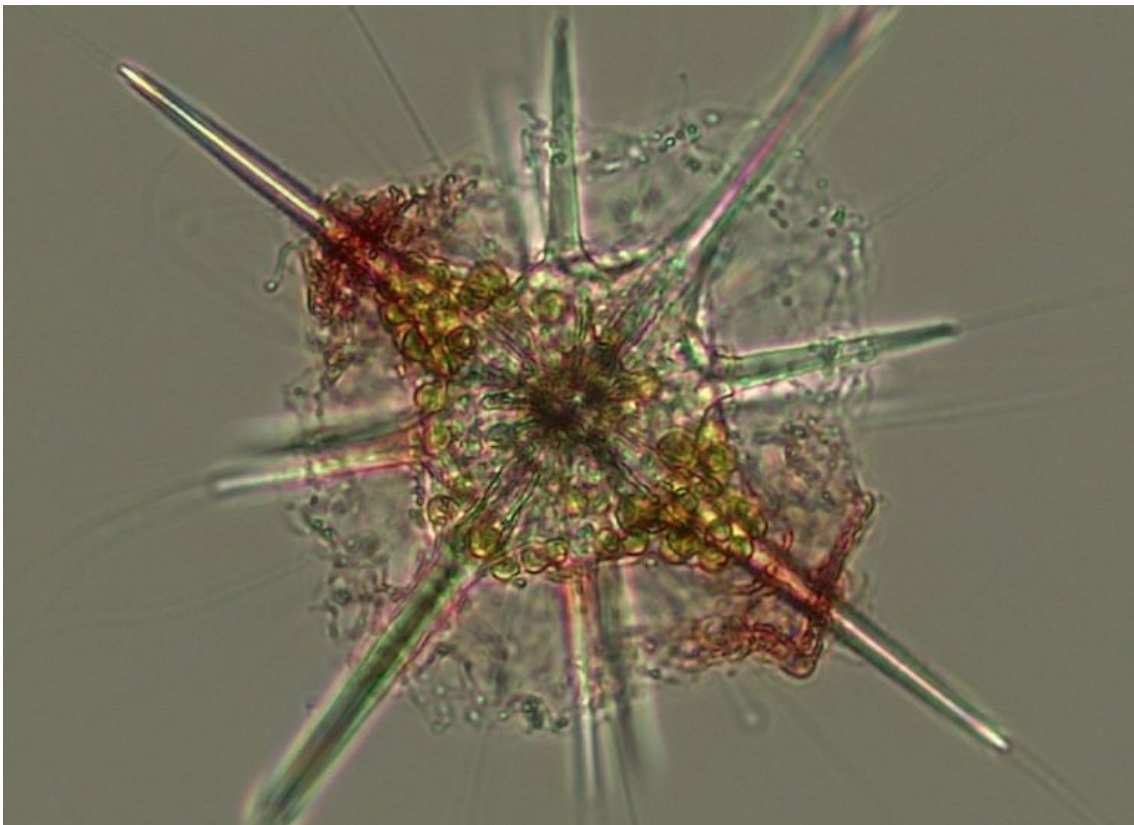
By combining FIB-SEM, nanoscale mass spectrometry X-ray fluorescence imaging, we investigated the transition between the free-living and symbiotic stages of microalgae at the subcellular level and determined the role of the host and the symbiont. These methods were complemented by physiological analyses to provide a complete picture of the physiology and metabolism of the entire relationship between the host (the radiolarian *Acantharia*) and its symbiont (the haptophyte *Phaeocystis*). We observed: (i) more plastids (from 2 to up to 30) and thylakoids in symbiotic *Phaeocystis*

than in free-living forms. (ii) higher photosynthetic efficiency (3–fold) in symbiotic *Phaeocystis* than do free-living cells, (iii) decreasing amount of phosphorous content in the plastids of symbiotic *Phaeocystis* and (iv) high concentrations of iron in vacuoles in symbiotic algae through nanoscale imaging.

Section 4.1 was from an article published in Current Biology in which I contributed by:

1. Computing the surface area occupied by the thylakoid membranes in the plastid of symbiotic and free-living *Phaeocystis* based on TEM images.
2. Analysing FIB-SEM images to reconstruct 3D models of *Phaeocystis* in free-living versus symbiotic stages.
3. Computing the surface and volume of individual plastids in free-living and symbiotic microalgal cells from a 3D reconstructed model.

I was in charge of Figure 1 (See Appendix A.1). In this study, only one symbiotic cell and few free-living cells were analysed, preventing any statistical analyses and robust conclusions.



Light microscopy image showing an acantharian cell (host) with its mineral skeleton and its intracellular symbiotic *Phaeocystis* cells (microalgae) in yellow.

Cytoklepty in the plankton: a host strategy to boost the bioenergetics of transformed endosymbiotic algae

Abstract

Using a quantitative subcellular 3D analysis protocol described in Chapter 2 of this Thesis, we reconstructed the three-dimensional cell architecture of twenty Haptophyte *Phaeocystis* cells and seven symbiotic cells. Thanks to the imaging workflow I developed, we could observe: (i) the invagination of the host-derived vacuole into the microalgal cell, highlighting cell-adaptation mechanisms in the host and providing evidence of host farming of algae; (ii) the organelle hypertrophy which multiplies cell volume by 80–times with a higher number of plastids (2 – 65) and a large central vacuole; (iii) the plastid multiplication, which may lead to a 100–fold increase in the total volume of plastids in a cell; (iv) the uncoupling mechanism between cell cycle evolution and plastid division, which suggests inhibition of communication between the plastid and the nucleus; (v) the volume of the mitochondrial network in symbiotic cells that grows up to 45 times in relation to the volume of the plastids. Altogether, these findings demonstrate an extraordinary morphological and metabolic transformation of microalgae after integration within a host and suggest that symbiosis is a farming strategy in which the host controls and exploits the microalgae (see in Appendix A.2 supplementary data related to single-cell transcriptomic and photo-physiology analysis).

Methods

Symbiotic acantharians harboring intracellular microalgal cells (*Phaeocystis*) were collected from surface seawaters (Mediterranean Sea, Villefranche-sur-Mer, France) as described in (Decelle et al. 2019). After collection, individual cells were isolated under a microscope with a micropipette, rapidly transferred into natural seawater, and maintained in the same controlled light ($100 \mu\text{mol photon m}^{-2}\text{s}^{-1}$) and temperature (20°C) conditions as the free-living stage. In parallel, cultures of the haptophyte *Phaeocystis cordata* RCC 1383 (the symbiont of Acantharia in the Mediterranean Sea) were maintained at 20°C in K/5 culture medium and at $100 \mu\text{mol photon m}^{-2}\text{s}^{-1}$. Microalga cells were cryofixed using high-pressure freezing, followed by freeze-substitution as indicated in Chapter 2.

Image processing, segmentation and quantitative analysis

Datasets were initially aligned¹ by the FIJI plugin ‘*Linear Stack Alignment with SIFT*’ (Lowe 2004), then finetuned by AMST (Hennies et al. 2020). Aligned FIB-SEM stacks were cropped and then binned in Fiji (<https://imagej.net/Fiji>). The regions of in-

¹**FIB-SEM acquisition and image registration:** Nicole Schieber & Yannick Schwab - Electron Microscopy Core Facility- EMBL- Heidelberg - Germany.

terest were annotated, and 3D reconstructed models were generated using the workflow described in Chapter 2 and geometry measurements were computed using an implementation of algorithms provided at (https://gitlab.com/clariaddy/stl_statistics) and (<https://gitlab.com/clariaddy/mindist>).

4.2 Results and Discussion

4.2.1 Integration of the microalgae into the host cell

The FIB-SEM tomography shows the external architectures of the microalga *Phaeocystis* in its free-living and symbiotic phases. Based on 3D reconstruction, we can visualise how the algae are integrated into the host and examine how the host interacts with the algae.

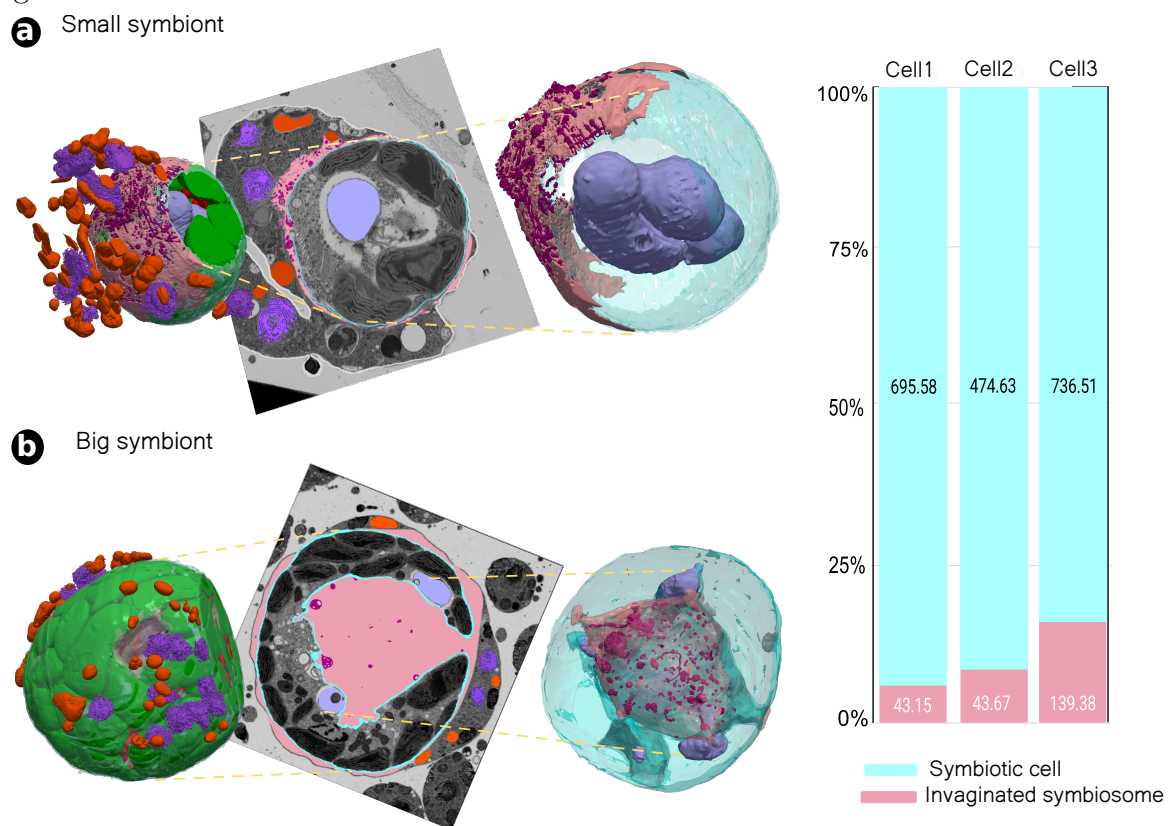


Figure 4.1 – The integration of the alga *Phaeocystis* in the host. (a) In the small symbiont (4 plastids), the symbiosome (pink) is associated with the microalgal cell while (b) in large symbionts, the symbiosome penetrates the microalgal cell. Both symbionts are surrounded by host mitochondria (red) and Golgi (purple). In the symbiosome, we can also note the presence of small vesicles (Bordeaux or dark red). The histogram shows the volume occupancy of the invaginated symbiosome in the symbiont space volume. In symbiosis, *Phaeocystis* cells exhibit large vacuoles (light purple) that increase with the number of plastids.

In photosymbiosis, the host phagocytes microalgal cells from the environment and

maintains them individually in a vacuole, called a symbiosome (Davy et al. 2012) (See Figure 4.1). The symbiosome is, therefore, a functional interface between the partners where metabolic exchanges take place. In small symbiotic *Phaeocystis* cells, the symbiosome membrane was tightly associated with the microalgal cell as observed in other photosymbioses (Davy et al. 2012). However, in larger microalgal cells (from 30 plastids), the symbiosome invades the symbiotic microalgal cell with a volume of up to $140 \mu m^3$ (Figure 4.1). We can predict that the invagination of the symbiosome occurred to optimise the exchange with the microalgal cell that became very large, so decreasing the surface to volume ratio.

This host-derived symbiosome invagination adds compelling evidence toward the concept that the acantharians host controls and parasites the microalgal cell, which is radically transformed. We also observed a high number of small round mitochondria of the host surrounding the symbiotic microalgae (Figure 4.1). They may bring ATP to support the transport of metabolites and nutrients via pumps and antiporters to symbiotic microalgae across the different membranes, including the symbiosome. Do morphological changes come with two different lifestyles? To address this question, we applied the same imaging approach to unveil *Phaeocystis* cellular architecture.

4.2.2 The architecture of *Phaeocystis* cell in free-living phase

FIB-SEM imaging was applied to unveil the subcellular organisation of the microalgal cell *Phaeocystis cordata* in culture “free-living phase” and inside a host cell “symbiosis phase”, to identify the structural changes following symbiotic condition. Twenty free-living cells and seven symbiotic cells were reconstructed and analysed with a 5 nm and 10 nm resolution, respectively.

Using electron microscopy, we identified the *Phaeocystis* cells in the free-living phase as unicellular and flagellar cells (Figure 4.2). The external architecture of *Phaeocystis* cell consists in a heart-shaped form, which is covered by two layers of thin scales. Then, we have identified specific subcellular features in *Phaeocystis* cells, focusing on particular organelle (plastid, mitochondria, and nucleus (see Figure 4.2 C)) modifications and interactions.

Amongst the twenty free-living *Phaeocystis* cells studied, with only one exception, *Phaeocystis* has typically two plastids (Figure 4.2 D) as reported in (Moisan et al. 2006; Medlin et al. 2007) with different mitochondria topologies (Figure 4.2 E) and a nucleus with the chromatin and a nucleolus (Figure 4.2 2).

From data volumes, the statistical analysis revealed a correlation between cell volume and plastid volume but not between the cell volume and the mitochondria or nucleus volume (see Figure 4.3).

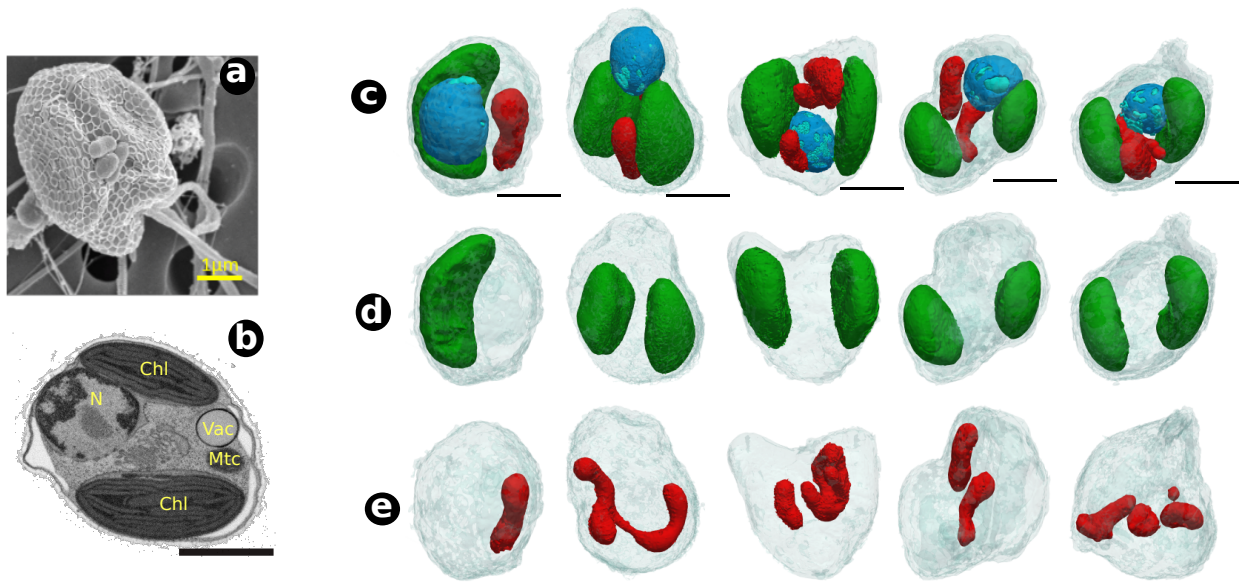


Figure 4.2 – Cell ultrastructure of *Phaeocystis* in the free-living phase. (a) The SEM image represents the *Phaeocystis* cell with flagella. (b) 2D FIB-SEM section shows the *Phaeocystis* inner structure. (c) The spatial localisation of organelles such as plastid (green), mitochondria (red) and nucleus (blue). (d) Plastids (green), (e) mitochondria (red) a. Abbreviations: Chl, plastid; N, nucleus; Mtc, mitochondrion; Vac, vacuole. Scale bars $1 \mu m$.

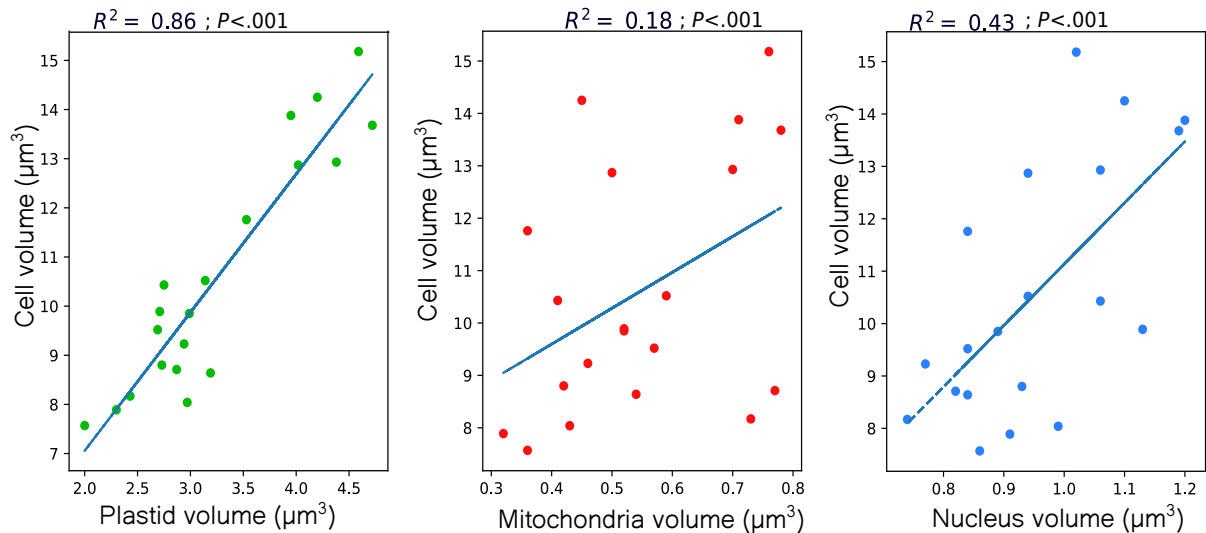


Figure 4.3 – The correlation between the cell volume and organelles. Plastid (green), mitochondria (red), and nucleus (blue).

4.2.3 Morphological change of *Phaeocystis* cells in symbiotic phase

We analysed 7 symbiotic microalgal cells within two distinct hosts, observing a fundamental morphological transformation, which tends to reflect different steps of algal metamorphosis.

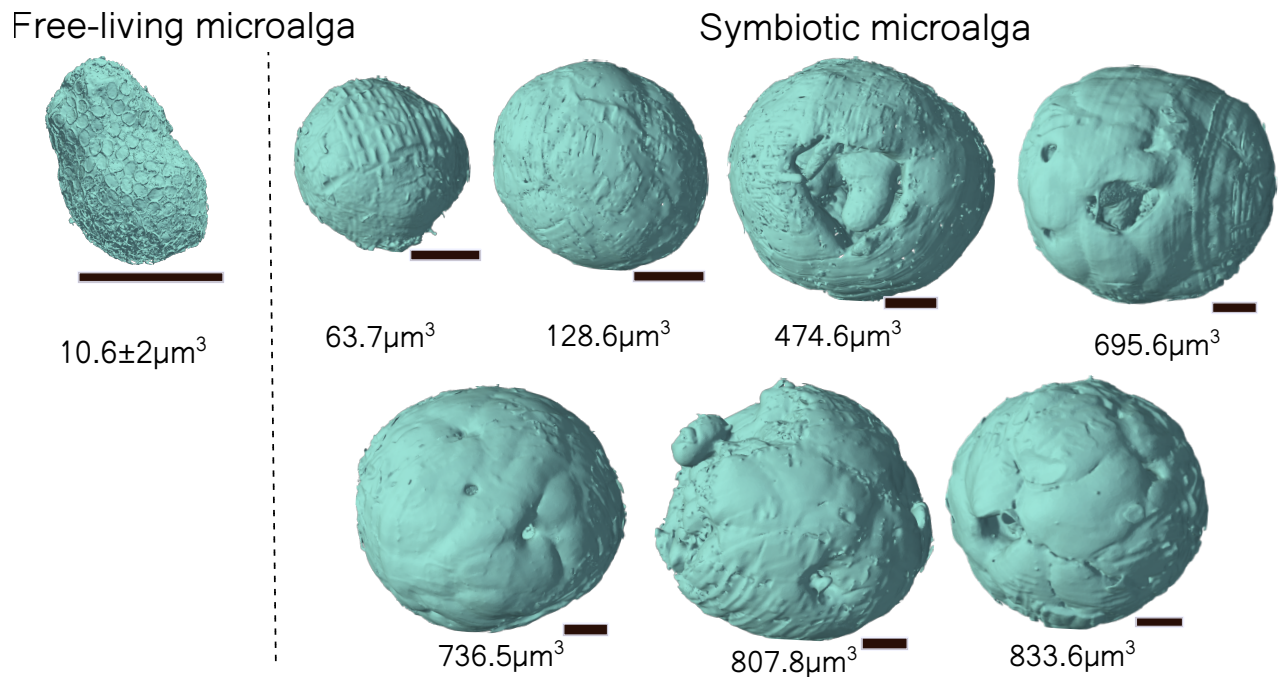


Figure 4.4 – Cellular architectures of *Phaeocystis* in free-living (first on the left) versus symbiotic phase. Scale bar: 2 μm

Quantitative analysis revealed a significant increase in cell volume and the disappearance of the flagella. The *Phaeocystis* cell volume can increase to 80–fold in symbiosis from 63.71 μm^3 to 833.6 μm^3 . In contrast, in free-living on the average of 20 cells, the cell volume is estimated at 10.6 μm^3 (Figure 4.4). Increased cell volume may stem from blockage of cell division in symbiosis and the consequent development of organelles.

Thanks to 3D imaging and morphometric analyses, we can propose that the cell volume adjusts in response to the increase in number and size of the intracellular organelles (Figure 4.5). The 3D reconstructed model highlight a change in organelles size and volume.

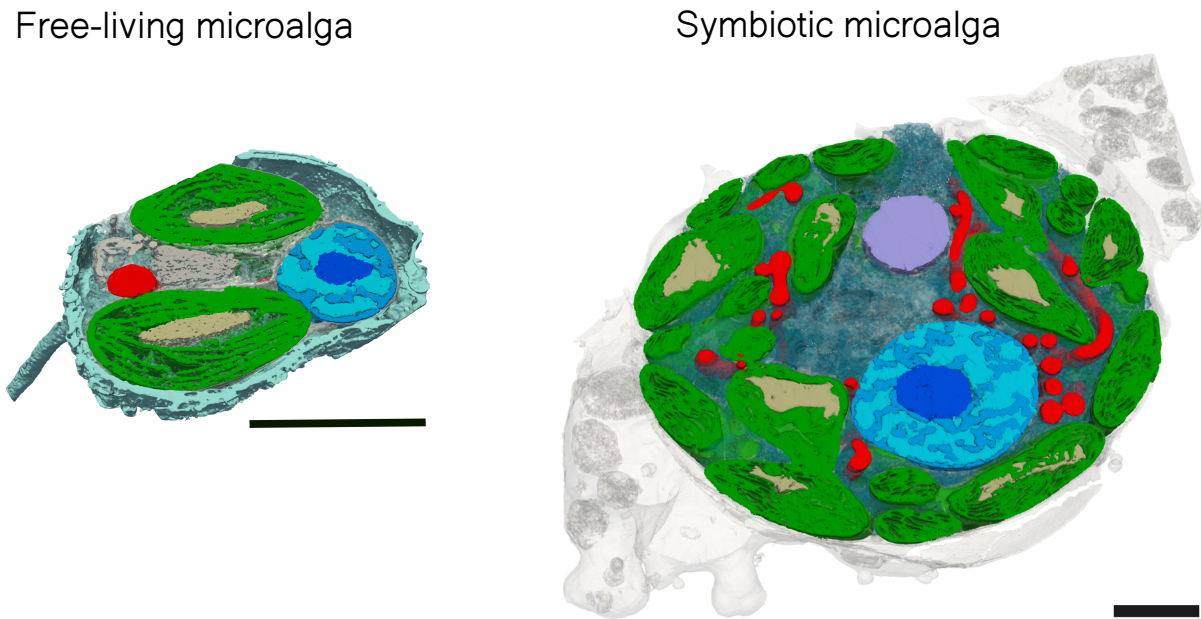


Figure 4.5 – 3D reconstructed model of *Phaeocystis* organelles in free-living versus symbiosis. Plastid (green), mitochondria (red), nucleus (blue) and vacuole (light purple).

Multiplication of the plastids in symbiosis

While in the free-living phase the cell has two plastids, the symbiotic phase induces plastids multiplication from 2 in free-living up to 65 (see Figure 4.6 A). Moreover, the plastids occupied 42 – 62% of the cell volume in symbiosis, compared to the fraction 30.8% occupied by the plastid in the free-living cell (see Figure 4.6 B).

In some cells it is possible to observe plastid division. A dense mitochondrial network surrounds the dividing plastids (see Figure 4.7 A) where individual large plastids enclose the differing state of pyrenoid dividing pyrenoid before a complete plastid division (Figure 4.7 B). We analyse the surface to volume ratio of individual plastids in the cell to understand the mechanisms behind the plastids division (Figure 4.7 C).

Based on previous observations made in mesophyll leaf cells (Jeong et al. 2002), one could hypothesise that a plastid division occurs once the plastids have reached a specific size (see the surface to volume ratio Figure 4.7 C). The assumptions would indicate why the photosynthetic cell in the symbiotic phase would contain many small plastids as reported in leaf cells (Trojan et al. 1996) instead of a couple of large plastids. A large population of small chloroplasts allows more effective chloroplast movement than a few enlarged chloroplasts (Jeong et al. 2002) probably aiding in efficient use of naturally fluctuating light intensities inside the host.

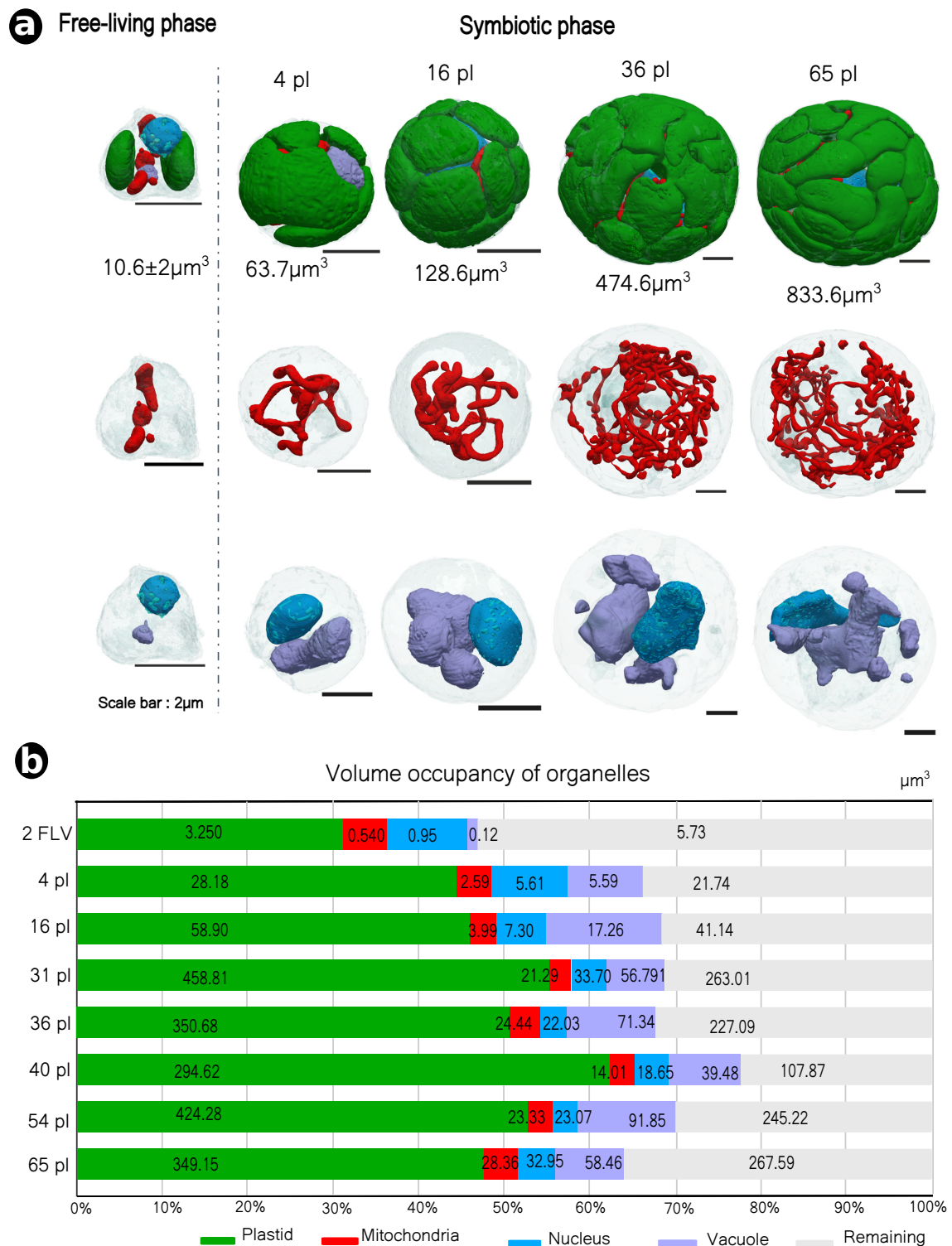


Figure 4.6 – Morphological transformation of the microalga in symbiosis. (a) 3D reconstructions of *Phaeocystis* in the free-living microalga (2 plastids) and different symbiotic microalgae with 4, 16, 36 and 65 plastids (green), mitochondria (red), nucleus (blue), and vacuoles (light purple) (scale bar: 2μm). (b) The volume of different organelles and cellular compartments as % occupancy in the cell (organelle volume/cell volume ratio) in free-living (2 plastids) and symbiotic microalgal cells and volume (μm³) of the cell, plastids, mitochondria, nucleus and vacuoles in free-living and symbiotic microalgae.

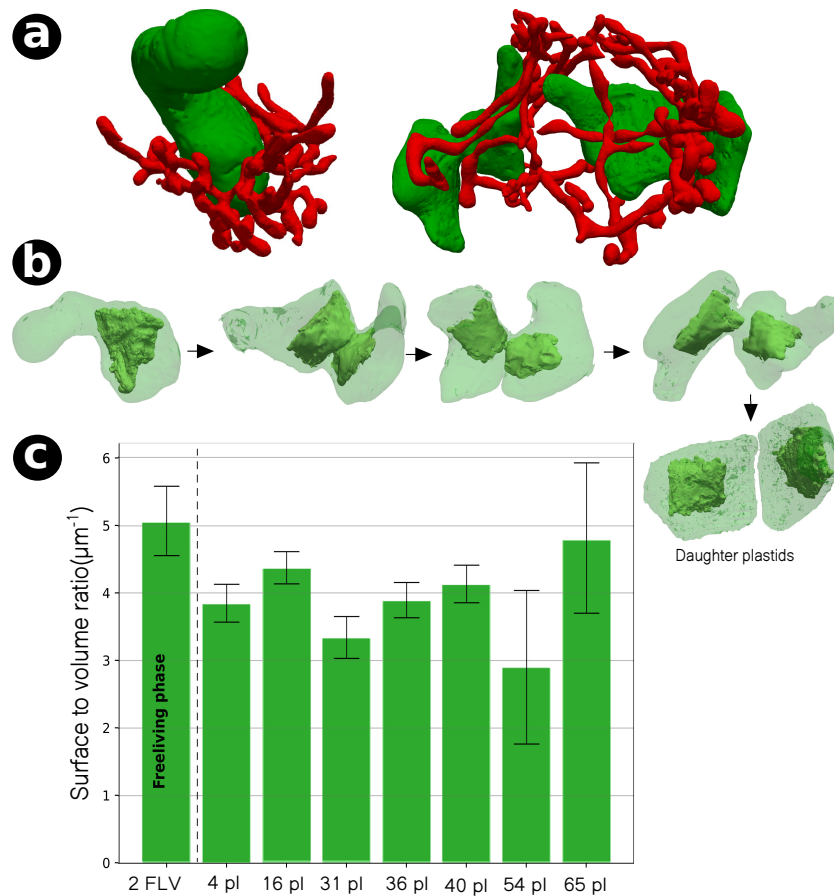


Figure 4.7 – The plastids division in symbiotic *Phaeocystis*. (a) 3D representation of the plastids (green) and mitochondria (red) shows a mitochondrial network, which surrounds the nucleus and plastids in the division. FIB-SEM tomography revealed different stages of pyrenoid and plastid division in symbiotic *Phaeocystis* cells. (b) Pyrenoid (light green) spatial localisation inside the plastid. (c) Surface to volume ratio of the individual plastids in the cell.

The FIB-SEM tomography provided images with a spatial resolution, which allowed investigating the internal organisation of the plastids. In Decelle et al. we report an increase in the fraction of thylakoid membrane in the plastid volume of symbiotic *Phaeocystis* cell compared to the fraction observed in free-living *Phaeocystis* cell (Decelle et al. 2019). We noticed that the thylakoid membranes of symbiotic *Phaeocystis* contained much denser networks of stacked thylakoid membranes, compared to the free-living microalgae. We believe that *Phaeocystis* cells expand their photosynthetic surfaces by increasing the thylakoid membranes and plastids volume. This observation corroborates a possible correlation between cell size and the number of plastids as supposed in higher plants (Dean et al. 1982; Ellis et al. 1983). However, the mechanism governing the plastid size and number in symbiotic *Phaeocystis* is still unclear.

We further investigate the inner structure of *Phaeocystis* plastids, highlighting the CO₂-fixing compartment - pyrenoid. More specifically, the localisation and archi-

texture of the pyrenoid were analysed in free-living and symbiotic cells. The pyrenoid occupies a central location in the plastid and exhibits different shapes that vary from a rectangle shape in free-living (Figure 4.8 A) to a triangle shape in symbiosis (Figure 4.8 B).

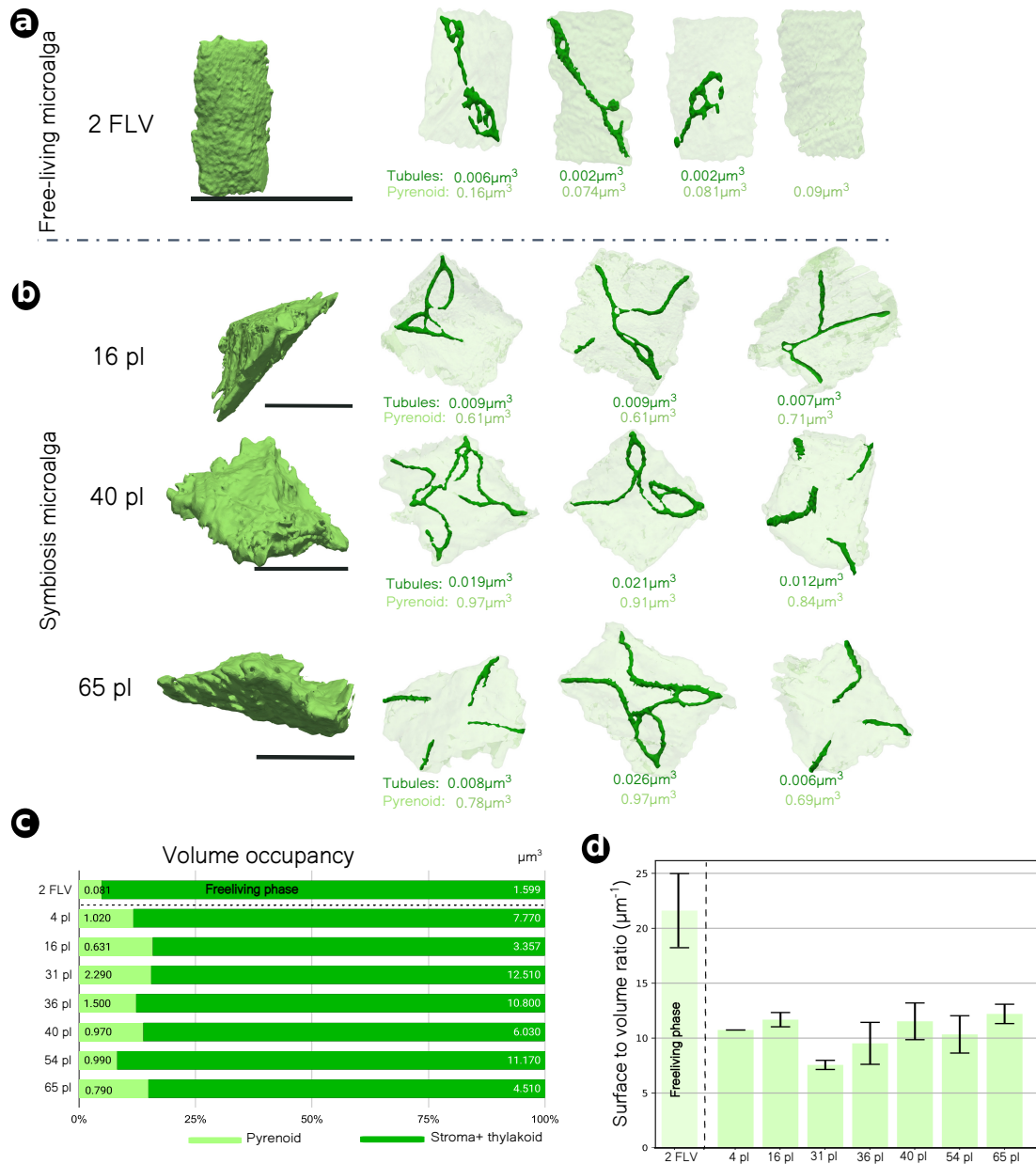


Figure 4.8 – Plastid architecture in *Phaeocystis* cell in free-living vs symbiotic phase. 3D reconstructed models represent the thylakoid membrane (dark green) and pyrenoid (light green). (a) The pyrenoid shows a rectangular shape in free-living with/without tubules and (b) a triangular form in symbiotic phase with different tubule structures. (c) The bar chart shows the averaged volume occupancy of the pyrenoid in each plastid of free-living (2 plastids) and symbiotic cells. Surface to volume ratio of the individual plastids in the cell. (d) The histogram represents the surface to volume ratio of the pyrenoid in both phases.

We compared the pyrenoid volume in free-living phase versus symbiotic phase and found an increase in pyrenoid volume from $0.08\mu\text{m}^3$ in free-living up to $1.5\mu\text{m}^3$ in symbiosis with an eventual growing up to $2.3\mu\text{m}^3$ when the plastids are dividing (Figure 4.8 C). The pyrenoid fraction in individual plastid volume is 4.8% in free-living while in symbiosis this fraction can increase up to 15.5% of the plastid volume (Figure 4.8 C). The average surface to volume ratio of pyrenoid in the free-living cell is 22 ± 3 while in the symbiotic cell the value reduces to 10.4 ± 2 and to 7.6 ± 2 when the plastids start to divide (Figure 4.8 D).

The pyrenoid architecture investigation highlighted different types of pyrenoid. In free-living cells, some pyrenoids contain crossing thylakoid membrane (tubule), while some others are lacking tubules (Figure 4.8 A). In symbiosis, we only observe pyrenoids with tubules, which are either separated in groups or fusing as a network. In symbiosis, the volume of tubules inside the pyrenoid is 9.5 fold more important than the single tubule in free-living pyrenoid (Figure 4.8 B). These tubules probably help maintaining CO_2 delivery to the Rubisco and ensure its diffusion for large pyrenoid as previously reported in *Chlamydomonas* (Meyer et al. 2017; Engel et al. 2015). The structural modifications found here corroborate our conclusions about the rules governing the pyrenoid architecture in different phytoplankton taxa (see results, Chapter 3).

Mitochondria expansion in symbiosis

The mitochondria of symbiotic *Phaeocystis* also underwent a significant expansion toward a well-developed network. Quantitative analysis indicates a volume increase from $0.5\mu\text{m}^3$ with a surface area of $7.4\mu\text{m}^2$ in free-living up to $28.4\mu\text{m}^3$ with an area expansion of $343.4\mu\text{m}^2$ in symbiosis (see Figure 4.6 A). However, compared to the cell volume, the fraction of mitochondria of 5.3% in free-living decreased to 3.1% in symbiosis (Figure 4.6 B).

In addition, we found a correlation between the plastid and mitochondria volume with $R^2 = 0.73$ and $p - \text{value} = 0.015$ in symbiosis. In contrast, no significant correlation was found between the volumes of plastid and mitochondria in fourteen *Phaeocystis* free-living cells ($R^2 = 0.07$ and $p - \text{value} = 0.38$) (see Figure 4.9 A). This analysis shows a common similarity to what has been previously observed in phytoplankton taxa (see Chapter 3), suggesting that coordination between plastids and mitochondria is an essential parameter in microalgae. In diatoms (Bailleul et al. 2015; Kim et al. 2016), it has been proposed that mitochondria and plastids are functionally related to optimize carbon assimilation.

Evaluating the possible physical contacts between plastid and mitochondria, based on the fact that plastid communicates with other cellular compartments to regulate their function and biogenesis as reported in (Mueller-Schuessele et al. 2018); we quantified the contact areas between plastids and mitochondria of *Phaeocystis* cells. Using

criteria discussed in (Scorrano et al. 2019) and in Chapter 3, contact areas below a distance of 50 nm between the two organelles was found in both phases (see Figure 4.9 B). Despite the increasing number of plastids in symbiosis, the surface area of the mitochondria in contact with plastids increases to about 8% in symbiosis compared to only $0.98 \pm 0.9\%$ in free-living cells (see Figure 4.9 C). This observation would suggest an interdependence of photosynthesis and mitochondrial metabolism, which need to be enhanced in symbiotic *Phaeocystis* cells.

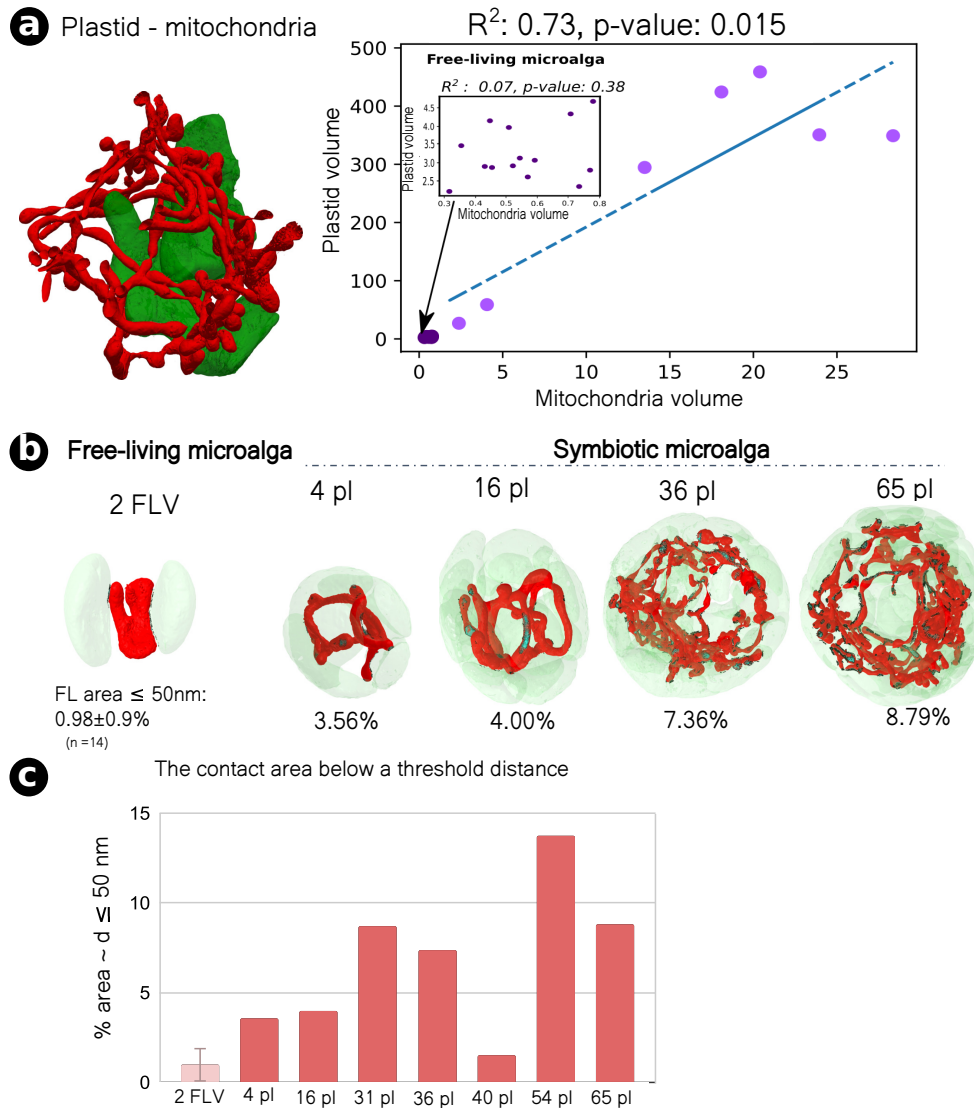


Figure 4.9 – The plastid-mitochondria interaction. 3D reconstructed models represent the thylakoid membrane (dark green) and pyrenoid (light green). (a) 3D representation of plastid (green) and mitochondria red (left panel and graph showing the correlation between the volume of the plastid and the volume of the mitochondria). (b) Proximity assessment ≤ 50 nm between the plastids (green) and mitochondria (red) is highlighted in light green. (c) Histogram recapitulates the contact area below a distance of 50 nm in free-living versus symbiotic phase.

Besides observing differences in shape (see Figure 4.10 A) and overall mitochondria surface and volume, among four symbiotic cells and fourteen free-living cells studied, we quantified the cristae which are the inner membrane folds of mitochondria. They provided an internal compartmentation of mitochondria for chemical reactions. We found that the fractions of cristae in mitochondria volumes are constant in both free living and symbiotic algae (Figure 4.10 B) as noted in the previous chapter for the mitochondria characterisation in different phytoplankton taxa studied by FIB-SEM tomography. This observation would suggest that the infolding of the inner membrane inside mitochondria is not a random process (Hackenbrock 1968).

By counting the number of cristae out of $1 \mu\text{m}^3$ in free-living versus symbiotic phase, we noticed an essential variation in the cristae density in both conditions (Figure 4.10 C). This variation perhaps reflects the dynamics of the inner membrane of the mitochondria, which can be adjusted and manage the volume of the cristae by a phase-independent fission and fusion mechanism (Cogliati et al. 2016; Picard et al. 2015; Muñoz-Gómez et al. 2015). Although both high-resolution images and further work are needed to study the shape and understand their physiological role in both phases, these preliminary results confirm the notion of cristae as a dynamic energy compartment.

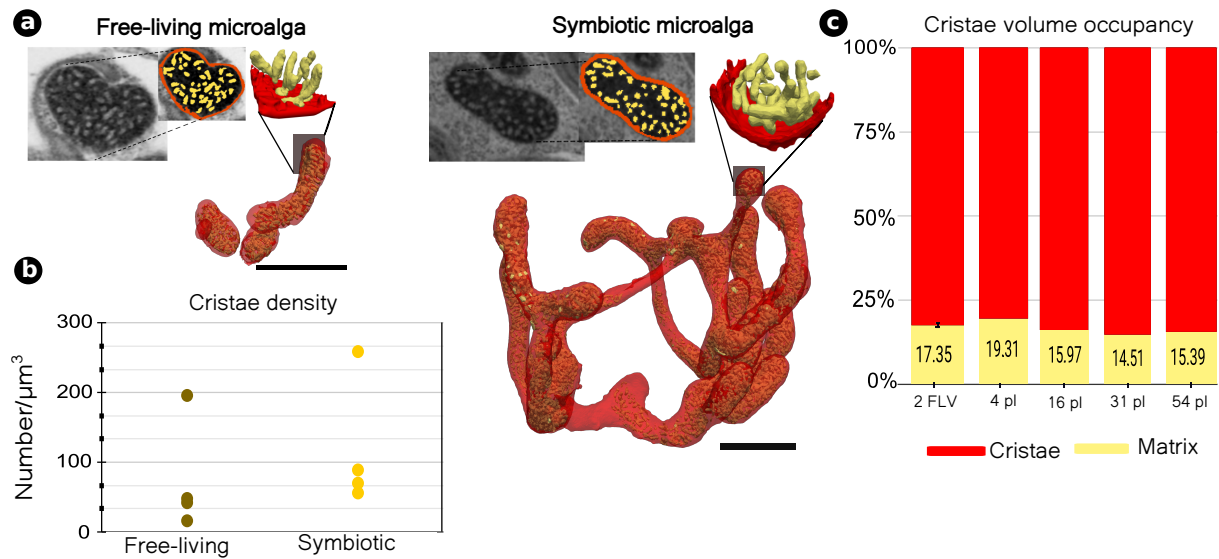


Figure 4.10 – Mitochondria features in both phases. (a) 3D reconstructed models showing the morphological change of the mitochondria in both stages with a focus on their cristae membranes (yellow) and matrix (red) (scale bar: $1 \mu\text{m}$). (b) Representation of the volume occupancy of the cristae membrane in both phases. (c) Plot Showing the cristae density.

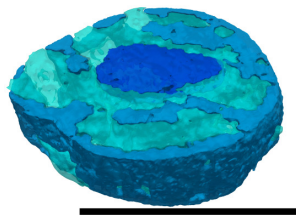
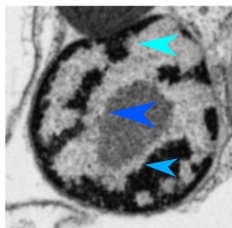
The internal organisation of the algae in symbiosis also displays an increase of the vacuole volume. The vacuole presents a dynamic morphology, probably depending on the cell function (Figure 4.6 A). This compartment gradually increased from $5.6 \mu\text{m}^3$

to $91.6 \mu\text{m}^3$ in larger symbiotic cells while in free-living, the volume of the vacuole is estimated at $0.12 \pm 0.05 \mu\text{m}^3$ (see Figure 4.6 B). In Decelle et al. we showed that these vacuoles contain trace metals iron and cobalt (Decelle et al. 2019), which may reflect the storage requirement for metabolism and photosynthetic activity.

Nucleus volume increase in symbiosis

The nucleus is the ‘control centre’ of the cell, enclosing most of the genetic material of the cell. FIB-SEM tomography distinguishes different cell compartments, including the nuclear organisation based on heavy-metal (uranyl-acetate and osmium) staining.

a Free-living microalga



b Symbiotic microalga

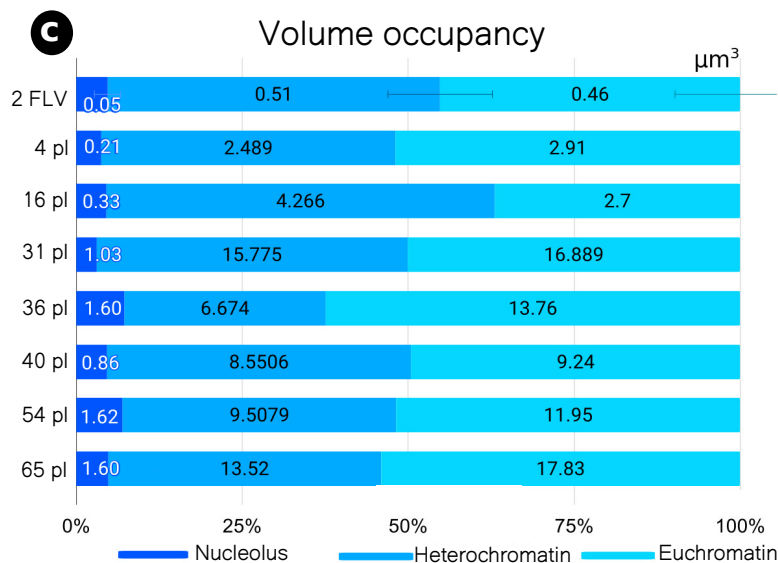
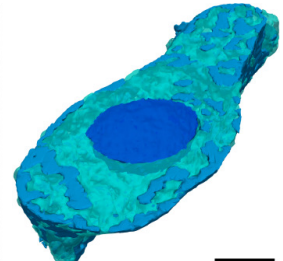
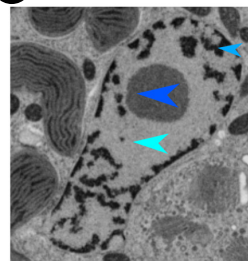


Figure 4.11 – Nucleus features in both phases. 3D reconstruction models distinguish nucleus compartments based on heavy-metal staining like uranyl-acetate and osmium with a (scale bar: $1 \mu\text{m}$). Heavy stained (blue) heterochromatin, low stained (light blue) euchromatin and medium stained (dark blue) nucleolus. (a) Free-living and (b) symbiotic phase. (c) The histogram shows the volume occupancy of each of these three nuclear compartments.

In the seven symbiotic cells as in the fourteen free-living cells, we observe only one nucleus. We separate heavy staining (blue), low staining (light blue) and medium staining (dark blue) (Figure 4.11). Based on literature indications, we assigned these staining levels to DNA compactness levels to set up the comparison in free-living (Figure 4.11

A) and symbiotic phases (Figure 4.11 B). Hence, the medium staining being nucleolus (known to synthesis RNA and ribosomes (Boisvert et al. 2007; Schöfer et al. 2018)), the heavy staining - heterochromatin (maintaining the structural and functional integrity of specific chromosomal regions (Guetg et al. 2012) and low staining - euchromatin (package and protect the DNA structure and sequence (Schöfer et al. 2018)).

Like for plastids and mitochondria, the volume of the nucleus largely increased (30–fold) in symbiosis compared to its estimation in free-living. However, the fraction of the nucleus in the cell volume of 9.2% in free-living reduces to 4.4% in symbiosis (Figure 4.6 B). Performing sub-organelle analysis, the volume of nuclear compartments increased in symbiosis to 32–fold the nucleolus, 31–fold the heterochromatin and 39–fold the chromatin, compared to the free-living phase (Figure 4.11 C). Based on these observations, we can assume that in symbiosis there is an active DNA replication and increased production of ribosomes. If we quantify the proximity area below 50 nm (see Figure 4.12 A), the physical contact between plastid and nucleus was preserved in free-living (12% on the average) while in symbiosis two cells out of seven had no physical contact area (Figure 4.12 B).

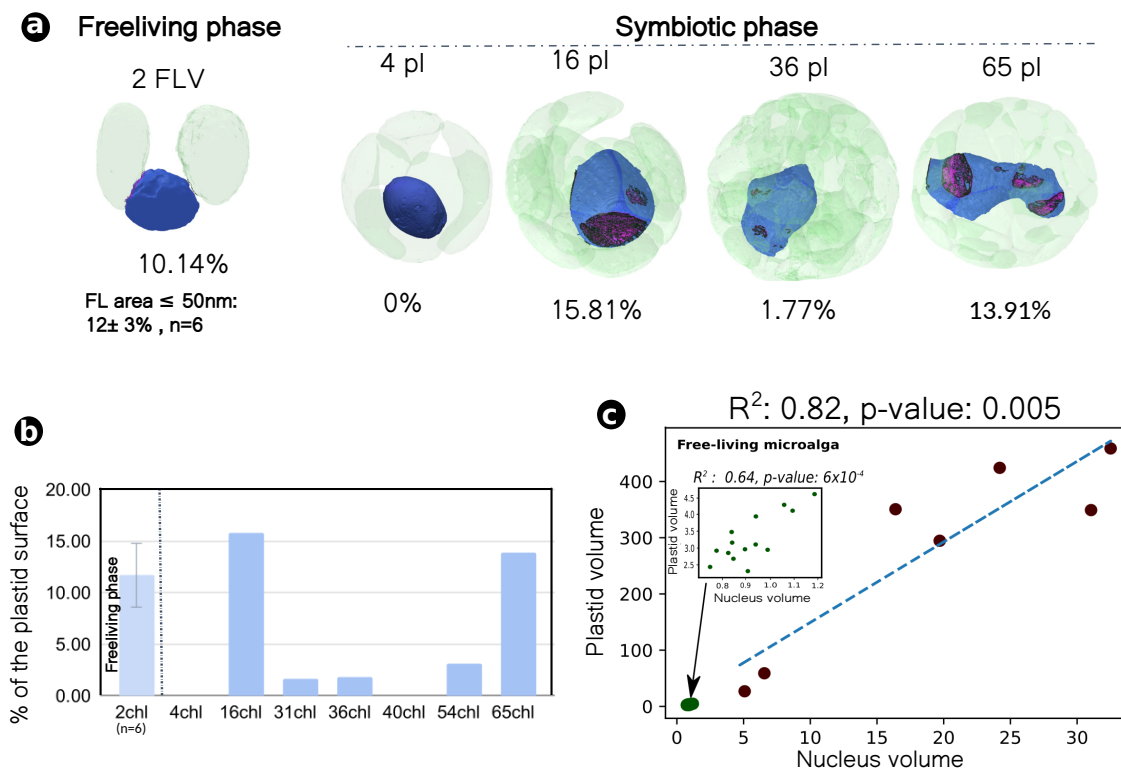


Figure 4.12 – Plastid-nucleus interactions.(a) Physical contacts between plastid (green) and nucleus (blue) corresponding to an area below a distance of 50 nm is represented in both phases (pink), (b) histogram recapitulating the contact area below a distance of 50 nm and (c) correlation between the plastids and nucleus volumes.

However, from volume data, the statistical analysis shows a poor correlation between the volume of plastid and nucleus with $R^2 = 0.64$ and $p - value = 0.0006$ in free-living and a better one ($R^2 = 0.82$ and $p - value = 0.005$) in symbiosis (Figure 4.12 C). This observation suggests that interactions between nucleus and plastid are also crucial in these microalgae (Mueller-Schuessele et al. 2018). Although many cells are needed to evaluate this possible linear trend between plastid and nucleus volume, the concept of how the plastid and nucleus keep functioning at optimal levels in symbiosis is not clear.

4.3 Conclusion and perspective

This work provides evidence that FIB-SEM imaging workflow described in Chapter 2 allows highlighting the significant cell morphological changes following symbiosis when the free-living *Phaeocystis* microalgae cells is hosted by acantharians to develop a photosymbiosis lifestyle. Using this imaging approach, we have been able to observe different organelles of the algae inside the host. Based on the observations made on seven symbiotic cells, we can raise several conclusions on the modifications of the alga following photosymbiosis. (i), the invagination of the host vacuole inside the symbiotic algae cell suggests how this symbiosis is mainly host-regulated. *Phaeocystis* cells transform themselves into powerful energy machinery where the plastids and mitochondria increase the volume up to 100 and 45 times, respectively. (ii) it appears that the symbiotic *Phaeocystis* cell does not divide. The multiplication of plastids is accompanied by the enlarged nucleus accumulating chromatin. (iii) the photosynthetic capacity of symbiotic *Phaeocystis*, including carbon fixation, is very likely boosted, with significant production of fixed carbon. This fixed carbon by photosynthesis is probably not deposited as carbon storage but used as photosynthates transferred to the hosts. Overall, the host seems to control the symbionts to optimise photosynthetic yield while controlling algal cell populations. An unknown mechanism inhibits plastid-to-nucleus communication, which is required to continue cell division. The integration of the alga in the host confirms the concept of algae culture where the host radically transforms and controls its symbiont, creating an irreversible evolutionary condition where *Phaeocystis* is enslaved. Combining these results with single-cell transcriptomic and photo-physiology could better explain this significant change in morphogenetic in the microalga *Phaeocystis* involved in a widely distributed photosymbiosis in the global ocean. This is the reason why I collaborated with different experts to prepare a manuscript, which can be found in Appendix A.2.

3D imaging to investigate chloroplast biogenesis during seedling emergence and transitory starch granules formation in *Arabidopsis thaliana* chloroplasts

Contents

5.1	Introduction	114
5.2	Preparation of plant material for SBF-SEM imaging	114
5.3	Background model	115
5.4	Segmentation and 3D analysis of SBF-SEM image datasets	116
5.5	Results and Discussion	117
5.5.1	Plastid development in germinating seedlings	117
5.5.2	Control of starch granule numbers in <i>Arabidopsis</i> chloroplasts	121
5.6	Conclusion and perspective	122

Summary

SBF-SEM imaging provides ultrastructural information from larger volumes of plant cells by giving the ability to generate 3D reconstructions of entire plant cells, including internal structures such as plastids. By adapting the 3D image processing workflow conceived for *FIB-SEM* to *SBF-SEM* datasets of plant cells, it has been possible to improve the resolution of Z-stacks of the existing model and extract quantitative data. Thanks to this approach, we have addressed two main biological questions: the etioplast - chloroplast transition in cotyledon cells and the process of starch granule formation in mature leaves. (i) Quantitative data and 3D reconstructions of the chloroplast and thylakoid membrane structures revealed the number and volume of chloroplasts as well as the extent of the thylakoid membrane surfaces during de-etiolation. Morphometric data showed a rapid formation of the thylakoid membrane, which demonstrates the efficiency of thylakoid biogenesis in the leaf cell of *Arabidopsis thaliana* to enable plants to optimise their light absorption capacity and ensure their primary energy source. (ii) A quantitative comparative analysis carried out on series of *SBF-SEM* images of wild-type *Arabidopsis thaliana* leaves and plants lacking soluble starch synthase 4 (*SS4*) showed that the number of starch granules per plastid in *Arabidopsis* leaf development depends on the duration of light exposure. A deficiency in *SS4* protein affects initiation and shape per chloroplast by counterbalancing the increase in starch granule volume.

Keywords: [SBF-SEM], [*Arabidopsis thaliana*], [chloroplast biogenesis], [ss4 mutant], [starch granule]

5.1 Introduction

Plants are well adapted to cope with changes in their environment. This is particularly true for light, probably the most important stimulus to which plants have to react. In addition to being the driving force for photosynthesis, light is involved in many developmental and regulatory processes. One of the well-known light regulated processes is de-etiolation, a switch in seedlings development from the skotomorphogenic program called etiolation to the photomorphogenic program. Photomorphogenesis involves a series of morphological changes, such as cotyledons expansion, hypocotyl growth inhibition and greening that accompany the onset of photosynthesis in the newly formed chloroplasts. We have followed the etioplast-chloroplast transition occurring during the etioplast-chloroplast transition. The results are a part of preprint of a bioRxiv paper submitted for publication and accepted in Elife on which I am the sixth author out of 10 (see Appendix A.3).

Another light-mediated effect is the accumulation of transitory starch, which is synthesized in the leaves during the day and is degraded in the following night (Pfister et al. 2016). Albeit transitory starch metabolism is important in the plant life cycle, many aspects of the synthesis and degradation of the starch granule are unknown.

In order to establish a comprehensive picture of chloroplast development and of transitory starch granules formation I have adapted the imaging protocol described in Chapter 2 of this Thesis to improve the segmentation process of SBF-SEM image datasets. Images were acquired during the etioplast-chloroplast transition of *Arabidopsis thaliana* seedlings for chloroplast biogenesis studies. To study the transitory starch granule formation, image datasets of wild type *Arabidopsis thaliana* leaves and plants lacking the soluble starch synthase 4 (SS4) (Roldán et al. 2007) were used.

5.2 Preparation of plant material for SBF-SEM imaging

Plant growth¹

Arabidopsis thaliana seeds were prepared and sown following the protocol described in (Pipitone et al. 2020). Briefly, the seeds were surface-sterilized with 70% (v/v) ethanol with 0.05% (v/v) Triton X-100, and then washed with 100% ethanol. Seeds were sown on agar plates containing 0.5×Murashige and Skoog salt mixture (MS, Duchefa) without sucrose. Following stratification in the dark for 3 days at 4°C, seeds were irradiated with 40 μmol m⁻²s⁻¹ for 2 h at 21°C and then transferred to the dark for 3 days growth at 21°C. Etiolated seedlings were collected in the dark (0 h of light; T_0) and at selected time points (T_0 , T_4 , T_{24} , T_{96}) upon continuous white light exposure (40 μmol m⁻²s⁻¹ at 21°C).

¹**Plant growth:**Rosa Pipitone, Felix Kessler, Emilie Demarsy - Neuchâtel Platform of Analytical Chemistry, University of Neuchâtel, Switzerland & Department of Botany and Plant Biology, University of Geneva, Switzerland

Sample preparation and SBF-SEM acquisition²

The plant material was prepared using the protocol developed by (Pipitone et al., 2020). Samples were fixed under vacuum (200 *mBar*) in 0.1M cacodylate buffer (pH 7.4) containing 2.5% (w/v) glutaraldehyde and 2% (w/v) formaldehyde (fresh from paraformaldehyde) for 4 *h* and left in the fixation solution for 16 *h* at 4°C. Samples were then incubated in a solution containing 3% (w/v) potassium ferrocyanide and 4 mM calcium chloride in 0.1M cacodylate buffer combined with an equal volume of 4% (w/v) aqueous osmium tetroxide (OsO₄) for 1 *h*, on ice. After the first heavy metal incubation, samples were rinsed with ddH₂O and treated with 1% (w/v) thiocarbohydrazide solution for 1 *h* at 60°C. Samples were rinsed (ddH₂O for 15 *min*) before the second exposure to 2% (w/v) OsO₄ aqueous solution for 30 *min* at room temperature. Following this second exposure to osmium, tissues were placed in 1% (w/v) uranyl acetate (aqueous) and left overnight at 4°C. The samples were rinsed with ddH₂O for 15 *min*, and placed in the lead aspartate solution for 30 *min* at 60°C. Samples were dehydrated in a series of aqueous ethanol solutions ranging from 50% (v/v) to 100%, and then embedded in Durcupan resin by successive changes of Durcupan resin/acetone mixes, with the last imbibition in 100% Durcupan resin. Polymerization of the resin was conducted for 48 *h* at 60°C.

SBF-SEM was performed on Durcupan resin-embedded cotyledons representing the four de-etiolation time points T_0 , T_4 , T_{24} , and T_{96} . Images were acquired using a variable pressure, field emission scanning electron microscope equipped with a Gatan 3View 2XP. Voxel size of T_4 zoomed stacks: $3.9 \times 3.9 \times 50 \text{ nm}$; T_{24} : $4.7 \times 4.7 \times 50 \text{ nm}$; T_{96} : $5.6 \times 5.6 \times 50 \text{ nm}$. Voxel size for T_0 overview: $9.5 \times 9.5 \times 100 \text{ nm}$; T_4 : $19.3 \times 19.3 \times 100 \text{ nm}$; T_{24} : $40 \times 40 \times 200 \text{ nm}$; T_{96} : $43.5 \times 43.5 \times 200 \text{ nm}$.

5.3 Background model

Previous studies on MRI (Magnetic Resonance Imaging) images (Mulder et al. 2019) and micro-MRI (Vasilic et al. 2008) have highlighted the trade-off between voxel size and quality of an image, when comparing 3D data acquired with an isotropic voxel size vs. an anisotropic voxel size. The comparison highlights the presence of gaps between adjacent slices when data volumes are acquired with a big step in z .

The same gaps were identified when Rosa Pipitone³ processed the SBF-SEM stack and performed the segmentation of the AOIs using the Amira software (FEI Visualisation Sciences group). The 3D reconstruction model of the extracted features had big gaps in geometry representation (Figure 5.1). The process of inferring geometry information from these models will be biased by their holey shape.

²**SBF-SEM acquisition:** Simona Eicke, Samuel Zeeman - Electron Microscopy Core Facility - ETH Zurich - Switzerland

³**Background 3D reconstructed model:** Rosa Pipitone - Neuchâtel Platform of Analytical Chemistry, University of Neuchâtel, Switzerland.

To improve the z -stack analysis in these datasets, where the voxel size was largely anisotropic (i.e. $5 \times 5 \times 20 \text{ nm}^3$) we have considered adding a z -stack interpolation in the pre-processing step after the stack registration described in chapter 2 of this manuscript. The approach allowed refining the structure and obtaining a continuous surface volume.

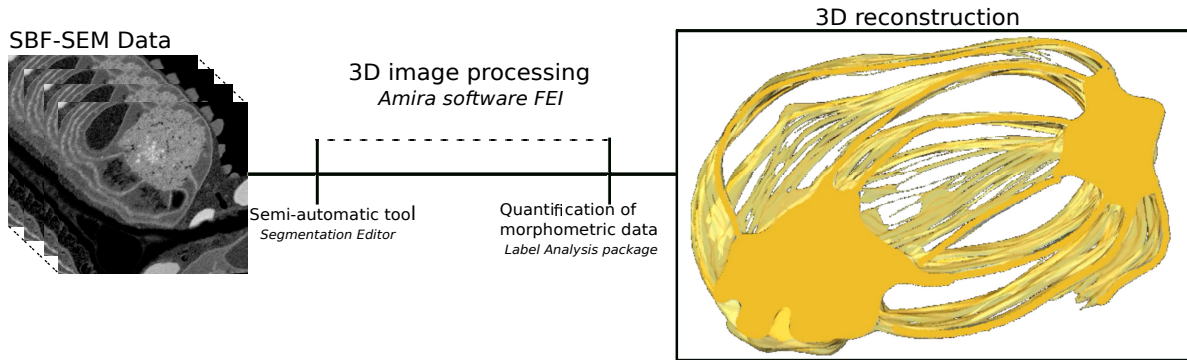


Figure 5.1 – 3D reconstruction of thylakoid membranes of an etioplast from 3 day-old. Partial growth of *Arabidopsis thaliana* seedlings illuminated for 0 *h*.

5.4 Segmentation and 3D analysis of SBF-SEM image datasets

SBF-SEM image datasets have been registered using the Fiji MultiStackReg plugin using affine transformation (Figure 5.2 A). The z -stack has to be well aligned before performing the z -stack resampling.

Using Fiji we performed a z -stack resampling using “*Image* → *Stacks* → *Reslice z*” mode and interpolate in z by setting a new z depth accordingly. The isotropic voxel size was automatically resampled after adjusting the depth parameter (Figure 5.2 B).

If necessary the resliced stack was binned twice to reduce the file size. Binning transformation would remove noise as well. However, in our cases, resliced stacks were filtered using a median filter with a window size of $5 \times 5 \times 5$ (Figure 5.2 C).

Segmentation and 3D reconstruction were performed using semi-automatic tools provided by 3D Slicer software as described in Chapter 2 of this Thesis (see also Figure 5.2 D). The surface mesh quality evaluation and geometry measurements were done in MeshLab software (Figure 5.2 E) and 2D pictures of 3D representations of reconstructed mode at different time points were performed using ParaView software.

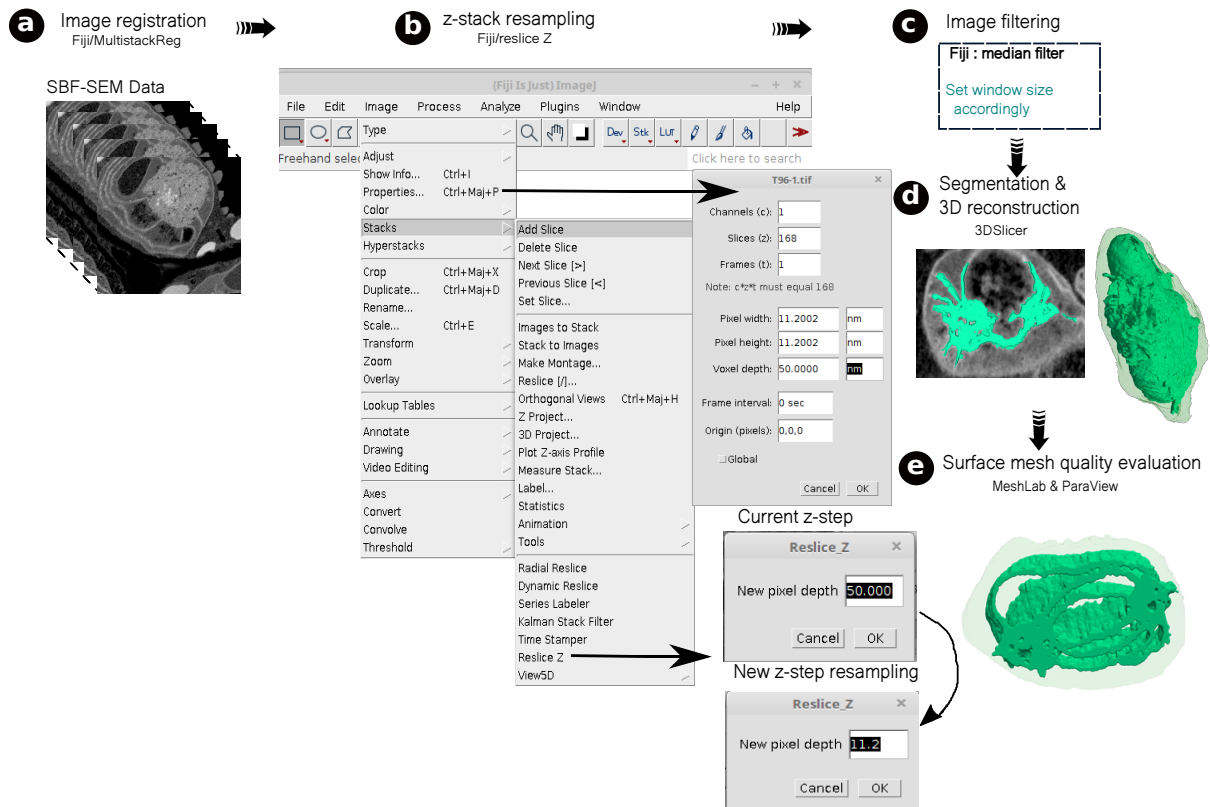


Figure 5.2 – SBF-SEM images processing and 3D reconstruction. (a) Stack registration -MultiStackReg from Fiji, (b) Interpolation of z -stack using resliced module from Fiji, ((c)) Stack filtering in Fiji, (d) Volume of interest segmentation and 3D reconstruction applying 3DSlicer and (e) 3D reconstructed model was evaluated in MeshLab and visualized in ParaView.

5.5 Results and Discussion

The workflow described in Chapter 2 of this Thesis with z -stack interpolation made it possible to represent a detailed picture of cotyledons plastids at different developmental stages of the de-etiolation process (Figure 5.3 A-D). From SBF-SEM image datasets (Figure 5.3 E-H), we also obtained morphometry information of the plastid and thylakoid surface area during differentiation.

5.5.1 Plastid development in germinating seedlings

The 3D reconstructed models revealed a change in plastid shape from ovoid at T_0 and T_4 to hemispheric at T_{24} and T_{96} (Figure 5.3 J-K). At T_0 , the dark-germinated seedlings contain undifferentiated plastids, the etioplasts, harbouring the characteristic lattice-like membranous structure known as the prolamellar body (PLB) and Prothylakoid (PT) structures (Pogson et al. 2011) to initiate the thylakoid membranes (Figure 5.3 E and I).

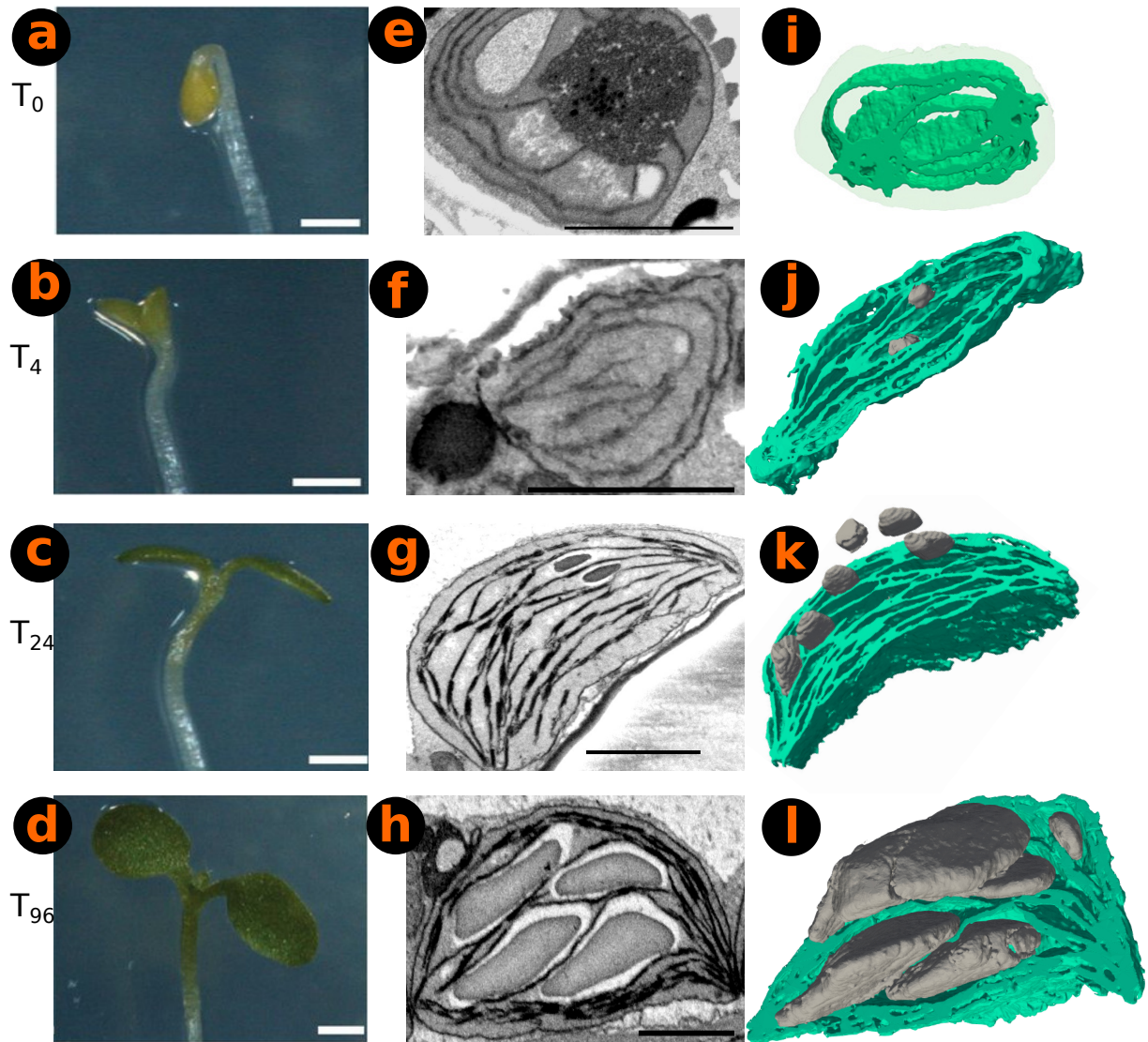


Figure 5.3 – 3D reconstructions of plastid and thylakoid membrane during de-etiolation. (a-d) Cotyledon phenotype of etiolated seedlings (T_0) after 4 h (T_4), 24 h (T_{24}), and 96 h (T_{96}) in continuous white light (scale bars: 0.5 mm). (e-h) 2D SBF-SEM sections highlighting the etioplast structure of cotyledons of dark grown *Arabidopsis thaliana* seedlings (T_0) and the thylakoid membrane evolution after 4 h (T_4), 24 h (T_{24}), and 96 h (T_{96}) of illumination (scale bars: 2 μm). (i-l) 3D reconstruction of the thylakoid membrane network (light green) from the etioplast (j) to a completely developed chloroplast (l). Starch granules are shown in grey.

After 4 h of illumination the prolamellar body is converted to thylakoid membrane. The typical structure of the PLB connected to PTs disappeared leaving only elongated lamellar structures, where the appearance of small amounts of starch granules shows excess energy, due to photosynthesis (Figure 5.3 F and J). At T_{24} and T_{96} , thylakoid membranes were organised in appressed and non-appressed regions and large spaces occupied by starch granules were observed (Figure 5.3 G-H and K-L).

Reconstructing the 3D thylakoid network for 3 or 4 chloroplasts for each developmental stage, we could extract quantitative data such as chloroplast volume and membrane surface areas (Figure 5.4 A and B). The total chloroplast volume increased about 12–fold from T_4 ($9.4 \mu\text{m}^3$) to T_{96} ($112.14 \mu\text{m}^3$). The surface area of the thylakoid membranes increased 10 times, from T_4 - $66.4 \pm 29 \mu\text{m}^2$ to T_{96} - $583.4 \pm 62.5 \mu\text{m}^2$ (Figure 5.4 B).

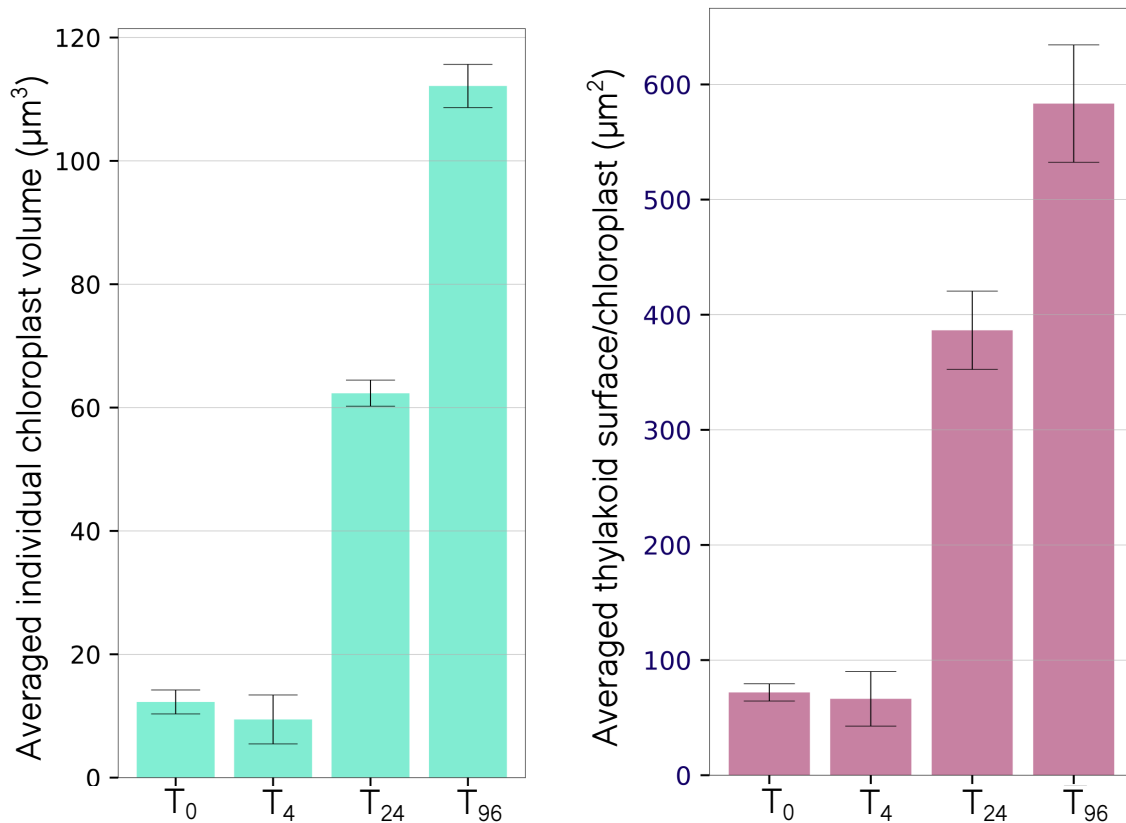


Figure 5.4 – Quantitative analysis of plastid and thylakoid membrane during de-etiolation. (a) Average individual plastid volume and (b) average thylakoid membrane area per plastid volume of 3 days old, dark grown *Arabidopsis thaliana* seedlings illuminated for 0 h, 4 h, 24 h and 96 h.

However, as observed in Figure 5.4, from T_0 to T_4 , the volume and the surface of both the plastid and thylakoid membrane do not change much. Both etioplasts (T_0) and developing chloroplasts (T_4) lack complete functional thylakoids. From T_4 to T_{24} , the thylakoid membrane area increased significantly (~ 6 fold) and still developed from T_{24} to T_{96} (about 1.5–fold). Our observations indicated that chloroplast development during the first 96 hours of de-etiolation can be separated into two phases: a first phase reflected by qualitative changes (i.e. structure establishment and reorganisation of the thylakoid network architecture) and a second phase (starting before T_{24}) during which the thylakoids surface increased due to the expansion and stacking of lamellae. The chloroplast volume expansion during the second phase may also reflect the enlargement of extra-thylakoidal spaces occupied by emerging starch granules. Indeed

starch granules were present at T_{24} , supporting the notion that these chloroplasts are photosynthetically functional and able to assimilate carbon dioxide (CO_2). The major differences observed between T_{24} and T_{96} were the increase in the overall chloroplast size and in starch granule size and number.

Our data also show that photosynthetically functional thylakoid membranes are formed rapidly during the first 24 h of de-etiolation. These results also suggest that large amounts of lipids and proteins are necessary to build up the thylakoid membrane until T_{24} , whereas increases in lipids and proteins between T_{24} and T_{96} enable the expansion of already functional thylakoid membranes in preparation for chloroplast division. Indeed, chloroplast number per cell increased during de-etiolation, a process that depends on the division of pre-existing chloroplasts.

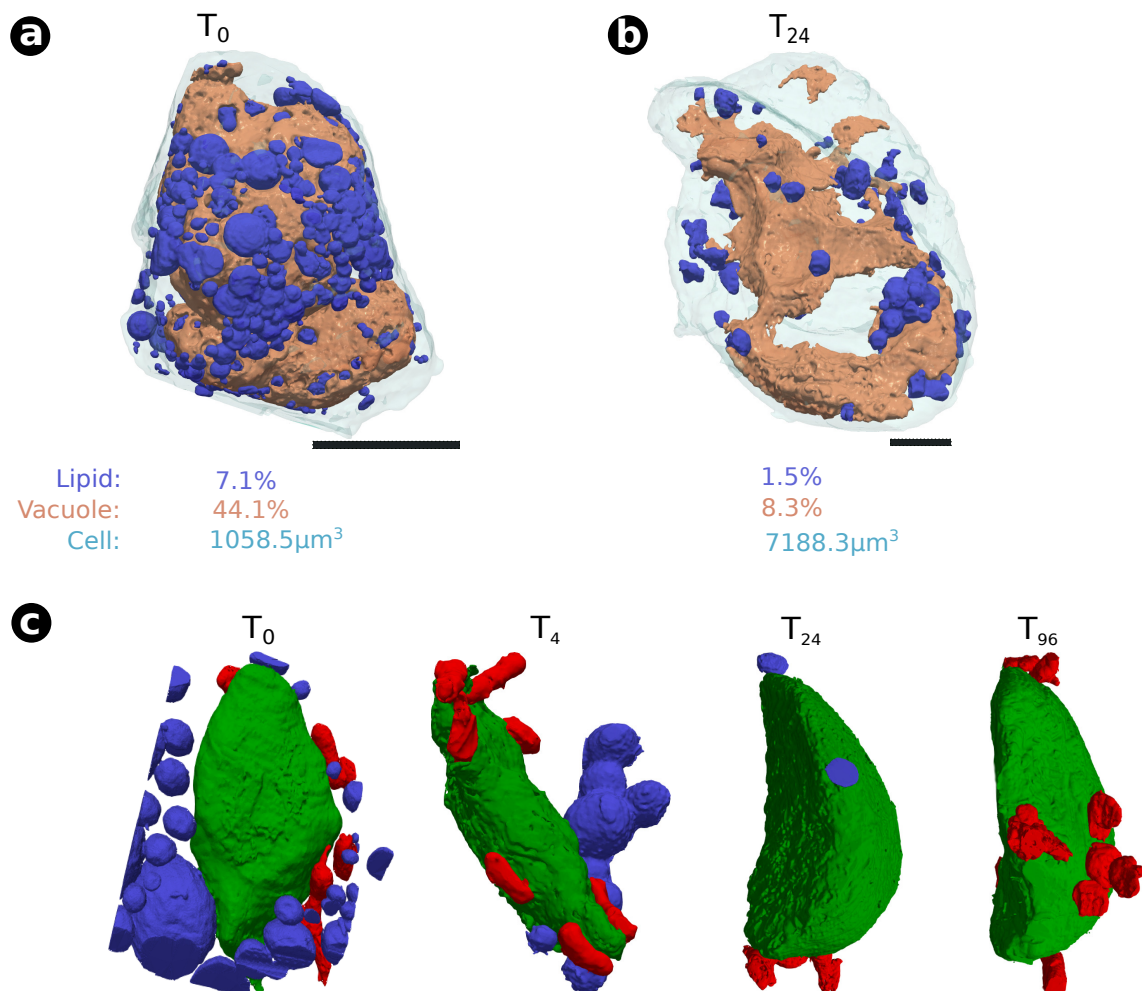


Figure 5.5 – 3D reconstruction of a 3–days old cotyledon cell revealed by SBF-SEM imaging. (a) after 0 h and 24 h (b) of illumination. The vacuole compartment (coral) and lipid body (blue) are shown. (c) Inside the cell, plastids (green) are surrounded by fragmented mitochondria (red) and lipid bodies (blue) that disappear after 96 h of illumination.

The data volume of a 3–days old cotyledon cell show that at T_0 , the cell (with a volume of $1058.5 \mu\text{m}^3$) contains about 20 chloroplasts and is filled with a large vacuole (44.1 % of the cell volume) and lipids bodies (7.1 % of the cell volume)(Figure 5.5 A). As stated above, these reserves are mobilized to fuel post-germination seedling growth associated with an increase in photosynthesis (Sela et al. 2020; Baud et al. 2008). After 24 hours of illumination, the cell volume rises to 7 times of its original size ($7188.3 \mu\text{m}^3$) and the storage system is diminished with lipid bodies filling a small portion of the cell (about 1.5 % of the cell volume) and the vacuole about 8.3 % of the cell volume (Figure 5.5 B). In addition to lipid bodies, the 3D reconstructed model unveiled the plastid-mitochondria interaction (Figure 5.5 C). Such interaction may reflect some energetic coupling between the two organelles during the etioplast/chloroplast transition.

5.5.2 Control of starch granule numbers in *Arabidopsis* chloroplasts

Previous studies on *Arabidopsis thaliana* developing leaves have shown that when plants are kept in continuous light for long periods, the starch granules change in size and shape (Zeeman et al. 2002). The authors hypothesized that the shape of the granules is defined by the space available between layers of thylakoid membranes within the plastid. Later, studies conducted to investigate the starch granule numbers in *Arabidopsis thaliana*, unveil a correlation between the starch granule numbers and plastid volume (Crumpton-Taylor et al. 2012). However, little is known about how granules are initiated and the factors that control the number and size of granules within the individual plastid. To address this question, we started from previous studies carried out to identify key proteins involved in granules size regulation and starch granule initiation in *Arabidopsis thaliana* during the leaf development (Seung et al. 2018; Crumpton-Taylor et al. 2013).

We thus focused on the morphological changes in *Arabidopsis* WT and *ss4* mutant strains. The latter lacks the sucrose synthase 4 protein, which is important for the starch granule formation (Lu et al. 2018). Using SBF-SEM⁴ image datasets, we investigated the role of SS4 protein in *Arabidopsis* leaf development by comparing the amount of starch granules per plastid of *Arabidopsis* wild-type (WT) leaf versus *ss4* mutant leaf. Both WT and *ss4* plants were grown in the dark for 16 hours and then illuminated in continuous white light ($150 \mu\text{mol m}^{-2}\text{s}^{-1}$) during 15 *min* and 8 hours.

3D reconstruction of starch granules in WT chloroplasts after 15 *min* of illumination reveals several small starch granules (Figure 5.6 A) when in *ss4* chloroplast a large starch granule is present (Figure 5.6 B). In WT plants, the number of initiated starch granules is different between plastids (24 ± 16). Quantitative analyse performed with 7 plastids shows that starch volume in *ss4* chloroplasts is greatly increase ($17.1 \pm 3 \mu\text{m}^3$) compared to the volume of wild-type starch granules ($0.2 \pm 0.1 \mu\text{m}^3$)

⁴SBF-SEM datasets of *Arabidopsis* WT and *ss4* mutant: Simona Eicke, Léo Bürgy, Samuel Zeeman - Electron Microscopy Core Facility - ETH Zurich -Switzerland

(Figure 5.6 C). In *ss4* quantitative analysis performed with 7 plastids shows that in *ss4* the starch granules volume content per plastid increases when compared to wild type.

After 8 h of illumination WT chloroplasts harbour the same number of starch granules between chloroplasts (25 ± 7) but with a drastic increase in granule volume ($15.7 \pm 4 \mu\text{m}^3$) (Figure 5.6 D). In the *ss4* mutants, a slight increase in starch granule number is observed (Figure 5.6 E-F) and the number of the starch granules per plastid grow to (4 ± 1) with an important increase in total volume ($65.9 \pm 24 \mu\text{m}^3$) (Figure 5.6 F).

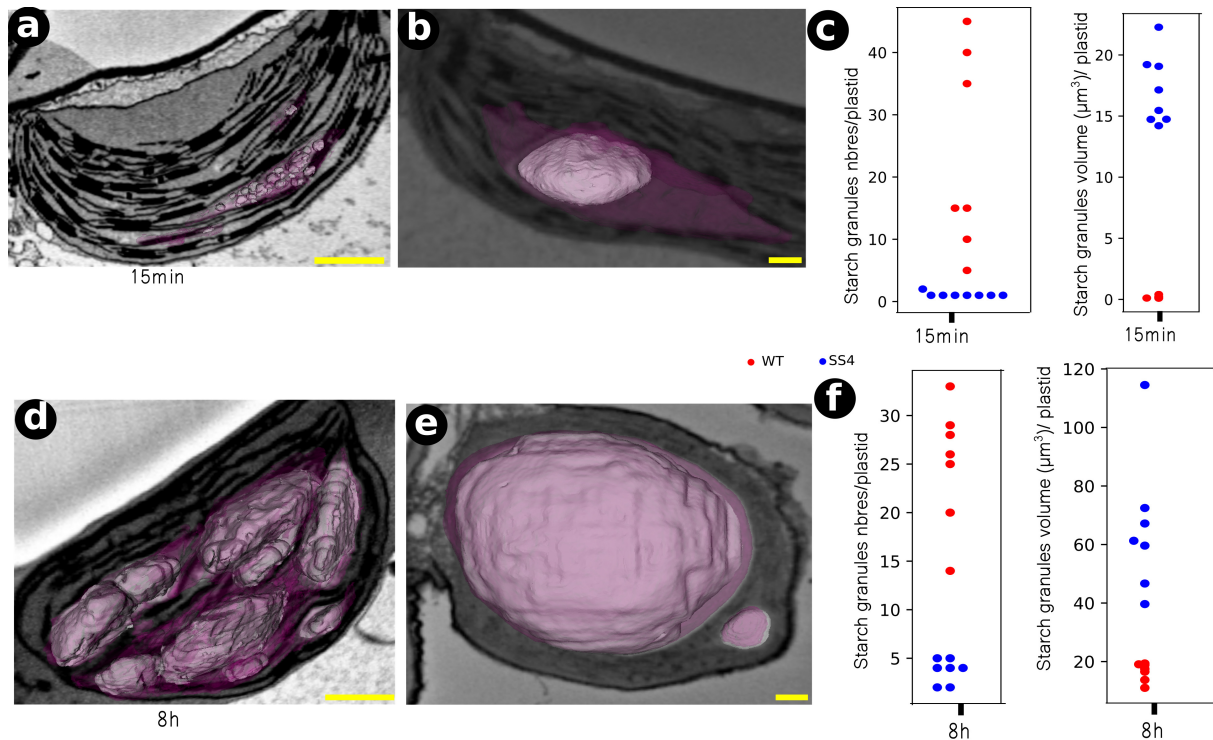


Figure 5.6 – Starch granules initiation in developing leaf cells of *Arabidopsis* WT vs. *ss4*. 3D reconstruction of starch granules (white) enclosed by stroma pocket (magenta). SBF-SEM gave a 2D picture of the plastid ultrastructure in *Arabidopsis* leaf cells of wild type and mutant plants grown in the dark for 16 h and then illuminated in the continuous white light of ($150 \mu\text{mol m}^{-2}\text{s}^{-1}$). (a) wild-type versus (b) *ss4* plants after 15 min of illumination. (c) Boxplots comparing both the volume and the number of starch granules per plastid. (d) wild-type versus (e) *ss4* plants after 8 h of illumination. (f) Boxplots comparing both the volume and the number of starch granules per plastids.

5.6 Conclusion and perspective

In comparison with FIB-SEM tomography, which has a limited volume of observation, SBF-SEM allows the acquisition of ultrastructural data from larger volumes of plant tissue and the generation of 3D reconstructions of whole plant cells, including internal structures such as plastids. Thanks to the image processing workflow described in

Chapter 2 of this manuscript, it has been possible to improve the z-stack resolution of the background model and perform quantitative analysis to address two distinct biological questions: the etioplast- chloroplast transition in cotyledons cells and the process of starch granule formation in mature leaves.

The proposed approach allowed us to obtain both qualitative and 3D representation of the plastid and thylakoid at different time points of development during de-etiolation at the whole plastid level. The 3D reconstructions revealed chloroplast number and volume and the extent of the thylakoid membrane surface during the de- etiolation process. The extent of thylakoid surface area emphasizes how fast and efficient the thylakoid biogenesis is. During plant development, extending thylakoids surface allows plants to optimize light absorption capacity, ensuring their primary source of energy.

SBF-SEM image datasets of *Arabidopsis* WT and *ss4* mutants confirmed that the number of starch granules per plastid in *Arabidopsis* leaf development depends on the length of the light utilization. Under continuous light (8 h) the starch granule number per chloroplast increases in WT and *ss4* mutant with different quantities as reported in (Malinova et al. 2017). However, the lack of SS4 protein has an impact on formation of starch granules and seems to be important in generating and regulating the volume and morphology of starch granules per plastid as recently expressed by (Malinova et al. 2018; Abt et al. 2020). The reduced number of starch granules in *ss4* mutants is compensated for by the increase in starch granules size.

The 3D quantitative and comparative analysis obtained from the SBF-SEM data of *Arabidopsis* WT and *ss4* mutants leaves open new perspectives to investigate other proteins targeting to starch protein involved in starch granules initiation as reported in (Seung et al. 2017; Seung et al. 2018).

Conclusion and perspectives

General conclusion

The objective of this PhD project was to implement 3D image processing and morphometric analysis workflow to generate 3D models describing the cell ultrastructure organization. The ultimate purpose of this work was to understand physiological responses of photosynthetic organisms (microalgal and plant cells) to environmental changes at the cellular and subcellular levels based on high-resolution 3D electron microscope techniques (FIB- SEM and SBF-SEM).

Volume EM imaging produces large datasets and has been the key starting material to investigate biological ultrastructures. However, the approach requires time for data analysis. Hence, 3D EM imaging faces data management challenges, including data processing. The challenge of the task is explained by: (*i*) the image analysis tools poorly described in literature and inaccessible to the microscopist community, (*ii*) the segmentation process limiting data reproducibility and (*iii*) the limited resolution of acquired images. Overcoming these challenges is the prerequisite to investigate cell structure organisation and perform quantitative analysis. Starting from these premises, this work proposes a 3D images processing pipeline, which optimizes image processing and provides quantitative data. From quantitative data, it is possible to understand the internal cell organisation and possible link to cell physiological responses.

The first chapter presents the biological material used in this study with a focus on the role of endosymbiosis events in the differentiation of phytoplankton species and plant cells. I also introduced the history of electron microscopy and its contribution to the identification and understanding of living organisms. This section includes a review of researches carried out with three-dimensional cellular investigation using EM imaging and the role of sample preparation in explaining cell ultrastructure towards scientific interpretation.

The second chapter focuses on the materials and the image methodology developed in this project. The culture conditions of the different algae together with the sample preparation methods used for EM observation are described. The main part of this chapter describes in detail the development of an optimised 3D imaging workflow needed to obtain three-dimensional information from high-resolution volumetric EM data. The idea behind the proposed workflow, entirely based on open access softwares, is to use supervised semi-automated segmentation that accelerates image analysis and 3D reconstruction and delivers quantitative data after image segmentation and volume reconstruction. First, the proposed workflow does not suffer from the automatic detection of wrong pixels in the segmentation process and the method can be applied to samples from any environment for quantitative analysis. Second, the geometry

processing offers to the user the possibility to automatically clean the reconstructed model, divide the clusters into independent structures and quantify the structural features to obtain volumes, surface areas and the proximity distances between nearby compartments. The different steps are described in a way that this protocol can be used by a large number of users.

The third chapter presents results from the application of the proposed 3D imaging workflow to observe morphological rearrangements following cell adaptation to abiotic and biotic stress. Using 3D EM (FIB-SEM) image data, we assessed subcellular features and their dynamic changes in algae representing major oceanic phytoplankton lineages and established laboratory models. The analysis done on cell architecture focused only on the relationships between the energy production compartments (plastids, mitochondria and energy storage compartments). The study showed the constant fraction occupancy of the energy production compartments in the different lineages as well as the interaction between plastid and mitochondria.

To understand how the cell architecture is remodeled in response to environmental change, I used this workflow to investigate the acclimation response of the diatom *Phaeodactylum tricornutum* to change in light intensity. When cells grown under a low light regime are transferred to high light, larger volume occupancy by the mitochondria and the plastid CO₂ -fixing pyrenoid are observed together with an increase in plastid-mitochondria surface contact. Overall, these changes reveal how cells modify their structure to regulate respiration and photosynthesis capacity.

I have also studied the change in trophic lifestyles when *Nannochloropsis gaditana* is grown under photoautotrophic conditions or in the presence of light plus reduced external carbon sources (mixotrophy). The change in the trophic lifestyle was also associated with substantial physiological and morphological changes. The observed increase in respiration and decrease in photosynthesis is also associated with enhanced surface contacts between both organelles thus probably favouring energy interaction between them. From these results, we propose that phytoplankton cell volume occupancy and organelles topology is possibly governed by energy management rules.

The fourth chapter deals with the application of the image processing workflow to unveil the morphological change following photosymbiosis (biotic constraint) when the free-living Haptophyte *Phaeocystis* undergoes a symbiotic lifestyle with an Acantharians host. I have reconstructed the cell architecture of the free-living and symbiotic *Phaeocystis*. The 3D reconstructed models of symbiotic *Phaeocystis* highlighted the invagination of the host vacuole into the algal, the increase in the symbiosome (the vacuole surrounding the symbiotic alga), the arrest of the algal cell division together with the drastic increase in plastids number and volume and the expansion of the mitochondrial network. Therefore, the observed cell modifications

demonstrate a substantial morphological adaptation of the microalgae after their integration within a host cell.

The fifth chapter focuses on the adaptation of the workflow to SBF-SEM image segmentation. 3D reconstructed models of chloroplast and thylakoid membranes helped establishing a complete picture of chloroplast development and transient starch granule initiation in *Arabidopsis thaliana*. The qualitative and quantitative imaging approaches reveal the transformation, the increase in the number and volume of chloroplasts as well as the surface area of the thylakoid membrane during the etioplast-chloroplast transition. The quantitative data pinpoints an extent of the thylakoid surface as a marker of the speed and efficiency of thylakoid biogenesis during plant development, providing to plants the ability to optimise their light absorption capacity.

Finally, the quantitative analyses done on SBF-SEM image datasets of *Arabidopsis* wild-type and mutants lacking the soluble starch synthase 4 protein (SS4) in developing leaf show that starch granules accumulation, an important energy reserve compartment of the plant, depends on the length of the light exposure. An important increase in the starch granule number is observed in WT chloroplasts. This increase is drastically reduced in *ss4* chloroplasts, but it is largely compensated by the augmentation in the starch granule volume.

Perspectives

Further important observations relevant to this project

Cell adaptation studies may require ‘omics’ approaches to identify genes and proteins associated with physiological transitions and to decipher mechanisms of acclimation. However, imaging approaches are needed to interpret acclimation responses at the cellular and subcellular levels as shown in this Thesis. Many other studies will emerge from the application of this workflow and some of them are actually ongoing such as:

1. Lipid droplets biogenesis in microalgae cells.
2. Morphological comparisons between many eukaryote - eukaryote and eukaryote - prokaryote photosymbiosis, parasitism in planktonic communities, etc.

Since the proposed 3D imaging workflow relies on sample preparation methods, data acquisition techniques and the images processing workflow, it requires interactions between people with different skills. Every step takes some time to be completed and probably will still needs to be optimized. This is actually a bottleneck to produce data. The image processing protocol described in chapter 2 of this manuscript outlines two potential approaches: (*i*) semi-automatic segmentation, and (*ii*) geometry processing, considered optimizing the 3D data analysis approach.

Improvements in image segmentation that can be expected in the future

It would be insightful to perform deep-learning based segmentation, which requires an intelligent segmentation to reduce human interaction to detect, observe and classify important features in an image. To do so, we have to build a model, which learns, identifies and detects certain features in 3D EM images, by manually building a rich training dataset representing different microalgae species, plants and complex intracellular structures models. This knowledge will allow training the same model with different observations. This approach showed robust extraction of relevant and high-quality information in small extracellular vesicles TEM images (Horwath et al. 2020). The authors noticed that clear edges are the most important factor in features identification of structure in the images and seemed to reduce the negative impact of any wrong detection.

The study of morphodynamics can improve the way we understand the adaptation of the cell to its environment

As cell morphology depends on its environment, understanding features that can regulate or modulate cell migration could bring other perspectives in cell structure to address some biological question on:

1. How do cells rearrange their morphology in order to travel more easily through its environment? This study will need a time-lapse 3D imaging.
2. Understanding temporal evolution of morphological features. It would suggest linking cell motility to cell structure, function and adaptation mechanism to classify and identify microalgae species, which resist the stress environment and those, which completely change morphology and function to adapt to the environment as reported in morphodynamics of 3D migrating cancer cells (Eddy et al. 2018).

Protein tags can help to interpret the biological processes involved in cell motility or membrane and organelle dynamics. It could be important to use time-lapse imaging to analyse the trajectory of a specific protein and get spatial temporal information of cell activity. Such information could bring new knowledge to reveal the link between cell topology and cell motility in order to figure out how a cell survives in extreme environmental fluctuations.

fluorescence microscopy can be employed to image specific features. In fixing fluorescent markers on samples, which exhibit targeted characteristics, we can produce a time-lapse image, which easily shows protein tags in the specific region:

- to specify resident protein composition and observe what happened to organelles machinery at contact sites.

- to investigate the stability of contact sites (D’Agostino et al. 2016).
- to study protein trafficking, organelle dynamics and division in order to understand trafficking function as reported in animal cell (Wu et al. 2017; Friedman et al. 2011; Friedman et al. 2013; Xu et al. 2020; Rowland et al. 2014).

We can finally state if physical contacts between organelles can refer to a metabolic exchange by showing factors and functions of organelles membranes at the contact using CryoET.

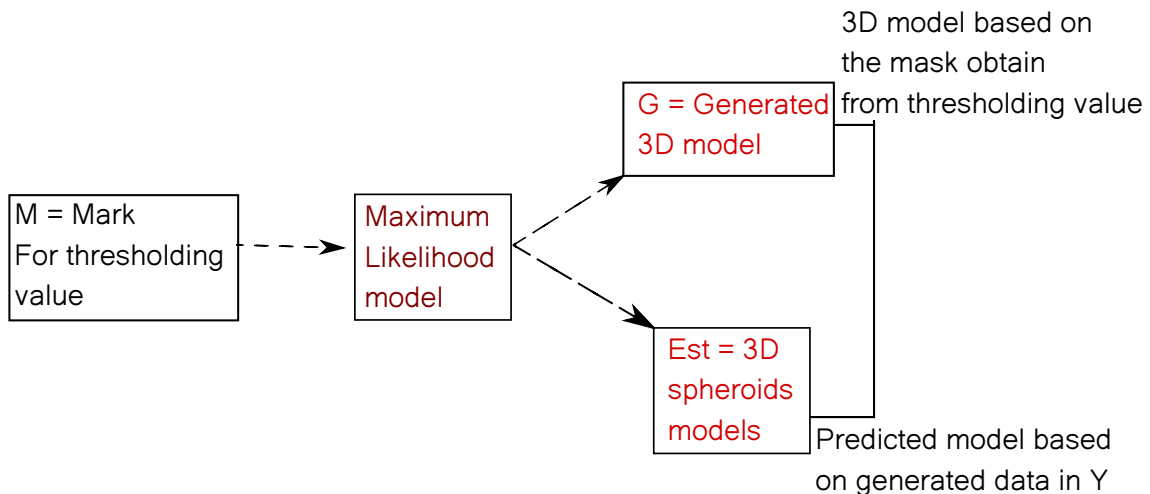
The acquisition of the images by FIB-SEM gives a detailed view of the internal structure of the cell but the method does not give the possibility to work on several cells. Depending on the cell size to be studied we can capture 4 to 20 cells per acquisition. If we consider the time of acquisition and the time it takes to prepare the sample for EM, it is difficult to obtain many cells in a short period of time.

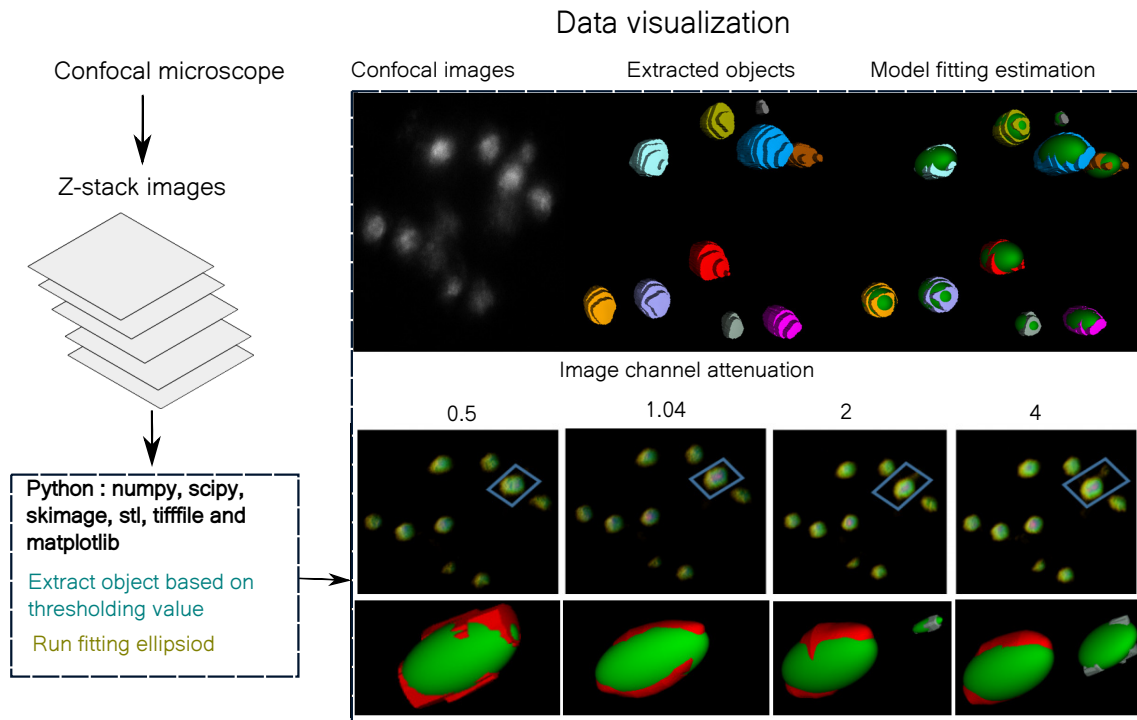
How to get more cells for statistical analysis?

3D confocal imaging approach

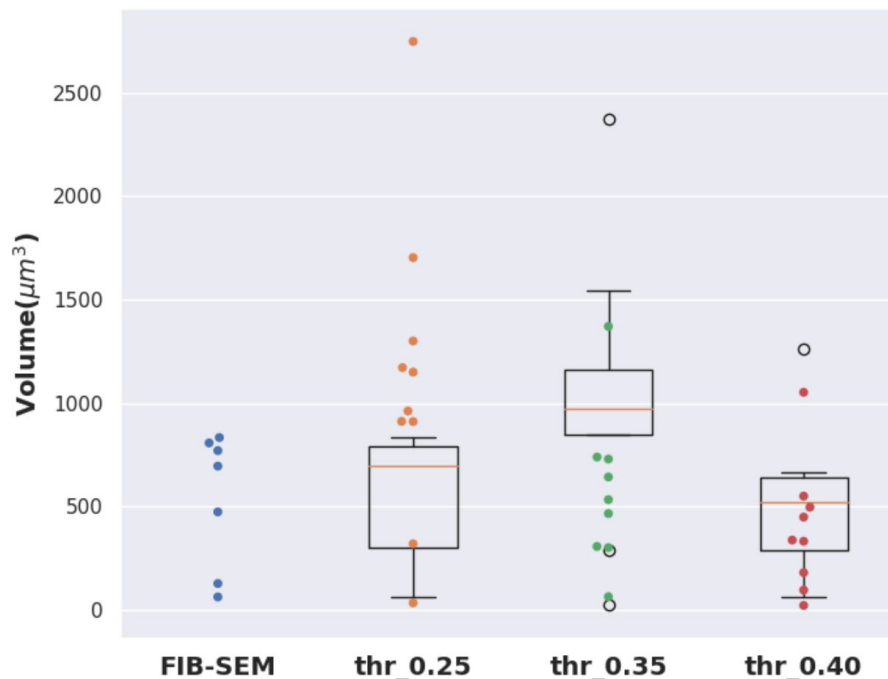
We have measured the fluorescence of different symbiotic algae in a acantharians host using a confocal microscope and we have reproduced the same images using four different intensities of confocal light, with a voxel size $\delta V(d_x, d_y, d_z) = (0.3095 \mu m, 0.3095 \mu m, 3.25 \mu m)$. The resulting images for each experiment were stacked to produce 3D images representing the sample in three-dimension.

Approach, method and strategy





A preliminary result shows the volume of detected symbiotic microalgal cells based on the thresholding pixels value range. When the estimated volume data were compared to volume information computed from FIB-SEM dataset the true thresholding value was obtained.



Using Gradient Descent methods for a linear regression estimation implemented in (Nedrich 2014) we can estimate organelles volume as a function of cell volume $\sim \beta X_i$ where $i = \text{chloroplast, mitochondria, nucleus, cother}$.

Appendices

Contents

A.1	Algal Remodeling in a Ubiquitous Planktonic Photosymbiosis	131
A.2	Cytoklepty in the plankton	148
A.3	A multifaceted analysis reveals two distinct phases of chloroplast biogenesis.	186

A.1 Algal Remodeling in a Ubiquitous Planktonic Photosymbiosis

Summary

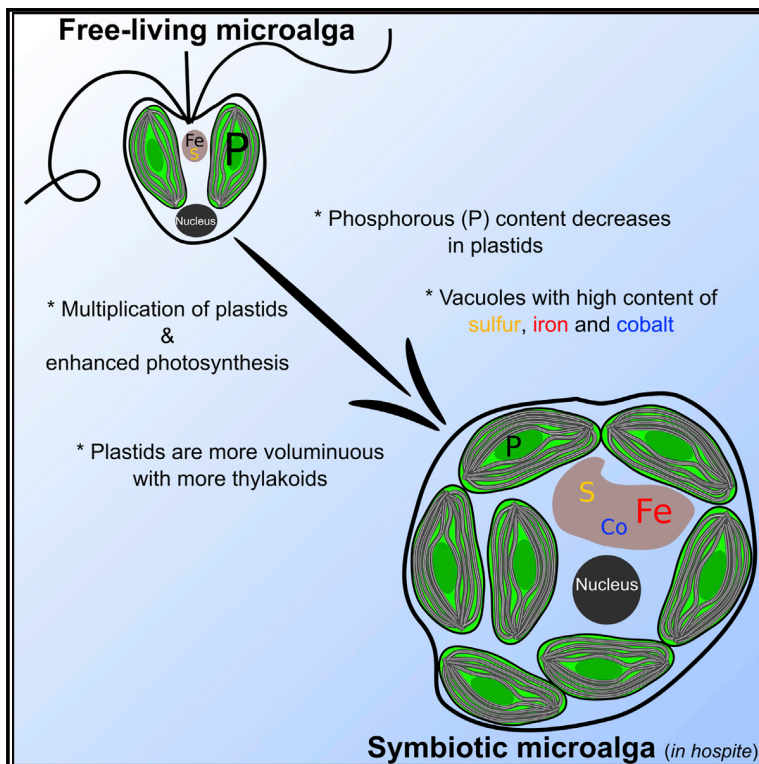
*Photosymbiosis between single-celled hosts and microalgae is common in oceanic plankton, especially in oligotrophic surface waters. However, the functioning of this ecologically important cell-cell interaction and the subcellular mechanisms allowing the host to accommodate and benefit from its micro-algae remain enigmatic. Here, using a combination of quantitative single-cell structural and chemical imaging techniques (FIB-SEM, nanoSIMS, Synchrotron X-ray fluorescence), we show that the structural organization, physiology, and trophic status of the algal symbionts (the haptophyte *Phaeocystis*) significantly change within their acantharian hosts compared to their free-living phase in culture. In symbiosis, algal cell division is blocked, photosynthesis is enhanced, and cell volume is increased by up to 10-fold with a higher number of plastids (from 2 to up to 30) and thylakoid membranes. The multiplication of plastids can lead to a 38-fold increase of the total plastid volume in a cell. Subcellular mapping of nutrients (nitrogen and phosphorous) and their stoichiometric ratios shows that symbiotic algae are impoverished in phosphorous and suggests a higher investment in energy-acquisition machinery rather than in growth. Nanoscale imaging also showed that the host supplies a substantial amount of trace metals (e.g., iron and cobalt), which are stored in algal vacuoles at high concentrations (up to 660 ppm). Sulfur mapping reveals a high concentration in algal vacuoles that may be a source of antioxidant molecules. Overall, this study unveils an unprecedented morphological and metabolic transformation of microalgae following their integration into a host, and it suggests that this widespread symbiosis is a farming strategy wherein the host engulfs and exploits microalgae.*

Keywords: symbiosis, plankton, microalga, single-cell imaging, photosynthesis, mass spectrometry imaging, 3D electron microscopy, eukaryotes, plastid, *Phaeocystis*.

Current Biology

Algal Remodeling in a Ubiquitous Planktonic Photosymbiosis

Graphical Abstract



Authors

Johan Decelle, Hryhoriy Stryhanyuk, Benoit Gallet, ..., Hans Richnow, Giovanni Finazzi, Niculina Musat

Correspondence

johan.decelle@univ-grenoble-alpes.fr

In Brief

The microalga *Phaeocystis* lives as an intracellular symbiont of acantharian hosts. Using single-cell imaging, Decelle et al. show that *Phaeocystis* is morphologically and metabolically transformed within a host, with a significant expansion of the photosynthetic machinery and alteration of nutrient homeostasis toward high productivity.

Highlights

- Symbiotic *Phaeocystis* has more plastids and thylakoids than do free-living forms
- Symbiotic *Phaeocystis* has a higher photosynthetic efficiency than do free-living cells
- Phosphorous content in symbiotic *Phaeocystis* decreases in the plastids
- Nanoscale imaging showed high concentrations of iron in vacuoles in symbiotic algae



Algal Remodeling in a Ubiquitous Planktonic Photosymbiosis

Johan Decelle,^{1,10,11,*} Hryhoriy Stryhanyuk,¹ Benoit Gallet,² Giulia Veronesi,^{3,4} Matthias Schmidt,¹ Sergio Balzano,⁵ Sophie Marro,⁶ Clarisse Uwizeye,⁷ Pierre-Henri Jouneau,⁸ Josselin Lupette,⁷ Juliette Jouhet,⁷ Eric Maréchal,⁷ Yannick Schwab,⁹ Nicole L. Schieber,⁹ Rémi Tucoulou,⁴ Hans Richnow,¹ Giovanni Finazzi,⁷ and Niculina Musat¹

¹Helmholtz Centre for Environmental Research – UFZ, Department of Isotope Biogeochemistry, 04318 Leipzig, Germany

²Institut de Biologie Structurale, Université Grenoble Alpes, CNRS, CEA, 71 Avenue des Martyrs, 38044 Grenoble, France

³Laboratoire de Chimie et Biologie des Métaux UMR 5249, Université Grenoble Alpes, CNRS, CEA, 17 Avenue des Martyrs, 38054 Grenoble, France

⁴ESRF, The European Synchrotron Radiation Facility, 71 Avenue des Martyrs, 38043 Grenoble, France

⁵NIOZ, Royal Netherlands Institute for Sea Research, Department of Marine Microbiology and Biogeochemistry, and Utrecht University, PO Box 59, 1790 AB Den Burg, the Netherlands

⁶Sorbonne Universités, UPMC Université Paris 06, CNRS, Laboratoire d’Océanographie de Villefranche UMR7093, Observatoire Océanologique, 06230 Villefranche-sur-Mer, France

⁷Cell & Plant Physiology Laboratory, University of Grenoble Alpes, CNRS, CEA, INRA, 38054 Grenoble Cedex 9, France

⁸Institut Nanosciences et Cryogénie, Université Grenoble Alpes, CEA, 38054 Grenoble, France

⁹Cell Biology and Biophysics Unit, European Molecular Biology Laboratory, 69117 Heidelberg, Germany

¹⁰Present address: Cell & Plant Physiology Laboratory, University of Grenoble Alpes, CNRS, CEA, INRA, 38054 Grenoble Cedex 9, France

¹¹Lead Contact

*Correspondence: johan.decelle@univ-grenoble-alpes.fr

<https://doi.org/10.1016/j.cub.2019.01.073>

SUMMARY

Photosymbiosis between single-celled hosts and microalgae is common in oceanic plankton, especially in oligotrophic surface waters. However, the functioning of this ecologically important cell-cell interaction and the subcellular mechanisms allowing the host to accommodate and benefit from its microalgae remain enigmatic. Here, using a combination of quantitative single-cell structural and chemical imaging techniques (FIB-SEM, nanoSIMS, Synchrotron X-ray fluorescence), we show that the structural organization, physiology, and trophic status of the algal symbionts (the haptophyte *Phaeocystis*) significantly change within their acantharian hosts compared to their free-living phase in culture. In symbiosis, algal cell division is blocked, photosynthesis is enhanced, and cell volume is increased by up to 10-fold with a higher number of plastids (from 2 to up to 30) and thylakoid membranes. The multiplication of plastids can lead to a 38-fold increase of the total plastid volume in a cell. Subcellular mapping of nutrients (nitrogen and phosphorous) and their stoichiometric ratios shows that symbiotic algae are impoverished in phosphorous and suggests a higher investment in energy-acquisition machinery rather than in growth. Nanoscale imaging also showed that the host supplies a substantial amount of trace metals (e.g., iron and cobalt), which are stored in algal vacuoles at high concentrations (up to 660 ppm). Sulfur mapping reveals a high concentration in algal vacu-

oles that may be a source of antioxidant molecules. Overall, this study unveils an unprecedented morphological and metabolic transformation of microalgae following their integration into a host, and it suggests that this widespread symbiosis is a farming strategy wherein the host engulfs and exploits microalgae.

INTRODUCTION

Acquisition of plastids by eukaryotic host cells via endosymbiosis with microalgae is heralded as one of the most important biological innovations [1, 2]. Prior to genetic integration, hosts had strong control over their photosynthetic symbionts by driving metabolic integration [3, 4]. In today’s oceanic plankton, living in symbiosis with microalgae (photosymbiosis) is a widespread and ecologically important phenomenon [5, 6]. The widely distributed photosymbiosis between heterotrophic radiolarian hosts and eukaryotic microalgae is abundant in surface oligotrophic waters [5, 7–9]. These organisms significantly contribute to planktonic biomass, carbon fixation (through photosynthesis of the algal symbionts), and carbon export to the deep ocean [9–12], making them important components of oceanic ecosystems. Photosymbiosis may become even more prominent in the oceans of the future, since oligotrophic provinces are expanding due to global warming [13]. While knowledge of the diversity of eukaryotic photosymbioses has greatly improved in the past decade (e.g., radiolarians, foraminiferans) [7, 14], their physiology and metabolism remain largely unexplored, as does their biogeochemical significance in marine ecosystems. In particular, investigating the structural and metabolic strategies that allow host cells to integrate and control intracellular microalgae has been a major challenge due to the highly complex nature of their intertwined partnerships, the lack of



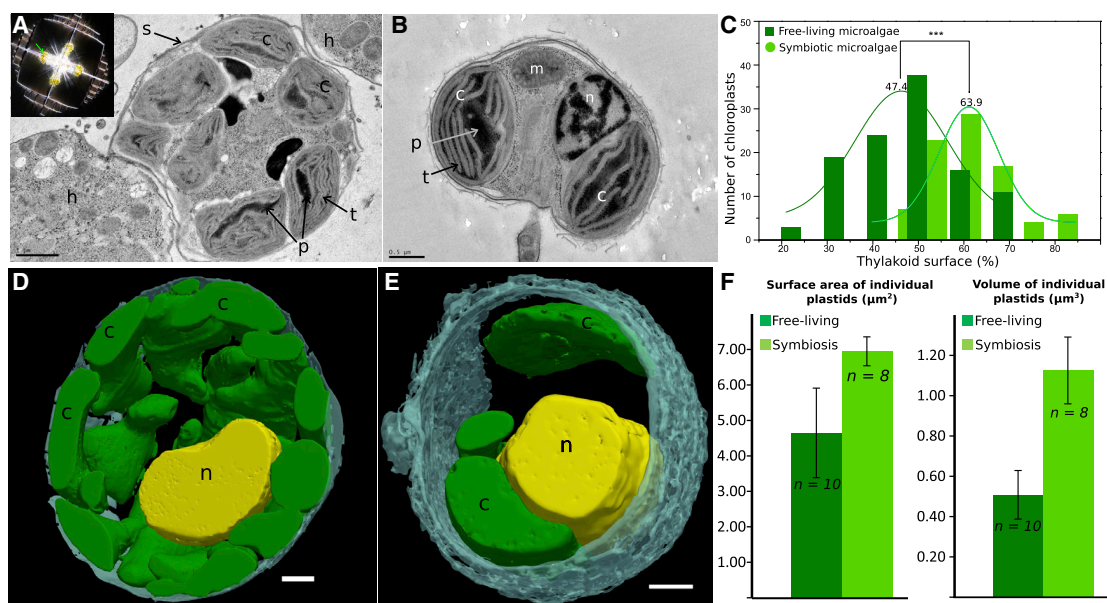


Figure 1. Morphological Transformation of the Microalga *Phaeocystis* between the Free-Living and Symbiotic Stages

(A) Ultrastructure of the symbiotic microalga *Phaeocystis cordata* within acantharian host unveiled by transmission electron microscopy (TEM). The scale bar represents 1 μm . Inset: light microscopy image showing an acantharian host cell with its star-shaped biomineralized skeleton and its intracellular microalgae *Phaeocystis* (yellow cells indicated by a green arrow).

(B) Ultrastructure in TEM of the free-living *Phaeocystis* cell grown in culture with two parietal plastids. The scale bar represents 0.5 μm . n, nucleus; c, plastid; p, pyrenoid; h, host; t, thylakoid membrane; s, symbiosome membrane; m, mitochondria.

(C) Surface occupied by thylakoid membranes per plastid in free-living (light green; 47.37% \pm 12.88%, n = 113 plastids) and symbiotic (dark green; 63.85% \pm 8.95%, n = 86 plastids) *Phaeocystis* calculated from TEM micrographs.

(D and E) 3D visualization with FIB-SEM (focused ion beam scanning electron microscopy) of the microalga *Phaeocystis* in symbiosis within a host (D) and in free-living phase (E) with plastids (green) and a nucleus (yellow). The scale bar represents 1 μm . (See also Video S1.)

(F) Surface area and volume of individual plastids in free-living (n = 10) and symbiotic (n = 8) microalgal cells were calculated from the 3D reconstructions. In symbiosis, the surface area and volume of plastids (6.95 \pm 1.22 μm^2 and 1.13 \pm 0.17 μm^3) were higher than those of free-living *Phaeocystis* cells in culture (4.65 \pm 0.85 μm^2 and 0.51 \pm 0.12 μm^3). (See also Video S1.)

stable cultures, and the scarcity of knowledge about their genomes and protein functions [15, 16]. In the ecologically successful symbiosis between Acantharia (radiolarian host) and the microalga *Phaeocystis*, the host depends entirely on engulfed symbiotic microalgae for growth and survival (i.e., obligatory symbiosis) [7]. By contrast, the microalga *Phaeocystis*, which is a keystone phytoplankton taxon that shapes the structure and function of marine ecosystems, can exist in free-living forms in the environment [17, 18]. Phylogenetic analyses including different nuclear and plastidial genes suggest that the free-living and symbiotic *Phaeocystis* populations are genetically identical in a given oceanic region (e.g., *Phaeocystis cordata* in the Mediterranean Sea [7]). Living with the locally adapted and abundant symbiont genotypes would be an advantageous strategy for acantharian hosts that must re-establish the symbiotic partnership at each generation (i.e., horizontal transmission).

We studied this ubiquitous symbiotic interaction between single-celled organisms, which represents a promising model to study the cellular integration of algae into a host and therefore to elucidate the possible processes underpinning plastid acquisition in eukaryotes. We used a combination of 3D electron microscopy, nanoscale mass spectrometry, and X-ray fluorescence imaging to investigate the transition between free-living and symbiotic stages of the microalgae at the subcellular level

and disentangle the role of each symbiotic partner. These techniques were complemented by physiological analyses to offer a comprehensive picture of the physiology and metabolism of the interaction. We showed that, within their host, division of algal cells is blocked, and their ultrastructure, physiology, and trophic state significantly change, transforming them into a highly productive photosynthetic machinery. This algal remodeling, presumably induced by the host, suggests that this widespread and abundant symbiosis could represent an algal farming strategy, providing a new paradigm for the ecological success of planktonic photosymbiosis in the oligotrophic oceans.

RESULTS AND DISCUSSION

Major Structural Transformation of Symbiotic Microalgae for Enhanced Photosynthesis

We investigated the ultrastructure of microalgal symbionts (*Phaeocystis cordata*) within their acantharian hosts (Figure 1A), collected from marine surface waters, and of their free-living phase (i.e., grown *ex hospite* in culture). To preserve their native ultrastructure and chemical composition, cells were cryofixed with high-pressure freezing, subjected to freeze substitution, and embedded in resin. Transmission electron microscopy of ultrathin sections showed that the free-living microalgae were

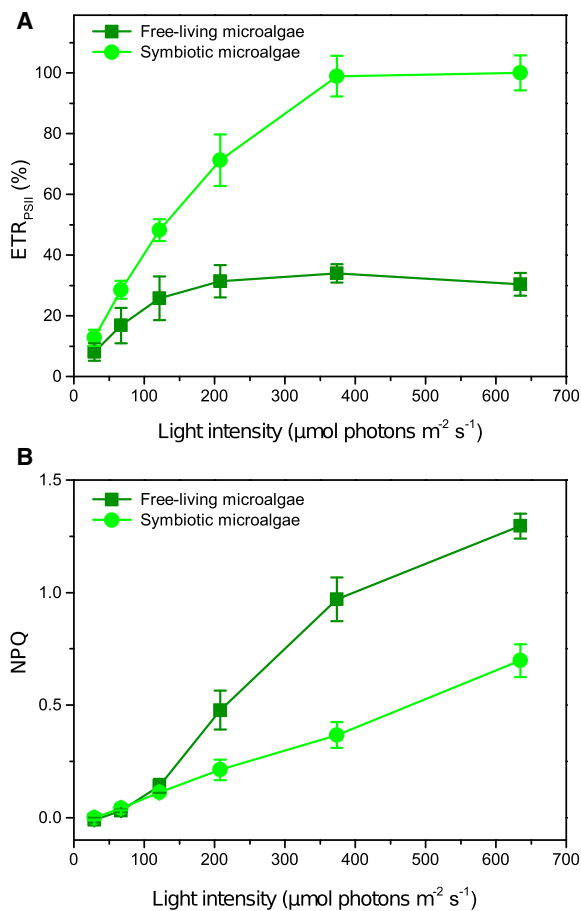


Figure 2. Photosynthetic Efficiency and Response to Light Stress in Free-Living and Symbiotic Microalgae *Phaeocystis*

(A) Photosynthetic efficiency measured by the relative electron transfer rate (ETR) for free-living (dark green squares; 23 measures from triplicates) and symbiotic (light green circles; 10 measures from triplicates) microalgae over a range of light intensities up to 700 $\mu\text{mol photons m}^{-2} \text{s}^{-1}$.

(B) The non-photochemical quenching (NPQ) parameter indicated that the light energy absorption of symbiotic microalgae *Phaeocystis* (light green line; 10 measures from triplicates) was less sensitive in high-light conditions than it was in free-living *Phaeocystis* grown in culture (dark green line; 23 measures from triplicates).

See also Table S1.

3–5 μm in size and typically possessed two parietal plastids (Figure 1B), as described in the taxonomic diagnosis of the species [19]. In stark contrast, the symbiotic microalgae were substantially larger (8–10 μm in size), with average volumes up to 10-fold larger than those of the free-living cells. In addition to a nucleus, symbiotic microalgae possessed up to 31 pyrenoid-containing plastids, located predominantly at the periphery of the cells (Figure 1). Three-dimensional subcellular reconstruction showed that the multiple interconnected plastids occupied most of the algal cell volume and were 3-fold more voluminous than were the plastids in the free-living microalgae (Figures 1D–1F; Video S1). In a single algal cell, our morphometric analyses based on 3D models revealed a 30-fold increase of the total surface of plastids (from 8.4 μm^2 in free-living to 251.6 μm^2 in symbiosis) and a 38-fold increase of the total volume of plastids (from 1 μm^3 in free-living to

38.6 μm^3 in symbiosis). In addition, the plastids of symbiotic microalgae contained far denser networks of stacked thylakoid membranes (17 nm thick), which occupied 64% ($\pm 9\%$) of the plastid surface area, compared to 47% ($\pm 13\%$) in the free-living microalgae (Figure 1C). Thus, microalgae in symbiosis significantly expand their photosynthetic surfaces by multiplication of voluminous plastids (from 2 to 31) and of thylakoid membranes.

To our knowledge, this significant morphological transformation of the photosynthetic machinery has not been reported in other symbiotic algae from terrestrial and marine ecosystems, such as coral or other planktonic symbioses [20, 21]. To test whether photosynthetic activity is affected by these morphological changes, we conducted *in vivo* photophysiology measurements based on measurements of chlorophyll fluorescence in the free-living and symbiotic microalgae. We found that the electron transfer rate (ETR), a widely used parameter to assess photosynthetic efficiency [22], was significantly higher (up to three times) in the symbiotic microalgae than in the free-living microalgae (Figure 2A). Within the host, photosynthesis was enhanced in a range of light conditions (29 to 672 $\mu\text{mol photons m}^{-2} \text{s}^{-1}$) encompassing values experienced by these organisms in the natural environment [23]. Based on the photosynthesis (ETR)-irradiance curves, different parameters of free-living and symbiotic microalgae were evaluated, such as the maximum photosynthetic capacity (Pm), the photosynthetic efficiency under light levels close to zero (the initial slope α), and the minimum photosynthetic saturation irradiance (Ek) [24]. Compared to free-living microalgae, we found higher values of Pm (128.85 ± 6.5 versus 41.34 ± 0.87), α (0.61 ± 0.04 versus 0.40 ± 0.02), and Ek (211.50 ± 16.32 versus 103.12 ± 6.03) in symbiotic microalgae, suggesting that the photosynthetic activity in limiting and saturating light levels was enhanced in symbiosis (Table S1). More particularly, we can conclude that light capture at limiting light was higher in symbiosis (1.5 times more) as well as carbon assimilation at saturating light (3.1 times more). In addition, excess light dissipation via non-photochemical quenching (NPQ) was diminished in symbiotic microalgae in high-light conditions (Figure 2B). This suggests that symbiotic microalgae were less exposed to excess light stress, confirming that the environment provided by the host is optimal for their photosynthesis.

High-Nitrogen and Low-Phosphorous Conditions in Symbiotic Microalgae

The structural and associated physiological changes of symbionts may be promoted by the host to maximize photosynthetic capacity and thereby fully benefit from the photosynthates, such as sugars. The transformed microalgal cells are maintained in an intracellular vacuole (symbiosome, Figure 1), where the host has to provide essential nutrients (nitrogen, phosphorous, and trace metals), which generally limit the primary productivity of phytoplankton in oceanic waters [25]. In order to highlight possible metabolic changes induced by symbiosis, we investigated the subcellular distribution and composition of nutrients in free-living and symbiotic microalgae. Note that we hereafter compared algal cells grown in an artificial culture medium (free-living condition) with algal cells maintained in the microhabitat provided by their host (Table S2).

The nitrogen (N)-to-phosphorus (P) ratio is generally considered to be a proxy for the metabolic investment of a cell [26].

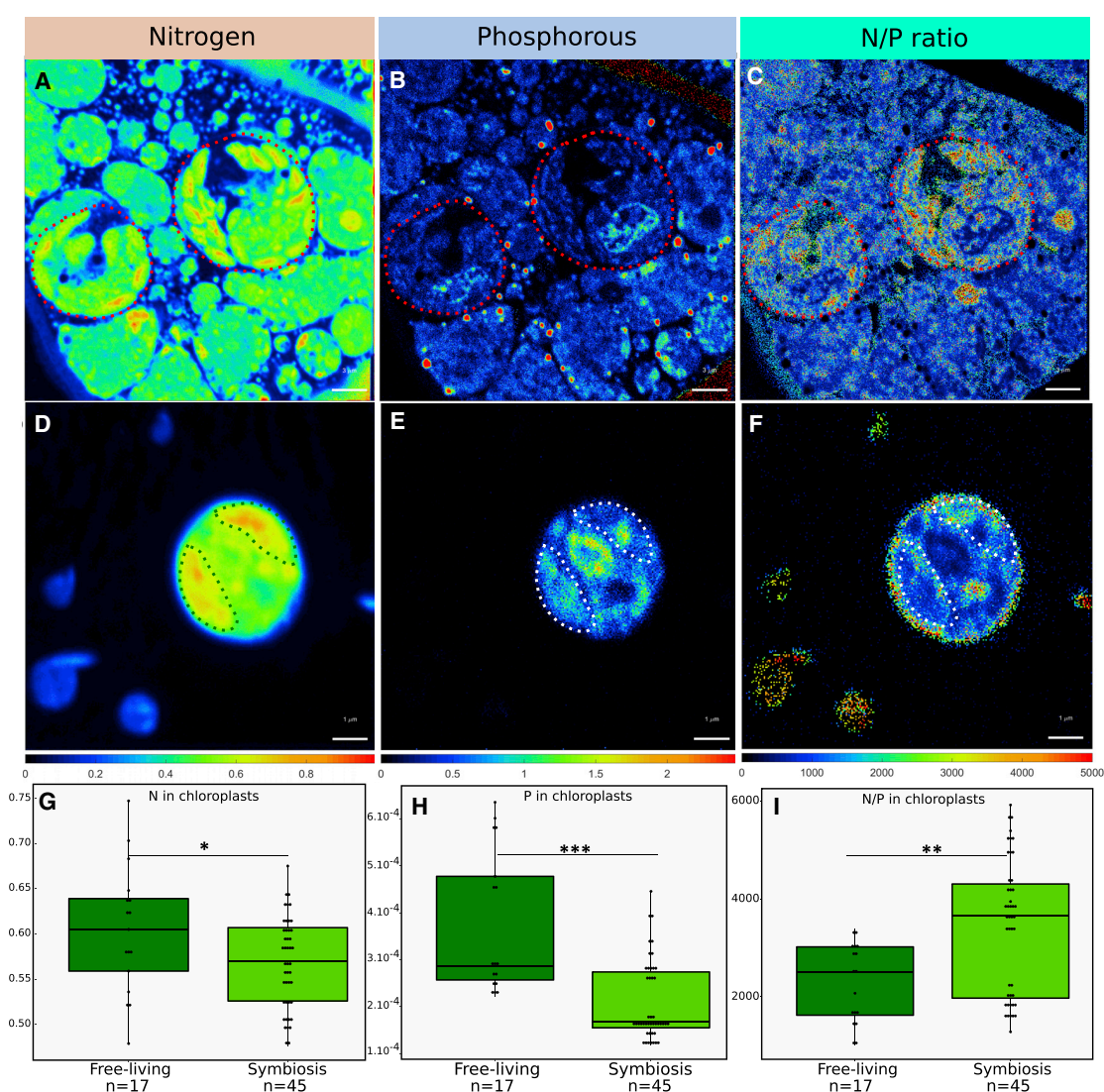


Figure 3. Subcellular Quantitative Mapping of Nitrogen, Phosphorous, and their Stoichiometric Ratios in Symbiotic and Free-Living *Phaeocystis* Cells, Measured by nanoSIMS

(A–C) Subcellular distribution of nitrogen ($^{12}\text{C}^{14}\text{N}/^{12}\text{C}_2$), phosphorous ($^{31}\text{P}^{16}\text{O}_2/^{12}\text{C}_2$), and the N/P ratio ($^{12}\text{C}^{14}\text{N}/^{31}\text{P}^{16}\text{O}_2$) in two symbiotic *Phaeocystis* algal cells highlighted by a red dashed line. Note that the two symbiotic microalgae are intracellular within their host cell. The scale bar represents 3 μm .

(D–F) Subcellular distribution of nitrogen ($^{12}\text{C}^{14}\text{N}/^{12}\text{C}_2$), phosphorous ($^{31}\text{P}^{16}\text{O}_2/^{12}\text{C}_2$) and the N/P ratio ($^{12}\text{C}^{14}\text{N}/^{31}\text{P}^{16}\text{O}_2$) in one free-living *Phaeocystis* algal cell. The two plastids of the algal cell are highlighted by a green and white dashed line. The scale bar represents 1 μm .

(G–I) Nitrogen ($^{12}\text{C}^{14}\text{N}/^{12}\text{C}_2$) and phosphorous ($^{31}\text{P}^{16}\text{O}_2/^{12}\text{C}_2$) content and the N/P stoichiometric ratio ($^{12}\text{C}^{14}\text{N}/^{31}\text{P}^{16}\text{O}_2$) in plastids of free-living and symbiotic microalgae. (See also [Data S1](#).) Statistical analyses were performed using ANOVA type-II tests based on 17 plastids of free-living microalgae and 45 plastids of symbiotic microalgae. $^{12}\text{C}^{14}\text{N}/^{12}\text{C}_2$ was log-transformed, and Tukey's Ladder for Power transformation was applied to $^{31}\text{P}^{16}\text{O}_2/^{12}\text{C}_2$ and $^{12}\text{C}^{14}\text{N}/^{31}\text{P}^{16}\text{O}_2$ (* $p < 0.05$, ** $p < 0.01$; *** $p < 0.001$, ANOVA test).

See also [Figures S1 and S4](#); [Data S1](#); and [Table S2](#).

Depending on environmental factors, microalgal cells are able to differentially allocate N and P into either energy-acquisition machinery (N-rich proteins; high N/P ratio) or growth machinery (P-rich RNA; low N/P ratio) [27, 28]. To reconstitute N/P ratios in host cells, symbiotic microalgae, and free-living microalgae, we mapped the content and distribution of N and P at a subcellular level using nanoSIMS. In order to compare the relative N and P content between the host and symbiotic and free-living microalgae, the total ion counts of these elements were normalized by

the total ion counts of carbon (C_2). We showed that symbionts have higher N/P ratios than their hosts (Figure 3C; [Data S1](#)), due to a higher N content of the plastids ($p < 0.05$; ANOVA; [Figure 3A](#); [Data S1](#)) and a lower cellular P content (Figure 3B). P in symbionts was mainly contained in the nucleus, with no evidence of cellular storage (Figure 3B). By contrast, the host cells contained cytosolic hotspots of P, where the content was 3- and 10-fold higher than that in the nucleus and plastids of the symbionts, respectively. Overall, N/P ratio mapping in cells suggests

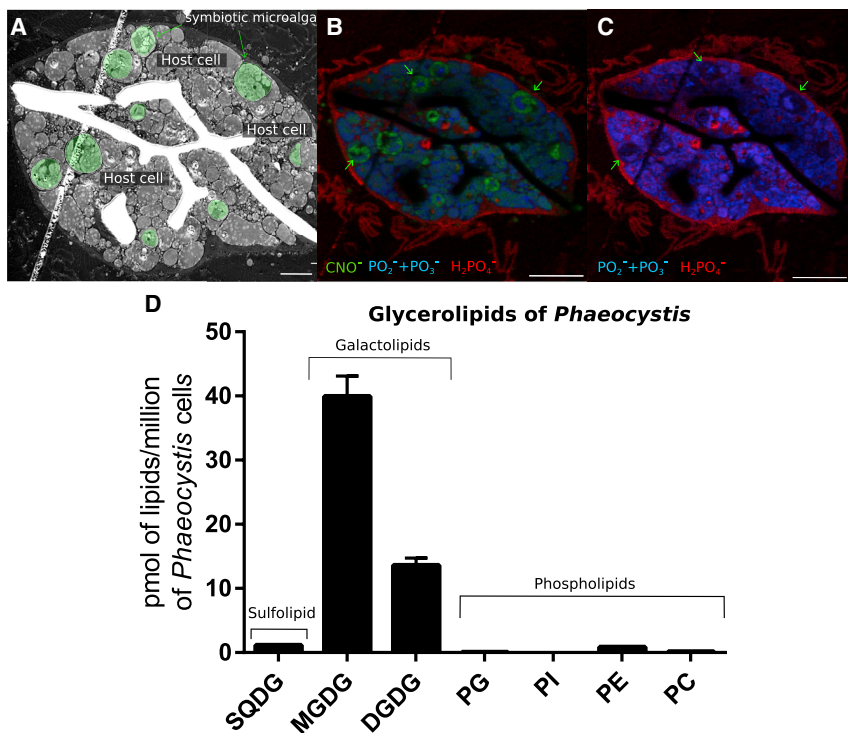


Figure 4. Subcellular Distribution of Phosphorous-Containing Molecules in the Host Acantharia and Lipid Composition of the Microalga *Phaeocystis*

(A) Scanning electron microscopy (SEM) image of a host acantharian cell containing endosymbiotic microalgae *Phaeocystis* artificially colored in green; the scale bar represents 10 μm .

(B and C) Corresponding ToF-SIMS images of the whole host cell showing the subcellular distribution of the accumulated phosphate ions PO_2^- (m/z 62.98) and PO_3^- (m/z 78.96) in blue, in lower concentration in plastids of the symbiotic *Phaeocystis* (highlighted by green arrows); in red, the ion fragment H_2PO_4^- (dihydrogen phosphate; m/z 96.96) located mainly in two cytoplasmic membranes of the host cell, and in green, nitrogen (CNO^- ; m/z 42.01) in high concentration in the symbiont plastids. The scale bar represents 20 μm .

(D) Lipidomics analyses showing the composition of glycerolipids (sulfolipids, galactolipids, and phospholipids) in the free-living *Phaeocystis* microalgae grown in a culture medium. SQDG, sulfoquinovosyldiacylglycerol; MGDG and DGDG, mono- and digalactosyldiacylglycerol, respectively; PG, phosphatidylglycerol; PI, phosphatidylinositol; PE, phosphatidylethanolamine; PC, phosphatidylcholine.

See also Figure S1 and Table S2.

the existence of an optimal metabolic coupling and labor division between the host (investment in growth) and symbionts (investment in energy acquisition), which likely provides a competitive edge in resource-limited oceanic waters, such as the Mediterranean Sea.

Compared to those in free-living cells, the N/P ratios of the symbiotic microalgae were 2-fold higher, especially in plastids ($p = 0.002$, ANOVA; Figure 3I). This was mainly caused by the lower P content of the plastids in the symbionts, since the N content was comparable in plastids of symbiotic and free-living cells ($p > 0.01$; ANOVA; Figures 3G–3I). The P content in symbiotic microalgae could be two times lower than that in free-living cells, and the plastids exhibited a significantly low P content with respect to the cytosol ($p < 0.05$; ANOVA; Figures 3B and 3E). By contrast, in free-living cells, P was homogeneously distributed and did not exhibit a lower concentration in the plastids (Figure 3E; Data S1). As the non-storage P in algae is mainly contained in RNA, followed by DNA and phospholipids [29, 30], subcellular P mapping suggests that these molecules were present in lower concentrations in symbiotic versus free-living microalgae. This could result from the increased primary productivity of the symbiotic microalgae that must adjust their nutrient homeostasis and/or from a lower availability of P in the symbiosome compared to that in the culture medium (Table S2). We hypothesize that the lower P content in symbiosis could reflect a limitation imposed by the host to control the symbiont population, as observed in reef photosymbioses [31, 32]. Under P limitation, cell division is blocked, but carbon fixation is maintained in some microalgae [33], which could be an optimal metabolic strategy for the host. Consistent with this hypothesis, we did not observe any *Phaeocystis* cell divisions within their hosts,

either from electron micrographs or by *in vivo* monitoring of isolated host cells over 7 days (Figure S1), whereas *Phaeocystis* cells in culture can divide every 6–7 h [34]. Inorganic P is scarce in oceanic waters, particularly in the Mediterranean Sea [35], and the association with symbiotic microalgae with naturally low phosphate requirements could be a selective pressure for the host. ToF-SIMS molecular mapping of PO_2^- and PO_3^- , which are characteristic phospholipid fragments [36], showed that the phospholipids were barely present in the plastids of the symbiotic microalgae (Figures 4B and 4C). Consistent with this finding, our lipidomics analyses revealed that free-living *Phaeocystis* cells, maintained in a culture medium where P was not limiting, contained an extremely low quantity of phospholipids (Figure 4D). In plastids, their thylakoid membranes consist mainly of non-phosphorous galactolipids (MGDG [monogalactosyldiacylglycerol] and DGDG [digalactosyldiacylglycerol]), and their extra-plastidial membranes are mainly composed of the non-phosphorous and N-containing betaine lipids (DGTA and DGCC). In *Phaeocystis*, P requirements for thylakoid lipid synthesis and high photosynthetic activity are therefore very low, which is highly advantageous for a host to accommodate a high number of plastids in an oligotrophic environment. Yet in order to sustain the enhanced primary productivity of its intracellular symbionts, the host must also deliver trace metals, such as iron, which are driving photosynthesis in the oceans [25, 37].

Altered Metal Homeostasis in Symbiotic Microalgae

Trace metals are essential for photosynthesis, N assimilation, antioxidant protection, and other essential biochemical functions of microalgae [37, 38]. The ecological success of the

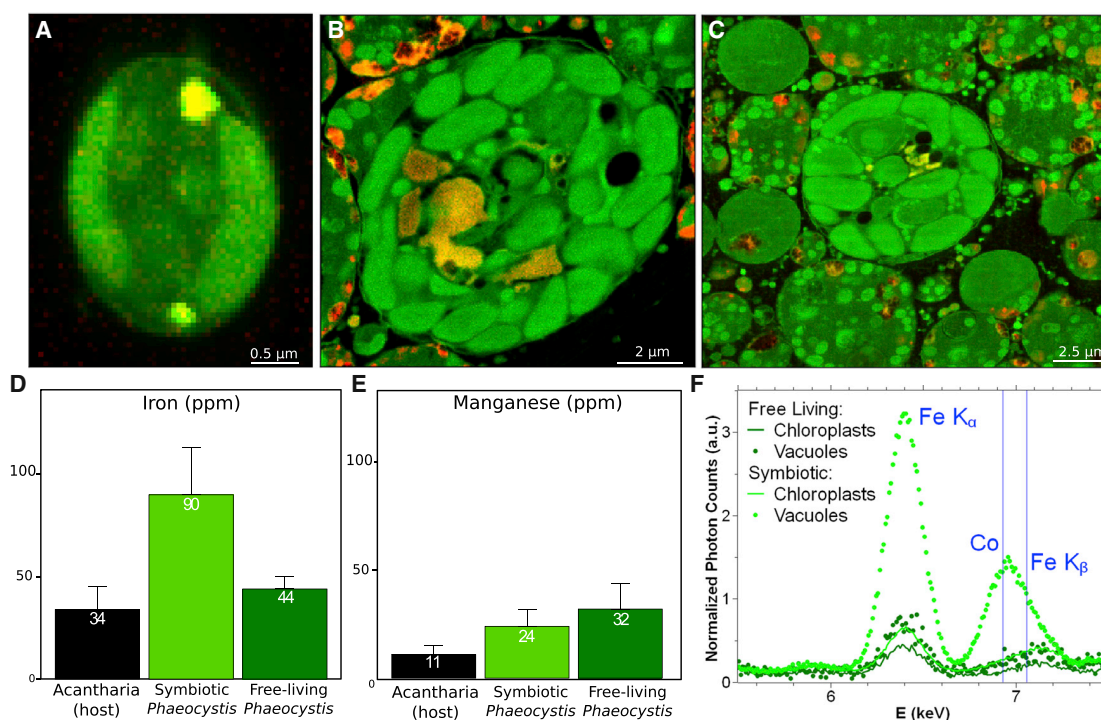


Figure 5. Subcellular Distribution and Quantification of Trace Metals—Fe, Mn, and Co—in Free-Living and Symbiotic Microalgae by Synchrotron X-Ray Fluorescence

(A) In free-living *Phaeocystis*, Fe (red) is localized in the two plastids and in vacuoles (osmium showing the ultrastructure, green). The co-localization of Fe and Os is indicated by the yellow color. (See also Tables S2–S4 and Figure S2.)

(B and C) In symbiosis, Fe concentration increases in *Phaeocystis* and is mainly stored in large vacuoles (yellow).

(D and E) Fe and Mn concentration in the host cells (black bars) and in the symbiotic and free-living *Phaeocystis* cells (light and dark green bars, respectively) (see also Table S3).

(F) Average S-XRF spectrum per pixel in subcellular compartments of *Phaeocystis* in free-living (dark green) and symbiotic (light green) stages, showing high Fe concentration in vacuoles of symbiotic microalgae (light green circles), where cobalt (Co) is also present (see also Figure S2 and Tables S2 and S4).

host-symbiont association must therefore rely on efficient mechanisms to uptake, sequester, and regulate the exchange of these extremely low-concentrated nutrients in the ocean. Here, we imaged and quantified the subcellular distribution of metals in host and symbiont cells with Synchrotron X-ray fluorescence. We found that the concentration of Fe in symbiotic microalgae was twice as high (90 ± 23 ppm) as that in free-living microalgae (44 ± 6 ppm) (Figure 5; Table S3). The higher concentration of Fe in symbiotic microalgae was mainly due to the presence of large Fe-rich vacuoles in the algal cytosol containing up to 660 ppm Fe (420 ± 210 ppm on average) (Figures 5B and 5C; Figure S2; Table S4). The same type of vacuole was also present in free-living microalgae, but these vacuoles were smaller, and their concentration of Fe was approximately decreased by 2-fold (160 ± 30 ppm) (Figures 5A and 5F; Table S4). The individual plastids of free-living and symbiotic *Phaeocystis* cells had similar Fe concentrations. Since they possess large storage vacuoles and numerous plastids, symbiotic microalgal cells contained substantially more Fe (from 0.77 to 5.50 fg, calculated from the analyzed surface area), than do free-living cells (0.25 ± 0.03 fg). This implies that a significant quantity of Fe is delivered by the host, and once sequestered in the intracellular microalgae, the homeostasis of this essential yet toxic metal could be regulated through storage vacuoles to minimize oxidative stress. In the host cell, Fe was

localized in high concentrations in specific subcellular structures but was, on average, 2.5 times less concentrated (34 ± 6 ppm) than in the symbiotic microalgae. Variability in metal homeostasis between symbiotic and free-living forms was also found for cobalt. Co was not detected in the free-living symbionts, although this metal was present in the culture medium (Table S2). By contrast, we detected Co in symbiotic microalgae (25 ± 17 ppm), specifically in the nucleus, some organelles, and the vacuole. In the latter cellular compartment, Co could be co-localized in high concentrations (up to 400 ppm) with Fe (Figure 5F and Figure S2). In the host cell, Co was homogeneously distributed in the cytoplasm (e.g., nucleus, Golgi apparatus) and was present at higher concentration (68 ppm) than in symbionts. For manganese, we found that the concentration was higher in symbiotic microalgae (24 ± 8 ppm) than in the host cell (11 ± 4 ppm) but was similar in free-living cells (32 ± 16 ppm) (Figure 5E; Table S3).

Overall, the subcellular quantitative mapping of metals showed that the metal homeostasis of microalgae was dramatically altered in symbiosis, implying specific mechanisms by which the host takes up and transfers these key elements to intracellular symbionts. Fe deprivation is known to decrease carbon fixation, N assimilation, and overall photosynthetic activity in microalgal cells [39]. We therefore hypothesize that the

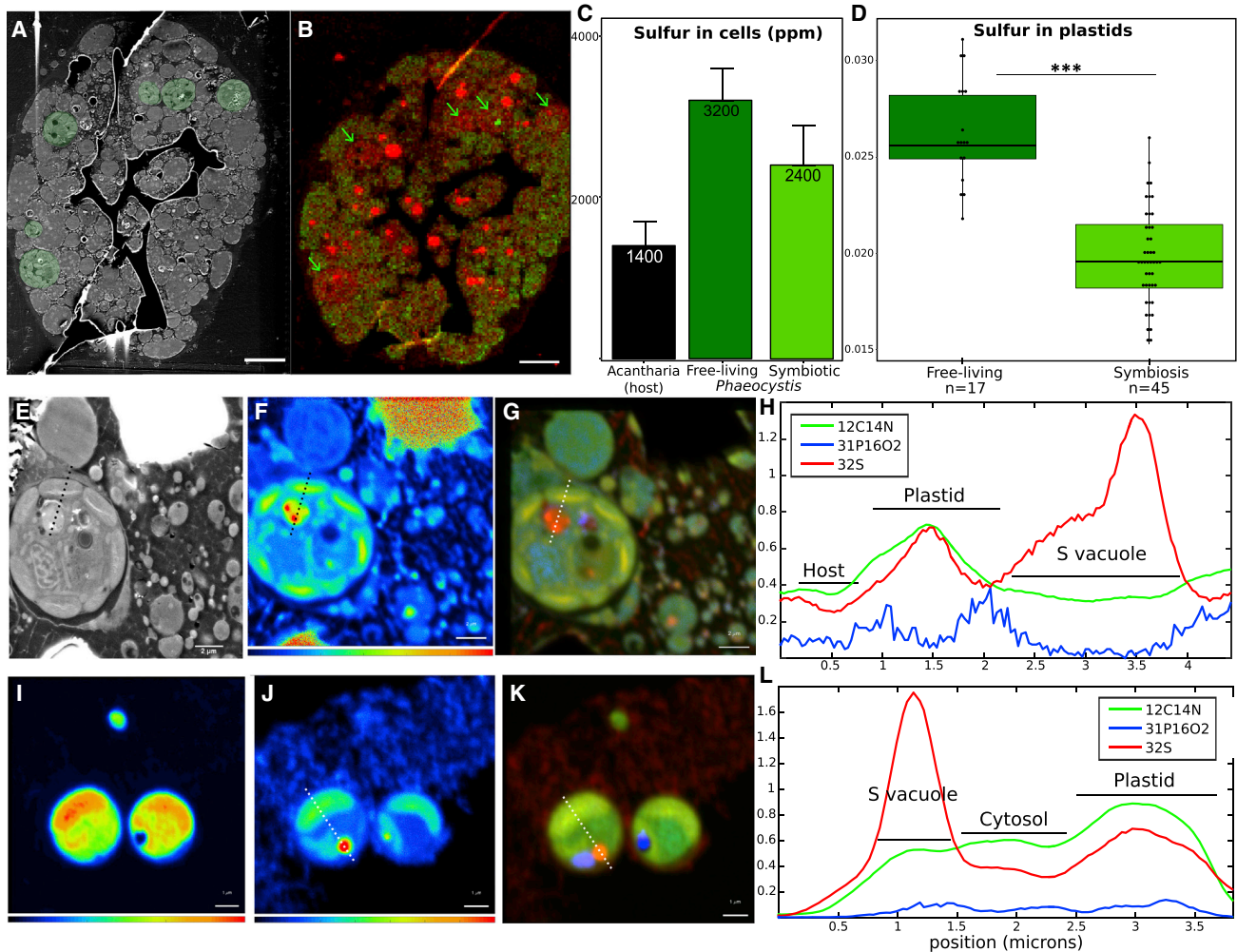


Figure 6. Subcellular Distribution and Quantification of Sulfur in the Symbiotic Partners

(A) Scanning electron microscopy (SEM) images of the host-symbiont partnership (symbiotic microalgae *Phaeocystis* are artificially colored in green).
 (B) Correlated Synchrotron X-ray Fluorescence (S-XRF) mapping of sulfur (red) and phosphorus (green) showing high sulfur concentration in microalgae (indicated by green arrows). The scale bar represents 20 μm .
 (C) Sulfur concentration (ppm) measured by S-XRF in the host cell (dark bar) and the free-living and symbiotic *Phaeocystis* cells (dark and light green, respectively).
 (D) Sulfur content ($^{32}\text{S}/^{12}\text{C}_2$) in plastids of free-living and symbiotic *Phaeocystis* measured by nanoSIMS. Statistical analyses were performed using ANOVA type-II tests, and the $^{32}\text{S}/^{12}\text{C}_2$ was log-transformed (** $p < 0.001$, ANOVA test). (See also [Data S1](#).)
 (E) SEM image of a single symbiont cell with a bright round vacuole.
 (F) Subcellular distribution of sulfur (^{32}S) in symbiotic *Phaeocystis*.
 (G) RGB image showing the subcellular distribution of sulfur $^{32}\text{S}^-$ (red), nitrogen $^{12}\text{C}^{14}\text{N}^-$ (green), and phosphorus $^{31}\text{P}^-$ (blue) in symbiotic cells.
 (H) Lateral profiling across the plastid and vacuole of the symbiotic microalga (dashed line in D, E, and F) showing the contribution of the nutrients S, N, and P (red, green, and blue solid lines, respectively).
 (I) Subcellular distribution of nitrogen ($^{12}\text{C}^{14}\text{N}^-$) in free-living *Phaeocystis*.
 (J) Subcellular distribution of sulfur (^{32}S) in free-living *Phaeocystis*.
 (K) RGB image showing the subcellular distribution of sulfur $^{32}\text{S}^-$ (red), nitrogen $^{12}\text{C}^{14}\text{N}^-$ (green), and phosphorus $^{31}\text{P}^-$ (blue) in free-living cells.
 (L) Lateral profiling across the free-living microalga (dashed line in I and J) showing the contribution of S, N, and P (red, green, and blue solid lines, respectively).
 See also [Tables S2](#) and [S3](#), [Figures S3](#) and [S4](#), and [Data S1](#).

host provides Fe in order to satisfy the high needs of the well-developed photosynthetic apparatus and antioxidant proteins [37]. The exclusive presence of cobalt in the symbiotic stage in the algal nucleus and vacuoles raises questions on the biological role of this element in the partnership. In microalgae, Co can be not only the metal center of important enzymes,

such as carbonic anhydrase for C fixation [37], but also the metal ligand of the essential vitamin B12 (cobalamin). Yet to fully interpret metal homeostasis changes, future molecular analyses should investigate the genes and proteins that are involved in the transport and regulation of metals in free-living and symbiotic microalgae.

High Sulfur Concentration in Symbiotic Microalgae

Enhanced intracellular photosynthetic activity performed by numerous plastids inevitably leads to the harmful production of reactive oxygen species (ROS) and implies the existence of antioxidant mechanisms. In microalgae, sulfur (S) metabolism plays a key role in antioxidant protection with the production of several S-containing compounds, such as glutathione and dimethylsulfoniopropionate (DMSP), which are also key components of the global S cycle of the ocean [40, 41]. Plastids have a central role in sulfate uptake and the production of DMSP [42–44]. It has been shown that the symbiont *Phaeocystis* can produce 100-fold more DMSP than free-living microalgae [7, 45], consistent with the notion that production of this compound increases with photosynthesis [46]. Here, we showed that the S concentration in symbiotic microalgae ($2,400 \pm 500$ ppm) was 1.7 times higher than that of their host ($1,400 \pm 300$ ppm) and similar to that of free-living microalgae ($3,200 \pm 400$ ppm) (Figure 6; Table S3). These concentrations may be underestimated, since small S-molecules can be lost during sample preparation [47]. In the microalgal cells, S was mainly contained in plastids and cytoplasmic vacuoles (Figures 6E, 6L, and S3). In symbiosis, the S content decreased in plastids and was mainly localized in vacuoles, which increased in size (1.5–2 μm in diameter) and contained up to 6.5 times more S than did the plastids (compared to 2.5 times more in free-living cells). In these vacuoles, S was the major macronutrient, P was not present, and N was very low, suggesting the absence of nucleic acids and phospholipids and a low amount of S-containing amino acids (Figures 6H and 6L). Based on previous evidence showing that DMSP is the main S-containing molecule in microalgal cells [48, 49] (i.e., representing more than 50% of the total organic S), is stored in *Phaeocystis* vesicles [50], and is produced in high amounts by symbiotic *Phaeocystis*, we speculate that these S-rich vacuoles may contain DMSP. The antioxidant properties of DMSP could reduce the oxidative stress of symbiotic *Phaeocystis*, which would be consistent with the enhanced oxidative stress scavenging during photosynthesis revealed by our photophysiology measurements (NPQ parameter, Figure 2B). The capacity to reduce sulfur and produce different S-containing compounds for intracellular antioxidant defense would enhance the suitability of microalgae to be symbionts. It may also partially explain why high-DMSP-producing red plastid lineages such as haptophytes and dinoflagellates are prevalent photosymbionts in oceanic waters [51].

Conclusions

This study shows that microalgae can be radically transformed at the morphological and metabolic levels following their integration into a host cell, a process that has not previously been reported in other algal symbioses. Specifically, by combining nanoscale imaging techniques and photophysiology, we provide evidence that host cells engulf ecologically successful microalgal cells from the environment and subsequently block cell proliferation without preventing plastid division to optimize the photosynthetic machinery (multiplication of voluminous plastids and thylakoids) for high productivity. In plants, the multiplication of plastids has been recognized as a means of increasing the surface exchange with the environment, in particular to enhance CO_2 diffusion [52]. The structural and functional changes of sym-

biotic microalgae are also paralleled by specific modifications of the trophic micro-environment (e.g., Fe). Considering the numerous N-rich plastids per symbiont cell and the low availability of N in oceanic waters [25], the host must transfer a substantial quantity of N to its intracellular symbionts. The recognized capacity of acantharian hosts to heterotrophically feed on a variety of prey could represent an essential source of N to sustain the photosynthesis of its symbionts [53].

Overall, this study sheds light on the capacity of a heterotrophic host to exploit and engineer photosynthetic cells in the ocean, and it paves the way for omics studies to fully understand the molecular mechanisms of this algal remodeling. Our findings challenge the common view of photosymbiosis as being mutualistic in nature. This Acantharia-*Phaeocystis* interaction could rather be considered as farming or inverted parasitism of microalgal cells where the host largely benefits from the symbiosis. This scenario is further supported by the fact that *Phaeocystis* cells cannot be grown after the symbiotic stage, do not divide within their host, and are very likely digested at the end of the life cycle of their host [7]. Available evidence suggests that the degree of host control seems to be less pronounced in other photosymbioses (e.g., reef invertebrates, foraminiferans) since the algal symbiont can divide within its host and can be grown in culture or survive in natural seawater after the symbiotic stage [6, 54]. In an evolutionary context, similar traits found in symbiotic *Phaeocystis* have been reported in *Paulinella chromatophora*, a recent primary endosymbiosis, where photosynthetic organelles (chromatophores) are 15–20 times larger than in free-living cyanobacteria [55, 56]. The Acantharia-*Phaeocystis* symbiotic partnership could therefore reflect a possible route for plastid acquisition where metabolic control of the host preceded the genetic integration and led to the morphological transformation of the photosynthetic endosymbiont. Alternatively, the expansion of the photosynthetic machinery in *Paulinella* and *Phaeocystis* could represent a host strategy to increase the photosynthetic yield while controlling a small number of symbionts. A comparison with other abundant planktonic photosymbioses using high-resolution imaging combined with transcriptomics and proteomics will certainly elucidate the different facets of microalgae in photosymbiosis and shed light on key evolutionary mechanisms in plastid acquisition.

STAR★METHODS

Detailed methods are provided in the online version of this paper and include the following:

- KEY RESOURCES TABLE
- CONTACT FOR REAGENT AND RESOURCE SHARING
- EXPERIMENTAL MODEL AND SUBJECT DETAILS
- METHOD DETAILS
 - Photophysiology measurements
 - Sample preparation for electron microscopy and chemical imaging
 - Transmission Electron Microscopy (TEM) and Scanning Electron Microscopy (SEM)
 - Focused Ion Beam Scanning Electron Microscopy (FIB-SEM)
 - Synchrotron X-ray fluorescence (S-XRF) imaging

- NanoSIMS acquisition and analyses
- ToF-SIMS acquisition and analyses
- Lipidomics analyses
- **QUANTIFICATION AND STATISTICAL ANALYSIS**

SUPPLEMENTAL INFORMATION

Supplemental Information includes four figures, four tables, one data file, and one video and can be found with this article online at <https://doi.org/10.1016/j.cub.2019.01.073>.

ACKNOWLEDGMENTS

This study and J.D. received funding from the European Union's Horizon 2020 research and innovation program under the Marie Skłodowska-Curie grant agreement 658442 (MSCA-IF-2014). J.D. was also supported by the LabEx GRAL (ANR-10-LABX-49-01) and Pôle CBS from the University of Grenoble Alpes. We are thankful for the use of the analytical facilities of the Centre for Chemical Microscopy (ProVIS) at UFZ Leipzig, which is supported by European Regional Development Funds (EFRE—Europe funds Saxony) and the Helmholtz Association. This research is also supported by EMBRC-France, whose French state funds are managed by the ANR within the Investments of the Future program under reference ANR-10-INBS-02. We are grateful to the Roscoff Culture Collection for providing the cultures and John Dolan and the marine service crew (Guillaume de Liège) from the Laboratoire d'Océanographie de Villefranche-sur-Mer (CNRS, UPMC). We also thank Guy Schoehn from the electron microscopy platform facilities, Christine Morisot for her technical assistance, and Ian Probert, Florin Musat, Chris Bowler, and Arthur R. Grossman for critically reading the manuscript and suggesting substantial improvements. The authors acknowledge the support and use of resources from Instruct (a Landmark ESFRI project) and the ESRF for providing beamtime (experiment LS-2625). This work used the platforms of the Grenoble Instruct center (ISBG; UMS 3518 CNRS-CEA-UJF-EMBL) with support from FRISBI (ANR-10-INBS-05-02) and GRAL (ANR-10-LABX-49-01) within the Grenoble Partnership for Structural Biology (PSB). The electron microscope facility is supported by the Rhône-Alpes Region, the Fondation Recherche Medicale (FRM), the fonds FEDER, the Centre National de la Recherche Scientifique (CNRS), the CEA, the University of Grenoble Alpes (UGA), EMBL, and the GIS-Infrastructures en Biologie Sante et Agronomie (IBISA). E.M. is supported by the ANR Oceanomics program (ANR-11-BTBR-0008). C.U. is supported by a joint UGA-ETH Zurich PhD grant in the framework of the "Investissements d'avenir" program (ANR-15-IDEX-02). G.F. is supported by the RGP0052 HFSP grant. P.-H.J. and G.F. are supported by the CEA_DRF_impulsion (Fib-Bio) grant.

AUTHOR CONTRIBUTIONS

J.D. designed research, collected samples, interpreted results, and drafted the manuscript. N.M. assisted experimental design and supervised the work. B.G. and J.D. jointly performed the sample preparation for high resolution microscopy. H.S., G.V., and R.T. conducted nanoSIMS, ToF-SIMS, and X-ray fluorescence imaging. H.S., N.M., and J.D. processed and interpreted nanoSIMS and ToFSIMS data. G.V. analyzed and interpreted the S-XRF data. S.M. maintained and provided the algal cultures, and S.B. and M.S. assisted with experiments. N.L.S., Y.S., and P.H.J. conducted FIB-SEM imaging, and C.U. analyzed the data. J.L., J.J., and E.M. performed and interpreted lipidomics analyses. G.F. performed and analyzed photophysiology measurements. J.D., G.F., and N.M. wrote the manuscript.

DECLARATION OF INTERESTS

The authors declare no competing interests.

Received: September 29, 2018

Revised: December 3, 2018

Accepted: January 28, 2019

Published: February 28, 2019

REFERENCES

1. Keeling, P.J. (2004). Diversity and evolutionary history of plastids and their hosts. *Am. J. Bot.* *91*, 1481–1493.
2. Embley, T.M., and Martin, W. (2006). Eukaryotic evolution, changes and challenges. *Nature* *440*, 623–630.
3. Ball, S., Colleoni, C., Cenci, U., Raj, J.N., and Tirtiaux, C. (2011). The evolution of glycogen and starch metabolism in eukaryotes gives molecular clues to understand the establishment of plastid endosymbiosis. *J. Exp. Bot.* *62*, 1775–1801.
4. Karkar, S., Facchinelli, F., Price, D.C., Weber, A.P.M., and Bhattacharya, D. (2015). Metabolic connectivity as a driver of host and endosymbiont integration. *Proc. Natl. Acad. Sci. USA* *112*, 10208–10215.
5. de Vargas, C., Audic, S., Henry, N., Decelle, J., Mahé, F., Logares, R., Lara, E., Berney, C., Le Bescot, N., Probert, I., et al.; Tara Oceans Coordinators (2015). Ocean plankton. Eukaryotic plankton diversity in the sunlit ocean. *Science* *348*, 1261605.
6. Decelle, J., Colin, S., and Foster, R.A. (2015). Photosymbiosis in marine planktonic protists. In *Marine Protists*, T. Suzuki, T. Horiguchi, F. Not, S. Ohtsuka, and N. Suzuki, eds. (Springer Japan), pp. 465–500.
7. Decelle, J., Probert, I., Bittner, L., Desdevises, Y., Colin, S., de Vargas, C., Galí, M., Simó, R., and Not, F. (2012). An original mode of symbiosis in open ocean plankton. *Proc. Natl. Acad. Sci. USA* *109*, 18000–18005.
8. Caron, D.A. (2016). Ocean science: the rise of Rhizaria. *Nature* *532*, 444–445.
9. Biard, T., Stemmann, L., Picheral, M., Mayot, N., Vandromme, P., Hauss, H., Gorsky, G., Guidi, L., Kiko, R., and Not, F. (2016). In situ imaging reveals the biomass of giant protists in the global ocean. *Nature* *532*, 504–507.
10. Guidi, L., Chaffron, S., Bittner, L., Eveillard, D., Larhlmi, A., Roux, S., Darzi, Y., Audic, S., Berline, L., Brum, J., et al.; Tara Oceans Coordinators (2016). Plankton networks driving carbon export in the oligotrophic ocean. *Nature* *532*, 465–470.
11. Caron, D.A., Michaels, A.F., Swanberg, N.R., and Howse, F.A. (1995). Primary productivity by symbiont-bearing planktonic sarcodines (Acantharia, Radiolaria, Foraminifera) in surface waters near Bermuda. *J. Plankton Res.* *17*, 103–129.
12. Lampitt, R.S., Salter, I., and Johns, D. (2009). Radiolaria: major exporters of organic carbon to the deep ocean. *Global Biogeochem. Cycles* *23*, GB1010.
13. Irwin, A.J., and Oliver, M.J. (2009). Are ocean deserts getting larger? *Geophys. Res. Lett.* *36*, 1–5.
14. Probert, I., Siano, R., Poirier, C., Decelle, J., Biard, T., Tuji, A., Suzuki, N., and Not, F. (2014). *Brandtodinium* gen. nov. and *B. nutricula* comb. Nov. (Dinophyceae), a dinoflagellate commonly found in symbiosis with polycystine radiolarians. *J. Phycol.* *50*, 388–399.
15. Caron, D.A., Alexander, H., Allen, A.E., Archibald, J.M., Armbrust, E.V., Bachy, C., Bell, C.J., Bharti, A., Dyhrman, S.T., Guida, S.M., et al. (2017). Probing the evolution, ecology and physiology of marine protists using transcriptomics. *Nat. Rev. Microbiol.* *15*, 6–20.
16. Worden, A.Z., Follows, M.J., Giovannoni, S.J., Wilken, S., Zimmerman, A.E., and Keeling, P.J. (2015). Environmental science. Rethinking the marine carbon cycle: factoring in the multifarious lifestyles of microbes. *Science* *347*, 1257594.
17. Smith, W.O., Codispoti, L.A., Nelson, D.M., Manley, T., Buskey, E.J., Niebauer, H.J., and Cota, G.F. (1991). Importance of *Phaeocystis* blooms in the high-latitude ocean carbon cycle. *Nature* *352*, 514–516.
18. Schoemann, V., Becquevort, S., Stefels, J., Rousseau, V., and Lancelot, C. (2005). *Phaeocystis* blooms in the global ocean and their controlling mechanisms: a review. *J. Sea Res.* *53*, 43–66.
19. Zingone, A., Chrétiennot-Dinet, M.J., Lange, M., and Medlin, L. (1999). Morphological and genetic characterization of *Phaeocystis cordata* and *P. jahni* (Prymnesiophyceae), two new species from the Mediterranean Sea. *J. Phycol.* *35*, 1322–1337.

20. Wakefield, T.S., Farmer, M.A., and Kempf, S.C. (2000). Revised description of the fine structure of *in situ* "zooxanthellae" genus *Symbiodinium*. *Biol. Bull.* *199*, 76–84.
21. Siano, R., Montresor, M., Probert, I., Not, F., and de Vargas, C. (2010). *Pelagodinium* gen. nov. and *P. béii* comb. nov., a dinoflagellate symbiont of planktonic foraminifera. *Protist* *161*, 385–399.
22. Genty, B., Briantais, J.M., and Baker, N.R. (1989). The relationship between the quantum yield of photosynthetic electron transport and quenching of chlorophyll fluorescence. *Biochimica et Biophysica Acta - General Subjects* *990*, 87–92.
23. Breitbarth, E., Wohlers, J., Kläs, J., LaRoche, J., and Peeken, I. (2008). Nitrogen fixation and growth rates of *Trichodesmium* IMS-101 as a function of light intensity. *Mar. Ecol. Prog. Ser.* *359*, 25–36.
24. Bouman, H.A., Platt, T., Doblin, M., Figueiras, F.G., Gudmundsson, K., Gudfinnsson, H.G., Huang, B., Hickman, A., Hiscock, M., Jackson, T., et al. (2018). Photosynthesis-irradiance parameters of marine phytoplankton: synthesis of a global data set. *Earth Syst. Sci. Data* *10*, 251–266.
25. Moore, C.M., Mills, M.M., Arrigo, K.R., Berman-Frank, I., Bopp, L., Boyd, P.W., Galbraith, E.D., Geider, R.J., Guieu, C., Jaccard, S.L., et al. (2013). Processes and patterns of oceanic nutrient limitation. *Nat. Geosci.* *6*, 701–710.
26. Quigg, A., Irwin, A.J., and Finkel, Z.V. (2011). Evolutionary inheritance of elemental stoichiometry in phytoplankton. *Proc. Biol. Sci.* *278*, 526–534.
27. Klausmeier, C.A., Litchman, E., Daufresne, T., and Levin, S.A. (2004). Optimal nitrogen-to-phosphorus stoichiometry of phytoplankton. *Nature* *429*, 171–174.
28. Arrigo, K.R. (2005). Marine microorganisms and global nutrient cycles. *Nature* *437*, 349–355.
29. Elser, J.J. (2012). Phosphorus: a limiting nutrient for humanity? *Curr. Opin. Biotechnol.* *23*, 833–838.
30. Raven, J.A. (2013). RNA function and phosphorus use by photosynthetic organisms. *Front. Plant Sci.* *4*, 536.
31. Miller, D.J., and Yellowlees, D. (1989). Inorganic nitrogen uptake by symbiotic marine cnidarians: a critical review. *Proc. R. Soc. Lond. B Biol. Sci.* *237*, 109–125.
32. Koop, K., Booth, D., Broadbent, A., Brodie, J., Bucher, D., Capone, D., Coll, J., Dennison, W., Erdmann, M., Harrison, P., et al. (2001). ENCORE: the effect of nutrient enrichment on coral reefs. Synthesis of results and conclusions. *Mar. Pollut. Bull.* *42*, 91–120.
33. Li, M., Shi, X., Guo, C., and Lin, S. (2016). Phosphorus deficiency inhibits cell division but not growth in the dinoflagellate *Amphidinium carterae*. *Front. Microbiol.* *7*, 826.
34. Jahnke, J. (1989). The light and temperature dependence of growth rate and elemental composition of *Phaeocystis globosa* scherffel and *P. Pouchetii* (HAR.) Lagerh. in batch cultures. *Neth. J. Sea Res.* *23*, 15–21.
35. Karl, D.M. (2014). Microbially mediated transformations of phosphorus in the sea: new views of an old cycle. *Annu. Rev. Mar. Sci.* *6*, 279–337.
36. Thiel, V., and Sjövall, P. (2011). Using time-of-flight secondary ion mass spectrometry to study biomarkers. *Annu. Rev. Earth Planet. Sci.* *39*, 125–156.
37. Morel, F.M.M., and Price, N.M. (2003). The biogeochemical cycles of trace metals in the oceans. *Science* *300*, 944–947.
38. Twining, B.S., and Baines, S.B. (2013). The trace metal composition of marine phytoplankton. *Annu. Rev. Mar. Sci.* *5*, 191–215.
39. Allen, A.E., Laroche, J., Maheswari, U., Lommer, M., Schauer, N., Lopez, P.J., Finazzi, G., Fernie, A.R., and Bowler, C. (2008). Whole-cell response of the pennate diatom *Phaeodactylum tricorutum* to iron starvation. *Proc. Natl. Acad. Sci. USA* *105*, 10438–10443.
40. Sunda, W., Kieber, D.J., Kiene, R.P., and Huntsman, S. (2002). An antioxidant function for DMSP and DMS in marine algae. *Nature* *418*, 317–320.
41. Simó, R. (2001). Production of atmospheric sulfur by oceanic plankton: biogeochemical, ecological and evolutionary links. *Trends Ecol. Evol.* *16*, 287–294.
42. Giordano, M., Norici, A., and Hell, R. (2005). Sulfur and phytoplankton: acquisition, metabolism and impact on the environment. *New Phytol.* *166*, 371–382.
43. Takahashi, H., Kopriva, S., Giordano, M., Saito, K., and Hell, R. (2011). Sulfur assimilation in photosynthetic organisms: molecular functions and regulations of transporters and assimilatory enzymes. *Annu. Rev. Plant Biol.* *62*, 157–184.
44. Curson, A.R.J., Williams, B.T., Pinchbeck, B.J., Sims, L.P., Martínez, A.B., Rivera, P.P.L., Kumaresan, D., Mercadé, E., Spurgin, L.G., Carrión, O., et al. (2018). DSYB catalyses the key step of dimethylsulfoniopropionate biosynthesis in many phytoplankton. *Nat. Microbiol.* *3*, 430–439.
45. Gutierrez-Rodriguez, A., Pillet, L., Biard, T., Said-Ahmad, W., Amrani, A., Simó, R., and Not, F. (2017). Dimethylated sulfur compounds in symbiotic protists: a potentially significant source for marine DMS(P). *Limnol. Oceanogr.* *1139*–1154.
46. Simo, R., Archer, S.D., Pedros Alio, C., Gilpin, L., and Stelfox Widdicombe, C.E. (2002). Coupled dynamics of dimethylsulfoniopropionate and dimethylsulfide cycling and the microbial food web in surface waters of the North Atlantic. *Limnol. Oceanogr.* *47*, 53–61.
47. Raina, J.B., Clode, P.L., Cheong, S., Bougoure, J., Kilburn, M.R., Reeder, A., Forêt, S., Stat, M., Beltran, V., Thomas-Hall, P., et al. (2017). Subcellular tracking reveals the location of dimethylsulfoniopropionate in microalgae and visualises its uptake by marine bacteria. *eLife* *6*, 1–17.
48. Matrai, P.A., and Keller, M.D. (1994). Total organic sulfur and dimethylsulfoniopropionate in marine phytoplankton: intracellular variations. *Mar. Biol.* *119*, 61–68.
49. Giordano, M., and Raven, J.A. (2014). Nitrogen and sulfur assimilation in plants and algae. *Aquat. Bot.* *118*, 45–61.
50. Orellana, M.V., Matrai, P.A., Janer, M., and Rauschenberg, C.D. (2011). Dimethylsulfoniopropionate storage in *Phaeocystis* (Prymnesiophyceae) secretory vesicles. *J. Phycol.* *47*, 112–117.
51. Decelle, J., Colin, S., and Foster, R.A. (2015). Photosymbiosis in marine planktonic protists. In *Marine Protists: Diversity and Dynamics*, S. Ohtsuka, T. Suzuki, T. Horiguchi, N. Suzuki, and F. Not, eds. (Springer Japan), pp. 1–637.
52. Xiong, D., Huang, J., Peng, S., and Li, Y. (2017). A few enlarged chloroplasts are less efficient in photosynthesis than a large population of small chloroplasts in *Arabidopsis thaliana*. *Sci. Rep.* *7*, 5782.
53. Swanberg, N.R., and Caron, D.A. (1991). Patterns of sarcodine feeding in epipelagic oceanic plankton. *J. Plankton Res.* *13*, 287–312.
54. Decelle, J., Carradec, Q., Pochon, X., Henry, N., Romac, S., Mahé, F., Dunthorn, M., Kourlaiev, A., Voolstra, C.R., Wincker, P., and de Vargas, C. (2018). Worldwide occurrence and activity of the reef-building coral symbiont symbiodinium in the open ocean. *Curr. Biol.* *28*, 3625–3633.e3.
55. Singer, A., Poschmann, G., Mühlich, C., Valadez-Cano, C., Hänsch, S., Hüren, V., Rensing, S.A., Stühler, K., and Nowack, E.C.M. (2017). Massive protein import into the early-evolutionary-etae photosynthetic organelle of the amoeba *Paulinella chromatophora*. *Curr. Biol.* *27*, 2763–2773.e5.
56. Nowack, E.C.M. (2014). *Paulinella chromatophora* - rethinking the transition from endosymbiont to organelle. *Acta Soc. Bot. Pol.* *83*, 387–397.
57. Fedorov, A., Beichel, R., Kalpathy-Cramer, J., Finet, J., Fillion-Robin, J.C., Pujol, S., Bauer, C., Jennings, D., Fennessy, F., Sonka, M., et al. (2012). 3D slicers as an image computing platform for the quantitative imaging network. *Magn. Reson. Imaging* *30*, 1323–1341.
58. Cignoni, P., Callieri, M., Corsini, M., Dellepiane, Ganovelli, F., and Ranzuglia, G. (2008). MeshLab: an open-source mesh processing tool, 6, V. Scarano, R. De Chiara, and U. Erra, eds. (Eurographics Italian Chapter Conference), pp. 129–136.
59. Solé, V.A., Papillon, E., Cotte, M., Walter, P., and Susini, J. (2007). A multi-platform code for the analysis of energy-dispersive X-ray fluorescence spectra. *Spectrochim. Acta B At. Spectrosc.* *62*, 63–68.

60. Polerecky, L., Adam, B., Milucka, J., Musat, N., Vagner, T., and Kuypers, M.M.M. (2012). Look@NanoSIMS—a tool for the analysis of nanoSIMS data in environmental microbiology. *Environ. Microbiol.* **14**, 1009–1023.
61. Johnson, X., Vandystadt, G., Bujaldon, S., Wollman, F.-A., Dubois, R., Roussel, P., Alric, J., and Béal, D. (2009). A new setup for in vivo fluorescence imaging of photosynthetic activity. *Photosynth. Res.* **102**, 85–93.
62. Maxwell, K., and Johnson, G.N. (2000). Chlorophyll fluorescence—a practical guide. *J. Exp. Bot.* **51**, 659–668.
63. Kashiv, Y., Austin, J.R.I., Lai, B., Rose, V., El-Muayed, M., and Vogt, S. (2016). Imaging trace element distributions in single organelles and sub-cellular features. *Scientific Reports* **6**, 1–9.
64. Moore, K.L., Schröder, M., Wu, Z., Martin, B.G.H., Hawes, C.R., McGrath, S.P., Hawkesford, M.J., Feng Ma, J., Zhao, F.-J., and Grovenor, C.R.M. (2011). High-resolution secondary ion mass spectrometry reveals the contrasting subcellular distribution of arsenic and silicon in rice roots. *Plant Physiol.* **156**, 913–924.
65. Smart, K.E., Smith, J.A.C., Kilburn, M.R., Martin, B.G.H., Hawes, C., and Grovenor, C.R.M. (2010). High-resolution elemental localization in vacuolate plant cells by nanoscale secondary ion mass spectrometry. *Plant J.* **63**, 870–879.
66. Pålsgård, E., Lindh, U., and Roomans, G.M. (1994). Comparative study of freeze-substitution techniques for X-ray microanalysis of biological tissue. *Microsc. Res. Tech.* **28**, 254–258.
67. Bernal, M., Sanchez-Testillano, P., Risueno, M.D.C., and Yruela, I. (2006). Excess copper induces structural changes in cultured photosynthetic soybean cells. *Funct. Plant Biol.* **33**, 1001–1012.
68. Clode, P.L., and Marshall, A.T. (2003). Calcium associated with a fibrillar organic matrix in the scleractinian coral *Galaxea fascicularis*. *Protoplasma* **220**, 153–161.
69. Marshall, A.T., Clode, P.L., Russell, R., Prince, K., and Stern, R. (2007). Electron and ion microprobe analysis of calcium distribution and transport in coral tissues. *J. Exp. Biol.* **210**, 2453–2463.
70. Kashiv, Y., Austin, J.R., 2nd, Lai, B., Rose, V., Vogt, S., and El-Muayed, M. (2016). Imaging trace element distributions in single organelles and sub-cellular features. *Sci. Rep.* **6**, 21437.
71. Lozić, I., Bartlett, C.A., Shaw, J.A., Iyer, K.S., Dunlop, S.A., Kilburn, M.R., and Fitzgerald, M. (2014). Changes in subtypes of Ca microdomains following partial injury to the central nervous system. *Metallomics* **6**, 455–464.
72. Chandra, S. (2005). Quantitative imaging of subcellular calcium stores in mammalian LLC-PK1 epithelial cells undergoing mitosis by SIMS ion microscopy. *Eur. J. Cell Biol.* **84**, 783–797.
73. Perrin, L., Carmona, A., Roudeau, S., and Ortega, R. (2015). Evaluation of sample preparation methods for single cell quantitative elemental imaging using proton or synchrotron radiation focused beams. *J. Anal. At. Spectrom.* **30**, 2525–2532.
74. Maco, B., Cantoni, M., Holtmaat, A., Kreshuk, A., Hamprecht, F.A., and Knott, G.W. (2014). Semiautomated correlative 3D electron microscopy of in vivo-imaged axons and dendrites. *Nat. Protoc.* **9**, 1354–1366.
75. Cotte, M., Pouyet, E., Salomé, M., Rivard, C., De Nolf, W., Castillo-Michel, H., Fabris, T., Monico, L., Janssens, K., Wang, T., et al. (2017). The ID21 X-ray and infrared microscopy beamline at the ESRF: status and recent applications to artistic materials. *J. Anal. At. Spectrom.* **32**, 477–493.
76. Martínez-Criado, G., Villanova, J., Tucoulou, R., Salomon, D., Suuronen, J.P., Labouré, S., Guilloud, C., Valls, V., Barrett, R., Gagliardini, E., et al. (2016). ID16B: a hard X-ray nanoprobe beamline at the ESRF for nano-analysis. *J. Synchrotron Radiat.* **23**, 344–352.
77. Vanbellingen, Q.P., Elie, N., Eller, M.J., Della-Negra, S., Touboul, D., and Brunelle, A. (2015). Time-of-flight secondary ion mass spectrometry imaging of biological samples with delayed extraction for high mass and high spatial resolutions. *Rapid Commun. Mass Spectrom.* **29**, 1187–1195.
78. Jouhet, J., Maréchal, E., Baldan, B., Bligny, R., Joyard, J., and Block, M.A. (2004). Phosphate deprivation induces transfer of DGDG galactolipid from chloroplast to mitochondria. *J. Cell Biol.* **167**, 863–874.
79. Jouhet, J., Maréchal, E., Bligny, R., Joyard, J., and Block, M.A. (2003). Transient increase of phosphatidylcholine in plant cells in response to phosphate deprivation. *FEBS Lett.* **544**, 63–68.
80. Jouhet, J., Lupette, J., Clerc, O., Magneschi, L., Bedhomme, M., Collin, S., Roy, S., Maréchal, E., and Rébeillé, F. (2017). LC-MS/MS versus TLC plus GC methods: consistency of glycerolipid and fatty acid profiles in microalgae and higher plant cells and effect of a nitrogen starvation. *PLoS ONE* **12**, e0182423.
81. Demé, B., Cataye, C., Block, M.A., Maréchal, E., and Jouhet, J. (2014). Contribution of galactoglycerolipids to the 3-dimensional architecture of thylakoids. *FASEB J.* **28**, 3373–3383.
82. Buseman, C.M., Tamura, P., Sparks, A.A., Baughman, E.J., Maatta, S., Zhao, J., Roth, M.R., Esch, S.W., Shah, J., Williams, T.D., and Welti, R. (2006). Wounding stimulates the accumulation of glycerolipids containing oxophytodienoic acid and dinor-oxophytodienoic acid in Arabidopsis leaves. *Plant Physiol.* **142**, 28–39.
83. Rainteau, D., Humbert, L., Delage, E., Vergnolle, C., Cantrel, C., Maubert, M.A., Lanfranchi, S., Maldiney, R., Collin, S., Wolf, C., et al. (2012). Acyl chains of phospholipase D transphosphatidylated products in Arabidopsis cells: a study using multiple reaction monitoring mass spectrometry. *PLoS ONE* **7**, e41985.

STAR★METHODS

KEY RESOURCES TABLE

REAGENT or RESOURCE	SOURCE	IDENTIFIER
Biological Samples		
Cultures of the microalga <i>Phaeocystis cordata</i>	Roscoff Culture Collection	RCC1383
Chemicals, Peptides, and Recombinant Proteins		
Araldite Resin 502	Electron Microscopy Sciences	Cat#13900
Software and Algorithms		
GIMP software	Open access	https://www.gimp.org/
StackReg (ImageJ plugin)	Open access	http://bigwww.epfl.ch/thevenaz/stackreg/
3D Slicer	[57]	https://www.slicer.org/
MeshLab	[58]	http://www.meshlab.net/
PyMca	[59]	http://pymca.sourceforge.net/
Look@NanoSIMS	[60]	http://nanosims.geo.uu.nl/nanosims-wiki/doku.php/nanosims:lans
R package “car”	Open access	https://cran.r-project.org/web/packages/car/index.html
R package “DescTools”	Open access	https://cran.r-project.org/web/packages/DescTools/index.html
R package “rcompanion”	Open access	https://cran.r-project.org/web/packages/rcompanion/index.html
SurfaceLab 6.7 software	ION-TOF GmbH	https://iontof-download.com/login.php

CONTACT FOR REAGENT AND RESOURCE SHARING

Further information and requests for resources and reagents should be directed to and will be fulfilled by the Lead Contact, Johan Decelle (johan.decelle@univ-grenoble-alpes.fr).

EXPERIMENTAL MODEL AND SUBJECT DETAILS

Symbiotic acantharians harboring intracellular microalgal cells (*Phaeocystis*) were gently collected by towing a plankton net with a large cod-end (1 L) for 1–2 min in surface waters (Mediterranean Sea, Villefranche-sur-Mer, France). After collection, the individual cells were isolated under a microscope with a micropipette as in [7], rapidly transferred into natural seawater, and maintained in the same controlled light ($100 \mu\text{mol photons m}^{-2}\text{s}^{-1}$) and temperature (20°C) conditions as the free-living stage. In parallel, cultures of the haptophyte *Phaeocystis cordata* RCC 1383 (the symbiont of Acantharia in the Mediterranean Sea) [7] were maintained at 20°C in K/5 culture medium and at $100 \mu\text{mol photons m}^{-2}\text{s}^{-1}$. Nutrient concentrations of the free-living (culture medium K/5) and symbiotic (natural seawater surrounding the host) conditions of microalgae are provided in Table S2.

METHOD DETAILS

Photophysiology measurements

Photosynthetic parameters were derived from chlorophyll fluorescence emission measured in cultures of the microalga *Phaeocystis cordata* (free-living) (23 measures from triplicates) and pools of 80–100 acantharian cells containing symbiotic *Phaeocystis* (10 measures from triplicates). For measurements, we employed a fluorescence imaging setup previously described in [61]. The system was modified by replacing the green LEDs for actinic light with red LEDs (emission peak 630 nm, Full Width at Half Maximum 40 nm), and the acquisition setup was an ORCA flash 4.0 LT camera (Hamamatsu, Japan). The photosynthetic electron transfer rate, ETR_{PSII} , was calculated as the product of the light intensity times the photochemical yield in the light: $I \cdot (F_m' - F) / F_m'$, where F and F_m' are the steady-state and maximum fluorescence intensities in light-acclimated cells, respectively, and I is the light irradiance in $\mu\text{mol quanta m}^{-2} \text{s}^{-1}$ (see previous work [62] for more details). The light intensity was increased stepwise from 29 to $672 \mu\text{mol quanta m}^{-2} \text{s}^{-1}$. At each light intensity, the cells were allowed to reach steady state fluorescence emissions before increasing the photon flux. Photosynthesis (ETR) - irradiance curves were then fitted with an exponential saturation function to evaluate the maximum photosynthetic capacity (P_m), the initial slope (α : which is the photosynthetic efficiency under light levels close to zero), and the minimum photosynthetic saturation irradiance ($E_k = P_m / \alpha$) of free-living and symbiotic cells [24] (See Table S1). The photoprotective responses were evaluated by measuring the non-photochemical quenching of fluorescence (NPQ [62]) using the fluorescence setup described above. The NPQ was calculated as $1 - (F_m' / F_m)$ where F_m is the maximum fluorescence emission in dark acclimated cells.

Sample preparation for electron microscopy and chemical imaging

Rapid freezing methods are recognized as superior to chemical fixation in preserving native-state cell ultrastructure and chemistry. Symbiotic acantharians (host and algal symbionts) and free-living microalgae in culture (*Phaeocystis cordata*) were therefore cryo-fixed using high-pressure freezing (HPM100, Leica) in which cells were subjected to a pressure of 210 MPa at -196°C , followed by freeze-substitution (EM ASF2, Leica). Prior to cryo-fixation, the microalgal cultures were concentrated by gentle centrifugation for 10 min. This cryo-preparation is recognized as the most suitable method to preserve the native chemistry of cells, including highly diffusible elements and trace elements [63–65]. For the freeze substitution (FS), a mixture of dried acetone and 1% osmium tetroxide was used. The FS machine was programmed as follows: 60–80 h at -90°C , heating rate of 2°C h^{-1} to -60°C (15 h), 10–12 h at -60°C , heating rate of 2°C h^{-1} to -30°C (15 h), and 10–12 h at -30°C . The cells were then washed several times in anhydrous acetone for 20 min at -30°C . Subsequently, the cells were gradually embedded in anhydrous araldite, a resin that contains negligible levels of the elements [66] and had been previously used in different analytical imaging studies [67–69]. A graded resin/acetone (v/v) series was used (30, 50 and 70% resin) with each step lasting 2 h at increased temperature: 30% resin/acetone bath from -30°C to -10°C , 50% resin/acetone bath from -10°C to 10°C , 70% resin/acetone bath from 10°C to 20°C . Samples were then placed in 100% resin for 8–10 h and in 100% resin with accelerator (BDMA) for 8 h at room temperature. Resin polymerization finally occurred at 65°C for 48 hours. The resin blocks and sections were stored in dry conditions before imaging. Prior to ultra-thin sectioning, symbiotic cells were observed in the resin block with a binocular and an inverted microscope to define the region of interest and the z-position of cells in the block, respectively. Trimming around the targeted cells was performed with razor blades and an EM Trimming Leica machine. Semi-thin sections (200–400 nm thick) were then obtained using an ultramicrotome (Leica EM) with an ultra-diamond knife (Diatome) and placed on 10-mm arsenic-doped silicon wafers for NanoSIMS and ToF-SIMS and on Si_3N_4 membrane windows for synchrotron X-ray fluorescence. Adjacent sections of 60- to 80-nm thick were also obtained for TEM analysis. Resin sections were rapidly collected on the water (< 30 s) of the diamond knife. Because it has been shown that some diffusible molecules and elements can be lost at this step [70, 71], we visualized the distribution of highly-diffusible elements (chlorine, potassium and calcium) with the synchrotron X-ray fluorescence. The presence of these mobile elements is a rule-of-thumb criterion to assess the chemical preservation of cells during the sample preparation [72, 73].

Transmission Electron Microscopy (TEM) and Scanning Electron Microscopy (SEM)

For TEM analysis, ultrathin sections of 60 nm thickness were mounted onto copper grids or slots coated with formvar and carbon. Sections were then stained in 1% uranyl acetate (10 min) and lead citrate (5 min). Micrographs were obtained using a Tecnai G2 Spirit BioTwin microscope (FEI) operating at 120 kV with an Orius SC1000 CCD camera (Gatan). From the TEM images, the surface area occupied by the thylakoid membranes in plastids of symbiotic ($n = 86$ plastids) and free-living ($n = 113$ plastids) cells was calculated. To calculate this area, we performed a manual area of interest extraction using GIMP software. By applying an adaptive thresholding technique, the pixels of the same greyscale were classified using computer vision library OpenCV linked to its python packages, and the classified pixels were computed for statistical analyses. Moreover, SEM was used to locate the cells on the sections, verify the quality of structural preservation, and identify the relevant regions of interest for subsequent chemical imaging with NanoSIMS, ToF-SIMS and S-XRF. The SEM micrographs were acquired at an electron energy of 5 kV using the secondary electron detector of the Zeiss Merlin VP Compact SEM at ProVIS.

Focused Ion Beam Scanning Electron Microscopy (FIB-SEM)

The sample was trimmed for FIB-SEM with a 90° diamond knife (Diatome) to expose cells at two surfaces (the imaging surface and the surface perpendicular to the focused ion beam, FIB) in order to optimize the acquisition [74]. After the sample was trimmed, it was mounted onto the edge of an SEM stub (Agar Scientific) using silver conductive epoxy (CircuitWorks) with the trimmed surfaces facing up and toward the edge of the stub. The sample was gold sputter coated (Quorum Q150RS; 180 s at 30 mA) and placed into the FIB-SEM for acquisition (Crossbeam 540, Carl Zeiss Microscopy GmbH). Once the ROI was located in the sample, Atlas3D software (Fibics Inc. and Carl Zeiss Microscopy GmbH) was used to perform sample preparation and 3D acquisitions. First, a $1\text{-}\mu\text{m}$ platinum protective coat ($20\ \mu\text{m} \times 20\ \mu\text{m}$) was deposited with a 1.5 nA FIB current. The rough trench was then milled to expose the imaging cross-section with a 15 nA FIB current, followed by a polish at 7 nA. The 3D acquisition milling was done with a 1.5 nA FIB current. For SEM imaging, the beam was operated at 1.5 kV/700 pA in analytic mode using an EsB detector (1.1 kV collector voltage) at a dwell time of 8 μs with no line averaging. Datasets were acquired (8 nm pixel size and 8 nm steps) in z and aligned using the plugins StackReg provided by the open source software ImageJ. Dataset quality improvement and noise reduction were performed by 3D median filtering using the SciPy python package. The segmentation and 3D models of cells were performed using the 3D Slicer [57] and MeshLab [58] open source software packages.

Synchrotron X-ray fluorescence (S-XRF) imaging

S-XRF hyperspectral images were acquired on the ID21 and ID16B-NA beamlines of the European Synchrotron Radiation Facility [75, 76]. Semi-thin sections (300 nm) were laid on Si_3N_4 membranes. On ID21, the incoming X-rays were tuned to the energy of 7.3 keV with a fixed-exit double crystal Si(111) monochromator and focused to $0.30 \times 0.75\ \mu\text{m}^2$ with a Kirkpatrick-Baez (KB) mirror system, yielding a flux of $4.7 \cdot 10^{10}$ ph/s. The experiment was performed under vacuum (10^{-5} – 10^{-4} mbar). The emitted fluorescence signal was detected with energy-dispersive, large area (80 mm^2) SDD detectors equipped either with polymer or with Be window (XFlash 5100 from Bruker and SGX from RaySpec, respectively). Images were acquired by raster scanning the sample in the

X-ray focal plane, with a $0.5 \times 0.5 \mu\text{m}^2$ step and a 1 s or 500 ms dwell time. The detector response was calibrated over a thin film reference sample consisting of layers of elements in ng/mm^2 concentration sputtered on a 200-nm thick Si_3N_4 membrane (RF7-200-S2371 from AXO), measured using the same acquisition parameters. Elemental mass fractions were calculated from fundamental parameters with the PyMca software package [59], assuming a biological matrix of light elements only (H, C, N, O). For comparison between concentrations in different samples and sample areas (host versus symbiont, free-living versus symbiotic), we performed the acquisitions in identical experimental conditions (Be-window detector, fixed detector-sample distance, 300 nm cuts, 500 ms/pixel dwell time) to ensure the comparability of the results. Areas were chosen by manually selecting the pixels in the region of interest and summing up their fluorescence signal; the sum spectrum normalized by the number of pixels was then subjected to spectral deconvolution, and the peak areas were converted in mass fractions. Three sections per sample were analyzed, and their average and standard deviation are reported in Table S3.

On ID16B-NA, a beam of 17.5 keV focused to $50 \times 50 \text{nm}^2$ through KB mirrors ($2 \cdot 10^{11}$ ph/s) was used to excite X-ray fluorescence from the samples. High-resolution XRF images ($50 \times 50 \text{nm}^2$ step size) were acquired in air, with a dwell time of 100 ms/pixel. Two 3-element SDD detector arrays were used to collect fluorescence from the sample. The detector response was calibrated over a thin film reference sample (RF8-200-S2453 from AXO). High-resolution images were acquired for free-living ($n = 4$) and symbiotic ($n = 6$) microalgae and in selected areas of the host (see also Table S4). Elemental quantification was extracted from fundamental parameters. To cross-check the consistency between data obtained with different experimental conditions (μm resolution and low excitation energy versus nm resolution and high energy, on ID21 and ID16B-NA, respectively), the estimated Fe concentrations in free-living *Phaeocystis* were compared: 44 ± 6 ppm (ID21) and 50 ± 5 ppm (ID16B-NA) lie within the error (see also Tables S3 and S4).

NanoSIMS acquisition and analyses

Semi-thin sections (200–300 nm) on silicon wafers were coated with 20-nm gold-palladium and analyzed with a nanoSIMS 50L (Cameca, Gennevilliers, France) at the ProVIS Centre (UFZ Leipzig). A 16-keV Cs^+ primary ion beam of 1–2 pA focused to approximately 70 nm was rastered over the sample area between $15 \times 15 \mu\text{m}^2$ and $70 \times 70 \mu\text{m}^2$ in size, with a dwelling time of 2 ms/pixel in a 512×512 or 1024×1024 pixel pattern, keeping the physical distance between pixels well below the beam size in order to avoid an ion beam induced surface roughening. The analysis areas were defined based on previous SEM observation. Before analysis, each area was pre-implanted with a 1 nA Cs^+ ion beam for 1–2 min to equilibrate the yield of negative secondary ions. Multiple analysis scans (up to 100) were recorded for each area. Secondary ions extracted from each pixel of the sample surface were analyzed for their mass to charge (m/z) ratio and counted separately with 7 electron multiplier detectors. The mass resolving power (MRP) of the spectrometer was set to 9000 ($M/\Delta M$) to resolve isobaric interferences. Different secondary ions ($^{12}\text{C}^{14}\text{N}$, ^{31}P or $^{31}\text{P}^{16}\text{O}_2$, ^{32}S , ^{16}O , $^{12}\text{C}_2$ or ^{12}C) were detected in simultaneous collection mode by pulse counting to generate 10–100 serial maps of secondary ion count for their further quantitative evaluation. The analyzed sample depth measured was between 50 nm and 200 nm.

For each nanoSIMS secondary ion count map, the regions of interest (ROI) were defined by manual drawing with the look@nanosims software [60], and ion counts (normalized by scans and pixels number) and ratios were calculated for each ROI (Data S1; Figure S4). In total, nine microalgal cells in symbiosis from three different host cells were analyzed. Four classes of ROIs were defined: host cell, whole microalgal cell (*Phaeocystis*), cytosol and plastid of the microalgal cell. In addition, eleven microalgal cells in the free-living stage were analyzed, where three ROIs classes were defined: entire cell, plastid of the alga and cytosol of the alga. Note that the cytosol of the microalgal cell can include the nucleus and vacuoles. In order to compare the relative N and P content between host, symbiotic and free-living microalgae, the total ions counts of elements (e.g., ^{31}P or $^{12}\text{C}^{14}\text{N}^-$) were normalized by the total ions counts of carbon (C_2). These analyses do not provide absolute quantification of N and P concentration but a comparison of the relative N and P content between ROIs of the algae and the host. For each ROI, the nitrogen, phosphorous and sulfur contents were therefore calculated by $^{12}\text{C}^{14}\text{N}/^{12}\text{C}_2$, $^{31}\text{P}^{16}\text{O}_2/^{12}\text{C}_2$ and $^{32}\text{S}/^{12}\text{C}_2$, respectively. Similarly, the stoichiometric ratio N/P was estimated by $^{12}\text{C}^{14}\text{N}/^{31}\text{P}^{16}\text{O}_2$. For comparison of different ROIs from the same acquisition, the homogeneity of variance was tested using Levene's test proposed in look@nanosims, and significant differences were tested using either the Kruskal-Wallis or ANOVA test. For cross-comparisons of different acquisitions, statistical significance was evaluated by performing ANOVAs with type II tests to account for unbalanced datasets. To meet the assumptions for ANOVA analysis, $^{12}\text{C}^{14}\text{N}/^{12}\text{C}_2$ was log-transformed, and Tukey's Ladder for Power transformation was applied to $^{31}\text{P}^{16}\text{O}_2/^{12}\text{C}_2$ and $^{12}\text{C}^{14}\text{N}/^{31}\text{P}^{16}\text{O}_2$. Confidence intervals were set to 95%. All statistical analyses were carried out using the R software (version 3.4.3, R Core Team 2017) with the packages 'car', 'DescTools' and 'rcompanion'.

ToF-SIMS acquisition and analyses

Qualitative analysis of molecular composition was performed on uncoated semi-thin sections, employing the time-of-flight secondary ion mass spectrometry technique (ToF-SIMS) with a ToF-SIMS.5 (ION-TOF GmbH, Münster) instrument. The ToF-SIMS experiment was performed using the imaging mode of ToF-SIMS.5 operation in combination with a delayed extraction [77] of negative secondary ions, providing a mass resolving power (MRP) above 3000 and a lateral resolution of approximately 150 nm. In these experimental conditions, the 30-keV NanoProbe LMIG source delivered 0.02 pA of primary Bi_3^{2+} cluster ions in 100 ns pulses with a 200 μs repetition period. The analysis has been done in 400 scans/plains with 5 shots of Bi_3^{2+} primary cluster ions per pixel distributed randomly in a 512×512 raster over a $56 \times 56 \mu\text{m}^2$ sample area. 30 keV Bi_3^+ ions from a NanoProbe source were employed for analysis. The 110- μs repetition period of primary ion pulse delivered 0.03 pA of Bi_3^+ . The analysis was performed by rastering the primary ion beam randomly in a 1024×1024 pixels pattern over a $110 \times 110 \mu\text{m}^2$ sample area. Each shot of analysis Bi_3^+ ion beam was followed by sample charge compensation implemented with 12 eV electrons from flooding e-gun and 2×10^{-7} mbar

partial pressure of Ar gas in the analysis chamber. The data were acquired in 306 planes. Each data plane was generated after 5 scans over the analysis area with 5 shots per pixel, and 5 keV [Ar]¹⁷⁵⁷ cluster ions from a GCIB source were used for sample sputtering in non-interlaced mode. The accumulation of acquired scans/plains was done after lateral drift correction, and the resulted total stack was analyzed for lateral distribution of ion yield using the SurfaceLab 6.7 software (ION-TOF GmbH).

Lipidomics analyses

Cultures of *Phaeocystis cordata* were concentrated, cryofixed in liquid nitrogen and lyophilized. Once freeze-dried, the pellet was suspended in 4 mL of boiling ethanol for 5 min to prevent lipid degradation and lipids were extracted according to Folch by addition of 2 mL methanol and 8 mL chloroform at room temperature [78, 79]. The mixture was then saturated with argon and stirred for 1 hour at room temperature. After filtration through glass wool, cell remains were rinsed with 3 mL chloroform/methanol 2:1, v/v and 5 mL of NaCl 1% were then added to the filtrate to initiate biphasic formation. The chloroform phase was dried under argon before solubilizing the lipid extract in pure chloroform. Total glycerolipids were quantified from their fatty acids: in an aliquot fraction of extracted lipids, a known quantity of 15:0 was added, and the fatty acids were converted into methyl esters (FAME) by a 1 hour incubation in 3 mL of 2.5% H₂SO₄ in pure methanol at 100°C [79]. The reaction was stopped by the addition of 3 mL of water and 3 mL of hexane. The hexane phase was analyzed using a gas chromatography-flame ionization detector and mass spectrometry (GC-FID/MS) (Perkin Elmer) on a BPX70 (SGE) column. FAME were identified by mass spectrometry and quantified by the surface peak method of the FID signal using 15:0 for calibration. For quantification of each lipid class by LC-MS/MS analysis, a fraction of extracted lipids corresponding to 25 nmol was resuspended in 100 μL of chloroform/methanol (2:1 v/v) containing 125 pmol of internal standards and analyzed as described in [80] or the total extract was re-suspended in 40 μL of chloroform/methanol (2:1 v/v) containing 50 pmol of internal standards. Internal standard used for DAG, TAG, MGDG and DGDG was DAG 18:0-22:6 from Avanti Polar Lipid. The internal standard for PE was PE 18:0-18:0 from Avanti Polar Lipid, and the internal standard for PC, PI, PS, PA, DPG, PG and SQDG was SQDG 16:0-18:0 extracted from spinach thylakoid [81] and hydrogenated as described before [82]. Lipids were then separated by HPLC and quantified by MS/MS. The high-performance liquid chromatography (HPLC) separation method was adapted from a previous study [83]. Lipid classes were separated using an Agilent 1200 HPLC system using a 150 mm × 3 mm (length × internal diameter) 5-μm diol column (Macherey-Nagel) at 40°C. The mobile phases consisted of hexane/isopropanol/water/ammonium acetate 1 M, pH 5.3 [625/350/24/1, (v/v/v/v)] (A), and isopropanol/water/ammonium acetate 1 M, pH 5.3 [850/149/1, (v/v/v)] (B). The injection volume was 20 μL. After 5 min, the percentage of B was increased linearly from 0% to 100% over 30 min and stayed at 100% for 15 min. This elution sequence was followed by a return to 100% A in 5 min and an equilibration for 20 min with 100% A before the next injection, leading to a total run time of 70 min. The flow rate of the mobile phase was 200 μL/min. The distinct glycerolipid classes were eluted successively as a function of the polar head group. Mass spectrometric analysis was done on a 6460 triple quadrupole mass spectrometer (Agilent) equipped with a Jet stream electrospray ion source under the following settings: drying gas heater, 260°C; drying gas flow 13 L.min⁻¹; sheath gas heater, 300°C; sheath gas flow; 11 L.min⁻¹; nebulizer pressure, 25 psi; capillary voltage, ± 5000 V; nozzle voltage, ± 1000. Nitrogen was used as collision gas. The quadrupoles Q1 and Q3 were operated at widest and unit resolution respectively. PC, DGTA and DGCC analysis were carried out in positive ion mode by scanning for precursors of m/z 184, 236 and 104 at collision energies (CE) of 34 eV, 52 eV and 40 eV, respectively. SQDG analysis was carried out in negative ion mode by scanning for precursors of m/z -225 at a CE of -56 eV. PE, PI, PG, MGDG and DGDG measurements were performed in positive ion mode by scanning for neutral losses of 141 Da, 277 Da, 189 Da, 179 Da and 341 Da at CEs of 20 eV, 12 eV, 16 eV, 8 eV and 8 eV, respectively. Quantification was performed using multiple reaction monitoring (MRM) with a 40-ms dwell time. Mass spectra were processed by MassHunter Workstation software (Agilent) for the identification and quantification of lipids. Lipid amounts (pmol) were corrected for response differences between internal standards and endogenous lipids and by comparison with a quality control (QC). The QC extract corresponded to a known *Phaeodactylum tricorutum* lipid extract qualified and quantified by TLC and GC-FID as previously described [80].

QUANTIFICATION AND STATISTICAL ANALYSIS

Statistical analysis and graph production were performed using R with specific libraries mentioned above. For nanoSIMS data, the homogeneity of variance was tested using Levene's test proposed in the software look@nanosims, and significant differences were tested using either the Kruskal-Wallis or ANOVA test. For cross-comparisons of different nanosims acquisitions, statistical significance was evaluated by performing ANOVAs with type II tests to account for unbalanced datasets based on 17 plastids of 12 free-living microalgae and 45 plastids of 10 symbiotic microalgae. To meet the assumptions for ANOVA analysis, ¹²C¹⁴N/¹²C₂ was log-transformed, and Tukey's Ladder for Power transformation was applied to ³¹P¹⁶O₂/¹²C₂ and ¹²C¹⁴N/³¹P¹⁶O₂. Confidence intervals were set to 95%. Statistical analyses were carried out using the R software (version 3.4.3, R Core Team 2017) with the packages 'car', 'DescTools' and 'rcompanion'. For the photophysiology measurements, 23 measures were conducted on cultures of free-living *Phaeocystis* in triplicate, and 10 measures on three pools of 80-100 acantharian cells containing symbiotic *Phaeocystis* (triplicate). Samples for lipidomics analyses were composed of two biological and three technical replicates. Synchrotron X-ray fluorescence was performed on 21 free-living *Phaeocystis* cells and 11 symbiotic *Phaeocystis* cells from three different host cells (Table S3). On the high resolution S-XRF beam line, four free-living and six symbiotic microalgae were also analyzed (see also Table S4).

A.2 Cytoklepty in the plankton: a host strategy to optimize the bioenergetic machinery of endosymbiotic algae

Summary

Endosymbioses have shaped the evolutionary trajectory of life and remain widespread and ecologically important. Investigating modern oceanic photosymbioses can illuminate how algal endosymbionts are energetically exploited by their heterotrophic hosts, and inform on putative initial steps of plastid acquisition in eukaryotes. By combining 3D subcellular imaging with photophysiology, carbon flux imaging and transcriptomics, we show that cell division of algal endosymbionts (Phaeocystis) is blocked within hosts (Acantharia), and that their cellular architecture and bioenergetic machinery are radically altered. Transcriptional evidence indicates that a nutrient-independent mechanism prevents symbiont cell division and decouples nuclear and plastid division. As endosymbiont plastids proliferate, the volume of the photosynthetic machinery volume increases 100-fold in correlation with expansion of a reticular mitochondrial network in close proximity to plastids. Photosynthetic efficiency tends to increase with cell size and photon propagation modeling indicates that the networked mitochondrial architecture enhances light capture. This is accompanied by 150-fold higher carbon uptake and upregulation of genes involved in photosynthesis and carbon fixation, which, in conjunction with a ca.15-fold size increase of pyrenoids demonstrates enhanced primary production in symbiosis. NanoSIMS analysis revealed major carbon allocation to plastids and transfer to the host cell. Invagination of the symbiosome into endosymbionts to optimize metabolic exchanges is strong evidence that the algal metamorphosis is irreversible. Hosts therefore trigger and unambiguously benefit from major bioenergetic remodeling of symbiotic microalgae with important consequences for the oceanic carbon cycle. Unlike other photosymbioses, this interaction represents a so-called cytoklepty, which is a putative initial step towards plastid acquisition.

Keywords: symbiosis, oceanic plankton, 3D electron microscopy, photosynthesis, single-cell, transcriptomics.

Cytoklepty in the plankton: a host strategy to optimize the bioenergetic machinery of endosymbiotic algae

Uwizeye Clarisse^{1*}, Mars Brisbin Margaret^{2,a*}, Gallet Benoit³, Chevalier Fabien¹, LeKieffre Charlotte¹, Schieber L. Nicole⁴, Falconet Denis¹, Wangpraseurt Daniel^{5,6,7}, Schertel Lukas⁶, Stryhanyuk Hryhoriy⁸, Musat Niculina⁸, Mitarai Satoshi², Schwab Yannick⁴, Finazzi Giovanni¹, Decelle Johan^{1§}

*: these authors contributed equally to the manuscript

^aPresent address: Biology and Marine Chemistry & Geochemistry departments, Woods Hole Oceanographic Institution, Woods Hole, USA

1- Univ. Grenoble Alpes, CNRS, CEA, INRAe, IRIG-LPCV, 38000 Grenoble, FRANCE

2- Marine Biophysics Unit, Okinawa Institute of Science and Technology, 1919-1 Tancha, Onna, Okinawa 904-0495, Japan

3-Institut de Biologie Structurale (IBS), University Grenoble Alpes, CEA, CNRS, 38044 Grenoble, France

4- Cell Biology and Biophysics Unit, European Molecular Biology Laboratory (EMBL), 69117 Heidelberg, Germany

5-Department of Nanoengineering, University of California San Diego, San Diego, CA, USA

6-Bioinspired Photonics Group, Department of Chemistry, University of Cambridge, Cambridge, UK

7-Scripps Institution of Oceanography, University of California San Diego, San Diego, USA

8-Helmholtz Centre for Environmental Research – UFZ, Department of Isotope Biogeochemistry, Leipzig, Germany

§: Johan Decelle, Cell and Plant Physiology Department, 17 rue des Martyrs, 38054 Grenoble, France

Email: johan.decelle@univ-grenoble-alpes.fr

Keywords: symbiosis; oceanic plankton; 3D electron microscopy, photosynthesis, single-cell transcriptomics

Author Contributions: C.U., M.M.B., S.M. and J.D. designed research; M.M.B. G.B., F.C., C.L., N.L.S., D.W., L.S., H.S., G.F. performed research; C.U., M.M.B., C.L., N.L.S., D.W., L.S., G.F., and J.D. analyzed data; and C.U., M.M.B. and J.D. wrote the paper, with assistance from D.F., G.F., Y.S., N.M., and S.M.

Abstract

Endosymbioses have shaped the evolutionary trajectory of life and remain widespread and ecologically important. Investigating modern oceanic photosymbioses can illuminate how algal endosymbionts are energetically exploited by their heterotrophic hosts, and inform on putative initial steps of plastid acquisition in eukaryotes. By combining 3D subcellular imaging with photophysiology, carbon flux imaging and transcriptomics, we show that cell division of algal endosymbionts (*Phaeocystis*) is blocked within hosts (Acantharia), and that their cellular architecture and bioenergetic machinery are radically altered. Transcriptional evidence indicates that a nutrient-independent mechanism prevents symbiont cell division and decouples nuclear and plastid division. As endosymbiont plastids proliferate, the volume of the photosynthetic machinery volume increases 100-fold in correlation with expansion of a reticular mitochondrial network in close proximity to plastids. Photosynthetic efficiency tends to increase with cell size and photon propagation modeling indicates that the networked mitochondrial architecture enhances light capture. This is accompanied by 150-fold higher carbon uptake and upregulation of genes involved in photosynthesis and carbon fixation, which, in conjunction with a ca.15-fold size increase of pyrenoids demonstrates enhanced primary production in symbiosis. NanoSIMS analysis revealed major carbon allocation to plastids and transfer to the host cell. Invagination of the symbiosome into endosymbionts to optimize metabolic exchanges is strong evidence that the algal metamorphosis is irreversible. Hosts therefore trigger and unambiguously benefit from major bioenergetic remodeling of symbiotic microalgae with important consequences for the oceanic carbon cycle. Unlike other photosymbioses, this interaction represents a so-called cytoklepty, which is a putative initial step towards plastid acquisition.

Introduction

Living with intracellular microalgae (photosymbiosis) is a globally widespread and ecologically important lifestyle. In marine benthic ecosystems, a wide diversity of animals (e.g. cnidarians, molluscs) host photosynthesizing microalgae in their tissues, sustaining coral reef habitats and their associated biodiversity worldwide. In the oceanic plankton, various unicellular heterotrophic eukaryotes (e.g. radiolarians, foraminiferans) also establish symbioses with intracellular microalgae (1, 2). These ubiquitous organisms contribute significantly to primary production (3) and carbon sequestration from surface waters to the deep sea (4–7). Photosymbioses are generally recognized as mutualistic partnerships with hosts providing nutrient-rich and protective microhabitats to algal symbionts, which in return provide energy-rich compounds produced via photosynthesis (e.g. sugars, lipids; (8)). This metabolic crosstalk between a heterotroph and an autotroph provides a competitive advantage in nutrient-poor habitats, such as the open ocean. However, it is difficult to demonstrate whether photosymbioses confer evolutionary advantages on algal symbionts, particularly in marine planktonic symbioses, which cannot be cultured in laboratory conditions and where the costs and benefits for each partner are not clearly defined (9). Therefore, whether photosymbioses are true mutualistic partnerships has long been debated (10).

In the evolutionary history of eukaryotes, photosymbiosis is recognized as a preliminary step leading to plastid acquisition and spread across photosynthetic lineages (11, 12). Interactions between host and endosymbiont evolved into inverted parasitism whereby the host exploited a prokaryotic (primary endosymbiosis) or plastid-bearing eukaryotic symbiont (secondary or tertiary endosymbiosis), leading to gradual cellular and genomic reduction of the symbiont and ultimately plastid acquisition by the host (13–15). However, the underlying cellular mechanisms that allow a host cell to take control and manipulate the bioenergetics of intracellular microalgae remain unknown. Several relevant models have been studied, but reduction of the microalgal cell and horizontal gene transfer to the host has already occurred in each of them (e.g. kleptoplastidy in dinoflagellates (16), *Paulinella chromatophora* (17)). Studying contemporary unicellular photosymbioses involving intact microalgae has the potential not only to lead to a better understanding of their ecological success in the ocean but also to provide evolutionary insights into the putative first steps of plastid acquisition and underlying host control.

The cosmopolitan planktonic photosymbiosis between acantharian hosts and intact microalgae (*Phaeocystis spp.*, Haptophyta) is characterized by a morphological transformation of symbionts,

wherein algal cell volume increases dramatically and there is a multiplication of enlarged plastids (18, 19). Free-living *Phaeocystis* cells can reach high population densities in many oceanic regions (20, 21), thus confounding any evolutionary advantages symbiosis may confer on this microalga. Conversely, the ecological success of free-living *Phaeocystis* benefits hosts since it increases opportunities to capture new symbionts throughout the life cycle (22). Hence, Acantharia-*Phaeocystis* photosymbioses are potentially exploitive symbioses with intact symbiont cells and represent an ideal system to investigate this oceanic interaction and bring new insights into the early transitional stages of more permanent algal endosymbioses.

To elucidate mechanisms involved in host exploitation of algal cells and the putative initial steps of plastid acquisition, the structural, physiological, and genetic changes of symbiotic microalgae need to be explored at the subcellular and molecular level. Here, the subcellular architecture of *Phaeocystis* cells outside (i.e. free-living in culture) and inside host cells was reconstructed in 3D to quantify structural changes of energy-producing organelles (plastid, mitochondria) and their interactions. In parallel, single-cell transcriptomics compared *Phaeocystis* gene expression in free-living and symbiotic stages. This combination of quantitative subcellular imaging and transcriptomics showed that the cell cycle of endosymbiotic microalgae is halted and the bioenergetic machinery is drastically enhanced. We observed a proliferation of plastids with enlarged pyrenoids and correlated extension of reticulated mitochondria in symbionts, accompanied by the upregulation of genes involved in photosynthesis and central carbon pathways. Photophysiology, photon propagation modeling and carbon flux imaging further demonstrated that algal energy production is significantly enhanced, leading to increased production of organic carbon, which is allocated to plastids and transferred to the host cell. This study deciphers mechanisms on how a microalgal cell is morphologically, metabolically and transcriptionally modified and ultimately exploited by a heterotrophic host cell in the oceanic plankton (i.e. cytotrophy).

Results and Discussion

***Phaeocystis* cell division is inhibited in symbiosis**

Using 3D electron microscopy (FIB-SEM: Focus Ion Beam - Scanning Electron Microscopy), we reconstructed and performed morphometric analyses of the subcellular architecture of the microalga *Phaeocystis* in the free-living ($n = 20$ cells) and endosymbiotic stage within two distinct acantharian hosts ($n = 7$ cells) (Fig. 1, Dataset S1). Alongside the disappearance of flagella and external scales, the total volume of symbiotic *Phaeocystis* cells increased 6- to 78-fold compared

to free-living cells and accommodated more organelles and larger vacuoles (Figs. 1 and 2). Such a dramatic increase in cell size indicates that *Phaeocystis* cell-division could be blocked while living symbiotically (23, 24). Consistent with this hypothesis, single-cell transcriptome analysis on twelve distinct hosts revealed that key *Phaeocystis* genes involved in DNA replication and progression through cell cycle stages (G1, S, G2, M) were downregulated in symbiosis (Fig. 2 and Fig. S1), including genes for DNA polymerase complexes, cyclins, cyclin-dependent kinases, and the anaphase-promoting complex. Additionally, nuclear volume increased in symbiotic cells up to 32-fold (Fig. 2, Dataset S1), although its relative occupancy decreased from $9.3 \pm 1.6\%$ in free-living cells to $4.7 \pm 2\%$ in symbiosis (Fig. 1D). Taking advantage of the varying electron densities of compartments within the nucleus, we separately quantified the volumes of the nucleolus (site of ribosome genesis) (25) and, eu- and hetero-chromatin (sites of DNA replication and gene expression) (26). The volume of these three nuclear compartments concomitantly increased in symbiosis (20-fold for the nucleolus, 18-fold for the heterochromatin, 23-fold for euchromatin) and their volume ratios remained relatively stable (Fig. S1, Dataset S1). While there is no reorganization of chromatin in symbiosis, the overall increase of its volume suggests that symbionts accumulate DNA. DNA synthesis occurs in symbiosis, but the final steps of mitosis and cytokinesis are prevented. Increased cell and nuclear volume alongside downregulation of DNA replication and cell-cycle pathways compile strong evidence for inhibited cell division in symbiotic *Phaeocystis*.

Preventing symbiont cell division is a host strategy for managing symbiont populations and limiting symbiont overgrowth (27). Hosts can regulate symbiont cell-division by controlling access to essential nutrients (e.g. nitrogen and phosphorus) (28), which has been previously hypothesized for the *Acantharia-Phaeocystis* symbiosis. We therefore investigated the expression level of marker genes for nutrient deprivation in microalgae: alkaline phosphatase genes for phosphorus limitation (29–31) and nitrate transporter genes for nitrogen limitation (28, 32, 33). Alkaline phosphatase genes (*phoA* and *ehp1*-like) that were expressed by free-living cells cultured in nutrient replete conditions were generally not expressed at detectable levels in symbionts, and the nitrate transporter gene (*Nrt*) was significantly downregulated in symbiotic cells compared to free-living cells (Fig. 2). Hence, symbiotic *Phaeocystis* in the host microhabitat does not appear to be limited by these major essential nutrients, despite very low nutrient availability in the waters from which hosts were collected. This is further supported by the increased nucleolar volume observed in symbiotic cells (Fig. S1), which reflects high rDNA transcription rates (34) and thus increased ribosome production and protein translation—that are processes typically reduced

under N-limitation (35). Similarly, the Translation, Translation initiation, and Protein folding GO terms, as well as the Ribosome KEGG pathway, were enriched among the significantly upregulated genes in symbiosis (Fig. S2, Dataset S1). Furthermore, the assimilatory nitrite reductase gene (*NirA*) was downregulated in symbiosis. In contrast, genes responsible for ammonia assimilation (*GS-GOGAT*, *CPS1*) were upregulated (Fig. 2D), indicating that ammonium may be readily available to symbionts, as has been shown in several other photosymbioses (36–38). Together, these results suggest that acantharian hosts may rely on a nutrient-independent mechanism to inhibit symbiont cell division and manage intracellular symbiont populations, a strategy that would give hosts finer control over symbionts while ensuring maximal symbiont productivity.

Enhanced photosynthesis and carbon fixation in symbiosis

Free-living, flagellated *Phaeocystis* cells usually have two plastids (Figs. 3A and S3). In symbiotic cells, there is a proliferation of enlarged plastids (18), and in this study, we observed 4–65 plastids in individual symbiotic *Phaeocystis* cells. 3D reconstructions allowed us to further determine that plastids occupied 42–62% of the total volume of symbiotic cells, compared to 31% in free-living cells, and that both the total volume and surface area of the photosynthetic machinery expanded up to app. 100 fold (Figs. 1 and 3, Dataset S1). In single-celled algae, plastid division is typically synchronized with cell division and is initiated by expression of nuclear-encoded plastid division genes during S-phase of the cell cycle (39). Several of these genes (*FtsZ*, *DRP5B*, and *PDR1*) were expressed at similar levels in symbiotic and free-living cells (Fig. S4), despite cell-cycle genes being significantly downregulated in symbiosis. Moreover, 3D reconstructions of symbiotic cells revealed several plastids in the process of dividing (Fig. S4). Continued plastid division without consequent cell division leads to the accumulation of plastids and indicates that plastid division has become decoupled from cell division in symbiotic *Phaeocystis*. Symbiotic cells may therefore be arrested in S-phase, thus allowing plastids to proliferate and explaining the build-up of chromatin, but ultimately keeping symbiont population density constrained.

In plants, plastid proliferation increases photosynthesis more efficiently than plastid enlargement and is recognized as a means of increasing surface exchange, particularly for CO₂ diffusion (40). Here, we found that the photosynthesis GO term and KEGG pathway were both enriched among genes upregulated in symbiotic *Phaeocystis* cells (Fig. S2). To further test whether morphological and transcriptional changes in symbiotic cells enhanced photosynthesis, we assessed the relationship between cell size (a proxy for number of chloroplasts) and photosynthetic efficiency

by analyzing photosynthetic parameters *in vivo* at the single-cell level. We found that photosynthetic capacity increased rapidly with cell size until size had doubled, at which point, further increase in photosynthetic capacity was limited (Fig. 3B). This suggests that increased cell size, and therefore expanded photosynthetic machinery, enhances photosynthesis in *Phaeocystis*. The presence of small and large algal cells within a host indicates that *Phaeocystis* cells with different photosynthetic capacity coexist (F_v/F_m ranging from 0.4 to 0.78). The smallest symbiotic algae had F_v/F_m values lower than those measured in free-living cells (0.54 ± 0.02). These algae could represent an early stage during the establishment of symbiosis, in which photosynthesis is transiently repressed.

Expansion of the photosynthetic machinery in symbiotic *Phaeocystis* should be accompanied by increased carbon fixation and production of organic compounds. Carbon uptake was measured in free-living *Phaeocystis* cells and symbiotic *Phaeocystis* within their host incubated with ^{13}C -bicarbonate for one hour. We found that symbiotic *Phaeocystis* cells took up approximately 150 times more ^{13}C (0.70 ± 0.19 pg of $^{13}\text{C}\cdot\text{cell}^{-1}$) than free-living cells (0.0043 ± 0.0004 pg of $^{13}\text{C}\cdot\text{cell}^{-1}$) (Dataset S2). Consistent with this, nearly all nuclear-encoded genes for Calvin-Benson cycle enzymes were upregulated in symbiosis (Fig. 3D). To further explain enhanced carbon fixation in symbiotic *Phaeocystis*, we resolved the internal organization of pyrenoids within plastids. Pyrenoids contain the majority of the Rubisco enzyme in plastids and separate it from the surrounding, more basic stroma to maximize the enzyme's efficiency and, therefore, the cell's carbon fixation potential (41). We found that the volume of pyrenoids increased 15 fold from 0.08 ± 0.02 μm^3 in free-living cells ($n = 27$ plastids, 14 cells) to 1.2 ± 0.6 μm^3 in symbionts ($n = 74$ plastids, 7 cells) and that they occupied a larger proportion of plastid volume ($13 \pm 2.8\%$ in symbiotic cells compared to $5 \pm 1.6\%$ in free-living cells, Fig. 3C, Fig. S5, Dataset S1). A consequence of enlarged pyrenoids in symbiosis is that their surface area:volume ratio inherently decreases (Fig. S5), potentially increasing the diffusion barrier for gas and metabolite exchange. Thylakoid tubules deliver CO_2 to Rubisco and transport glycerate-3-phosphate product to the stroma, where the remainder of the Calvin-Benson cycles occurs (42, 43). In symbiosis, pyrenoids were always crossed by multiple tubules, whereas pyrenoids in free-living cells either lacked tubules (type 1) or were crossed by one small tubule (type 2) (Fig. 3C). When present, tubules in the pyrenoids of free-living cells were 9.5 times less voluminous than those in symbiotic cells. We hypothesize that multiple tubules in the pyrenoids counterbalance the lower surface area: volume ratio in symbiosis and maintain optimal delivery of CO_2 . These fine-scale changes in pyrenoid

structure, alongside upregulation of Calvin-Benson cycle genes, explain the mechanisms underpinning enhanced carbon fixation in symbiotic *Phaeocystis*.

Symbionts may themselves take advantage of the additional organic carbon produced from enhanced carbon fixation—either immediately or after synthesizing storage molecules—or they could transfer the additional fixed carbon to hosts. Based on the transcriptome analyses, symbiotic cells do not seem to be storing more fixed carbon than free-living cells. Key genes for the biosynthesis of triacylglycerol (TAG)—the preferred storage molecule among microalgae in oligotrophic regions (44)—were downregulated in symbiosis, including those for acyl-CoA binding proteins and acyltransferases that are involved in the production of TAG precursors (e.g. phosphatidic acid) and diacylglycerol transferase (DGAT), which performs the terminal step in TAG synthesis (Fig. 3E). Likewise, starch synthase was significantly downregulated in symbiosis (Fig. 3E). Symbiotic cells may store less carbon than free-living cells and instead produce ATP to meet energetic requirements (plastid division, protein synthesis) and relinquish surplus photosynthate to hosts. NanoSIMS analyses incorporating a 5-hour incubation with ^{13}C -labelled bicarbonate on four algal cells from two distinct hosts showed that symbiotic *Phaeocystis* cells mainly allocated carbon to their multiple plastids and small vacuoles (Fig. 3F, Fig. S6). These analyses also demonstrated that photosynthetically fixed carbon is transferred to the host cell (Fig. 3F), thus providing direct evidence that the host benefits from the boosted primary production of its symbiotic microalgae.

Transformation of the mitochondria into a reticulated fine network connected to plastids

Like plastids, mitochondria underwent an extensive expansion in symbiosis, forming a well-developed fine reticular network with mitochondrial volume and surface area increasing up to 52 and 47 fold, respectively (Fig. 4A, Dataset S1). Such reticular and fused networks are characteristic of actively respiring cells in eukaryotes (45). Yet, in relation to cell volume, the contribution of mitochondria was relatively constant (from $5.3 \pm 1.5\%$ in free-living to $3.3 \pm 0.6\%$ in symbiosis) (Fig. 1C and Dataset S1). At the sub-organelle level, the total volume of mitochondrial cristae (i.e. membrane invaginations, which are respiratory units), increased by up to 38-fold in symbiosis, but volume occupancy was similar in both stages ($17.4 \pm 3.9\%$ in free-living and $16.3 \pm 2.1\%$ in symbiosis) (Fig. S7). The GO terms for Respiration and Oxidative phosphorylation were enriched among genes downregulated in symbiosis (Fig. S2) and the majority of genes in the TCA cycle and respiratory oxidative phosphorylation KEGG pathways

were downregulated in symbiosis (Fig. S8). The morphology of the mitochondria and downregulation of respiratory pathways indicates that symbiotic cells may not respire at a higher rate than free-living cells. The mitochondria may, therefore, have a different primary role in symbiotic cells.

Other metabolic functions could provide a functional rationale for the morphological modification of mitochondria in symbiotic *Phaeocystis*. Mitochondrial interaction with plastids is an essential aspect of the bioenergetics of photosynthetic cells (46–48). In symbiotic *Phaeocystis*, mitochondrial volume tended to increase as plastid volume increased ($R^2 = 0.74$, $p = 4.8 \text{ E}10^{-11}$), whereas this relationship was not observed for free-living cells ($R^2 = 0.07$, $p = 0.38$) (Fig. 4B). We further found that mitochondrial surface area in contact with plastids ($\leq 50 \text{ nm}$ distance) increased from $2.63 \pm 2.1\%$ in free-living ($n = 14$ cells) to up to 8.8% in the largest symbiotic cell that was imaged (65 plastids, Fig. 4A, Dataset S1), with mitochondria interacting with multiple plastids in symbiotic cells. This indicates that the expansion of the reticulated mitochondria is likely related to plastid proliferation, where mitochondria may serve to maintain minimal diffusion distance between the two organelles and ensure optimal metabolic exchange (e.g. lipids, ammonium, ATP; (47, 48)). Consistent with this possibility, a brief incubation with mitochondrial inhibitors (Antimycin A, Salicylhydroxamic acid) at concentrations blocking respiration (47) decreased the F_v/F_m in symbiosis to 0.55 ± 0.05 (Fig. 4C). We interpret this observation in terms of a reduction of the electron acceptors between the two photosystems, due to increased cellular reducing power upon blocking consumption of reducing equivalents by the respiratory chain, as shown in other microalgae (49). This effect of inhibitors was less pronounced in free-living cells, indicating less interaction between the two organelles in this life stage. Overall, these results show that mitochondria contribute to the enhanced physiological performance of symbiotic *Phaeocystis*.

Symbiont photosynthesis within multicellular hosts is strongly affected by the light scattering properties of cells (50, 51). At the cellular level, mitochondria are known to be efficient light scatterers (52). We, therefore, tested whether the well-developed mitochondrial network of symbiotic cells could improve light distribution for photosynthesis. We used Finite-Difference-Time-Domain (FDTD) calculations to model the 3D light propagation in free-living (2 plastids) and symbiotic cells (16 plastids) using the 3D architectures of plastids and mitochondria. We observed that the reticular mitochondrial network homogeneously distributed the incident electric field due to its high scattering cross-section and intricate spatial distribution (Fig. 4D). Contrary to scattering in free-living microalgae, which is small and unidirectional with the incident light, the reticular mitochondrial network of symbiotic microalgae increases the photon pathlength within the algal

cell (Fig. 4D and Fig. S9), consequently enhancing the chance of light absorption (51). Thus, mitochondria-induced light scattering may contribute to the optimized photosynthetic performance of *Phaeocystis* in symbiosis. This is consistent with earlier measurements, showing that symbiotic cells have improved photosynthetic efficiency under limiting light (the initial slope α of the photosynthesis-irradiance curve, (18)) than their free-living counterparts.

Physical integration of microalgae into the host cell: symbiosome invagination into symbionts

In photosymbioses, hosts phagocytize microalgal cells from the environment and maintain them individually in a vacuole, or symbiosome, where metabolic exchanges take place. For small symbiotic *Phaeocystis* cells, the symbiosome surrounds the microalgal cell as observed in other photosymbioses (53) (Fig. 5A). Remarkably, in larger symbiotic cells (> 31 plastids), an invagination of the symbiosome vacuole into the microalgal cell was observed in different host cells (Fig. 5B). This invagination can represent a volume of up to $139.4 \mu\text{m}^3$ (one-fifth of symbiont volume) with a tendency to increase with symbiont size (Fig. 5C). We predict that symbiosome invagination maintains/optimizes metabolic exchanges with very large symbionts that would otherwise have decreased surface area for exchange. Of note, small vesicles were visible in the symbiosome space around symbionts, as well as within the invaginated symbiosome in larger symbionts (Fig. 5A and 5B). These vesicles could represent a route for transferring photosynthetic products from symbiont to host or metabolites and signaling molecules from host to symbiont. Indeed, free-living *Phaeocystis* are often considered “secretory cells” because they excrete vesicles rich in organic carbon (polysaccharides) into the environment (54). Penetration of the symbiosome represents a profound morphological manipulation and adds compelling evidence for the concept that symbionts are too far changed to return to their free-living form. Thus, the acantharian host hijacks and parasitizes the microalgal cell, ultimately performing “cytoklepty”. Cytoklepty can be defined as an evolutionarily one-sided endosymbiosis, in which the host captures and physiologically exploits endosymbionts, which eventually die and must be replaced by uptake of new endosymbionts from a wild population.

Conclusions The combination of nanoscale imaging with single-cell transcriptomics in this study illuminates the drastic morpho-genetic manipulation of endosymbiotic microalgae involved in a globally distributed and ecologically relevant photosymbiosis. Acantharian hosts prevent *Phaeocystis* cell division, leading to a complete cellular overhaul that improves symbiont bioenergetic performance, enhances photosynthesis and carbon fixation, and ultimately results in

substantial organic carbon production and transfer to hosts. More specifically, there is a structural remodeling of the bioenergetic machinery at multiple scales within the algal cell: plastids proliferate and pyrenoids develop with an immersed thylakoid network, which is accompanied by an extension of reticulated mitochondria that maintains contact with plastids and optimizes light distribution within the algal cell. These modifications are clearly beneficial to single-celled planktonic hosts, which gain an additional energy source and avoid symbiont overgrowth. The observation that host symbiosomes intrude into symbiont cells is unique among marine photosymbioses and provides new evidence supporting the idea that the metamorphosis of *Phaeocystis* is unidirectional, making the relationship an evolutionary dead-end for symbionts. Such extreme manipulation of microalgae suggests that this relationship, named cytoklepty, may represent a first step toward a more complete integration of endosymbionts.

Aspects of the symbiont remodeling observed here, such as hypertrophy of the photosynthetic machinery, are also observed in the *Paulinella chromatophora* endosymbiosis, the most recent known example of primary plastid acquisition (55), and in the *Hatena* endosymbiosis, a contemporary example of secondary endosymbiosis in progress (56). Expansion of the photosynthetic machinery may, therefore, represent a common stepping stone towards plastid acquisition. Enlarged nuclei and increased genome ploidy, observed here and in several examples of kleptoplastidy, may represent another commonality in plastid acquisition that serves to support photosynthetic expansion (57, 58).

The uncoupling between cell cycle progression and plastid division in symbiotic *Phaeocystis* suggests that the plastid-to-nucleus signal required to continue cell division is inhibited and deciphering the mechanism involved warrants further attention. Canonical cell-signalling pathways are a promising target for future work, as they have been implicated in mediating other endosymbioses as well as the morphological transformation between flagellate and colonial *Phaeocystis* cells (59, 60). As this cytoklepty shares important similarities with kleptoplastidy and may represent an early intermediary step between photosymbiosis and more permanent incorporation of the photosynthetic machinery, further elucidation of the mechanisms involved should pave the way to a more complete understanding of how eukaryotes acquire new organelles.

Materials and methods

Sampling and preparation for electron microscopy

Symbiotic acantharians harboring intracellular microalgal cells (*Phaeocystis cordata*) were collected from surface waters as in (18) (Mediterranean Sea, Villefranche-sur-Mer, France). After collection, individual cells were isolated under a microscope with a micropipette, rapidly transferred into filtered natural seawater, and maintained in the same controlled light (100 $\mu\text{mol photons m}^{-2}\text{s}^{-1}$) and temperature (20°C) conditions as the free-living stage. In parallel, cultures of the haptophyte *Phaeocystis cordata* (the symbiont of Acantharia in the Mediterranean Sea) (1) (strain RCC1383 from the Roscoff Culture Collection) were maintained at 20°C in K5 culture medium and at 100 $\mu\text{mol photons m}^{-2}\text{s}^{-1}$.

Sample preparation protocols were adapted from (18) to optimize the contrast for 3D electron microscopy imaging and facilitate pixel classification. Symbiotic acantharians (with algal endosymbionts) and free-living *Phaeocystis cordata* in culture were cryofixed using high-pressure freezing (HPM100, Leica), in which, cells were subjected to a pressure of 210 MPa at 196°C, followed by freeze-substitution (EM ASF2, Leica). Prior to cryo-fixation, the microalgal cultures were concentrated by gentle centrifugation for 10 min. For freeze-substitution (FS), a mixture of dried acetone, and 2% osmium tetroxide and 0.5% uranyl acetate was used as contrasting agents. The FS machine was programmed as follows: 60–80 h at –90°C, heating rate of 2°C h⁻¹ to –60°C (15 h), 10–12 h at –60°C, heating rate of 2°C h⁻¹ to –30°C (15 h), and 10–12 h at –30°C, quickly heated to 0°C for 1 h to enhance the staining efficiency of osmium tetroxide and uranyl acetate and then back to –30°C. Cells were then washed in anhydrous acetone for 20 min at 30°C and gradually embedded in anhydrous Araldite (resin). A graded resin/acetone (v/v) series was used (30, 50 and 70% resin) with each step lasting 2 h at increased temperature: 30% resin/acetone bath from –30°C to –10°C, 50% resin/acetone bath from –10°C to 10°C, 70% resin/acetone bath from 10°C to 20°C. Samples were then placed in 100% resin for 8–10 h and in 100% resin with the accelerator BDMA for 8 h at room temperature. Resin polymerization finally occurred at 65°C for 48 h.

Focused Ion Beam Scanning Electron Microscopy (FIB-SEM)

For FIB-SEM, the sample was trimmed with a 90° diamond knife (Diatome) to expose cells at two surfaces (the imaging surface and the surface perpendicular to the focused ion beam) and optimize acquisition (61). For symbiotic *Phaeocystis cordata*, trimming was targeted towards the periphery of hosts where microalgae were more abundant. After the sample was trimmed, it was mounted onto the edge of an SEM stub (Agar Scientific) using silver conductive epoxy (CircuitWorks) with the trimmed surfaces facing up and towards the edge of the stub. The sample was gold sputter-coated (Quorum Q150RS; 180 s at 30 mA) and placed into the FIB-SEM for acquisition (Crossbeam 540, Carl Zeiss Microscopy GmbH). Once the Region of Interest (ROI) was located in the sample, Atlas3D software (Fibics Inc. and Carl Zeiss Microscopy GmbH) was used to perform sample preparation and 3D acquisitions. First, a 1 μm platinum protective coat was deposited with a 1.5 nA FIB current. The rough trench was then milled to expose the imaging

cross-section with a 15 nA FIB current, followed by a polish at 7 nA. The 3D acquisition milling was conducted with a 1.5 nA FIB current. For SEM imaging, the beam was operated at 1.5 kV/700 pA in analytic mode using an EsB detector (1.1 kV grid collector voltage) at a dwell time of 8 μ s with no line averaging. The voxel size used throughout acquisitions was 5 or 10 nm. Datasets were initially aligned by the Fiji plugin “Linear Stack Alignment with SIFT” (62) then fine-tuned by AMST (63). Raw electron microscopy data are deposited in EMPIAR, accession code EMPIAR-XXX.

FIB-SEM Image analysis: segmentation and morphometric analyses

From the aligned FIB-SEM stack, images were binned in Fiji (<https://imagej.net/Fiji>), and regions of interest representing *Phaeocystis* cells were cropped. Segmentation and 3D reconstruction were performed using the work-flow developed in (64), and geometry measurements were provided using algorithms provided at (https://gitlab.com/clariaddy/stl_statistics and <https://gitlab.com/clariaddy/mindist>). Briefly, segmentation of organelles and vacuoles of *Phaeocystis* (considered as regions of interest) was carried out with 3DSlicer software (65) (www.slicer.org), using a supervised semi-automatic pixel classification mode (3 to 10 slices automatically segmented for each ROI). Each region was “colored” using paint tools and adjusting the threshold range of pixels values of the images. The Model maker module from 3D slicer was then used to generate corresponding 3D models which were exported in STL format. 3D reconstructed models were imported into the MeshLab software (66) to clean the model and reduce file size by model decimation. Metrics for volumes, surface area, and the area below the minimum distance between meshes were computed using Numpy-STL (<https://pypi.org/project/numpy-stl/>) and TRIMESH (<https://trimsh.org/trimesh.html>) python packages. Surfaces and volumes were computed using the discrete mesh geometry, the surface being computed directly from mesh triangles, and volume being obtained from the signed volume of individual tetrahedrons, assuming a watertight model. Proximity distance between organelles was calculated based on the closest points between two triangular meshes. The surface area below the proximity distance was quantified based on (i) the minimal distance between each vertex of the plastid mesh to the mitochondria mesh, and (ii) matching surface using face data according to a given distance threshold. A distance threshold ≤ 50 nm was chosen as representative of an interaction between nearby organelles, based on previous morphometric analyses in animal and plant cells (48, 67). Morphometric data are available in Dataset S1.

Single-cell chlorophyll fluorescence imaging

Single-cell chlorophyll fluorescence was detected with an imaging system (JBeamBio, France), mounted on an optical microscope (CKX 53 Olympus, Japan). The imaging setup consists of a high sensitivity camera (Orca Flash 4.0 LT, Hamamatsu, Japan) equipped with a near-infrared long-pass filter (RG 695 Schott, Germany). Regions of Interest (ROIs) containing host cells were identified using the microscope in transmission mode. The photosynthetic capacity of symbiotic *Phaeocystis* was quantified as the photochemical quantum yield of Photosystem II (F_v/F_m), calculated as $(F_m - F_o)/F_m$ (68). Cells were excited with blue light pulses ($\lambda = 470 \text{ nm} \pm 12 \text{ nm}$, duration 260 μ s) to evaluate minimum fluorescence emission F_o . Short green saturating pulses (λ

= 520 nm \pm 20 nm, intensity 3000 $\mu\text{mol photons m}^{-2} \text{s}^{-1}$, duration 250 ms) were used to reach maximum fluorescence emission (F_m). F_m was evaluated with the same blue pulses used for F_o , fired 10 μs after the saturating light was switched off. We used a 20X (NA = 0.45) objective to scan the slits. Single algal cells within a given ROI were imaged separately, with a pixel resolution of 1.7 μm^2 .

Comparative transcriptomics for symbiotic and free-living *Phaeocystis*

Individual acantharians ($n = 12$) were collected for single-host RNA-seq from the western subtropical North Pacific. RNA-seq was also performed with biological culture replicates ($n = 3$) of *Phaeocystis cordata* CCMP3104 (synonymous to RCC1383) to assemble a *de novo* reference transcriptome and to provide a comparison point for changes in symbiotic gene expression. Raw sequencing reads are available from the NCBI Sequencing Read Archive with accession PRJNA603434. Detailed descriptions of sampling, culturing, RNA extraction, sequencing, transcriptome assembly and annotation, differential expression and functional enrichment testing are presented in the SI Appendix and in Tables S1 and S2 and Fig. S10. All code and data analysis pipelines are available from GitHub (<https://maggimars.github.io/PcordataSymbiosisDGE/analysis.html>). Genes were considered significantly differentially expressed when the False Discovery Rate adjusted p -value (padj) was less than 0.05 and the log₂ fold-change was greater than |1|. Likewise, Gene Ontology (GO) and KEGG (Kyoto Encyclopedia of Genes and Genomes) pathways were considered significantly enriched among up- or downregulated genes when the padj from the respective enrichment test was less than 0.05.

¹³C bulk enrichment (EA-IRMS) and isotope analysis

Symbiotic acantharia were sampled as described above. Between 54 and 78 individual acantharian cells were pooled together. Two control samples were kept in unspiked filtered seawater (FSW, 0.22 μm) to obtain natural (background) ¹³C cell content and two experimental samples were incubated for one hour in ¹³C-bicarbonate spiked FSW at 20°C under constant light (100 $\mu\text{mol photons m}^{-2}\text{s}^{-1}$). To start the incubation, H¹³CO₃ (99%¹³C; Cambridge Isotopes Laboratory Inc.) was added to the FSW (0.2 mM, 10% final concentration). After one hour, acantharian cells were immediately harvested by centrifugation and rinsed three times with FSW and one time with Milli-Q water. All individuals in each sample were then transferred to tin capsules and dried at room temperature for three days.

In parallel, cultures of free-living *Phaeocystis cordata* RCC1383 maintained at 20°C in K5 culture medium and at 100 $\mu\text{mol photons m}^{-2}\text{s}^{-1}$ were also incubated for 1 hour with ¹³C-bicarbonate spiked K5 medium (0.2 mM, 10% final concentration). As for symbiotic cells, two samples were used as controls to obtain natural (background) ¹³C cell content and were kept in unspiked K5 medium. To harvest cells, cultures were centrifuged and rinsed four times with FSW (0.22 μm). Before free-living were transferred to tin capsules, an aliquot was taken from each sample to count the number of cells per sample (Dataset S2). Tin capsules were dried for one day at 37°C.

Samples were analyzed for ^{13}C -enrichment using an Elemental Analyser (Flash 2000, Thermo scientific, Milan, Italy) coupled to an Isotopic Ratio Mass Spectrometer (IRMS Delta V Plus with a Conflo IV Interface, Thermo scientific, Bremen, Germany). Atom% of samples was derived from isotope ratio data and calculated using the Vienna Pee Dee Belemnite standard ($R_{\text{VPDB}} = 0.0112372$)

$$R_{\text{sample}} = (X_{\text{sample}}/1000 + 1) \times R_{\text{standard}} \quad (1)$$

$$\text{atom}\%X[\%] = R_{\text{sample}}/(1 + R_{\text{sample}}) \quad (2)$$

The uptake of ^{13}C (I_{isotope}) in acantharia and *Phaeocystis* cells was obtained from the excess E of the ^{13}C stable isotope in the sample above background ($E = \text{atom}\%X_{\text{sample}} - \text{atom}\%X_{\text{control}}$), and total carbon content in the sample or cell.

$$I_{\text{isotope}} = E \times \mu\text{g C per sample (per cell)} \quad (3)$$

To measure ^{13}C uptake of symbiotic *Phaeocystis* cells in Acantharia, we estimated that one acantharian cell harbors an average of 30 cells (29 ± 27 , (1)). Note that we also added the values calculated for 60 symbiotic *Phaeocystis* per Acantharia to have conservative estimations of ^{13}C -uptake in Acantharia cells (Dataset S2). The uptake of ^{13}C (I_{isotope} , pg. cell $^{-1}$) for symbiotic *Phaeocystis* cells was calculated using these estimations. A short incubation (1 hour) was chosen to reduce the effect of cell respiration and C-compound exudation on measured ^{13}C uptake values.

NanoSIMS imaging and associated sample preparation

Upon collection, symbiotic acantharians were maintained in filtered seawater for 24 hours. Cells were then incubated with ^{13}C -labelled bicarbonate (0.4 mM, corresponding to a 16% ^{13}C labeling) for five hours and cryofixed as for electron microscopy according to a freeze substitution protocol from (18). Semi-thin sections (200 nm) were placed on boron-doped silicon wafers, coated with a 20 nm Au/Pd (80/20) layer and analyzed with a nanoSIMS 50L (Cameca) at the ProVIS Centre for Chemical Microscopy (UFZ Leipzig). The analysis areas involving symbiotic algal cells were defined from SEM observations on consecutive sections. Before analysis, pre-implantation with 200 pA of 16 keV Cs^+ ion beam was performed for 15–20 min in 100x100 μm^2 area to equilibrate the yield of negative secondary ions. Upon analysis, a 16 keV Cs^+ primary ion beam of 1–2 pA focused to approximately 70 nm was rastered over the sample area between 15x15 μm^2 and 70x70 μm^2 , with a dwelling time of 2 ms pixel $^{-1}$ in a 512x512 or 1024x1024 pixel pattern, keeping the physical pixel size well below the beam-spot size in order to avoid an ion-beam induced surface roughening. Secondary ions extracted from each pixel of the sample surface were analyzed for their mass to charge (m/z) ratio and counted separately with seven electron multiplier detectors. To resolve isobaric interferences, the mass resolving power (MRP) of the spectrometer was set > 8000 (M/DM) with the entrance slit of 20x140 μm (width x height; nominal size), 200x200 μm aperture, 40x1800 μm exit slits and the energy slit cutting-off 20% of $^{12}\text{C}^{14}\text{N}^-$ ions at their high-energy distribution site. Secondary ion species ($^{16}\text{O}^-$, $^{12}\text{C}_2^-$, $^{12}\text{C}^{13}\text{C}^-$, $^{12}\text{C}^{14}\text{N}^-$, $^{13}\text{C}^{14}\text{N}^-$, $^{31}\text{P}^-$, $^{32}\text{S}^-$) were simultaneously detected in single-ion counting mode. The acquired 40 serial maps of secondary ion count were corrected for lateral drift and accumulated with the

Look@NanoSims software (69). Isotope ratios were calculated for each ROI defined with LANS either in automatic thresholding mode or by manual drawing over cell compartments recognized in ion-count/ratio maps (normalized by scans and pixel number) and correlative SEM images. The fraction of assimilated carbon relative to its initial content (relative carbon assimilation, K_a) was derived from the changes in carbon-isotope composition as described in (70).

Photon propagation model: Finite-difference time-domain simulations

To study the role of light scattering from the 3D mitochondrial network we performed 3D finite-difference time-domain (FDTD) calculations using a Maxwell equation solver (Lumerical FDTD Solutions 8.16). FDTD allows for discretizing the real-space time-domain Maxwell equations onto a regular lattice in time and space with equidistant time steps and cubic voxels on the Yee grid. The propagation of the electromagnetic field is modelled by time stepwise forward integration. For plastids, we assumed that the real part of the refractive index was minimally wavelength dependent (between 1.352–1.364 for 400–700 nm), while the imaginary part of the refractive index (k) was governed by the characteristic absorption profile of chlorophyll *a* (71). The real refractive index (n) of mitochondria was assumed to be 1.4, which is a moderate estimate for such strongly light scattering structures (52, 72) with a reduced scattering coefficient about two orders of magnitude greater than the absorption coefficient ($\mu_s' > 100 \mu_a$) (52). The background n of the cell was similar to water ($n = 1.34$). For each cell type (i.e. free-living and symbiotic) we performed calculations in the presence and absence of mitochondria. Additionally, we replaced the mitochondria with a solid sphere of the same volume, to visualise the beneficial light spreading by the intricate mitochondrial network over a solid sphere with the same refractive index properties. For each simulation, excitation was provided by a plane wave that was incident in either the x , y or z plane. Only one plane is shown as the results were largely independent of the incident plane. The numerical stability of the simulation was ensured by selecting boundary conditions and simulation times (> 150 fs) that confirmed that the electric field in the structure decayed prior to the end of the simulation, such that all of the incident excitation was lost from the grid.

Acknowledgments

This project received funding from the ATIP-Avenir program, a Défi X-Life grant from CNRS, the LabEx GRAL (ANR-10-LABX-49-01), financed within the University Grenoble Alpes graduate school (Ecoles Universitaires de Recherche) CBH-EUR-GS (ANR-17-EURE-0003). J.D. was supported by the ATIP-Avenir program. C.U. was supported by a joint UGA-ETH Zurich PhD grant in the framework of the "Investissements d'avenir" programme (ANR-15-IDEX-02). M.M.B. was supported by a DC1 graduate fellowship awarded by the Japan Society for the Promotion of Science. D.W. was funded by the Gordon and Betty Moore Foundation and L.S. was supported by the Isaac Newton Trust. G.F. and D.F. received funding from the European Research Council: ERC Chloro-mito (grant no. 833184). This project also received funds from the European Union's Horizon 2020 research and innovation programme CORBEL under the grant agreement No 654248. We thank the institutes that supported the collection of samples: EMBRC-France and the Laboratoire d'Océanographie de Villefranche-sur-Mer (John Dolan and the marine crew). This

work used the platforms of the Grenoble Instruct-ERIC centre (ISBG ; UMS 3518 CNRS-CEA-UGA-EMBL) within the Grenoble Partnership for Structural Biology (PSB), supported by FRISBI (ANR-10-INBS-05-02) and GRAL, financed within the University Grenoble Alpes graduate school (Ecoles Universitaires de Recherche) CBH-EUR-GS (ANR-17-EURE-0003). We thank Guy Schoehn and the electron microscope facility, which is supported by the Auvergne-Rhône-Alpes Region, the Fondation Recherche Medicale (FRM), the fonds FEDER and the GIS-Infrastructures en Biologie Sante et Agronomie (IBISA). We are thankful for the use of the analytical facilities of the Centre for Chemical Microscopy (ProVIS) at UFZ Leipzig, which is supported by European Regional Development Funds (EFRE—Europe funds Saxony) and the Helmholtz Association. Sampling and molecular work for transcriptome analysis was funded by the Marine Biophysics Unit of the Okinawa Institute of Science and Technology (OIST) Graduate University. We thank the captain and crew of the JAMSTEC R/V *Mirai* for their assistance and support in sample collection. Hiromi Watanabe, Dhugal Lindsay, and Yuko Hasagawa were instrumental in organizing and facilitating cruise sampling. Lisa Mesrop and Dave Caron collaborated to optimize single-host RNA-seq. Hiroki Goto and the OIST DNA Sequencing Section performed sequencing and provided guidance. We also thank Gaël Guillou, Benoit Lebreton and the Plateforme de Spectrométrie Isotopique of the La Rochelle University, which is funded by FEDER Poitou-Charentes and the Région Nouvelle Aquitaine (2017-2021).

References

1. J. Decelle, *et al.*, An original mode of symbiosis in open ocean plankton. *Proc. Natl. Acad. Sci. U. S. A.* **109**, 18000–18005 (2012).
2. J. Decelle, S. Colin, R. A. Foster, “Photosymbiosis in Marine Planktonic Protists” in *Marine Protists: Diversity and Dynamics*, S. Ohtsuka, T. Suzuki, T. Horiguchi, N. Suzuki, F. Not, Eds. (Springer Japan, 2015), pp. 465–500.
3. D. A. Caron, A. F. Michaels, N. R. Swanberg, F. A. Howse, Primary productivity by symbiont-bearing planktonic sarcodines (Acantharia, Radiolaria, Foraminifera) in surface waters near Bermuda. *J. Plankton Res.* **17**, 103–129 (1995).
4. A. F. Michaels, Acantharian abundance and symbiont productivity at the VERTEX seasonal station. *J. Plankton Res.* **13**, 399–418 (1991).
5. A. F. Michaels, D. A. Caron, N. R. Swanberg, F. A. Howse, C. M. Michaels, Planktonic sarcodines (Acantharia, Radiolaria, Foraminifera) in surface waters near Bermuda: abundance, biomass and vertical flux. *J. Plankton Res.* **17**, 131–163 (1995).
6. P. Martin, *et al.*, Sedimentation of acantharian cysts in the Iceland Basin: Strontium as a ballast for deep ocean particle flux, and implications for acantharian reproductive strategies. *Limnol. Oceanogr.* **55**, 604–614 (2010).
7. A. Gutierrez-Rodriguez, *et al.*, High contribution of Rhizaria (Radiolaria) to vertical export in the California Current Ecosystem revealed by DNA metabarcoding. *ISME J.* **13**, 964–976 (2019).

8. D. Yellowlees, T. A. V. Rees, W. Leggat, Metabolic interactions between algal symbionts and invertebrate hosts. *Plant Cell Environ.* **31**, 679–694 (2008).
9. J. Decelle, New perspectives on the functioning and evolution of photosymbiosis in plankton: Mutualism or parasitism? *Commun. Integr. Biol.* **6**, e24560 (2013).
10. A. E. Douglas, D. C. Smith, Are endosymbioses mutualistic? *Trends Ecol. Evol.* **4**, 350–352 (1989).
11. S. Karkar, F. Facchinelli, D. C. Price, A. P. M. Weber, D. Bhattacharya, Metabolic connectivity as a driver of host and endosymbiont integration. *Proc. Natl. Acad. Sci. U. S. A.* **112**, 10208–10215 (2015).
12. D. Bhattacharya, J. M. Archibald, A. P. M. Weber, A. Reyes-Prieto, How do endosymbionts become organelles? Understanding early events in plastid evolution. *Bioessays* **29**, 1239–1246 (2007).
13. P. J. Keeling, The number, speed, and impact of plastid endosymbioses in eukaryotic evolution. *Annu. Rev. Plant Biol.* **64**, 583–607 (2013).
14. J. M. Archibald, Endosymbiosis and Eukaryotic Cell Evolution. *Curr. Biol.* **25**, R911–21 (2015).
15. J. M. Archibald, The puzzle of plastid evolution. *Curr. Biol.* **19**, R81–8 (2009).
16. E. Hehenberger, R. J. Gast, P. J. Keeling, A kleptoplastidic dinoflagellate and the tipping point between transient and fully integrated plastid endosymbiosis. *Proc. Natl. Acad. Sci. U. S. A.* **116**, 17934–17942 (2019).
17. E. C. M. Nowack, M. Melkonian, G. Glöckner, Chromatophore genome sequence of *Paulinella* sheds light on acquisition of photosynthesis by eukaryotes. *Curr. Biol.* **18**, 410–418 (2008).
18. J. Decelle, *et al.*, Algal Remodeling in a Ubiquitous Planktonic Photosymbiosis. *Curr. Biol.* **29**, 968–978.e4 (2019).
19. J. Febvre, C. Febvre-Chevalier, Ultrastructural study of zooxanthellae of three species of *Acantharia* (Protozoa: Actinopoda), with details of their taxonomic position in the prymnesiales (Prymnesiophyceae, Hibberd, 1976). *J. Mar. Biol. Assoc. U. K.* **59**, 215–226 (1979).
20. P. G. Verity, V. Smetacek, Organism life cycles, predation, and the structure of marine pelagic ecosystems. *Mar. Ecol. Prog. Ser.* **130**, 277–293 (1996).
21. V. Schoemann, S. Becquevort, J. Stefels, V. Rousseau, C. Lancelot, *Phaeocystis* blooms in the global ocean and their controlling mechanisms: a review. *J. Sea Res.* **53**, 43–66 (2005).
22. M. Mars Brisbin, L. Y. Mesrop, M. M. Grossmann, S. Mitarai, Intra-host Symbiont Diversity and Extended Symbiont Maintenance in Photosymbiotic *Acantharea* (Clade F). *Front. Microbiol.* **9**, 1998 (2018).
23. A. R Jones, *et al.*, Cell-size dependent progression of the cell cycle creates homeostasis and flexibility of plant cell size. *Nat. Commun.* **8**, 15060 (2017).

24. A. R. Jones, W. Dewitte, Cell size and cell cycle progression: the cyclin-dependent kinase link in green algae. *J. Exp. Bot.* **70**, 731–733 (2019).
25. F.-M. Boisvert, S. van Koningsbruggen, J. Navascués, A. I. Lamond, The multifunctional nucleolus. *Nat. Rev. Mol. Cell Biol.* **8**, 574–585 (2007).
26. H. Tamaru, Confining euchromatin/heterochromatin territory: jumonji crosses the line. *Genes Dev.* **24**, 1465–1478 (2010).
27. E. A. Titlyanov, *et al.*, Degradation of zooxanthellae and regulation of their density in hermatypic corals. *Marine Ecology Progress Series* **139**, 167–178 (1996).
28. T. Xiang, *et al.*, Symbiont population control by host-symbiont metabolic interaction in Symbiodiniaceae-cnidarian associations. *Nat. Commun.* **11**, 108 (2020).
29. E. R. Annis, C. B. Cook, Alkaline phosphatase activity in symbiotic dinoflagellates (zooxanthellae) as a biological indicator of environmental phosphate exposure. *Mar. Ecol. Prog. Ser.* **245**, 11–20 (2002).
30. L. Alipanah, *et al.*, Molecular adaptations to phosphorus deprivation and comparison with nitrogen deprivation responses in the diatom *Phaeodactylum tricornutum*. *PLoS One* **13**, e0193335 (2018).
31. T. Li, *et al.*, Identification and Expression Analysis of an Atypical Alkaline Phosphatase in *Emiliana huxleyi*. *Front. Microbiol.* **9**, 2156 (2018).
32. E. Sanz-Luque, A. Chamizo-Ampudia, A. Llamas, A. Galvan, E. Fernandez, Understanding nitrate assimilation and its regulation in microalgae. *Front. Plant Sci.* **6**, 899 (2015).
33. L. Alipanah, J. Rohloff, P. Winge, A. M. Bones, T. Brembu, Whole-cell response to nitrogen deprivation in the diatom *Phaeodactylum tricornutum*. *J. Exp. Bot.* **66**, 6281–6296 (2015).
34. D. Rudra, J. R. Warner, What better measure than ribosome synthesis? *Genes Dev.* **18**, 2431–2436 (2004).
35. P. W. Siersma, K. S. Chiang, Conservation and degradation of cytoplasmic and chloroplast ribosomes in *Chlamydomonas reinhardtii*. *J. Mol. Biol.* **58**, 167–185 (1971).
36. C. LeKieffre, *et al.*, Ammonium is the preferred source of nitrogen for planktonic foraminifer and their dinoflagellate symbionts. *Proc. Biol. Sci.* **287**, 20200620 (2020).
37. Z. Liu, L. Y. Mesrop, S. K. Hu, D. A. Caron, Transcriptome of *Thalassicolla nucleata* holobiont reveals details of a radiolarian symbiotic relationship. *Frontiers in Marine Science* (2019).
38. K. Maor-Landaw, M. J. H. van Oppen, G. I. McFadden, Symbiotic lifestyle triggers drastic changes in the gene expression of the algal endosymbiont *Breviolum minutum* (Symbiodiniaceae). *Ecol. Evol.* **10**, 451–466 (2020).
39. N. Sumiya, Mechanism of coordination between cell and chloroplast division in unicellular algae. *PLANT MORPHOLOGY* **30**, 83–89 (2018).
40. D. Xiong, J. Huang, S. Peng, Y. Li, A few enlarged chloroplasts are less efficient in

photosynthesis than a large population of small chloroplasts in *Arabidopsis thaliana*. *Sci. Rep.* **7**, 5782 (2017).

41. J. V. Moroney, R. A. Ynalvez, Proposed carbon dioxide concentrating mechanism in *Chlamydomonas reinhardtii*. *Eukaryot. Cell* **6**, 1251–1259 (2007).
42. B. D. Engel, *et al.*, Native architecture of the *Chlamydomonas* chloroplast revealed by in situ cryo-electron tomography. *Elife* **4** (2015).
43. J.-D. Rochaix, The Pyrenoid: An Overlooked Organelle Comes out of Age. *Cell* **171**, 28–29 (2017).
44. K. W. Becker, *et al.*, Daily changes in phytoplankton lipidomes reveal mechanisms of energy storage in the open ocean. *Nat. Commun.* **9**, 5179 (2018).
45. B. Westermann, Bioenergetic role of mitochondrial fusion and fission. *Biochim. Biophys. Acta* **1817**, 1833–1838 (2012).
46. J. B. Spinelli, M. C. Haigis, The multifaceted contributions of mitochondria to cellular metabolism. *Nat. Cell Biol.* **20**, 745–754 (2018).
47. B. Bailleul, *et al.*, Energetic coupling between plastids and mitochondria drives CO₂ assimilation in diatoms. *Nature* **524**, 366–369 (2015).
48. S. J. Mueller-Schuessele, M. Michaud, “Plastid Transient and Stable Interactions with Other Cell Compartments” in *Plastids: Methods and Protocols*, E. Maréchal, Ed. (Springer US, 2018), pp. 87–109.
49. B. Ghysels, D. Godaux, R. F. Matagne, P. Cardol, F. Franck, Function of the chloroplast hydrogenase in the microalga *Chlamydomonas*: the role of hydrogenase and state transitions during photosynthetic activation in anaerobiosis. *PLoS One* **8**, e64161 (2013).
50. A. L. Holt, S. Vahidinia, Y. L. Gagnon, D. E. Morse, A. M. Sweeney, Photosymbiotic giant clams are transformers of solar flux. *J. R. Soc. Interface* **11**, 20140678 (2014).
51. D. Wangpraseurt, *et al.*, Bionic 3D printed corals. *Nat. Commun.* **11**, 1748 (2020).
52. B. Beauvoit, T. Kitai, B. Chance, Contribution of the mitochondrial compartment to the optical properties of the rat liver: a theoretical and practical approach. *Biophys. J.* **67**, 2501–2510 (1994).
53. S. K. Davy, D. Allemand, V. M. Weis, Cell biology of cnidarian-dinoflagellate symbiosis. *Microbiol. Mol. Biol. Rev.* **76**, 229–261 (2012).
54. W.-C. Chin, M. V. Orellana, I. Quesada, P. Verdugo, Secretion in unicellular marine phytoplankton: demonstration of regulated exocytosis in *Phaeocystis globosa*. *Plant Cell Physiol.* **45**, 535–542 (2004).
55. E. C. M. Nowack, *Paulinella chromatophora* – rethinking the transition from endosymbiont to organelle. *Acta Soc. Bot. Pol.* **83**, 387–397 (2014).
56. N. Okamoto, I. Inouye, A secondary symbiosis in progress? *Science* **310**, 287 (2005).

57. R. Onuma, *et al.*, Changes in the transcriptome, ploidy, and optimal light intensity of a cryptomonad upon integration into a kleptoplastic dinoflagellate. *ISME J.* **14**, 2407–2423 (2020).
58. M. D. Johnson, The acquisition of phototrophy: adaptive strategies of hosting endosymbionts and organelles. *Photosynth. Res.* **107**, 117–132 (2011).
59. S.-F. Zhang, K. Zhang, H.-M. Cheng, L. Lin, D.-Z. Wang, Comparative transcriptomics reveals colony formation mechanism of a harmful algal bloom species *Phaeocystis globosa*. *Sci. Total Environ.* **719**, 137454 (2020).
60. M. Mars Brisbin, S. Mitarai, Differential Gene Expression Supports a Resource-Intensive, Defensive Role for Colony Production in the Bloom-Forming Haptophyte, *Phaeocystis globosa*. *J. Eukaryot. Microbiol.* **66**, 788–801 (2019).
61. B. Maco, *et al.*, Semiautomated correlative 3D electron microscopy of in vivo-imaged axons and dendrites. *Nat. Protoc.* **9**, 1354–1366 (2014).
62. D. G. Lowe, Distinctive Image Features from Scale-Invariant Keypoints. *Int. J. Comput. Vis.* **60**, 91–110 (2004).
63. J. Hennies, *et al.*, AMST: Alignment to Median Smoothed Template for Focused Ion Beam Scanning Electron Microscopy Image Stacks. *Sci. Rep.* **10**, 2004 (2020).
64. C. Uwizeye, *et al.*, In-cell quantitative structural imaging of phytoplankton using 3D electron microscopy. *Cold Spring Harbor Laboratory*, 2020.05.19.104166 (2020).
65. R. Kikinis, S. D. Pieper, K. G. Vosburgh, “3D Slicer: A Platform for Subject-Specific Image Analysis, Visualization, and Clinical Support” in *Intraoperative Imaging and Image-Guided Therapy*, F. A. Jolesz, Ed. (Springer New York, 2014), pp. 277–289.
66. P. Cignoni, *et al.*, Meshlab: an open-source mesh processing tool in *Eurographics Italian Chapter Conference*, (Salerno, 2008), pp. 129–136.
67. L. Scorrano, *et al.*, Coming together to define membrane contact sites. *Nat. Commun.* **10**, 1287 (2019).
68. W. L. Butler, Energy Distribution in the Photochemical Apparatus of Photosynthesis. *Annu. Rev. Plant Physiol.* **29**, 345–378 (1978).
69. L. Polerecky, *et al.*, Look@ NanoSIMS--a tool for the analysis of nanoSIMS data in environmental microbiology. *Environ. Microbiol.* **14**, 1009–1023 (2012).
70. H. Stryhanyuk, *et al.*, Calculation of Single Cell Assimilation Rates From SIP-NanoSIMS-Derived Isotope Ratios: A Comprehensive Approach. *Front. Microbiol.* **9**, 2342 (2018).
71. H. Qi, Z.-Z. He, F.-Z. Zhao, L.-M. Ruan, Determination of the spectral complex refractive indices of microalgae cells by light reflectance-transmittance measurement. *Int. J. Hydrogen Energy* **41**, 4941–4956 (2016).
72. J. D. Wilson, W. J. Cottrell, T. H. Foster, Index-of-refraction-dependent subcellular light scattering observed with organelle-specific dyes. *J. Biomed. Opt.* **12**, 014010 (2007).

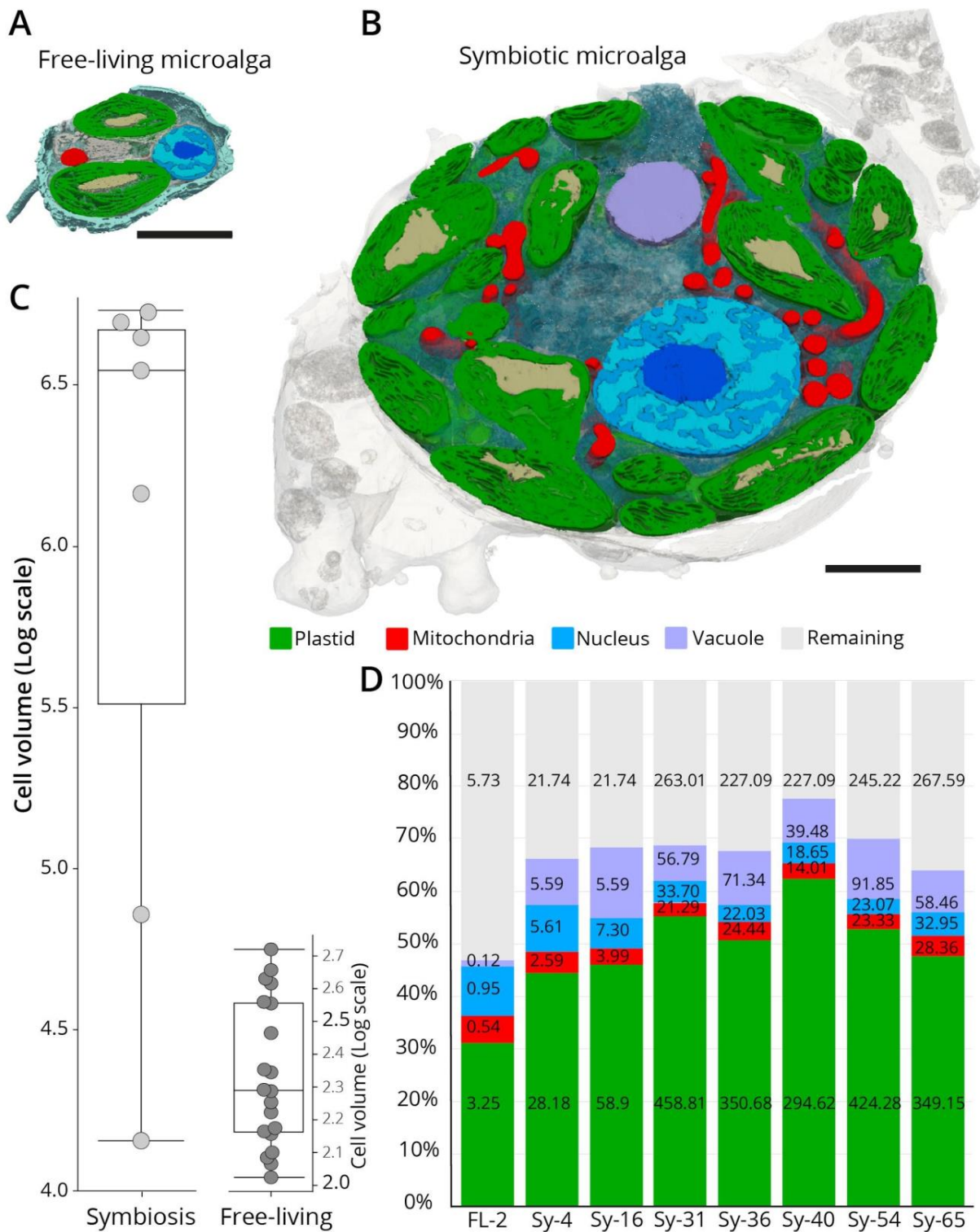


Figure 1. Morphological transformation of the microalga *Phaeocystis cordata* in symbiosis unveiled by FIB-SEM.

A–B) Sections of the 3D reconstruction of the free-living (A) and symbiotic (B) *Phaeocystis* cells as revealed by FIB-SEM (Focused Ion Beam-Scanning Electron Microscopy), showing multiplication of plastids (green) with immersed pyrenoids (light brown), extension of the mitochondria (red), nuclear compartments (nucleolus in dark blue, heterochromatin in blue, and euchromatin in light blue), and vacuoles (purple). Scale bar: 2 μm . **C)** Box plots showing the increase of the cell volume (log scale, μm^3) in symbiotic *Phaeocystis* (left) compared to the free-living cells (right). **D)** Relative volume occupancy of different organelles and cellular compartments (plastid, mitochondria, nucleus, vacuole) as % occupancy in the cell (organelle volume/cell volume ratio) in free-living (FL-2 plastids) and seven different symbiotic microalgal cells (Sy) having 2, 4, 16, 31, 36, 40, 54, 65 plastids. The volumes (μm^3) of organelles and cellular compartments are given within respective bar segments, and in Dataset S1

expression of *Phaeocystis* genes in the KEGG cell cycle reference pathway (ko04110). Blocks representing protein and enzymes are colored according to differential gene expression results. Solid blue indicates genes that were significantly downregulated in symbiosis ($\text{padj} < 0.05$, $\log_2\text{FC} < -1$); transparent blue indicates genes that had a negative fold-change in symbiosis but the difference was not statistically significant; transparent red indicates genes that had a positive, but statistically insignificant, fold-change in symbiosis; white indicates proteins without annotated genes. **C)** Heatmap of alkaline phosphatase gene expression (*phoA* and *ehp1*-like) as log normalized counts in free-living *Phaeocystis cordata* cultures ($n = 3$) and in individual hosts ($n = 12$). Alkaline phosphatase expression is a marker for phosphorus limitation in microalgae and these genes were mostly not expressed in symbiosis. **D)** Differential expression of genes in the Nitrogen metabolism KEGG reference pathway (ko00910). Inorganic nitrogen transporters, especially those encoded by *Nrt*, are marker genes for nitrogen limitation in microalgae. Genes that were significantly downregulated in symbiosis are colored blue and those that were significantly upregulated are red. The \log_2 fold-change values for differentially expressed genes are indicated next to or below the gene name.

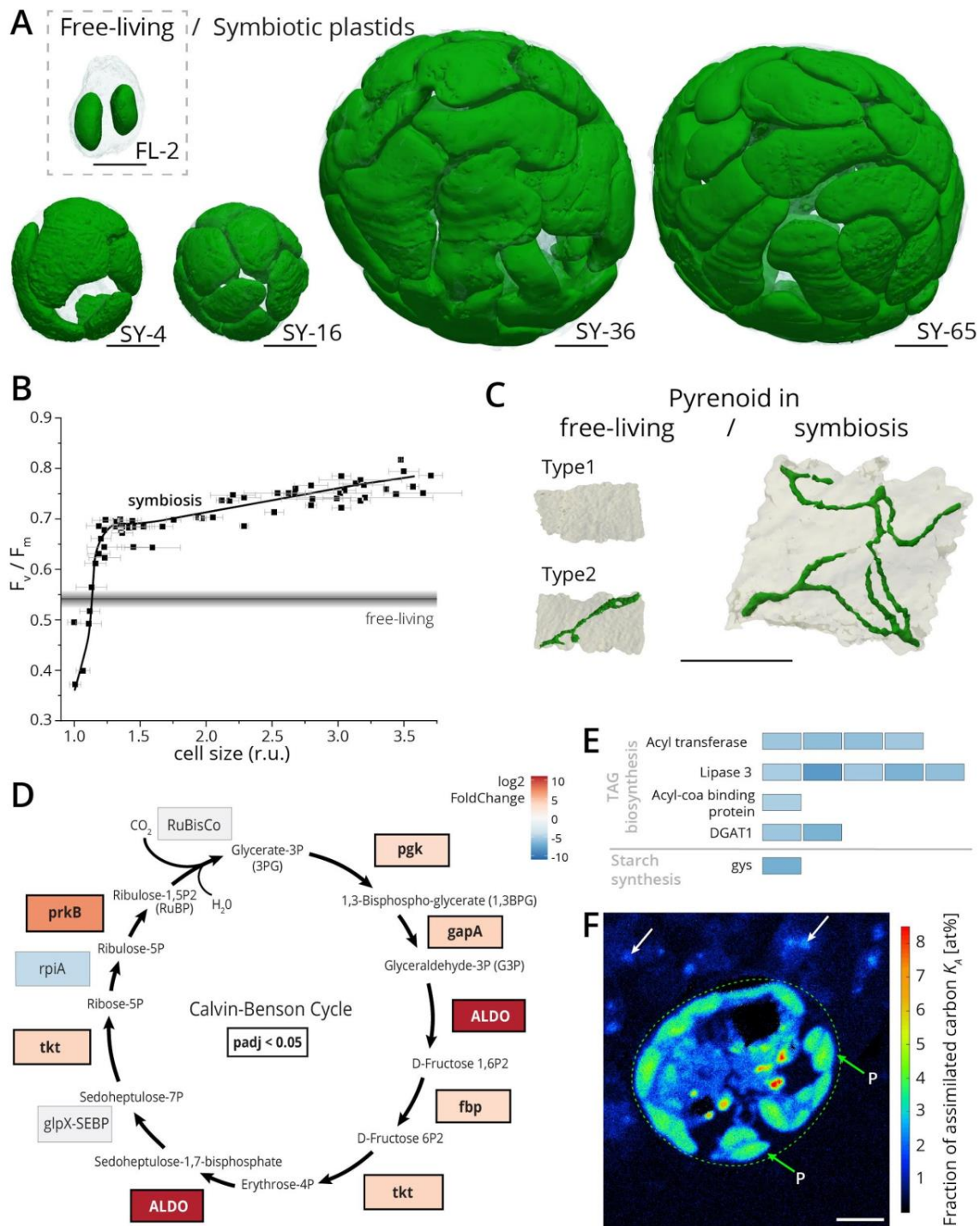


Figure 3. Morphological transformation of the photosynthetic machinery in symbiosis and associated physiological and gene expression activity.

A) Multiplication of plastids in *Phaeocystis* cells unveiled by FIB-SEM from two in free-living stage (top left) to up to 65 plastids (Sy-65) in symbiosis (see also Fig. S3 and S4). Scale bar: 2 μ m. **B)**

Single-cell chlorophyll fluorescence imaging showing that the photosynthetic capacity (F_v/F_m parameter) changes as a function of the relative cell size of symbiotic *Phaeocystis* (symbols). The black line represents the mean F_v/F_m value in free-living cells (\pm s.d., grey lines). **C**) Architecture and organization of pyrenoids in plastids of free-living (two types: with and without tubule) and symbiotic *Phaeocystis*, showing the increased volume of the pyrenoid in symbiosis with multiple thylakoids crossing the pyrenoid (dark green tubules). Scale bar: 1 μ m. (See also Fig. S5). **D–E**) Differential expression results for genes encoding enzymes of the Calvin-Benson Cycle (D) and proteins involved in storage molecule biosynthesis (E). The color scale indicates log₂ fold-change in symbiosis so that positive values (red) represent upregulation in symbiotic cells and negative values (blue) represent downregulation in symbiotic cells. Significantly differentially expressed genes (false discovery rate adjusted p -value, $p_{adj} < 0.05$) are highlighted with bolded gene names and black boxes in D; all results were significant in E. When several isoforms were expressed for a single gene (Acyl transferase, Ligase 3, and DGAT1), the log₂ fold-change is shown for each isoform. TAG stands for triacylglycerol. **F**) Single Isotope Probing-NanoSIMS-derived map of carbon relative assimilation (K_a , (70)) showing the fraction of carbon (relative to its initial content) assimilated during 5 hours of incubation with ¹³C-labelled bicarbonate in one symbiotic *Phaeocystis* cell (mainly allocated to plastids) and transferred to the host cytoplasm in specific cellular locations (See also Fig. S6). Green arrows indicate the plastids (P) of symbiotic microalgae (surrounded by the dashed circle) showing about 5 at% of relative carbon assimilation. White arrows indicate host areas revealing about 1–3 at% of the assimilated carbon fraction. Scale bar: 3 μ m.

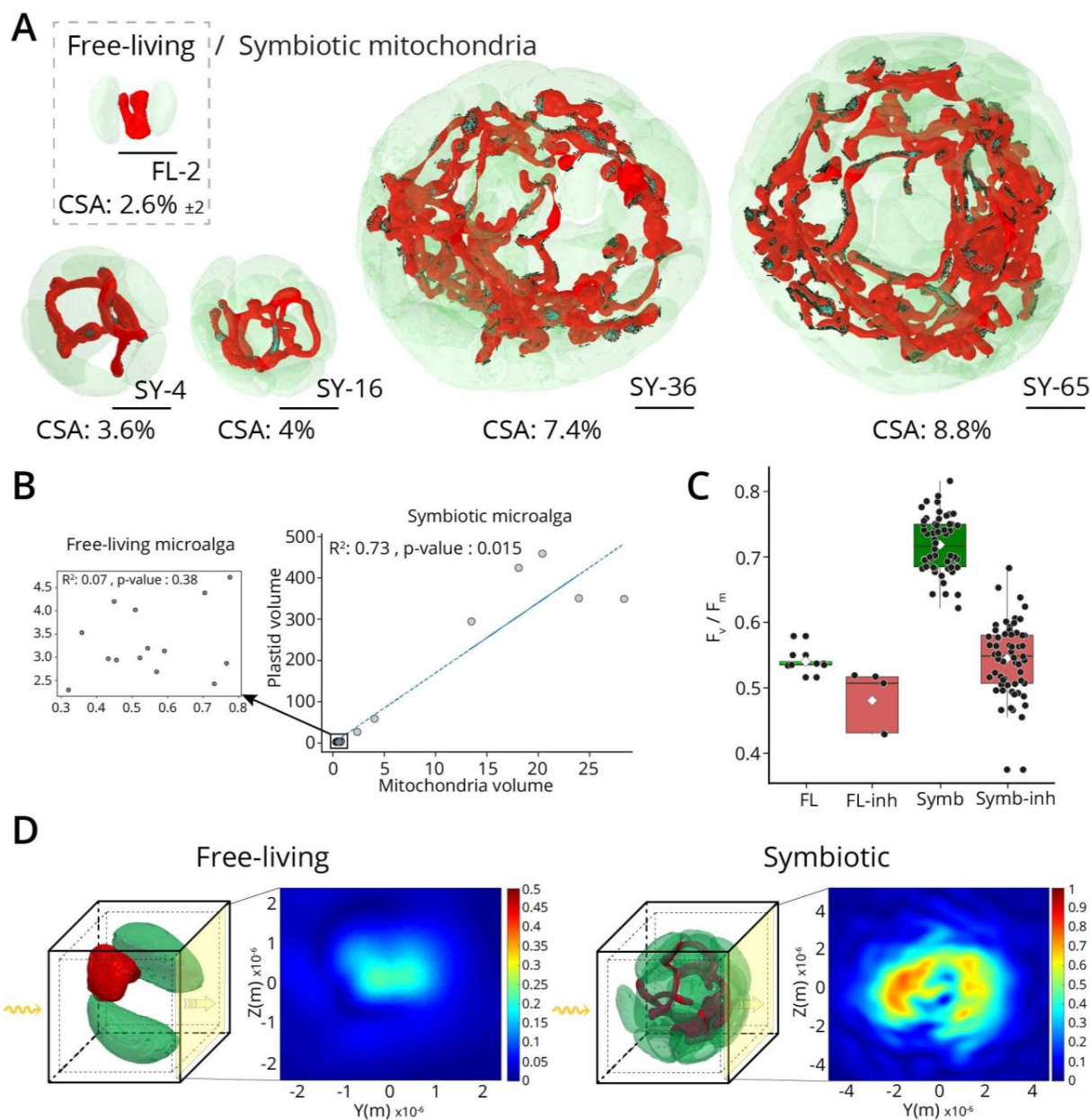


Figure 4. Expansion of the reticulate mitochondria in symbiosis and its interaction with plastids and role in light capture.

A) Extension of the mitochondria (red) in symbiotic *Phaeocystis* cell towards a fine reticular network in contact with plastids. A free-living *Phaeocystis* cell (top left) and four symbiotic *Phaeocystis* cells (Sy) are represented with their 4, 16, 36 and 65 plastids in transparency. Contact surface area (≤ 50 nm, CSA) between the mitochondria and the plastids have been quantified and represented in dark green colors. The mitochondrial surface area in contact with plastids (CSA) increased from $2.6 \pm 2\%$ ($n = 14$) in free-living to up to 8.79% in symbiosis (Sy-

65). (See also Fig. S7). Scale bar: 2 μm . **B)** Scatter plot showing the correlation between the volume of the plastid and the volume of the mitochondria in 20 free-living cells (left insert) and in seven symbiotic *Phaeocystis* cells. **C)** Box plot showing the effect of mitochondrial inhibitors (inh: 5 μM Antimycin A and 1 mM Salicylhydroxamic acid-SHAM) on the F_v/F_m parameter of free-living (left) and symbiotic (right) *Phaeocystis* cells. **D)** Finite-difference-time-domain (FDTD) model calculating the distribution of the light scattering cross-section (σ) based on 3D architectures of microalgal cells. Light scattering by free-living cells (left) is forward directed while light scattering by symbiotic cells (right, 16 plastids) is distributed, yielding an enhanced electric field distribution. Note that due to small light scattering by free-living cells, the scale was adjusted for improved visualisation. The outer and inner boxes represent the scattering monitor and the absorption monitor, respectively. Behind the cell, the yellow plane is measuring the transmitted field direction flow (poynting vector). The yellow arrows correspond to the incident plane wave (See also Fig. S9).

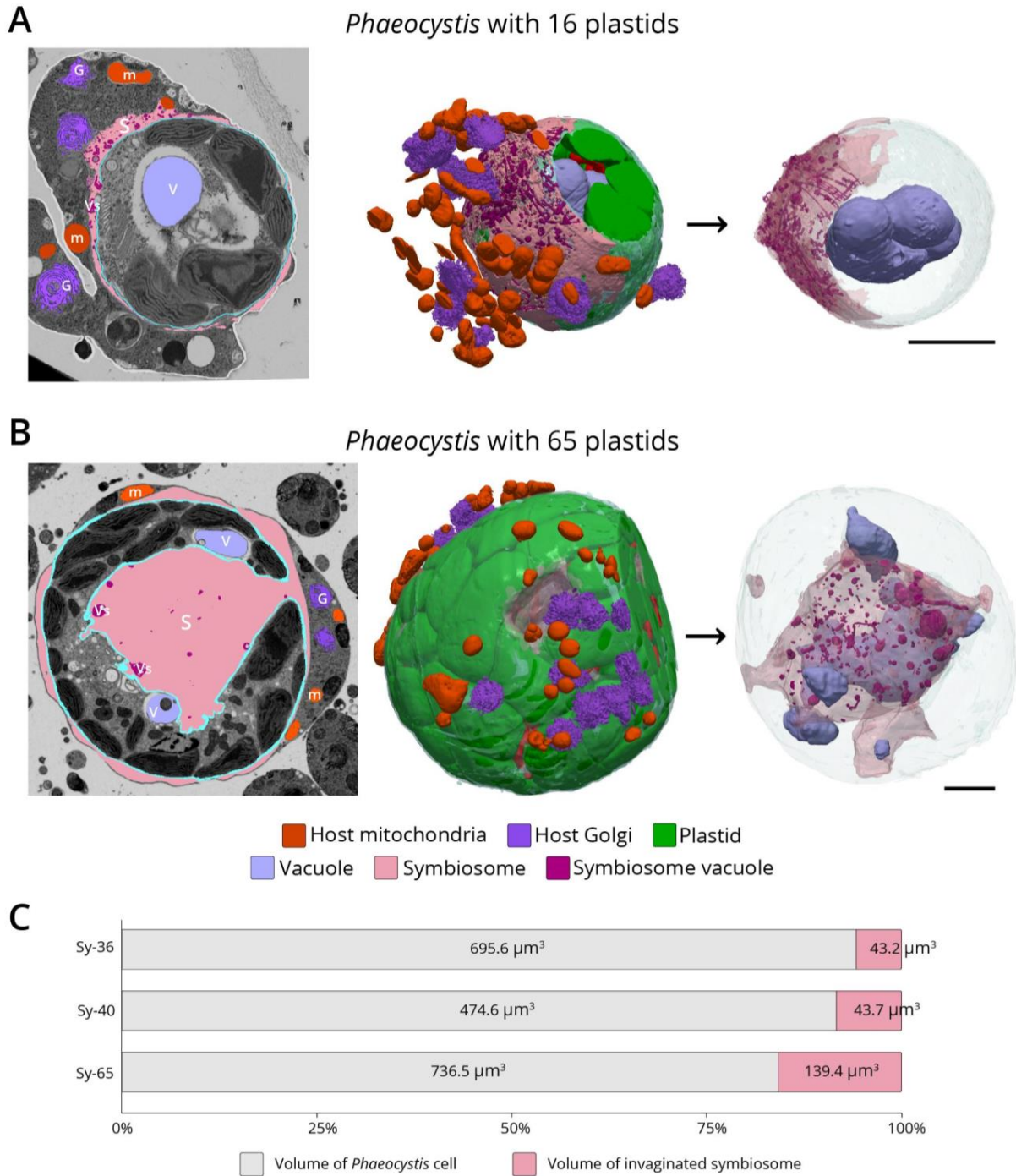
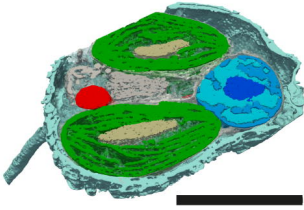


Figure 5. Host-symbiont integration and morphometrics of the symbiosome invagination in large symbiotic microalgae.

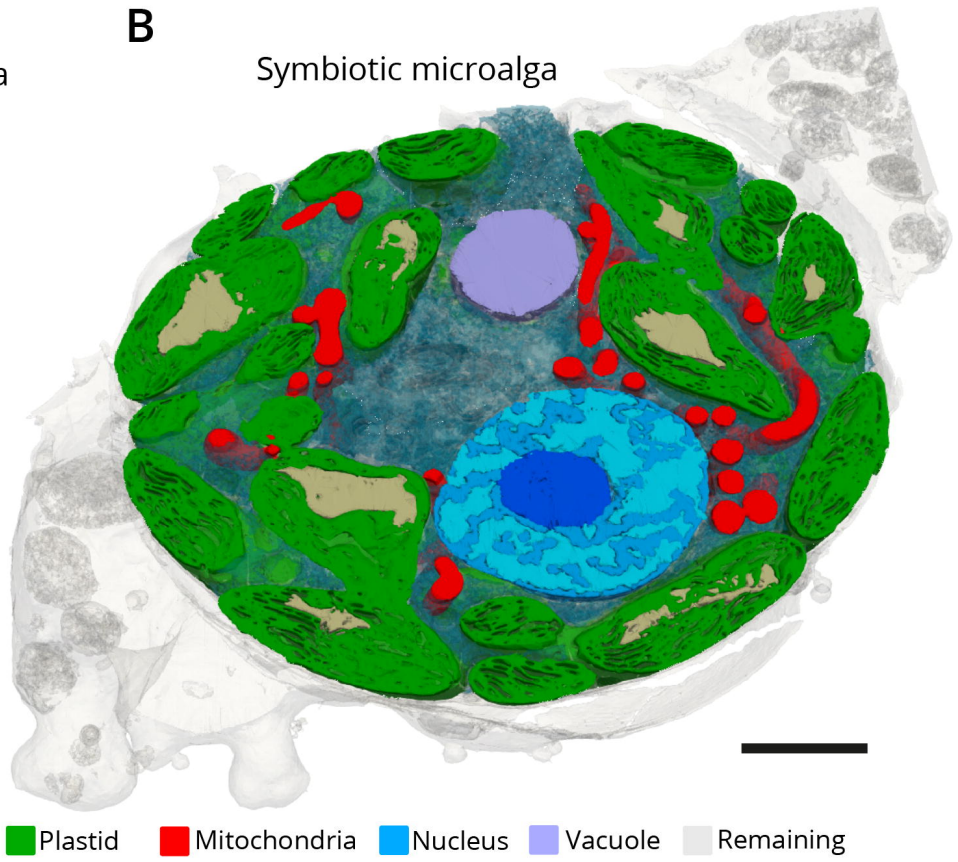
A) 3D reconstruction following FIB-SEM of a symbiotic microalga with 16 plastids surrounded by mitochondria (red) and Golgi apparatus (dark purple) of the host. The different organelles and compartments reconstructed in 3D are highlighted in the FIB-SEM electron micrograph frame

(left). 3D reconstruction (right) of a large vacuole in the symbiotic microalga (light purple), which is surrounded by a symbiosome (pink) containing small vesicles (dark red). Scale bar: 2 μm . **B)** 3D reconstruction of a large symbiotic microalga with 65 plastids surrounded by mitochondria (m; red) and Golgi apparatus (G; dark purple) of the host. The different organelles and compartments reconstructed in 3D are highlighted in the FIB-SEM electron micrograph frame (left). In large symbionts (> 31 plastids), there is an invagination of the symbiosome (S; pink) in the algal cell. Note the presence of small vesicles (Vs; dark red) in the symbiosome and large vacuoles (V; light purple) close to the symbiosome. Scale bar: 2 μm . **C)** Cell volume of different symbiotic microalgae with 36, 40 and 65 plastids and the associated invaginated symbiosome that increases in volume.

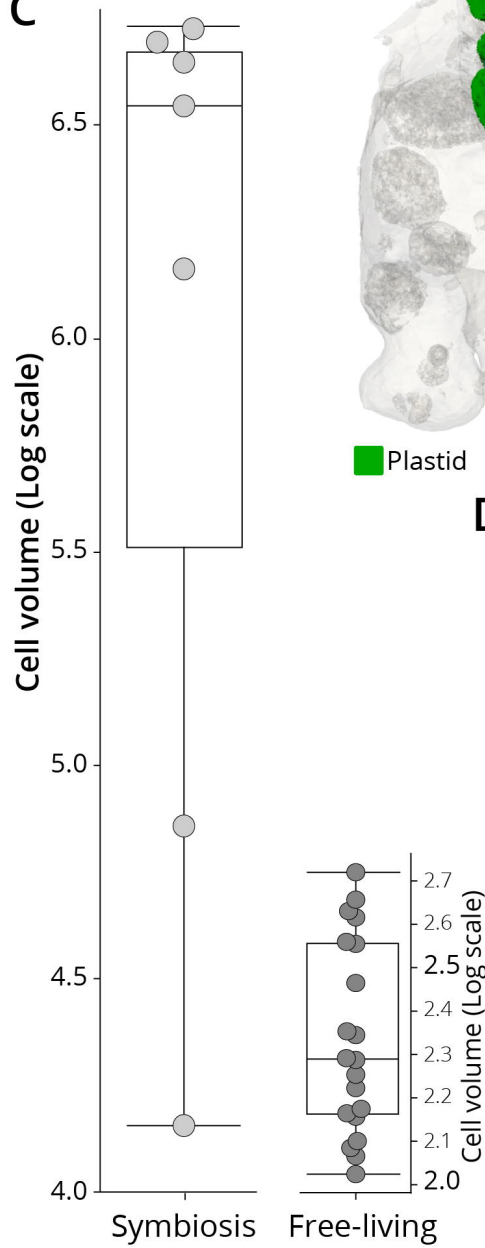
A Free-living microalga



B Symbiotic microalga

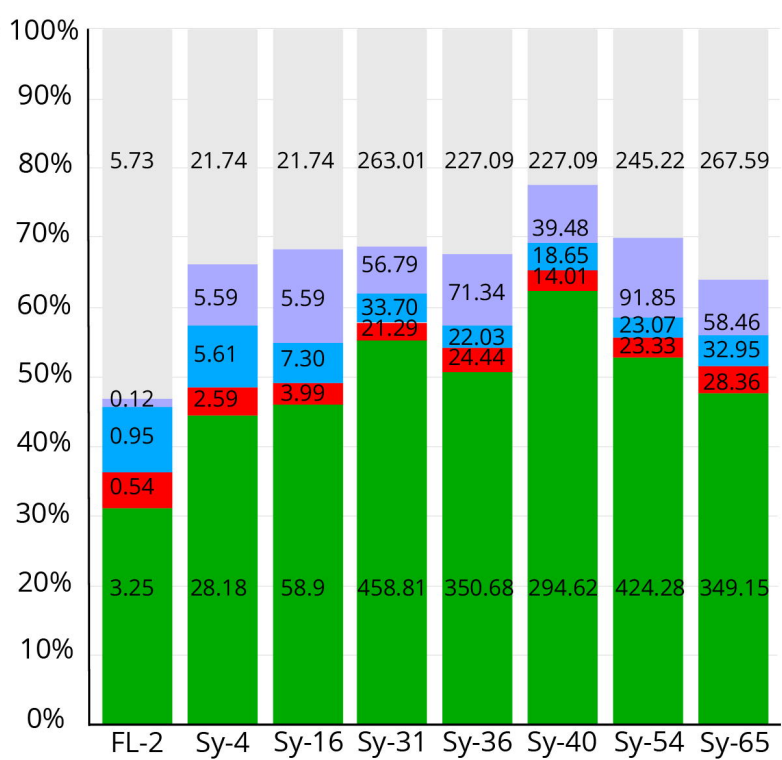


C

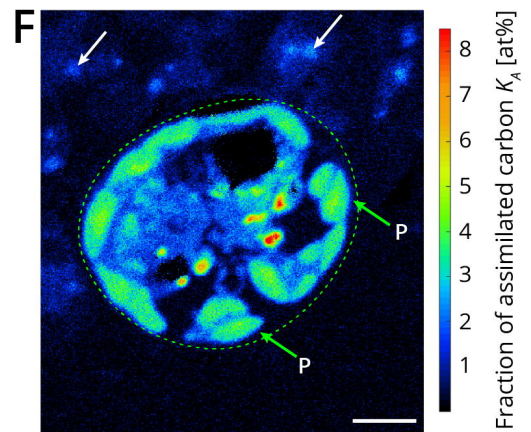
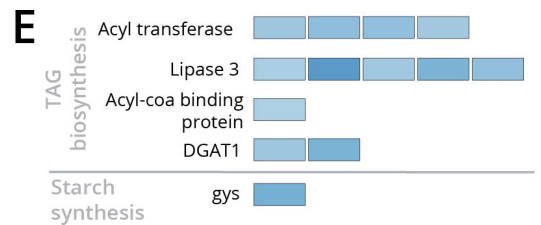
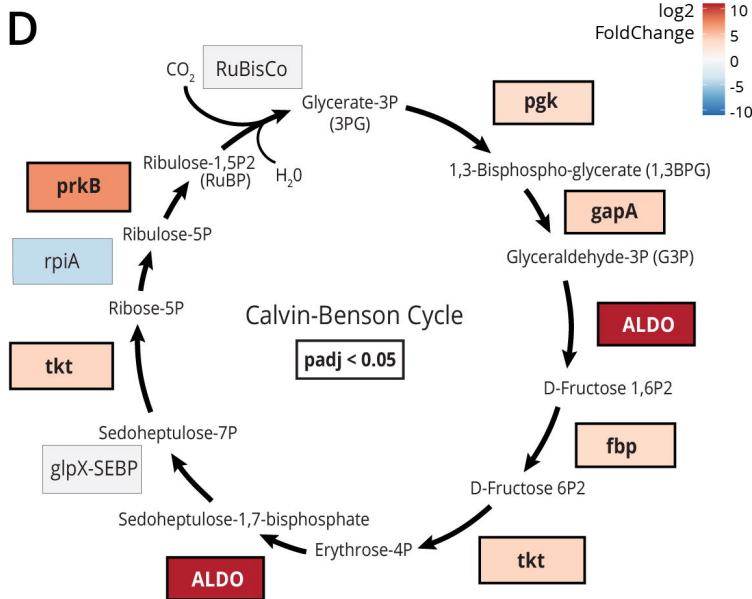
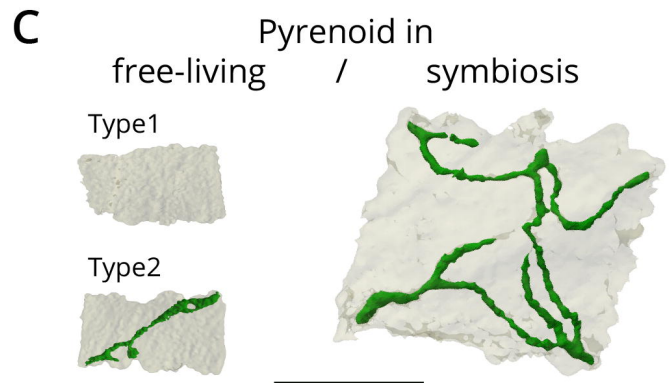
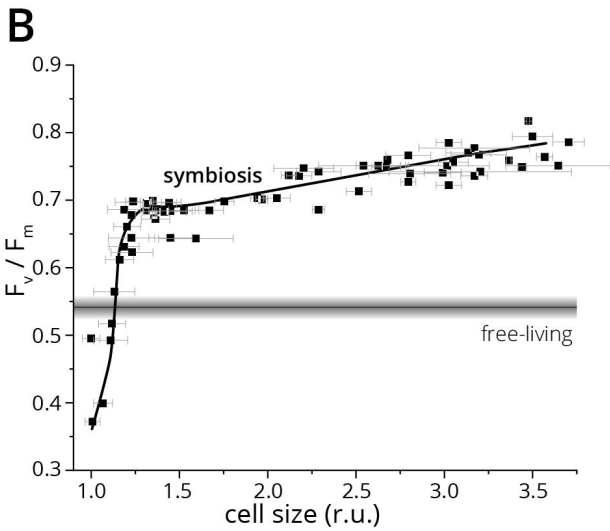
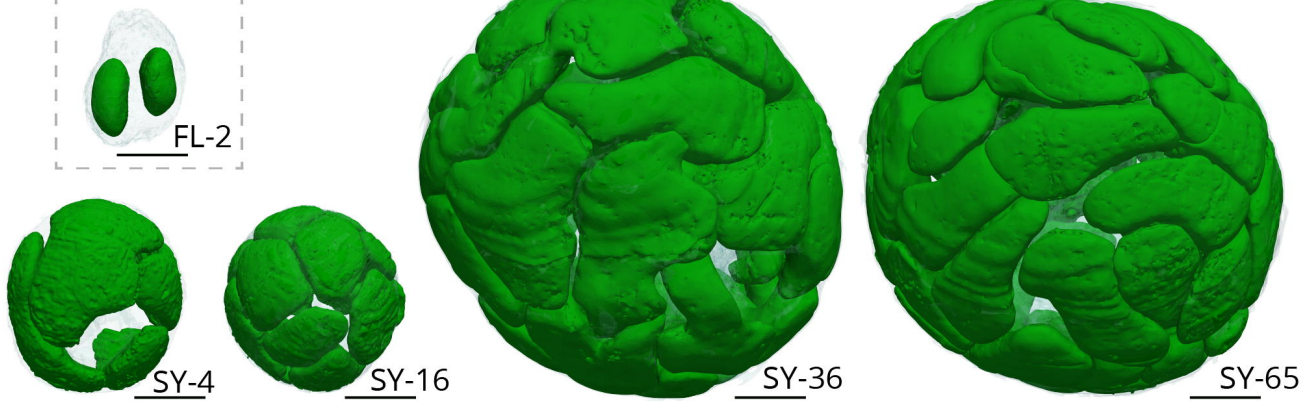


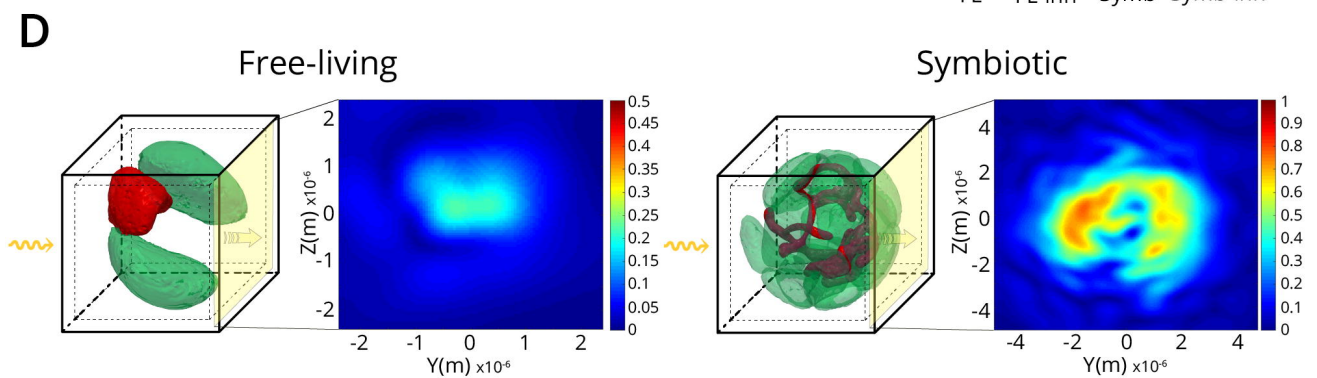
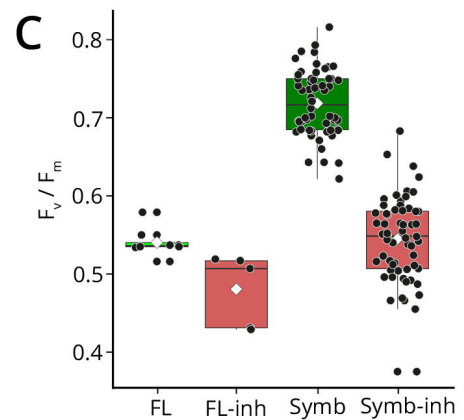
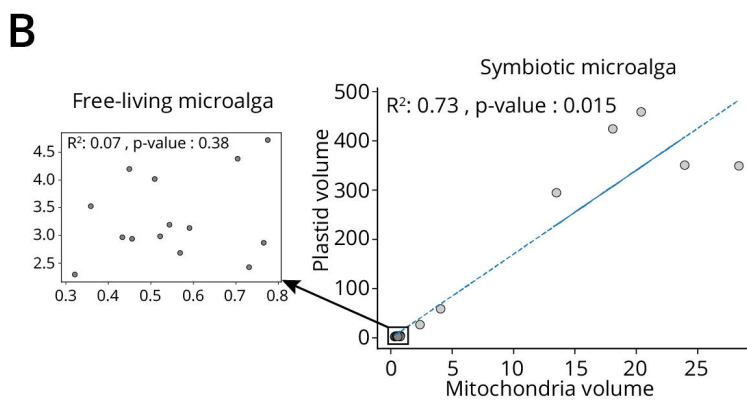
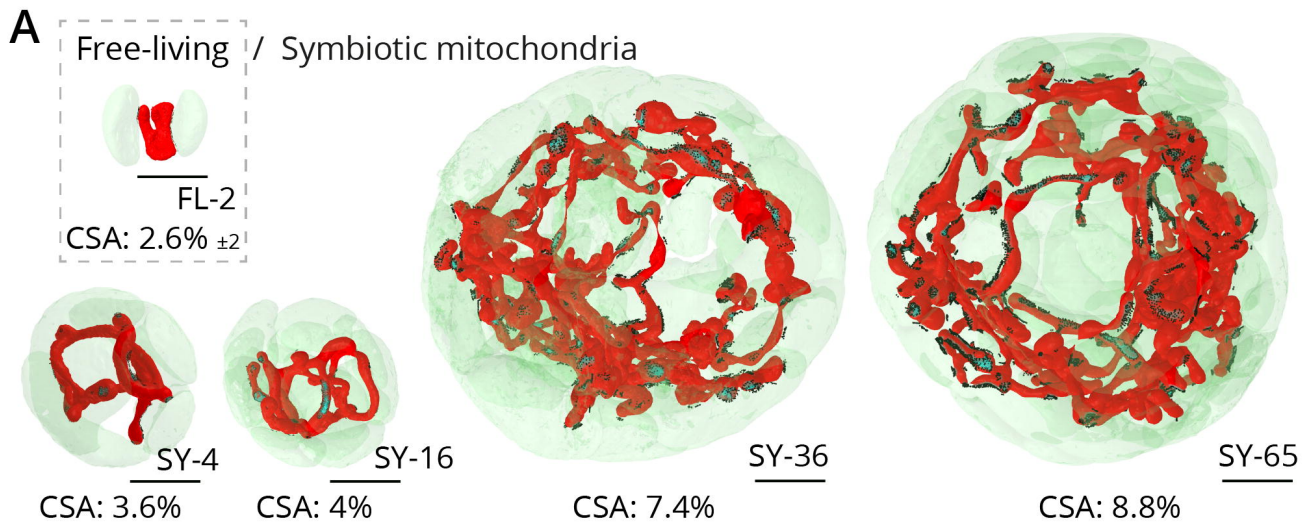
■ Plastid
 ■ Mitochondria
 ■ Nucleus
 ■ Vacuole
 ■ Remaining

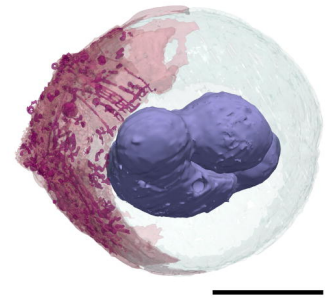
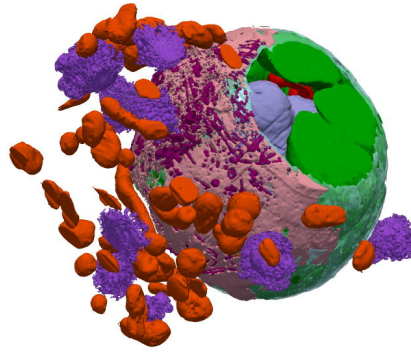
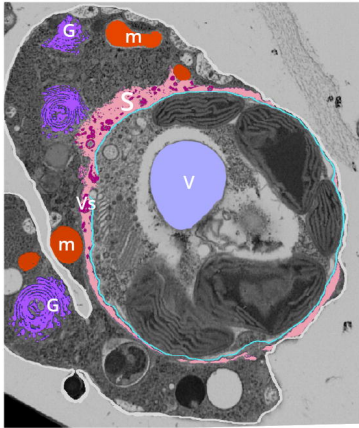
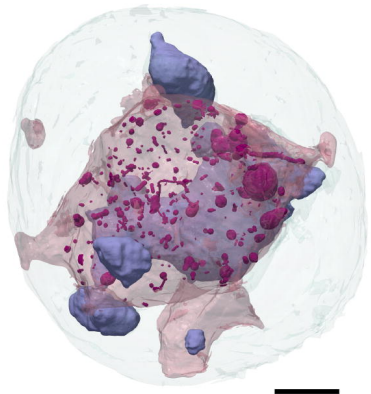
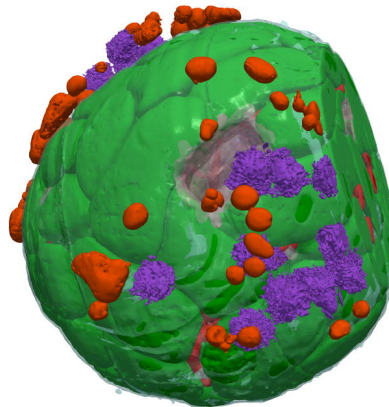
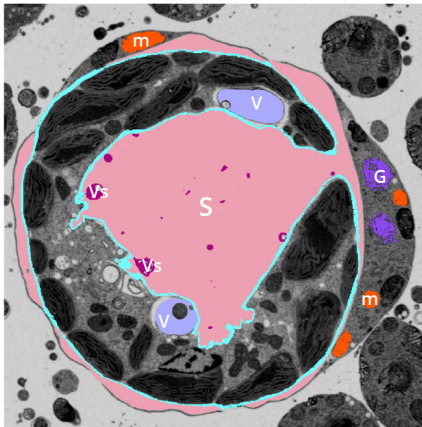
D



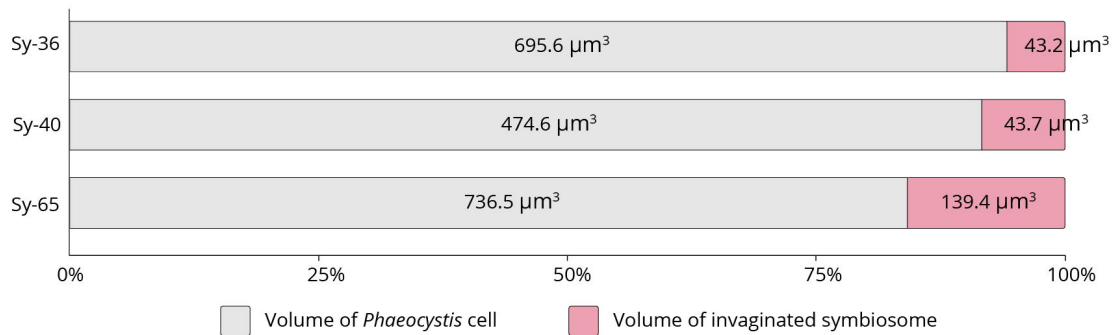
A Free-living / Symbiotic plastids





A*Phaeocystis* with 16 plastids**B***Phaeocystis* with 65 plastids

■ Host mitochondria ■ Host Golgi ■ Plastid
■ Vacuole ■ Symbiosome ■ Symbiosome vacuole

C

A.3 A multifaceted analysis reveals two distinct phases of chloroplast biogenesis during de-etiolation in *Arabidopsis*

Summary

Light triggers chloroplast differentiation whereby the etioplast transforms into a photosynthesizing chloroplast and the thylakoid rapidly emerges. However, the sequence of events during chloroplast differentiation remains poorly understood. Using Serial Block Face Scanning Electron Microscopy (SBF-SEM), we generated a series of chloroplast 3D reconstructions during differentiation, revealing chloroplast number and volume and the extent of envelope and thylakoid membrane surfaces. Furthermore, we used quantitative lipid and whole proteome data to complement the (ultra)structural data, providing a time-resolved, multi-dimensional description of chloroplast differentiation. This showed two distinct phases of chloroplast biogenesis: an initial photosynthesis-enabling ‘Structure Establishment Phase’ followed by a ‘Chloroplast Proliferation Phase’ during cell expansion. Moreover, these data detail thylakoid membrane expansion during de-etiolation at the seedling level and the relative contribution and differential regulation of proteins and lipids at each developmental stage. Altogether, we establish a roadmap for chloroplast differentiation, a critical process for plant photoautotrophic growth and survival.

Keywords: Thylakoid, Chloroplast, Photosynthesis, SBF-SEM, Proteomics, *Arabidopsis*.

A multifaceted analysis reveals two distinct phases of chloroplast biogenesis during de-etiolation in *Arabidopsis*

Rosa Pipitone¹, Simona Eicke², Barbara Pfister², Gaetan Glauser³, Denis Falconet⁴, Clarisse UWIZEYE⁴, Thibaut Pralon¹, Samuel C Zeeman², Felix Kessler^{1*}, Emilie Demarsy^{1,5*}

¹Plant Physiology Laboratory, University of Neuchâtel, Neuchâtel, Switzerland; ²Institute of Molecular Plant Biology, Department of Biology ETH Zurich, Zurich, Switzerland; ³Neuchâtel Platform of Analytical Chemistry, University of Neuchâtel, Neuchâtel, Switzerland; ⁴Université Grenoble Alpes, CNRS, CEA, INRAE, IRIG-DBSCI-LPCV, Grenoble, France; ⁵Department of Botany and Plant Biology, University of Geneva, Geneva, Switzerland

Abstract Light triggers chloroplast differentiation whereby the etioplast transforms into a photosynthesizing chloroplast and the thylakoid rapidly emerges. However, the sequence of events during chloroplast differentiation remains poorly understood. Using Serial Block Face Scanning Electron Microscopy (SBF-SEM), we generated a series of chloroplast 3D reconstructions during differentiation, revealing chloroplast number and volume and the extent of envelope and thylakoid membrane surfaces. Furthermore, we used quantitative lipid and whole proteome data to complement the (ultra)structural data, providing a time-resolved, multi-dimensional description of chloroplast differentiation. This showed two distinct phases of chloroplast biogenesis: an initial photosynthesis-enabling 'Structure Establishment Phase' followed by a 'Chloroplast Proliferation Phase' during cell expansion. Moreover, these data detail thylakoid membrane expansion during de-etiolation at the seedling level and the relative contribution and differential regulation of proteins and lipids at each developmental stage. Altogether, we establish a roadmap for chloroplast differentiation, a critical process for plant photoautotrophic growth and survival.

*For correspondence: felix.kessler@unine.ch (FK); emilie.demarsy@unige.ch (ED)

Competing interests: The authors declare that no competing interests exist.

Funding: See page 27

Received: 02 September 2020
Accepted: 04 February 2021

Reviewing editor: Caroline Gutjahr, Technical University of Munich, Germany

© Copyright Pipitone et al. This article is distributed under the terms of the [Creative Commons Attribution License](https://creativecommons.org/licenses/by/4.0/), which permits unrestricted use and redistribution provided that the original author and source are credited.

Introduction

Seedling development relies on successful chloroplast biogenesis, ensuring the transition from heterotrophic to autotrophic growth. Light is a crucial factor for chloroplast differentiation. For seeds that germinate in the light, chloroplasts may differentiate directly from proplastids present in cotyledons. However, as seeds most often germinate underneath soil, seedling development typically begins in darkness and follows a skotomorphogenic program called etiolation, characterized by rapid hypocotyl elongation and etioplast development. Light promotes seedling de-etiolation, which involves a series of morphological changes, such as cotyledon expansion, hypocotyl growth inhibition, and greening, that accompanies the onset of photosynthesis in chloroplasts. During de-etiolation, etioplast–chloroplast transition is thereby rapidly triggered by light following seedling emergence at the soil surface (*Jarvis and López-Juez, 2013; Solymosi and Schoefs, 2010; Weier and Brown, 1970*). A hallmark of chloroplast differentiation is the biogenesis of thylakoids, a network of internal membranes where the components of the photosynthetic electron transport chain assemble. Thylakoid biogenesis and the onset of photosynthesis rely on the concerted synthesis and coordinated assembly of chlorophylls, lipids, and proteins in both space and time (*Jarvis and López-Juez, 2013*).

The thylakoids harbor the photosynthetic electron transport chain, which is composed of three complexes: photosystem II (PSII), the cytochrome b_6f complex (Cyt b_6f), and photosystem I (PSI). Electron transfer between these complexes is facilitated by mobile electron carriers, specifically the low-molecular-weight, membrane-soluble plastoquinone (electron transfer from PSII to Cyt b_6f) and the luminal protein plastocyanin (electron transfer from Cyt b_6f to PSI; [Eberhard et al., 2008](#)). Electron transfer leads to successive reduction and oxidation of electron transport chain components. The final reduction step catalyzed by ferredoxin-NADP(+) reductase (FNR) leads to NADPH production. Oxidation of water by PSII and of plastoquinone by Cyt b_6f releases protons into the lumen, generating a proton gradient across the thylakoid membrane that drives the activity of the thylakoid-localized chloroplast ATP synthase complex. Each of the photosynthetic complexes consists of multiple subunits encoded by the plastid or nuclear genome ([Allen et al., 2011](#); [Jarvis and López-Juez, 2013](#)) PSII and PSI have core complexes comprising 25–30 and 15 proteins, respectively ([Amunts and Nelson, 2009](#); [Caffarri et al., 2014](#)). The antenna proteins from the Light Harvesting Complexes (LHC) surround the PSI and PSII core complexes contributing to the formation of super-complexes. Cyt b_6f is an eight-subunit dimeric complex ([Schöttler et al., 2015](#)). Each complex of the electron transport chain has a specific dimension, orientation, and location within the thylakoid membrane, occupying a defined surface, and their dimensions have been reported in several studies giving congruent results ([Caffarri et al., 2014](#); [Kurusu et al., 2003](#); [van Bezouwen et al., 2017](#)). During de-etiolation, massive protein synthesis is required for assembly of the highly abundant photosynthetic complexes embedded in thylakoids. Photomorphogenic program is controlled by regulation of gene expression at different levels ([Wu, 2014](#)). Transcriptome analyses have revealed that upon light exposure, up to one-third of Arabidopsis genes are differentially expressed, with 3/5 being upregulated and 2/5 downregulated ([Ma et al., 2001](#)). Chloroplast proteins encoded by the nuclear genome must be imported from the cytoplasm ([Jarvis and López-Juez, 2013](#)). The general chloroplast protein import machinery is composed of the multimeric complexes Translocon of Outer membrane Complex (TOC) and Translocon of Inner membrane Complex (TIC), and selective import is based on specific recognition of transit peptide sequences and TOC receptors ([Agne and Kessler, 2010](#); [Richardson and Schnell, 2020](#)).

Reminiscent of their cyanobacterial origin, chloroplast membranes are composed mostly of glycolipids (mono- and di-galactosyldiacylglycerol; MGDG and DGDG) and are poor in phospholipids compared to other membranes in the cell ([Bastien et al., 2016](#); [Block et al., 1983](#); [Kobayashi, 2016](#)). Galactolipids comprise a glycerol backbone esterified to contain a single (MGDG) or double (DGDG) galactose units at the *sn1* position and two fatty acid chains at the *sn2* and *sn3* positions. In addition to the number of galactose units at *sn1*, galactolipids also differ by the length and degrees of saturation of the fatty acid chains. In some species, including Arabidopsis, galactolipid synthesis relies on two different pathways, defined as the eukaryotic and prokaryotic pathway depending on the organellar origin of the diacylglycerol precursor. The eukaryotic pathway requires the import of diacyl-glycerol (DAG) synthesized in the endoplasmic reticulum (ER) into the plastids and is referred to as the ER pathway, whereas the prokaryotic pathway is entirely restricted to the plastid (PL) and is referred to as the PL pathway ([Ohlrogge and Browse, 1995](#)). As signatures, ER pathway-derived galactolipids harbor an 18-carbon chain, whereas PL pathway-derived galactolipids harbor a 16-carbon chain at the *sn2* position. In addition to constituting the lipid bilayer, galactolipids are integral components of photosystems and thereby contribute to photochemistry and photo-protection ([Aronsson et al., 2008](#); [Kobayashi, 2016](#)). Thylakoids also contain neutral lipids such as chlorophyll, carotenoids, tocopherols, and plastoquinone. These may exist freely or be associated with the photosynthetic complexes, having either a direct role in photosynthesis (chlorophyll, carotenoids, plastoquinone) or participating indirectly in the optimization of light usage and/or mitigation of potentially damaging effects (tocopherols in addition to carotenoids and plastoquinone; [Hashimoto et al., 2003](#); [van Wijk and Kessler, 2017](#)).

Past studies used conventional electron microscopy to first describe the architecture of the thylakoid membrane network. Based on these 2D observations, researchers proposed that plant thylakoid membranes are organized as single lamellae connected to appressed multi-lamellar regions called grana. How these lamellae are interconnected was revealed only later following the development of 3D electron microscopic techniques ([Staehelein and Paolillo, 2020](#)). Tremendous technological progress in the field of electron microscopy has been made recently, leading to improved descriptions of chloroplast ultrastructure ([Daum et al., 2010](#); [Daum and Kühlbrandt, 2011](#)). Electron tomography

substantially improved our comprehension of the 3D organization of the thylakoid network in chloroplasts at different developmental stages and in different photosynthetic organisms, including *Arabidopsis* (Austin and Staehelin, 2011; Liang et al., 2018), *Chlamydomonas* (Engel et al., 2015), runner bean (Kowalewska et al., 2016), and *Phaeodactylum tricornutum* (Flori et al., 2017). Electron tomography also provided quantitative information on thylakoid structure such as the thylakoid layer number within the grana stack and the thickness of the stacking repeat distance of grana membrane (Daum et al., 2010; Kirchhoff et al., 2011). These quantitative data allowed a greater understanding of the spatial organization of the thylakoid membrane in relation to the embedded photosynthetic complexes (Wietrzynski et al., 2020). Although electron tomography offers extraordinary resolution at the nanometer level, its main drawback is a limit to the volume of the observation, enabling only a partial 3D reconstruction of a chloroplast. Serial Block Face-Scanning Electron Microscopy (SBF-SEM) is a technique where the embedded specimen is imaged by scanning the face of the block with an electron beam. After imaging, the face of the block is shaved automatically (e.g. 60-nm-thick slices) by an ultramicrotome mounted in the vacuum chamber. The section is discarded and the newly revealed block face is imaged again. Repeated imaging and cutting allows the collection of a tomographic sequence of hundreds of images of the same area. Thereby, a much larger volume can be reconstructed in 3D to show cellular organization (Peddie and Collinson, 2014; Pinali and Kitmitto, 2014).

In combination with electron microscopy, biochemical fractionation of thylakoids has revealed differential lipid and protein compositions of the grana and the stroma lamellae. The grana are enriched in DGDG and PSII, whereas the stroma lamellae are enriched in MGDG, Cyt *b6/f*, and PSI (Demé et al., 2014; Koochak et al., 2019; Tomizioli et al., 2014; Wietrzynski et al., 2020). Changes in lipid and protein compositions during etioplast–chloroplast transition are tightly linked to the thylakoid architecture. In particular, changes in MGDG to DGDG ratio are correlated with the transition from prolamellar body (PLB) and prothylakoid (PT) structures (tubular membrane) to thylakoid membranes (lamellar structure; Bottier et al., 2007; Demé et al., 2014; Mazur et al., 2019).

Individual studies have provided much insight regarding specific dynamics of the soluble chloroplast proteome, the chloroplast transcriptome, photosynthesis-related protein accumulation and photosynthetic activity, chloroplast lipids, and changes in thylakoid architecture (Armarego-Marriott et al., 2019; Dubreuil et al., 2018; Kleffmann et al., 2007; Kowalewska et al., 2016; Liang et al., 2018; Rudowska et al., 2012). However, these studies were mostly qualitative, focused on one or two aspects, and were performed in different model organisms. Therefore, chemical data related to thylakoid biogenesis remain sparse and quantitative information is rare. Here, we present a systems-level study that integrates quantitative information on ultrastructural changes of the thylakoids with lipid and protein composition during de-etiolation of *Arabidopsis* seedlings.

Results

The photosynthetic machinery is functional after 14 hr of de-etiolation

We analyzed etioplast–chloroplast transition in *Arabidopsis* seedlings grown in the absence of exogenous sucrose for 3 days in darkness and then exposed to constant white light (Figure 1A). These experimental conditions were chosen to avoid effects of exogenous sucrose on seedling development and variations due to circadian rhythm. Upon illumination, the etiolated seedlings switched from the skotomorphogenic to the photomorphogenic developmental program, evidenced by opening of the apical hook and cotyledon greening and expansion (Figure 1B; Kami et al., 2010). We stopped the analysis following 96 hr of illumination (T96), before the emergence of the primary leaves. Samples were collected at different selected time points during de-etiolation (Figure 1A).

In angiosperms, chlorophyll synthesis arrests in the dark but starts immediately upon seedling irradiation (Von Wettstein et al., 1995). Chlorophyll levels in whole seedlings increased within the first 4 hr of illumination (T4) and continued to increase linearly during subsequent illumination as the seedlings grew (Figure 1C). To evaluate photosynthetic efficiency during de-etiolation, we measured chlorophyll fluorescence and calculated the maximum quantum yield of PSII (Fv/Fm, Figure 1D and Figure 1—figure supplement 1). PSII maximum quantum yield increased during the initial period of illumination and was near the maximal value of 0.8 at 14 hr of light exposure (T14), independent of light intensity (Figure 1D and Figure 1—figure supplement 1A). Other photosynthetic parameters

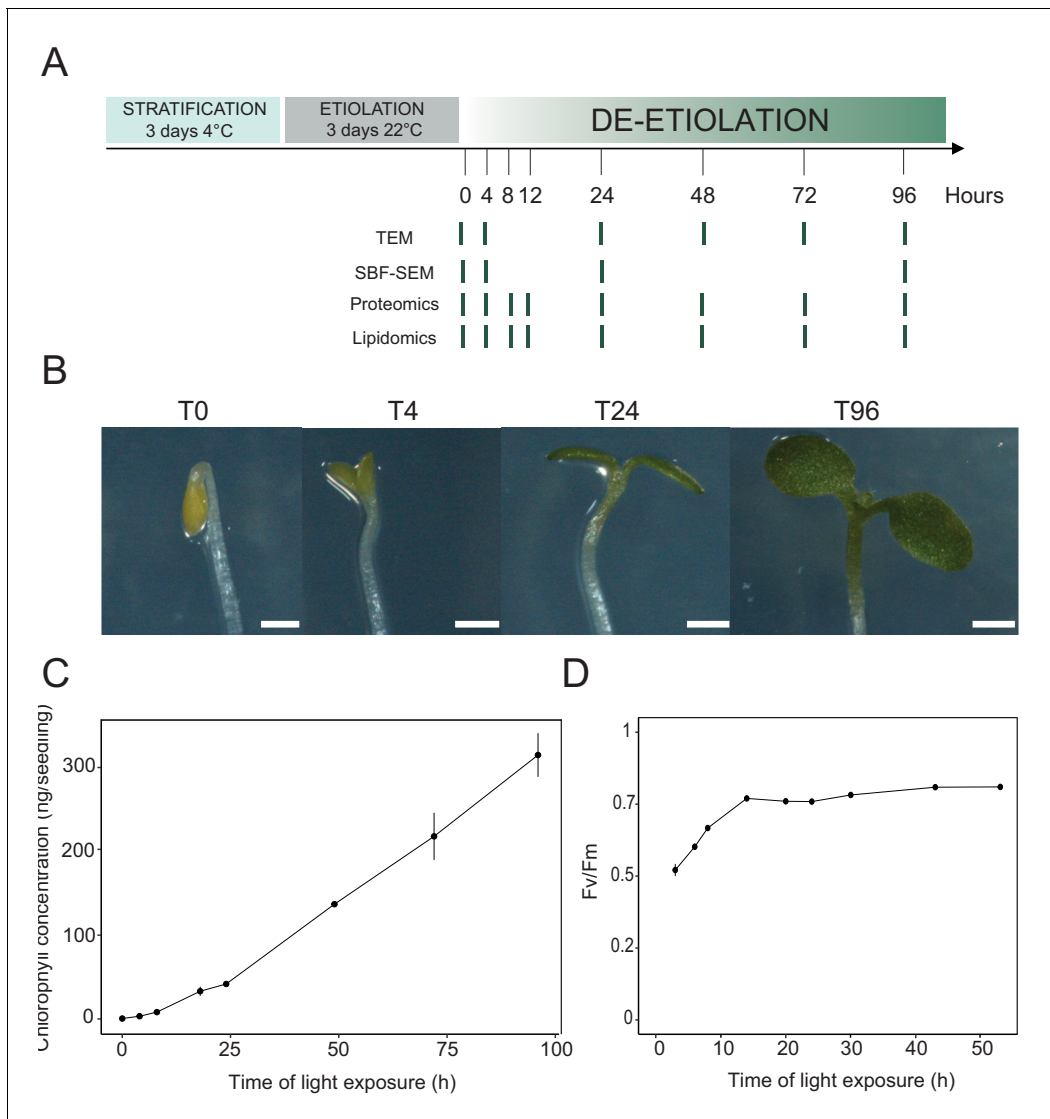


Figure 1. Photosynthesis onset during de-etiolation. (A) Scheme of the experimental design. Seeds of *Arabidopsis thaliana* (Columbia) sown on agar plates were stratified for three days at 4°C and then transferred to 22°C in the dark. After 3 days, etiolated seedlings were exposed to continuous white light (40 $\mu\text{mol}/\text{m}^2/\text{s}$) and harvested at different time points during de-etiolation. Selected time points used for different analyses are indicated. (B) Cotyledon phenotype of etiolated seedlings (T0) after 4 hr (T4), 24 hr (T24), and 96 (T96) hr in continuous white light. Scale bars: 0.5 mm. (C) Chlorophyll quantification at different time points upon illumination. Error bars indicate \pm SD ($n = 3$). (D) Maximum quantum yield of photosystem II (Fv/Fm). Error bars indicate \pm SD ($n = 4-10$). For some data points, the error bars are inferior to the size of the symbol. Measurements of further photosynthetic parameters are presented in **Figure 1—figure supplement 1**.

The online version of this article includes the following figure supplement(s) for figure 1:

Figure supplement 1. Photosynthesis parameters during de-etiolation.

(photochemical quenching, qP and PSII quantum yield in the light, ΦPSII , **Figure 1—figure supplement 1B and C**) reached maximum values at T14 and remained stable thereafter, indicating that the assembly of fully functional photosynthetic machinery occurs within the first 14 hr of de-etiolation, and that further biosynthesis of photosynthesis related compounds is efficiently coordinated.

Major thylakoid structural changes occur within 24 hr of de-etiolation

We determined the dynamics of thylakoid biogenesis during the etioplast–chloroplast transition by observing chloroplast ultrastructure in cotyledons using transmission electron microscopy (TEM)

(Figure 2). Plastids present in cotyledons of etiolated seedlings displayed the typical etioplast ultrastructure with a paracrystalline PLB and tubular PTs (Figure 2A). The observed PLBs were constituted of hexagonal units with diameters of 0.8–1 μm (Figure 2E). By T4, the highly structured PLBs progressively disappeared and thylakoid lamellae were formed (Figure 2B). The lamellae were blurry and their thickness varied between 15 and 70 nm (Figure 2F). After 24 hr of illumination (T24), the density of lamellae per chloroplast was higher than that at T4 due to an increase in lamellar length and number. Appressed regions corresponding to developing grana stacks also appeared by T24 (Figure 2C and G). These early grana stacks consisted of 2–6 lamellae with a thickness of 13 nm each (Figure 2—figure supplement 1). In addition, starch granules were present at T24, supporting the notion that these chloroplasts are photosynthetically functional and able to assimilate carbon dioxide (CO_2). At T96, thylakoid membrane organization was visually similar to that at T24, but with more layers per grana (up to 10 lamellae per grana; Figure 2D and H). In addition, singular lamella thickness at T96 increased by 2–3 nm compared to that at T24 (Figure 2—figure supplement 1). The major differences observed between T24 and T96 were increases in starch granule size and number and overall chloroplast size (Figure 2C and D and Table 1). Etioplast average length (estimated by measuring the maximum distance on individual slices) was 2 μm (± 0.9 , $n = 10$) in the dark

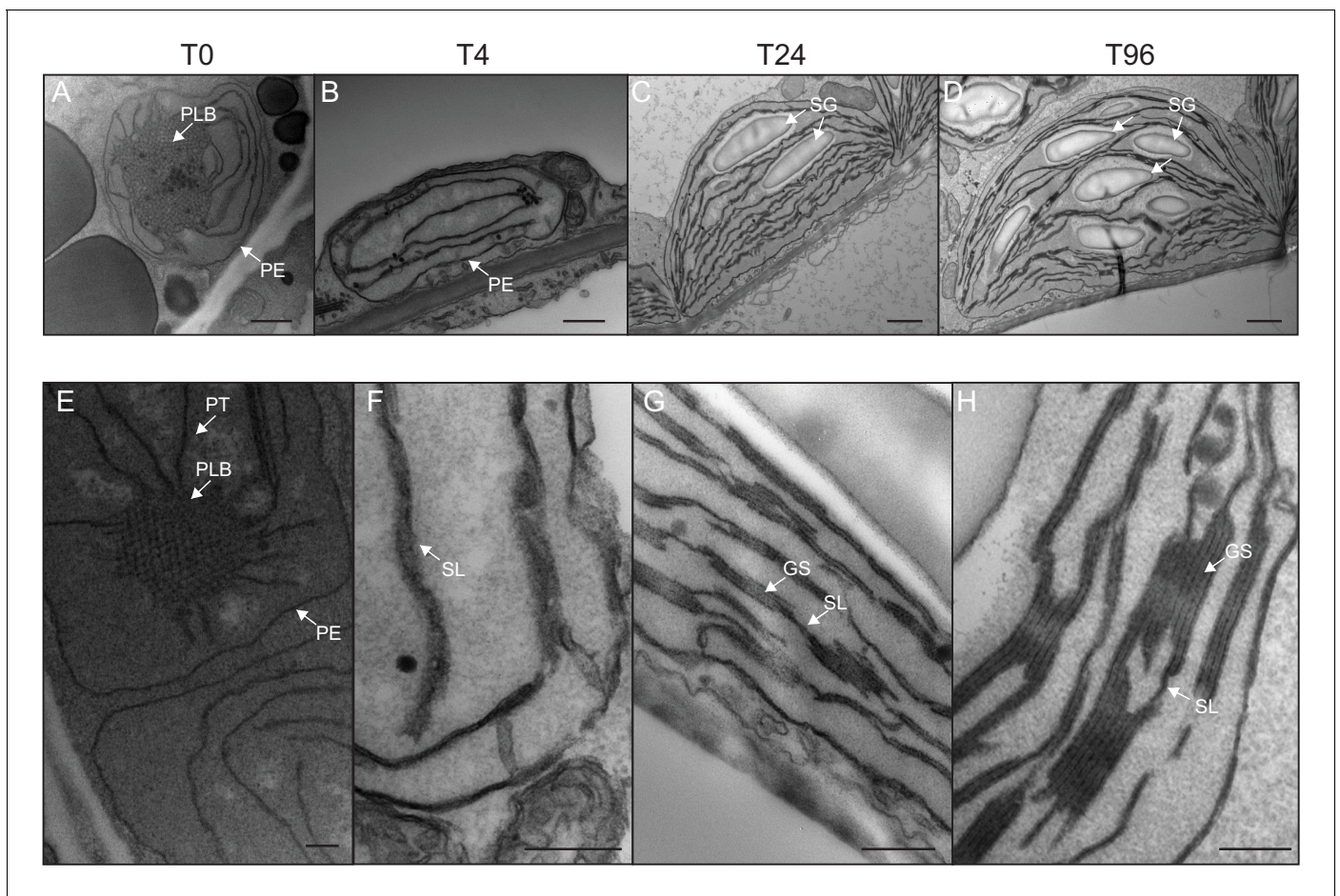


Figure 2. Qualitative analysis of chloroplast ultrastructure during de-etiolation. Transmission electron microscopy (TEM) images of cotyledon cells of 3-day-old, dark-grown *Arabidopsis thaliana* (Columbia) seedlings illuminated for 0 hr (T0, A and E), 4 hr (T4, B and F), 24 hr (T24, C and G), and 96 hr (T96, D and H) in continuous white light (40 $\mu\text{mol}/\text{m}^2/\text{s}$). (A–D) Scale bars: 500 nm, (E–H) higher magnification of A–D images; Scale bars: 200 nm. PLB: prolamellar body; PT: prothylakoid; PE: plastid envelope; SG: starch grain; GS: grana stack; SL: single lamella. Specific details for measurements of lamella thickness are provided in Figure 2—figure supplement 1.

The online version of this article includes the following figure supplement(s) for figure 2:

Figure supplement 1. Measurement of lamella thickness.

Table 1. Collection of quantitative data.

Morphometric data corresponding to thylakoid surfaces and volumes, thylakoid/envelope surface ratio, and chloroplast and cell volumes were collected after 3View analysis. Chloroplast and cell volumes were also quantified by subsequent confocal microscopy analysis, whereas plastid length was measured using TEM images. Molecular data for galactolipids (GLs) were analyzed by lipidomics, whereas PsbA, PsaC, and PetC were quantified by quantitative immunodetection.

	Method	T0	T4	T8	T12	T24	T48	T72	T96
Chloroplast volume (μm^3)	SBF-SEM	12.27 (± 2.3)	9.4 (± 4.8)	-	-	62 (± 2.04)	-	-	112.14 (± 4.3)
Thylakoid surface (μm^2)	SBF-SEM	-	67 (± 29.5)	-	-	1476 (± 146)	-	-	2086 (± 393)
Grana lamellae/total thylakoid surface		-	-	-	-	2.55 (± 0.11)	-	-	2.08 (± 0.57)
Thylakoid/envelope surface		-	1.02 (± 0.15)	-	-	7.37 (± 0.51)	-	-	6.83 (± 1.40)
Length of plastid (μm)	TEM	2 (± 0.90)	2.8 (± 0.90)	-	-	5.1 (± 1.47)	-	-	6 (± 1.62)
Stroma lamellae volume (μm^3)	SBF-SEM		2.43 (± 0.95)	-	-	17.87 (± 1.04)	-	-	29.17 (± 1.94)
Chloroplast volume (μm^3)	Confocal	-	-	-	-	61.5 (± 11.2)	70.1 (± 10.2)	85 (± 22)	-
Cell volume (μm^3)	SBF-SEM	1173 (± 284)	1891 (± 362)	-	-	6103 (± 1309)	-	-	52597 (± 12671)
Cell perimeter (μm)	TEM					55.3 (± 14.1)	46.4 (± 6.1)	71.7 (± 19.1)	92.8 (± 22.1)
Number of chloroplast per cell	SBF-SEM	22 (± 6)	25 (± 8)	-	-	26 (± 6)	-	-	112 (± 29)
Number of cells per seedling		-	-	-	-	~3000	-	-	~3000
Protein / GLs surface		0.19 (± 0.05)	0.23 (± 0.04)	0.34 (± 0.03)	0.52 (± 0.07)	0.80 (± 0.14)	0.80 (± 0.17)	0.78 (0.07)	0.87 (± 0.25)
GLs (nmol/seedling)	Lipidomics	0.31 (± 0.03)	0.31 (± 0.02)	0.32 (± 0.02)	0.54 (± 0.02)	0.67 (± 0.04)	1.28 (± 0.12)	1.84 (± 0.01)	2.20 (± 0.09)
PsbA (nmol/seedling)	Immuno-detection	6.9E-06 ($\pm 1.8E-06$)	9.2E-06 ($\pm 1.7E-06$)	1.5E-05 ($\pm 0.07E-05$)	3.2E-05 ($\pm 0.4E-05$)	9.3E-05 ($\pm 2E-05$)	2.0E-04 ($\pm 0.6E-04$)	3.9E-04 ($\pm 0.4E-04$)	6.2E-04 ($\pm 1.7E-04$)
PsaC (nmol/seedling)	Immuno-detection				1.6E-05 ($\pm 0.2E-05$)	7.3E-05 ($\pm 2E-05$)	1.1E-04 ($\pm 0.7E-04$)	1.7E-04 ($\pm 0.4E-04$)	2.3E-04 ($\pm 1E-04$)
PetC (nmol /seedling)	Immuno-detection	2.7E-05 ($\pm 0.8E-05$)	2.8E-05 ($\pm 1E-05$)	2.5E-05 ($\pm 0.4E-05$)	5.3E-05 ($\pm 2.2E-05$)	1.2E-04 ($\pm 0.4E-04$)	1.8E-04 ($\pm 0.4E-04$)	5.7E-04 ($\pm 1.8E-04$)	7.9E-04 ($\pm 3.7E-04$)

(T0), whereas chloroplast average length was 6 μm (± 1.62 , $n = 10$) at T96 (**Table 1**). Collectively, these data show that photosynthetically functional thylakoid membranes form rapidly during the first 24 hr of de-etiolation. This implies that there are efficient mechanisms for thylakoid assembly and structural organization. Subsequent changes seem to involve the expansion of pre-existing structures (i.e. lamellae length and grana size) and the initiation of photosynthetic carbon fixation (reflected by starch content).

Quantitative analysis of thylakoid surface area per chloroplast during de-etiolation

To visualize entire chloroplasts and thylakoid networks in 3D, and to obtain a quantitative view of the total thylakoid surface area during chloroplast development, we prepared and imaged cotyledons at different developmental stages by SBF-SEM (**Figure 3A–D**). PLBs, thylakoids, and envelope membranes were selected, and segmented images were used for 3D reconstruction (**Figure 3E–L**, and **Videos 1–4**; see also **Figure 2—figure supplement 1** and **Figure 3—figure supplement 1** for grana segmentation). Similar to that observed by TEM (**Figure 2**), a drastic switch from PLB to

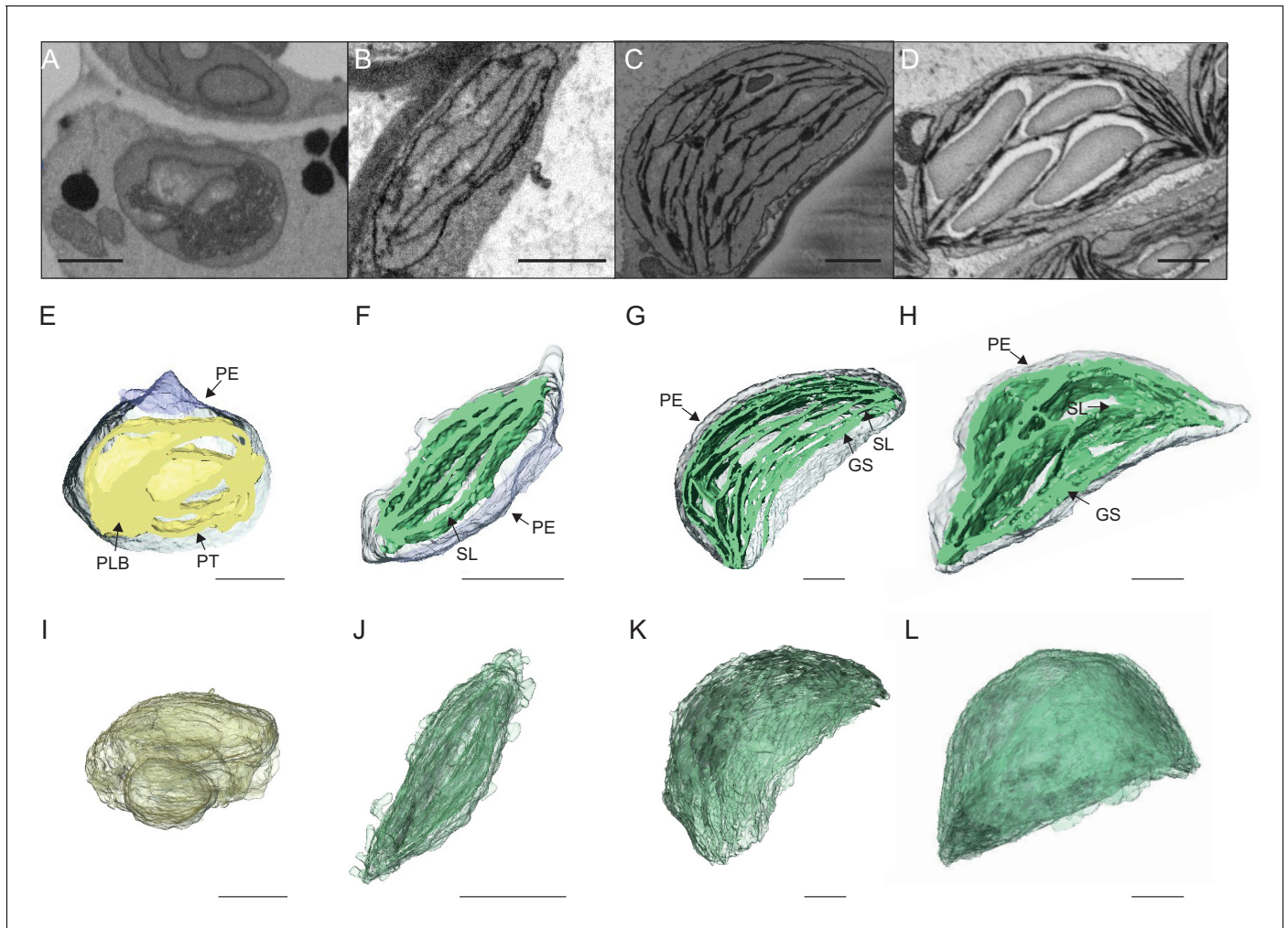


Figure 3. 3D reconstructions of chloroplast thylakoid network during de-etiolation. (A–D) Scanning electron microscopy (SEM) micrographs of representative etioplasts and chloroplasts from 3-day-old, dark-grown *Arabidopsis thaliana* seedlings illuminated for 0 hr (T0; A), 4 hr (T4; B), 24 hr (T24; C), and 96 hr (T96; D) in continuous white light ($40 \mu\text{mol}/\text{m}^2/\text{s}$). (E–H) Partial 3D reconstruction of thylakoid membranes (green) and envelope (blue) at T0 (E), T4 (F), T24 (G), and T96 (H). Z-depth of thylakoid membrane reconstruction corresponds to $0.06 \mu\text{m}$ (E), $0.10 \mu\text{m}$ (F), $0.13 \mu\text{m}$ (G), and $0.15 \mu\text{m}$ (H). (I–L) 3D reconstruction of a thylakoid membrane of an etioplast at T0 (I) or a chloroplast at T4 (J), T24 (K), and T96 (L). Scale bars = $1 \mu\text{m}$. Details of grana segmentation at T24 are provided in **Figure 3—figure supplement 1**. PLB: prolamellar body; PT: prothylakoid; PE: plastid envelope; SG: starch granule; GS: grana stack; SL: single lamella.

The online version of this article includes the following figure supplement(s) for figure 3:

Figure supplement 1. Grana segmentation (T24).

thylakoid membrane occurred by T4: the typical structure of the PLB connected to PTs disappeared leaving only elongated lamellar structures (**Figure 3E–F** and **Videos 1** and **2**). At T24 and T96, thylakoid membranes were organized in appressed and non-appressed regions and large spaces occupied by starch granules were observed (**Figure 3G–H** and **Videos 3** and **4**). 3D reconstruction revealed a change in plastid shape from ovoid at T0 and T4 to hemispheric at T24 and T96 (**Figure 3I–L**).

Using 3D reconstruction of the thylakoid network for three or four chloroplasts for each developmental stage, quantitative data such as chloroplast volume and membrane surface area were extracted and calculated (**Figure 4A and B**, **Figure 3—figure supplement 1** and **Table 1**). The total chloroplast volume increased about 11-fold from T4 ($9.4 \mu\text{m}^3$) to T96 ($112.14 \mu\text{m}^3$) (**Table 1**). In parallel, the thylakoid surface area (stroma side) increased about 30-fold reaching $2086 (\pm 393) \mu\text{m}^2$ per chloroplast at T96 (**Figure 4A** and **Table 1**). The surface area increased drastically between T4 and



Video 1. Representative sequential sections showing etioplasts (T0) followed by segmentation and 3D reconstruction of envelope (blue), and prothylakoids and prolamellar body (yellow) of a single etioplast. The tour of the etioplast reveals its ovoid shape. The sequential view of the 3D reconstruction and final partial 3D visualization reveals a single prolamellar body and interconnected prothylakoids.

<https://elifesciences.org/articles/62709#video1>

ation. Total proteins were prepared from 3-day-old etiolated seedlings exposed to light for 0–96 hr (eight time points; **Figure 1A**) and quantified by label-free shot-gun mass spectrometry. For relative quantification of protein abundances between different samples, peptide ion abundances were normalized to total protein (see Materials and methods). We considered further only those proteins that were identified with a minimum of two different peptides (with at least one being unique; see Materials and methods for information on protein grouping), resulting in the robust identification and quantification of more than 5000 proteins.

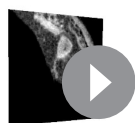
Based on this proteomic approach, the first 12 hr of illumination (T12) saw very few statistically significant changes in protein abundance (**Figure 5—source data 1**). Considering a q-value <0.01 as a stringent threshold value, significant changes were observed only after 8 hr of illumination. These changes correspond to the decreased abundance of only one protein (the photoreceptor cryptochrome 2, consistent with its photolabile property) and increased levels of only three proteins,

T24 (about 22-fold) and much less (about 1.4-fold) between T24 and T96. Accordingly, quantification of the envelope surface area indicated that the ratio of the thylakoid to envelope surface area increased drastically from T4 to T24, but decreased slightly between T24 and T96 (**Table 1**).

Our quantitative observations confirmed that during chloroplast development the major ultra-structural changes (disappearance of prolamellar body, build-up of the thylakoids and their organization into grana) occurs within the first 24 hr of de-etiolation, and no drastic changes occurs thereafter. We further analyzed these temporal processes at the molecular level focusing on proteins and lipids that constitute the thylakoid membrane.

Dynamics of plastid proteins related to thylakoid biogenesis

We analyzed the full proteome to reveal the dynamics of protein accumulation during de-etio-



Video 2. Representative sequential sections of a chloroplast (T4) followed by segmentation and 3D reconstruction of envelope (blue), and thylakoids (green). The tour of the chloroplast reveals its ovoid/discoid shape. The sequential view of the 3D reconstruction and final partial 3D visualization reveals that thylakoids are constituted by lamellae parallelly oriented.

<https://elifesciences.org/articles/62709#video2>



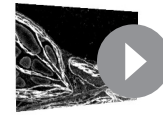
Video 3. Representative sequential sections of a chloroplast (T4) followed by segmentation and 3D reconstruction of envelope (blue), and thylakoids (green). The tour of the chloroplast reveals its hemispheric shape. The sequential view of the sections reveals the presence of starch granules (8). The sequential view of the 3D reconstruction and final partial 3D visualization reveals that thylakoids are constituted by non-appressed (stroma lamellae) and appressed regions (grana).

<https://elifesciences.org/articles/62709#video3>

which belonged to the chlorophyll a/b binding proteins category involved in photoprotection (AT1G44575 = PsbS; AT4G10340 = Lhcb5; AT1G15820 = Lhcb6; *Chen et al., 2018; Li et al., 2000*). Relaxing the statistical threshold value to 0.05, cryptochrome 2 and Lhcb6 levels were respectively decreased and increased already after 4 hr of illumination and the abundance of two other proteins (ATCG00790 = Ribosomal protein L16; AT4G15630 = Uncharacterized protein family UPF0497) increased slightly (fold changes of 1.9 and 1.7, respectively). At 8 hr, a total of 36 proteins displayed a change in abundance with a q-value <0.05. A drastic change of proteome composition occurred by T24, with 402 proteins showing a significant increase in abundance with over two-fold change (FC >2; q-value <0.01) compared with the etiolated stage, and 107 proteins showing a significant decrease with over twofold change (FC <0.5; q-value <0.01). As expected, the 100 most-upregulated proteins comprised proteins related to photosynthesis, proteins constituting the core and antennae of photosystems, and proteins involved in carbon fixation (*Figure 5—source data 1*).

To monitor the dynamics of the plastidial proteome, we selected proteins predicted to localize to the plastid (consensus localization from SUBA4; *Hooper et al., 2017*). Generation of a global heatmap for each of the 1112 potential plastidial proteins revealed different accumulation patterns (*Figure 5—figure supplement 1* and *Figure 5—figure supplement 1—source data 1*). Hierarchical clustering showed a categorization into six main clusters. Cluster 1 (purple) contained proteins whose relative amounts decreased during de-etiolation. Clusters 2, 5, and 6 (pink, light green, and dark green, respectively) contained proteins whose relative amounts increased during de-etiolation but differed with respect to the amplitude of variations. Proteins in clusters 2 and 6 displayed the largest amplitude of differential accumulation. Gene ontology (GO) analysis (*Mi et al., 2019*) indicated a statistically significant overrepresentation of proteins related to the light reactions of photosynthesis in clusters 2 and 6 (*Figure 5—figure supplement 1—source data 1*). Underrepresentation of organic acid metabolism, in particular carboxylic acid metabolism, characterized cluster 2, whereas overrepresentation of carboxylic acid biosynthesis and underrepresentation of photosynthetic light reactions were clear features of cluster 3. Protein levels in cluster 3 changed only moderately during de-etiolation in contrast with proteins levels in cluster 2. No biological processes were significantly over- or underrepresented in clusters 1, 4, and 5.

To analyze the dynamics of proteins related to thylakoid biogenesis, we selected specific proteins and represented their pattern of accumulation during de-etiolation (*Figure 5*). We included proteins constituting protein complexes located in thylakoids (complexes constituting the electron transport chain and the ATP synthase complex) and proteins involved in chloroplast lipid metabolism, chlorophyll synthesis, and protein import into the chloroplast. In agreement with that depicted in the global heatmap (*Figure 5—figure supplement 1*), all photosynthesis-related proteins increased in abundance during de-etiolation (*Figure 5A*). However, our hierarchical clustering did not show any particular clustering per complex. Only few chloroplast-localized proteins related to lipid biosynthesis were present in our proteomics data set. Among the eight detected proteins, two appeared differentially regulated; fatty acid binding protein 1 (FAB1) and fatty acid desaturase 7 (FAD7) levels increased only between 72 hr of illumination (T72) and T96, whereas the other proteins gradually accumulated over the course of de-etiolation (*Figure 5B*). Etioplasts initiate synthesis of chlorophyll precursors that are blocked at the level of protochlorophyllide synthesis, with protochlorophyllide oxidoreductase A (PORA) in its inactive form accumulating to high levels in the etioplast before subsequently decreasing at the protein level upon activation and degradation following light exposure



Video 4. Representative sequential sections of a chloroplast (T4) followed by segmentation and 3D reconstruction of envelope (blue), and thylakoids (green). The tour of the chloroplast reveals its hemispheric shape. The sequential view of the sections reveals the presence of large starch granules (11). The sequential view of the 3D reconstruction and final partial 3D visualization reveals that thylakoids are constituted by non-appressed (stroma lamellae) and appressed regions (grana), with large spaces between lamellae occupied by starch granules.

<https://elifesciences.org/articles/62709#video4>

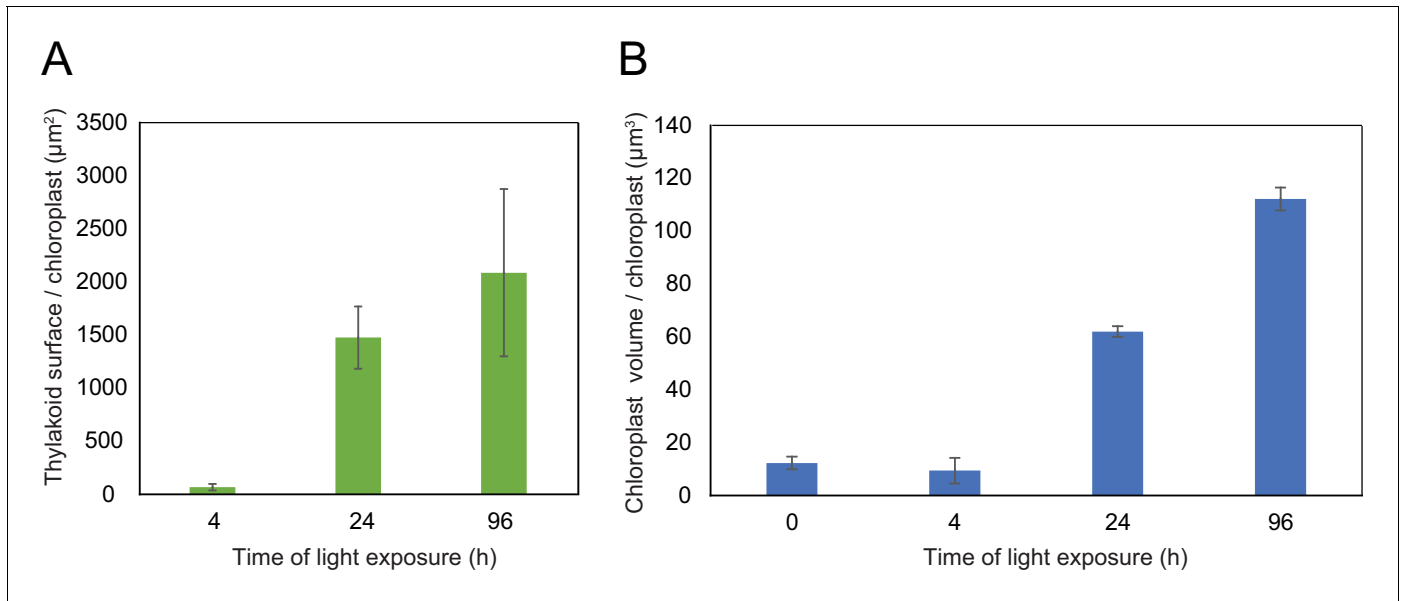


Figure 4. Quantitative analysis of chloroplast volume and thylakoid surface during de-etiolation. Quantification of thylakoid surface per chloroplast (A) and chloroplast volume (B) using 3-day-old, dark-grown *Arabidopsis thaliana* (Columbia) seedlings illuminated for 0 hr, 4 hr, 24 hr, and 96 hr in continuous white light (40 µmol/m²/s). Morphometric data were quantified by Labels analysis module of Amira software. Error bars indicate ± SD (n = 3). The total thylakoid surface indicated in A corresponds to the thylakoid surface exposed to the stroma, calculated in Amira software, in addition to the percentage of the grana surface (%Gs) calculated as described in **Figure 3—figure supplement 1**.

The online version of this article includes the following source data for figure 4:

Source data 1.

(Blomqvist et al., 2008; Runge et al., 1996; Von Wettstein et al., 1995). In agreement, illumination resulted in increased amounts of most of all detected proteins of the chlorophyll biosynthesis pathway, except PORA and to a lesser extent PORB, which clearly decreased and was separated from other chlorophyll-related proteins (**Figure 5C** and **Figure 5—source data 1**). We also selected proteins involved in protein import in chloroplasts, focusing on the TOC-TIC machinery (**Figure 5D**) that is the major route for plastid protein import and essential for chloroplast biogenesis (Kessler and Schnell, 2006). Past studies identified several TOC preprotein receptors that are proposed to display differential specificities for preprotein classes (Bauer et al., 2000; Bischof et al., 2011). The composition of plastid import complexes varies with developmental stages and in different tissues, thereby adjusting the selectivity of the import apparatus to the demands of the plastid and influencing its proteome composition (Demarsy et al., 2014; Kubis et al., 2003). Accordingly, the TOC receptors TOC120 and TOC132, which are important for the import of proteins in non-photosynthetic tissues, were more abundant in etioplasts compared to fully-developed chloroplasts (compare T0 and T96). TOC120 and TOC132 were part of a cluster separated from other components of the plastid machinery, such as the TOC159 receptor associated with large-scale import of proteins in chloroplasts. The general import channel TOC75 (TOC75 III) maintained stable expression levels throughout de-etiolation, reflecting its general role in protein import. All other components clustered with TOC159 and displayed gradual increases in accumulation during de-etiolation. Most of these components have not been reported to confer selectivity to the import machinery, which suggests an overall increase of chloroplast protein import capacity.

To validate and complement our proteomic data, we used immunoblot analysis to detect and quantify representative proteins linked to photomorphogenesis and etioplast-to-chloroplast transition.

Our proteomic data indicated a significant decrease of the abundance of the photoreceptor phyA between 48 and 72 hr of illumination (**Figure 5—source data 1**). However, immunoblots revealed that the abundance of phyA dropped already during the first 4 hr of light exposure (**Figure 6**), as previously reported (e.g. Debrieux and Fankhauser, 2010). The transcription factor

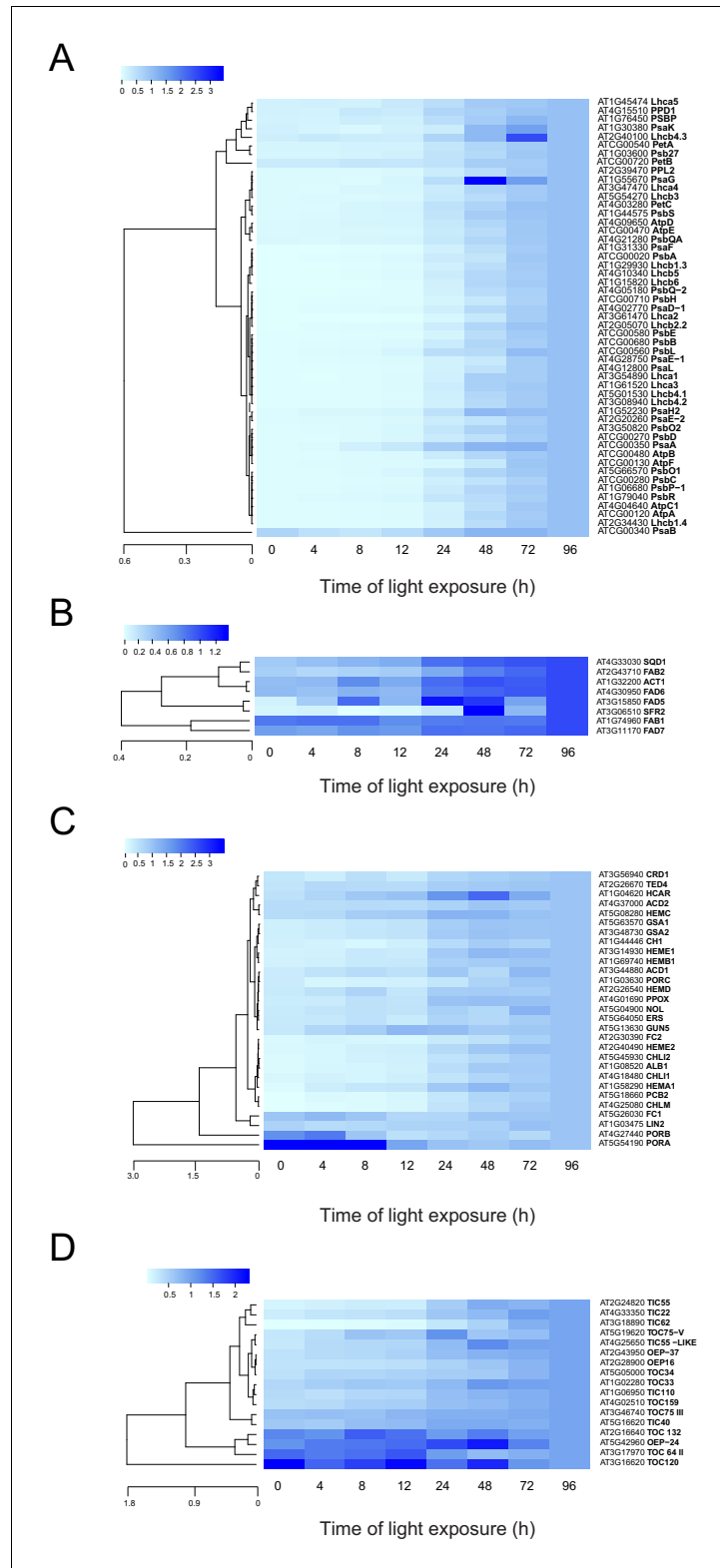


Figure 5. Accumulation dynamics of plastid proteins during de-etiolation. Three-day-old etiolated seedlings of *Arabidopsis thaliana* were illuminated for 0 hr (T0), 4 hr (T4), 8 hr (T8), 12 hr (T12), 24 hr (T24), 48 hr (T48), 72 hr (T72), and 96 hr (T96) under white light (40 $\mu\text{mol}/\text{m}^2/\text{s}$). Hierarchical clustering (Euclidean, average linkage) of normalized protein abundance for photosynthesis-(A), galactolipid metabolism- (B), chlorophyll metabolism- (C), *Figure 5 continued on next page*

Figure 5 continued

and protein import-related proteins during de-etiolation (D). Protein abundance was quantified by shot-gun proteomics and heatmap colors indicate the fold change (average of 3–4 replicates) of each selected protein at each time point of de-etiolation (T0 to T96), relative to the last time point (T96). Note that some PORA values in panel D were higher than 3.5 and outside of the color range limits. Further hierarchical clustering based on the accumulation dynamics of all plastid-localized proteins is provided in **Figure 5—figure supplement 1**.

The online version of this article includes the following source data and figure supplement(s) for figure 5:

Source data 1.

Figure supplement 1. Accumulation dynamics of selected plastid proteins during de-etiolation.

Figure supplement 1—source data 1.

ELONGATED HYPOCOTYL 5 (HY5) is a positive marker of photomorphogenesis, and accumulates during light exposure (*Osterlund and Deng, 1998*). The increase of HY5 peptide abundance was not significant by proteomics but we observed a transient accumulation of the protein between 4 and 72 hr by immunoblot (**Figure 5—source data 1; Figure 6**) and consistent with the previously reported regulation of abundance during seedling development (*Hardtke et al., 2000*).

We further compared data obtained by proteomics and immunoblot focusing on chloroplast localized proteins. Overall, immunoblot and proteomics provided similar results (**Figure 6** and **Figure 6—figure supplement 1**). PsbA and PsbD (PSII reaction center core), PsbO (oxygen evolving complex), and Lhcb2 (outer antenna complex) proteins were detectable in seedlings at T4, gradually increasing thereafter. Accumulation of the PSI proteins PsaC and PsaD and the Cyt *b₆f* complex protein PetC started later; these proteins were detectable starting at T8 (**Figure 6A** and **Figure 6—figure supplement 1**). Interestingly, AtpC (ATP synthase complex) was detectable in the etioplast, as described previously (*Plösch et al., 2011*). Other proteins were selected as markers of etioplast–chloroplast transition. As expected, ELIPs (early light-induced protein) transiently accumulated upon the dark-to-light transition (**Figure 6A; Kimura et al., 2003**). As in the proteome analysis, PORA accumulated in etiolated seedlings (T0) and then progressively disappeared upon light exposure. We performed absolute quantification for PsbA, PsaC, and PetC proteins using recombinant proteins as standards (**Figure 6B and C** and **Figure 6—figure supplement 1**). Quantitative data (nmol/seedling) were obtained and normalized using the last time point (**Figure 6C**) to compare the dynamics of protein accumulation. In addition, the comparison of PsbA and PsaC (representative proteins of PSII and PSI, respectively) showed that PsbA levels were about twice that of PsaC at T96 (**Figure 6B and C**).

Dynamics of chloroplast membrane lipids

Total lipids were extracted from seedlings collected at different time points during de-etiolation (T0, T4, T8, T12, T24, T48, T72, and T96), analyzed by ultra-high-pressure liquid chromatography–mass spectrometry (UHPLC-MS), and quantified against pure standards (**Figure 7—source data 1**). We analyzed the quantity and kinetics of accumulation of 12 different species of galactolipids (**Figure 7A and B**). MGDG 18:3/16:3, MGDG 18:3/18:3, MGDG 18:3/16:1, DGDG 18:3/18:3, and DGDG 18:3/16:0 were the most abundant lipids detected at all time points. Accumulation of all galactolipids increased upon de-etiolation; however, clustering analysis identified two distinct kinetic patterns. One group displayed a leap between T8 and T12, whereas the other group increased later during the de-etiolation period (**Figure 7C**). Interestingly, the two clusters separated the lipids according to the two pathways described for galactolipid synthesis, namely the ER and PL pathways (**Figure 7A and B; Marechal et al., 1997; Ohlrogge and Browse, 1995**). During early stages of de-etiolation (T0–T24), we observed an incremental accumulation of MGDG and DGDG galactolipids derived from the ER pathway, whereas galactolipids from the PL pathway started to accumulate at T24 (**Figure 7A and B**). The MGDG/DGDG ratio decreased between T0 and T8. This was associated with the transition from PLB (cubic lipid phase) to thylakoid membrane (lamellar structure) (*Bottier et al., 2007*). The MGDG/DGDG ratio started to increase gradually at T8 and was constant by T72 and T96 (**Figure 7D**).

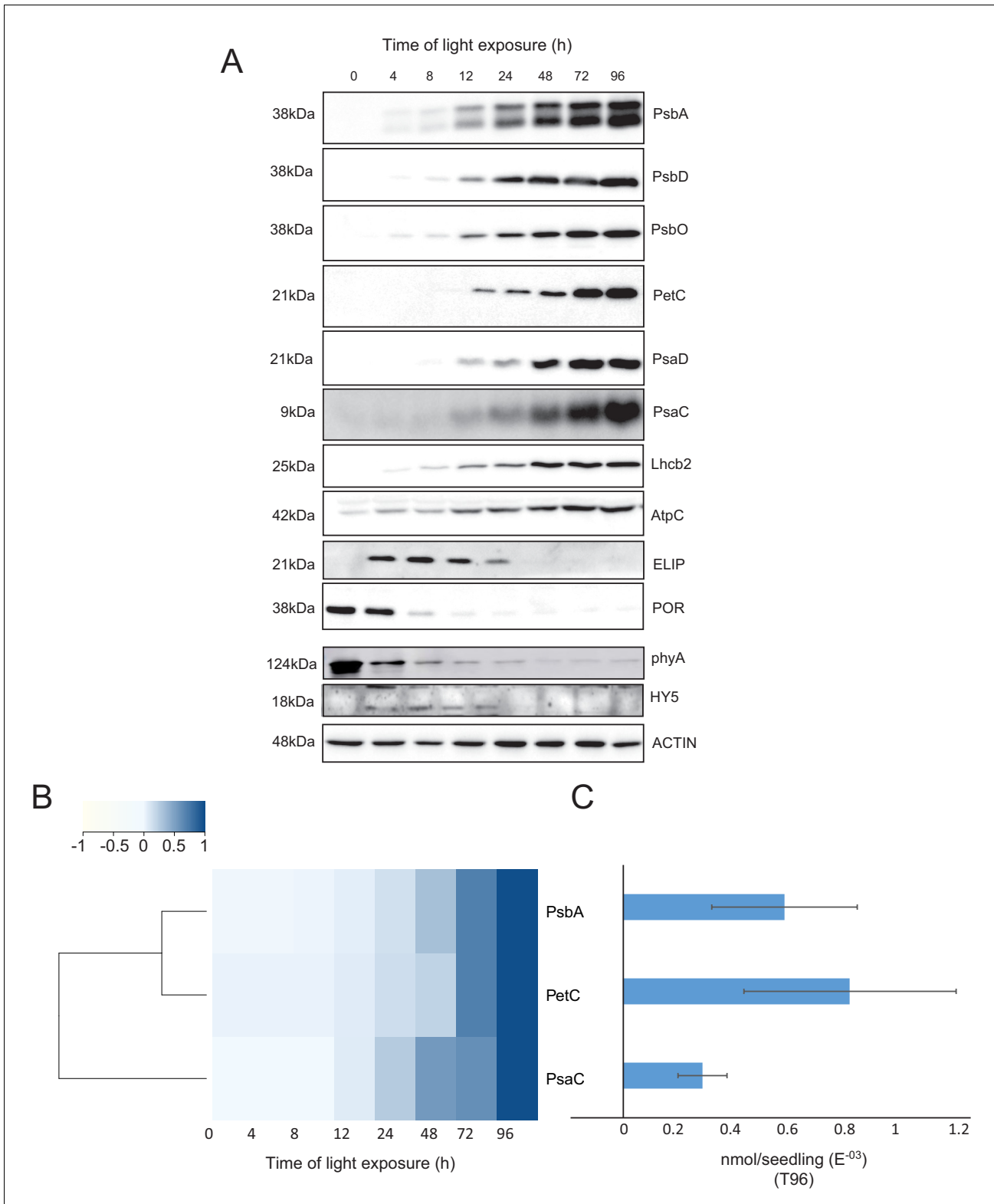


Figure 6. Accumulation dynamics of photosynthesis-related proteins during de-etiolation. Three-day-old etiolated seedlings of *Arabidopsis thaliana* were illuminated for 0 hr (T0), 4 hr (T4), 8 hr (T8), 12 hr (T12), 24 hr (T24), 48 hr (T48), 72 hr (T72), and 96 hr (T96) under white light ($40 \mu\text{mol}/\text{m}^2/\text{s}$). (A) Proteins were separated by SDS-PAGE and transferred onto nitrocellulose membrane and immunodetected with antibodies against PsbA, PsbD, PsbO, PetC, PsaD, PsaC, Lhcb2, AtpC, ELIP, POR, phyA, HY5, and ACTIN proteins. (B–C) Quantification of PsbA, PetC, and PsaC during de-etiolation. *Figure 6 continued on next page*

Figure 6 continued

Heatmap (B) was generated after normalization of the amount of each protein relative to the last time point (T96). Graph (C) corresponds to the absolute quantification of proteins at T96. Error bars indicate \pm SD ($n = 3$). Quantification of photosystem-related proteins during de-etiolation is detailed in **Figure 6—figure supplement 1**.

The online version of this article includes the following source data and figure supplement(s) for figure 6:

Source data 1.

Figure supplement 1. Quantification of photosynthesis-related proteins.

Identification of a chloroplast division phase

We observed a massive increase in the accumulation of photosynthesis-related proteins and galactolipids between T24 and T96, corresponding to $FC > 2$ in the levels of all major chloroplast proteins and lipids (**Figures 6** and **7**). Intriguingly, the total thylakoid surface per chloroplast increased by only 41% between these two time points (**Figure 4A** and **Table 1**). We reasoned that the increase in chloroplast proteins and lipids between T24 and T96 could be explained by increased chloroplast number (per cell and thus per seedling) and thus total thylakoid surface per seedling. We therefore determined chloroplast number per cell and the cell number and volume for each developmental stage through SBF-SEM analysis (T0, T4, T24, and T96) and confocal microscopy analysis for intermediary time points (T24–T96) (**Figure 8** and **Figure 8—figure supplement 1**). The chloroplast number per cell was constant from T4 (25 ± 8) to T24 (26 ± 6); however, in parallel with cell expansion (**Figure 8A and B**), chloroplast number increased sharply (fourfold increase) between T24 (26 ± 6) and T96 (112 ± 29), indicating that two rounds of chloroplast division occurred during this time. Immunoblot analysis of filamentous temperature-sensitive FtsZ1, FtsZ2-1, and FtsZ2-2 proteins showed that these key components of the chloroplast division machinery were already present during the early time points of de-etiolation. We observed considerably increased accumulation of these proteins between T24 and T48, consistent with the idea that activation of chloroplast division takes place at T24, leading the proliferation of chloroplasts (**Figure 8C**). However, levels of accumulation and replication of chloroplast 5 (ARC5) protein, another key component of the chloroplast division machinery, clearly increased during de-etiolation between T8 and T12, presumably reflecting assembly of the chloroplast division machinery before its activation and the proliferation of chloroplasts (**Figure 8D**). To test whether there is a correlation between chloroplast division and either volume or developmental stage, we measured the volume of dividing chloroplasts (selected visually based on the presence of a constriction ring, see **Figure 8—figure supplement 1**) at T24 and T96 using images acquired by SBF-SEM. The average volume of dividing chloroplasts at T24 and T96 were consistently higher than the average volume of all chloroplasts ($96 \mu\text{m}^3$ and $136 \mu\text{m}^3$ compared to $62 \mu\text{m}^3$ and $112 \mu\text{m}^3$, respectively) (**Figure 4B**, **Figure 8E** and **Figure 8—source data 1**) indicating that smaller chloroplasts are not dividing. This indicates that developing chloroplasts only divide once a certain chloroplast volume is reached.

Model of thylakoid surface expansion over time

The quantitative molecular data for the major compounds of thylakoids (galactolipids and proteins) and estimation of chloroplast number per cell allowed us to mathematically determine the thylakoid membrane surface area per seedling and its expansion over time (molecular approach hereafter) and compare it to the surface estimated from the 3D reconstruction (morphometric approach hereafter). First, we calculated the surface area occupied by the main galactolipids (MGDG and DGDG) and photosynthesis-related complexes (PSII, Cyt *b₆f*, and PSI) per seedling (**Table 2**), assuming a 1:1 ratio between number of PsbA, PetC, and PsaC subunits with their corresponding complexes (**Amunts and Nelson, 2009; Caffari et al., 2014; Schöttler et al., 2015**).

$$\text{Surface/seedling} = \text{nmol/seedling} * N * \text{nm}^2 \text{ per molecule} \quad (1)$$

Quantitative data for MGDG, DGDG, PsbA, PetC, and PsaC (nmol/seedling) obtained from lipiomic and immunological analyses (**Figures 6** and **7**) were converted into number of molecules/seedling using the Avogadro constant (N). To calculate the surface area of outer membrane of thylakoids (i.e. surface exposed to the stroma in lamellae and facing the other thylakoid in appressed regions) and account for the lipid double layer of the membrane, corresponding values of lipids

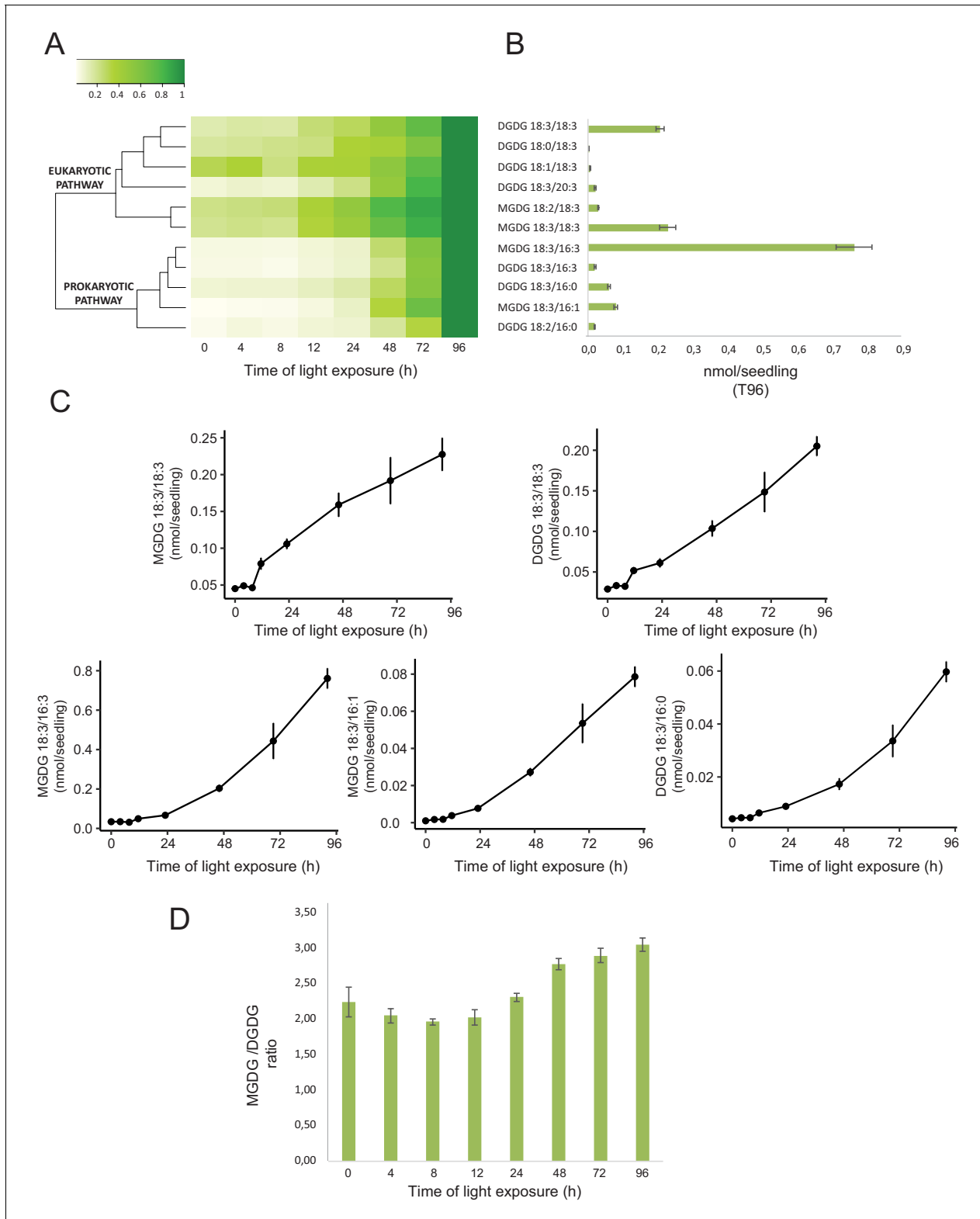


Figure 7. Accumulation dynamics of galactolipids during de-etiolation. Three-day-old etiolated seedlings of *Arabidopsis thaliana* were illuminated for 0 hr (T0), 4 hr (T4), 8 hr (T8), 12 hr (T12), 24 hr (T24), 48 hr (T48), 72 hr (T72), and 96 hr (T96) under white light (40 $\mu\text{mol}/\text{m}^2/\text{s}$). (A) Heatmap representation of galactolipids (MGDG and DGDG) during de-etiolation. Samples were normalized to the last time point (T96). (B) Absolute quantification at T96 expressed in nmol/seedling. Error bars indicate \pm SD ($n = 4$). (C) Absolute quantification (nmol/seedling) of the most abundant chloroplast galactolipids
 Figure 7 continued on next page

Figure 7 continued

MGDG (MGDG 18:3/18:3, MGDG 18:3/16:3, MGDG 18:3/16:1) and DGDG (DGDG 18:3/18:3, DGDG 18:3/16:0) at different time points during de-etiolation. Error bars indicate \pm SD ($n = 4$). (D) The MGDG/DGDG ratio was calculated using all 12 species of galactolipids detected during de-etiolation. Error bars indicate \pm SD ($n = 4$).

The online version of this article includes the following source data for figure 7:

Source data 1.

(Figure 7—source data 1, Table 2) were divided by 2. In addition, the lipid values were corrected by subtracting the portion of lipids incorporated into the envelope rather than present in the thylakoids (Table 1). The surface area occupied by molecules of MGDG and DGDG, and that of PSII, Cyt b_6f , and PSI photosynthetic complexes (nm^2 per molecule, corresponding to stroma-exposed surface) were retrieved from the literature (Table 3). Specifically, we used the minimal molecular area of MGDG and DGDG (Bottier et al., 2007). To quantify the surface area occupied by the galactolipids and photosynthetic complexes in thylakoids per seedling, the number of molecules per seedling of galactolipids was multiplied by the corresponding molecular surface area, whereas the number of molecules per seedling of PsbA, PetC, and PsaC (subunits of PSII, Cyt b_6f , and PSI, respectively) were multiplied by the surface area of the corresponding complex (see Table 3).

We calculated thylakoid surface (S) per seedling for each time point (t) as the sum of the surface occupied by MGDG, DGDG, photosynthetic complexes (PS), and ε per seedling, the latter of which corresponds to compounds such as other lipids (e.g. sulfoquinovosyldiacylglycerol, plastoquinone) or protein complexes (ATP synthase and NDH) that were not quantified.

$$S_{\text{thylakoid}}(t)/\text{seedling} = (S_{\text{MGDG}}(t) + S_{\text{DGDG}}(t) + S_{\text{PS}}(t) + \varepsilon)/\text{seedling} \quad (2)$$

Omitting the unknown ε factor, we plotted the thylakoid surface calculated for each time point where quantitative molecular data were available (T0, T4, T8, T12, T24, T48, T72, and T96) as a function of the duration of light exposure (Figure 9—figure supplement 1). The best fitting curve corresponded to a S-shaped logistic function, characterized by a lag phase at early time points (T0–T8), followed by a phase of near-linear increase, and a final plateau at the final time points (T72–T96). To model this function, a four-parameter logistic non-linear regression equation was used to describe the dynamics of the total thylakoid surface over time (Figure 9—figure supplement 1C).

Superimposition of molecular and morphometric data

We compared the values of thylakoid surface, as obtained with the model based on molecular data, with the values obtained from the morphometric analysis (Figure 9). The total thylakoid surface per seedling ($S_{\text{thylakoid_morpho}}$) was calculated by multiplying the thylakoid surface ($S_{\text{thylakoid}}$) per chloroplast obtained by morphometrics (Figure 4A) by the number of chloroplasts (nb.cp) per cell (Figure 8A) and the number of cells (nb.cells) per seedlings for each time point (t).

$$\frac{S_{\text{thylakoid_morpho}}(t)}{\text{seedling}} = \quad (3)$$

$$S_{\text{thylakoid}}(t)/\text{chloroplast} * \text{nb.cp}(t)/\text{cell} * \text{nb.cells}(t)/\text{seedling}$$

We estimated cell number per seedling by measuring the total volume occupied by palisade and spongy cells in cotyledons (that corresponded to 50% of total cotyledon volume; Figure 9—figure supplement 2) and dividing this by the average cell volume (Table 1). As reported previously (Pyke and Leech, 1994), cell number was constant during cotyledon development. We estimated this number as 3000 mesophyll and palisade cells per seedling at T24 and T96 (Figure 9—figure supplement 2). The thylakoid membrane surface quantified by the morphometric approach was also estimated at T4, assuming that cell number per cotyledon remained similar between T4 and T24. We compared the thylakoid surface predicted by our mathematical model to the surface estimated experimentally with our 3D thylakoid reconstruction and morphometric measurements (Figure 9 and Table 1). As shown in Figure 9, the two approaches showed very similar total thylakoid surface area per seedling at T4 and T24 and differences in this parameter by T96. This indicates that the plateau

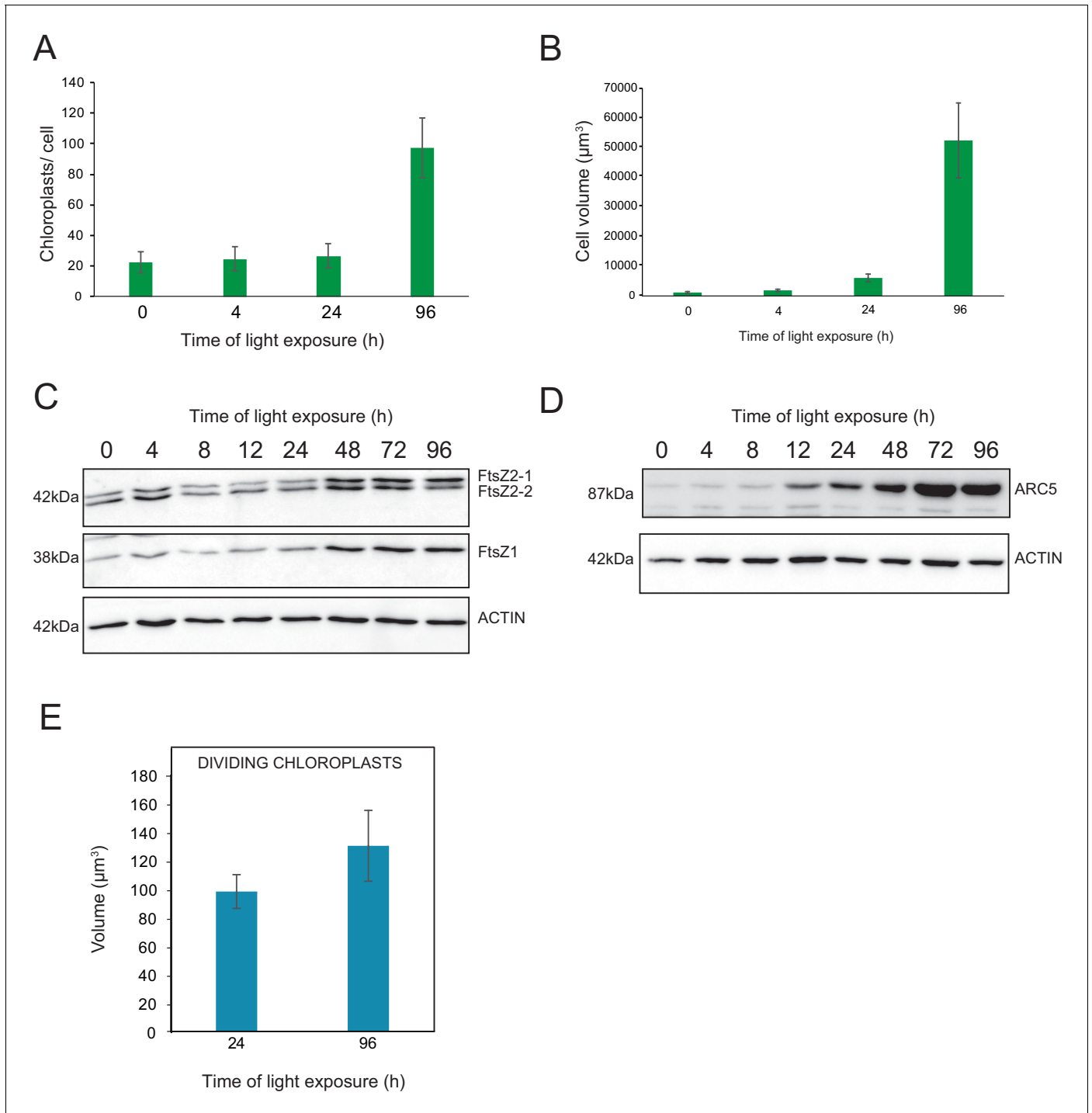


Figure 8. Relationship between chloroplast proliferation and chloroplast volume. (A–B) Chloroplast number and cell volume in cotyledons of 3-day-old, dark-grown *Arabidopsis thaliana* seedlings illuminated for 0 hr (T0), 4 hr (T4), 24 hr (T24), and 96 hr (T96) in continuous white light ($40 \mu\text{mol}/\text{m}^2/\text{s}$). (A) Chloroplast number per cell during de-etiolation. Error bars indicate \pm SD ($n = 6$ for T0 and T4; seven for T24; five for T96). (B) Cell volume was quantified by the Labels analysis module of Amira software. Error bars indicate \pm SD ($n = 5$ –6). (C–D) Total proteins were extracted from T0–T96 seedlings, separated on SDS-PAGE, and transferred onto nitrocellulose. Proteins involved in plastid division (C, FtsZ; D, ARC5) and loading control (actin) were detected using specific antibodies (FtsZ2 antibody recognizes both FtsZ2-1 and FtsZ2-2). (E) Volume of dividing chloroplast at T24 and T96. Error bars indicate \pm SD ($n = 3$). Further details of chloroplast proliferation in parallel with cell expansion are provided in **Figure 8—figure supplement 1**.

Figure 8 continued on next page

Figure 8 continued

The online version of this article includes the following source data and figure supplement(s) for figure 8:

Source data 1.

Figure supplement 1. Chloroplast proliferation in parallel with cell expansion.

phase suggested by the model is not validated and that other components that were not included in the model probably contributed to the expansion of thylakoids at later time points of de-etiolation.

Discussion

Here, the analysis of 3D structures of entire chloroplasts in Arabidopsis in combination with proteomic and lipidomic analyses provide an overview of thylakoid biogenesis. **Figure 10** depicts a summary of the changes that occur during the de-etiolation process. When considering chloroplast development, our study shows that de-etiolation is divided into two phases. We documented structural changes (disassembly of the PLB and the gradual formation of thylakoid lamellae) and initial increases of ER- and PL-pathway galactolipids and photosynthesis-related proteins (PSII, PSI, and Cyt *b₆f*) during the ‘Structure Establishment Phase’, which was followed by increased chloroplast number in parallel with cell expansion in the ‘Chloroplast Proliferation Phase’. Collection of quantitative data allowed us to create a mathematical model of thylakoid membrane expansion and describe this process during de-etiolation.

A set of 3D reconstructions of whole chloroplasts by SBF-SEM

In contrast to electron tomography, which is limited in the volume of observation, SBF-SEM allows the acquisition of ultrastructural data from large volumes of mesophyll tissue and the generation of 3D reconstructions of entire cells and chloroplasts (**Figure 3** and **Figure 8—figure supplement 1, Videos 1–4**). SEM image resolution was sufficient to visualize stromal lamellae and grana contours, whereas grana segmentation in different lamellae was deduced according to our own TEM analysis and literature data (**Figure 2—figure supplement 1** and **Figure 3—figure supplement 1**). This approach allowed us to obtain quantitative data of chloroplast and thylakoid structure at different developmental stages during de-etiolation at the whole-chloroplast level. By T96, the latest time point of our analysis, the total surface area of thylakoids present in the seedling cotyledons was about 700 mm² (see values in **Table 1** for calculation), about 500-fold greater than the surface area of one cotyledon at this developmental stage. This result is supported by previous estimates made regarding thylakoid surface area relative to leaf surface area (**Bastien et al., 2016; Demé et al., 2014**). Moreover, the extent of thylakoid surface area emphasizes how fast and efficient thylakoid

Table 2. Surface area occupied by the main galactolipids (MGDG and DGDG) and photosynthetic complexes (PSII, cyt *b₆f*, and PSI). Shown are values at different time points following illumination of 3-day-old etiolated seedlings. Each value (in bold) indicates the calculated surface area in μm² and corresponds to the average of three biological replicates. Errors indicate SD.

	T0	T4	T8	T12	T24	T48	T72	T96
MGDG	1.11E+07 (±0.03E+07)	1.15E+07 (±0.1E+07)	1.11E+07 (±0.1E+07)	1.75E+07 (±0.18E+07)	4.16E+07 (±0.4E+07)	8.65E+07 (±0.6E+07)	1.68E+08 (±0.09E+08)	2.35E+08 (±0.2E+07)
DGDG	3.64E+06 (±0.4E+06)	4.23E+06 (±0.5E+06)	4.10E+06 (±0.1E+06)	6.26E+06 (±0.5E+05)	1.32E+07 (±0.107)	2.32E+07 (±0.2E+07)	3.97E+07 (±0.3E+07)	5.48E+07 (±0.41E+07)
PSII	2.04E+06 (±0.5E+05)	2.74E+06 (±0.5E+05)	4.40E+06 (±0.2E+06)	9.91E+06 (±1.3E+06)	2.75E+07 (±0.6E+07)	6.06E+07 (±0.2E+07)	1.15E+08 (±0.2E+08)	1.83E+08 (±0.5E+08)
PSI	0E+00 (±0E+00)	0E+00 (±0E+00)	0E+00 (±0E+00)	8.95E+05 (±4.49E+05)	1.33E+07 (±0.4E+07)	2.10E+07 (±1.30E+07)	3.04E+07 (±0.8E+07)	4.24E+07 (±1.89E+07)
Cyt <i>b₆f</i>	7.99E+05 (±2.33E+05)	8.43E+05 (±2.91E+05)	7.5E+05 (±1.33E+05)	1.57E+06 (±0.7E+06)	3.44E+06 (±1.22E+06)	5.30E+06 (±1.01E+06)	1.69E+07 (±0.5E+06)	2.37E+07 (±1.11E+07)

The online version of this article includes the following source data for Table 2:

Source data 1.

Table 3. Surface area occupied by galactolipid and photosynthetic complexes.

(A) Values were retrieved from the corresponding references. MGDG and DGDG surfaces correspond to the minimal molecular area. The surfaces of PSII-LHCII, PSI, and Cyt *b₆f* complexes correspond to the surface exposed to the stroma (19*26 nm, 20*15 nm, and 90*55 Å, respectively). (B) Values from the table in panel A were used to calculate the total surface per seedling corresponding to MGDG and DGDG galactolipids, and PSII, PSI, and Cyt *b₆f* complexes.

	Surface in nm ²	reference
MGDG	0,82	<i>Bottier et al., 2007</i>
DGDG	0,64	<i>Bottier et al., 2007</i>
PSII - LHCII (C2 S2 M2)	494	<i>Caffarri et al., 2014</i>
Cyt <i>b₆f</i>	49,5	<i>Kurusu et al., 2003</i>
PSI	300	<i>Caffarri et al., 2014</i>

biogenesis is during plant development, allowing plants to optimize light absorption capacity, ensuring their primary source of energy.

Chloroplast development: 'structure establishment phase'

We observed TEM images and quantified 3D chloroplast ultrastructure by SBF-SEM analysis during chloroplast differentiation. Typical etioplast structure of the PLB connected with tubular PTs was replaced by lamellar thylakoids by T4. Measurements of PLB diameter and thylakoid length and thickness were comparable with literature values (*Biswal et al., 2013; Daum et al., 2010; Kirchoff et al., 2011*), indicating that these morphometric values are conserved between various model organisms. Thylakoid surface area per chloroplast increased 20-fold between T4 and T24.

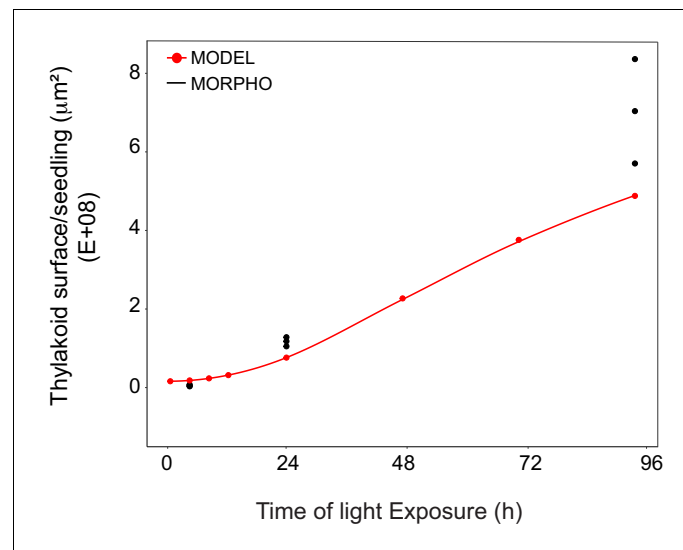


Figure 9. Superimposition of thylakoid surface per seedling obtained from morphometric analysis and mathematical modeling. Thylakoid surface per seedling was estimated using quantitative data from 3View analysis ('MORPHO' black dots at T4, T24, and T96; and see *Figure 4* and *Table 1*) and model generated using the quantitative data from proteomics and lipidomics ('MODEL' red line at T0, T4, T8, T12, T24, T48, T72, and T96, and *Table 1*). Further details are provided in *Figure 9—figure supplements 1* and *2*.

The online version of this article includes the following source data and figure supplement(s) for figure 9:

Source data 1.

Figure supplement 1. Non-linear mixed effect model of thylakoid surface during de-etiolation.

Figure supplement 2. Morphometric analysis of cotyledons.

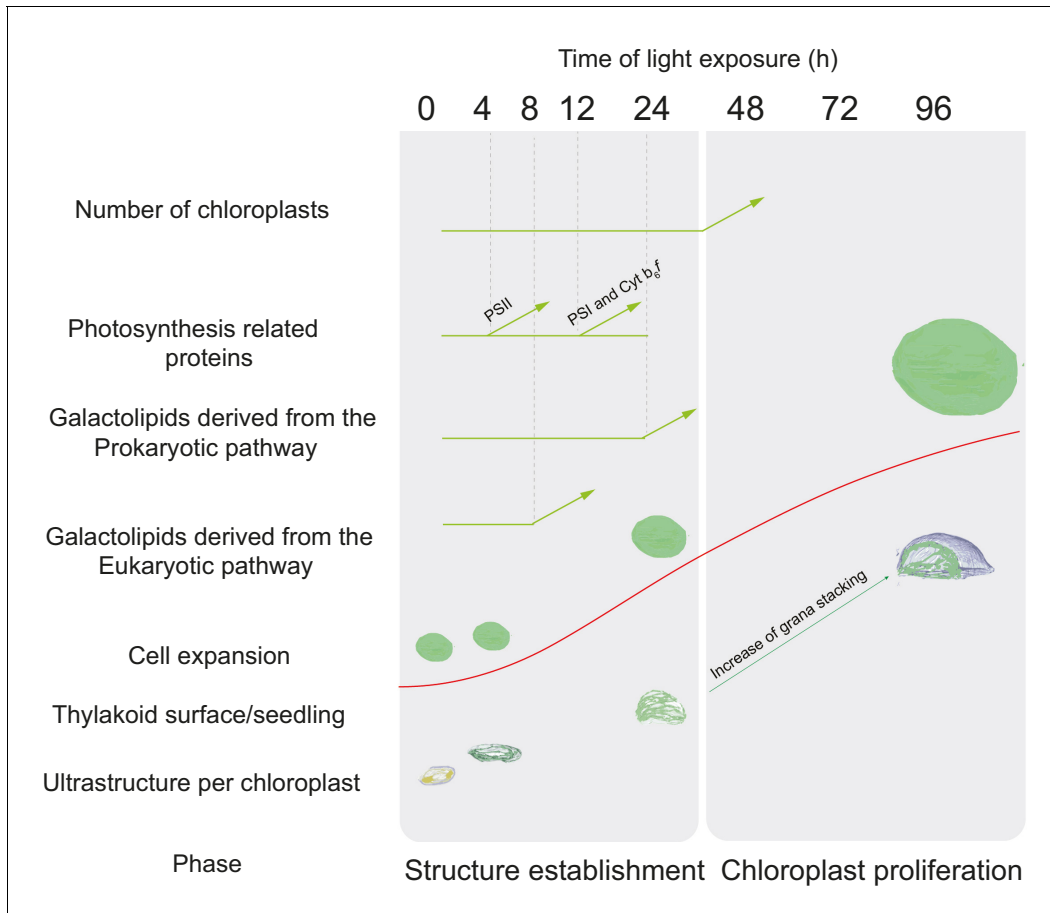


Figure 10. Overview of changes observed during the de-etiolation process in *Arabidopsis thaliana* seedlings. The ‘Structure Establishment Phase’ is correlated with disassembly of the PLB and gradual formation of the thylakoid membrane as well as an initial increase of eukaryotic (after 8 hr) and prokaryotic (after 24 hr) galactolipids and photosynthesis-related proteins (PSII subunits at 4 hr, PSI and *cyt b₆f* at 12 hr). The subsequent ‘Chloroplast Proliferation Phase’ is associated with an increase in chloroplast number in concomitance with cell expansion, a linear increase of prokaryotic and eukaryotic galactolipids and photosynthesis-related proteins, and increased grana stacking. The red curve (retrieved from the **Figure 9**) shows thylakoid surface/seedling dynamics during the de-etiolation process.

Remarkably, PSII maximum quantum yield (F_v/F_m) reached the maximal value (0.8) by T14, independent of light intensity (**Figure 1D** and **Figure 1—figure supplement 1**). This shows that PSII assembly, and more globally assembly of the photosynthetic machinery, occurs simultaneously with thylakoid membrane formation and that photosynthesis is operational almost immediately upon greening.

Our proteomic and lipidomic analyses suggest that chloroplast ultrastructural changes rely on specifically timed molecular changes. Proteomic analysis revealed the accumulation patterns of more than 5000 unique proteins at eight time points during de-etiolation. These data provide information for plastid development and more widely on light-regulated developmental processes (**Figure 5—source data 1**). Our dataset is more exhaustive regarding temporal resolution and the number of unique proteins detected than that of previous reports on chloroplast differentiation and de-etiolation (**Brütigam and Weber, 2009; Plösch et al., 2011; Reiland et al., 2011; Wang et al., 2006**). Overall, the dynamics of the accumulation of proteins revealed by proteomics was similar to the dynamics observed by immunoblots (**Figure 6; Figure 6—figure supplement 1** and **Figure 5—source data 1**), although not totally identical for some proteins (e.g. *phyA*, *HY5*). The observed differences may be due to the detection methods of the two approaches (detection and relative quantification of individual peptides in proteomics versus detection of the full-length protein by

immunoblot analysis) or other inherent limitations of proteomics when faced with low-abundance proteins like transcription factors.

Here, we focused on chloroplast-localized proteins, specifically on thylakoid membrane proteins. According to the SUBA4 localization consensus, 1112 proteins were assigned to plastids, which covers about a third of the total plastid proteome (Ferro et al., 2003; Hooper et al., 2017; Kleffmann et al., 2007). We observed striking changes at the chloroplast ultrastructural levels, and in particular the formation of thylakoids between T0 and T4. However, our proteomic analysis indicated only a few changes in abundance of proteins between these time points, including proteins constituting the photosynthetic machinery (Figure 8—figure supplement 1 and Figure 5—source data 1). Also, we did not observe a significant increase in the major galactolipids constituting the lipid bilayer (Figure 7 and Figure 7—source data 1). Therefore, our data suggest that the reorganization of pre-existing molecules rather than de novo synthesis is responsible for the major chloroplast ultrastructural changes that occur between T0 and T4. These results are consistent with other studies reporting only minor increases in protein accumulation and translation during initial chloroplast differentiation (Dubreuil et al., 2018; Kleffmann et al., 2007; Reiland et al., 2011). A significant change in the proteome was observed when comparing T24 and T0 but overall this change appeared gradual, indicating that increase of chloroplast associated proteins does not exactly follow the two-step induction of corresponding nuclear encoded transcripts reported previously (Dubreuil et al., 2018). At T96 the abundance of 607 proteins (12% of the identified) was increased which confirm the massive reorganization of the proteome following the reorganization of the transcriptome during photomorphogenesis (Ma et al., 2001). Proteins whose transcript levels decreases in response to light exposure were also downregulated at the protein levels (e.g. phyA and PORA) (Figure 6; Ma et al., 2001). GO analysis combined with expression pattern-based hierarchical clustering highlighted that most photosynthesis-related proteins are globally coregulated (Figure 5—figure supplement 1, clusters 2 and 6) which correlates as well with the overall increase of their corresponding transcripts upon light exposure (Ma et al., 2001). However, targeted immunoblot analysis revealed different accumulation dynamics for specific photosystem subunits: PSI subunits were detected at later time points than PSII subunits, but thereafter PSI subunit accumulation was faster (Figure 6). The kinetics of different photosynthetic parameters were consistent with the sequential activation of PSII and PSI, in particular photochemical quenching, which showed increased oxidation of the plastoquinone pool by T14 (Figure 1—figure supplement 1). Early accumulation of proteins such as Lhcb5, -6, and PSBS could be a way to quickly induce photoprotective mechanisms such as non-photochemical quenching to prevent PSII photodamage during initial photosynthetic machinery assembly. Differences in PSI and PSII accumulation dynamics and activity have been consistently observed in other chloroplast development experimental systems, including in Arabidopsis cell cultures, during germination and development of Arabidopsis seedlings in the light, and in tobacco leaves upon reillumination after dark adaptation (Armarego-Marriott et al., 2019; Dubreuil et al., 2018; Liang et al., 2018). The molecular mechanisms underlying this differential accumulation are currently unknown; however, it is intriguing to observe that PSII protein abundance is higher at early stages of thylakoid formation when grana have not yet been organized. Preferential localization of the PSI and PSII protein complexes in specific thylakoid membrane domains have been reported (lamellae and grana, respectively) (Wietrzynski et al., 2020). Therefore, the timing of PSII/PSI relative abundance do not match with their preferential localization. It is possible that the formation of PSI still needs to be delayed until grana formation and PSII relocalization is initiated, which can prevent spillover between the two photosystems (Anderson, 1981).

Chloroplast membranes have a specific composition that differs from that of other cell membranes. Galactolipids constitute the bulk of the thylakoid membranes, but are mostly absent from other membrane systems under growth conditions where phosphorus nutrient is available (Jouhet et al., 2007). MGDG and DGDG represent around 80% of the thylakoid membrane lipids. The absolute quantification of 12 types of MGDG and DGDG galactolipids (representing the major forms) revealed specific patterns of accumulation (Figure 7). Results showed a gradual accumulation of MGDG and DGDG galactolipids derived from the ER pathway from T8 to T24, whereas galactolipids from the PL pathway started to accumulate after 1 day of light exposure (T24). This illustrates the different galactolipid compositions of etioplasts and chloroplasts: ER-pathway galactolipids are predominant in the etioplast whereas PL-pathway galactolipids are predominant in the chloroplast. As no significant changes in lipid accumulation were observed by T4, it appears likely that the

emergence of PTs relies on the existing lipids in the etioplast PLB, as suggested also by *Armarego-Marriott et al., 2019*. At later time points, galactolipids from both the ER and PL pathways constitute the lipid matrix of the thylakoid membrane. How the two galactolipid biosynthesis pathways are regulated during development and/or upon light treatment remains to be elucidated; however, we hypothesize that the PL pathway gains traction after T24 when photosynthetic capacity is fully established.

Chloroplast development: 'chloroplast proliferation phase'

Chloroplast development continued between T24 and T96, during which thylakoid membranes acquired grana stacks with more clearly defined organization (*Figure 2*). Thylakoid surface increased by only 41%; however, chloroplasts continued to enlarge at a rate comparable to previous de-etiolation stages (T0–T24). This chloroplast volume expansion may be caused by enlargement of extra-thylakoidal spaces occupied by emerging starch granules. These results suggest that large amounts of lipids and proteins are necessary to build up the thylakoid membrane until T24, whereas increases in lipids and proteins between T24 and T96 enable the expansion of already functional thylakoid membranes in preparation for chloroplast division. Indeed, chloroplast number per cell increased during de-etiolation, a process that depends on the division of pre-existing chloroplasts.

Both chloroplasts and mitochondria divide through the activity of supramolecular complexes that constitute the organelle division machineries (*Yoshida, 2018*). As chloroplast proliferation was observed between T24 and T96, chloroplast division may correlate with developmental stage of the organelle. Components of the chloroplast division machinery (e.g. FtsZ and ARC5) were detectable in etioplasts; however, their protein levels accumulated significantly during de-etiolation as chloroplasts proliferated (*Figure 8C and D*). Interestingly, the capacity to divide appeared to correlate with a minimum chloroplast volume of about $100 \mu\text{m}^3$, even at T24 when most chloroplasts were smaller (*Figure 8E and Figure 4B*). On the other hand, plastid division and volume seem not to correlate with light and chloroplast photosynthetic capacity in monocots, as etioplasts can divide and increase in size with leaf cell development in absence of light (*Robertson and Laetsch, 1974; Klein and Mullet, 1986*). Whether and how cell, chloroplast size and developmental stage can be sensed to activate the chloroplast division machinery remains poorly understood and requires further study.

A model of thylakoid expansion

Our mathematical model describing the expansion of thylakoid surface per seedling over time considered the surface area occupied by the membrane lipids MGDG and DGDG and the major photosynthetic complexes PSII, PSI, and Cyt *b₆f*. We omitted some components that contribute to the total thylakoid membrane surface (e.g. the protein complexes ATP synthase and NDH, and the lipid sulfoquinovosyldiacylglycerol; together grouped as 'ε' in *Equation 2*). The predictions made by our model fit the surface estimated by SBF-SEM at T4 and T24, whereas they do not fit that at T96. This means that compounds used to generate the mathematical model appear to contribute most to changes in thylakoid surface during early stages of de-etiolation (the structure establishment phase). By contrast, during the later stages of de-etiolation (the chloroplast proliferation phase), the contribution of other compounds omitted in our model is obviously required to build up thylakoid surface.

Our proteomics data (*Figure 5—figure supplement 1* and Dataset 2) revealed some proteins that increased between T24 and T96, such as the FtsH protease (AT2G30950). FtsH proteases have a critical function during thylakoid biogenesis. In Arabidopsis, they constitute a hetero-hexameric complex of four FtsH subunits, which is integrated in the thylakoid membrane (*Kato and Sakamoto, 2018*). Although the FtsH complex surface area is unknown in Arabidopsis, it can be considered as a potential compound contributing to the thylakoid surface changes missing from our mathematical model. Other proteins, such as those involved in carotenoid biosynthesis (AT3G10230) or fatty acid metabolism (AT1G08640), also increased significantly after T24, implying that they contribute to the 'ε' factor.

A follow-up study would be to test the model under different conditions to investigate how this biological system responds to internal (perturbing hormone concentrations, genetic modification of thylakoid lipid and protein composition) or external (different qualities of light) factors. This could be

instrumental in revealing new potential regulatory mechanisms of thylakoid biogenesis and maintenance.

Upon de-etiolation, the development of photosynthetic capacity relies on successful chloroplast biogenesis. At the cellular level, this process is expected to be highly coordinated with the metabolism and development of other organelles. Lipid synthesis involves lipid exchanges between chloroplasts and the endoplasmic reticulum. How lipid trafficking is organized remains poorly understood, but could require membrane contact sites between these two organelles (Michaud and Jouhet, 2019). Physical interaction between mitochondria and chloroplasts have been reported previously in diatoms (Bailleul et al., 2015; Flori et al., 2017). Whether such contact sites occur and are functional in plants is unknown; however, these mechanisms are hypothesized to exist since it is necessary that chloroplasts exchange metabolites with mitochondria and peroxisomes to ensure activation of photorespiration concomitantly with photosynthesis. The study of membrane contact sites is an emerging field in cell biology (Scorrano et al., 2019). Future work will focus on analysing the dynamics and functionality of contact sites between chloroplast membranes and other organelles, and investigate the general coordination of plant cell metabolism during de-etiolation. These questions could be further addressed using the SBF-SEM stacks and proteomic resource described here.

Materials and methods

Plant material and growth conditions

Arabidopsis thaliana seeds (Columbia ecotype) were surface-sterilized with 70% (v/v) ethanol with 0.05% (v/v) Triton X-100, then washed with 100% ethanol. Seeds were sown in spot containing 50 seeds (to facilitate rapid harvest) on agar plates containing 0.5 × Murashige and Skoog salt mixture (Duchefa Biochemie, Haarlem, Netherlands) without sucrose. Following stratification in the dark for 3 days at 4°C, seeds were irradiated with 40 μmol m⁻² s⁻¹ for 2 hr at 21°C and then transferred to the dark (plates were covered with three layers of aluminium foil) for 3 days growth at 21°C. For chlorophyll, protein and lipid analyses, 50 etiolated seedlings per time point and replicate were collected in a dark room using a dim green LED lamp as light source (0 hr of light; T0) and at selected time points (T4, T8, T12, T24, T48, T72, T96) upon continuous white light exposure (40 μmol m⁻² s⁻¹ at 21°C), transferred into 1.5 ml tube, flash-frozen in liquid nitrogen and stored at -80°C until further use. For TEM and SBF-SEM microscopy, seedlings were directly immersed into fixation buffer at the corresponding time point.

Photosynthetic parameters

Maximum quantum yield of photosystem II ($\Phi_{MAX} = F_v/F_M = (F_m - F_o)/F_m$ where F_m is the maximal fluorescence in dark adapted state, F_o is minimal fluorescence in dark adapted state, F_v is the variable fluorescence ($F_m - F_o$)), photosystem II quantum yield in the light (Φ_{PSII}), and photochemical quenching (qP) were determined using a Fluorcam (Photon Systems Instruments) with blue-light LEDs (470 nm). Plants were dark adapted for a minimum of 5 min before measurement.

Chlorophyll concentration

Chlorophylls were extracted in 4 volumes of dimethylformamide (DMF) (v/w) overnight at 4°C. After centrifugation, chlorophylls were measured using a NanoDrop instrument at 647 nm and 664 nm. Chlorophyll contents were calculated according to previously described methods (Porra et al., 1989).

Transmission electron microscopy

Samples were fixed under vacuum (200 mBar) in 0.1 M cacodylate buffer (pH 7.4) containing 2.5% (w/v) glutaraldehyde and 2% (w/v) formaldehyde (fresh from paraformaldehyde) for 4 hr and left in the fixation solution for 16 hr at 4°C. Samples were then incubated in a solution containing 3% (w/v) potassium ferrocyanide and 4 mM calcium chloride in 0.1 M cacodylate buffer combined with an equal volume of 4% (w/v) aqueous osmium tetroxide (OsO₄) for 1 hr, on ice. After the first heavy metal incubation, samples were rinsed with ddH₂O and treated with 1% (w/v) thiocarbonylhydrazide solution for 1 hr at 60°C. Samples were rinsed (ddH₂O for 15 min) before the second exposure to 2% (w/v) OsO₄ aqueous solution for 30 min at room temperature. Following this second exposure to

osmium, tissues were placed in 1% (w/v) uranyl acetate (aqueous) and left overnight at 4°C. The samples were rinsed with ddH₂O for 15 min, and placed in the lead aspartate solution for 30 min at 60°C. Samples were dehydrated in a series of aqueous ethanol solutions ranging from 50% (v/v) to 100%, then embedded in Durcupan resin by successive changes of Durcupan resin/acetone mixes, with the last imbibition in 100% Durcupan resin. Polymerization of the resin was conducted for 48 hr at 60°C (Deerinck *et al.*, 2010). Ultra-thin sections (70 nm) were cut using Ultrathin-E microtome (Reichert-Jung) equipped with a diamond knife. The sections were analyzed with a Philips CM-100 electron microscope operating at 60 kV.

Confocal microscopy

To derive the chloroplast and cell volumes, images of 1–5 μm thick sections of cotyledon cells were acquired with ×10 and ×40 oil immersion objectives using a LEICA TCS SP5 confocal laser scanning microscope. Chlorophyll was excited using a red laser (33%) and spectral detection channel was PMT3.

SBF-SEM

SBF-SEM was performed on Durcupan resin-embedded cotyledons representing the four de-etiolation time points T0, T4, T24, and T96. Overview of the mesophyll tissue (≈600 images) and zoomed stacks of the chloroplasts (≈300 images) were acquired. Voxel size of T4 zoomed stacks: 3.9 × 3.9 × 50 nm; T24: 4.7 × 4.7 × 50 nm; T96: 5.6 × 5.6 × 50 nm. Voxel size for T0 overview: 9.5 × 9.5 × 100 nm; T4: 19.3 × 19.3 × 100 nm; T24: 40 × 40 × 200 nm; T96: 43.5 × 43.5 × 200 nm.

Acquired datasets were aligned and smoothed respectively, using the plugins MultiStackReg and 3D median filter, provided by the open-source software Fiji.

We performed a stack-reslice from Fiji to generate a new stack by reconstructing the slices at a new pixel depth to obtain isotropic voxel size and improve z-resolution. The segmentation and 3D mesh geometry information of plastid /thylakoid (T0, T4, T24 and T96) were implemented by open-source software 3D Slicer (Fedorov *et al.*, 2012) and MeshLab (Cignoni *et al.*, 2008) respectively.

Segmentation, 3D reconstruction, and surface and volume quantification

Segmentation and 3D reconstruction of 3View and confocal images were performed using Amira software (FEI Visualization Sciences Group). Specifically, prolamellar body, thylakoids, and envelope membranes as well as the cells were selected using a semi-automatic tool called Segmentation Editor. From the segmented images, triangulated 3D surfaces were created using Generate Surface package. Quantification of morphometric data (Area 3D and volume 3D) was acquired using Label Analysis package.

Analysis of grana segmentation

Grana structures acquired from SBF-SEM were selected in Amira. The grana selections were converted in line set view in Amira software using the Generate Contour line package. To complete the grana segmentation, the line set views were imported into the Rhino six software (Robert McNeel and Associates, USA). Every granum was segmented in layers with a specific thickness and distance according to quantitative data collected (Figure 2—figure supplement 1 and Figure 3—figure supplement 1). After segmentation, images were re-imported in Amira software to quantify perimeter using the Label Analysis package.

Chloroplast number determination

Chloroplasts per cell were counted manually using Image J software (Wayne Rasband, National Institutes of Health). From the same SBF-SEM stack, five and/or 6 cells were cropped at each time point (T0, T4, T24, and T96) to quantify chloroplast number per cell. From TEM images, chloroplast number/cell was determined at T24 (16 cells), T48 (12 cells), T72 (12 cells), and T96 (17 cells). TEM images were acquired from two independent experiments.

Liquid chromatography–mass spectrometry analysis and protein quantification

Etiolated seedlings were grown as described above. At each time point, ca. 80 seedlings were pooled, frozen in liquid nitrogen, and stored at -80°C until use. Frozen material was ground with a mortar and pestle, and 40–80 mg of plant material was used for protein and peptide preparation using the iST kit for plant tissues (PreOmics, Germany). Briefly, each sample was resuspended in 100 μL of the provided 'Lysis' buffer and processed with High Intensity Focused Ultrasound (HIFU) for 1 min by setting the ultrasonic amplitude to 65% to enhance solubilization. For each sample, 100 μg of protein was transferred to the cartridge and digested by adding 50 μL of the provided 'Digest' solution. After 180 min of incubation at 37°C , the digestion was stopped with 100 μL of the provided 'Stop' solution. The solutions in the cartridge were removed by centrifugation at 3,800 g , whereas the peptides were retained on the iST filter. Finally, the peptides were washed, eluted, dried, and re-solubilized in 18.7 μL of solvent (3% (v/v) acetonitrile, 0.1% (v/v) formic acid).

Mass spectrometry (MS) analysis was performed on a Q Exactive HF-X mass spectrometer (Thermo Scientific) equipped with a Digital PicoView source (New Objective) and coupled to a M-Class UPLC (Waters). Solvent composition at the two channels was 0.1% (v/v) formic acid for channel A and 0.1% formic acid, 99.9% (v/v) acetonitrile for channel B. For each sample, 2 μL of peptides were loaded on a commercial MZ Symmetry C18 Trap Column (100 \AA , 5 μm , 180 μm \times 20 mm, Waters) followed by nanoEase MZ C18 HSS T3 Column (100 \AA , 1.8 μm , 75 μm \times 250 mm, Waters). The peptides were eluted at a flow rate of 300 nL/min by a gradient of 8–27% B in 85 min, 35% B in 5 min, and 80% B in 1 min. Samples were acquired in a randomized order. The mass spectrometer was operated in data-dependent mode (DDA), acquiring a full-scan MS spectra (350–1400 m/z) at a resolution of 120,000 at 200 m/z after accumulation to a target value of 3,000,000, followed by HCD (higher-energy collision dissociation) fragmentation on the 20 most intense signals per cycle. HCD spectra were acquired at a resolution of 15,000 using a normalized collision energy of 25 and a maximum injection time of 22 ms. The automatic gain control (AGC) was set to 100,000 ions. Charge state screening was enabled. Singly, unassigned, and charge states higher than seven were rejected. Only precursors with intensity above 250,000 were selected for MS/MS. Precursor masses previously selected for MS/MS measurement were excluded from further selection for 30 s, and the exclusion window was set at 10 ppm. The samples were acquired using internal lock mass calibration on m/z 371.1012 and 445.1200. The mass spectrometry proteomics data were handled using the local laboratory information management system (LIMS) (Türker *et al.*, 2010).

Protein quantification based on precursor signal intensity was performed using ProgenesisQI for Proteomics (v4.0.6403.35451; nonlinear dynamics, Waters). Raw MS files were loaded into ProgenesisQI and converted to mzIn files. To select the alignment reference, a group of samples that had been measured in the middle of the run (to account for drifts in retention times) and derived from de-etiolation time point T12 or later (to account for increasing sample complexity) was preselected, from which replicate 3 of time point T48 was then automatically chosen as best alignment reference. After automatic peak picking, precursor ions with charges other than 2+, 3+, or 4+ were discarded. The five highest-ranked MS/MS spectra, at most, for each peptide ion were exported, using the deisotoping and charge deconvolution option and limiting the fragment ion count to 200 peaks per MS/MS. The resulting Mascot generic file (.mgf) was searched with Mascot Server version 2.6.2 (<http://www.matrixscience.com>) using the following settings: trypsin digest with up to two missed cleavages allowed; carbamidomethylation of cysteine as fixed modification; N-terminal acetylation and oxidation of methionine residue as variable modifications; precursor ion mass tolerance 10 ppm; fragment ion (MS/MS) tolerance 0.04 kDa. This search was performed against a forward and reverse (decoy) Araport11 database that included common MS contaminants and iRT peptides. The mascot result was imported into Scaffold Q+S (v4.8.9; Proteome Software Inc), where a spectrum report was created using a false discovery rate (FDR) of 10% and 0.5% at the protein and peptide level, respectively, and a minimum of one identified peptide per protein. After loading the spectrum report into ProgenesisQI, samples were normalized using the 'normalize to all proteins' default settings (i.e. normalization was performed to all ions with charges 2+, 3+ or 4+). Samples were grouped according to de-etiolation time point in a between-group analysis with four replicates for each condition, except for time point T0 and T48, where $n = 3$. For these two time points, one replicate each had been discarded it appeared as an outlier in principal component analysis (PCA) of protein

abundances between different runs (**Figure 5—source data 1**). Quantification employed the Hi-N method, measuring the three most abundant peptides for each protein (**Grossmann et al., 2010**). Associated statistics (p-values, PCA etc.) were calculated in ProgenesisQI, except for the q-values, which were calculated from the p-values using the Benjamini-Hochberg (BH) method, with FDR-adjustment to enforce monotonicity. Quantification also used protein grouping, which assigns proteins for which only shared but no unique peptides were identified to a 'lead' identifier containing all these shared peptides and thus having the greatest coverage among all grouped identifiers or highest score where coverage is equal. Quantification was restricted to protein (groups) with at least two identified peptides among which at least one is unique to the protein (group). Using these requirements, 5082 Arabidopsis proteins (or groups) were identified. Since 13 additional identifications were exclusively associated with decoy proteins, the false discovery rate at the protein level is estimated to be 0.3%.

Immunoblot analysis

Proteins were extracted from whole seedlings in four volumes (w/v) of SDS-PAGE sample buffer (0.2 M Tris/HCL pH 6.8, 0.4 M dithiothreitol, 8% (w/v) SDS, 0.4% (w/v) Bromophenol blue, and 40% (v/v) glycerol).

Proteins were denatured for 15 min at 65°C and cell debris were removed by centrifugation for 5 min at 16,000 g. Proteins were separated on SDS-PAGE (10–15% (w/v) polyacrylamide concentrations depending on the molecular weight of the protein of interest) and transferred onto a nitrocellulose membrane for immunoblotting (overnight at 4°C) in Dunn buffer (10 mM NaHCO₃, 3 mM Na₂CO₃, 0.01% (w/v) SDS, and 20% ethanol).

Absolute quantification of PsbA, PetC, and PsdC was performed according to Agrisera instructions and using recombinant proteins (PsbA AS01 0116S, PetC AS08 330S, and PsdC AS04 042S; Agrisera, Vännäs, SWEDEN). Three respective calibration curves for the three recombinant proteins were created. Concentrations used to generate the PsbA and PetC calibration curves were 1.75, 2.5, 5, and 10 (ng/μL). Concentrations used to generate the PsdC calibration curve were 0.375, 0.75, 1.5, and 3 (ng/μL). Immunodetections were performed using specific antibodies: anti-Actin (Sigma, A0 480) at 1/3000 dilution in 5% (w/v) milk in Tris-buffered saline (TBS); anti-Lhcb2 (Agrisera, AS01 003), anti-D1(PsbA) (Agrisera, AS05 084), anti-PsbO (Agrisera, AS14 2825), anti-PsbD (Agrisera, AS06 146), anti-PetC (Agrisera, AS08 330), and anti-AtpC (Agrisera, AS08 312) at 1/5000 dilution in 5% milk/TBS; Anti-PsdA (Agrisera, AS09 461) at 1/2000 in 5% milk/TBS; and anti-PsdC (Agrisera, AS042P) and anti-ARC5 (Agrisera, AS13 2676) at 1/2000 in 3% (w/v) bovine serum albumin (BSA) in TBS. Anti-FtsZ-1 and anti-FtsZ2-1/FtsZ 2-2 (**El-Shami et al., 2002**; **Karamoko et al., 2011**) were used at 1/2000 dilution in 5% milk/TBS. After incubation with primary antibodies overnight at 4°C, blots were washed three times in TBS containing 0.1% (v/v) Tween without antibodies for 10 min and incubated for 1 hr at RT with horseradish peroxidase-conjugated secondary antibodies (1/3000 (v/v) anti-rabbit or anti-mouse secondary antibodies, Agrisera). For Anti-HY5 (1/1000 dilution; **Oravecz et al., 2006**) and anti-phyA (1/1000 dilution; **Shinomura et al., 1996**), TBS was replaced by Phosphate Buffer Saline (PBS). Chemiluminescence signals were generated with Enhanced chemiluminescence reagent (1 M Tris/HCL pH 8.5, 90 mM coumaric acid, and 250 mM luminol) and detected with a Fujifilm Image – Quant LAS 4000 mini CCD (GE Healthcare). Quantifications were performed with ImageQuant TL software (GE Healthcare).

Lipid profiling

Lipids were extracted from whole seedlings ground in a mortar and pestle under liquid nitrogen. Ground plant material corresponding to 40–80 mg fresh weight was suspended in tetrahydrofuran: methanol (THF/MeOH) 50:50 (v/v). 10–15 glass beads (1 mm in diameter) were added followed by homogenization (3 min, 30 Hz,) and centrifugation (3 min, 14 000 g, at 4°C). The supernatant was removed and transferred to an HPLC vial. Lipid profiling was carried out by ultra-high pressure liquid chromatography coupled with atmospheric pressure chemical ionization-quadrupole time-of-flight mass spectrometry (UHPLC-APCI-QTOF-MS; **Martinis et al., 2011**). Reverse-phase separation was performed at 60°C on an Acquity BEH C18 column (50 × 2.1 mm, 1.7 μm). The conditions were the following: solvent A = water; solvent B = methanol; 80–100% B in 3 min, 100% B for 2 min, re-equilibration at 80% B for 0.5 min. Flow rate was 0.8 ml min⁻¹ and the injection volume 2.5 μl. Data were

acquired using MassLynx version 4.1 (Waters), and processed with MarkerLynx XS (Waters). Peak lists consisting of variables described by mass-to-charge ratio and retention time were generated (Martinis et al., 2011; Spicher et al., 2016).

Absolute quantification of mono- (MGDG) and di-galactosyldiacylglycerol (DGDG) was conducted by creating calibration curves using MGDG (reference number 840523) and DGDG (reference number 840523) products of Avanti Company. Calibration curves were prepared using the following concentrations: 0.08, 0.4, 2, 10, and 50 $\mu\text{g ml}^{-1}$ of MGDG or DGDG.

Mathematical model

A non-linear mixed effects model (with fixed effect of time and random effect of replicates on 3 of the parameters), built on a four-parameter logistic function, was implemented in R (free software created by Ross Ihaka and Robert Gentleman, Auckland University, New Zealand), following the examples in Pinheiro and Bates, 2000. The R-packages used are: nlme (Pinheiro and Bates, 2000), effects, lattice and car (Fox and Weisberg, 2018). To account for self-correlation at the replicate level, we proceeded to fit an overall mixed-effects model to the data (package 'nlme' from R), using the replicate's as random effect term (Figure 9—figure supplement 1). The four parameters *a*, *b*, *c*, and *d* have been calculated (Figure 9—figure supplement 1) and the three plots (one for each biological replicate) (Figure 9—figure supplement 1) indicated the fitting curve for a series of data points.

Acknowledgements

This work was supported by the University of Neuchâtel and ETH Zurich, a grant from the Swiss National Science Foundation (3100A0-112638) to ED, and grants 31003A_156998 and 31003A_176191 to FK. We thank Jonas Grossmann, Laura Kunz and Paolo Nanni from the Functional Genomic Center Zurich (FGCZ) for peptide preparation for mass spectrometry, acquisition of the raw data and help with associated data analysis, the ETH Zurich microscopy facility (ScopeM) for advice in conducting SBF-SEM analysis. We thank Slobodeanu Radu Alexandru and Federico Giacomarra for help with bioinformatics analysis, and Romain Bessire for help with image processing software. We thank Christian Fankhauser for kindly providing anti-phyA antibodies. We thank Roman Ulm and Michel Goldschmidt-Clermont for critical reading of the manuscript.

Additional information

Funding

Funder	Grant reference number	Author
Schweizerischer Nationalfonds zur Förderung der Wissenschaftlichen Forschung	3100A0-112638	Emilie Demarsy
Schweizerischer Nationalfonds zur Förderung der Wissenschaftlichen Forschung	31003A_156998	Felix Kessler
Schweizerischer Nationalfonds zur Förderung der Wissenschaftlichen Forschung	31003A_176191	Felix Kessler

The funders had no role in study design, data collection and interpretation, or the decision to submit the work for publication.

Author contributions

Rosa Pipitone, Conceptualization, Data curation, Software, Formal analysis, Validation, Investigation, Visualization, Methodology, Writing - original draft, Writing - review and editing; Simona Eicke, Barbara Pfister, Conceptualization, Data curation, Formal analysis, Validation, Investigation, Visualization, Methodology, Writing - review and editing; Gaetan Glauser, Conceptualization, Resources, Formal analysis, Validation, Methodology, Writing - review and editing; Denis Falconet, Resources, Data curation, Formal analysis, Validation, Investigation, Visualization, Methodology, Writing - review

and editing; Clarisse UWIZEYE, Conceptualization, Data curation, Software, Formal analysis, Investigation, Visualization, Methodology, Writing - review and editing; Thibaut Pralon, Formal analysis, Investigation, Writing - review and editing; Samuel C Zeeman, Conceptualization, Resources, Funding acquisition, Validation, Writing - review and editing; Felix Kessler, Conceptualization, Resources, Supervision, Funding acquisition, Validation, Project administration, Writing - review and editing; Emilie Demarsy, Conceptualization, Resources, Data curation, Formal analysis, Supervision, Funding acquisition, Validation, Investigation, Visualization, Methodology, Writing - original draft, Project administration, Writing - review and editing

Author ORCIDs

Simona Eicke  <http://orcid.org/0000-0003-4180-2440>

Denis Falconet  <http://orcid.org/0000-0001-8182-1182>

Felix Kessler  <https://orcid.org/0000-0001-6409-5043>

Emilie Demarsy  <http://orcid.org/0000-0002-0638-0812>

Decision letter and Author response

Decision letter <https://doi.org/10.7554/eLife.62709.sa1>

Author response <https://doi.org/10.7554/eLife.62709.sa2>

Additional files

Supplementary files

- Transparent reporting form

Data availability

All data generated or analysed during this study are included in the manuscript and supporting files. Sources data files for figures 4, 5 6 7 8 and 9 and associated figure supplements have been provided.

References

- Agne B**, Kessler F. 2010. Modifications at the A-domain of the chloroplast import receptor Toc159. *Plant Signaling & Behavior* **5**:1513–1516. DOI: <https://doi.org/10.4161/psb.5.11.13707>, PMID: 21057194
- Allen JF**, de Paula WB, Puthiyaveetil S, Nield J. 2011. A structural phylogenetic map for chloroplast photosynthesis. *Trends in Plant Science* **16**:645–655. DOI: <https://doi.org/10.1016/j.tplants.2011.10.004>, PMID: 22093371
- Amunts A**, Nelson N. 2009. Plant photosystem I design in the light of evolution. *Structure* **17**:637–650. DOI: <https://doi.org/10.1016/j.str.2009.03.006>, PMID: 19446520
- Anderson JM**. 1981. Consequences of spatial separation of photosystem 1 and 2 in thylakoid membranes of higher plant chloroplasts. *FEBS Letters* **124**:1–10. DOI: [https://doi.org/10.1016/0014-5793\(81\)80041-5](https://doi.org/10.1016/0014-5793(81)80041-5)
- Armarego-Marriott T**, Kowalewska Ł, Burgos A, Fischer A, Thiele W, Erban A, Strand D, Kahlau S, Hertle A, Kopka J, Walther D, Reich Z, Schöttler MA, Bock R. 2019. Highly resolved systems biology to dissect the Etioplast-to-Chloroplast transition in tobacco leaves. *Plant Physiology* **180**:654–681. DOI: <https://doi.org/10.1104/pp.18.01432>, PMID: 30862726
- Aronsson H**, Schöttler MA, Kelly AA, Sundqvist C, Dörmann P, Karim S, Jarvis P. 2008. Monogalactosyldiacylglycerol deficiency in Arabidopsis affects pigment composition in the prolamellar body and impairs thylakoid membrane energization and photoprotection in leaves. *Plant Physiology* **148**:580–592. DOI: <https://doi.org/10.1104/pp.108.123372>, PMID: 18641085
- Austin JR**, Staehelin LA. 2011. Three-dimensional architecture of grana and stroma thylakoids of higher plants as determined by electron tomography. *Plant Physiology* **155**:1601–1611. DOI: <https://doi.org/10.1104/pp.110.170647>, PMID: 21224341
- Bailleul B**, Berne N, Murik O, Petroustos D, Prihoda J, Tanaka A, Villanova V, Bligny R, Flori S, Falconet D, Krieger-Liszka A, Santabarbara S, Rappaport F, Joliot P, Tirichine L, Falkowski PG, Cardol P, Bowler C, Finazzi G. 2015. Energetic coupling between plastids and mitochondria drives CO₂ assimilation in diatoms. *Nature* **524**:366–369. DOI: <https://doi.org/10.1038/nature14599>, PMID: 26168400
- Bastien O**, Botella C, Chevalier F, Block MA, Jouhet J, Breton C, Girard-Egrot A, Maréchal E. 2016. New insights on thylakoid biogenesis in plant cells. *International Review of Cell and Molecular Biology* **323**:1–30. DOI: <https://doi.org/10.1016/bs.ircmb.2015.12.001>, PMID: 26944617

- Bauer J, Chen K, Hiltbunner A, Wehrli E, Eugster M, Schnell D, Kessler F. 2000. The major protein import receptor of plastids is essential for chloroplast biogenesis. *Nature* **403**:203–207. DOI: <https://doi.org/10.1038/35003214>, PMID: 10646606
- Bischof S, Baerenfaller K, Wildhaber T, Troesch R, Vidi PA, Roschitzki B, Hirsch-Hoffmann M, Hennig L, Kessler F, Gruissem W, Baginsky S. 2011. Plastid proteome assembly without Toc159: photosynthetic protein import and accumulation of N-acetylated plastid precursor proteins. *The Plant Cell* **23**:3911–3928. DOI: <https://doi.org/10.1105/tpc.111.092882>, PMID: 22128122
- Biswal B, Krupinska K, Biswal U. 2013. *Plastid Development in Leaves During Growth and Senescence*. Netherlands: Springer. DOI: <https://doi.org/10.1007/978-94-007-5724-0>
- Block MA, Dorne AJ, Joyard J, Douce R. 1983. Preparation and characterization of membrane fractions enriched in outer and inner envelope membranes from spinach chloroplasts. II. biochemical characterization. *Journal of Biological Chemistry* **258**:13281–13286. DOI: [https://doi.org/10.1016/S0021-9258\(17\)44113-5](https://doi.org/10.1016/S0021-9258(17)44113-5), PMID: 6630230
- Blomqvist LA, Ryberg M, Sundqvist C. 2008. Proteomic analysis of highly purified prolamellar bodies reveals their significance in chloroplast development. *Photosynthesis Research* **96**:37–50. DOI: <https://doi.org/10.1007/s11120-007-9281-y>, PMID: 18071923
- Bottier C, Géan J, Artzner F, Desbat B, Pézolet M, Renault A, Marion D, Vié V. 2007. Galactosyl headgroup interactions control the molecular packing of wheat lipids in Langmuir films and in hydrated liquid-crystalline mesophases. *Biochimica Et Biophysica Acta (BBA) - Biomembranes* **1768**:1526–1540. DOI: <https://doi.org/10.1016/j.bbamem.2007.02.021>, PMID: 17459332
- Bräutigam A, Weber AP. 2009. Proteomic analysis of the proplastid envelope membrane provides novel insights into small molecule and protein transport across proplastid membranes. *Molecular Plant* **2**:1247–1261. DOI: <https://doi.org/10.1093/mp/ssp070>, PMID: 19995728
- Caffarri S, Tibiletti T, Jennings RC, Santabarbara S. 2014. A comparison between plant photosystem I and photosystem II architecture and functioning. *Current Protein & Peptide Science* **15**:296–331. DOI: <https://doi.org/10.2174/1389203715666140327102218>, PMID: 24678674
- Chen YE, Ma J, Wu N, Su YQ, Zhang ZW, Yuan M, Zhang HY, Zeng XY, Yuan S. 2018. The roles of Arabidopsis proteins of Lhcb4, Lhcb5 and Lhcb6 in oxidative stress under natural light conditions. *Plant Physiology and Biochemistry* **130**:267–276. DOI: <https://doi.org/10.1016/j.plaphy.2018.07.014>, PMID: 30032070
- Cignoni P, Callieri M, Corsini M, Dellepiane M, Ganovelli F, Ranzuglia G. 2008. MeshLab: an open-source mesh processing tool. 6th Eurographics Ital Chapter Conf 129–133.
- Daum B, Nicastro D, McIntosh JR, Ku W. 2010. Arrangement of photosystem II and ATP synthase in chloroplast. Membranes of Spinach and Pea 1299–1312.
- Daum B, Kühlbrandt W. 2011. Electron tomography of plant thylakoid membranes. *Journal of Experimental Botany* **62**:2393–2402. DOI: <https://doi.org/10.1093/jxb/err034>, PMID: 21441405
- Debrieux D, Fankhauser C. 2010. Light-induced degradation of phyA is promoted by transfer of the photoreceptor into the nucleus. *Plant Molecular Biology* **73**:687–695. DOI: <https://doi.org/10.1007/s11103-010-9649-9>, PMID: 20473552
- Deerinck TJ, Bushong EA, Thor A, Ellisman MH. 2010. NCMIR methods for 3D EM : a new protocol for preparation of biological specimens for serial block face scanning electron microscopy. *Microscopy* **1**:6–8.
- Demarsy E, Lakshmanan AM, Kessler F. 2014. Border control: selectivity of chloroplast protein import and regulation at the TOC-complex. *Frontiers in Plant Science* **5**:483. DOI: <https://doi.org/10.3389/fpls.2014.00483>, PMID: 25278954
- Demé B, Cataye C, Block MA, Maréchal E, Jouhet J. 2014. Contribution of galactoglycerolipids to the 3-dimensional architecture of thylakoids. *The FASEB Journal* **28**:3373–3383. DOI: <https://doi.org/10.1096/fj.13-247395>, PMID: 24736411
- Dubreuil C, Jin X, Barajas-López JD, Hewitt TC, Tanz SK, Dobrenel T, Schröder WP, Hanson J, Pesquet E, Grönlund A, Small I, Strand Å. 2018. Establishment of photosynthesis through chloroplast development is controlled by two distinct regulatory phases. *Plant Physiology* **176**:1199–1214. DOI: <https://doi.org/10.1104/pp.17.00435>, PMID: 28626007
- Eberhard S, Finazzi G, Wollman FA. 2008. The dynamics of photosynthesis. *Annual Review of Genetics* **42**:463–515. DOI: <https://doi.org/10.1146/annurev.genet.42.110807.091452>, PMID: 18983262
- El-Shami M, El-Kafafi S, Falconet D, Lerbs-Mache S. 2002. Cell cycle-dependent modulation of FtsZ expression in synchronized tobacco BY2 cells. *Molecular Genetics and Genomics* **267**:254–261. DOI: <https://doi.org/10.1007/s00438-002-0660-y>, PMID: 11976969
- Engel BD, Schaffer M, Kuhn Cuellar L, Villa E, Plietzko JM, Baumeister W. 2015. Native architecture of the chlamydomonas chloroplast revealed by in situ cryo-electron tomography. *eLife* **4**:e04889. DOI: <https://doi.org/10.7554/eLife.04889>, PMID: 25584625
- Fedorov A, Beichel R, Kalpathy-Cramer J, Finet J, Fillion-Robin JC, Pujol S, Bauer C, Jennings D, Fennessy F, Sonka M, Buatti J, Aylward S, Miller JV, Pieper S, Kikinis R. 2012. 3D slicer as an image computing platform for the quantitative imaging network. *Magnetic Resonance Imaging* **30**:1323–1341. DOI: <https://doi.org/10.1016/j.mri.2012.05.001>, PMID: 22770690
- Ferro M, Salvi D, Brugière S, Miras S, Kowalski S, Louwagie M, Garin J, Joyard J, Rolland N. 2003. Proteomics of the chloroplast envelope membranes from *Arabidopsis thaliana*. *Molecular & Cellular Proteomics* **2**:325–345. DOI: <https://doi.org/10.1074/mcp.M300030-MCP200>, PMID: 12766230
- Flori S, Jouneau PH, Bailleul B, Gallet B, Estrozi LF, Moriscot C, Bastien O, Eicke S, Schober A, Bártulos CR, Maréchal E, Kroth PG, Petroustos D, Zeeman S, Breyton C, Schoehn G, Falconet D, Finazzi G. 2017. Plastid

- thylakoid architecture optimizes photosynthesis in diatoms. *Nature Communications* **8**:15885. DOI: <https://doi.org/10.1038/ncomms15885>, PMID: 28631733
- Fox J, Weisberg S. 2018. Visualizing fit and lack of fit in complex regression models with predictor effect plots and partial residuals. *Journal of Statistical Software* **87**:i09. DOI: <https://doi.org/10.18637/jss.v087.i09>
- Grossmann J, Roschitzki B, Panse C, Fortes C, Barkow-Oesterreicher S, Rutishauser D, Schlapbach R. 2010. One master protein that is identified by a set of peptides that are not included (all together) in any other protein group. all proteins that are identified by the same set or a subset of those peptides. *Journal of Proteomics* **73**: 1740–1746. DOI: <https://doi.org/10.1016/j.jprot.2010.05.011>
- Hardtke CS, Gohda K, Osterlund MT, Oyama T, Okada K, Deng XW. 2000. HY5 stability and activity in Arabidopsis is regulated by phosphorylation in its COP1 binding domain. *The EMBO Journal* **19**:4997–5006. DOI: <https://doi.org/10.1093/emboj/19.18.4997>, PMID: 10990463
- Hashimoto M, Endo T, Peltier G, Tasaka M, Shikanai T. 2003. A nucleus-encoded factor, CRR2, is essential for the expression of chloroplast ndhB in Arabidopsis. *The Plant Journal : For Cell and Molecular Biology* **36**:541–549. DOI: <https://doi.org/10.1046/j.1365-313x.2003.01900.x>, PMID: 14617084
- Hooper CM, Castleden IR, Tanz SK, Aryamanesh N, Millar AH. 2017. SUBA4: the interactive data analysis centre for Arabidopsis subcellular protein locations. *Nucleic Acids Research* **45**:D1064–D1074. DOI: <https://doi.org/10.1093/nar/gkw1041>, PMID: 27899614
- Jarvis P, López-Juez E. 2013. Biogenesis and homeostasis of chloroplasts and other plastids. *Nature Reviews Molecular Cell Biology* **14**:787–802. DOI: <https://doi.org/10.1038/nrm3702>, PMID: 24263360
- Jouhet J, Maréchal E, Block MA. 2007. Glycerolipid transfer for the building of membranes in plant cells. *Progress in Lipid Research* **46**:37–55. DOI: <https://doi.org/10.1016/j.plipres.2006.06.002>, PMID: 16970991
- Kami C, Lorrain S, Hornitschek P, Fankhauser C. 2010. Light-regulated plant growth and development. *Current Topics in Developmental Biology* **91**:29–66. DOI: [https://doi.org/10.1016/S0070-2153\(10\)91002-8](https://doi.org/10.1016/S0070-2153(10)91002-8), PMID: 20705178
- Karamoko M, El-Kafafi el-S, Mandaron P, Lerbs-Mache S, Falconet D. 2011. Multiple FtsZ2 isoforms involved in chloroplast division and biogenesis are developmentally associated with thylakoid membranes in Arabidopsis. *FEBS Letters* **585**:1203–1208. DOI: <https://doi.org/10.1016/j.febslet.2011.03.041>, PMID: 21439281
- Kato Y, Sakamoto W. 2018. FtsH protease in the thylakoid membrane: physiological functions and the regulation of protease activity. *Frontiers in Plant Science* **9**:1–8. DOI: <https://doi.org/10.3389/fpls.2018.00855>, PMID: 29973948
- Kessler F, Schnell DJ. 2006. The function and diversity of plastid protein import pathways: a multilane GTPase highway into plastids. *Traffic* **7**:248–257. DOI: <https://doi.org/10.1111/j.1600-0854.2005.00382.x>, PMID: 16497220
- Kimura M, Manabe K, Abe T, Yoshida S, Matsui M, Yamamoto YY. 2003. Analysis of hydrogen peroxide-independent expression of the high-light-inducible ELIP2 gene with the aid of the ELIP2 promoter-luciferase fusions. *Photochemistry and Photobiology* **77**:668–674. DOI: [https://doi.org/10.1562/0031-8655\(2003\)077<0668:AOHPEO>2.0.CO;2](https://doi.org/10.1562/0031-8655(2003)077<0668:AOHPEO>2.0.CO;2), PMID: 12870854
- Kirchhoff H, Hall C, Wood M, Herbstová M, Tsabari O, Nevo R, Charuvi D, Shimoni E, Reich Z. 2011. Dynamic control of protein diffusion within the granal thylakoid lumen. *PNAS* **108**:20248–20253. DOI: <https://doi.org/10.1073/pnas.1104141109>, PMID: 22128333
- Kleffmann T, von Zychlinski A, Russenberger D, Hirsch-Hoffmann M, Gehrig P, Gruissem W, Baginsky S. 2007. Proteome dynamics during plastid differentiation in rice. *Plant Physiology* **143**:912–923. DOI: <https://doi.org/10.1104/pp.106.090738>, PMID: 17189339
- Klein RR, Mullet JE. 1986. Regulation of chloroplast-encoded chlorophyll-binding protein translation during higher plant chloroplast biogenesis. *Journal of Biological Chemistry* **261**:11138–11145. DOI: [https://doi.org/10.1016/S0021-9258\(18\)67359-4](https://doi.org/10.1016/S0021-9258(18)67359-4), PMID: 3525563
- Kobayashi K. 2016. Role of membrane glycerolipids in photosynthesis, thylakoid biogenesis and chloroplast development. *Journal of Plant Research* **129**:565–580. DOI: <https://doi.org/10.1007/s10265-016-0827-y>, PMID: 27114097
- Koochak H, Puthiyaveetil S, Mullendore DL, Li M, Kirchhoff H. 2019. The structural and functional domains of plant thylakoid membranes. *The Plant Journal* **97**:412–429. DOI: <https://doi.org/10.1111/tpj.14127>, PMID: 30312499
- Kowalewska Ł, Mazur R, Suski S, Garstka M, Mostowska A. 2016. Three-Dimensional visualization of the Tubular-Lamellar transformation of the internal plastid membrane network during runner bean chloroplast biogenesis. *The Plant Cell* **28**:875–891. DOI: <https://doi.org/10.1105/tpc.15.01053>, PMID: 27002023
- Kubis S, Baldwin A, Patel R, Razzaq A, Dupree P, Lilley K, Kurth J, Leister D, Jarvis P. 2003. The Arabidopsis ppi1 mutant is specifically defective in the expression, chloroplast import, and accumulation of photosynthetic proteins. *The Plant Cell* **15**:1859–1871. DOI: <https://doi.org/10.1105/tpc.012955>, PMID: 12897258
- Kurisu G, Zhang H, Smith JL, Cramer WA. 2003. Structure of the cytochrome b6f complex of oxygenic photosynthesis: tuning the cavity. *Science* **302**:1009–1014. DOI: <https://doi.org/10.1126/science.1090165>, PMID: 14526088
- Li XP, Björkman O, Shih C, Grossman AR, Rosenquist M, Jansson S, Niyogi KK. 2000. A pigment-binding protein essential for regulation of photosynthetic light harvesting. *Nature* **403**:391–395. DOI: <https://doi.org/10.1038/35000131>, PMID: 10667783
- Liang Z, Zhu N, Mai KK, Liu Z, Tzeng D, Osteryoung KW, Zhong S, Staehelin LA, Kang BH. 2018. Thylakoid-Bound polysomes and a Dynamin-Related protein, FZL, mediate critical stages of the linear chloroplast

- biogenesis program in greening *Arabidopsis* cotyledons. *The Plant Cell* **30**:1476–1495. DOI: <https://doi.org/10.1105/tpc.17.00972>, PMID: 29880711
- Ma L, Li J, Qu L, Hager J, Chen Z, Zhao H, Deng XW. 2001. Light control of *Arabidopsis* development entails coordinated regulation of genome expression and cellular pathways. *The Plant Cell* **13**:2589–2607. DOI: <https://doi.org/10.1105/tpc.010229>, PMID: 11752374
- Marechal E, Block MA, Dorne A-J, Douce R, Joyard J. 1997. Lipid synthesis and metabolism in the plastid envelope. *Physiologia Plantarum* **100**:65–77. DOI: <https://doi.org/10.1111/j.1399-3054.1997.tb03455.x>
- Martinis J, Kessler F, Glauser G. 2011. A novel method for prenylquinone profiling in plant tissues by ultra-high pressure liquid chromatography-mass spectrometry. *Plant Methods* **7**:23. DOI: <https://doi.org/10.1186/1746-4811-7-23>, PMID: 21777468
- Mazur R, Mostowska A, Szach J, Gieczewska K, Wójtowicz J, Bednarska K, Garstka M, Kowalewska Ł. 2019. Galactolipid deficiency disturbs spatial arrangement of the thylakoid network in *Arabidopsis thaliana* plants. *Journal of Experimental Botany* **70**:4689–4704. DOI: <https://doi.org/10.1093/jxb/erz219>, PMID: 31087066
- Mi H, Muruganujan A, Huang X, Ebert D, Mills C, Guo X, Thomas PD. 2019. Protocol update for large-scale genome and gene function analysis with the PANTHER classification system (v.14.0). *Nature Protocols* **14**:703–721. DOI: <https://doi.org/10.1038/s41596-019-0128-8>, PMID: 30804569
- Michaud M, Jouhet J. 2019. Lipid trafficking at membrane contact sites during plant development and stress response. *Frontiers in Plant Science* **10**:2. DOI: <https://doi.org/10.3389/fpls.2019.00002>, PMID: 30713540
- Ohlrogge J, Browse J. 1995. Lipid biosynthesis. *The Plant Cell* **7**:957–970. DOI: <https://doi.org/10.1105/tpc.7.7.957>, PMID: 7640528
- Oravec A, Baumann A, Máté Z, Brzezinska A, Molinier J, Oakeley EJ, Adám E, Schäfer E, Nagy F, Ulm R. 2006. CONSTITUTIVELY PHOTOMORPHOGENIC1 is required for the UV-B response in *Arabidopsis*. *The Plant Cell* **18**:1975–1990. DOI: <https://doi.org/10.1105/tpc.105.040097>, PMID: 16829591
- Osterlund MT, Deng XW. 1998. Multiple photoreceptors mediate the light-induced reduction of GUS-COP1 from *Arabidopsis* hypocotyl nuclei. *The Plant Journal* **16**:201–208. DOI: <https://doi.org/10.1046/j.1365-313x.1998.00290.x>, PMID: 9839465
- Peddie CJ, Collinson LM. 2014. Exploring the third dimension: volume electron microscopy comes of age. *Micron* **61**:9–19. DOI: <https://doi.org/10.1016/j.micron.2014.01.009>, PMID: 24792442
- Pinali C, Kitmitto A. 2014. Serial block face scanning electron microscopy for the study of cardiac muscle ultrastructure at nanoscale resolutions. *Journal of Molecular and Cellular Cardiology* **76**:1–11. DOI: <https://doi.org/10.1016/j.yjmcc.2014.08.010>, PMID: 25149127
- Pinheiro J, Bates M. 2000. *Mixed Effects Models in S & S PLUS*. Springer. DOI: <https://doi.org/10.1007/b98882>
- Plösch M, Reisinger V, Eichacker LA. 2011. Proteomic comparison of etioplast and chloroplast protein complexes. *Journal of Proteomics* **74**:1256–1265. DOI: <https://doi.org/10.1016/j.jprot.2011.03.020>, PMID: 21440687
- Porra RJ, Thompson WA, Kriedemann PE. 1989. Determination of accurate extinction coefficients and simultaneous equations for assaying chlorophylls a and b extracted with four different solvents: verification of the concentration of chlorophyll standards by atomic absorption spectroscopy. *Biochimica Et Biophysica Acta (BBA) - Bioenergetics* **975**:384–394. DOI: [https://doi.org/10.1016/S0005-2728\(89\)80347-0](https://doi.org/10.1016/S0005-2728(89)80347-0)
- Pyke KA, Leech RM. 1994. A genetic analysis of chloroplast division and expansion in *Arabidopsis thaliana*. *Plant Physiology* **104**:201–207. DOI: <https://doi.org/10.1104/pp.104.1.201>, PMID: 12232072
- Reiland S, Grossmann J, Baerenfaller K, Gehrig P, Nunes-Nesi A, Fernie AR, Gruissem W, Baginsky S. 2011. Integrated proteome and metabolite analysis of the de-etiolation process in plastids from rice (*Oryza sativa* L.). *Proteomics* **11**:1751–1763. DOI: <https://doi.org/10.1002/pmic.201000703>, PMID: 21433289
- Richardson LGL, Schnell DJ. 2020. Origins, function, and regulation of the TOC-TIC general protein import machinery of plastids. *Journal of Experimental Botany* **71**:1226–1238. DOI: <https://doi.org/10.1093/jxb/erz517>, PMID: 31730153
- Robertson D, Laetsch WM. 1974. Structure and function of developing barley plastids. *Plant Physiology* **54**:148–159. DOI: <https://doi.org/10.1104/pp.54.2.148>, PMID: 16658850
- Rudowska L, Gieczewska K, Mazur R, Garstka M, Mostowska A. 2012. Chloroplast biogenesis - correlation between structure and function. *Biochimica Et Biophysica Acta (BBA) - Bioenergetics* **1817**:1380–1387. DOI: <https://doi.org/10.1016/j.bbabi.2012.03.013>, PMID: 22465024
- Runge S, Sperling U, Frick G, Apel K, Armstrong GA. 1996. Distinct roles for light-dependent NADPH: protochlorophyllide oxidoreductases (POR) A and B during greening in higher plants. *The Plant Journal* **9**:513–523. DOI: <https://doi.org/10.1046/j.1365-313x.1996.09040513.x>, PMID: 8624514
- Schöttler MA, Tóth SZ, Boulouis A, Kahlau S. 2015. Photosynthetic complex stoichiometry dynamics in higher plants: biogenesis, function, and turnover of ATP synthase and the cytochrome b6f complex. *Journal of Experimental Botany* **66**:2373–2400. DOI: <https://doi.org/10.1093/jxb/eru495>, PMID: 25540437
- Scorrano L, De Matteis MA, Emr S, Giordano F, Hajnóczky G, Kornmann B, Lackner LL, Levine TP, Pellegrini L, Reinisch K, Rizzuto R, Simmen T, Stenmark H, Ungermann C, Schuldiner M. 2019. Coming together to define membrane contact sites. *Nature Communications* **10**:1287. DOI: <https://doi.org/10.1038/s41467-019-09253-3>, PMID: 30894536
- Shinomura T, Nagatani A, Hanzawa H, Kubota M, Watanabe M, Furuya M. 1996. Action spectra for phytochrome A- and B-specific photoinduction of seed germination in *Arabidopsis thaliana*. *PNAS* **93**:8129–8133. DOI: <https://doi.org/10.1073/pnas.93.15.8129>, PMID: 8755615

- Solymosi K**, Schoefs B. 2010. Etioplast and etio-chloroplast formation under natural conditions: the dark side of chlorophyll biosynthesis in angiosperms. *Photosynthesis Research* **105**:143–166. DOI: <https://doi.org/10.1007/s11120-010-9568-2>, PMID: 20582474
- Spicher L**, Glauser G, Kessler F. 2016. Lipid antioxidant and galactolipid remodeling under temperature stress in tomato plants. *Frontiers in Plant Science* **7**:167. DOI: <https://doi.org/10.3389/fpls.2016.00167>, PMID: 26925083
- Staehelein LA**, Paolillo DJ. 2020. A brief history of how microscopic studies led to the elucidation of the 3D architecture and macromolecular organization of higher plant thylakoids. *Photosynthesis Research* **145**:237–258. DOI: <https://doi.org/10.1007/s11120-020-00782-3>, PMID: 33017036
- Tomizioli M**, Lazar C, Brugière S, Burger T, Salvi D, Gatto L, Moyet L, Breckels LM, Hesse AM, Lilley KS, Seigneurin-Berny D, Finazzi G, Rolland N, Ferro M. 2014. Deciphering thylakoid sub-compartments using a mass spectrometry-based approach. *Molecular & Cellular Proteomics* **13**:2147–2167. DOI: <https://doi.org/10.1074/mcp.M114.040923>, PMID: 24872594
- Türker C**, Akal F, Joho D, Panse C, Barkow-Oesterreicher S, Rehrauer H, Schlapbach R. 2010. B-Fabric The Swiss Army Knife for Life Sciences Proceedings of the 13th International Conference on Extending Database Technology. Association for Computing Machinery 717–720.
- van Bezouwen LS**, Caffarri S, Kale RS, Kouřil R, Thunnissen AWH, Oostergetel GT, Boekema EJ. 2017. Subunit and chlorophyll organization of the plant photosystem II supercomplex. *Nature Plants* **3**:17080. DOI: <https://doi.org/10.1038/nplants.2017.80>, PMID: 28604725
- van Wijk KJ**, Kessler F. 2017. Plastoglobuli: plastid microcompartments with integrated functions in metabolism, plastid developmental transitions, and environmental adaptation. *Annual Review of Plant Biology* **68**:253–289. DOI: <https://doi.org/10.1146/annurev-arplant-043015-111737>, PMID: 28125283
- Von Wettstein D**, Gough S, Kannangara CG. 1995. Chlorophyll biosynthesis. *The Plant Cell* **7**:1039–1057. DOI: <https://doi.org/10.2307/3870056>, PMID: 12242396
- Wang B-C**, Pan Y-H, Meng D-Z, Zhu Y-X. 2006. Identification and quantitative analysis of significantly accumulated proteins during the Arabidopsis seedling De-etiolation process. *Journal of Integrative Plant Biology* **48**:104–113. DOI: <https://doi.org/10.1111/j.1744-7909.2006.00215.x>
- Weier TE**, Brown DL. 1970. Formation of the prolamellar body in 8-day, dark-grown seedlings. *American Journal of Botany* **57**:267–275. DOI: <https://doi.org/10.1002/j.1537-2197.1970.tb09815.x>
- Wietrzynski W**, Schaffer M, Tegenov D, Albert S, Kanazawa A, Plitzko JM, Baumeister W, Engel BD. 2020. Charting the native architecture of *Chlamydomonas* thylakoid membranes with single-molecule precision. *eLife* **9**:e53740. DOI: <https://doi.org/10.7554/eLife.53740>, PMID: 32297859
- Wu SH**. 2014. Gene expression regulation in photomorphogenesis from the perspective of the central dogma. *Annual Review of Plant Biology* **65**:311–333. DOI: <https://doi.org/10.1146/annurev-arplant-050213-040337>, PMID: 24779996
- Yoshida Y**. 2018. Insights into the mechanisms of chloroplast division. *International Journal of Molecular Sciences* **19**:733. DOI: <https://doi.org/10.3390/ijms19030733>, PMID: 29510533

Bibliography

- Abbe, Ernst (1873). “Beiträge zur Theorie des Mikroskops und der mikroskopischen Wahrnehmung”. In: *Archiv für mikroskopische Anatomie* 9.1, pp. 413–468 (cit. on p. 6).
- Abt, Melanie R, Barbara Pfister, Mayank Sharma, Simona Eicke, Léo Bürgy, Isabel Neale, David Seung, and Samuel C Zeeman (2020). “STARCH SYNTHASE5, a Noncanonical Starch Synthase-Like Protein, Promotes Starch Granule Initiation in Arabidopsis”. In: *The Plant Cell* 32.8, pp. 2543–2565 (cit. on p. 123).
- Ahrens, James, Berk Geveci, and Charles Law (2005). “Paraview: An end-user tool for large data visualization”. In: *The visualization handbook* 717.8 (cit. on p. 76).
- Allen, Mary Belle (1959). “Studies with *Cyanidium caldarium*, an anomalously pigmented chlorophyte”. In: *Archiv für Mikrobiologie* 32.3, pp. 270–277 (cit. on pp. 16, 73).
- Andersen, Robert A, Gary W Saunders, Michael P Paskind, and Julianne P Sexton (1993). “Ultrastructure and 18s RRNA gene sequence for pelagomonas calceolata gen. Et Sp. nov. and the description of a new algal class, the pelagophyceae classis nov. 1”. In: *Journal of Phycology* 29.5, pp. 701–715 (cit. on pp. 63, 67).
- Andersen, Robert A, J Craig Bailey, Johan Decelle, and Ian Probert (2015). “Phaeocystis rex sp. nov.(Phaeocystales, Prymnesiophyceae): a new solitary species that produces a multilayered scale cell covering”. In: *European Journal of Phycology* 50.2, pp. 207–222 (cit. on p. 61).
- Archibald, John M (2015). “Endosymbiosis and eukaryotic cell evolution”. In: *Current Biology* 25.19, R911–R921 (cit. on pp. 2, 96).
- Asano, Shoh, Benjamin D Engel, and Wolfgang Baumeister (2016). “In situ cryo-electron tomography: a post-reductionist approach to structural biology”. In: *Journal of molecular biology* 428.2, pp. 332–343 (cit. on p. 61).
- Austin, Jotham R and L Andrew Staehelin (2011). “Three-dimensional architecture of grana and stroma thylakoids of higher plants as determined by electron tomography”. In: *Plant physiology* 155.4, pp. 1601–1611 (cit. on p. 10).
- Awcock, Graeme J and Ray Thomas (1995). *Applied image processing*. Macmillan International Higher Education (cit. on p. 33).
- Badger, Murray R and G Dean Price (1994). “The role of carbonic anhydrase in photosynthesis”. In: *Annual review of plant biology* 45.1, pp. 369–392 (cit. on p. 67).
- Bailleul, Benjamin, Nicolas Berne, Omer Murik, Dimitris Petroustos, Judit Prihoda, Atsuko Tanaka, Valeria Villanova, Richard Bligny, Serena Flori, Denis Falconet, et al. (2015). “Energetic coupling between plastids and mitochondria drives CO₂ assimilation in diatoms”. In: *Nature* 524.7565, pp. 366–369 (cit. on pp. 4, 61, 66, 69, 71, 78, 107).
- Basu, Samarпита and Katherine RM Mackey (2018). “Phytoplankton as key mediators of the biological carbon pump: Their responses to a changing climate”. In: *Sustainability* 10.3, p. 869 (cit. on p. 4).
- Baud, Sébastien, Bertrand Dubreucq, Martine Miquel, Christine Rochat, and Loïc Lepiniec (2008). “Storage reserve accumulation in Arabidopsis: metabolic and developmental con-

- trol of seed filling”. In: *The Arabidopsis book/American Society of Plant Biologists* 6 (cit. on p. 121).
- Baumeister, Wolfgang (2002). “Electron tomography: towards visualizing the molecular organization of the cytoplasm”. In: *Current opinion in structural biology* 12.5, pp. 679–684 (cit. on p. 10).
- Bereiter-Hahn, J and M Vöth (1994). “Dynamics of mitochondria in living cells: shape changes, dislocations, fusion, and fission of mitochondria”. In: *Microscopy research and technique* 27.3, pp. 198–219 (cit. on p. 63).
- Berges, John A, Daniel J Franklin, and Paul J Harrison (2001). “Evolution of an artificial seawater medium: improvements in enriched seawater, artificial water over the last two decades”. In: *Journal of Phycology* 37.6, pp. 1138–1145 (cit. on pp. 16, 73).
- Bhattacharya, Debashish, John M Archibald, Andreas PM Weber, and Adrian Reyes-Prieto (2007). “How do endosymbionts become organelles? Understanding early events in plastid evolution”. In: *Bioessays* 29.12, pp. 1239–1246 (cit. on p. 96).
- Blank, RJ (1987). “Cell architecture of the dinoflagellate *Symbiodinium* sp. inhabiting the Hawaiian stony coral *Montipora verrucosa*”. In: *Marine Biology* 94.1, pp. 143–155 (cit. on p. 63).
- Bock, Davi D, Wei-Chung Allen Lee, Aaron M Kerlin, Mark L Andermann, Greg Hood, Arthur W Wetzell, Sergey Yurgenson, Edward R Soucy, Hyon Suk Kim, and R Clay Reid (2011). “Network anatomy and in vivo physiology of visual cortical neurons”. In: *Nature* 471.7337, pp. 177–182 (cit. on p. 8).
- Bogner, Agnes, P-H Jouneau, Gilbert Thollet, D Basset, and Catherine Gauthier (2007). “A history of scanning electron microscopy developments: Towards “wet-STEM” imaging”. In: *Micron* 38.4, pp. 390–401 (cit. on p. 6).
- Boisvert, François-Michel, Silvana van Koningsbruggen, Joaquín Navascués, and Angus I Lamond (2007). “The multifunctional nucleolus”. In: *Nature reviews Molecular cell biology* 8.7, pp. 574–585 (cit. on p. 111).
- Briggman, Kevin L and Winfried Denk (2006). “Towards neural circuit reconstruction with volume electron microscopy techniques”. In: *Current opinion in neurobiology* 16.5, pp. 562–570 (cit. on p. 8).
- Briggman, Kevin L, Moritz Helmstaedter, and Winfried Denk (2011). “Wiring specificity in the direction-selectivity circuit of the retina”. In: *Nature* 471.7337, pp. 183–188 (cit. on p. 11).
- Briggman, Kevin L and Davi D Bock (2012). “Volume electron microscopy for neuronal circuit reconstruction”. In: *Current opinion in neurobiology* 22.1, pp. 154–161 (cit. on p. 10).
- Buckley, Genevieve, Gediminas Gervinskis, Cyntia Taveneau, Hariprasad Venugopal, James C Whisstock, and Alex de Marco (2020). “Automated cryo-lamella preparation for high-throughput in-situ structural biology”. In: *Journal of Structural Biology*, p. 107488 (cit. on p. 11).
- Bushby, Andrew J, Kenneth MY P’ng, Robert D Young, Christian Pinali, Carlo Knupp, and Andrew J Quantock (2011). “Imaging three-dimensional tissue architectures by focused ion beam scanning electron microscopy”. In: *Nature protocols* 6.6, pp. 845–858 (cit. on p. 9).

- Callieri, Marco, Guido Ranzuglia, Matteo Dellepiane, Paolo Cignoni, and Roberto Scopigno (2012). “Meshlab as a complete open tool for the integration of photos and colour with high-resolution 3D geometry data”. In: *Comput Appl Quant Methods Archaeol*, pp. 406–16 (cit. on p. 76).
- Cardona, Albert, Stephan Saalfeld, Johannes Schindelin, Ignacio Arganda-Carreras, Stephan Preibisch, Mark Longair, Pavel Tomancak, Volker Hartenstein, and Rodney J Douglas (2012). “TrakEM2 software for neural circuit reconstruction”. In: *PloS one* 7.6, e38011 (cit. on p. 33).
- Cignoni, Paolo, Marco Callieri, Massimiliano Corsini, Matteo Dellepiane, Fabio Ganovelli, and Guido Ranzuglia (2008). “Meshlab: an open-source mesh processing tool.” In: *Eurographics Italian chapter conference*. Vol. 2008. Salerno, Italy, pp. 129–136 (cit. on pp. 75, 76).
- Cocks, Erin, Michael Taggart, FC Rind, and Kathryn White (2018). “A guide to analysis and reconstruction of serial block face scanning electron microscopy data”. In: *Journal of microscopy* 270.2, pp. 217–234 (cit. on pp. 9, 13, 33).
- Cogliati, Sara, Jose A Enriquez, and Luca Scorrano (2016). “Mitochondrial cristae: where beauty meets functionality”. In: *Trends in biochemical sciences* 41.3, pp. 261–273 (cit. on p. 109).
- Colin, Sébastien, Luis Pedro Coelho, Shinichi Sunagawa, Chris Bowler, Eric Karsenti, Peer Bork, Rainer Pepperkok, and Colomban De Vargas (2017). “Quantitative 3D-imaging for cell biology and ecology of environmental microbial eukaryotes”. In: *Elife* 6, e26066 (cit. on p. 61).
- Cross, Wyatt F, James M Hood, Jonathan P Benstead, Alexander D Huryn, and Daniel Nelson (2015). “Interactions between temperature and nutrients across levels of ecological organization”. In: *Global change biology* 21.3, pp. 1025–1040 (cit. on p. 58).
- Crumpton-Taylor, Matilda, Scott Grandison, Kenneth MY Png, Andrew J Bushby, and Alison M Smith (2012). “Control of starch granule numbers in Arabidopsis chloroplasts”. In: *Plant physiology* 158.2, pp. 905–916 (cit. on p. 121).
- Crumpton-Taylor, Matilda, Marilyn Pike, Kuan-Jen Lu, Christopher M Hylton, Regina Feil, Simona Eicke, John E Lunn, Samuel C Zeeman, and Alison M Smith (2013). “Starch synthase 4 is essential for coordination of starch granule formation with chloroplast division during Arabidopsis leaf expansion”. In: *New Phytologist* 200.4, pp. 1064–1075 (cit. on p. 121).
- D’Agostino, Massimo, Herre Jelger Risselada, and Andreas Mayer (2016). “Steric hindrance of SNARE transmembrane domain organization impairs the hemifusion-to-fusion transition”. In: *EMBO reports* 17.11, pp. 1590–1608 (cit. on p. 129).
- Dall’Oglio, Aline, Denise Ferme, Janaína Brusco, Jorge E Moreira, and Alberto A Rasia-Filho (2010). “The “single-section” Golgi method adapted for formalin-fixed human brain and light microscopy”. In: *Journal of neuroscience methods* 189.1, pp. 51–55 (cit. on p. 5).
- Das, Probir, Wang Lei, Siti Sarah Aziz, and Jeffrey Philip Obbard (2011). “Enhanced algae growth in both phototrophic and mixotrophic culture under blue light”. In: *Bioresource Technology* 102.4, pp. 3883–3887 (cit. on p. 71).
- Daum, Bertram, Daniela Nicastro, Jotham Austin, J Richard McIntosh, and Werner Kühlbrandt (2010). “Arrangement of photosystem II and ATP synthase in chloroplast membranes of spinach and pea”. In: *The Plant Cell* 22.4, pp. 1299–1312 (cit. on p. 10).

- Dauvillée, David, Philippe Deschamps, Jean-Philippe Ral, Charlotte Plancke, Jean-Luc Putaux, Jimi Devassine, Amandine Durand-Terrasson, Aline Devin, and Steven G Ball (2009). “Genetic dissection of floridean starch synthesis in the cytosol of the model dinoflagellate *Cryptothecodinium cohnii*”. In: *Proceedings of the National Academy of Sciences* 106.50, pp. 21126–21130 (cit. on p. 68).
- Davidson, Keith, Richard J Gowen, Paul Tett, Eileen Bresnan, Paul J Harrison, April McKinney, Stephen Milligan, David K Mills, Joe Silke, and Anne-Marie Crooks (2012). “Harmful algal blooms: how strong is the evidence that nutrient ratios and forms influence their occurrence?” In: *Estuarine, Coastal and Shelf Science* 115, pp. 399–413 (cit. on p. 58).
- Davy, Simon K, Denis Allemand, and Virginia M Weis (2012). “Cell biology of cnidarian-dinoflagellate symbiosis”. In: *Microbiology and Molecular Biology Reviews* 76.2, pp. 229–261 (cit. on p. 100).
- De Broglie, Louis (1924). “Recherches sur la théorie des quanta”. PhD thesis. Migration-université en cours d’affectation (cit. on p. 6).
- De Clerck, Olivier, Kenny A Bogaert, and Frederik Leliaert (2012). “Diversity and evolution of algae: primary endosymbiosis”. In: *Advances in botanical research*. Vol. 64. Elsevier, pp. 55–86 (cit. on p. 2).
- De Vargas, Colomban, Stéphane Audic, Nicolas Henry, Johan Decelle, Frédéric Mahé, Ramiro Logares, Enrique Lara, Cédric Berney, Noan Le Bescot, Ian Probert, et al. (2015). “Eukaryotic plankton diversity in the sunlit ocean”. In: *Science* 348.6237 (cit. on p. 61).
- Dean, Caroline and Rachel M. Leech (1982). “Genome Expression during Normal Leaf Development”. In: *Plant Physiology* 69.4, pp. 904–910. eprint: <http://www.plantphysiol.org/content/69/4/904.full.pdf> (cit. on p. 105).
- Decelle, Johan, Sébastien Colin, and Rachel A Foster (2015a). “Photosymbiosis in marine planktonic protists”. In: *Marine protists*, pp. 465–500 (cit. on p. 96).
- Decelle, Johan, Sarah Romac, Rowena F Stern, El Mahdi Bendif, Adriana Zingone, Stéphane Audic, Michael D Guiry, Laure Guillou, Désiré Tessier, Florence Le Gall, et al. (2015b). “Phyto REF: a reference database of the plastidial 16S rRNA gene of photosynthetic eukaryotes with curated taxonomy”. In: *Molecular ecology resources* 15.6, pp. 1435–1445 (cit. on pp. 14, 62).
- Decelle, Johan, Hryhoriy Stryhanyuk, Benoit Gallet, Giulia Veronesi, Matthias Schmidt, Sergio Balzano, Sophie Marro, Clarisse Uwizeye, Pierre-Henri Jouneau, Josselin Lupette, et al. (2019). “Algal remodeling in a ubiquitous planktonic photosymbiosis”. In: *Current Biology* 29.6, pp. 968–978 (cit. on pp. 11, 16, 17, 58, 61, 74, 79, 98, 105, 110).
- Decelle, Johan, Giulia Veronesi, Benoit Gallet, Hryhoriy Stryhanyuk, Pietro Benettoni, Matthias Schmidt, Rémi Tucoulou, Melissa Passarelli, Sylvain Bohic, Peta Clode, et al. (2020). “Subcellular chemical imaging: new avenues in cell biology”. In: *Trends in cell biology* 30.3, pp. 173–188 (cit. on p. 73).
- Deerinck, TJ, EA Bushong, V Lev-Ram, X Shu, RY Tsien, and MH Ellisman (2010). “Enhancing serial block-face scanning electron microscopy to enable high resolution 3-D nanohistology of cells and tissues”. In: *Microscopy and Microanalysis* 16.S2, pp. 1138–1139 (cit. on p. 9).
- Degli Esposti, Mauro (2014). “Bioenergetic evolution in proteobacteria and mitochondria”. In: *Genome biology and evolution* 6.12, pp. 3238–3251 (cit. on p. 2).

- Denk, Winfried and Heinz Horstmann (2004). “Serial block-face scanning electron microscopy to reconstruct three-dimensional tissue nanostructure”. In: *PLoS Biol* 2.11, e329 (cit. on p. 9).
- Denk, Winfried, Kevin L Briggman, and Moritz Helmstaedter (2012). “Structural neurobiology: missing link to a mechanistic understanding of neural computation”. In: *Nature Reviews Neuroscience* 13.5, pp. 351–358 (cit. on p. 9).
- Dionísio, Gisela João Ribeiro Lemos (2017). “Effects of Climate Change on the Physiology and Photobiology of Photosynthetic Sea Slugs”. PhD thesis. Universidade de Aveiro (Portugal) (cit. on p. 4).
- Dolch, Lina-Juana, Camille Rak, Giorgio Perin, Guillaume Tourcier, Richard Broughton, Marina Leterrier, Tomas Morosinotto, Frédérique Tellier, Jean-Denis Faure, Denis Falconet, et al. (2017). “A palmitic acid elongase affects eicosapentaenoic acid and plastidial monogalactosyldiacylglycerol levels in *Nannochloropsis*”. In: *Plant Physiology* 173.1, pp. 742–759 (cit. on pp. 16, 73).
- Dos Santos, Adriana Lopes, Thibaut Pollina, Priscillia Gourvil, Erwan Corre, Dominique Marie, José Luis Garrido, Francisco Rodríguez, Mary-Hélène Noël, Daniel Vaultot, and Wenche Eikrem (2017). “Chloropicophyceae, a new class of picophytoplanktonic prasino-phytes”. In: *Scientific reports* 7.1, pp. 1–20 (cit. on p. 63).
- Dyall, Sabrina D, Mark T Brown, and Patricia J Johnson (2004). “Ancient invasions: from endosymbionts to organelles”. In: *Science* 304.5668, pp. 253–257 (cit. on p. 2).
- Eddy, Christopher Z, Xinyao Wang, Fuxin Li, and Bo Sun (2018). “The morphodynamics of 3D migrating cancer cells”. In: *arXiv preprint arXiv:1807.10822* (cit. on p. 128).
- Ellis, J Raymond, Antia J Jellings, and Rachel M Leech (1983). “Nuclear DNA content and the control of chloroplast replication in wheat leaves”. In: *Planta* 157.4, pp. 376–380 (cit. on p. 105).
- Embleton, KV, CE Gibson, and SI Heaney (2003). “Automated counting of phytoplankton by pattern recognition: a comparison with a manual counting method”. In: *Journal of Plankton Research* 25.6, pp. 669–681 (cit. on p. 61).
- Embley, T Martin and William Martin (2006). “Eukaryotic evolution, changes and challenges”. In: *Nature* 440.7084, pp. 623–630 (cit. on p. 96).
- Engel, Benjamin D, Miroslava Schaffer, Luis Kuhn Cuellar, Elizabeth Villa, Jürgen M Plitzko, and Wolfgang Baumeister (2015). “Native architecture of the *Chlamydomonas* chloroplast revealed by in situ cryo-electron tomography”. In: *Elife* 4, e04889 (cit. on pp. 11, 61, 67, 107).
- Erdman, Natasha, Bell C David, and Rudolf Reichelt (2019). “Scanning Electron Microscopy.” In: *Springer Handbook of Microscopy* (cit. on p. 6).
- Falconet, Denis (2012). “Origin, evolution and division of plastids”. In: *Photosynthesis*. Springer, pp. 35–61 (cit. on p. 2).
- Falkowski, Paul G (2002). “The ocean’s invisible forest”. In: *Scientific American* 287.2, pp. 54–61 (cit. on pp. 4, 58).
- Falkowski, Paul G, Miriam E Katz, Andrew H Knoll, Antonietta Quigg, John A Raven, Oscar Schofield, and FJR Taylor (2004). “The evolution of modern eukaryotic phytoplankton”. In: *science* 305.5682, pp. 354–360 (cit. on p. 4).

- Fang, Xu, Cong Wei, Cai Zhao-Ling, and Ouyang Fan (2004). “Effects of organic carbon sources on cell growth and eicosapentaenoic acid content of *Nannochloropsis* sp.” In: *Journal of Applied Phycology* 16.6, pp. 499–503 (cit. on p. 71).
- Fedorov, Andriy, Reinhard Beichel, Jayashree Kalpathy-Cramer, Julien Finet, Jean-Christophe Fillion-Robin, Sonia Pujol, Christian Bauer, Dominique Jennings, Fiona Fennesy, Milan Sonka, et al. (2012). “3D Slicer as an image computing platform for the Quantitative Imaging Network”. In: *Magnetic resonance imaging* 30.9, pp. 1323–1341 (cit. on p. 35).
- Field, Christopher B, Michael J Behrenfeld, James T Randerson, and Paul Falkowski (1998). “Primary production of the biosphere: integrating terrestrial and oceanic components”. In: *science* 281.5374, pp. 237–240 (cit. on pp. 4, 58, 60).
- Flegler, Stanley L and Stanley L Flegler (1997). *Scanning & Transmission Electron Microscopy*. Oxford University Press (cit. on p. 6).
- Flori, Serena, Pierre-Henri Jouneau, Giovanni Finazzi, Eric Maréchal, and Denis Falconet (2016). “Ultrastructure of the periplastidial compartment of the diatom *Phaeodactylum tricorutum*”. In: *Protist* 167.3, pp. 254–267 (cit. on pp. 2, 11, 63, 78).
- Flori, Serena, Pierre-Henri Jouneau, Benjamin Bailleul, Benoit Gallet, Leandro F Estrozi, Christine Moriscot, Olivier Bastien, Simona Eicke, Alexander Schober, Carolina Río Bártulos, et al. (2017). “Plastid thylakoid architecture optimizes photosynthesis in diatoms”. In: *Nature communications* 8.1, pp. 1–9 (cit. on pp. 11, 55, 58, 61, 66).
- Flori, Serena, Pierre-Henri Jouneau, Benoit Gallet, Leandro F Estrozi, Christine Moriscot, Guy Schoehn, Giovanni Finazzi, and Denis Falconet (2018). “Imaging Plastids in 2D and 3D: confocal and electron microscopy”. In: *Plastids*. Springer, pp. 113–122 (cit. on pp. 12, 17).
- Fornasiero, Eugenio F and Felipe Opazo (2015). “Super-resolution imaging for cell biologists: Concepts, applications, current challenges and developments”. In: *Bioessays* 37.4, pp. 436–451 (cit. on p. 6).
- Frank, Joachim (2013). *Electron tomography: three-dimensional imaging with the transmission electron microscope*. Springer Science & Business Media (cit. on p. 8).
- Friedman, Jonathan R, Laura L Lackner, Matthew West, Jared R DiBenedetto, Jodi Nunnari, and Gia K Voeltz (2011). “ER tubules mark sites of mitochondrial division”. In: *Science* 334.6054, pp. 358–362 (cit. on p. 129).
- Friedman, Jonathan R, Jared R DiBenedetto, Matthew West, Ashley A Rowland, and Gia K Voeltz (2013). “Endoplasmic reticulum–endosome contact increases as endosomes traffic and mature”. In: *Molecular biology of the cell* 24.7, pp. 1030–1040 (cit. on p. 129).
- Gal, Assaf, Andrea Sorrentino, Keren Kahil, Eva Pereiro, Damien Faivre, and André Scheffel (2018). “Native-state imaging of calcifying and noncalcifying microalgae reveals similarities in their calcium storage organelles”. In: *Proceedings of the National Academy of Sciences* 115.43, pp. 11000–11005 (cit. on p. 63).
- Gallagher, JC, AM Wood, and RS Alberte (1984). “Ecotypic differentiation in the marine diatom *Skeletonema costatum*: influence of light intensity on the photosynthetic apparatus”. In: *Marine biology* 82.2, pp. 121–134 (cit. on p. 69).
- García-Cerdán, José G, Eva M Schmid, Tomomi Takeuchi, Ian McRae, Kent L McDonald, Nichakarn Yordduangjun, Ahmed M Hassan, Patricia Grob, C Shan Xu, Harald F Hess,

- et al. (2020). “Chloroplast Sec14-like 1 (CPSFL1) is essential for normal chloroplast development and affects carotenoid accumulation in *Chlamydomonas*”. In: *Proceedings of the National Academy of Sciences* 117.22, pp. 12452–12463 (cit. on p. 11).
- Gavelis, Gregory S, Maria Herranz, Kevin C Wakeman, Christina Ripken, Satoshi Mitarai, Gillian H Gile, Patrick J Keeling, and Brian S Leander (2019). “Dinoflagellate nucleus contains an extensive endomembrane network, the nuclear net”. In: *Scientific reports* 9.1, pp. 1–9 (cit. on p. 58).
- Gest, Howard (2004). “The discovery of microorganisms by Robert Hooke and Antoni Van Leeuwenhoek, fellows of the Royal Society”. In: *Notes and records of the Royal Society of London* 58.2, pp. 187–201 (cit. on p. 5).
- Gonzalez, Rafael C and E Richard (2002). “Woods, digital image processing”. In: *ed: Prentice Hall Press, ISBN 0-201-18075* 8 (cit. on p. 31).
- Gray, Michael W, Gertraud Burger, and B Franz Lang (1999). “Mitochondrial evolution”. In: *Science* 283.5407, pp. 1476–1481 (cit. on p. 2).
- Guérin, Christopher J, Anna Kremer, Peter Borghgraef, and Saskia Lippens (2019). “Targeted studies using serial block face and focused ion beam scan electron microscopy”. In: *JoVE (Journal of Visualized Experiments)* 150, e59480 (cit. on p. 19).
- Guetg, Claudio and Raffaella Santoro (2012). “Formation of nuclear heterochromatin: the nucleolar point of view”. In: *Epigenetics* 7.8, pp. 811–814 (cit. on p. 111).
- Guidi, Lionel, Samuel Chaffron, Lucie Bittner, Damien Eveillard, Abdelhalim Larhlimi, Simon Roux, Youssef Darzi, Stéphane Audic, Léo Berline, Jennifer R Brum, et al. (2016). “Plankton networks driving carbon export in the oligotrophic ocean”. In: *Nature* 532.7600, pp. 465–470 (cit. on p. 96).
- Hackenbrock, Charles R (1968). “Ultrastructural bases for metabolically linked mechanical activity in mitochondria II. Electron transport-linked ultrastructural transformations in mitochondria”. In: *Journal of Cell Biology* 37.2, pp. 345–369 (cit. on p. 109).
- Hallegraeff, Gustaaf M (2010). “Ocean climate change, phytoplankton community responses, and harmful algal blooms: a formidable predictive challenge 1”. In: *Journal of phycology* 46.2, pp. 220–235 (cit. on p. 58).
- Haralick, Robert M and Linda G Shapiro (1985). “Image segmentation techniques”. In: *Computer vision, graphics, and image processing* 29.1, pp. 100–132 (cit. on p. 31).
- Harris, Kristen M, Elizabeth Perry, Jennifer Bourne, Marcia Feinberg, Linnaea Ostroff, and Jamie Hurlburt (2006). “Uniform serial sectioning for transmission electron microscopy”. In: *Journal of Neuroscience* 26.47, pp. 12101–12103 (cit. on p. 8).
- Harwood, Richard, Elinor Goodman, Marin Gudmundsdottir, Minh Huynh, Quinn Musulin, Magnolia Song, and Margaret M Barbour (2020). “Cell and chloroplast anatomical features are poorly estimated from 2D cross-sections”. In: *New Phytologist* 225.6, pp. 2567–2578 (cit. on p. 11).
- Hayworth, KJ, N Kasthuri, R Schalek, and JW Lichtman (2006). “Automating the collection of ultrathin serial sections for large volume TEM reconstructions”. In: *Microscopy and Microanalysis* 12.S02, pp. 86–87 (cit. on p. 9).
- Helle, Sebastian CJ, Gil Kanfer, Katja Kolar, Alexander Lang, Agnès H Michel, and Benoît Kornmann (2013). “Organization and function of membrane contact sites”. In: *Biochimica et Biophysica Acta (BBA)-Molecular Cell Research* 1833.11, pp. 2526–2541 (cit. on p. 76).

- Helmchen, Fritjof and Winfried Denk (2005). “Deep tissue two-photon microscopy”. In: *Nature methods* 2.12, pp. 932–940 (cit. on p. 8).
- Hennies, Julian, José Miguel Serra Lleti, Nicole L Schieber, Rachel M Templin, Anna M Steyer, and Yannick Schwab (2020). “AMST: alignment to median smoothed template for focused ion beam scanning electron microscopy image stacks”. In: *Scientific reports* 10.1, pp. 1–10 (cit. on p. 98).
- Hense, Burkhard A, Peter Gais, Uta Jütting, Hagen Scherb, and Karsten Rodenacker (2008). “Use of fluorescence information for automated phytoplankton investigation by image analysis”. In: *Journal of Plankton Research* 30.5, pp. 587–606 (cit. on p. 61).
- Heymann, Jurgen AW, Dan Shi, Sang Kim, Donald Bliss, Jacqueline LS Milne, and Sriram Subramaniam (2009). “3D imaging of mammalian cells with ion-abrasion scanning electron microscopy”. In: *Journal of structural biology* 166.1, pp. 1–7 (cit. on p. 11).
- Hildrew, Alan G, David G Raffaelli, and Ronni Edmonds-Brown (2007). *Body size: the structure and function of aquatic ecosystems*. Cambridge University Press (cit. on p. 79).
- Hoppe, W (1974). “Towards three-dimensional “electron microscopy” at atomic resolution”. In: *Naturwissenschaften* 61.6, pp. 239–249 (cit. on p. 8).
- Horwath, James P, Dmitri N Zakharov, Remi Megret, and Eric A Stach (2020). “Understanding important features of deep learning models for segmentation of high-resolution transmission electron microscopy images”. In: *npj Computational Materials* 6.1, pp. 1–9 (cit. on p. 128).
- Hughes, Louise, Chris Hawes, Sandy Monteith, and Sue Vaughan (2014). “Serial block face scanning electron microscopy—the future of cell ultrastructure imaging”. In: *Protoplasma* 251.2, pp. 395–401 (cit. on p. 11).
- Jantschke, Anne, Iddo Pinkas, Anna Hirsch, Nadav Elad, Andreas Schertel, Lia Addadi, and Steve Weiner (2019). “Anhydrous β -guanine crystals in a marine dinoflagellate: Structure and suggested function”. In: *Journal of structural biology* 207.1, pp. 12–20 (cit. on p. 11).
- Jantschke, Anne, Iddo Pinkas, Andreas Schertel, Lia Addadi, and Steve Weiner (2020). “Biom mineralization pathways in calcifying dinoflagellates: Uptake, storage in MgCaP-rich bodies and formation of the shell”. In: *Acta Biomaterialia* 102, pp. 427–439 (cit. on p. 11).
- Jeong, Won Joong, Youn-Il Park, KyeHong Suh, John A Raven, Ook Joon Yoo, and Jang Ryol Liu (2002). “A large population of small chloroplasts in tobacco leaf cells allows more effective chloroplast movement than a few enlarged chloroplasts”. In: *Plant Physiology* 129.1, pp. 112–121 (cit. on p. 103).
- Kanaya, K a and S Okayama (1972). “Penetration and energy-loss theory of electrons in solid targets”. In: *Journal of Physics D: Applied Physics* 5.1, p. 43 (cit. on p. 8).
- Kasthuri, Narayanan, Kenneth Jeffrey Hayworth, Daniel Raimund Berger, Richard Lee Schalek, José Angel Conchello, Seymour Knowles-Barley, Dongil Lee, Amelio Vázquez-Reina, Verena Kaynig, Thouis Raymond Jones, et al. (2015). “Saturated reconstruction of a volume of neocortex”. In: *Cell* 162.3, pp. 648–661 (cit. on p. 11).
- Keeling, Patrick J (2004). “Diversity and evolutionary history of plastids and their hosts”. In: *American journal of botany* 91.10, pp. 1481–1493 (cit. on p. 96).
- (2010). “The endosymbiotic origin, diversification and fate of plastids”. In: *Philosophical Transactions of the Royal Society B: Biological Sciences* 365.1541, pp. 729–748 (cit. on p. 2).

- (2013). “The number, speed, and impact of plastid endosymbioses in eukaryotic evolution”. In: *Annual review of plant biology* 64, pp. 583–607 (cit. on pp. 2, 3, 96).
- Kikinis, Ron, Steve D Pieper, and Kirby G Vosburgh (2014). “3D Slicer: a platform for subject-specific image analysis, visualization, and clinical support”. In: *Intraoperative imaging and image-guided therapy*. Springer, pp. 277–289 (cit. on p. 75).
- Kim, Joomi, Michele Fabris, Gino Baart, Min K Kim, Alain Goossens, Wim Vyverman, Paul G Falkowski, and Desmond S Lun (2016). “Flux balance analysis of primary metabolism in the diatom *Phaeodactylum tricornutum*”. In: *The plant journal* 85.1, pp. 161–176 (cit. on pp. 66, 107).
- Kittelmann, Maïke, Chris Hawes, and Louise Hughes (2016). “Serial block face scanning electron microscopy and the reconstruction of plant cell membrane systems”. In: *Journal of microscopy* 263.2, pp. 200–211 (cit. on p. 11).
- Kizilyaprak, C, J Daraspe, and BM Humbel (2014). “Focused ion beam scanning electron microscopy in biology”. In: *Journal of microscopy* 254.3, pp. 109–114 (cit. on pp. 11, 58).
- Knoll, Andrew H, Roger E Summons, Jacob R Waldbauer, and John E Zumberge (2007). “The geological succession of primary producers in the oceans”. In: *Evolution of primary producers in the sea*. Elsevier, pp. 133–163 (cit. on p. 4).
- Knoll, Max and Ernst Ruska (1932). “Das elektronenmikroskop”. In: *Zeitschrift für physik* 78.5-6, pp. 318–339 (cit. on p. 6).
- Knott, Graham and Christel Genoud (2013). “Is EM dead?” In: *Journal of cell science* 126.20, pp. 4545–4552 (cit. on p. 8).
- Kowalewska, Lucja, Radosław Mazur, Szymon Suski, Maciej Garstka, and Agnieszka Mostowska (2016). “Three-dimensional visualization of the tubular-lamellar transformation of the internal plastid membrane network during runner bean chloroplast biogenesis”. In: *The Plant Cell* 28.4, pp. 875–891 (cit. on p. 10).
- Kremer, Anna, Stefaan Lippens, Sonia Bartunkova, Bob Asselbergh, Cendric Blanpain, Matyas Fendrych, Alain Goossens, Matthew Holt, Sophie Janssens, Michiel Kroels, et al. (2015). “Developing 3D SEM in a broad biological context”. In: *Journal of microscopy* 259.2, pp. 80–96 (cit. on p. 6).
- Kreshuk, Anna, Christoph N Straehle, Christoph Sommer, Ullrich Koethe, Marco Cantoni, Graham Knott, and Fred A Hamprecht (2011). “Automated detection and segmentation of synaptic contacts in nearly isotropic serial electron microscopy images”. In: *PloS one* 6.10, e24899 (cit. on p. 33).
- Lampitt, RS, I Salter, and D Johns (2009). “Radiolaria: Major exporters of organic carbon to the deep ocean”. In: *Global Biogeochemical Cycles* 23.1 (cit. on p. 96).
- Leighton, Stephen B (1981). “SEM images of block faces, cut by a miniature microtome within the SEM—a technical note.” In: *Scanning electron microscopy Pt 2*, p. 73 (cit. on p. 9).
- Lewandowska, Aleksandra M, Daniel G Boyce, Matthias Hofmann, Birte Matthiessen, Ulrich Sommer, and Boris Worm (2014). “Effects of sea surface warming on marine plankton”. In: *Ecology letters* 17.5, pp. 614–623 (cit. on p. 58).
- Liang, Zizhen, Ning Zhu, Keith K Mai, Zhongyuna Liu, David Tzeng, Katherine W Osteryoung, Silin Zhong, L Andrew Staehelin, and Byung-Ho Kang (2018). “Thylakoid-bound polysomes and a dynamin-related protein, FZL, mediate critical stages of the linear chloro-

- plast biogenesis program in greening *Arabidopsis* cotyledons”. In: *The Plant Cell* 30.7, pp. 1476–1495 (cit. on p. 10).
- Lodish, Harvey, Arnold Berk, S Lawrence Zipursky, Paul Matsudaira, David Baltimore, and James Darnell (2000). “Molecular cell biology 4th edition”. In: *National Center for Biotechnology Information, Bookshelf* 9 (cit. on p. 85).
- Lopez-Haro, Miguel, Tonggang Jiu, Pascale Bayle-Guillemaud, Pierre-Henri Jouneau, and Frédéric Chandezon (2013). “Multiscale tomographic analysis of polymer–nanoparticle hybrid materials for solar cells”. In: *Nanoscale* 5.22, pp. 10945–10955 (cit. on p. 11).
- Lowe, David G (2004). “Distinctive image features from scale-invariant keypoints”. In: *International journal of computer vision* 60.2, pp. 91–110 (cit. on p. 98).
- Lu, Kuan-Jen, Barbara Pfister, Camilla Jenny, Simona Eicke, and Samuel C Zeeman (2018). “Distinct functions of STARCH SYNTHASE 4 domains in starch granule formation”. In: *Plant physiology* 176.1, pp. 566–581 (cit. on p. 121).
- Lupette, Josselin, Antoine Jaussaud, Khawla Seddiki, Christian Morabito, Sabine Brugière, Hubert Schaller, Marcel Kuntz, Jean-Luc Putaux, Pierre-Henri Jouneau, Fabrice Rébeillé, et al. (2019). “The architecture of lipid droplets in the diatom *Phaeodactylum tricornum*”. In: *Algal Research* 38, p. 101415 (cit. on p. 63).
- Mackinder, Luke CM, Moritz T Meyer, Tabea Mettler-Altmann, Vivian K Chen, Madeline C Mitchell, Oliver Caspari, Elizabeth S Freeman Rosenzweig, Leif Pallesen, Gregory Reeves, Alan Itakura, et al. (2016). “A repeat protein links Rubisco to form the eukaryotic carbon-concentrating organelle”. In: *Proceedings of the National Academy of Sciences* 113.21, pp. 5958–5963 (cit. on p. 67).
- Malathi, G and V Shanthi (2011). “Statistical measurement of ultrasound placenta images complicated by gestational diabetes mellitus using segmentation approach”. In: *Journal of Information Hiding and Multimedia Signal Processing* 2.4, pp. 332–343 (cit. on p. 31).
- Malinova, Irina, Saleh Alseekh, Regina Feil, Alisdair R Fernie, Otto Baumann, Mark Aurel Schöttler, John E Lunn, and Joerg Fettke (2017). “Starch synthase 4 and plastidal phosphorylase differentially affect starch granule number and morphology”. In: *Plant physiology* 174.1, pp. 73–85 (cit. on p. 123).
- Malinova, Irina, Hadeel M Qasim, Henrike Brust, and Joerg Fettke (2018). “Parameters of starch granule genesis in chloroplasts of *Arabidopsis thaliana*”. In: *Frontiers in plant science* 9, p. 761 (cit. on p. 123).
- Maor-Landaw, Keren, Hiba Waldman Ben-Asher, Sarit Karako-Lampert, Mali Salmon-Divon, Fiorella Prada, Erik Caroselli, Stefano Goffredo, Giuseppe Falini, Zvy Dubinsky, and Oren Levy (2017). “Mediterranean versus Red sea corals facing climate change, a transcriptome analysis”. In: *Scientific reports* 7.1, pp. 1–8 (cit. on p. 4).
- Margulis, Lynn (1970). *Origin of eukaryotic cells: Evidence and research implications for a theory of the origin and evolution of microbial, plant and animal cells on the precambrian Earth*. Yale University Press (cit. on p. 96).
- Marudhupandi, Thangapandi, Ramamoorthy Sathishkumar, and Thipramalai Thankappan Ajith Kumar (2016). “Heterotrophic cultivation of *Nannochloropsis salina* for enhancing biomass and lipid production”. In: *Biotechnology Reports* 10, pp. 8–16 (cit. on p. 72).

- McEwen, Bruce F and Michael Marko (2001). “The emergence of electron tomography as an important tool for investigating cellular ultrastructure”. In: *Journal of Histochemistry & Cytochemistry* 49.5, pp. 553–563 (cit. on p. 8).
- McFadden, Geoffrey Ian (2001). “Primary and secondary endosymbiosis and the origin of plastids”. In: *Journal of Phycology* 37.6, pp. 951–959 (cit. on p. 78).
- Medeiros, Lia Carolina Soares, Wanderley De Souza, Chengge Jiao, Hector Barrabin, and Kildare Miranda (2012). “Visualizing the 3D architecture of multiple erythrocytes infected with Plasmodium at nanoscale by focused ion beam-scanning electron microscopy”. In: *PLoS One* 7.3, e33445 (cit. on p. 11).
- Medlin, Linda and Adriana Zingone (2007). “A taxonomic review of the genus *Phaeocystis*”. In: *Phaeocystis, major link in the biogeochemical cycling of climate-relevant elements*, pp. 3–18 (cit. on p. 100).
- Mellard, Jarad P, Kohei Yoshiyama, Christopher A Klausmeier, and Elena Litchman (2012). “Experimental test of phytoplankton competition for nutrients and light in poorly mixed water columns”. In: *Ecological Monographs* 82.2, pp. 239–256 (cit. on p. 58).
- Merola, Aldo, Rosa Castaldo, Paolo De Luca, Raffaele Gambardella, Aldo Musacchio, and Roberto Taddei (1981). “Revision of *Cyanidium caldarium*. Three species of acidophilic algae”. In: *Plant Biosystem* 115.4-5, pp. 189–195 (cit. on p. 67).
- Meyer, Moritz T, Alistair J McCormick, and Howard Griffiths (2016). “Will an algal CO₂-concentrating mechanism work in higher plants?” In: *Current opinion in plant biology* 31, pp. 181–188 (cit. on p. 67).
- Meyer, Moritz T, Charles Whittaker, and Howard Griffiths (2017). “The algal pyrenoid: key unanswered questions”. In: *Journal of experimental botany* 68.14, pp. 3739–3749 (cit. on pp. 67, 68, 78, 107).
- Michaels, Anthony F, David A Caron, Neil R Swanberg, Frances A Howse, and Claire M Michaels (1995). “Planktonic sarcodines (*Acantharia*, *Radiolaria*, *Foraminifera*) in surface waters near Bermuda: abundance, biomass and vertical flux”. In: *Journal of Plankton Research* 17.1, pp. 131–163 (cit. on p. 96).
- Minichino, Joe and Joseph Howse (2015). *Learning OpenCV 3 Computer Vision with Python*. Packt Publishing Ltd (cit. on p. 75).
- Mock, Thomas, Stuart J Daines, Richard Geider, Sinead Collins, Metodi Metodiev, Andrew J Millar, Vincent Moulton, and Timothy M Lenton (2016). “Bridging the gap between omics and earth system science to better understand how environmental change impacts marine microbes”. In: *Global Change Biology* 22.1, pp. 61–75 (cit. on p. 79).
- Moisan, Tiffany A and B Greg Mitchell (1999). “Photophysiological acclimation of *Phaeocystis antarctica* Karsten under light limitation”. In: *Limnology and Oceanography* 44.2, pp. 247–258 (cit. on p. 10).
- Moisan, Tiffany A, Mark H Ellisman, Casey W Buitenhuis, and Gina E Sosinsky (2006). “Differences in chloroplast ultrastructure of *Phaeocystis antarctica* in low and high light”. In: *Marine Biology* 149.6, pp. 1281–1290 (cit. on pp. 10, 70, 86, 100).
- Moroney, James V and Catherine B Mason (1991). “The role of the chloroplast in inorganic carbon acquisition by *Chlamydomonas reinhardtii*”. In: *Canadian journal of botany* 69.5, pp. 1017–1024 (cit. on p. 67).

- Mueller-Schuessle, Stefanie J and Morgane Michaud (2018). “Plastid transient and stable interactions with other cell compartments”. In: *Plastids*. Springer, pp. 87–109 (cit. on pp. 66, 76, 107, 112).
- Mulder, Martijn J, Max C Keuken, Pierre-Louis Bazin, Anneke Alkemade, and Birte U Forstmann (2019). “Size and shape matter: The impact of voxel geometry on the identification of small nuclei”. In: *PloS one* 14.4, e0215382 (cit. on p. 115).
- Muñoz-Gómez, Sergio A, Claudio H Slamovits, Joel B Dacks, Kaitlyn A Baier, Katelyn D Spencer, and Jeremy G Wideman (2015). “Ancient homology of the mitochondrial contact site and cristae organizing system points to an endosymbiotic origin of mitochondrial cristae”. In: *Current Biology* 25.11, pp. 1489–1495 (cit. on p. 109).
- Murata, Kenji and David F Kyser (1987). “Monte Carlo methods and microlithography simulation for electron and X-ray beams”. In: *Advances in electronics and electron physics*. Vol. 69. Elsevier, pp. 175–259 (cit. on p. 7).
- Mustárdy, László and Győző Garab (2003). “Granum revisited. A three-dimensional model—where things fall into place”. In: *Trends in plant science* 8.3, pp. 117–122 (cit. on p. 63).
- Narayan, Kedar and Sriram Subramaniam (2015). “Focused ion beams in biology”. In: *Nature methods* 12.11, p. 1021 (cit. on pp. 11, 58).
- Nedrich, Matt (2014). “An introduction to gradient descent and linear regression”. In: *Atomic Spin*. June 24 (cit. on p. 130).
- Nellist, Peter D, Matthew F Chisholm, N Dellby, OL Krivanek, MF Murfitt, ZS Szilagy, Andrew R Lupini, A Borisevich, WH Sides, and Stephen J Pennycook (2004). “Direct sub-angstrom imaging of a crystal lattice”. In: *Science* 305.5691, pp. 1741–1741 (cit. on p. 8).
- Nicolas, William J, Emmanuelle Bayer, and Lysiane Brocard (2018). “Electron tomography to study the three-dimensional structure of Plasmodium in plant tissues—from high pressure freezing preparation to ultrathin section collection”. In: *Bio-protocol* 8.1, e2681–e2681 (cit. on p. 18).
- Not, Fabrice, Raffaele Siano, Wiebe H.C.F. Kooistra, Nathalie Simon, Daniel Vaultot, and Ian Probert (2012). “Chapter One - Diversity and Ecology of Eukaryotic Marine Phytoplankton”. In: *Genomic Insights into the Biology of Algae*. Ed. by Gwenaél Piganeau. Vol. 64. Advances in Botanical Research. Academic Press, pp. 1–53 (cit. on p. 60).
- Oi, Takao, Sakiko Enomoto, Tomoyo Nakao, Shigeo Arai, Koji Yamane, and Mitsutaka Taniguchi (2017). “Three-dimensional intracellular structure of a whole rice mesophyll cell observed with FIB-SEM”. In: *Annals of botany* 120.1, pp. 21–28 (cit. on p. 11).
- Oliphant, Travis E (2007). “Python for scientific computing”. In: *Computing in Science & Engineering* 9.3, pp. 10–20 (cit. on p. 75).
- O’Mara, Joseph G (1979). “On Leeuwenhoek’s magnifications”. In: *Antonie van Leeuwenhoek* 45.2, pp. 161–164 (cit. on p. 5).
- Ota, Shuhei, Mai Yoshihara, Tomokazu Yamazaki, Tsuyoshi Takeshita, Aiko Hirata, Mami Konomi, Kenshiro Oshima, Masahira Hattori, Kateřina Bišová, Vilém Zachleder, et al. (2016a). “Deciphering the relationship among phosphate dynamics, electron-dense body and lipid accumulation in the green alga *Parachlorella kessleri*”. In: *Scientific reports* 6.1, pp. 1–11 (cit. on p. 10).

- Ota, Shuhei, Kenshiro Oshima, Tomokazu Yamazaki, Sangwan Kim, Zhe Yu, Mai Yoshihara, Kohei Takeda, Tsuyoshi Takeshita, Aiko Hirata, Kateřina Bišová, et al. (2016b). “Highly efficient lipid production in the green alga *Parachlorella kessleri*: draft genome and transcriptome endorsed by whole-cell 3D ultrastructure”. In: *Biotechnology for biofuels* 9.1, p. 13 (cit. on p. 10).
- Pachauri, Rajendra K, Myles R Allen, Vicente R Barros, John Broome, Wolfgang Cramer, Renate Christ, John A Church, Leon Clarke, Qin Dahe, Purnamita Dasgupta, et al. (2014). *Climate change 2014: synthesis report. Contribution of Working Groups I, II and III to the fifth assessment report of the Intergovernmental Panel on Climate Change*. Ipcc (cit. on p. 73).
- Pal, Nikhil R and Sankar K Pal (1993). “A review on image segmentation techniques”. In: *Pattern recognition* 26.9, pp. 1277–1294 (cit. on p. 33).
- Pandey, Prachi, Vadivelmurugan Irulappan, Muthukumar V Bagavathiannan, and Muthappa Senthil-Kumar (2017). “Impact of combined abiotic and biotic stresses on plant growth and avenues for crop improvement by exploiting physio-morphological traits”. In: *Frontiers in plant science* 8, p. 537 (cit. on p. 58).
- Peddie, Christopher J and Lucy M Collinson (2014). “Exploring the third dimension: volume electron microscopy comes of age”. In: *Micron* 61, pp. 9–19 (cit. on p. 9).
- Petroutsos, Dimitris, Souad Amiar, Heni Abida, Lina-Juana Dolch, Olivier Bastien, Fabrice Rébeillé, Juliette Jouhet, Denis Falconet, Maryse A Block, Geoffrey I McFadden, et al. (2014). “Evolution of galactoglycerolipid biosynthetic pathways—from cyanobacteria to primary plastids and from primary to secondary plastids”. In: *Progress in lipid research* 54, pp. 68–85 (cit. on pp. 2, 78).
- Pfister, Barbara and Samuel C Zeeman (2016). “Formation of starch in plant cells”. In: *Cellular and Molecular Life Sciences* 73.14, pp. 2781–2807 (cit. on p. 114).
- Phan, Sébastien, Daniela Boassa, Phuong Nguyen, Xiaohua Wan, Jason Lanman, Albert Lawrence, and Mark H Ellisman (2016). “3D reconstruction of biological structures: automated procedures for alignment and reconstruction of multiple tilt series in electron tomography”. In: *Advanced structural and chemical imaging* 2.1, pp. 1–18 (cit. on p. 10).
- Phillips, Melissa J and Gia K Voeltz (2016). “Structure and function of ER membrane contact sites with other organelles”. In: *Nature reviews Molecular cell biology* 17.2, pp. 69–82 (cit. on p. 66).
- Picard, Martin, Meagan J McManus, György Csordás, Péter Várnai, Gerald W Dorn II, Dewight Williams, György Hajnóczky, and Douglas C Wallace (2015). “Trans-mitochondrial coordination of cristae at regulated membrane junctions”. In: *Nature communications* 6.1, pp. 1–8 (cit. on p. 109).
- Pipitone, Rosa, Simona Eicke, Barbara Pfister, Gaetan Glauser, Denis Falconet, Clarisse Uwizeye, Thibaut Pralon, Samuel Zeeman, Felix Kessler, and Emilie Demarsy (2020). “Two distinct phases of chloroplast biogenesis during de-etiolation in *Arabidopsis thaliana*”. In: *bioRxiv* (cit. on pp. 11, 114).
- Pogson, Barry J and Verónica Albrecht (2011). “Genetic dissection of chloroplast biogenesis and development: an overview”. In: *Plant Physiology* 155.4, pp. 1545–1551 (cit. on p. 117).
- Poole, Anthony and David Penny (2007). “Engulfed by speculation”. In: *Nature* 447.7147, pp. 913–913 (cit. on p. 2).

- Pörtner, Hans-Otto, David M Karl, Philip W Boyd, William Cheung, Salvador E Lluch-Cota, Yukihiro Nojiri, Daniela N Schmidt, Peter O Zavialov, Jürgen Alheit, Javier Aristegui, et al. (2014). “Ocean systems”. In: *Climate change 2014: impacts, adaptation, and vulnerability. Part A: global and sectoral aspects. contribution of working group II to the fifth assessment report of the intergovernmental panel on climate change*. Cambridge University Press, pp. 411–484 (cit. on p. 58).
- Prepelitã, Sebastian, Michele Geronazzo, Federico Avanzini, and Lauri Savioja (2016). “Influence of voxelization on finite difference time domain simulations of head-related transfer functions”. In: *The Journal of the Acoustical Society of America* 139.5, pp. 2489–2504 (cit. on p. 46).
- Prieto, Daniel, Gonzalo Aparicio, Pablo E Morande, and Flavio R Zolessi (2014). “A fast, low cost, and highly efficient fluorescent DNA labeling method using methyl green”. In: *Histochemistry and cell biology* 142.3, pp. 335–345 (cit. on p. 79).
- Prinz, William A (2014). “Bridging the gap: membrane contact sites in signaling, metabolism, and organelle dynamics”. In: *Journal of Cell Biology* 205.6, pp. 759–769 (cit. on p. 66).
- Rajapakse, Jagath C, Jay N Giedd, and Judith L Rapoport (1997). “Statistical approach to segmentation of single-channel cerebral MR images”. In: *IEEE transactions on medical imaging* 16.2, pp. 176–186 (cit. on p. 33).
- Ramazanov, Ziyadin, Mamta Rawat, Margaret C Henk, Catherine B Mason, Sharon W Matthews, and James V Moroney (1994). “The induction of the CO₂-concentrating mechanism is correlated with the formation of the starch sheath around the pyrenoid of *Chlamydomonas reinhardtii*”. In: *Planta* 195.2, pp. 210–216 (cit. on p. 78).
- Reimer, Ludwig (2013). *Transmission electron microscopy: physics of image formation and microanalysis*. Vol. 36. Springer (cit. on p. 6).
- Rigort, Alexander, Elizabeth Villa, Felix JB Bäuerlein, Benjamin D Engel, and Jürgen M Plitzko (2012). “Integrative approaches for cellular cryo-electron tomography: correlative imaging and focused ion beam micromachining”. In: *Methods in cell biology*. Vol. 111. Elsevier, pp. 259–281 (cit. on p. 11).
- Robinson, JM and T Takizawa (2009). “Correlative fluorescence and electron microscopy in tissues: immunocytochemistry”. In: *Journal of microscopy* 235.3, pp. 259–272 (cit. on p. 79).
- Rodenacker, Karsten, Burkhard Hense, Uta Jütting, and Peter Gais (2006). “Automatic analysis of aqueous specimens for phytoplankton structure recognition and population estimation”. In: *Microscopy research and technique* 69.9, pp. 708–720 (cit. on p. 61).
- Rogowska, Jadwiga (2000). “Overview and fundamentals of medical image segmentation”. In: *Handbook of medical imaging, processing and analysis*, pp. 69–85 (cit. on p. 31).
- Roldán, Isaac, Fabrice Wattebled, M Mercedes Lucas, David Delvallé, Veronique Planchot, Sebastian Jiménez, Ricardo Pérez, Steven Ball, Christophe d’Hulst, and Ángel Mérida (2007). “The phenotype of soluble starch synthase IV defective mutants of *Arabidopsis thaliana* suggests a novel function of elongation enzymes in the control of starch granule formation”. In: *The Plant Journal* 49.3, pp. 492–504 (cit. on p. 114).
- Rossoll, Dennis, Rafael Bermúdez, Helena Hauss, Kai G Schulz, Ulf Riebesell, Ulrich Sommer, and Monika Winder (2012). “Ocean acidification-induced food quality deterioration constrains trophic transfer”. In: *PLoS one* 7.4, e34737 (cit. on p. 79).

- Rowland, Ashley A and Gia K Voeltz (2012). “Endoplasmic reticulum–mitochondria contacts: function of the junction”. In: *Nature reviews Molecular cell biology* 13.10, pp. 607–615 (cit. on p. 66).
- Rowland, Ashley A, Patrick J Chitwood, Melissa J Phillips, and Gia K Voeltz (2014). “ER contact sites define the position and timing of endosome fission”. In: *Cell* 159.5, pp. 1027–1041 (cit. on p. 129).
- Russo, Fabrizio (2002). “An image enhancement technique combining sharpening and noise reduction”. In: *IEEE Transactions on Instrumentation and Measurement* 51.4, pp. 824–828 (cit. on p. 75).
- Sands, Gregory B, Dane A Gerneke, Darren A Hooks, Colin R Green, Bruce H Smaill, and Ian J Legrice (2005). “Automated imaging of extended tissue volumes using confocal microscopy”. In: *Microscopy research and technique* 67.5, pp. 227–239 (cit. on p. 8).
- Sartori, Anna, Rudolf Gatz, Florian Beck, Alexander Rigort, Wolfgang Baumeister, and Juer-gen M Plitzko (2007). “Correlative microscopy: bridging the gap between fluorescence light microscopy and cryo-electron tomography”. In: *Journal of structural biology* 160.2, pp. 135–145 (cit. on p. 73).
- Schaffer, Miroslava, Benjamin D Engel, Tim Laugks, Julia Mahamid, Jürgen M Plitzko, and Wolfgang Baumeister (2015). “Cryo-focused ion beam sample preparation for imaging vitreous cells by cryo-electron tomography”. In: *Bio-protocol* 5.17 (cit. on p. 11).
- Schöfer, Christian and Klara Weipoltshammer (2018). “Nucleolus and chromatin”. In: *Histo-chemistry and cell biology* 150.3, pp. 209–225 (cit. on p. 111).
- Schulze, Katja, Ulrich M Tillich, Thomas Dandekar, and Marcus Frohme (2013). “PlanktoVision-an automated analysis system for the identification of phytoplankton”. In: *BMC bioinformatics* 14.1, pp. 1–10 (cit. on p. 61).
- Schwarz, Michael and Hans-Peter Seidel (2010). “Fast parallel surface and solid voxelization on GPUs”. In: *ACM transactions on graphics (TOG)* 29.6, pp. 1–10 (cit. on p. 46).
- Scorrano, Luca, Maria Antonietta De Matteis, Scott Emr, Francesca Giordano, György Hajnóczky, Benoît Kornmann, Laura L Lackner, Tim P Levine, Luca Pellegrini, Karin Reinisch, et al. (2019). “Coming together to define membrane contact sites”. In: *Nature communications* 10.1, pp. 1–11 (cit. on pp. 66, 76, 108).
- Sela, Ayala, Urszula Piskurewicz, Christian Megies, Laurent Mène-Saffrané, Giovanni Finazzi, and Luis Lopez-Molina (2020). “Embryonic photosynthesis affects post-germination plant growth”. In: *Plant physiology* 182.4, pp. 2166–2181 (cit. on p. 121).
- Seung, David, Julien Boudet, Jonathan Monroe, Tina B Schreier, Laure C David, Melanie Abt, Kuan-Jen Lu, Martina Zanella, and Samuel C Zeeman (2017). “Homologs of PROTEIN TARGETING TO STARCH control starch granule initiation in Arabidopsis leaves”. In: *The Plant Cell* 29.7, pp. 1657–1677 (cit. on p. 123).
- Seung, David, Tina B Schreier, Léo Bürgy, Simona Eicke, and Samuel C Zeeman (2018). “Two plastidial coiled-coil proteins are essential for normal starch granule initiation in Arabidopsis”. In: *The Plant Cell* 30.7, pp. 1523–1542 (cit. on pp. 121, 123).
- Sforza, Eleonora, Renato Cipriani, Tomas Morosinotto, Alberto Bertucco, and Giorgio M Giacometti (2012). “Excess CO₂ supply inhibits mixotrophic growth of *Chlorella protothecoides* and *Nannochloropsis salina*”. In: *Bioresource technology* 104, pp. 523–529 (cit. on p. 71).

- Shimoni, Eyal, Ophir Rav-Hon, Itzhak Ohad, Vlad Brumfeld, and Ziv Reich (2005). “Three-dimensional organization of higher-plant chloroplast thylakoid membranes revealed by electron tomography”. In: *The Plant Cell* 17.9, pp. 2580–2586 (cit. on p. 10).
- Sibbald, Shannon J and John M Archibald (2020). “Genomic insights into plastid evolution”. In: *Genome biology and evolution* 12.7, pp. 978–990 (cit. on p. 60).
- Sim, KS, JTL Thong, and JCH Phang (2004a). “Effect of shot noise and secondary emission noise in scanning electron microscope images”. In: *Scanning: The Journal of Scanning Microscopies* 26.1, pp. 36–40 (cit. on p. 28).
- Sim, KS and Nidal S Kamel (2004b). “Image signal-to-noise ratio estimation using the autoregressive model”. In: *Scanning: The Journal of Scanning Microscopies* 26.3, pp. 135–139 (cit. on p. 28).
- Smith, David J (2010). “Progress & perspectives for atomic-resolution electron microscopy”. In: *Materials Today* 12, pp. 10–16 (cit. on p. 6).
- Sosik, Heidi M and Robert J Olson (2007). “Automated taxonomic classification of phytoplankton sampled with imaging-in-flow cytometry”. In: *Limnology and Oceanography: Methods* 5.6, pp. 204–216 (cit. on p. 61).
- Stadtländer, CTKH (2007). “Scanning electron microscopy and transmission electron microscopy of mollicutes: challenges and opportunities”. In: *Modern research and educational topics in microscopy* 1, pp. 122–131 (cit. on p. 6).
- Stephens, David J and Victoria J Allan (2003). “Light microscopy techniques for live cell imaging”. In: *science* 300.5616, pp. 82–86 (cit. on p. 73).
- Stillman, Jonathon H and Eric Armstrong (2015). “Genomics are transforming our understanding of responses to climate change”. In: *BioScience* 65.3, pp. 237–246 (cit. on p. 4).
- Suetens, Paul, Erwin Bellon, Dirk Vandermeulen, M Smet, Guy Marchal, Johan Nuyts, and Luc Mortelmans (1993). “Image segmentation: methods and applications in diagnostic radiology and nuclear medicine”. In: *European journal of radiology* 17.1, pp. 14–21 (cit. on p. 33).
- Sviben, Sanja, Assaf Gal, Matthew A Hood, Luca Bertinetti, Yael Politi, Mathieu Bennet, Praveen Krishnamoorthy, Andreas Schertel, Richard Wirth, Andrea Sorrentino, et al. (2016). “A vacuole-like compartment concentrates a disordered calcium phase in a key coccolithophorid alga”. In: *Nature communications* 7, p. 11228 (cit. on pp. 11, 63).
- Swanberg, Neil R and David A Caron (1991). “Patterns of sarcodine feeding in epipelagic oceanic plankton”. In: *Journal of Plankton Research* 13.2, pp. 287–312 (cit. on p. 96).
- Takemura, Shin-ya, Arjun Bharioke, Zhiyuan Lu, Aljoscha Nern, Shiv Vitaladevuni, Patricia K Rivlin, William T Katz, Donald J Olbris, Stephen M Plaza, Philip Winston, et al. (2013). “A visual motion detection circuit suggested by Drosophila connectomics”. In: *Nature* 500.7461, pp. 175–181 (cit. on p. 8).
- Tapia, Juan Carlos, Narayanan Kasthuri, Kenneth J Hayworth, Richard Schalek, Jeff W Lichtman, Stephen J Smith, and JoAnn Buchanan (2012). “High-contrast en bloc staining of neuronal tissue for field emission scanning electron microscopy”. In: *Nature protocols* 7.2, p. 193 (cit. on p. 9).
- Taylor, FJR and TAYLOR FJR (1982). “Symbioses in marine microplankton”. In: (cit. on p. 96).

- Titze, Benjamin and Christel Genoud (2016). “Volume scanning electron microscopy for imaging biological ultrastructure”. In: *Biology of the Cell* 108.11, pp. 307–323 (cit. on p. 9).
- Toyooka, Kiminori and Byung-Ho Kang (2014). “Reconstructing plant cells in 3D by serial section electron tomography”. In: *Plant Cell Morphogenesis*. Springer, pp. 159–170 (cit. on p. 10).
- Trojan, Anna and Halina Gabrys (1996). “Chloroplast distribution in *Arabidopsis thaliana* (L.) depends on light conditions during growth”. In: *Plant Physiology* 111.2, pp. 419–425 (cit. on p. 103).
- Tu, Zhuowen and Xiang Bai (2009). “Auto-context and its application to high-level vision tasks and 3d brain image segmentation”. In: *IEEE transactions on pattern analysis and machine intelligence* 32.10, pp. 1744–1757 (cit. on p. 33).
- Uwizeye, Clarisse, Johan Decelle, Pierre-Henri Jouneau, Benoit Gallet, Jean-Baptiste Keck, Christine Moriscot, Fabien Chevalier, Nicole Schieber, Rachel Templin, Gilles Curien, et al. (2020). “In-cell quantitative structural imaging of phytoplankton using 3D electron microscopy”. In: (cit. on p. 56).
- Van Leeuwenhoek, Antoni (1800). *The select works of anthony van leeuwenhoek: containing his microscopical discoveries in many of the works of nature*. Vol. 1. translator (cit. on p. 5).
- Van Thinh, Luong, DJ Griffiths, and H Winsor (1986). “Ultrastructure of *Symbiodinium microadriaticum* (Dinophyceae) symbiotic with *Zoanthus* sp.(Zoanthidea)”. In: *Phycologia* 25.2, pp. 178–184 (cit. on p. 68).
- Vasilic, B, J Magland, M Wald, and FW Wehrli (2008). “Advantages of isotropic voxel size for classification of trabecular bone struts and plates in micro-MR images”. In: *Proceedings of the International Society for Magnetic Resonance Imaging* 16, p. 3627 (cit. on p. 115).
- Vaulot, Daniel, Florence Le Gall, Dominique Marie, Laure Guillou, and Frédéric Partensky (2004). “The Roscoff Culture Collection (RCC): a collection dedicated to marine picoplankton”. In: *Nova Hedwigia* 79.1-2, pp. 49–70 (cit. on pp. 16, 73).
- Vihinen, Helena, Ilya Belevich, and Eija Jokitalo (2013). “Three dimensional electron microscopy of cellular organelles by serial block face SEM and ET”. In: *Microsc. Anal* 27, pp. 7–10 (cit. on p. 11).
- Wayama, Marina, Shuhei Ota, Hazuki Matsuura, Nobuhito Nango, Aiko Hirata, and Shigeyuki Kawano (2013). “Three-dimensional ultrastructural study of oil and astaxanthin accumulation during encystment in the green alga *Haematococcus pluvialis*”. In: *PloS one* 8.1, e53618 (cit. on p. 10).
- Wei, Dongguang, Scott Jacobs, Shannon Modla, Shuang Zhang, Carissa L Young, Robert Cirino, Jeffrey Caplan, and Kirk Czymmek (2012). “High-resolution three-dimensional reconstruction of a whole yeast cell using focused-ion beam scanning electron microscopy”. In: *Biotechniques* 53.1, pp. 41–48 (cit. on p. 11).
- White, Edward L and Michael P Rock (1981). “A comparison of thalamocortical and other synaptic inputs to dendrites of two non-spiny neurons in a single barrel of mouse SmI cortex”. In: *Journal of Comparative Neurology* 195.2, pp. 265–277 (cit. on p. 10).
- White, John G, Eileen Southgate, J Nichol Thomson, and Sydney Brenner (1986). “The structure of the nervous system of the nematode *Caenorhabditis elegans*”. In: *Philos Trans R Soc Lond B Biol Sci* 314.1165, pp. 1–340 (cit. on p. 10).

- Wierzbicki, Rafał, Carsten Købler, Mikkel RB Jensen, Joanna Lopacińska, Michael S Schmidt, Maciej Skolimowski, Fabien Abeille, Klaus Qvortrup, and Kristian Mølhav (2013). “Mapping the complex morphology of cell interactions with nanowire substrates using FIB-SEM”. In: *PloS one* 8.1, e53307 (cit. on p. 11).
- Wietrzynski, Wojciech, Mirosława Schaffer, Dimitry Tegunov, Sahrada Albert, Atsuko Kanazawa, Jürgen M Plitzko, Wolfgang Baumeister, and Benjamin D Engel (2020). “Charting the native architecture of Chlamydomonas thylakoid membranes with single-molecule precision”. In: *Elife* 9, e53740 (cit. on p. 61).
- Wu, Yumei, Christina Whiteus, C Shan Xu, Kenneth J Hayworth, Richard J Weinberg, Harald F Hess, and Pietro De Camilli (2017). “Contacts between the endoplasmic reticulum and other membranes in neurons”. In: *Proceedings of the National Academy of Sciences* 114.24, E4859–E4867 (cit. on p. 129).
- Xu, C Shan, Kenneth J Hayworth, Zhiyuan Lu, Patricia Grob, Ahmed M Hassan, Jose G Garcia-Cerdan, Krishna K Niyogi, Eva Nogales, Richard J Weinberg, and Harald F Hess (2017). “Enhanced FIB-SEM systems for large-volume 3D imaging”. In: *Elife* 6, e25916 (cit. on p. 11).
- Xu, Lingna, Xi Wang, Jia Zhou, Yunyi Qiu, Weina Shang, Jun-Ping Liu, Liquan Wang, and Chao Tong (2020). “Miga-mediated endoplasmic reticulum–mitochondria contact sites regulate neuronal homeostasis”. In: *Elife* 9, e56584 (cit. on p. 129).
- Yamane, Koji, Takao Oi, Sakiko Enomoto, Tomoyo Nakao, Shigeo Arai, Hiroshi Miyake, and Mitsutaka Taniguchi (2018). “Three-dimensional ultrastructure of chloroplast pockets formed under salinity stress”. In: *Plant, Cell & Environment* 41.3, pp. 563–575 (cit. on p. 11).
- Yoon, Hwan Su, Wendy Nelson, Sandra C Lindstrom, Sung Min Boo, Curt Pueschel, Huanhuan Qiu, and Debashish Bhattacharya (2017). “Rhodophyta”. In: *Handbook of the Protists: Second Edition*. Springer International Publishing, pp. 89–133 (cit. on p. 58).
- Young, RJ, T Dingle, K Robinson, and PJA Pugh (1993). “An application of scanned focused ion beam milling to studies on the internal morphology of small arthropods”. In: *Journal of Microscopy* 172.1, pp. 81–88 (cit. on p. 9).
- Zeeman, Samuel C, Axel Tiessen, Emma Pilling, K Lisa Kato, Athene M Donald, and Alison M Smith (2002). “Starch synthesis in Arabidopsis. Granule synthesis, composition, and structure”. In: *Plant physiology* 129.2, pp. 516–529 (cit. on p. 121).
- Zhang, Cha and Tsuhan Chen (2001). “Efficient feature extraction for 2D/3D objects in mesh representation”. In: *Proceedings 2001 International Conference on Image Processing (Cat. No. 01CH37205)*. Vol. 3. IEEE, pp. 935–938 (cit. on p. 76).
- Zhang, Ray R, Alexandra B Schroeder, Joseph J Grudzinski, Eben L Rosenthal, Jason M Warram, Anatoly N Pinchuk, Kevin W Eliceiri, John S Kuo, and Jamey P Weichert (2017). “Beyond the margins: real-time detection of cancer using targeted fluorophores”. In: *Nature reviews Clinical oncology* 14.6, p. 347 (cit. on p. 79).

Approches quantitatives d'imagerie pour étudier la physiologie des cellules photosynthétiques

Résumé — Le phytoplancton est composé de micro-organismes photosynthétiques (microalgues et cyanobactéries) vivant en suspension dans les eaux marines et douces. Grâce à la photosynthèse, le phytoplancton produit de grandes quantités d'oxygène indispensable à la vie marine et terrestre, et fixe le CO₂ de l'atmosphère. Les microalgues marines sont également des organismes prometteurs pour les applications biotechnologiques (alimentation humaine et animale, biocarburants). En raison de leur importance écologique et économique, l'étude des réponses du phytoplancton aux défis environnementaux (y compris ceux induits par l'activité humaine et le réchauffement climatique) est un domaine de recherche en plein développement. L'activité du phytoplancton est influencée par les changements dans la stratification verticale de la colonne d'eau qui module, en fonction de la température, la disponibilité de l'énergie lumineuse ainsi que l'apport de nutriments aux cellules du phytoplancton. En raison de la disponibilité de la lumière et des nutriments, les cellules du phytoplancton ont évolué vers différents modes de vie : phototrophie (activité photosynthétique), mixotrophie (utilisation simultanée de la photosynthèse et de la respiration de sources de carbone organique extérieures pour la croissance) et photosymbiose (interactions symbiotiques à l'intérieur de cellules animales). Dans cette thèse, j'ai étudié les réponses physiologiques des cellules du phytoplancton aux changements environnementaux en regardant aux niveaux cellulaires et subcellulaires. Pour atteindre cet objectif, j'ai mis au point un processus d'imagerie complet permettant d'effectuer des analyses morphométriques quantitatives de cellules entières d'algues représentatives à la fois d'espèces à succès écologique et de modèles de laboratoire. Le protocole commence avec l'acquisition de séries d'images hautes résolutions soit par FIB-SEM (Focused Ion Beam - Scanning Electron Microscopy) ou SBF-SEM (Serial Block Face - Scanning Electron Microscopy). Le protocole d'analyse d'images 3D développé dans ce travail permet d'obtenir des modèles tridimensionnels à haute résolution de cellules entières permettant la réalisation d'analyses quantitatives. Grâce à ces outils, j'ai pu imager des cellules du phytoplancton dans diverses conditions environnementales révélant ainsi : 1) le changement de taille et de morphologie des plastes et des mitochondries lors de l'acclimatation à la lumière dans les diatomées, 2) le changement dans l'interaction des organites chez *Nannochloropsis* lors de l'acclimatation aux nutriments, 3) les changements morphologiques qui surviennent lors de la photosymbiose dans l'algue *Phaeocystis*. Ces travaux révèlent plusieurs scénarios d'acclimatation du phytoplancton au niveau cellulaire et subcellulaire. J'ai également pu valider l'utilisation de ce protocole chez les plantes pour répondre à deux questions biologiques principales : la transition étioplaste - chloroplaste dans les cellules du cotylédon et le processus de formation des granules d'amidon dans les feuilles matures d'*Arabidopsis*.

Mots clés : Imagerie 3D, Analyse morphométriques, Phytoplancton, Photosymbiose, Organites, Plantes.

Quantitative imaging methods to investigate the physiology of photosynthetic cells

Abstract — Phytoplankton is composed of photosynthetic microorganisms (microalgae and cyanobacteria) living in suspension in marine and fresh waters. Through photosynthesis, phytoplankton produce large amounts of the oxygen essential for marine and terrestrial life, and captures CO₂ from the atmosphere. Marine microalgae are also promising organisms for biotechnological applications (human and animal food, biofuels). Because of their ecological and economic importance, the study of the phytoplankton responses to environmental challenges (including the ones induced by human activity and global warming) is a developing field of research. Phytoplankton activity is influenced by changes in the vertical stratification of the water column, which modulate light energy availability as well as nutrient supply to phytoplankton cells in a temperature-dependent manner. Based on light and nutrient availability, phytoplankton cells have evolved different lifestyles: autotrophy (photosynthetic activity), mixotrophy (simultaneous use of photosynthesis and respiration of exogenous organic carbon sources for growth) and photosymbiosis (endosymbiotic interactions within animal cells). In this thesis, I have studied phytoplankton cells and their responses to environmental changes at the cellular and subcellular levels. To achieve this goal, I have developed a complete imaging workflow to perform quantitative morphometric analyses of entire algal cells, representatives of ecologically-successful and laboratory-model microalgal species. This protocol starts with FIB-SEM (Focused Ion Beam-Scanning Electron Microscopy) or SBF-SEM (Serial Block Face-Scanning Electron Microscopy), to acquire high-resolution images. By implementing the 3D image analysis protocol, it is possible to obtain high-resolution whole cells models in three dimensions, suitable to perform quantitative analyses. Thanks to these tools, I have been able to image phytoplankton cells in various environmental conditions: (i) changes in the size and morphology of plastids and mitochondria during light acclimation in diatoms, (ii) Changes in organelles interaction during nutrient acclimation in *Nannochloropsis*, (iii) morphological changes occurring during photosymbiosis in *Phaeocystis*. Overall, this work reveals several scenarios of phytoplankton acclimation at both the cellular and subcellular levels. I have also validated the use of this protocol in plants to answer two main biological questions: the etioplast - chloroplast transition in cotyledon cells and the process of starch granule formation in mature leaves of *Arabidopsis*.

Keywords: 3D imaging, Morphometric analyses, Phytoplankton, Photosymbiosis, Organelles, Plants.

Plant & Cell Physiology lab (LPCV) - UMR 5168 - IRIG
17 rue des Martyrs
38054 Grenoble cedex 9
France